



# Physics Reference Manual

*Release 11.3*

Geant4 Collaboration

Rev9.0: December 6th, 2024



## **CONTENTS:**

<b>I</b>	<b>Introduction</b>	<b>1</b>
1	Definition of Terms Used in this Guide	3
2	Monte Carlo Methods	5
3	Particle Transport	7
3.1	Particle transport . . . . .	7
3.2	True Step Length . . . . .	7
3.2.1	The Interaction Length or Mean Free Path . . . . .	7
3.2.2	Determination of the Interaction Point . . . . .	8
3.2.3	Step Limitations . . . . .	8
3.2.4	Updating the Particle Time . . . . .	9
3.3	Transportation . . . . .	9
3.3.1	Some additional details on motion in fields . . . . .	9
	Bibliography	11
<b>II</b>	<b>Decay</b>	<b>13</b>
4	Particle Decay	15
4.1	Mean Free Path for Decay in Flight . . . . .	15
4.2	Branching Ratios and Decay Channels . . . . .	15
4.2.1	G4PhaseSpaceDecayChannel . . . . .	16
4.2.2	G4DalitzDecayChannel . . . . .	16
4.2.3	Muon Decay . . . . .	16
4.2.4	Leptonic Tau Decay . . . . .	17
4.2.5	Kaon Decay . . . . .	17
5	Decays of orthopositronium at rest to 3 photons	19
5.1	Random polarization . . . . .	19
5.1.1	Validation . . . . .	20
5.2	Polarized model . . . . .	20
5.2.1	Validation . . . . .	21
	Bibliography	23
<b>III</b>	<b>Electromagnetic</b>	<b>25</b>
6	Electromagnetic Physics in GEANT4	27

6.1	Introduction . . . . .	27
6.2	EM physics sub-packages . . . . .	27
6.3	Low Energy Livermore Model . . . . .	28
6.4	Penelope Models . . . . .	29
6.5	Generic Calculation of Total Cross Sections . . . . .	29
<b>7</b>	<b>Gamma incident</b>	<b>31</b>
7.1	Introduction to Gamma Processes . . . . .	31
7.1.1	General Interfaces . . . . .	31
7.2	Elastic Scattering . . . . .	32
7.2.1	Penelope Model . . . . .	32
7.2.2	Livermore Model . . . . .	34
7.2.3	JAEA Elastic Scattering Model . . . . .	35
7.3	PhotoElectric Effect . . . . .	35
7.3.1	Cross Section . . . . .	36
7.3.2	Final State . . . . .	36
7.3.3	Relaxation . . . . .	37
7.3.4	Penelope Model . . . . .	38
7.3.5	Livermore Model . . . . .	38
7.4	Compton scattering . . . . .	40
7.4.1	Cross Section . . . . .	40
7.4.2	Sampling the Final State . . . . .	40
7.4.3	Atomic shell effects . . . . .	42
7.4.4	Penelope Model . . . . .	42
7.4.5	Livermore Model . . . . .	43
7.4.6	Monash University Low Energy Model . . . . .	44
7.5	Gamma Conversion into $e^+e^-$ Pair . . . . .	46
7.5.1	Cross Section . . . . .	46
7.5.2	Final State . . . . .	49
7.5.3	Ultra-Relativistic Model . . . . .	50
7.5.4	Five-dimensional (5D) Bethe-Heitler gamma Conversion to $e^+e^-$ . . . . .	50
7.5.5	Penelope Model . . . . .	53
7.5.6	Livermore Model . . . . .	54
7.6	Livermore Triple Gamma Conversion . . . . .	55
7.6.1	Method . . . . .	55
7.6.2	Azimuthal Distribution for Electron Recoil . . . . .	55
7.6.3	Monte Carlo Simulation of the Asymptotic Expression . . . . .	56
7.6.4	Algorithm for Non Polarized Radiation . . . . .	56
7.6.5	Algorithm for Polarized Radiation . . . . .	58
7.6.6	Sampling of Energy . . . . .	59
7.7	Gamma Conversion into Lepton Pair . . . . .	60
7.7.1	Cross Section and Energy Sharing . . . . .	60
7.7.2	Parameterization of the Total Cross Section . . . . .	61
7.7.3	Multi-differential Cross Section and Angular Variables . . . . .	64
7.7.4	Procedure for the Generation of $\mu^+\mu^-$ Pairs . . . . .	65
7.7.5	Five-dimensional (5D) Bethe-Heitler gamma Conversion to $\mu^+\mu^-$ . . . . .	70
7.8	X-ray reflection . . . . .	70
7.8.1	Activation . . . . .	72
7.8.2	Reflectivity model . . . . .	72
7.8.3	Surface roughness model . . . . .	73
<b>8</b>	<b>Energy Loss of Charged Particles</b>	<b>75</b>
8.1	Discrete Processes for Charged Particles . . . . .	75
8.2	Mean Energy Loss . . . . .	76

8.2.1	Method . . . . .	76
8.2.2	General Interfaces . . . . .	77
8.2.3	Step-size Limit . . . . .	78
8.2.4	Run Time Energy Loss Computation . . . . .	79
8.2.5	Energy Loss by Heavy Charged Particles . . . . .	79
8.3	Energy Loss Fluctuations . . . . .	80
8.3.1	Fluctuations in Thick Absorbers . . . . .	80
8.3.2	Fluctuations in Thin Absorbers . . . . .	81
8.3.3	Width Correction Algorithm . . . . .	82
8.3.4	Sampling of Energy Loss . . . . .	82
8.4	Correcting the Cross Section for Energy Variation . . . . .	83
8.5	Conversion from Cut in Range to Energy Threshold . . . . .	84
8.6	Photoabsorption Ionisation Model . . . . .	85
8.6.1	Cross Section for Ionising Collisions . . . . .	85
8.6.2	Energy Loss Simulation . . . . .	86
8.6.3	Photoabsorption Cross Section at Low Energies . . . . .	87
8.7	ATIMA energy-loss model . . . . .	87
8.7.1	Continuous energy loss . . . . .	88
8.7.2	Fluctuations of energy loss . . . . .	89
<b>9</b>	<b>Elastic scattering</b>	<b>91</b>
9.1	Multiple Scattering . . . . .	91
9.1.1	Introduction . . . . .	91
9.1.2	Definition of Terms . . . . .	92
9.1.3	Path Length Correction . . . . .	93
9.1.4	Angular Distribution . . . . .	94
9.1.5	Determination of the Model Parameters . . . . .	95
9.1.6	Step Limitation Algorithm . . . . .	96
9.1.7	Boundary Crossing Algorithm . . . . .	97
9.1.8	Implementation Details . . . . .	98
9.2	Single Scattering . . . . .	99
9.2.1	Coulomb Scattering . . . . .	99
9.2.2	Implementation Details . . . . .	100
9.3	Ion Scattering . . . . .	100
9.3.1	Method . . . . .	100
9.3.2	Implementation Details . . . . .	103
9.4	Single Scattering, Screened Coulomb Potential and NIEL . . . . .	103
9.4.1	Nucleus–Nucleus Interactions . . . . .	103
9.4.2	Nuclear Stopping Power . . . . .	105
9.4.3	Non-Ionizing Energy Loss due to Coulomb Scattering . . . . .	106
9.4.4	G4IonCoulombScatteringModel . . . . .	107
9.4.5	The Method . . . . .	108
9.4.6	Implementation Details . . . . .	108
9.5	Electron Screened Single Scattering and NIEL . . . . .	109
9.5.1	Scattering Cross Section of Electrons on Nuclei . . . . .	109
9.5.2	Nuclear Stopping Power of Electrons . . . . .	116
9.5.3	Non-Ionizing Energy-Loss of Electrons . . . . .	117
9.6	<i>G4eSingleScatteringModel</i> . . . . .	117
9.6.1	The method . . . . .	118
9.6.2	Implementation Details . . . . .	119
<b>10</b>	<b>Atomic Relaxation</b>	<b>121</b>
10.1	Atomic relaxation . . . . .	121
10.1.1	Fluorescence . . . . .	121

10.1.2	Auger process . . . . .	122
10.1.3	PIXE . . . . .	122
10.2	Alternative models for impact ionisation by hadrons and PIXE . . . . .	123
<b>11</b>	<b>Electron and Positron Incident</b>	<b>127</b>
11.1	Ionisation . . . . .	127
11.1.1	Method . . . . .	127
11.1.2	Continuous Energy Loss . . . . .	127
11.1.3	Total Cross Section per Atom and Mean Free Path . . . . .	129
11.1.4	Simulation of Delta-ray Production . . . . .	129
11.1.5	Penelope Model . . . . .	130
11.1.6	Livermore Model . . . . .	134
11.2	Bremsstrahlung . . . . .	135
11.2.1	Seltzer-Berger bremsstrahlung model . . . . .	135
11.2.2	Bremsstrahlung of high-energy electrons . . . . .	137
11.2.3	Penelope Model . . . . .	139
11.2.4	Livermore Model . . . . .	141
11.3	Positron - Electron Annihilation . . . . .	146
11.3.1	Introduction . . . . .	146
11.3.2	Cross Section . . . . .	146
11.3.3	Sampling the final state . . . . .	146
11.3.4	Sampling the Gamma Energy . . . . .	147
11.3.5	Penelope Model for positron-electron annihilation . . . . .	147
11.4	Positron Annihilation into $\mu^+ \mu^-$ Pair in Media . . . . .	148
11.4.1	Total Cross Section . . . . .	148
11.4.2	Sampling of Energies and Angles . . . . .	149
11.4.3	Validity . . . . .	151
11.5	Positron Annihilation into Hadrons in Media . . . . .	151
11.5.1	Introduction . . . . .	151
11.5.2	Cross Section . . . . .	151
11.5.3	Sampling the final state . . . . .	151
<b>12</b>	<b>Muon incident</b>	<b>153</b>
12.1	Muon Ionisation . . . . .	153
12.2	Bremsstrahlung . . . . .	154
12.2.1	Differential Cross Section . . . . .	154
12.2.2	Continuous Energy Loss . . . . .	155
12.2.3	Total Cross Section . . . . .	155
12.2.4	Sampling . . . . .	155
12.3	Positron - Electron Pair Production by Muons . . . . .	156
12.3.1	Differential Cross Section . . . . .	157
12.3.2	Total Cross Section and Restricted Energy Loss . . . . .	159
12.3.3	Sampling of Positron - Electron Pair Production . . . . .	159
12.4	Muon Photonuclear Interaction . . . . .	160
12.4.1	Differential Cross Section . . . . .	160
12.4.2	Sampling . . . . .	161
<b>13</b>	<b>Charged Hadron Incident</b>	<b>163</b>
13.1	Hadron and Ion Ionisation . . . . .	163
13.1.1	Method . . . . .	163
13.1.2	Continuous Energy Loss . . . . .	163
13.1.3	Nuclear Stopping . . . . .	167
13.1.4	Total Cross Section per Atom . . . . .	167
13.1.5	Simulating Delta-ray Production . . . . .	168

13.1.6	Ion Effective Charge . . . . .	168
13.2	Low energy extensions . . . . .	169
13.2.1	Energy losses of slow negative particles . . . . .	169
13.2.2	Energy losses of hadrons in compounds . . . . .	169
13.2.3	Fluctuations of energy losses of hadrons . . . . .	171
13.2.4	ICRU 73-based energy loss model . . . . .	172
<b>14</b>	<b>Polarized Electron/Positron/Gamma Incident</b>	<b>173</b>
14.1	Introduction . . . . .	173
14.1.1	Stokes vector . . . . .	174
14.1.2	Transfer matrix . . . . .	174
14.1.3	Coordinate transformations . . . . .	175
14.1.4	Polarized beam and material . . . . .	176
14.2	Ionisation . . . . .	177
14.2.1	Method . . . . .	177
14.2.2	Total cross section and mean free path . . . . .	177
14.2.3	Sampling the final state . . . . .	181
14.3	Positron - Electron Annihilation . . . . .	183
14.3.1	Method . . . . .	183
14.3.2	Total cross section and mean free path . . . . .	184
14.3.3	Sampling the final state . . . . .	186
14.3.4	Annihilation at Rest . . . . .	188
14.4	Polarized Compton scattering . . . . .	189
14.4.1	Method . . . . .	189
14.4.2	Total cross section and mean free path . . . . .	189
14.4.3	Sampling the final state . . . . .	191
14.5	Polarized Bremsstrahlung for electron and positron . . . . .	193
14.5.1	Method . . . . .	193
14.5.2	Polarization in gamma conversion and bremsstrahlung . . . . .	193
14.5.3	Polarization transfer from the lepton $e^+e^-$ to a photon . . . . .	194
14.5.4	Remaining polarization of the lepton after emitting a bremsstrahlung photon . . . . .	195
14.6	Polarized Gamma conversion into an electron–positron pair . . . . .	196
14.6.1	Method . . . . .	196
14.6.2	Polarization transfer from the photon to the two leptons . . . . .	196
14.7	Polarized Photoelectric Effect . . . . .	197
14.7.1	Method . . . . .	197
14.7.2	Polarization transfer . . . . .	198
14.8	Compton Scattering by Linearly Polarized Gamma Rays - Livermore Model . . . . .	199
14.8.1	The Cross Section . . . . .	199
14.8.2	Angular Distribution . . . . .	199
14.8.3	Polarization Vector . . . . .	199
14.8.4	Unpolarized Photons . . . . .	200
14.9	Pair production by Linearly Polarized Gamma Rays - Livermore Model . . . . .	200
14.9.1	Relativistic cross section for linearly polarized gamma ray . . . . .	200
14.9.2	Spatial azimuthal distribution . . . . .	201
14.9.3	Unpolarized Photons . . . . .	202
14.10	Pair production by Linearly Polarized Gamma Rays - Five-dimensional (5D) Bethe-Heitler Model . . . . .	202
<b>15</b>	<b>X-Ray production</b>	<b>203</b>
15.1	Transition radiation . . . . .	203
15.1.1	The Relationship of Transition Radiation to X-ray Čerenkov Radiation . . . . .	203
15.1.2	Calculating the X-ray Transition Radiation Yield . . . . .	204
15.1.3	Simulating X-ray Transition Radiation Production . . . . .	205
15.2	Scintillation . . . . .	207

15.3	Čerenkov Effect . . . . .	207
15.4	Synchrotron Radiation . . . . .	208
15.4.1	Photon spectrum . . . . .	208
15.4.2	Validity . . . . .	209
15.4.3	Direct inversion and generation of the photon energy spectrum . . . . .	210
15.4.4	Properties of the Power Spectra . . . . .	213
<b>16</b>	<b>Optical Photons</b>	<b>215</b>
16.1	Interactions of optical photons . . . . .	215
16.1.1	Physics processes for optical photons . . . . .	215
16.1.2	Photon polarization . . . . .	216
16.1.3	Tracking of the photons . . . . .	216
16.1.4	Mie Scattering in Henyey-Greenstein Approximation . . . . .	219
<b>17</b>	<b>GEANT4-DNA</b>	<b>221</b>
17.1	GEANT4-DNA physics processes and models . . . . .	221
<b>18</b>	<b>Microelectronics</b>	<b>223</b>
18.1	The MicroElec extension for microelectronics applications . . . . .	223
<b>19</b>	<b>Shower Parameterizations</b>	<b>225</b>
19.1	Gflash Shower Parameterizations . . . . .	225
19.1.1	Parameterization Ansatz . . . . .	225
19.1.2	Longitudinal Shower Profiles . . . . .	225
19.1.3	Radial Shower Profiles . . . . .	226
19.1.4	Gflash Performance . . . . .	227
<b>Bibliography</b>		<b>229</b>
<b>IV</b>	<b>Hadronic</b>	<b>249</b>
<b>20</b>	<b>Hadronic Cross Sections in GEANT4</b>	<b>251</b>
20.1	Hadron-nucleus Cross Sections . . . . .	251
20.1.1	Hadron-nucleon cross sections . . . . .	251
20.1.2	Neutron-Nucleus cross sections . . . . .	251
20.1.3	Other Hadron-Nucleus cross sections . . . . .	251
20.1.4	Extraction of CHIPS kaon and hyperon nuclear cross sections . . . . .	252
20.2	Total Reaction Cross Section in Nucleus-nucleus Reactions . . . . .	254
20.2.1	Nucleus-nucleus cross sections . . . . .	254
20.2.2	Antinucleus–nucleus cross sections . . . . .	254
20.2.3	Alternative nucleus-nucleus cross sections . . . . .	255
<b>21</b>	<b>Coherent elastic scattering</b>	<b>257</b>
21.1	Nucleon-Nucleon elastic Scattering . . . . .	257
<b>22</b>	<b>Hadron-nucleus Elastic Scattering at Medium and High Energy</b>	<b>259</b>
22.1	Method of Calculation . . . . .	259
<b>23</b>	<b>Parton string model</b>	<b>273</b>
23.1	Reaction initial state simulation. . . . .	273
23.1.1	Allowed projectiles and bombarding energy range for interaction with nucleon and nuclear targets . . . . .	273
23.1.2	MC initialization procedure for nucleus . . . . .	273
23.1.3	Random choice of the impact parameter . . . . .	274

23.2	Sample of collision participants in nuclear collisions . . . . .	274
23.2.1	MC procedure to define collision participants . . . . .	274
23.2.2	Separation of hadron diffraction excitation . . . . .	275
23.3	Longitudinal string excitation . . . . .	276
23.3.1	Hadron–nucleon inelastic collision . . . . .	276
23.3.2	The diffractive string excitation . . . . .	276
23.3.3	The string excitation by parton exchange . . . . .	276
23.3.4	Transverse momentum sampling . . . . .	276
23.3.5	Sampling x-plus and x-minus . . . . .	276
23.3.6	The diffractive string excitation . . . . .	277
23.3.7	The string excitation by parton rearrangement . . . . .	277
23.4	Longitudinal string decay . . . . .	278
23.4.1	Hadron production by string fragmentation . . . . .	278
23.4.2	The hadron formation time and coordinate . . . . .	279
<b>24</b>	<b>Fritiof (FTF) Model</b>	<b>281</b>
24.1	Introduction . . . . .	281
24.1.1	Main assumptions of the FTF model . . . . .	282
24.1.2	General properties of hadron–nucleon interactions . . . . .	283
24.1.3	Cross sections of hadron–nucleon processes . . . . .	290
24.1.4	Simulation of hadron-nucleon interactions . . . . .	293
24.1.5	Flowchart of the FTF model . . . . .	297
24.1.6	Simulation of nuclear interactions . . . . .	297
<b>25</b>	<b>The GEANT4 Bertini Intranuclear Cascade Model</b>	<b>311</b>
25.1	Introduction . . . . .	311
25.2	The GEANT4 Cascade Model . . . . .	311
25.2.1	Model Limits . . . . .	312
25.2.2	Intranuclear Cascade Model . . . . .	312
25.2.3	Nuclear Model . . . . .	312
25.2.4	Pre-equilibrium Model . . . . .	314
25.2.5	Break-up models . . . . .	314
25.2.6	Evaporation Model . . . . .	314
25.3	Interfacing Bertini implementation . . . . .	314
<b>26</b>	<b>The GEANT4 Binary Cascade Model</b>	<b>317</b>
26.1	Modeling overview . . . . .	317
26.1.1	The transport algorithm . . . . .	317
26.1.2	The description of the target nucleus and fermi motion . . . . .	318
26.1.3	Optical and phenomenological potentials . . . . .	319
26.1.4	Pauli blocking simulation . . . . .	319
26.1.5	The scattering term . . . . .	319
26.1.6	Total inclusive cross-sections . . . . .	320
26.1.7	Nucleon Nucleon elastic collisions . . . . .	321
26.1.8	Generation of transverse momentum . . . . .	321
26.1.9	Decay of strong resonances . . . . .	322
26.1.10	The escaping particle and coherent effects . . . . .	322
26.1.11	Light ion reactions . . . . .	323
26.1.12	Transition to pre-compound modeling . . . . .	323
26.1.13	Calculation of excitation energies and residuals . . . . .	323
26.2	Comparison with experiments . . . . .	324
26.3	Neutrons Comparison with Experimental Data . . . . .	324
<b>27</b>	<b>INCL++: the Liège Intranuclear Cascade Model</b>	<b>329</b>
27.1	Introduction . . . . .	329

27.1.1	Suitable application fields . . . . .	331
27.2	Generalities of the <code>INCL++</code> cascade . . . . .	332
27.2.1	Model limits . . . . .	333
27.3	Physics ingredients . . . . .	333
27.3.1	Emission of composite particles . . . . .	334
27.3.2	Cascade stopping time . . . . .	334
27.3.3	Conservation laws . . . . .	334
27.3.4	Initialisation of composite projectiles . . . . .	334
27.3.5	Two meson resonances implemented: $\eta$ and $\omega$ . . . . .	335
27.3.6	Strangeness added: <i>Kaon</i> , $\Lambda$ and $\Sigma$ . . . . .	335
27.3.7	De-excitation phase . . . . .	335
27.4	Physics performance . . . . .	335
<b>28</b>	<b>Precompound model</b>	<b>339</b>
28.1	Reaction initial state. . . . .	339
28.2	Simulation of pre-compound reaction . . . . .	339
28.2.1	Statistical equilibrium condition . . . . .	339
28.2.2	Level density of excited (n-exciton) states . . . . .	339
28.2.3	Transition probabilities . . . . .	340
28.2.4	Emission probabilities for nucleons . . . . .	341
28.2.5	Emission probabilities for complex fragments . . . . .	341
28.2.6	The total probability . . . . .	342
28.2.7	Calculation of kinetic energies for emitted particle . . . . .	342
28.2.8	Parameters of residual nucleus . . . . .	342
<b>29</b>	<b>Evaporation Model</b>	<b>343</b>
29.1	Introduction . . . . .	343
29.2	Evaporation model . . . . .	343
29.2.1	Cross sections for inverse reactions . . . . .	344
29.2.2	Coulomb barriers . . . . .	344
29.2.3	Level densities . . . . .	344
29.2.4	Maximum energy available for evaporation . . . . .	345
29.2.5	Total decay width . . . . .	345
29.3	GEM model . . . . .	345
29.4	Nuclear fission . . . . .	346
29.4.1	The fission total probability . . . . .	346
29.4.2	The fission barrier . . . . .	347
29.5	Photon evaporation . . . . .	347
29.5.1	Computation of probability . . . . .	347
29.5.2	Discrete photon evaporation . . . . .	348
29.5.3	Internal conversion electron emission . . . . .	348
29.6	Sampling procedure . . . . .	349
<b>30</b>	<b>Fission model</b>	<b>351</b>
30.1	Reaction initial state. . . . .	351
30.2	Fission process simulation. . . . .	351
30.2.1	Atomic number distribution of fission products. . . . .	351
30.2.2	Charge distribution of fission products. . . . .	352
30.2.3	Kinetic energy distribution of fission products. . . . .	353
30.2.4	Calculation of the excitation energy of fission products. . . . .	353
30.2.5	Excited fragment momenta. . . . .	354
<b>31</b>	<b>Fermi Break-up Model</b>	<b>355</b>
31.1	Fermi break-up simulation for light nuclei . . . . .	355
31.1.1	Allowed channels . . . . .	355

31.1.2	Break-up probability . . . . .	356
31.1.3	Fragment characteristics . . . . .	356
31.1.4	Sampling procedure . . . . .	356
<b>32</b>	<b>Multifragmentation Model</b>	<b>357</b>
32.1	Multifragmentation process simulation . . . . .	357
32.1.1	Multifragmentation probability . . . . .	357
32.1.2	Direct simulation of the low multiplicity multifragment disintegration . . . . .	359
32.1.3	Fragment multiplicity distribution . . . . .	359
32.1.4	Atomic number distribution of fragments . . . . .	359
32.1.5	Charge distribution of fragments . . . . .	360
32.1.6	Kinetic energy distribution of fragments . . . . .	360
32.1.7	Calculation of the fragment excitation energies . . . . .	360
<b>33</b>	<b>ABLA++ evaporation/fission model</b>	<b>361</b>
33.1	Introduction . . . . .	361
33.2	Evaporation . . . . .	361
33.3	Level densities . . . . .	362
33.4	Fission . . . . .	363
33.5	Multifragmentation . . . . .	365
33.6	External data file required . . . . .	365
33.7	How to use ABLA++ . . . . .	365
<b>34</b>	<b>Quantum Molecular Dynamics for Heavy Ions</b>	<b>367</b>
34.1	Equations of Motion . . . . .	367
34.2	Ion-ion Implementation . . . . .	369
34.3	Cross Sections . . . . .	369
<b>35</b>	<b>Abrasion-ablation Model</b>	<b>371</b>
35.1	Introduction . . . . .	371
35.2	Initial nuclear dynamics and impact parameter . . . . .	371
35.3	Abrasion process . . . . .	372
35.4	Abraded nucleon spectrum . . . . .	374
35.5	De-excitation of the projectile and target nuclear pre-fragments by standard GEANT4 de-excitation physics . . . . .	375
35.6	De-excitation of the projectile and target nuclear pre-fragments by nuclear ablation . . . . .	375
35.7	Definition of the functions P and F used in the abrasion model . . . . .	376
<b>36</b>	<b>Electromagnetic Dissociation Model</b>	<b>379</b>
36.1	The Model . . . . .	379
<b>37</b>	<b>Interactions of Stopping Particles</b>	<b>383</b>
37.1	Complementary parameterised and theoretical treatment . . . . .	383
37.2	Pion absorption at rest . . . . .	383
<b>38</b>	<b>Low Energy Neutron Interactions</b>	<b>385</b>
38.1	Introduction . . . . .	385
38.2	Physics and Verification . . . . .	385
38.2.1	Inclusive Cross-sections . . . . .	385
38.3	Elastic Scattering . . . . .	386
38.4	Radiative Capture . . . . .	386
38.5	Fission . . . . .	388
38.6	Inelastic Scattering . . . . .	391
38.7	Unresolved Resonance Region (URR) description with Probability Tables (PT) . . . . .	391
38.8	Neutron Data Library (G4NDL) Format . . . . .	392

38.8.1	Cross Section . . . . .	392
38.8.2	Final State . . . . .	392
38.8.3	Thermal Scattering Cross Section . . . . .	393
38.8.4	Coherent Final State . . . . .	393
38.8.5	Incoherent Final State . . . . .	394
38.8.6	Inelastic Final State . . . . .	395
38.8.7	Further Information . . . . .	396
38.9	High Precision Models and Low Energy Parameterized Models . . . . .	396
38.10	NUDEX . . . . .	397
38.11	Summary and Important Remark . . . . .	398
<b>39</b>	<b>LowEnergyChargedParticles</b>	<b>399</b>
39.1	Low Energy Charged Particle Interactions . . . . .	399
39.1.1	Introduction . . . . .	399
39.1.2	Physics and Verification . . . . .	399
39.1.3	Neutron-induced alpha production reactions on carbon . . . . .	400
39.1.4	Data Format . . . . .	400
<b>40</b>	<b>GEANT4 Low Energy Nuclear Data (LEND) Package</b>	<b>401</b>
40.1	Low Energy Nuclear Data . . . . .	401
<b>41</b>	<b>Radioactive Decay</b>	<b>403</b>
41.1	The Radioactive Decay Module . . . . .	403
41.2	Alpha Decay . . . . .	403
41.3	Beta Decay . . . . .	403
41.4	Electron Capture . . . . .	404
41.5	Recoil Nucleus Correction . . . . .	404
41.6	Biasing Methods . . . . .	404
<b>Bibliography</b>		<b>407</b>
<b>V</b>	<b>Photolepton</b>	<b>423</b>
<b>42</b>	<b>Introduction</b>	<b>425</b>
<b>43</b>	<b>Cross-sections in Photonuclear and Electronuclear Reactions</b>	<b>427</b>
43.1	Approximation of Photonuclear Cross Sections . . . . .	427
43.2	Electronuclear Cross Sections and Reactions . . . . .	429
43.3	Common Notation for Different Approaches to Electronuclear Reactions . . . . .	429
<b>44</b>	<b>Gamma-nuclear Interactions</b>	<b>435</b>
44.1	Process and Cross Section . . . . .	435
44.2	Final State Generation . . . . .	435
44.3	Low Energy Nuclear Data Model . . . . .	435
<b>45</b>	<b>Electro-nuclear Interactions</b>	<b>437</b>
45.1	Process and Cross Section . . . . .	437
45.2	Final State Generation . . . . .	437
<b>46</b>	<b>Muon-nuclear Interactions</b>	<b>439</b>
46.1	Process and Cross Section . . . . .	439
46.2	Final State Generation . . . . .	439
<b>Bibliography</b>		<b>441</b>

<b>VI Neutrino</b>	<b>443</b>
<b>47 GEANT4 neutrino interaction processes</b>	<b>445</b>
47.1 Neutrino oscillation process . . . . .	445
47.2 Neutrino-electron process . . . . .	445
47.3 Neutrino-nucleus process . . . . .	446
47.4 Example . . . . .	446
<b>Bibliography</b>	<b>447</b>
<b>VII Solid State</b>	<b>449</b>
<b>48 Phonon-Lattice interactions</b>	<b>451</b>
48.1 Introduction . . . . .	451
48.2 Phonon Propagation . . . . .	451
48.3 Lattice Parameters . . . . .	452
48.4 Scattering and Mode Mixing . . . . .	452
48.5 Anharmonic Downconversion . . . . .	452
<b>49 Crystal Channeling Physics</b>	<b>455</b>
49.1 Channeling of relativistic particles . . . . .	455
49.2 Channeling Fast Simulation Model . . . . .	456
49.2.1 Applicability range . . . . .	457
49.2.2 Trajectory simulation . . . . .	457
49.2.3 Coulomb scattering and ionization losses . . . . .	457
49.2.4 Baier-Katkov Model . . . . .	458
49.2.5 Coherent Pair Production Model . . . . .	458
<b>Bibliography</b>	<b>461</b>



# **Part I**

# **Introduction**



---

CHAPTER  
ONE

---

## DEFINITION OF TERMS USED IN THIS GUIDE

Several terms used throughout the Physics Reference Manual have specific meaning within GEANT4, but are not well-defined in general usage. The definitions of these terms are given here.

- **process** - a C++ class which describes how and when a specific kind of physical interaction takes place along a particle track. A given particle type typically has several processes assigned to it. Occasionally “process” refers to the interaction which the process class describes.
- **model** - a C++ class whose methods implement the details of an interaction, such as its kinematics. One or more models may be assigned to each process. In sections discussing the theory of an interaction, “model” may refer to the formulae or parameterization on which the model class is based.
- **Geant3** - a previous physics simulation tool written in Fortran, and the direct predecessor of GEANT4. Although some references are still made to Geant3, no knowledge of it is required to understand this manual.
- **Verification** - in terms of physics modelling we define verification of testing a model at the thin target level to determine if it performs as expected normally in terms of double differential cross-sections. This is as much a computational unit test as a theoretical investigation.
- **Validation** - a comparison between a physics model and real experimental data. This may be at the microscopic (thin target) level whereby the experiment have provided derived cross sections from their data, or at a larger macroscopic (thick target) level whereby experimental data are directly compared with experiment.



---

CHAPTER  
TWO

---

## MONTE CARLO METHODS

The GEANT4 toolkit [eal16, JA09, SA03] uses a combination of the composition and rejection Monte Carlo methods. Only the basic formalism of these methods is outlined here. For a complete account of the Monte Carlo methods, the interested user is referred to the publications of Butcher and Messel, Messel and Crawford, or Ford and Nelson [BM60, MC70, NHR85].

Suppose we wish to sample  $x$  in the interval  $[x_1, x_2]$  from the distribution  $f(x)$  and the *normalised* probability density function can be written as :

$$f(x) = \sum_{i=1}^n N_i f_i(x) g_i(x)$$

where  $N_i > 0$ ,  $f_i(x)$  are *normalised* density functions on  $[x_1, x_2]$ , and  $0 \leq g_i(x) \leq 1$ .

According to this method,  $x$  can sampled in the following way:

1. select a random integer  $i \in \{1, 2, \dots, n\}$  with probability proportional to  $N_i$
2. select a value  $x_0$  from the distribution  $f_i(x)$
3. calculate  $g_i(x_0)$  and accept  $x = x_0$  with probability  $g_i(x_0)$ ;
4. if  $x_0$  is rejected restart from step 1.

It can be shown that this scheme is correct and the mean number of tries to accept a value is  $\sum_i N_i$ .

In practice, a good method of sampling from the distribution  $f(x)$  has the following properties:

- all the subdistributions  $f_i(x)$  can be sampled easily;
- the rejection functions  $g_i(x)$  can be evaluated easily/quickly;
- the mean number of tries is not too large.

Thus the different possible decompositions of the distribution  $f(x)$  are not equivalent from the practical point of view (e.g. they can be very different in computational speed) and it can be useful to optimise the decomposition.

A remark of practical importance : if our distribution is not normalised

$$\int_{x_1}^{x_2} f(x) dx = C > 0$$

the method can be used in the same manner; the mean number of tries in this case is  $\sum_i N_i/C$ .



## PARTICLE TRANSPORT

### 3.1 Particle transport

Particle transport in GEANT4 [SA03] is the result of the combined actions of the GEANT4 kernel's Stepping Manager class and the actions of processes which it invokes—physics processes and the Transportation ‘process’ which identifies the next volume boundary and also the geometrical volume that lies behind it, when the track has reached it.

The expected length at which an interaction is expected to occur is determined by polling all processes applicable at each step.

Then it is determined whether the particle will remain within the current volume long enough, otherwise it will cross into a different volume before this potential interaction occurs.

The most important processes for determining the trajectory of a charged particle, including boundary crossing and the effects of external fields are the multiple scattering process and the Transportation process, which is discussed in the second following section.

### 3.2 True Step Length

GEANT4 simulation of particle transport is performed step by step [SA03]. A *true step length* for a next physics interaction is randomly sampled using the *mean free path* of the interaction or by various *step limitations* established by different GEANT4 components. The smallest step limit defines the new true step length.

#### 3.2.1 The Interaction Length or Mean Free Path

Computation of mean free path of a particle in a media is performed in GEANT4 using cross section of a particular physics process and density of atoms. In a simple material the number of atoms per volume is:

$$n = \frac{\mathcal{N}\rho}{A}$$

where:

$\mathcal{N}$  = Avogadro's number

$\rho$  = density of the medium

$A$  = mass of a mole

In a compound material the number of atoms per volume of the  $i^{th}$  element is:

$$n_i = \frac{\mathcal{N}\rho w_i}{A_i}$$

where:

$$w_i = \text{proportion by mass of the } i^{\text{th}} \text{ element}$$

$$A_i = \text{mass of a mole of the } i^{\text{th}} \text{ element}$$

The **mean free path** of a process,  $\lambda$ , also called the **interaction length**, can be given in terms of the total cross section:

$$\lambda(E) = \left( \sum_i [n_i \cdot \sigma(Z_i, E)] \right)^{-1}$$

where  $\sigma(Z, E)$  is the total cross section per atom of the process and  $\sum_i$  runs over all elements composing the material.  $\sum_i [n_i \sigma(Z_i, E)]$  is also called the *macroscopic cross section*. The mean free path is the inverse of the macroscopic cross section.

Cross sections per atom and mean free path values may be tabulated during initialisation.

### 3.2.2 Determination of the Interaction Point

The mean free path,  $\lambda$ , of a particle for a given process depends on the medium and cannot be used directly to sample the probability of an interaction in a heterogeneous detector. The number of mean free paths which a particle travels is:

$$n_\lambda = \int_{x_1}^{x_2} \frac{dx}{\lambda(x)},$$

which is independent of the material traversed. If  $n_r$  is a random variable denoting the number of mean free paths from a given point to the point of interaction, it can be shown that  $n_r$  has the distribution function:

$$P(n_r < n_\lambda) = 1 - e^{-n_\lambda}$$

The total number of mean free paths the particle travels before reaching the interaction point,  $n_\lambda$ , is sampled at the beginning of the trajectory as:

$$n_\lambda = -\log(\eta)$$

where  $\eta$  is a random number uniformly distributed in the range  $(0, 1)$ .  $n_\lambda$  is updated after each step  $\Delta x$  according the formula:

$$n'_\lambda = n_\lambda - \frac{\Delta x}{\lambda(x)}$$

until the step originating from  $s(x) = n_\lambda \cdot \lambda(x)$  is the shortest and this triggers the specific process.

### 3.2.3 Step Limitations

The short description given above is the *differential approach* to particle transport, which is used in many other simulation codes. In this approach besides the other (*discrete*) processes the continuous energy loss and multiple scattering imposes a limit on the step-size too [eal16, JA09], because the cross section of different processes depend of the energy of the particle. Then it is assumed that the step is small enough so that the particle cross sections remain approximately constant during the step. In principle, one must use very small steps in order to insure an accurate simulation, but computing time increases as the step-size decreases and the default model of energy loss fluctuations will not be accurate for extremely small steps. A good compromise depends on required accuracy of a concrete simulation. The problem is reduced using integral approach, which is described below in *Correcting the Cross Section for Energy Variation*. However, this only provides effectively correct cross sections but step limitation is needed also for more precise tracking. Thus, in GEANT4 any process may establish additional step limitation, the most important limits come from ionisation and multiple scattering (see details in sub-chapters *Step-size Limit* and *Step Limitation Algorithm* correspondingly).

### 3.2.4 Updating the Particle Time

The laboratory time of a particle should be updated after each step:

$$\Delta t_{lab} = 0.5\Delta x \left( \frac{1}{v_1} + \frac{1}{v_2} \right),$$

where  $\Delta x$  is a true step length traveled by the particle,  $v_1$  and  $v_2$  are particle velocities at the beginning and at the end of the step correspondingly.

## 3.3 Transportation

The transportation process is responsible for determining the geometrical limits of a step. It calculates the length of step with which a track will cross into another volume. When the track actually arrives at a boundary, the transportation process locates the next volume that it enters.

If the particle is charged and there is an electromagnetic (or potentially other) field, it is responsible for propagating the particle in this field. It does this according to an equation of motion. This equation can be provided by GEANT4, for the case a magnetic or EM field, or can be provided by the user for other fields.

$$\frac{d\mathbf{p}}{ds} = \frac{1}{v}\mathbf{F} = \frac{q}{v}(\mathbf{E} + \mathbf{v} \times \mathbf{B})$$

Extensions are provided for the propagation of the polarisation, and the effect of a gravitational field, of potential interest for cases of slow neutral particles.

### 3.3.1 Some additional details on motion in fields

In order to intersect the model GEANT4 geometry of a detector or setup, the curved trajectory followed by a charged particle is split into ‘chords segments’. A chord is a straight line segment between two trajectory points. Chords are created utilizing a criterion for the maximum estimated value of the sagitta—the distance between the further curve point and the chord.

The equations of motions are solved utilising Runge Kutta methods. For the simplest case of a pure magnetic field, only the position and momentum are integrated. If an electric field is present, the time of flight is also integrated since the velocity changes along the step.

A Runge Kutta integration method for a vector  $\mathbf{y}$  starting at  $\mathbf{y}_{start}$  and given its derivative  $d\mathbf{y}'(s)$  as a function of  $s$  and  $y$ . For a given interval  $h$  it provides an estimate of the endpoint  $\mathbf{y}_{end}$  and of the integration error  $\mathbf{y}_{error}$ , due to the truncation errors of the RK method and the variability of the derivative.

The position and momentum as used as parts of the vector  $\mathbf{y}$ , and optionally the time of flight in the lab frame and the polarisation.

A proposed step is accepted if the magnitude of the location components of the error is below a tolerated fraction  $\epsilon$  of the step length  $s$

$$|\Delta\mathbf{x}| = |\mathbf{x}_{error}| < \epsilon * s$$

and the relative momentum error is also below  $\epsilon$ :

$$|\Delta\mathbf{p}| = |\mathbf{p}_{error}| < \epsilon$$

The transportation also updates the time of flight of a particle. In case of a neutral particle or of a charged particle in a pure magnetic field it utilises the average inverse velocity (average of the initial and final value of the inverse velocity.)

In case of a charged particle in an electric field or other field which does not preserve the energy, an explicit integration of time along the track is used. This is done by integrating the inverse velocity along the track:

$$t_1 = t_0 + \int_{s_0}^{s_1} \frac{1}{v} ds$$

Runge Kutta methods of different order can be utilised for fields depending on the numerical method utilised for approximating the field. Specialised methods for near-constant magnetic fields are also available.

## BIBLIOGRAPHY

- [BM60] J.C. Butcher and H. Messel. *Nucl. Phys.*, 20(15):, 1960.
- [eal16] J. Allison et al. Recent developments in geant4. *Nuclear Instruments and Methods in Physics Research Section A: Accelerators, Spectrometers, Detectors and Associated Equipment*, 835:186–225, nov 2016. URL: <https://doi.org/10.1016/j.nima.2016.06.125>, doi:10.1016/j.nima.2016.06.125.
- [JA09] et al. J. Apostolakis. Geometry and physics of the geant4 toolkit for high and medium energy applications. *Radiation Physics and Chemistry*, 78(10):859–873, oct 2009. URL: <https://doi.org/10.1016/j.radphyschem.2009.04.026>, doi:10.1016/j.radphyschem.2009.04.026.
- [MC70] H. Messel and D. Crawford. *Electron-Photon shower distribution*. Pergamon Press, 1970.
- [NHR85] W.R. Nelson, H. Hirayama, and D.W.O. Rogers. *EGS4 code system*. SLAC, Dec 1985. SLAC-265, UC-32.
- [SA03] et al. S. Agostinelli. Geant4—a simulation toolkit. *Nuclear Instruments and Methods in Physics Research Section A: Accelerators, Spectrometers, Detectors and Associated Equipment*, 506(3):250–303, jul 2003. URL: [https://doi.org/10.1016/S0168-9002\(03\)01368-8](https://doi.org/10.1016/S0168-9002(03)01368-8), doi:10.1016/s0168-9002(03)01368-8.
- [eal16] J. Allison et al. Recent developments in geant4. *Nuclear Instruments and Methods in Physics Research Section A: Accelerators, Spectrometers, Detectors and Associated Equipment*, 835:186–225, nov 2016. URL: <https://doi.org/10.1016/j.nima.2016.06.125>, doi:10.1016/j.nima.2016.06.125.
- [JA09] et al. J. Apostolakis. Geometry and physics of the geant4 toolkit for high and medium energy applications. *Radiation Physics and Chemistry*, 78(10):859–873, oct 2009. URL: <https://doi.org/10.1016/j.radphyschem.2009.04.026>, doi:10.1016/j.radphyschem.2009.04.026.
- [SA03] et al. S. Agostinelli. Geant4—a simulation toolkit. *Nuclear Instruments and Methods in Physics Research Section A: Accelerators, Spectrometers, Detectors and Associated Equipment*, 506(3):250–303, jul 2003. URL: [https://doi.org/10.1016/S0168-9002\(03\)01368-8](https://doi.org/10.1016/S0168-9002(03)01368-8), doi:10.1016/s0168-9002(03)01368-8.



# **Part II**

# **Decay**



---

CHAPTER  
FOUR

---

## PARTICLE DECAY

The decay of particles in flight and at rest is simulated by the G4Decay class.

### 4.1 Mean Free Path for Decay in Flight

The mean free path  $\lambda$  is calculated for each step using

$$\lambda = \gamma \beta c \tau$$

where  $\tau$  is the lifetime of the particle and

$$\gamma = \frac{1}{\sqrt{1 - \beta^2}}.$$

$\beta$  and  $\gamma$  are calculated using the momentum at the beginning of the step. The decay time in the rest frame of the particle (proper time) is then sampled and converted to a decay length using  $\beta$ .

### 4.2 Branching Ratios and Decay Channels

G4Decay selects a decay mode for the particle according to branching ratios defined in the G4DecayTable class, which is a member of the G4ParticleDefinition class. Each mode is implemented as a class derived from G4VDecayChannel and is responsible for generating the secondaries and the kinematics of the decay. In a given decay channel the daughter particle momenta are calculated in the rest frame of the parent and then boosted into the laboratory frame. Polarization is not currently taken into account for either the parent or its daughters.

A large number of specific decay channels may be required to simulate an experiment, ranging from two-body to many-body decays and V-A to semi-leptonic decays. Most of these are covered by the five decay channel classes provided by GEANT4:

G4PhaseSpaceDecayChannel	phase space decay
G4DalitzDecayChannel	dalitz decay
G4MuonDecayChannel	muon decay
G4TauLeptonicDecayChannel	tau leptonic decay
G4KL3DecayChannel	semi-leptonic decays of kaon

## 4.2.1 G4PhaseSpaceDecayChannel

The majority of decays in GEANT4 are implemented using the `G4PhaseSpaceDecayChannel` class. It simulates phase space decays with isotropic angular distributions in the center-of-mass system. Three private methods of `G4PhaseSpaceDecayChannel` are provided to handle two-, three- and N-body decays: `TwoBodyDecayIt()`, `ThreeBodyDecayIt()`, `ManyBodyDecayIt()`.

Some examples of decays handled by this class are:

$$\begin{aligned}\pi^0 &\rightarrow \gamma\gamma, \\ \Lambda &\rightarrow p\pi^-\end{aligned}$$

and

$$K^0_L \rightarrow \pi^0\pi^+\pi^-.$$

## 4.2.2 G4DalitzDecayChannel

The Dalitz decay

$$\pi^0 \rightarrow \gamma + e^+ + e^-$$

and other Dalitz-like decays, such as

$$K^0_L \rightarrow \gamma + e^+ + e^-$$

and

$$K^0_L \rightarrow \gamma + \mu^+ + \mu^-$$

are simulated by the `G4DalitzDecayChannel` class. In general, it handles any decay of the form

$$P^0 \rightarrow \gamma + l^+ + l^-,$$

where  $P^0$  is a spin-0 meson of mass  $M$  and  $l^\pm$  are leptons of mass  $m$ . The angular distribution of the  $\gamma$  is isotropic in the center-of-mass system of the parent particle and the leptons are generated isotropically and back-to-back in their center-of-mass frame. The magnitude of the leptons' momentum is sampled from the distribution function

$$f(t) = \left(1 - \frac{t}{M^2}\right)^3 \left(1 + \frac{2m^2}{t}\right) \sqrt{1 - \frac{4m^2}{t}},$$

where  $t$  is the square of the sum of the leptons' energy in their center-of-mass frame.

## 4.2.3 Muon Decay

`G4MuonDecayChannel` simulates muon decay according to  $V-A$  theory. The electron energy is sampled from the following distribution:

$$d\Gamma = \frac{G_F^2 m_\mu^5}{192\pi^3} 2\epsilon^2 (3 - 2\epsilon)$$

where:

$$\Gamma = \text{decay rate}$$

$$\epsilon = E_e/E_{max}$$

$$E_e = \text{electron energy}$$

$$E_{max} = \text{maximum electron energy} = m_\mu/2$$

The magnitudes of the two neutrino momenta are also sampled from the  $V-A$  distribution and constrained by energy conservation. The direction of the electron neutrino is sampled using

$$\cos(\theta) = 1 - 2/E_e - 2/E_{\nu e} + 2/E_e/E_{\nu e}$$

and the muon anti-neutrino momentum is chosen to conserve momentum. Currently, neither the polarization of the muon nor the electron is considered in this class.

#### 4.2.4 Leptonic Tau Decay

`G4TauLeptonicDecayChannel` simulates leptonic tau decays according to  $V-A$  theory. This class is valid for both

$$\tau^\pm \rightarrow e^\pm + \nu_\tau + \nu_e$$

and

$$\tau^\pm \rightarrow \mu^\pm + \nu_\tau + \nu_\mu$$

modes.

The energy spectrum is calculated without neglecting lepton mass as follows:

$$d\Gamma = \frac{G_F^2 m_\tau^3}{24\pi^3} p_l E_l (3E_l m_\tau^2 - 4E_l^2 m_\tau - 2m_\tau m_l^2)$$

where:

- $\Gamma$  = decay rate
- $E_l$  = daughter lepton energy (total energy)
- $p_l$  = daughter lepton momentum
- $m_l$  = daughter lepton mass

As in the case of muon decay, the energies of the two neutrinos are not sampled from their  $V-A$  spectra, but are calculated so that energy and momentum are conserved. Polarization of the  $\tau$  and final state leptons is not taken into account in this class.

#### 4.2.5 Kaon Decay

The class `G4KL3DecayChannel` simulates the following four semi-leptonic decay modes of the kaon:

$$\begin{aligned} K^\pm_{e3} : K^\pm &\rightarrow \pi^0 + e^\pm + \nu \\ K^\pm_{\mu 3} : K^\pm &\rightarrow \pi^0 + \mu^\pm + \nu \\ K^0_{e3} : K_L^0 &\rightarrow \pi^\pm + e^\mp + \nu \\ K^0_{\mu 3} : K_L^0 &\rightarrow \pi^\pm + \mu^\mp + \nu \end{aligned}$$

Assuming that only the vector current contributes to  $K \rightarrow l\pi\nu$  decays, the matrix element can be described by using two dimensionless form factors,  $f_+$  and  $f_-$ , which depend only on the momentum transfer  $t = (P_K - P_\pi)^2$ . The Dalitz plot density used in this class is as follows [LMCG72]:

$$\rho(E_\pi, E_\mu) \propto f_+^2(t) \left[ A + B\xi(t) + C\xi(t)^2 \right]$$

where:

$$\begin{aligned} A &= m_K(2E_\mu E_\nu - m_K E'_\pi) + m_\mu^2 \left( \frac{1}{4} E'_\pi - E_\nu \right) \\ B &= m_\mu^2 \left( E_\nu - \frac{1}{2} E'_\pi \right) \\ C &= \frac{1}{4} m_\mu^2 E'_\pi \\ E'_\pi &= E_\pi^{max} - E_\pi \end{aligned}$$

Here  $\xi(t)$  is the ratio of the two form factors

$$\xi(t) = f_-(t)/f_+(t).$$

$f_+(t)$  is assumed to depend linearly on t, i.e.,

$$f_+(t) = f_+(0)[1 + \lambda_+(t/m_\pi^2)]$$

and  $f_-(t)$  is assumed to be constant due to time reversal invariance.

Two parameters,  $\lambda_+$  and  $\xi(0)$  are then used for describing the Dalitz plot density in this class. The values of these parameters are taken to be the world average values given by the Particle Data Group [eal00].

## DECAYS OF ORTHOPOSITRIONIUM AT REST TO 3 PHOTONS

Triplet state positronium, “orthopositronium”, is a spin-one state that decays to three photons. For a decay at rest, the three photons are emitted in a plane. The orientation of that plane and the polarization of the photons in the final state depend on the polarization of the positronium in the initial state.

For positronium decay at rest two ortho-positronium decay into 3 gamma models are available: `G4OrePowellAtRestModel` with random polarization and `G4PolarizedOrePowellAtRestModel` for arbitrary positronium and photon polarization.

### 5.1 Random polarization

The decay for a positronium random polarization and summing on the polarization of the photons is provided by `G4OrePowellAtRestModel`. The differential decay rate is [OP49]:

$$P \propto \left[ (1 - \cos(\theta_{23}))^2 + (1 - \cos(\theta_{31}))^2 + (1 - \cos(\theta_{12}))^2 \right] dk_1 dk_2 d\Omega_1, \quad (5.1)$$

where  $k_i$  and  $\Omega_i$  are the energy and solid angle of photon  $i$  and  $\theta_{ij}$  is the angle between the photon momenta  $\vec{k}_i$  and  $\vec{k}_j$ .  $k_3$  and the directions of photons 2 and 3 are obtained from energy-momentum conservation. The photon energies sum up to  $k_1 + k_2 + k_3 = 2m$ , given the positronium mass is approximately equal to twice the electron mass,  $m$ . Upon integration, one obtains the inclusive photon energy spectrum [OP49]:

$$P \propto F(x) \equiv \left[ \frac{x(1-x)}{(2-x)^2} - \frac{2(1-x)^2}{(2-x)^3} \ln(1-x) + \frac{2-x}{x} + \frac{2(1-x)}{x^2} \ln(1-x) \right] dx, \quad (5.2)$$

with  $x \equiv k/m$ , and  $0 \leq x \leq 1$ , that is,

The graph of  $F(x)$  is given in Fig. 5.1.

The model samples the final state as follows

- take  $k_1$  and  $k_2$  at random in  $[0, m]$ ; compute  $k_3 = 2m - (k_1 + k_2)$ ;
- assume  $k_1$  along  $\vec{x}$ ; compute  $\cos \theta_{1i}$ ,  $i = 2, 3$  from momentum conservation; request  $|\cos \theta_{1i}| \leq 1$ ,  $i = 2, 3$ ; compute  $\cos \theta_{23}$  from  $\vec{k}_2 \cdot \vec{k}_3$ ;
- generate events from pdf (5.1).

The direction of  $\vec{k}_1$  in the plane and the direction of the normal to the plane in the local frame are then taken at random and the final state rotated to the local frame accordingly.

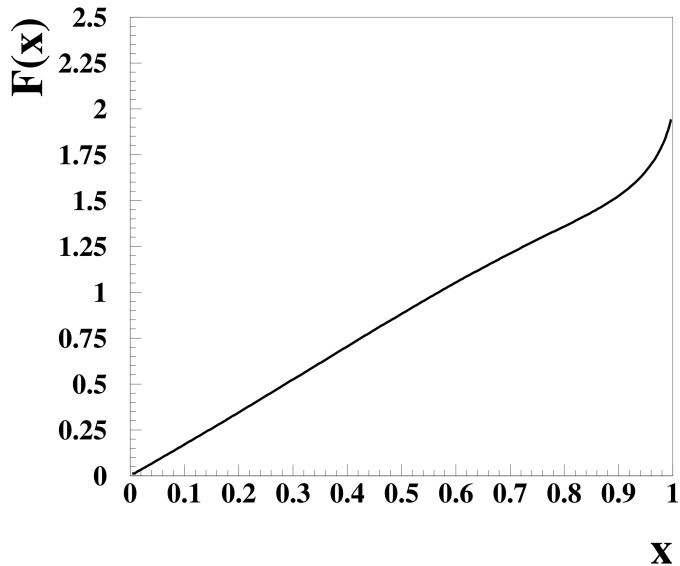


Fig. 5.1: Graph of  $F(x)$  ((5.2)).

### 5.1.1 Validation.

The photon energy spectra are found to be compatible with (5.2) and Fig. 5.1.

## 5.2 Polarized model

The decay for arbitrary positronium and photon polarizations is provided by G4PolarizedOrePowellAtRestModel. The differential decay rate becomes proportional to  $|(\vec{t}_1 + \vec{t}_2 + \vec{t}_3) \cdot \vec{u}|^2$  [Dri56, OP49],

- $\vec{u}$  is a complex unit vector which characterizes the initial triplet state of the positronium atom;
- $\vec{t}_1 = -\vec{a}_3(\vec{a}_1 \cdot \vec{a}_2) + \vec{a}_1(\vec{a}'_2 \cdot \vec{a}'_3) - \vec{a}'_2(\vec{a}'_3 \cdot \vec{a}_1) - \vec{a}'_3(\vec{a}_1 \cdot \vec{a}'_2)$  and  $\vec{t}_2$  and  $\vec{t}_3$  are obtained by permutation of the photon indices (terms that cancel upon the sum  $(\vec{t}_1 + \vec{t}_2 + \vec{t}_3)$  have been removed).
- $\vec{a}_i$  is the polarization vector of photon  $i$  and  $\vec{a}'_i = \vec{a}_i \times \vec{n}_i$ ,  $\vec{n}_i = \vec{k}_i/k_i$ .

$\vec{u}$  depends on the value of the positronium polarization quantum number,  $m$ . If the quantization axis is perpendicular to the decay plane [Dri56, OP49]:

- $m = 0$ ,  $\vec{u} = (0, 0, 1)$ ,
- $m = +1$ ,  $\vec{u} = (1, i, 0)/\sqrt{2}$ ,
- $m = -1$ ,  $\vec{u} = (1, -i, 0)/\sqrt{2}$ ,

where  $i$  is the imaginary unit.

The model samples the final state as follows

- The direction of the positronium quantization axis is assumed to be  $\vec{z}$  in the local frame. Fill  $\vec{u}$  depending on input value of  $m$ .
- Take the orientation of the decay frame with respect to the local frame at random.
- Generate a decay in the decay plane.

- For each photon  $i$ , compute  $\vec{n}_i$ ; compute vector perpendicular to  $\vec{n}_i$  in the horizontal plane,  $\vec{m}_i$ ; take polarization vector in  $(\vec{m}_i, \vec{z})$  plane,  $\vec{z}$  perpendicular to the decay plane (take  $\phi_i$  at random flat,  $\vec{a}_i = \cos(\phi_i)\vec{m}_i + \sin(\phi_i)\vec{z}$ ); compute  $\vec{a}'_i = \vec{a}_i \times \vec{n}_i$ ;
- Compute  $\vec{t} = (\vec{t}_1 + \vec{t}_2 + \vec{t}_3)$ ; rotate  $\vec{t}$  to the local frame. Compute  $|\vec{t} \cdot \vec{u}|^2$ ;
- Generate events from pdf proportional to  $|\vec{t} \cdot \vec{u}|^2$ .

### 5.2.1 Validation.

The inclusive energy spectra are found to be compatible with (5.2) and Fig. 5.1.

The distribution of the angle  $\theta$  between the quantization axis and the normal to the plane is found to be compatible with  $1/\Gamma d\Gamma/d\Omega$  [BN81] ( $d\Omega = \sin \theta d\theta$ ), that is, proportional to  $(1 + \cos^2 \theta)$  for  $m = 0$  and to  $(3 - \cos^2 \theta)$  for  $m = \pm 1$ .

Also in a dedicated version of the model for which the normal to the plane was set parallel to the quantization axis, it was checked that in the symmetric equipartition case, ( $\theta_{12} = \theta_{23} = \theta_{13} = 120^\circ$ ,  $k_1 = k_2 = k_3 = 2m/3$ ), “the ratio of the number of quanta polarized perpendicular to the plane of the quanta to the number polarized in the plane of detection of the quanta is 5:1 when the positronium atom annihilates from the triplet  $m = 0$  state, 2:1 for the  $m = \pm 1$  states” [Dri56].

The polarized model `G4PolarizedOrePowellAtRestModel` is approximately one order of magnitude slower than the random polarization model `G4OrePowellAtRestModel`.



## BIBLIOGRAPHY

- [eal00] D.E. Groom et al. Review of Particle Physics. *The European Physical Journal*, C15:1+, 2000. URL: <http://pdg.lbl.gov>.
- [LMCG72] L.M. Chouinet, J.M. Gaillard and M.K. Gaillard. *Phys. Reports* 4C, 199, 1972.
- [BN81] W. Bernreuther and O. Nachtmann. Weak interaction effects in positronium. *Zeitschrift für Physik C Particles and Fields*, 11(3):235–245, September 1981. URL: <http://dx.doi.org/10.1007/BF01545680>, doi:10.1007/bf01545680.
- [Dri56] R. M. Drisko. Spin and polarization effects in the annihilation of triplet positronium. *Physical Review*, 102(6):1542–1544, June 1956. URL: <http://dx.doi.org/10.1103/PhysRev.102.1542>, doi:10.1103/physrev.102.1542.
- [OP49] A. Ore and J. L. Powell. Three-photon annihilation of an electron-positron pair. *Physical Review*, 75(11):1696–1699, June 1949. URL: <http://dx.doi.org/10.1103/PhysRev.75.1696>, doi:10.1103/physrev.75.1696.



# **Part III**

# **Electromagnetic**



## ELECTROMAGNETIC PHYSICS IN GEANT4

### 6.1 Introduction

The GEANT4 set of electromagnetic (EM) physics processes and models [eal16, eal09, eal03, eal11] are used in practically all types of simulation applications including high energy and nuclear physics experiments, beam transport, medical physics, cosmic ray interactions and radiation effects in space. In addition to models for low and high energy EM physics for simulation of radiation effects in media, a sub-library of very low energy models was developed within the framework of the GEANT4-DNA project, with the goal of simulating radiation effects involving physics and chemistry at the sub-cellular level [eal14].

### 6.2 EM physics sub-packages

In the early stages of GEANT4, low and high energy electromagnetic processes were developed independently, with the result that these processes could not be used in the same run. To resolve this problem, the interfaces were unified so that the standard, muon, high energy, low energy and DNA EM physics sub-packages now follow the same design [eal11].

All GEANT4 physical processes, including transportation, decay, EM, hadronic, optical and others, were implemented via the unique general interface `G4VProcess`. Three EM process interfaces inherit from it via the intermediate classes [eal09]:

- `G4VEnergyLossProcess`, which is active along the step and post step,
- `G4VMultipleScattering`, which is active along the step,
- `G4VEmProcess`, which is active post step and at rest.

These three base classes are responsible for interfacing to the GEANT4 kernel, initializing the electromagnetic physics, managing the energy loss, range and cross sections tables, managing the electromagnetic models, and the built-in biasing options. These based classes are also responsible for managing of EM classes in the multi threaded mode of Geant4 [eal16]. Most part of EM internal data objects are shared between threads and are destructed end of run these data objects and all models.

A concrete physics process class inherits from one of these base classes, and has one or more physics models. EM physics models were implemented via the `G4VEmModel` interface. A model is applied for a defined energy range and `gclass{G4Region}`, allowing, for example, one model from the low energy and one from the high energy sub-package to be assigned to a process for a given particle type. Each of these processes have following phases:

- initial initialisation at time of construction, when the default set of EM parameters is defined;
- possible modification of EM parameters by a user;
- initialisation before the run, which includes preparation of tables with cross sections, energy losses, ranges, and other values;

- initialisation of the main tables is carried out only in the master thread at the beginning of a run and these tables are shared between threads at run time;
- run time access to the cross section or computation it by a selected model on-fly;
- sampling of final state via the model;
- destruction of EM objects at the end of simulation.

The EM model classes are responsible for concrete computations of cross sections and for sampling of final state. If a model class has a private objects, which does not inherit of the `G4VEmModel` interface, then deletion end of run of these objects is a responsibility of this model class. The EM process based classes select a model for the given energy and region and communicate with the GEANT4 kernel in a generic way in all phases.

Migration to this common design resulted in an improvement of overall CPU performance, and made it possible to provide several helper classes which are useful for a variety of user applications:

- `G4EmParameters`: class which keep the set of EM parameters, which may be changed via C++ access methods or UI commands, the access is opened for all parameters in the `PreInit` state of GEANT4 and for part of parameters in the `Idle` state;
- `G4EmCalculator`: accesses or computes cross section, energy loss, and range;
- `G4EmConfigurator`: adds extra physics models per particle type, energy, and geometry region;
- `G4EmSaturation`: adds Birks saturation of visible energy in sensitive detectors;
- `G4ElectronIonPair`: samples ionisation clusters in tracking devices.

Further improvements were made through the factorization of secondary energy and angle sampling. `G4VEmAngularDistribution` common interface allows the reuse of angular generator code by models in all EM sub-packages. The implementation of a unified interface for atomic de-excitation, `G4VAtomDeexcitation` provides the possibility of sampling atomic de-excitation by models from all EM sub-packages.

## 6.3 Low Energy Livermore Model

Additional electromagnetic physics processes for photons, electrons, hadrons and ions have been implemented in GEANT4 in order to extend the validity range of particle interactions to lower energies than those available in the standard GEANT4 EM [eal99]. Since the atomic shell structure is more important in most cases at low energies than it is at higher energies, the low energy processes make direct use of shell cross section data. The standard processes, which are optimized for high energy physics applications, often rely on parameterizations of these data.

Low energy processes include the photo-electric effect, Compton scattering, Rayleigh scattering, gamma conversion, bremsstrahlung and ionisation. Also atomic de-excitation module is implemented within this sub-package, which includes fluorescence and Auger electron emission of excited atoms. The implementation of low energy processes is valid for elements with atomic number between 1 and 99, and for energies down to 10 eV, upper limit depends on the process.

The data used for the determination of cross-sections and for sampling of the final state are extracted from a set of publicly distributed evaluated data libraries:

- EPDL97 (Evaluated Photons Data Library) [[CHK89](#)];
- EPICS2014 (Evaluated Photons Data Library) [[NEAa](#)];
- EPICS2017 (Evaluated Photons Data Library) [[NEAa](#)];
- EEDL (Evaluated Electrons Data Library) [[STPerkins89](#)];
- EADL (Evaluated Atomic Data Library) [[PCeal](#)];
- binding energy values based on data of Scofield [[Sco75](#)].

Evaluated data sets are produced through the process of critical comparison, selection, renormalization and averaging of the available experimental data, normally complemented by model calculations. These libraries provide the following data:

- total cross-sections for photoelectric effect, Compton scattering, Rayleigh scattering, pair production and bremsstrahlung;
- subshell integrated cross sections for photo-electric effect and ionisation;
- energy spectra of the secondaries for electron processes;
- scattering functions for the Compton effect;
- binding energies for electrons for all subshells;
- transition probabilities between subshells for fluorescence and the Auger effect.

These data are used directly or are transformed into Geant4 format specific for each model. The author of EPDL97, who is also responsible for the EPICS2014, EEDL, and EADL data libraries, Dr. Red Cullen, has kindly permitted the libraries and their related documentation to be distributed with the GEANT4 toolkit. The data are reformatted for GEANT4 input and are inside the G4LEDATA data set, which may be downloaded from the GEANT4 [download page](#).

The EADL, EPICS2014, EEDL and EPDL97 data-sets are also available from several public distribution centres in a format different from the one used by GEANT4 [[NEAb](#)].

## 6.4 Penelope Models

Physics processes for photons, electrons and positrons have been implemented in GEANT4 according to the PENELOPE code (PENetration and Energy LOss of Positrons and Electrons), version 2008. Models for the following processes have been included: Compton scattering, photoelectric effect, Rayleigh scattering, gamma conversion, bremsstrahlung, ionisation and positron annihilation and are described in more detail in Ref.[[eal01](#)]. The Penelope models have been specifically developed for Monte Carlo simulation and great care was given to the low energy description (i.e. atomic effects, etc.). Hence, these implementations provide reliable results for energies from 100 eV up to 6 GeV [[eal01](#), [SFernandezVAS03](#)], in GEANT4 the upper limit 1 GeV is used. These models may be used as an alternative to standard and Livermore models.

## 6.5 Generic Calculation of Total Cross Sections

In GEANT4 EM interpolation of physics tables (energy loss, ranges, cross sections) is performed by the G4PhysicsVector class using linear or logarithmic scale with linear or spline interpolation. For a number of models the energy dependence of the total cross section is not so regular. For example, the Livermore evaluated data libraries with a scale of the concrete data. Thus, for some models the total cross is obtained by interpolation according to the formula [[Ste03](#)]:

$$\log(\sigma(E)) = \frac{\log(\sigma_1) \log(E_2/E) + \log(\sigma_2) \log(E/E_1)}{\log(E_2/E_1)} \quad (6.1)$$

where  $E$  is actual energy,  $E_1$  and  $E_2$  are respectively the closest lower and higher energy points for which data ( $\sigma_1$  and  $\sigma_2$ ) are available. For other processes interpolation method is chosen depending on cross section shape.



## GAMMA INCIDENT

### 7.1 Introduction to Gamma Processes

All processes of gamma interaction with media in GEANT4 happen at the end of the step, so these interactions are *discrete* and corresponding processes are following the *G4VDiscreteProcess* interface.

#### 7.1.1 General Interfaces

There are a number of similar functions for discrete electromagnetic processes and for electromagnetic (EM) packages an additional base classes were designed to provide common computations [eal09]. Common calculations for discrete EM processes are performed in the class *G4VEmProcess*. Derived classes (Table 7.1) are concrete processes providing initialisation. The physics models are implemented using the *G4VEmModel* interface. Each process may have one or many models defined to be active over a given energy range and set of *G4Regions*. Models are implementing computations of cross section and sampling of final state. The list of EM processes and models for gamma incident is shown in Table 7.1.

Table 7.1: List of process and model classes for gamma.

EM process	EM model	Ref.
G4PhotoElectricEffect	G4PEEffectFluoModel	Section 7.3
	G4LivermorePhotoElectricModel	Section 7.3.5
	G4PenelopePhotoElectricModel	Section 7.3.4
G4PolarizedPhotoElectricEffect	G4PolarizedPEEffectModel	Section 14.7
	G4LivermorePolarizedPhotoElectricModel	
G4ComptonScattering	G4KleinNishinaCompton	Section 7.4
	G4KleinNishinaModel	Section 7.4
	G4LivermoreComptonModel	Section 7.4.5
	G4LivermoreComptonModelRC	
	G4LowEPComptonModel	Section 7.4.6
	G4PenelopeComptonModel	Section 7.4.4
G4PolarizedCompton	G4PolarizedComptonModel	Section 14.4
	G4LivermorePolarizedComptonModel	Section 14.4
G4GammaConversion	G4BetheHeitlerModel	Section 7.5
	G4BetheHeitler5DModel	Section 7.5.4
	G4BetheHeitler5DModel	Section 14.10
	G4PairProductionRelModel	
	G4LivermoreGammaConversionModel	Section 7.5.6
	G4LivermoreGammaConversion5DModel	<i>Livermore Model</i>
	G4BoldyshevTripletModel	Section 7.6
	G4LivermoreNuclearGammaConversionModel	

continues on next page

Table 7.1 – continued from previous page

EM process	EM model	Ref.
	G4PenelopeGammaConversion	Section 7.5.5
G4PolarizedGammaConversion	G4PolarizedGammaConversionModel	Section 14.6
	G4LivermorePolarizedGammaConversionModel	
G4RayleighScattering	G4LivermoreRayleighModel	Section 7.2.2
	G4LivermorePolarizedRayleighModel	
	G4PenelopeRayleighModel	Section 7.2.1
G4JAEAelasticScattering	G4JAEAelasticScatteringModel	Section 7.2.3
G4GammaConversionToMuons		Section 7.7
G4XrayReflection		Section 7.8

## 7.2 Elastic Scattering

Elastic scattering of gammas can involve Rayleigh, nuclear Thomson and Delbrück scattering. The Rayleigh process in GEANT4 can be simulated with either the Penelope (*Penelope Models*) or Livermore models (*Low Energy Livermore Model*). A more detailed model involving atomic and molecular interactions is included as a JAEA model (*JAEA Elastic Scattering Model*). These specific implementations are described in more detail below.

### 7.2.1 Penelope Model

#### Total cross section

The total cross section of the Rayleigh scattering process is determined from an analytical parameterization. The atomic cross section for coherent scattering is given approximately by [Bor69]

$$\sigma(E) = \pi r_e^2 \int_{-1}^1 \frac{1 + \cos^2 \theta}{2} [F(q, Z)]^2 d\cos \theta, \quad (7.1)$$

where  $F(q, Z)$  is the atomic form factor,  $Z$  is the atomic number and  $q$  is the magnitude of the momentum transfer, i.e.

$$q = 2 \frac{E}{c} \sin\left(\frac{\theta}{2}\right).$$

In the numerical calculation the following analytical approximations are used for the form factor:

$$F(q, Z) = f(x, Z) = \begin{cases} Z \frac{1+a_1x^2+a_2x^3+a_3x^4}{(1+a_4x^2+a_5x^4)^2} & \text{or} \\ \max[f(x, Z), F_K(x, Z)] & \text{if } Z > 10 \text{ and } f(x, Z) < 2 \end{cases}$$

where

$$F_K(x, Z) = \frac{\sin(2b \arctan Q)}{bQ(1+Q^2)^b},$$

with

$$x = 20.6074 \frac{q}{m_e c}, \quad Q = \frac{q}{2m_e c a}, \quad b = \sqrt{1 - a^2}, \quad a = \alpha \left( Z - \frac{5}{16} \right),$$

where  $\alpha$  is the fine-structure constant. The function  $F_K(x, Z)$  is the contribution to the atomic form factor due to the two K-shell electrons (see [eal94]). The parameters of expression  $f(x, Z)$  have been determined in Ref. [eal94] for  $Z = 1$  to 92 by numerically fitting the atomic form factors tabulated in Ref. [eal75]. The integration of Eq.(7.1) is performed numerically using the 20-point Gaussian method. For this reason the initialization of the Penelope Rayleigh process is somewhat slower than the Low Energy Livermore process.

## Form Factor for compounds and mixtures

In the case of compounds and mixtures, the form factor is calculated, by default, through a weighted sum of the atomic form factors of the elements composing the material and using their mass fractions as weights. However, this approach, which is called independent atom model (IAM) and is natively adopted by all the particle tracking codes, does not consider the interference effect of the photons scattered by the bound electrons in molecules. As a consequence, the scattering pattern will not feature the peaks at small values of momentum transfer that characterize the considered material. To take into account the molecular interference effect (MI), form factors extracted from the measured scattering (diffraction) patterns can be used. A database of form factors including MI effect for a variety of materials, mainly biological tissue and plastics, is available. In order to use the files of the database, the user has to label the defined materials according to the following table:

material	label
fat	Fat_MI
water	Water_MI
collagen	BoneMatrix_MI
hydroxyapatite	Mineral_MI
PMMA	PMMA_MI
adipose	adipose_MI
glandular	glandular_MI
breast (50%fat + 50%water)	breast5050_MI
liver	liver_MI
kidney	kidney_MI
muscle	muscle_MI
heart	heart_MI
blood	blood_MI
bone	bone_MI
carcinoma	carcinoma_MI
white matter of brain	whiteMatter_MI
gray matter of brain	grayMatter_MI
fat (ext. to low q)	FatLowX_MI
collagen (ext. to low q)	BoneMatrixLowX_MI
dry bone (ext. to low q)	dryBoneLowX_MI
lexan	Lexan_MI
kapton	Kapton_MI
nylon	Nylon_MI
polyethylene	Polyethylene_MI
polystyrene	Polystyrene_MI
formaline	Formaline_MI
acetone	Acetone_MI
Hydrogen peroxide	Hperoxide_MI
CIRS30-70	CIRS30-70_MI
CIRS50-50	CIRS50-50_MI
CIRS70-30	CIRS70-30_MI
RMI454	RMI454_MI

Due to the tissue variability, the measured diffraction patterns of two samples of the same tissue type may differ significantly. To overcome this problem, a generic tissue can be decomposed in simpler basis materials with well-defined elemental composition. In particular, each tissue is considered as a composition of four components, namely fat, water, collagen or bone matrix, and hydroxyapatite (see [PaternoCC+18], [PaternoCGT20]). The form factor of a generic tissue can be then expressed through the mixture rule using tissues (molecules or supramolecules) instead of

atoms as:

$$\frac{F^2(q)}{W} = \sum_{i=1}^4 \frac{a_i F_i^2(q)}{W_i}, \quad (7.2)$$

where  $a_i$  is the mass fraction of  $i$ -th basis component.

In order to enable this functionality, the user has to create the mixture of basis materials (whose composition and density are defined in [PaternoCGT20] and label the material as *MedMat\_a1\_a2\_a3\_a4*, where  $a_i$  are three digit numbers representing the mass fraction of the basis components. Then, the form factor of the material is automatically calculated according to Eq.(7.2).

In order to gain generality, the user has the faculty of providing the form factor of the materials he wants to consider. This is obtained by defining a material as *G4ExtendedMaterial* and registering *G4MIData* extension. The *SetFilenameFF()* method of this class allows to specify the path of the file with the form factor of the material. This functionality is particularly suited for modeling materials with partial crystalline behaviour, such as powder and polycrystals, which are characterized by a large number of sharp diffraction peaks.

### Sampling of the final state

The angular deflection  $\cos \theta$  of the scattered photon is sampled from the probability distribution function

$$P(\cos \theta) = \frac{1 + \cos^2 \theta}{2} [F(q, Z)]^2.$$

For details on the sampling algorithm (which is quite heavy from the computational point of view) see Ref. [eal01]. The azimuthal scattering angle  $\phi$  of the photon is sampled uniformly in the interval  $(0, 2\pi)$ .

## 7.2.2 Livermore Model

Rayleigh scattering is described by *G4LivermoreRayleighModel*.

### Total Cross Section

The total cross section for the Rayleigh scattering process is based on either EPDL97 or EPICS2017 data as described in *Low Energy Livermore Model*, and determined from the data as described in *Generic Calculation of Total Cross Sections*.

### Sampling of the Final State

The coherent scattered photon angle  $\theta$  is sampled according to the distribution obtained from the product of the Rayleigh formula  $(1 + \cos^2 \theta) \sin \theta$  and the square of Hubbel's form factor  $FF^2(q)$  [eal79] [Cul95]

$$\Phi(E, \theta) = [1 + \cos^2 \theta] \sin \theta \times FF^2(q),$$

where  $q = 2E \sin(\theta/2)$  is the momentum transfer.

Form factors introduce a dependency on the initial energy  $E$  of the photon that is not taken into account in the Rayleigh formula. At low energies, form factors are isotropic and do not affect angular distribution, while at high energies they are forward peaked. For effective sampling of final state a method proposed by D.E. Cullen [Cul95] has been implemented: form factor data were fitted and fitted parameters included in the *G4RayleighAngularGenerator*.

The sampling procedure is following:

1. atom is selected randomly according to cross section;

2.  $\cos \theta$  is sampled as proposed in [Cul95];
3. azimuthal angle is sampled uniformly.

### 7.2.3 JAEA Elastic Scattering Model

The  $\gamma$ -ray elastic scattering process in GEANT4 is a process that takes into consideration the different mechanisms in which a high-energy photon may be elastically scattered by an atom. These mechanisms include Rayleigh scattering, nuclear Thomson scattering, and Delbrück scattering. A new model developed by JAEA includes all these scattering mechanisms collectively as elastic scattering. A more detailed description can be found in Ref. [OH18].

#### Total cross section

The total cross section is given by [OH17]

$$\sigma = 4\pi \int_0^\pi \frac{d\sigma}{d\Omega} d\cos\theta$$

where

$$\frac{d\sigma}{d\Omega} = |A|^2 = |A^R + A^T + A^D|^2$$

Here  $A^R$  is the Rayleigh scattering amplitude,  $A^T$  is the nuclear Thomson scattering amplitude,  $A^D$  is the Delbrück scattering amplitude, and  $A$  is the resultant scattering amplitude. The resultant amplitude is a function of the incident photon energy  $E$ , scattering angle  $\theta$ , and the atomic number of the scattering atom  $Z$ . The total and differential cross sections are pre-calculated and prepared in data files for all elements with  $1 \leq Z \leq 100$  and  $10 \text{ keV} \leq E \leq 3 \text{ MeV}$  over the whole angular range. The structure of the data file is explained in Ref. [OH18].

#### Sampling of the Final States

Sampling procedure is as the following:

1. atom is selected randomly according to the total cross section.
2. angular distribution functions are retrieved from data files according to the incident photon energy and atomic number of the scattering atom.
3. polar angle is sampled based on the angular distribution function retrieved in 2.
4. azimuthal angle is sampled uniformly.

## 7.3 PhotoElectric Effect

The photoelectric effect is the ejection of an electron from a material after a photon has been absorbed by that material. In the standard model *G4PEEffectFluoModel* it is simulated by using a parameterized photon absorption cross section to determine the mean free path, atomic shell data to determine the energy of the ejected electron, and the K-shell angular distribution to sample the direction of the electron.

### 7.3.1 Cross Section

The parameterization of the photoabsorption cross section proposed by Biggs et al.[BL88] was used:

$$\sigma(Z, E_\gamma) = \frac{a(Z, E_\gamma)}{E_\gamma} + \frac{b(Z, E_\gamma)}{E_\gamma^2} + \frac{c(Z, E_\gamma)}{E_\gamma^3} + \frac{d(Z, E_\gamma)}{E_\gamma^4} \quad (7.3)$$

Using the least-squares method, a separate fit of each of the coefficients  $a, b, c, d$  to the experimental data was performed in several energy intervals [VMAPeal94, AGU+00]. As a rule, the boundaries of these intervals were equal to the corresponding photoabsorption edges. The cross section (and correspondingly mean free path) are discontinuous and must be computed ‘on the fly’ from the formula (7.3). Coefficients are defined for each Sandia table energy interval.

If photon energy is below the lowest Sandia energy for the material the cross section is computed for this lowest energy, so gamma is absorbed by photoabsorption at any energy. This approach is implemented coherently for models of photoelectric effect of GEANT4. As a result, any media become not transparent for low-energy gammas.

The class `G4StaticSandiaData.hh` contains the corrected data table for the cross-section applied according to the Sandia table with extra data taken from the Lebedev report. The coefficients are from Ref.[BL88].

The first energy intervals and coefficients for Xe are corrected to correspond perfectly to the data of J.B. West et al.[WM78]. The coefficients are checked to correspond perfectly to the data from B.L. Henke et al. [eal82]. The coefficients for Carbon are checked to correspond perfectly to the data of B.L. Henke et al. (as Xe). The first three energy intervals and coefficients for C are corrected to correspond perfectly to the data of Gallagher et al. [eal88]. The coefficients for Oxygen are checked to correspond perfectly to the data of B.L. Henke et al. (as Xe). The first two energy intervals and coefficients for O are corrected to correspond perfectly to the data of Gallagher et al. (as C). The coefficients for Hydrogen are checked to correspond perfectly to the data of B.L. Henke et al. (as Xe). The first three energy intervals and coefficients for H are corrected to correspond perfectly to the data of L.C. Lee et al.[eal77]. The first energy intervals and coefficients for He, Ne, Ar, and Kr are corrected to correspond perfectly to the data of G.V. Marr et al.[MW76].

The most of ionisation energies are taken from S. Ruben[Rub85]. Twenty-eight of the ionisation energies have been changed slightly to bring them up to date (changes from W.C. Martin and B.N. Taylor of the National Institute of Standards and Technology, January 1990). Here the ionisation energy is the least energy necessary to remove to infinity one electron from an atom of the element.

### 7.3.2 Final State

#### Choosing an Element

The binding energies of the shells depend on the atomic number  $Z$  of the material. In compound materials the  $i^{th}$  element is chosen randomly according to the probability:

$$Prob(Z_i, E_\gamma) = \frac{n_{ati}\sigma(Z_i, E_\gamma)}{\sum_i[n_{ati} \cdot \sigma_i(E_\gamma)]}.$$

## Shell

A quantum can be absorbed if  $E_\gamma > B_{shell}$  where the shell energies are taken from `G4AtomicShells` data: the closest available atomic shell is chosen. The photoelectron is emitted with kinetic energy:

$$T_{photoelectron} = E_\gamma - B_{shell}(Z_i)$$

## Theta Distribution of the Photoelectron

The polar angle of the photoelectron is sampled from the Sauter-Gavrila distribution (for K-shell) [Gav59], which is correct only to zero order in  $\alpha Z$ :

$$\frac{d\sigma}{d(\cos \theta)} \sim \frac{\sin^2 \theta}{(1 - \beta \cos \theta)^4} \left\{ 1 + \frac{1}{2} \gamma(\gamma - 1)(\gamma - 2)(1 - \beta \cos \theta) \right\}$$

where  $\beta$  and  $\gamma$  are the Lorentz factors of the photoelectron.

Introducing the variable transformation  $\nu = 1 - \cos \theta_e$ , as done in Penelope, the angular distribution can be expressed as

$$p(\nu) = (2 - \nu) \left[ \frac{1}{A + \nu} + \frac{1}{2} \beta \gamma (\gamma - 1)(\gamma - 2) \right] \frac{\nu}{(A + \nu)^3},$$

where

$$\gamma = 1 + \frac{E_e}{m_e c^2}, \quad A = \frac{1}{\beta} - 1,$$

$E_e$  is the electron energy,  $m_e$  its rest mass and  $\beta$  its velocity in units of the speed of light  $c$ .

Though the Sauter distribution, strictly speaking, is adequate only for ionisation of the K-shell by high-energy photons, in many practical simulations it does not introduce appreciable errors in the description of any photoionisation event, irrespective of the atomic shell or of the photon energy.

### 7.3.3 Relaxation

Atomic relaxations can be sampled using the de-excitation module of the low-energy sub-package `Atomic relaxation`. For that atomic de-excitation option should be activated. In the `physics_list` sub-library this activation is done automatically for `G4EmLivermorePhysics`, `G4EmPenelopePhysics`, `G4EmStandardPhysics_option3` and `G4EmStandardPhysics_option4`. For other standard physics constructors the de-excitation module is already added but is disabled. The simulation of fluorescence and Auger electron emission may be enabled for all geometry via UI commands:

```
/process/em/fluo true
/process/em/auger true
/process/em/pixe true
```

Please see further detailed information on atomic deexcitation [here](#).

There is a possibility to enable atomic deexcitation only for `G4Region` by its name:

```
/process/em/deexcitation myregion true true false
```

where three Boolean arguments enable/disable fluorescence, Auger electron production and PIXE (deexcitation induced by ionisation).

## 7.3.4 Penelope Model

### Total cross section

The total photoelectric cross section at a given photon energy  $E$  is calculated from the data [CHK89], as described in *Generic Calculation of Total Cross Sections*.

### Sampling of the final state

The subshell from which the electron is emitted is randomly selected according to the relative cross sections of subshells, determined at the energy  $E$  by interpolation of the data of Ref. [eal69]. The electron kinetic energy is the difference between the incident photon energy and the binding energy of the electron before the interaction in the sampled shell. The interaction leaves the atom in an excited state; the subsequent de-excitation is simulated as described in *Atomic relaxation*.

## 7.3.5 Livermore Model

Three model classes are available *G4LivermorePhotoElectricModel*, *G4LivermorePolarizedPhotoElectricModel*, and *G4LivermorePolarizedPhotoelectricGDMModel*.

### Cross sections

The total photoelectric and single shell cross-sections are based on either EPICS2014 or EPICS2017 data as described in *Low Energy Livermore Model*. They are tabulated from threshold to the low energy limit of the fit. Above it, they are parameterised in two different energy intervals, as following:

$$\sigma(E) = \frac{a_1}{E} + \frac{a_2}{E^2} + \frac{a_3}{E^3} + \frac{a_4}{E^4} + \frac{a_5}{E^5} + \frac{a_6}{E^6}.$$

The intervals ranges are set dynamically and they depend on the atomic number of the element and the corresponding k-shell binding energy. The accuracy of such parameterisation is better than 1%. To avoid tracking problems for very low-energy gamma the photoelectric cross section is not zero below first ionisation potential but stay constant, so all types of media are not transparent for gamma.

### Sampling of the final state

The incident photon is absorbed and an electron is emitted.

The electron kinetic energy is the difference between the incident photon energy and the binding energy of the electron before the interaction. The sub-shell, from which the electron is emitted, is randomly selected according to the relative cross-sections of all subshells, determined at the given energy. The interaction leaves the atom in an excited state. The deexcitation of the atom is simulated as described in *Atomic relaxation*.

## Angular distribution of the emitted photoelectron

For sampling of the direction of the emitted photoelectron by default the angular generator *G4SauterGavrilaAngularDistribution* is used. The algorithm is described in [PhotoElectric Effect](#).

For polarized models alternative angular generators are applied.

*G4LivermorePolarizedPhotoElectricModel* uses the *G4PhotoElectricAngularGeneratorPolarized* angular generator.

This model models the double differential cross section (for angles  $\theta$  and  $\phi$ ) and thus it is capable of account for polarization of the incident photon. The developed generator was based in the research of Sauter in 1931 [[RHPA64](#), [Sau31](#)]. Sauter's formula was recalculated by Gavrila in 1959 for the K-shell [[Gav59](#)] and in 1961 for the L-shells [[Gav61](#)]. These new double differential formulas have some limitations,  $\alpha Z \ll 1$  and have a range between  $0.1 < \beta < 0.99c$ .

The double differential photoeffect for K–shell can be written as [[Gav59](#)]:

$$\frac{d\sigma}{d\omega}(\theta, \phi) = \frac{4}{m^2} \alpha^6 Z^5 \frac{\beta^3 (1 - \beta^2)^3}{[1 - (1 - \beta^2)^{1/2}]} \left( F \left( 1 - \frac{\pi \alpha Z}{\beta} \right) + \pi \alpha Z G \right)$$

where

$$F = \frac{\sin^2 \theta \cos^2 \phi}{(1 - \beta \cos \theta)^4} - \frac{1 - (1 - \beta^2)^{1/2}}{2(1 - \beta^2)} \frac{\sin^2 \theta \cos^2 \phi}{(1 - \beta \cos \theta)^3} + \frac{[1 - (1 - \beta^2)^{1/2}]^2}{4(1 - \beta^2)^{3/2}} \frac{\sin^2 \theta}{(1 - \beta \cos \theta)^3}$$

$$G = \frac{[1 - (1 - \beta^2)^{1/2}]^{1/2}}{2^{7/2} \beta^2 (1 - \beta \cos \theta)^{5/2}} \left[ \frac{4\beta^2}{(1 - \beta^2)^{1/2}} \frac{\sin^2 \theta \cos^2 \phi}{1 - \beta \cos \theta} + \frac{4\beta}{1 - \beta^2} \cos \theta \cos^2 \phi - 4 \frac{1 - (1 - \beta^2)^{1/2}}{1 - \beta^2} (1 - \cos^2 \phi) - \beta^2 \frac{1 - (1 - \beta^2)^{1/2}}{1 - \beta^2} \frac{\sin^2 \theta}{1 - \beta \cos \theta} - 4\beta^2 \frac{1 - (1 - \beta^2)^{1/2}}{(1 - \beta^2)^{3/2}} - 4\beta \frac{[1 - (1 - \beta^2)^{1/2}]^2}{(1 - \beta^2)^{3/2}} \right] + \frac{1 - (1 - \beta^2)^{1/2}}{4\beta^2 (1 - \beta \cos \theta)^2} \left[ \frac{\beta}{1 - \beta^2} - \frac{2}{1 - \beta^2} \cos \theta \cos^2 \phi + \frac{1 - (1 - \beta^2)^{1/2}}{(1 - \beta^2)^{3/2}} \cos \theta - \beta \frac{1 - (1 - \beta^2)^{1/2}}{(1 - \beta^2)^{3/2}} \right]$$

where  $\beta$  is the electron velocity,  $\alpha$  is the fine–structure constant,  $Z$  is the atomic number of the material and  $\theta, \phi$  are the emission angles with respect to the electron initial direction.

The double differential photoeffect distribution for L1–shell is the same as for K–shell aside from a constant [[Gav61](#)]:

$$B = \xi \frac{1}{8}$$

where  $\xi$  is equal to 1 when working with unscreened Coulomb wave functions as it is done in this development.

Since the polarized Gavrila cross–section is a 2–dimensional non–factorized distribution an acceptance–rejection technique was the adopted [[LP03](#)]. For the Gavrila distribution, two functions were defined  $g_1(\phi)$  and  $g_2(\theta)$ :

$$g_1(\phi) = a$$

$$g_2(\theta) = \frac{\theta}{1 + c\theta^2}$$

such that:

$$A g_1(\phi) g_2(\theta) \geq \frac{d^2 \sigma}{d\phi d\theta}$$

where  $A$  is a global constant. The method used to calculate the distribution is the same as the one used in Low Energy 2BN Bremsstrahlung Generator, being the difference  $g_1(\phi) = a$ .

*G4LivermorePolarizedPhotoElectricGDModel* uses its own methods to produce the angular distribution of the photo-electron. The method to sample the azimuthal angle  $\phi$  is described in [DL06].

## 7.4 Compton scattering

The Compton scattering is an inelastic gamma scattering on atom with the ejection of an electron. In the standard sub-package two model *G4KleinNishinaCompton* and *G4KleinNishinaModel* are available. The first model is the fastest, in the second model atomic shell effects are taken into account.

### 7.4.1 Cross Section

When simulating the Compton scattering of a photon from an atomic electron, an empirical cross section formula is used, which reproduces the cross section data down to 10 keV:

$$\sigma(Z, E_\gamma) = \left[ P_1(Z) \frac{\log(1+2X)}{X} + \frac{P_2(Z) + P_3(Z)X + P_4(Z)X^2}{1+aX+bX^2+cX^3} \right].$$

where

$$\begin{aligned} Z &= \text{atomic number of the medium} \\ E_\gamma &= \text{energy of the photon} \\ X &= E_\gamma/mc^2 \\ m &= \text{electron mass} \\ P_i(Z) &= Z(d_i + e_iZ + f_iZ^2). \end{aligned}$$

The values of the parameters can be found within the method which computes the cross section per atom. A fit of the parameters was made to over 511 data points [JHHOverbo80, SI70] chosen from the intervals

$$1 \leq Z \leq 100$$

$$E_\gamma \in [10 \text{ keV}, 100 \text{ GeV}].$$

The accuracy of the fit was estimated to be

$$\frac{\Delta\sigma}{\sigma} = \begin{cases} \approx 10\% & \text{for } E_\gamma \simeq 10 \text{ keV} - 20 \text{ keV} \\ \leq 5 - 6\% & \text{for } E_\gamma > 20 \text{ keV} \end{cases}$$

To avoid sampling problems in the Compton process the cross section is set to zero at low-energy limit of cross section table, which is 100 eV in majority of EM Physics Lists.

### 7.4.2 Sampling the Final State

The Klein-Nishina differential cross section per atom is [KN29]:

$$\frac{d\sigma}{d\epsilon} = \pi r_e^2 \frac{m_e c^2}{E_0} Z \left[ \frac{1}{\epsilon} + \epsilon \right] \left[ 1 - \frac{\epsilon \sin^2 \theta}{1 + \epsilon^2} \right]$$

where

$$\begin{aligned} r_e &= \text{classical electron radius} \\ m_e c^2 &= \text{electron mass} \\ E_0 &= \text{energy of the incident photon} \\ E_1 &= \text{energy of the scattered photon} \\ \epsilon &= E_1/E_0 \end{aligned}$$

Assuming an elastic collision, the scattering angle  $\theta$  is defined by the Compton formula:

$$E_1 = E_0 \frac{m_e c^2}{m_e c^2 + E_0(1 - \cos \theta)}.$$

### Sampling the Photon Energy

The value of  $\epsilon$  corresponding to the minimum photon energy (backward scattering) is given by

$$\epsilon_0 = \frac{m_e c^2}{m_e c^2 + 2E_0},$$

hence  $\epsilon \in [\epsilon_0, 1]$ . Using the combined composition and rejection Monte Carlo methods described in [MC70, NHR85, BM60] one may set

$$\Phi(\epsilon) \simeq \left[ \frac{1}{\epsilon} + \epsilon \right] \left[ 1 - \frac{\epsilon \sin^2 \theta}{1 + \epsilon^2} \right] = f(\epsilon) \cdot g(\epsilon) = [\alpha_1 f_1(\epsilon) + \alpha_2 f_2(\epsilon)] \cdot g(\epsilon),$$

where

$$\begin{aligned} \alpha_1 &= \ln(1/\epsilon_0) & ; & \quad f_1(\epsilon) = 1/(\alpha_1 \epsilon) \\ \alpha_2 &= (1 - \epsilon_0^2)/2 & ; & \quad f_2(\epsilon) = \epsilon/\alpha_2. \end{aligned}$$

$f_1$  and  $f_2$  are probability density functions defined on the interval  $[\epsilon_0, 1]$ , and

$$g(\epsilon) = \left[ 1 - \frac{\epsilon}{1 + \epsilon^2} \sin^2 \theta \right]$$

is the rejection function  $\forall \epsilon \in [\epsilon_0, 1] \implies 0 < g(\epsilon) \leq 1$ . Given a set of 3 random numbers  $r, r', r''$  uniformly distributed on the interval  $[0, 1]$ , the sampling procedure for  $\epsilon$  is the following:

1. decide whether to sample from  $f_1(\epsilon)$  or  $f_2(\epsilon)$ : if  $r < \alpha_1/(\alpha_1 + \alpha_2)$  select  $f_1(\epsilon)$ , otherwise select  $f_2(\epsilon)$
2. sample  $\epsilon$  from the distributions corresponding to  $f_1$  or  $f_2$ :
  - for  $f_1 : \epsilon = \epsilon_0^{r'} \quad (\equiv \exp(-r' \alpha_1))$
  - for  $f_2 : \epsilon^2 = \epsilon_0^2 + (1 - \epsilon_0^2)r'$
3. calculate  $\sin^2 \theta = t(2 - t)$  where  $t \equiv (1 - \cos \theta) = m_e c^2 (1 - \epsilon)/(E_0 \epsilon)$
4. test the rejection function: if  $g(\epsilon) \geq r''$  accept  $\epsilon$ , otherwise go to step 1.

### Compute the Final State Kinematics

After the successful sampling of  $\epsilon$ , the polar angles of the scattered photon with respect to the direction of the parent photon are generated. The azimuthal angle,  $\phi$ , is generated isotropically and  $\theta$  is as defined in the previous section.

The momentum vector of the scattered photon,  $\overrightarrow{P_{\gamma 1}}$ , is then transformed into the World coordinate system. The kinetic energy and momentum of the recoil electron are then

$$T_{el} = E_0 - E_1$$

$$\overrightarrow{P_{el}} = \overrightarrow{P_{\gamma 0}} - \overrightarrow{P_{\gamma 1}}.$$

Doppler broadening of final electron momentum due to electron motion is implemented only in *G4KleinNishinaModel*. For that empirical electron density profile function is used.

### 7.4.3 Atomic shell effects

The differential cross-section described above is valid only for those collisions in which the energy of the recoil electron is large compared to its binding energy (which is ignored). In the alternative model (*G4KleinNishinaModel*) atomic shell effects are taken into account. For that a sampling of a shell is performed with the weight proportional to number of shell electrons. Electron energy distribution function is approximated via simplified form

$$F(T) = \exp(-T/E_b)/E_b,$$

where  $E_b$  is shell bound energy,  $T$  is the kinetic energy of the electron.

The value  $T$  is sampled and scattering is sampled in the rest frame of the electron according the algorithm described in the previous sub-chapter. After sampling an inverse Lorentz transformation to the laboratory frame is performed. Potential energy ( $E_b + T$ ) is subtracted from the scattered electron kinetic energy. If final electron energy becomes negative then sampling is repeated. Atomic relaxation are sampled if deexcitation module is enabled. Enabling of atomic relaxation for Compton scattering is performed in the same way as for photoelectric effect *Relaxation*.

### 7.4.4 Penelope Model

#### Total cross section

The total cross section of the Compton scattering process is determined from an analytical parameterization. For  $\gamma$  energy  $E$  greater than 5 MeV, the usual Klein-Nishina formula is used for  $\sigma(E)$ . For a more accurate parameterization is used, which takes into account atomic binding effects and Doppler broadening [eal96]:

$$\sigma(E) = 2\pi \int_{-1}^1 \frac{r_e^2}{2} \frac{E_C^2}{E^2} \left( \frac{E_C}{E} + \frac{E}{E_C} - \sin^2 \theta \right) \times \sum_{shells} f_i \Theta(E - U_i) n_i(p_z^{max}) d(\cos \theta) \quad (7.4)$$

where:

$r_e$  = classical radius of the electron;

$m_e$  = mass of the electron;

$\theta$  = scattering angle;

$E_C$  = Compton energy

$$= \frac{E}{1 + \frac{E}{m_e c^2} (1 - \cos \theta)}$$

$f_i$  = number of electrons in the  $i$ -th atomic shell;

$U_i$  = ionisation energy of the  $i$ -th atomic shell;

$\Theta$  = Heaviside step function;

$p_z$  = projection of the initial momentum of the electron in the direction of the scattering angle

$p_z^{max}$  = highest possible value of  $p_z$

$$= \frac{E(E - U_i)(1 - \cos \theta) - m_e c^2 U_i}{c \sqrt{2E(E - U_i)(1 - \cos \theta) + U_i^2}}.$$

Finally,

$$n_i(x) = \begin{cases} \frac{1}{2} e^{[\frac{1}{2} - (\frac{1}{2} - \sqrt{2}J_{i0}x)^2]} & \text{if } x < 0 \\ 1 - \frac{1}{2} e^{[\frac{1}{2} - (\frac{1}{2} + \sqrt{2}J_{i0}x)^2]} & \text{if } x > 0 \end{cases}$$

where  $J_{i0}$  is the value of the  $p_z$ -distribution profile  $J_i(p_z)$  for the i-th atomic shell calculated in  $p_z = 0$ . The values of  $J_{i0}$  for the different shells of the different elements are tabulated from the Hartree-Fock atomic orbitals of Ref. [eal75].

The integration of Eq.(7.4) is performed numerically using the 20-point Gaussian method. For this reason, the initialization of the Penelope Compton process is somewhat slower than the Low Energy Livermore process.

### Sampling of the final state

The polar deflection  $\cos \theta$  is sampled from the probability density function

$$P(\cos \theta) = \frac{r_e^2}{2} \frac{E_C^2}{E^2} \left( \frac{E}{E_C} + \frac{E}{E_C} - \sin^2 \theta \right) \sum_{\text{shells}} f_i \Theta(E - U_i) n_i(p_z^{\max})$$

(see Ref. [eal01] for details on the sampling algorithm). Once the direction of the emerging photon has been set, the active electron shell  $i$  is selected with relative probability equal to  $Z_i \Theta(E - U_i) n_i(p_z^{\max}(E, \theta))$ .

A random value of  $p_z$  is generated from the analytical Compton profile [eal75]. The energy of the emerging photon is

$$E' = \frac{E\tau}{1 - \tau t} \left[ (1 - \tau t \cos \theta) + \frac{p_z}{|p_z|} \sqrt{(1 - \tau t \cos \theta)^2 - (1 - \tau^2)(1 - t)} \right],$$

where

$$t = \left( \frac{p_z}{m_e c} \right)^2 \quad \text{and} \quad \tau = \frac{E_C}{E}.$$

The azimuthal scattering angle  $\phi$  of the photon is sampled uniformly in the interval  $(0, 2\pi)$ . It is assumed that the Compton electron is emitted with energy  $E_e = E - E' - U_i$ , with polar angle  $\theta_e$  and azimuthal angle  $\phi_e = \phi + \pi$ , relative to the direction of the incident photon. In this case  $\cos \theta_e$  is given by

$$\cos \theta_e = \frac{E - E' \cos \theta}{\sqrt{E^2 + E'^2 - 2EE' \cos \theta}}.$$

Since the active electron shell is known, characteristic x-rays and electrons emitted in the de-excitation of the ionized atom can also be followed. The de-excitation is simulated as described in [Atomic relaxation](#). For further details see [eal01].

## 7.4.5 Livermore Model

### Total Cross Section

The total cross section for the Compton scattering process is based on either EPDL97 or EPICS2017 data as described in [Low Energy Livermore Model](#), and determined from the data as described in [Generic Calculation of Total Cross Sections](#). To avoid sampling problems in the Compton process the cross section is set to zero at low-energy limit of cross section table, which is 100 eV in majority of EM Physics Lists.

## Sampling of the Final State

For low energy incident photons, the simulation of the Compton scattering process is performed according to the same procedure used for the “standard” Compton scattering simulation, with the addition that Hubbel’s atomic form factor [Hub97] or scattering function,  $SF$ , is taken into account. The angular and energy distribution of the incoherently scattered photon is then given by the product of the Klein-Nishina formula  $\Phi(\epsilon)$  and the scattering function,  $SF(q)$  [Cul95]

$$P(\epsilon, q) = \Phi(\epsilon) \times SF(q).$$

$\epsilon$  is the ratio of the scattered photon energy  $E'$ , and the incident photon energy  $E$ . The momentum transfer is given by  $q = \frac{1}{\lambda} \sin(\theta/2)$ , where  $\theta$  is the polar angle of the scattered photon with respect to the direction of the parent photon.  $\Phi(\epsilon)$  is given by

$$\Phi(\epsilon) \cong \left[ \frac{1}{\epsilon} + \epsilon \right] \left[ 1 - \frac{\epsilon}{1 + \epsilon^2} \sin^2 \theta \right].$$

The effect of the scattering function becomes significant at low energies, especially in suppressing forward scattering [Cul95].

The sampling method of the final state is based on composition and rejection Monte Carlo methods [MC70, NHR85, BM60], with the  $SF$  function included in the rejection function

$$g(\epsilon) = \left[ 1 - \frac{\epsilon}{1 + \epsilon^2} \sin^2 \theta \right] \times SF(q),$$

with  $0 < g(\epsilon) < Z$ . Values of the scattering functions at each momentum transfer,  $q$ , are obtained by interpolating the evaluated data for the corresponding atomic number,  $Z$ .

The polar angle  $\theta$  is deduced from the sampled  $\epsilon$  value. In the azimuthal direction, the angular distributions of both the scattered photon and the recoil electron are considered to be isotropic [NSJC04, Ste03].

Since the incoherent scattering occurs mainly on the outermost electronic subshells, the binding energies can be neglected, as stated in reference [NSJC04, Ste03]. The momentum vector of the scattered photon,  $\vec{P}_\gamma'$ , is transformed into the World coordinate system. The kinetic energy and momentum of the recoil electron are then

$$\begin{aligned} T_{el} &= E - E' \\ \vec{P}_{el} &= \vec{P}_\gamma' - \vec{P}_\gamma. \end{aligned}$$

## 7.4.6 Monash University Low Energy Model

### Introduction

The Monash Compton Scattering models, for polarised (*G4LowEPPolarizedComptonModel*) and non-polarised (*G4LowEPComptonModel*) photons, are an alternative set of Compton scattering models to those of Livermore and Penelope that were constructed using Ribberfors’ theoretical framework [eal96, Kip04, Rib75]. The limitation of the Livermore and Penelope models is that only the components of the pre-collision momentum of the target electron contained within the photon plane, two-dimensional plane defined by the incident and scattered photon, is incorporated into their scattering frameworks [eal01]. Both models are forced to constrain the ejected direction of the Compton electron into the photon plane as a result. The Monash Compton scattering models avoid this limitation through the use of a two-body fully relativistic three-dimensional scattering framework to ensure the conservation of energy and momentum in the Relativistic Impulse Approximation (RIA) [eal14, Mon29].

## Physics and Simulation

### Total Cross Section

The Monash Compton scattering models were built using the Livermore and Polarised Livermore Compton scattering models as templates. As a result the total cross section for the Compton scattering process and handling of polarisation effects mimic those outlined in [Low Energy Livermore Model](#).

### Sampling of the Final State

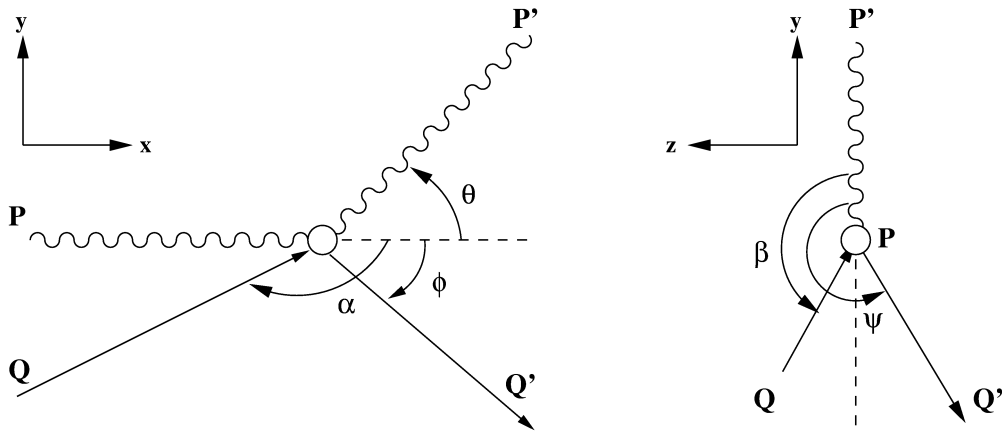


Fig. 7.1: Scattering diagram of atomic bound electron Compton scattering.  $\mathbf{P}$  is the incident photon momentum,  $\mathbf{Q}$  the electron pre-collision momentum,  $\mathbf{P}'$  the scattered photon momentum and  $\mathbf{Q}'$  the recoil electron momentum.

The scattering diagram seen in Fig. 7.1 outlines the basic principles of Compton scattering with an electron of non-zero pre-collision momentum in the RIA.

The process of sampling the target atom, atomic shell and target electron pre-collision momentum mimic that outlined in [Low Energy Livermore Model](#). After the sampling of these parameters the following four equations are utilised to model the scattered photon energy  $E'$ , recoil electron energy  $T_{el}$  and recoil electron polar and azimuthal angles ( $\phi$  and  $\psi$ ) with respect to the incident photon direction and out-going plane of polarisation:

$$E' = \frac{\gamma mc(c - u \cos \alpha)}{1 - \cos \theta + \frac{\gamma mc(c - u \cos \theta \cos \alpha - u \sin \theta \sin \alpha \cos \beta)}{E}},$$

$$T_{el} = E - E' - E_B,$$

$$\cos \phi = \frac{-Y \pm \sqrt{Y^2 - 4WZ}}{2W},$$

$$\cos \psi = \frac{C - B \cos \phi}{A \sin \phi},$$

where:

$$A = E' u' \sin \theta,$$

$$B = E' u' \cos \theta - Eu',$$

$$C = c(E' - E) - \frac{EE'}{\gamma' mc}(1 - \cos \theta),$$

$$\begin{aligned}
 D &= \frac{\gamma m E'}{c} (c - u \cos \theta \cos \alpha - u \sin \theta \cos \beta \sin \alpha) + m^2 c^2 (\gamma \gamma' - 1) - \gamma' m E', \\
 F &= \left( \gamma \gamma' m^2 u u' \cos \beta \sin \alpha - \frac{\gamma' m E' u'}{c} \sin \theta \right), \\
 G &= \gamma \gamma' m^2 u u' \sin \beta \sin \alpha, \\
 H &= \left( \gamma \gamma' m^2 u u' \cos \alpha - \frac{\gamma' m E'}{c} u' \cos \theta \right), \\
 W &= (F B - H A)^2 + G^2 A^2 + G^2 B^2, \\
 Y &= 2 ((A D - F C) (F B - H A) - G^2 B C), \\
 Z &= (A D - F C)^2 + G^2 (C^2 - A^2),
 \end{aligned}$$

and  $c$  is the speed of light,  $m$  is the rest mass of an electron,  $u$  is the speed of the target electron,  $u'$  is the speed of the recoil electron,  $\gamma = (1 - (u^2/c^2))^{-1/2}$  and  $\gamma' = (1 - (u'^2/c^2))^{-1/2}$ . Further information regarding the Monash Compton scattering models can be found in [eal14].

## 7.5 Gamma Conversion into $e^+e^-$ Pair

In the standard sub-package two models are available. The first model is implemented in the class *G4BetheHeitlerModel*, it was derived from Geant3 and is applicable below 100 GeV. In the second (*G4PairProductionRelModel*) Landau-Pomeranchuk-Migdal (LPM) effect is taken into account and this model can be applied for high energy gammas (above 100 MeV). Alternative models for moderate energies are *G4BetheHeitler5DModel*, *G4LivermoreGammaConversionModel*, and *G4PenelopeGammaConversionModel*.

### 7.5.1 Cross Section

According [JHHOverbo80], [Hei54] the total cross-section per atom for the conversion of a  $\gamma$  into an  $(e^+, e^-)$  pair has been parameterized as

$$\sigma(Z, E_\gamma) = Z(Z+1) \left[ F_1(X) + F_2(X) Z + \frac{F_3(X)}{Z} \right], \quad (7.5)$$

where  $E_\gamma$  is the incident gamma energy and  $X = \ln(E_\gamma/m_e c^2)$ . The functions  $F_n$  are given by

$$\begin{aligned}
 F_1(X) &= a_0 + a_1 X + a_2 X^2 + a_3 X^3 + a_4 X^4 + a_5 X^5 \\
 F_2(X) &= b_0 + b_1 X + b_2 X^2 + b_3 X^3 + b_4 X^4 + b_5 X^5 \\
 F_3(X) &= c_0 + c_1 X + c_2 X^2 + c_3 X^3 + c_4 X^4 + c_5 X^5,
 \end{aligned}$$

with the parameters  $a_i, b_i, c_i$  taken from a least-squares fit to the data [JHHOverbo80]. Their values can be found in the function which computes formula (7.5). This parameterization describes the data in the range

$$1 \leq Z \leq 100$$

and

$$E_\gamma \in [1.5 \text{ MeV}, 100 \text{ GeV}].$$

The accuracy of the fit was estimated to be  $\Delta \sigma/\sigma \leq 5\%$  with a mean value of  $\approx 2.2\%$ . Above 100 GeV the cross section is constant. Below  $E_{low} = 1.5$  MeV the extrapolation

$$\sigma(E) = \sigma(E_{low}) \cdot \left( \frac{E - 2m_e c^2}{E_{low} - 2m_e c^2} \right)^2$$

is used.

In a given material the mean free path,  $\lambda$ , for a photon to convert into an  $(e^+, e^-)$  pair is

$$\lambda(E_\gamma) = \left( \sum_i n_{ati} \cdot \sigma(Z_i, E_\gamma) \right)^{-1}$$

where  $n_{ati}$  is the number of atoms per volume of the  $i^{th}$  element of the material.

### Corrected Bethe-Heitler Cross Section

As written in [Hei54], the Bethe-Heitler formula corrected for various effects is

$$\begin{aligned} \frac{d\sigma(Z, \epsilon)}{d\epsilon} = & \alpha r_e^2 Z [Z + \xi(Z)] \left\{ [\epsilon^2 + (1 - \epsilon)^2] \left[ \Phi_1(\delta(\epsilon)) - \frac{F(Z)}{2} \right] \right. \\ & \left. + \frac{2}{3} \epsilon (1 - \epsilon) \left[ \Phi_2(\delta(\epsilon)) - \frac{F(Z)}{2} \right] \right\} \end{aligned} \quad (7.6)$$

where  $\alpha$  is the fine-structure constant and  $r_e$  the classical electron radius. Here  $\epsilon = E/E_\gamma$ ,  $E_\gamma$  is the energy of the photon and  $E$  is the total energy carried by one particle of the  $(e^+, e^-)$  pair. The kinematical limits of  $\epsilon$  are therefore

$$\frac{m_e c^2}{E_\gamma} = \epsilon_0 \leq \epsilon \leq 1 - \epsilon_0.$$

### Screening Effect

The *screening variable*,  $\delta$ , is a function of  $\epsilon$

$$\delta(\epsilon) = \frac{136}{Z^{1/3}} \frac{\epsilon_0}{\epsilon(1 - \epsilon)},$$

and measures the ‘impact parameter’ of the projectile. Two screening functions are introduced in the Bethe-Heitler formula:

$$\begin{aligned} \text{for } \delta \leq 1 \quad \Phi_1(\delta) &= 20.867 - 3.242\delta + 0.625\delta^2 \\ \Phi_2(\delta) &= 20.209 - 1.930\delta - 0.086\delta^2 \\ \text{for } \delta > 1 \quad \Phi_1(\delta) &= \Phi_2(\delta) = 21.12 - 4.184 \ln(\delta + 0.952). \end{aligned}$$

Because the formula (7.6) is symmetric under the exchange  $\epsilon \leftrightarrow (1 - \epsilon)$ , the range of  $\epsilon$  can be restricted to

$$\epsilon \in [\epsilon_0, 1/2].$$

### Born Approximation

The Bethe-Heitler formula is calculated with plane waves, but Coulomb waves should be used instead. To correct for this, a *Coulomb correction function* is introduced in the Bethe-Heitler formula :

$$\begin{aligned} \text{for } E_\gamma < 50 \text{ MeV} : \quad F(z) &= 8/3 \ln Z \\ \text{for } E_\gamma \geq 50 \text{ MeV} : \quad F(z) &= 8/3 \ln Z + 8f_c(Z) \end{aligned}$$

with

$$f_c(Z) = (\alpha Z)^2 \left[ \frac{1}{1 + (\alpha Z)^2} + 0.20206 - 0.0369(\alpha Z)^2 + 0.0083(\alpha Z)^4 - 0.0020(\alpha Z)^6 + \dots \right].$$

It should be mentioned that, after these additions, the cross section becomes negative if

$$\delta > \delta_{max}(\epsilon_1) = \exp \left[ \frac{42.24 - F(Z)}{8.368} \right] - 0.952.$$

This gives an additional constraint on  $\epsilon$  :

$$\delta \leq \delta_{max} \implies \epsilon \geq \epsilon_1 = \frac{1}{2} - \frac{1}{2} \sqrt{1 - \frac{\delta_{min}}{\delta_{max}}}$$

where

$$\delta_{min} = \delta \left( \epsilon = \frac{1}{2} \right) = \frac{136}{Z^{1/3}} 4\epsilon_0$$

has been introduced. Finally the range of  $\epsilon$  becomes

$$\epsilon \in [\epsilon_{min} = \max(\epsilon_0, \epsilon_1), 1/2].$$

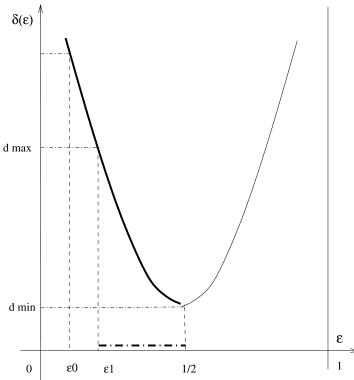


Fig. 7.2: Calculation of  $\epsilon$  for gamma conversion.

### Gamma Conversion in the Electron Field

The electron cloud gives an additional contribution to pair creation, proportional to  $Z$  (instead of  $Z^2$ ). This is taken into account through the expression

$$\xi(Z) = \frac{\ln(1440/Z^{2/3})}{\ln(183/Z^{1/3}) - f_c(Z)}.$$

### Factorization of the Cross Section

$\epsilon$  is sampled using the techniques of ‘composition+rejection’, as treated in [MC70, BM60, FN78]. First, two auxiliary screening functions should be introduced:

$$F_1(\delta) = 3\Phi_1(\delta) - \Phi_2(\delta) - F(Z)$$

$$F_2(\delta) = \frac{3}{2}\Phi_1(\delta) - \frac{1}{2}\Phi_2(\delta) - F(Z)$$

It can be seen that  $F_1(\delta)$  and  $F_2(\delta)$  are decreasing functions of  $\delta$ ,  $\forall \delta \in [\delta_{min}, \delta_{max}]$ . They reach their maximum for  $\delta_{min} = \delta(\epsilon = 1/2)$ :

$$F_{10} = \max F_1(\delta) = F_1(\delta_{min})$$

$$F_{20} = \max F_2(\delta) = F_2(\delta_{min}).$$

After some algebraic manipulations the formula (7.6) can be written:

$$\frac{d\sigma(Z, \epsilon)}{d\epsilon} = \alpha r_e^2 Z [Z + \xi(Z)] \frac{2}{9} \left[ \frac{1}{2} - \epsilon_{min} \right] [N_1 f_1(\epsilon) g_1(\epsilon) + N_2 f_2(\epsilon) g_2(\epsilon)], \quad (7.7)$$

where

$$N_1 = \left[ \frac{1}{2} - \epsilon_{min} \right]^2 F_{10} \quad f_1(\epsilon) = \frac{3}{\left[ \frac{1}{2} - \epsilon_{min} \right]^3} \left[ \frac{1}{2} - \epsilon \right]^2 \quad g_1(\epsilon) = \frac{F_1(\epsilon)}{F_{10}}$$

$$N_2 = \frac{3}{2} F_{20} \quad f_2(\epsilon) = \text{const} = \frac{1}{\left[ \frac{1}{2} - \epsilon_{min} \right]} \quad g_2(\epsilon) = \frac{F_2(\epsilon)}{F_{20}}.$$

$f_1(\epsilon)$  and  $f_2(\epsilon)$  are probability density functions on the interval  $\epsilon \in [\epsilon_{min}, 1/2]$  such that

$$\int_{\epsilon_{min}}^{1/2} f_i(\epsilon) d\epsilon = 1,$$

and  $g_1(\epsilon)$  and  $g_2(\epsilon)$  are valid rejection functions:  $0 < g_i(\epsilon) \leq 1$ .

## 7.5.2 Final State

The differential cross section depends on the atomic number  $Z$  of the material in which the interaction occurs. In a compound material the element  $i$  in which the interaction occurs is chosen randomly according to the probability

$$Prob(Z_i, E_\gamma) = \frac{n_{ati}\sigma(Z_i, E_\gamma)}{\sum_i [n_{ati} \cdot \sigma_i(E_\gamma)]}.$$

### Sampling the Energy

Given a triplet of uniformly distributed random numbers  $(r_a, r_b, r_c)$ :

1. use  $r_a$  to choose which decomposition term in (7.7) to use:

$$\begin{aligned} \text{if } r_a < N_1/(N_1 + N_2) &\rightarrow f_1(\epsilon) g_1(\epsilon) \\ \text{otherwise} &\rightarrow f_2(\epsilon) g_2(\epsilon) \end{aligned}$$

2. sample  $\epsilon$  from  $f_1(\epsilon)$  or  $f_2(\epsilon)$  with  $r_b$ :

$$\epsilon = \frac{1}{2} - \left( \frac{1}{2} - \epsilon_{min} \right) r_b^{1/3} \quad \text{or} \quad \epsilon = \epsilon_{min} + \left( \frac{1}{2} - \epsilon_{min} \right) r_b$$

3. reject  $\epsilon$  if  $g_1(\epsilon)$  or  $g_2(\epsilon) < r_c$

---

**Note:** below  $E_\gamma = 2$  MeV it is enough to sample  $\epsilon$  uniformly on  $[\epsilon_0, 1/2]$ , without rejection.

---

## Charge

The charge of each particle of the pair is fixed randomly.

## Polar Angle of the Electron or Positron

The polar angle of the electron (or positron) is defined with respect to the direction of the parent photon. The energy-angle distribution given by Tsai [Tsa74, Tsa77] is quite complicated to sample and can be approximated by a density function suggested by Urban [eal93] :

$$\forall u \in [0, \infty[ \quad f(u) = \frac{9a^2}{9+d} [u \exp(-au) + d u \exp(-3au)] \quad (7.8)$$

with

$$a = \frac{5}{8} \quad d = 27 \quad \text{and } \theta_{\pm} = \frac{mc^2}{E_{\pm}} u.$$

A sampling of the distribution (7.8) requires a triplet of random numbers such that

$$\text{if } r_1 < \frac{9}{9+d} \rightarrow u = \frac{-\ln(r_2 r_3)}{a} \quad \text{otherwise } u = \frac{-\ln(r_2 r_3)}{3a}.$$

The azimuthal angle  $\phi$  is generated isotropically. The  $e^+$  and  $e^-$  momenta are assumed to be coplanar with the parent photon. This information, together with energy conservation, is used to calculate the momentum vectors of the  $(e^+, e^-)$  pair and to rotate them to the global reference system.

### 7.5.3 Ultra-Relativistic Model

It is implemented in the class *G4PairProductionRelModel* and is configured above 80 GeV in all reference Physics lists. The cross section is computed using direct integration of differential cross section [Tsa74, Tsa77] and not its parameterisation described in *Cross Section*. LPM effect is taken into account in the same way as for bremsstrahlung *Bremsstrahlung of high-energy electrons*. Secondary generation algorithm is the same as in the standard Bethe-Heitler model.

### 7.5.4 Five-dimensional (5D) Bethe-Heitler gamma Conversion to $e^+e^-$

The *G4BetheHeitler5DModel* generates the five-dimensional Bethe-Heitler differential cross section, that is, with a correct target recoil momentum distribution both in magnitude and in direction (not necessarily in the pair plane). Therefore the pair itself is also kicked transversely and the photon direction does not lie in the pair plane. This model can be applied to both  $e^+e^-$  pairs (described here) and  $\mu^+\mu^-$  pair production (section *Five-dimensional (5D) Bethe-Heitler gamma Conversion to* ).

The nuclear or triplet conversion of polarized or non-polarized photons on atomic or isolated-charge targets can be performed.

## Total cross-section

The total cross section is inherited from the *G4BetheHeitlerModel* physics model. We take the nuclear, triplet share to be  $Z/(Z + 1), 1/(Z + 1)$ . Pure nuclear or pure triplet samples can also be generated.

## Sampling of the final state

In the conversion of a high-energy photon to an  $(e^+, e^-)$  pair by interaction with the field of a nucleus or of an electron of the detector, the final state contains three particles (electron, positron, “recoiling” target) and therefore is described in a five-dimensional phase space.

Bethe and Heitler (BH) have obtained an analytical expression of the differential cross section for non-polarized photons, in the first-order Born approximation and for a point-like, isolated charged-particle target [BH34]. The final-state variables are the azimuthal angles  $\phi_+$  and  $\phi_-$  and the polar angles  $\theta_+$  and  $\theta_-$  of the positron and of the electron, respectively, and the fraction of the photon energy carried away by the positron  $x_+ \equiv E_+/E$ .

The differential cross section for fully polarized photons has been obtained by [BM50], put in BH notation by [May51], after which [JR76] have corrected a numerical factor. At this first order of the Born development, only the linear photon polarization takes part to the differential cross section. Therefore no polarization is transferred to the final leptons.

The generation of the probability density function for this differential cross section is made difficult by the presence of a number of divergences, in  $1/(E_+ - P_+ \cos \theta_+)$ , in  $1/(E_- - P_- \cos \theta_-)$  and in  $1/q^4$ , where  $q$  is the “recoil” momentum, that is, the momentum transferred to the target. Further more the divergences take place in functions of several of the kinematical variables in which the differential cross section is written,  $(\phi_+, \phi_-, \theta_+, \theta_-, x_+)$ , that is, in a correlated way in their space.

The correlation issue is solved in the usual way in high-energy physics: each step is performed in the appropriate Lorentz frame. The interaction between the photon and the target is performed in the center-of-mass system (CMS); an object having an invariant mass  $\sqrt{s}$  is “created”. The invariant mass of the pair is taken at random. The “decay” of that  $\sqrt{s}$  thing to the recoiling target and to the pair is generated in the CMS. The decay of the pair to an actual electron and a positron is performed in the pair Lorentz frame. The two leptons are then boosted back to the CMS. Finally every body is boosted back to the laboratory frame. The variables used to do so are defined in Table 7.3.

Table 7.3: Kinematic variables and the Lorentz frame in which they are defined.

	variable	Lorentz frame
$\theta$	target and pair polar angle	CMS
$\mu$	$e^+e^-$ invariant mass	
$\theta_\ell$	$e^+$ and $e^-$ polar angle	pair frame
$\phi_\ell$	$e^+$ and $e^-$ azimuthal angle	pair frame
$\phi$	target and pair azimuthal angle	CMS

As the distribution of these variables still show divergences, a change of variables is used ( Table 7.4 ). The  $x_i, i = 1 \dots 5$  are taken flat. The photon-energy-dependent bounds of the  $x_1$  segment and the  $x_i$  distributions can be found in Fig. 1 and in Fig. 3, respectively, of [Ber18].

Table 7.4: Relationship between the generator variables,  $x_i, i = 1 \dots 5$ , and the kinematic variables, and their range.

$i$		Jacobian	$x_i$ range
1	$\cos \theta = \frac{y-1}{1+y}, y = \exp(x_1)$	$\frac{y}{(1+y)^2}$	$[x_{1l}, x_{1u}]$
2	$\mu = \mu_{min} \times (\mu_{range})^{x_2^2}$	$2x_2 \log(\mu_{range})\mu$	$[0, 1]$
3	$\cos \theta_\ell = x_3$	$ \sin \theta_\ell $	$[0, \pi]$
4	$\phi_\ell = x_4$	1	$[-\pi, \pi]$
5	$\phi = x_5$	1	$[-\pi, \pi]$

The algorithm is described with some detail in the documentation of the fortran demonstration model [Ber18] and its C++ implementation in [SB19]. The normalization of the phase space of the final state in this case of cascade “decays” is described in the PDG, Sect. 47.4.3 of [Gro16]. We get:

$$d\sigma = \frac{1}{(2\pi)^5} \frac{1}{32M\sqrt{s}E} |\mathcal{M}|^2 |p_+^*| |p_r| d\mu d\Omega_+^* d\Omega_r,$$

where  $(p_+^*, \Omega_+^*)$  refers to the kinematic variables of the positron in the pair rest frame and  $(p_r, \Omega_r)$  to the kinematic variables of the target recoil in the CMS. We obtain:

$$d\sigma = H \times X d\mu d\Omega_+^* d\Omega_r, \quad \text{with :} \quad H = \frac{-\alpha Z^2 r_0^2}{(2\pi)^2} \frac{|p_+^*| |p_r| m^2 M}{E^3 \sqrt{s} |\vec{q}|^4}.$$

For an unpolarized photon [BH34]:

$$\begin{aligned} X_u = & \left( \frac{p_+ \sin \theta_+}{E_+ - p_+ \cos \theta_+} \right)^2 (4E_-^2 - q^2) + \left( \frac{p_- \sin \theta_-}{E_- - p_- \cos \theta_-} \right)^2 (4E_+^2 - q^2) + \\ & \frac{2p_+ p_- \sin \theta_+ \sin \theta_- \cos(\phi_+ - \phi_-)}{(E_- - p_- \cos \theta_-)(E_+ - p_+ \cos \theta_+)} (4E_+ E_- + q^2 - 2E^2) - 2E^2 \frac{(p_+ \sin \theta_+)^2 + (p_- \sin \theta_-)^2}{(E_+ - p_+ \cos \theta_+)(E_- - p_- \cos \theta_-)}, \end{aligned} \quad (7.9)$$

For a polarized photon [BM50, JR76, May51]:

$$\begin{aligned} X_f = & 2 \left[ \left( 2E_+ \frac{p_- \sin \theta_- \cos \phi_-}{E_- - p_- \cos \theta_-} + 2E_- \frac{p_+ \sin \theta_+ \cos \phi_+}{E_+ - p_+ \cos \theta_+} \right)^2 - q^2 \left( \frac{p_- \sin \theta_- \cos \phi_-}{E_- - p_- \cos \theta_-} - \frac{p_+ \sin \theta_+ \cos \phi_+}{E_+ - p_+ \cos \theta_+} \right)^2 \right. \\ & \left. - E^2 \frac{(p_+ \sin \theta_+)^2 + (p_- \sin \theta_-)^2 + 2p_+ p_- \sin \theta_+ \sin \theta_- \cos(\phi_+ - \phi_-)}{(E_- - p_- \cos \theta_-)(E_+ - p_+ \cos \theta_+)} \right], \end{aligned} \quad (7.10)$$

with  $|\vec{q}|^2 = |\vec{p}_+ + \vec{p}_- - \vec{k}|^2$ .

In case the nucleus or the electron are not isolated but are part of an atom, the screening of the target field by the (other) electrons of the atom is described by a function of  $q^2$ , a coherent form factor [NFM34] for nuclear conversion, an incoherent form factor [WL39] for triplet conversion.

In contrast with the BH expressions taken at face value, for which the recoil energy is neglected and the electron energy is taken to be  $E_- = E - E_+$ , here a strict energy-momentum conservation is achieved.

A number of approximations are used:

- For triplet conversions, BH neglects the  $e - \gamma$  exchange diagrams, which might be an issue at low energy (see Table 1, Fig.3 and their discussion in [Mor67]).
- Landau-Pomeranchuk-Migdal (LPM) suppression effects at very high energies are neglected.
- The finite size of the nucleus is neglected.
- Any pre-existing non-zero momentum of the target prior to the conversion, such as in the case of Compton “Doppler” broadening, is not considered.

A number of verifications of the model have been performed by comparison with analytical expressions of the distribution of one of the kinematic variables, obtained in the past from partial integrations of the BH differential cross section. In particular the distribution of the pair opening angle is found [Ber13] to take its most probable value at the high-energy asymptotic value of 1.6 MeV rad [Ols63]. The *G4BetheHeitler5DModel* is the only gamma-conversion physics model for which the recoil momentum distribution is found [Ber13b, GB17b] to be compatible with the analytical expression of [JLS50]. See also the extended electromagnetic example *TestEm15* and its README.

The verification of the integral of the differential cross section over the full  $x_i, i = 1 \dots 5$  phase space can be found in Fig. 4 of [Ber18], for atomic targets (comparison with total cross section NIST data) and for isolated charges (comparison with total cross section asymptotic expressions).

The verification of the polarization properties of the model are addressed in Section 14.10.

## 7.5.5 Penelope Model

### Total cross section

The total cross section of the  $\gamma$  conversion process is determined from the data [BH87], as described in *Generic Calculation of Total Cross Sections*.

### Sampling of the final state

The energies  $E_-$  and  $E_+$  of the secondary electron and positron are sampled using the Bethe-Heitler cross section with the Coulomb correction, using the semiempirical model of Ref. [eal94]. If

$$\epsilon = \frac{E_- + m_e c^2}{E}$$

is the fraction of the  $\gamma$  energy  $E$  which is taken away from the electron,

$$\kappa = \frac{E}{m_e c^2} \quad \text{and} \quad a = \alpha Z,$$

the differential cross section, which includes a low-energy correction and a high-energy radiative correction, is

$$\frac{d\sigma}{d\epsilon} = r_e^2 a (Z + \eta) C_r \frac{2}{3} \left[ 2 \left( \frac{1}{2} - \epsilon \right)^2 \phi_1(\epsilon) + \phi_2(\epsilon) \right], \quad (7.11)$$

where:

$$\begin{aligned} \phi_1(\epsilon) &= \frac{7}{3} - 2 \ln(1 + b^2) - 6b \arctan(b^{-1}) \\ &\quad - b^2 [4 - 4b \arctan(b^{-1}) - 3 \ln(1 + b^{-2})] \\ &\quad + 4 \ln(R m_e c / \hbar) - 4f_C(Z) + F_0(\kappa, Z) \end{aligned}$$

and

$$\begin{aligned} \phi_2(\epsilon) &= \frac{11}{6} - 2 \ln(1 + b^2) - 3b \arctan(b^{-1}) \\ &\quad + \frac{1}{2} b^2 [4 - 4b \arctan(b^{-1}) - 3 \ln(1 + b^{-2})] \\ &\quad + 4 \ln(R m_e c / \hbar) - 4f_C(Z) + F_0(\kappa, Z), \end{aligned}$$

with

$$b = \frac{R m_e c}{\hbar} \frac{1}{2\kappa} \frac{1}{\epsilon(1-\epsilon)}.$$

In this case  $R$  is the screening radius for the atom  $Z$  (tabulated in [JHHOverbo80] for  $Z = 1$  to 92) and  $\eta$  is the contribution of pair production in the electron field (rather than in the nuclear field). The parameter  $\eta$  is approximated as

$$\eta = \eta_\infty (1 - e^{-v}),$$

where

$$\begin{aligned} v &= (0.2840 - 0.1909a) \ln(4/\kappa) + (0.1095 + 0.2206a) \ln^2(4/\kappa) \\ &\quad + (0.02888 - 0.04269a) \ln^3(4/\kappa) + (0.002527 + 0.002623) \ln^4(4/\kappa) \end{aligned}$$

and  $\eta_\infty$  is the contribution for the atom  $Z$  in the high-energy limit and is tabulated for  $Z = 1$  to 92 in Ref. [JHHOverbo80]. In the Eq.(7.11), the function  $f_C(Z)$  is the high-energy Coulomb correction of Ref. [eal54], given by

$$f_C(Z) = a^2[(1 + a^2)^{-1} + 0.202059 - 0.03693a^2 + 0.00835a^4 - 0.00201a^6 + 0.00049a^8 - 0.00012a^{10} + 0.00003a^{12}];$$

$C_r = 1.0093$  is the high-energy limit of Mork and Olsen's radiative correction (see Ref. [JHHOverbo80]);  $F_0(\kappa, Z)$  is a Coulomb-like correction function, which has been analytically approximated as [eal01]

$$\begin{aligned} F_0(\kappa, Z) = & (-0.1774 - 12.10a + 11.18a^2)(2/\kappa)^{1/2} \\ & + (8.523 + 73.26a - 44.41a^2)(2/\kappa) \\ & - (13.52 + 121.1a - 96.41a^2)(2/\kappa)^{3/2} \\ & + (8.946 + 62.05a - 63.41a^2)(2/\kappa)^2. \end{aligned}$$

The kinetic energy  $E_+$  of the secondary positron is obtained as

$$E_+ = E - E_- - 2m_e c^2.$$

The polar angles  $\theta_-$  and  $\theta_+$  of the directions of movement of the electron and the positron, relative to the direction of the incident photon, are sampled from the leading term of the expression obtained from high-energy theory (see Ref.[eal69])

$$p(\cos \theta_\pm) = a(1 - \beta_\pm \cos \theta_\pm)^{-2},$$

where  $a$  is the a normalization constant and  $\beta_\pm$  is the particle velocity in units of the speed of light. As the directions of the produced particles and of the incident photon are not necessarily coplanar, the azimuthal angles  $\phi_-$  and  $\phi_+$  of the electron and of the positron are sampled independently and uniformly in the interval  $(0, 2\pi)$ .

### 7.5.6 Livermore Model

*G4LivermoreGammaConversionModel* and *G4LivermoreGammaConversion5DModel* are available.

#### Total cross-section

The total cross-section of the Gamma Conversion process is based on either EPDL97 or EPICS2017 data as described in *Low Energy Livermore Model*, and determined from the data as described in *Generic Calculation of Total Cross Sections*.

#### Sampling of the final state

For low energy incident photons, the simulation of the Gamma Conversion final state is performed according to *Final State*.

The secondary  $e^\pm$  energies are sampled using the Bethe-Heitler cross-sections with Coulomb correction.

The Bethe-Heitler differential cross-section with the Coulomb correction for a photon of energy  $E$  to produce a pair with one of the particles having energy  $\epsilon E$  ( $\epsilon$  is the fraction of the photon energy carried by one particle of the pair) is given by [FN78]:

$$\frac{d\sigma(Z, E, \epsilon)}{d\epsilon} = \frac{r_0^2 \alpha Z (Z + \xi(Z))}{E^2} \left[ (\epsilon^2 + (1 - \epsilon)^2) \left( \Phi_1(\delta) - \frac{F(Z)}{2} \right) + \frac{2}{3} \epsilon (1 - \epsilon) \left( \Phi_2(\delta) - \frac{F(Z)}{2} \right) \right] \quad (7.12)$$

where  $\Phi_i(\delta)$  are the screening functions depending on the screening variable  $\delta$  [eal93].

The value of  $\epsilon$  is sampled using composition and rejection Monte Carlo methods [MC70, eal93, BM60].

After the successful sampling of  $\epsilon$ , the process generates the polar angles of the electron with respect to an axis defined along the direction of the parent photon. The electron and the positron are assumed to have a symmetric angular distribution. The energy-angle distribution is given by [Tsa74, Tsa77]:

$$\frac{d\sigma}{dpd\Omega} = \frac{2\alpha^2 e^2}{\pi km^4} \left[ \left( \frac{2x(1-x)^2}{(1+l)} - \frac{12lx(1-x)}{(1+l)^4} \right) (Z^2 + Z) + \left( \frac{2x^2 - 2x + 1}{(1+l)^2} + \frac{4lx(1-x)}{(1+l)^4} \right) (X - 2Z^2 f((\alpha Z)^2)) \right]$$

where  $k$  is the photon energy,  $p$  the momentum and  $E$  the energy of the electron of the  $e^\pm$  pair  $x = E/k$  and  $l = E^2\theta^2/m^2$ . The sampling of this cross-section is obtained according to [eal93].

The azimuthal angle  $\phi$  is generated isotropically.

This information together with the momentum conservation is used to calculate the momentum vectors of both decay products and to transform them to the GEANT4 coordinate system. The choice of which particle in the pair is the electron/positron is made randomly.

## 7.6 Livermore Triple Gamma Conversion

The class *G4BoldyshevTripletModel* was developed to simulate the pair production by linearly polarized gamma rays on electrons. For the angular distribution of electron recoil we used the cross section by Vinokurov and Kuraev [VK72, VK73] using the Borsellino diagrams in the high energy. For energy distribution for the pair, we used Boldyshev [VFBP94] formula that differs only in the normalization from Wheeler-Lamb. The cross sections include a cut off for momentum detections [MLI11].

### 7.6.1 Method

The first step is sample the probability to have an electron recoil with momentum greater than a threshold define by the user (by default, this value is  $p_0 = 1$  in units of  $mc$ ). This probability is

$$\sigma(p \geq p_0) = \alpha r_0^2 \left( \frac{82}{27} - \frac{14}{9} \ln X_0 + \frac{4}{15} X_0 - 0.0348 X_0^2 + 0.008 X_0^3 - \dots \right)$$

$$X_0 = 2 \left( \sqrt{p_0^2 + 1} \right).$$

Since that total cross section is  $\sigma = \alpha r_0^2 \left( \frac{28}{4} \ln 2E_\gamma - \frac{218}{27} \right)$ , if a random number is  $\xi \geq \sigma(p \geq p_0)/\sigma$  we create the electron recoil, otherwise we deposited the energy in the local point.

### 7.6.2 Azimuthal Distribution for Electron Recoil

The expression for the differential cross section is composed of two terms which express the azimuthal dependence as follows:

$$d\sigma = d\sigma^{(t)} - P d\sigma^{(l)} \cos(2\varphi)$$

Where both  $d\sigma_{(t)}$  and  $d\sigma_{(l)}$  are independent of the azimuthal angle,  $\varphi$ , referred to an origin chosen in the direction of the polarization vector  $\vec{P}$  of the incoming photons.

### 7.6.3 Monte Carlo Simulation of the Asymptotic Expression

In this section we present an algorithm for Monte Carlo simulation of the asymptotic expressions calculate by Vinokurov et.al. [VK72, VK73].

We must generate random values of  $\theta$  and  $\varphi$  distributed with probability proportional to the following function  $f(\theta, \varphi)$ , for  $\theta$  restricted inside of its allowed interval value [VFBP94] (0, or  $\theta_{max}(p_0)$ ):

$$f(\theta, \varphi) = \frac{\sin \theta}{\cos^3 \theta} (F_1(\theta) - P \cos(2\varphi) F_P(\theta)) \quad (7.13)$$

$$F_1(\theta) = 1 - \frac{1 - 5 \cos^2 \theta}{\cos \theta} \ln(\cot(\theta/2))$$

$$F_P(\theta) = 1 - \frac{\sin^2 \theta}{\cos \theta} \ln(\cot(\theta/2))$$

As we will see, for  $\theta < \pi/2$ ,  $F_1$  is several times greater than  $F_P$ , and since both are positive, it follows that  $f$  is positive for any possible value of  $P$  ( $0 \leq P \leq 1$ ).

Since  $F_1$  is the dominant term in expression (7.13), it is more convenient to begin developing the algorithm of this term, belonging to the unpolarized radiation.

### 7.6.4 Algorithm for Non Polarized Radiation

The algorithm was described in Ref.[DI09]. We must generate random values of  $\theta$  between 0 and  $\theta_{max} = \arccos\left(\frac{E_1 - mc^2}{p_0} + mc^2 \frac{E_1 + mc^2}{E_\gamma p_0}\right)$ ,  $E_1 = \sqrt{p_0^2 + (mc^2)^2}$  distributed with probability proportional to the following function  $f_1(\theta)$ :

$$f_1(\theta) = \frac{\sin(\theta)}{\cos^3(\theta)} \left( 1 - \frac{1 - 5 \cos^2(\theta)}{\cos(\theta)} \ln(\cot(\theta/2)) \right)$$

$$= \frac{\sin(\theta)}{\cos^3(\theta)} \times F_1(\theta)$$

By substitution  $\cos(\theta/2) = \sqrt{\frac{1+\cos\theta}{2}}$  and  $\sin(\theta/2) = \sqrt{\frac{1-\cos\theta}{2}}$ , we can write:

$$\ln(\cot(\theta/2)) = \frac{1}{2} \ln\left(\frac{1 + \cos\theta}{1 - \cos\theta}\right)$$

In order to simulate the  $f_1$  function, it may be decomposed in two factors: the first,  $\sin(\theta)/\cos^3(\theta)$ , easy to integrate, and the other,  $F_1(\theta)$ , which may constitute a reject function, on despite of its  $\theta = 0$  divergence. This is possible because they have very low probability. On other hand,  $\theta$  values near to zero are not useful to measure polarization because for those angles it is very difficult to determine the azimuthal distribution (due to multiple scattering).

Then, it is possible to choose some value of  $\theta_0$ , small enough that it is not important that the sample is fitted rigorously for  $\theta < \theta_0$ , and at the same time  $F_1(\theta_0)$  is not too big.

Modifying  $F_1$  so that it is constant for  $\theta \leq \theta_0$ , we may obtain an adequate reject function. Doing this, we introduce only a very few missed points, all of which lie totally outside of the interesting region.

Expanding  $F_1$  for great values of  $\theta$ , we see it is proportional to  $\cos^2\theta$ :

$$F_1(\theta) \rightarrow \frac{14}{3} \cos^2 \theta \left( 1 + \frac{33}{35} \cos^2 \theta + \dots \right), \quad \text{if } \theta \rightarrow \pi/2$$

Thus, it is evident that  $F_1$  divided by  $\cos^2(\theta)$  will be a better reject function, because it tends softly to a some constant value ( $14/3 = 4,666\dots$ ) for large  $\theta$ , whereas its behavior is not affected in the region of small  $\theta$ , where  $\cos(\theta) \rightarrow 1$ .

It seems adequate to choose  $\theta_0$  near  $5^\circ$ , and, after some manipulation looking for round numbers we obtain:

$$\frac{F_1(4.47^\circ)}{\cos^2(4.47^\circ)} \cong 14.00$$

Finally we define a reject function:

$$\begin{aligned} r(\theta) &= \frac{1}{14} \frac{F_1(\theta)}{\cos^2(\theta)} = \frac{1}{14 \cos^2(\theta)} \\ &\quad \left( 1 - \frac{1-5 \cos^2(\theta)}{2 \cos(\theta)} \ln \left( \frac{1+\cos\theta}{1-\cos\theta} \right) \right) ; \quad \text{for } \theta \geq 4.47^\circ \\ r(\theta) &= 1 \quad ; \quad \text{for } \theta \leq 4.47^\circ \end{aligned}$$

Now we have a probability distribution function (PDF) for  $\theta$ ,  $p(\theta) = C f_1(\theta)$ , expressed as a product of another PDF,  $\pi(\theta)$ , by the reject function:

$$p(\theta) = C f_1(\theta) \cong C' \pi(\theta) r(\theta)$$

where  $C$  is the normalization constant belonging to the function  $p(\theta)$ .

One must note that the equality between  $C \sim f_1(\theta)$  and  $C' \pi(\theta) r(\theta)$  is not exact for small values of  $\theta$ , where we have truncated the infinity of  $F_1(\theta)$ ; but this can not affect appreciably the distribution because  $f_1 \rightarrow 0$  there. Now the PDF  $\pi(\theta)$  is:

$$\pi(\theta) = C_\pi \frac{14 \sin(\theta)}{\cos(\theta)}$$

From the normalization, the constant  $C_\pi$  results:

$$C_\pi = \frac{1}{14 \int_0^{\theta_{max}} \frac{\sin(\theta)}{\cos(\theta)} d\theta} = \frac{-1}{14 \ln(\cos(\theta_{max}))} = \frac{1}{7} \ln\left(\frac{\omega}{4m}\right)$$

And the relation with  $C$  is given by:

$$C = \frac{1}{\int_0^{\theta_{max}} f_1(\theta) d\theta} \cong C' C_\pi$$

Then we obtain the cumulative probability by integrating the PDF  $\pi(\theta)$ :

$$P_\pi = \int_0^\theta \pi(\theta') d\theta' = \frac{-14 \ln(\cos(\theta))}{7 \ln\left(\frac{\omega}{4m}\right)} = \frac{2 \ln(\cos(\theta))}{\ln(4m/\omega)}$$

Finally for the Monte Carlo method we sample a random number  $\xi_1$  (between 0 and 1), which is defined as equal to  $P_\pi$ , and obtain the corresponding  $\theta$  value:

$$\xi_1 = \frac{2 \ln(\cos \theta)}{\ln(4m/\omega)} = \frac{\ln(\cos \theta)}{\ln(\cos(\theta_{max}))}$$

Then,

$$\theta = \arccos \left( \left( \frac{4m}{\omega} \right)^{\frac{\xi_1}{2}} \right)$$

Another random number  $\xi_2$  is sampled for the reject process: the  $\theta$  value is accepted if  $\xi_2 \leq r(\theta)$ , and reject in the contrary.

For  $\theta \leq 4.47^\circ$  all values are accepted. It happens automatically without any modification in the algorithm previously defined (it is not necessary to define the truncated reject function for  $\theta < \theta_0$ ).

## 7.6.5 Algorithm for Polarized Radiation

The algorithm was also described in Ref.[DI09]. As we have seen, the azimuthal dependence of the differential cross section is given by the expressions and:

$$f(\theta, \varphi) = \frac{\sin \theta}{\cos^3 \theta} (F_1(\theta) - P \cos(2\varphi) F_P(\theta))$$

$$F_P(\theta) = 1 - \frac{\sin^2 \theta}{\cos \theta} \ln(\cot(\theta/2))$$

We see that  $F_P$  tends to 1 at  $\theta = 0$ , decreases monotonically to 0 as  $\theta$  goes to  $\pi/2$ .

Furthermore, the expansion of  $F_P$  for  $\theta$  near  $\pi/2$  shows that it is proportional to  $\cos^2(\theta)$ , in virtue of which  $F_P/\cos^2(\theta)$  tends to a non null value,  $2/3$ . This value is exactly 7 times the value of  $F_1/\cos^2(\theta)$ .

This suggests applying the combination method, rearranging the whole function as follows:

$$f(\theta, \varphi) = \tan(\theta) \frac{F_1(\theta)}{\cos^2(\theta)} \left( 1 - \cos(2\varphi) P \frac{F_P(\theta)}{F_1(\theta)} \right)$$

and the normalized PDF  $p(\theta, \varphi)$ :

$$p(\theta, \varphi) = C f(\theta, \varphi)$$

where  $C$  is the normalization constant

$$\frac{1}{C} = \int_0^{\theta_{\max}} \int_0^{2\pi} f(\theta, \varphi) d\varphi d\theta$$

Taking account that  $\int_0^{2\pi} \cos(2\varphi) d\varphi = 0$ , then:

$$\frac{1}{C} = 2\pi \int_0^{\theta_{\max}} \tan(\theta) \frac{F_1(\theta)}{\cos^2(\theta)} d\theta$$

On the other hand the integration over the azimuthal angle is straightforward and gives:

$$q(\theta) = \int_0^{2\pi} p(\theta, \varphi) d\varphi = 2\pi C \tan(\theta) \frac{F_1(\theta)}{\cos^2(\theta)}$$

and  $p(\varphi/\theta)$  is the conditional probability of  $\varphi$  given  $\theta$ :

$$p(\varphi/\theta) = \frac{p(\theta, \varphi)}{q(\theta)} = \frac{1}{2\pi C \tan(\theta) \frac{F_1(\theta)}{\cos^2(\theta)}} C \frac{\sin(\theta)}{\cos^3(\theta)} F_1(\theta) \left( 1 - \cos(2\varphi) P \frac{F_P(\theta)}{F_1(\theta)} \right)$$

$$= \frac{1}{2\pi} \left( 1 - \cos(2\varphi) P \frac{F_P(\theta)}{F_1(\theta)} \right)$$

Now the procedure consists of sampling  $\theta$  according the PDF  $q(\theta)$ ; then, for each value of  $\theta$  we must sample  $\varphi$  according to the conditional PDF  $p(\varphi/\theta)$ .

Knowing that  $F_1$  is several times greater than  $F_P$ , we can see that  $P F_1/F_P \ll 1$ , and thus  $p(\varphi/\theta)$  maintains a nearly constant value slightly diminished in some regions of  $\varphi$ . Consequently the  $\varphi$  sample can be done directly by the rejecting method with high efficiency.

On the other hand,  $q(\theta)$  is the same function  $p(\theta)$  given by , that is the PDF for unpolarized radiation,  $q(\theta) \cong C' \pi(\theta) r(\theta)$ , so we can sample  $\theta$  with exactly the same procedure, specified as follows:

1. We begin sampling a random number  $\xi_1$  and obtain  $\theta$  from :

$$\theta = \arccos \left( \left( \frac{4m}{\omega} \right)^{\frac{\xi_1}{2}} \right)$$

2. Then we sample a second random number  $\xi_2$  and accept the values of  $\theta$  if  $\xi_2 \leq r(\theta)$ , where  $r(\theta)$  is the same expression defined before:

$$r(\theta) = \frac{1}{14 \cos^2 \theta} \left[ 1 - \frac{1 - 5 \cos^2 \theta}{2 \cos \theta} \ln \left( \frac{1 + \cos \theta}{1 - \cos \theta} \right) \right]$$

For  $\theta \geq 4.47^\circ$  and for  $\theta \leq 4.47^\circ$  all values are accepted.

3. Now we sample  $\varphi$ . According to the reject method, we sample a third random number  $\xi_3$  (which is defined as  $\varphi/2\pi$ ) and evaluate the reject function (which is essentially):

$$\begin{aligned} r_\theta(\xi_3) &= \frac{1}{2\pi} \left( 1 - \cos(4\pi\xi_3) P \frac{F_P(\theta)}{F_1(\theta)} \right) \\ &= \frac{1}{2\pi} \left( 1 - \cos(4\pi\xi_3) P \frac{\cos \theta - \sin^2 \theta \ln(\cot(\frac{\theta}{2}))}{\cos \theta - (1 - 5 \cos^2 \theta) \ln(\cot(\frac{\theta}{2}))} \right) \end{aligned}$$

4. Finally, with a fourth random number  $\xi_4$ , we accept the values of  $\varphi = 2\pi\xi_4$  if  $\xi_4 \leq r_\theta(\xi_3)$ .

## 7.6.6 Sampling of Energy

For the electron recoil we calculate the energy from the maximum momentum that can take according with the  $\theta$  angle

$$E_r = mc^2 \frac{(S + (mc^2)^2)}{D2}$$

where

$$\begin{aligned} S &= mc^2 (2E_{gamma} + mc^2) \\ D2 &= 4Smc^2 + (S - (mc^2)^2)^2 \sin^2(\theta) \end{aligned}$$

The remnant energy is distributed to the pair according to the Boldyshev formula [VFBP94] ( $x$  is the fraction of the positron energy):

$$\begin{aligned} 2\pi \frac{d^2\sigma}{dxd\phi} &= 2\alpha r_0^2 \{ [1 - 2x(1-x)] J_1(p_0) + 2x(1-x) [1 - P \cos(\phi)] J_2(p_0) \} \\ J_1(p_0) &= 2 \left( t \frac{\cosh(t)}{\sinh(t)} - \ln(2 \sinh(t)) \right) \\ J_2(p_0) &= -\frac{2}{3} \ln(2 \sinh(t)) + t \frac{\cosh(t)}{\sinh(t)} + \frac{\sinh(t) - t \cosh^3(t)}{3 \sinh^3(t)}, \quad \sinh(2t) = p_0 \end{aligned}$$

This distribution can be written like a PDF for  $x$ :

$$P(x) = N(1 - Jx(1-x))$$

where  $N$  is a normalization constant and  $J = (J_1 - J_2)/J_1$ . Solving for  $x$  ( $\xi$  is a random number):

$$\begin{aligned} x &= \frac{c_1^{1/3}}{2J} + \frac{J-4}{2c_1^{1/3}} + \frac{1}{2} \\ c_1 &= (-6 + 12r_n + J + 2a) J^2 \\ a &= \left( \frac{16 - 3J - 36r_n + 36Jr_n^2 + 6r_n J^2}{J} \right) \\ r_n &= \xi \left( 1 - \frac{J}{6} \right) \end{aligned}$$

## 7.7 Gamma Conversion into Lepton Pair

The class *G4GammaConversionToMuons* simulates the process of gamma conversion into muon or tau-lepton pairs. The same formulas are used in both case with the only difference in lepton mass. So, below only the case of the muon pair production will be described. Given the photon energy and  $Z$  and  $A$  of the material in which the photon converts, the probability for the conversions to take place is calculated according to a parameterized total cross section. Next, the sharing of the photon energy between the  $\mu^+$  and  $\mu^-$  is determined. Finally, the directions of the muons are generated. Details of the implementation are given below and can be also found in [BKK02].

### 7.7.1 Cross Section and Energy Sharing

Muon pair production on atomic electrons,  $\gamma + e \rightarrow e + \mu^+ + \mu^-$ , has a threshold of  $2m_\mu(m_\mu + m_e)/m_e \approx 43.9$  GeV. Up to several hundred GeV this process has a much lower cross section than the corresponding process on the nucleus. At higher energies, the cross section on atomic electrons represents a correction of  $\sim 1/Z$  to the total cross section.

For the approximately elastic scattering considered here, momentum, but no energy, is transferred to the nucleon. The photon energy is fully shared by the two muons according to

$$E_\gamma = E_\mu^+ + E_\mu^-$$

or in terms of energy fractions

$$x_+ = \frac{E_\mu^+}{E_\gamma}, \quad x_- = \frac{E_\mu^-}{E_\gamma}, \quad x_+ + x_- = 1.$$

The differential cross section for electromagnetic pair creation of muons in terms of the energy fractions of the muons is

$$\frac{d\sigma}{dx_+} = 4 \alpha Z^2 r_c^2 \left(1 - \frac{4}{3} x_+ x_-\right) \log(W), \quad (7.14)$$

where  $Z$  is the charge of the nucleus,  $r_c$  is the classical radius of the particles which are pair produced (here muons) and

$$W = W_\infty \frac{1 + (D_n \sqrt{e} - 2) \delta / m_\mu}{1 + B Z^{-1/3} \sqrt{e} \delta / m_e} \quad (7.15)$$

where

$$W_\infty = \frac{B Z^{-1/3}}{D_n} \frac{m_\mu}{m_e} \quad \delta = \frac{m_\mu^2}{2 E_\gamma x_+ x_-} \quad \sqrt{e} = 1.6487 \dots$$

For hydrogen,  $B = 202.4$  and  $D_n = 1.49$ . For all other nuclei,  $B = 183$  and  $D_n = 1.54 A^{0.27}$ .

These formulae are obtained from the differential cross section for muon bremsstrahlung [KKP95] by means of crossing relations. The formulae take into account the screening of the field of the nucleus by the atomic electrons in the Thomas-Fermi model, as well as the finite size of the nucleus, which is essential for the problem under consideration. The above parameterization gives good results for  $E_\gamma \gg m_\mu$ . The fact that it is approximate close to threshold is of little practical importance. Close to threshold, the cross section is small and the few low energy muons produced will not travel very far. The cross section calculated from Eq.(7.14) is positive for  $E_\gamma > 4m_\mu$  and

$$x_{\min} \leq x \leq x_{\max} \quad \text{with} \quad x_{\min} = \frac{1}{2} - \sqrt{\frac{1}{4} - \frac{m_\mu}{E_\gamma}} \quad x_{\max} = \frac{1}{2} + \sqrt{\frac{1}{4} - \frac{m_\mu}{E_\gamma}},$$

except for very asymmetric pair-production, close to threshold, which can easily be taken care of by explicitly setting  $\sigma = 0$  whenever  $\sigma < 0$ .

Note that the differential cross section is symmetric in  $x_+$  and  $x_-$  and that

$$x_+ x_- = x - x^2$$

where  $x$  stands for either  $x_+$  or  $x_-$ . By defining a constant

$$\sigma_0 = 4 \alpha Z^2 r_c^2 \log(W_\infty) \quad (7.16)$$

the differential cross section Eq.(7.14) can be rewritten as a normalized and symmetric as function of  $x$ :

$$\frac{1}{\sigma_0} \frac{d\sigma}{dx} = \left[ 1 - \frac{4}{3} (x - x^2) \right] \frac{\log W}{\log W_\infty}. \quad (7.17)$$

This is shown in Fig. 7.3 for several elements and a wide range of photon energies. The asymptotic differential cross section for  $E_\gamma \rightarrow \infty$

$$\frac{1}{\sigma_0} \frac{d\sigma_\infty}{dx} = 1 - \frac{4}{3} (x - x^2)$$

is also shown.

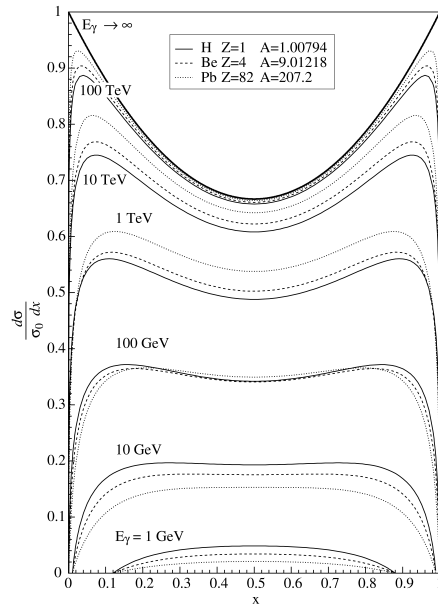


Fig. 7.3: Normalized differential cross section for pair production as a function of  $x$ , the energy fraction of the photon energy carried by one of the leptons in the pair. The function is shown for three different elements, hydrogen, beryllium and lead, and for a wide range of photon energies.

## 7.7.2 Parameterization of the Total Cross Section

The total cross section is obtained by integration of the differential cross section Eq.(7.14), that is

$$\sigma_{\text{tot}}(E_\gamma) = \int_{x_{\min}}^{x_{\max}} \frac{d\sigma}{dx_+} dx_+ = 4 \alpha Z^2 r_c^2 \int_{x_{\min}}^{x_{\max}} \left( 1 - \frac{4}{3} x_+ x_- \right) \log(W) dx_+. \quad (7.18)$$

$W$  is a function of  $(x_+, E_\gamma)$  and  $(Z, A)$  of the element (see Eq.(7.15)). Numerical values of  $W$  are given in Table 7.5.

Table 7.5: Numerical values of  $W$  for  $x_+ = 0.5$  for different elements.

$E_\gamma$ [GeV]	W for H	W for Be	W for Cu	W for Pb
1	2.11	1.594	1.3505	5.212
10	19.4	10.85	6.803	43.53
100	191.5	102.3	60.10	332.7
1000	1803	919.3	493.3	1476.1
10000	11427	4671	1824	1028.1
$\infty$	28087	8549	2607	1339.8

Values of the total cross section obtained by numerical integration are listed in Table 7.6 for four different elements. Units are in  $\mu\text{barn}$ , where  $1 \mu\text{barn} = 10^{-34} \text{ m}^2$ .

Table 7.6: Numerical values for the total cross section

$E_\gamma$ [GeV]	$\sigma_{\text{tot}}$ , H [ $\mu\text{barn}$ ]	$\sigma_{\text{tot}}$ , Be [ $\mu\text{barn}$ ]	$\sigma_{\text{tot}}$ , Cu [ $\mu\text{barn}$ ]	$\sigma_{\text{tot}}$ , Pb [ $\mu\text{barn}$ ]
1	0.01559	0.1515	5.047	30.22
10	0.09720	1.209	49.56	334.6
100	0.1921	2.660	121.7	886.4
1000	0.2873	4.155	197.6	1476
10000	0.3715	5.392	253.7	1880
$\infty$	0.4319	6.108	279.0	2042

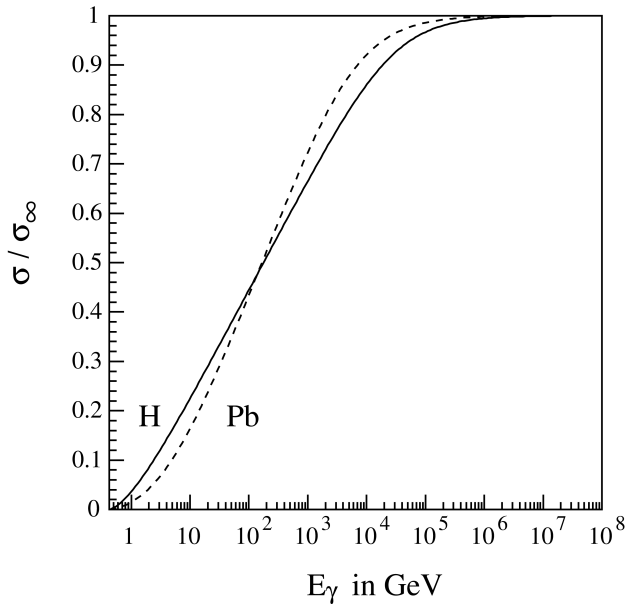


Fig. 7.4: Total cross section for the Bethe-Heitler process  $\gamma \rightarrow \mu^+ \mu^-$  as a function of the photon energy  $E_\gamma$  in hydrogen and lead, normalized to the asymptotic cross section  $\sigma_\infty$ .

Well above threshold, the total cross section rises about linearly in  $\log(E_\gamma)$  with the slope

$$W_M = \frac{1}{4 D_n \sqrt{e} m_\mu}$$

until it saturates due to screening at  $\sigma_\infty$ . Fig. 7.4 shows the normalized cross section where

$$\sigma_\infty = \frac{7}{9} \sigma_0 \quad \text{and} \quad \sigma_0 = 4 \alpha Z^2 r_c^2 \log(W_\infty) .$$

Numerical values of  $W_M$  are listed in Table 7.7.

Table 7.7: Numerical values of  $W_M$ .

Element	$W_M$ [1/GeV]
H	0.963169
Be	0.514712
Cu	0.303763
Pb	0.220771

The total cross section can be parameterized as

$$\sigma_{\text{par}} = \frac{28 \alpha Z^2 r_c^2}{9} \log(1 + W_M C_f E_g) , \quad (7.19)$$

with

$$E_g = \left(1 - \frac{4m_\mu}{E_\gamma}\right)^t (W_{\text{sat}}^s + E_\gamma^s)^{1/s} .$$

and

$$W_{\text{sat}} = \frac{W_\infty}{W_M} = B Z^{-1/3} \frac{4\sqrt{e} m_\mu^2}{m_e} .$$

The threshold behavior in the cross section was found to be well approximated by  $t = 1.479 + 0.00799 D_n$  and the saturation by  $s = -0.88$ . The agreement at lower energies is improved using an empirical correction factor, applied to the slope  $W_M$ , of the form

$$C_f = \left[ 1 + 0.04 \log \left( 1 + \frac{E_c}{E_\gamma} \right) \right] ,$$

where

$$E_c = \left[ -18. + \frac{4347.}{B Z^{-1/3}} \right] \text{ GeV} .$$

A comparison of the parameterized cross section with the numerical integration of the exact cross section shows that the accuracy of the parametrization is better than 2%, as seen in Fig. 7.5.

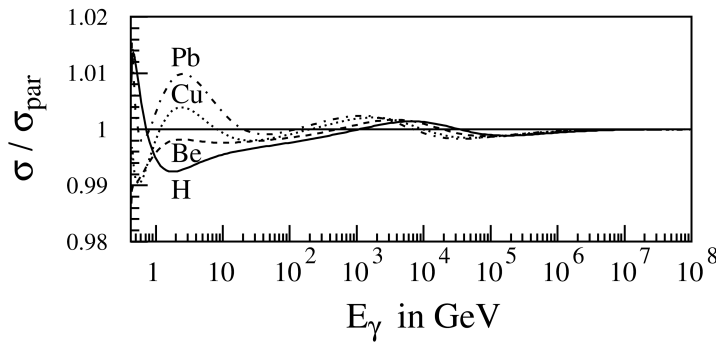


Fig. 7.5: Ratio of numerically integrated and parametrized total cross sections as a function of  $E_\gamma$  for hydrogen, beryllium, copper and lead.

### 7.7.3 Multi-differential Cross Section and Angular Variables

The angular distributions are based on the multi-differential cross section for lepton pair production in the field of the Coulomb center

$$\frac{d\sigma}{dx_+ du_+ du_- d\varphi} = \frac{4Z^2\alpha^3}{\pi} \frac{m_\mu^2}{q^4} u_+ u_- \times \\ \times \left\{ \frac{u_+^2 + u_-^2}{(1+u_+^2)(1+u_-^2)} - 2x_+ x_- \left[ \frac{u_+^2}{(1+u_+^2)^2} + \frac{u_-^2}{(1+u_-^2)^2} \right] - \frac{2u_+ u_- (1-2x_+ x_-) \cos \varphi}{(1+u_+^2)(1+u_-^2)} \right\}. \quad (7.20)$$

Here

$$u_\pm = \gamma_\pm \theta_\pm \quad , \quad \gamma_\pm = \frac{E_\mu^\pm}{m_\mu} \quad , \quad q^2 = q_\parallel^2 + q_\perp^2 \quad , \quad (7.21)$$

where

$$q_\parallel^2 = q_{\min}^2 (1 + x_- u_+^2 + x_+ u_-^2)^2, \\ q_\perp^2 = m_\mu^2 [(u_+ - u_-)^2 + 2u_+ u_- (1 - \cos \varphi)]. \quad (7.22)$$

$q^2$  is the square of the momentum  $\mathbf{q}$  transferred to the target and  $q_\parallel^2$  and  $q_\perp^2$  are the squares of the components of the vector  $\mathbf{q}$ , which are parallel and perpendicular to the initial photon momentum, respectively. The minimum momentum transfer is  $q_{\min} = m_\mu^2 / (2E_\gamma x_+ x_-)$ . The muon vectors have the components

$$\begin{aligned} \mathbf{p}_+ &= p_+ (\sin \theta_+ \cos(\varphi_0 + \varphi/2), \sin \theta_+ \sin(\varphi_0 + \varphi/2), \cos \theta_+), \\ \mathbf{p}_- &= p_- (-\sin \theta_- \cos(\varphi_0 - \varphi/2), -\sin \theta_- \sin(\varphi_0 - \varphi/2), \cos \theta_-), \end{aligned} \quad (7.23)$$

where  $p_\pm = \sqrt{E_\pm^2 - m_\mu^2}$ . The initial photon direction is taken as the  $z$ -axis. The cross section of Eq.(7.20) does not depend on  $\varphi_0$ . Because of azimuthal symmetry,  $\varphi_0$  can simply be sampled at random in the interval  $(0, 2\pi)$ .

Eq.(7.20) is too complicated for efficient Monte Carlo generation. To simplify, the cross section is rewritten to be symmetric in  $u_+$ ,  $u_-$  using a new variable  $u$  and small parameters  $\xi, \beta$ , where  $u_\pm = u \pm \xi/2$  and  $\beta = u \varphi$ . When higher powers in small parameters are dropped, the differential cross section in terms of  $u, \xi, \beta$  becomes

$$\frac{d\sigma}{dx_+ d\xi d\beta u du} = \frac{4Z^2\alpha^3}{\pi} \frac{m_\mu^2}{\left(q_\parallel^2 + m_\mu^2(\xi^2 + \beta^2)\right)^2} \times \\ \times \left\{ \xi^2 \left[ \frac{1}{(1+u^2)^2} - 2x_+ x_- \frac{(1-u^2)^2}{(1+u^2)^4} \right] + \frac{\beta^2(1-2x_+ x_-)}{(1+u^2)^2} \right\}, \quad (7.24)$$

where, in this approximation,

$$q_\parallel^2 = q_{\min}^2 (1+u^2)^2.$$

For Monte Carlo generation, it is convenient to replace  $(\xi, \beta)$  by the polar coordinates  $(\rho, \psi)$  with  $\xi = \rho \cos \psi$  and  $\beta = \rho \sin \psi$ . Integrating Eq.(7.24) over  $\psi$  and using symbolically  $du^2 = 2u du$  yields

$$\frac{d\sigma}{dx_+ d\rho du^2} = \frac{4Z^2\alpha^3}{m_\mu^2} \frac{\rho^3}{(q_\parallel^2/m_\mu^2 + \rho^2)^2} \left\{ \frac{1-x_+ x_-}{(1+u^2)^2} - \frac{x_+ x_- (1-u^2)^2}{(1+u^2)^4} \right\}. \quad (7.25)$$

Integration with logarithmic accuracy over  $\rho$  gives

$$\int \frac{\rho^3 d\rho}{(q_\parallel^2/m_\mu^2 + \rho^2)^2} \approx \int_{q_\parallel/m_\mu}^1 \frac{d\rho}{\rho} = \log \left( \frac{m_\mu}{q_\parallel} \right).$$

Within the logarithmic accuracy,  $\log(m_\mu/q_{\parallel})$  can be replaced by  $\log(m_\mu/q_{\min})$ , so that

$$\frac{d\sigma}{dx_+ du^2} = \frac{4Z^2\alpha^3}{m_\mu^2} \left\{ \frac{1-x_+x_-}{(1+u^2)^2} - \frac{x_+x_-(1-u^2)^2}{(1+u^2)^4} \right\} \log\left(\frac{m_\mu}{q_{\min}}\right).$$

Making the substitution  $u^2 = 1/t - 1$ ,  $du^2 = -dt/t^2$  gives

$$\frac{d\sigma}{dx_+ dt} = \frac{4Z^2\alpha^3}{m_\mu^2} [1 - 2x_+x_- + 4x_+x_-t(1-t)] \log\left(\frac{m_\mu}{q_{\min}}\right). \quad (7.26)$$

Atomic screening and the finite nuclear radius may be taken into account by multiplying the differential cross section determined by Eq.(7.24) with the factor

$$(F_a(q) - F_n(q))^2,$$

where  $F_a$  and  $F_n$  are atomic and nuclear form factors. Please note that after integrating Eq.(7.25) over  $\rho$ , the  $q$ -dependence is lost.

#### 7.7.4 Procedure for the Generation of $\mu^+\mu^-$ Pairs

Given the photon energy  $E_\gamma$  and  $Z$  and  $A$  of the material in which the  $\gamma$  converts, the probability for the conversions to take place is calculated according to the parametrized total cross section Eq.(7.19). The next step, determining how the photon energy is shared between the  $\mu^+$  and  $\mu^-$ , is done by generating  $x_+$  according to Eq.(7.14). The directions of the muons are then generated via the auxilliary variables  $t$ ,  $\rho$ ,  $\psi$ . In more detail, the final state is generated by the following five steps, in which  $R_{1,2,3,4,\dots}$  are random numbers with a flat distribution in the interval  $[0,1]$ . The generation proceeds as follows.

1. Sampling of the positive muon energy  $E_\mu^+ = x_+ E_\gamma$ . This is done using the rejection technique.  $x_+$  is first sampled from a flat distribution within kinematic limits using

$$x_+ = x_{\min} + R_1(x_{\max} - x_{\min})$$

and then brought to the shape of Eq.(7.14) by keeping all  $x_+$  which satisfy

$$\left(1 - \frac{4}{3}x_+x_-\right) \frac{\log(W)}{\log(W_{\max})} < R_2.$$

Here  $W_{\max} = W(x_+ = 1/2)$  is the maximum value of  $W$ , obtained for symmetric pair production at  $x_+ = 1/2$ . About 60% of the events are kept in this step. Results of a Monte Carlo generation of  $x_+$  are illustrated in Fig. 7.6. The shape of the histograms agrees with the differential cross section illustrated in Fig. 7.3.

2. Generate  $t (= \frac{1}{\gamma^2\theta^2+1})$ . The distribution in  $t$  is obtained from Eq.(7.26) as

$$f_1(t) dt = \frac{1 - 2x_+x_- + 4x_+x_-t(1-t)}{1 + C_1/t^2} dt, \quad 0 < t \leq 1.$$

with form factors taken into account by

$$C_1 = \frac{(0.35 A^{0.27})^2}{x_+x_- E_\gamma/m_\mu}.$$

In the interval considered, the function  $f_1(t)$  will always be bounded from above by

$$\max[f_1(t)] = \frac{1 - x_+x_-}{1 + C_1}.$$

For small  $x_+$  and large  $E_\gamma$ ,  $f_1(t)$  approaches unity, as shown in Fig. 7.7.

The Monte Carlo generation is done using the rejection technique. About 70% of the generated numbers are kept in this step. Generated  $t$ -distributions are shown in Fig. 7.9.

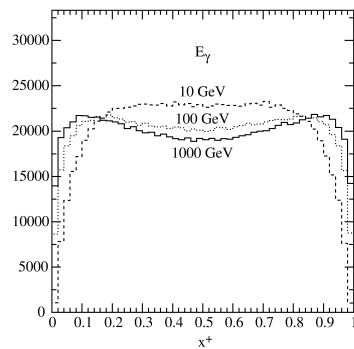


Fig. 7.6: Histogram of generated  $x_+$  distributions for beryllium at three different photon energies. The total number of entries at each energy is  $10^6$ .

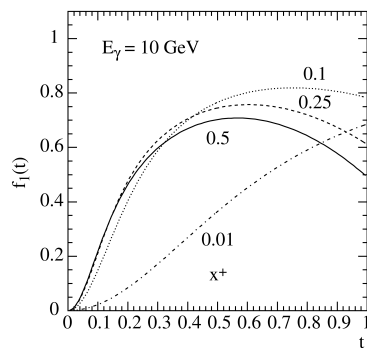


Fig. 7.7: The function  $f_1(t)$  at  $E_\gamma = 10$  GeV in beryllium for different values of  $x_+$ .

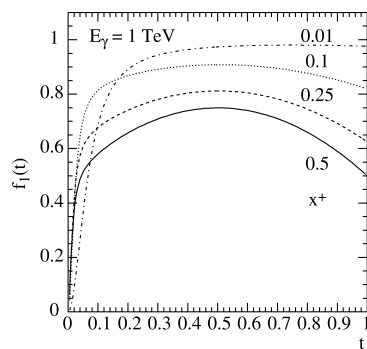


Fig. 7.8: The function  $f_1(t)$  at  $E_\gamma = 1$  TeV in beryllium for different values of  $x_+$ .

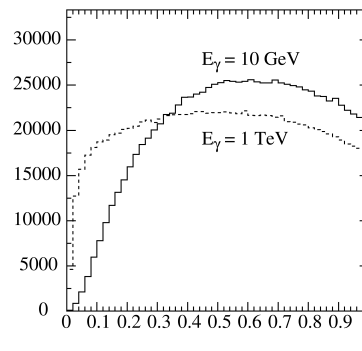


Fig. 7.9: Histograms of generated  $t$  distributions for  $E_\gamma = 10 \text{ GeV}$  (solid line) and  $E_\gamma = 100 \text{ GeV}$  (dashed line) with  $10^6$  events each.

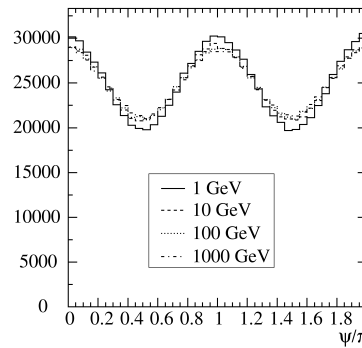


Fig. 7.10: Histograms of generated  $\psi$  distributions for beryllium at four different photon energies.

3. Generate  $\psi$  by the rejection technique using  $t$  generated in the previous step for the frequency distribution

$$f_2(\psi) = \left[ 1 - 2x_+x_- + 4x_+x_-t(1-t)(1+\cos(2\psi)) \right], \quad 0 \leq \psi \leq 2\pi.$$

The maximum of  $f_2(\psi)$  is

$$\max[f_2(\psi)] = 1 - 2x_+x_- [1 - 4t(1-t)].$$

Generated distributions in  $\psi$  are shown in Fig. 7.10.

4. Generate  $\rho$ . The distribution in  $\rho$  has the form

$$f_3(\rho) d\rho = \frac{\rho^3 d\rho}{\rho^4 + C_2}, \quad 0 \leq \rho \leq \rho_{\max},$$

where

$$\rho_{\max}^2 = \frac{1.9}{A^{0.27}} \left( \frac{1}{t} - 1 \right),$$

and

$$C_2 = \frac{4}{\sqrt{x_+x_-}} \left[ \left( \frac{m_\mu}{2E_\gamma x_+x_- t} \right)^2 + \left( \frac{m_e}{183 Z^{-1/3} m_\mu} \right)^2 \right]^2.$$

The  $\rho$  distribution is obtained by a direct transformation applied to uniform random numbers  $R_i$  according to

$$\rho = [C_2(\exp(\beta R_i) - 1)]^{1/4},$$

where

$$\beta = \log \left( \frac{C_2 + \rho_{\max}^4}{C_2} \right).$$

Generated distributions of  $\rho$  are shown in Fig. 7.11

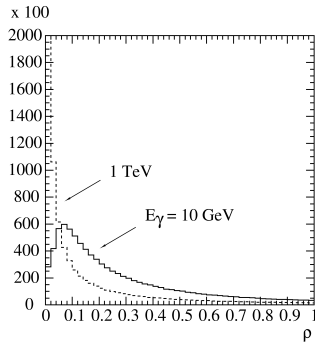


Fig. 7.11: Histograms of generated  $\rho$  distributions for beryllium at two different photon energies. The total number of entries at each energy is  $10^6$ .

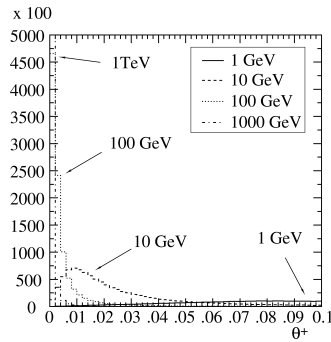


Fig. 7.12: Histograms of generated  $\theta_+$  distributions at different photon energies.

5. Calculate  $\theta_+, \theta_-$  and  $\varphi$  from  $t, \rho, \psi$  with

$$\gamma_{\pm} = \frac{E_{\mu}^{\pm}}{m_{\mu}} \quad \text{and} \quad u = \sqrt{\frac{1}{t} - 1}. \quad (7.27)$$

according to

$$\theta_+ = \frac{1}{\gamma_+} \left( u + \frac{\rho}{2} \cos \psi \right), \quad \theta_- = \frac{1}{\gamma_-} \left( u - \frac{\rho}{2} \cos \psi \right) \quad \text{and} \quad \varphi = \frac{\rho}{u} \sin \psi.$$

The muon vectors can now be constructed from Eq.(7.23), where  $\varphi_0$  is chosen randomly between 0 and  $2\pi$ . Fig. 7.12 shows distributions of  $\theta_+$  at different photon energies (in beryllium). The spectra peak around  $1/\gamma$  as expected.

The most probable values are  $\theta_+ \sim m_{\mu}/E_{\mu}^+ = 1/\gamma_+$ . In the small angle approximation used here, the values of  $\theta_+$  and  $\theta_-$  can in principle be any positive value from 0 to  $\infty$ . In the simulation, this may lead (with a very small probability, of the order of  $m_{\mu}/E_{\gamma}$ ) to unphysical events in which  $\theta_+$  or  $\theta_-$  is greater than  $\pi$ . To avoid this, a limiting angle  $\theta_{\text{cut}} = \pi$  is introduced, and the angular sampling repeated, whenever  $\max(\theta_+, \theta_-) > \theta_{\text{cut}}$ .

Fig. 7.13, Fig. 7.14 and Fig. 7.15 show distributions of the simulated angular characteristics of muon pairs in comparison with results of exact calculations. The latter were obtained by means of numerical integration of the squared

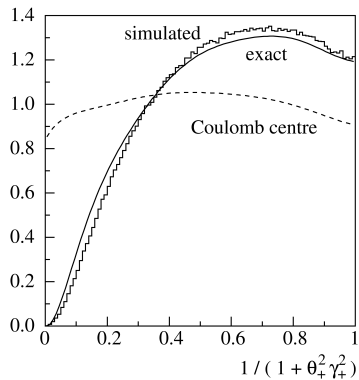


Fig. 7.13: Angular distribution of positive (or negative) muons. The solid curve represents the results of the exact calculations. The histogram is the simulated distribution. The angular distribution for pairs created in the field of the Coulomb centre (point-like target) is shown by the dashed curve for comparison.

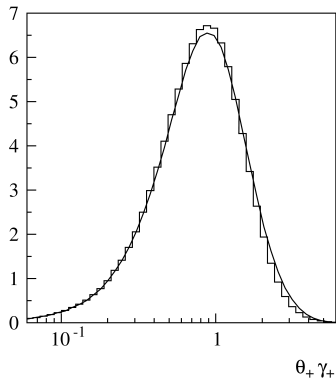


Fig. 7.14: Angular distribution in logarithmic scale. The curve corresponds to the exact calculations and the histogram is the simulated distribution.

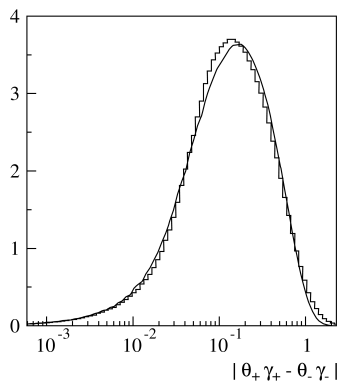


Fig. 7.15: Distribution of the difference of transverse momenta of positive and negative muons (with logarithmic x-scale).

matrix elements with respective nuclear and atomic form factors. All these calculations were made for iron, with  $E_\gamma = 10 \text{ GeV}$  and  $x_+ = 0.3$ . As seen from Fig. 7.13, wide angle pairs (at low values of the argument in the figure) are suppressed in comparison with the Coulomb center approximation. This is due to the influence of the finite nuclear size which is comparable to the inverse mass of the muon. Typical angles of particle emission are of the order of  $1/\gamma_\pm = m_\mu/E_\mu^\pm$  (Fig. 7.14). Fig. 7.15 illustrates the influence of the momentum transferred to the target on the angular characteristics of the produced pair. In the frame of the often used model which neglects target recoil, the pair particles would be symmetric in transverse momenta, and coplanar with the initial photon.

### 7.7.5 Five-dimensional (5D) Bethe-Heitler gamma Conversion to $\mu^+\mu^-$

Since release 10.6, the G4BetheHeitler5DModel physics model for  $\gamma$ -ray conversions to  $e^+e^-$  pairs (section [Five-dimensional \(5D\) Bethe-Heitler gamma Conversion to  \$e^+e^-\$](#) ) has been extended to the conversions to  $\mu^+\mu^-$  pairs, sampling the 5D Bethe-Heitler differential cross section as described in the preceding section. For decays to muon pairs, G4BetheHeitler5DModel is a low-energy complement to the former G4GammaConversionToMuons model that is using high-energy approximations, that has been verified above 10 GeV and that is described above ([Gamma Conversion into Lepton Pair](#)). G4BetheHeitler5DModel is expected to be valid down to threshold and the algorithm has been verified down to a couple of hundred keV above threshold [Ber19]. Conversions of linearly polarised or non-polarised incident photons can be generated. The energy threshold is

$$E_{\text{threshold}} = 2(m_\mu^2/M + m_\mu)c^2,$$

where M is the target mass.

- For triplet conversion ( $\gamma e^- \rightarrow \mu^+\mu^- e^-$ ),  $E_{\text{threshold}}$  is close to 44 GeV.
- For nuclear conversion ( $\gamma Z \rightarrow \mu^+\mu^- Z$ ),  $E_{\text{threshold}}$  ranges from 223 MeV for hydrogen targets down to almost  $2m_\mu c^2 \approx 211 \text{ MeV}$  for heavy nuclei.

Fig. 7.16 presents distributions of kinematic variables of interest for several incident-photon energies for  $\gamma$ -ray nuclear conversion on Argon:

- $\theta_{\mu^+\mu^-} \times E$ , the pair opening angle multiplied by the incident-photon energy; the vertical line shows the most probable value of the distribution,  $3.2m_\mu c^2$ , obtained by Olsen in the high-energy approximation [Ols63];
- $\log_{10}(q)$ , where  $q$  is the (nucleus) recoil momentum;
- $\phi_{\text{recoil}}$ , azimuthal angle of the (nucleus) recoil momentum (for a fully linearly polarized  $\gamma$ -ray beam);
- $E_{\mu^+}/E$ , the fraction of the incident-photon energy that is carried away by the positive muon

Note that G4BetheHeitler5DModel does not take the finite size of the nucleus into account.

## 7.8 X-ray reflection

X-rays impacting at small angles on surfaces can undergo specular reflection. This is simulated by the class G4XrayReflection implemented as a standard electromagnetic X-ray process for the gamma particle. Design criteria were, clarity, speed and modularity.

The implementation has a default reflection model and data for all stable elements and a simple surface roughness model. For specific cases like multilayer surfaces, it should be straightforward to replace the default reflection and roughness model by user provided models. The reflection model implemented is the one used by the *Center for X-Ray Optics* at Lawrence Berkeley National Laboratory CXRO for single layers, described and illustrated in the [X-Ray Data Booklet](#) as well as in [X-Ray Interactions With Matter](#) based on the paper from Henke et al. [HGD93] and their [element data](#) available in G4EMLOW since version 8.5 as formatted tables with 3 columns E(eV), f1, f2. The minimum energy is 10 eV and the maximum energy 30 keV spaced by 0.1 eV close to absorption edges. The number

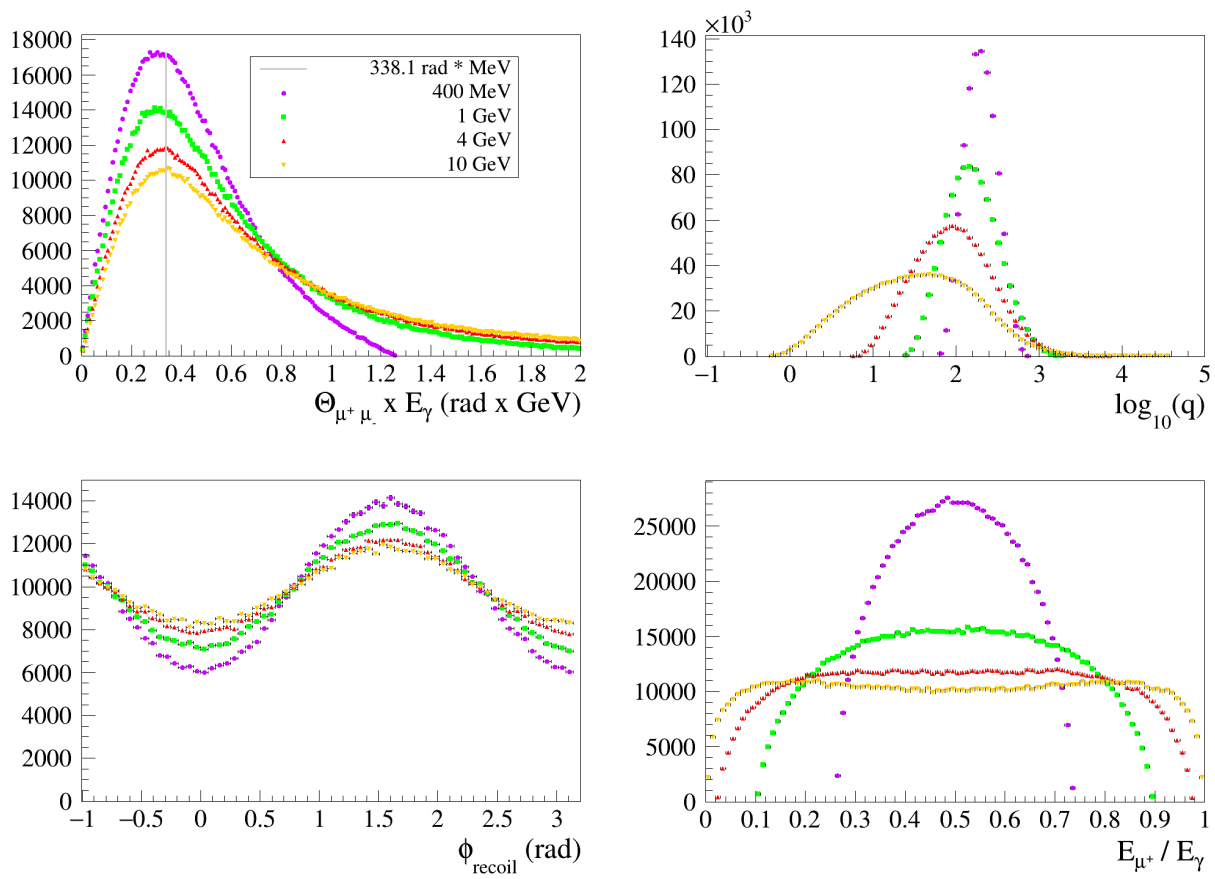


Fig. 7.16: *G4BetheHeitler5DModel*:  $\gamma$ -ray conversions to  $\mu^+ \mu^-$  pairs on Argon atoms (see text), for various incident-photon energies (bullets 400 MeV, squares 1 GeV, upper triangle 4 GeV, down triangle 10 GeV).

of points varies depending on the element between 505 and 909 points. The data below 30 eV has  $f_1=-9999$  and is not used in G4XrayReflection.

The wavelength  $\lambda$  of a photon is inversely proportional to its energy  $E$ , according to

$$\lambda = \frac{hc}{E}$$

where  $h$  is the Planck constant and  $c$  the speed of light. Numerically  $hc = 1.239\,842\,\text{keV nm}$ . The data can be used to calculate the complex reflection index

$$n = 1 - \delta - i\beta$$

as a function of energy, where  $\delta$  and  $\beta$  are obtained from  $f_1, f_2$  by multiplication with the number of atoms per unit volume  $N$ , the classical electron radius  $r_e$  and the wavelength squared, according to

$$\delta = \frac{N r_e \lambda^2}{2\pi} f_1$$

$$\beta = \frac{N r_e \lambda^2}{2\pi} f_2$$

The values of  $\delta, \beta$  are calculated and saved in the material tables by G4XrayReflection::SaveHenkeDataAsMaterialProperty from the values of  $f_1, f_2$  read from the data files by G4XrayReflection::ReadHenkeXrayData for all elements used in a particular simulation. This is done when the G4XrayReflection class is first created. For more details see [Bur25]. An example of how to use this process is provided with the extended electromagnetic example TestEm16.

### 7.8.1 Activation

The modeling is launched from G4XrayReflection::GetMeanFreePath for gamma energies between 30 eV and 30 keV when the gamma particle reaches a new volume. At this point the previous and new volume media, the gamma energy and direction and the surface normal are known and can be used to calculate the reflection probability. Reflection is only considered when the new medium has a higher density than the previous volume.

### 7.8.2 Reflectivity model

The reflectivity model implemented is that described by Henke et al. in section C. as “Non-Bragg Fresnel Reflection at Small Angles for the Semi-Infinite; Solid 1. Reflection from an Ideally Smooth Surface”. The reflection probability for the impact angle  $\theta$  is calculated as the average value of the  $\sigma$  and  $\pi$  polarization reflectivities

$$R_\sigma = \frac{\rho^2(\sin \theta - \rho)^2 + \beta^2}{\rho^2(\sin \theta + \rho)^2 + \beta^2}$$

and

$$R_\pi = R_\sigma \frac{\rho^2(\rho - \cos \theta \cot \theta)^2 + \beta^2}{\rho^2(\rho + \cos \theta \cot \theta)^2 + \beta^2}$$

where

$$\rho^2 = \frac{1}{2} \left[ \sin^2 \theta - 2\delta + \sqrt{(\sin^2 \theta - 2\delta)^2 + 4\beta^2} \right] .$$

using the  $\delta, \beta$  values at the current gamma energy. Fig. 7.17 shows the reflectivity for copper calculated as described here and used by default in G4XrayReflection as a function of energy for three different impact angles.

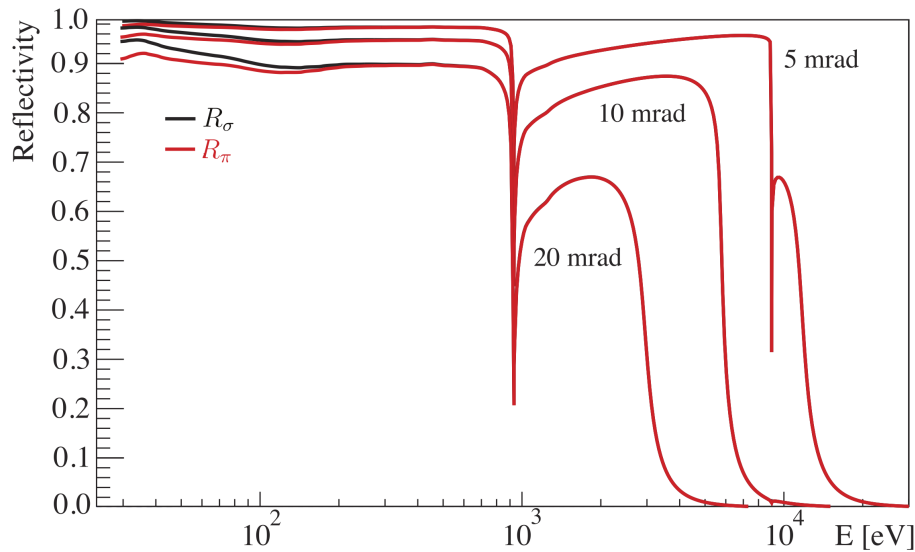


Fig. 7.17: Reflectivity of copper as a function of the photon energy for different impact angles  $\theta$ .

### 7.8.3 Surface roughness model

Implemented is a simple exponential Névot–Croce [NC80] attenuation factor  $f$ :

$$\begin{aligned} k_{iz} &= \frac{\sin \theta E_\gamma}{\hbar c} \\ k_{jz} &= (1 - \delta) \frac{\sin \theta E_\gamma}{\hbar c} \\ f &= \exp(-2 k_{i,z} k_{j,z} \sigma^2) \end{aligned}$$

where  $\sigma$  is the surface roughness. A typical value for a metallic surface can be 5 nm.



---

CHAPTER  
**EIGHT**

---

## ENERGY LOSS OF CHARGED PARTICLES

### 8.1 Discrete Processes for Charged Particles

Some processes for charged particles following the same interface *G4VEmProcess* as gamma processes described in *Introduction to Gamma Processes*.

- G4CoulombScattering;
- G4eplusAnnihilation (with additional `AtRest` methods);
- G4eplusPolarizedAnnihilation (with additional `AtRest` methods);
- G4eeToHadrons;
- G4MicroElecElastic;
- G4MicroElecInelastic.

Corresponding model classes follow the *G4VEmModel* interface:

- G4DummyModel (zero cross section, no secondaries);
- G4eCoulombScatteringModel;
- G4eSingleCoulombScatteringModel;
- G4IonCoulombScatteringModel;
- G4eeToTwoGammaModel;
- G4eplusTo2GammaOKVIModel;
- G4eeToHadronsModel;
- G4PenelopeAnnihilationModel;
- G4PolarizedAnnihilationModel;
- G4MicroElecElasticModel;
- G4MicroElecInelasticModel.

Some processes do not follow described EM interfaces but provide direct implementations of the basic *G4VDiscreteProcess* process:

- G4AnnihiToMuPair;
- G4ScreenedNuclearRecoil;
- G4Cerenkov;
- G4Scintillation;

- G4SynchrotronRadiation;

## 8.2 Mean Energy Loss

Energy loss processes are very similar for  $e^+/e^-$ ,  $\mu^+/\mu^-$  and charged hadrons, so a common description for them was a natural choice in GEANT4 [eal03], [eal09]. Any energy loss process must calculate the continuous and discrete energy loss in a material. Below a given energy threshold the energy loss is continuous and above it the energy loss is simulated by the explicit production of secondary particles - gammas, electrons, and positrons.

### 8.2.1 Method

Let

$$\frac{d\sigma(Z, E, T)}{dT}$$

be the differential cross-section per atom (atomic number  $Z$ ) for the ejection of a secondary particle with kinetic energy  $T$  by an incident particle of total energy  $E$  moving in a material of density  $\rho$ . The value of the *kinetic energy cut-off* or *production threshold* is denoted by  $T_{cut}$ . Below this threshold the soft secondaries ejected are simulated as continuous energy loss by the incident particle, and above it they are explicitly generated. The mean rate of energy loss is given by:

$$\frac{dE_{soft}(E, T_{cut})}{dx} = n_{at} \cdot \int_0^{T_{cut}} \frac{d\sigma(Z, E, T)}{dT} T \, dT \quad (8.1)$$

where  $n_{at}$  is the number of atoms per volume in the material. The total cross section per atom for the ejection of a secondary of energy  $T > T_{cut}$  is

$$\sigma(Z, E, T_{cut}) = \int_{T_{cut}}^{T_{max}} \frac{d\sigma(Z, E, T)}{dT} \, dT \quad (8.2)$$

where  $T_{max}$  is the maximum energy transferable to the secondary particle.

If there are several processes providing energy loss for a given particle, then the total continuous part of the energy loss is the sum:

$$\frac{dE_{soft}^{tot}(E, T_{cut})}{dx} = \sum_i \frac{dE_{soft,i}(E, T_{cut})}{dx}. \quad (8.3)$$

These values are pre-calculated during the initialization phase of GEANT4 and stored in the  $dE/dx$  table. Using this table the ranges of the particle in given materials are calculated and stored in the *Range* table. The *Range* table is then inverted to provide the *InverseRange* table. At run time, values of the particle's continuous energy loss and range are obtained using these tables. Concrete processes contributing to the energy loss are not involved in the calculation at that moment. In contrast, the production of secondaries with kinetic energies above the production threshold is sampled by each concrete energy loss process.

The default energy interval for these tables extends from 100 eV to 100 TeV and the default number of bins is 84. For muons and for heavy particles energy loss processes models are valid for higher energies and can be extended. For muons the upper limit may be set to 1000 PeV.

## 8.2.2 General Interfaces

There are a number of similar functions for discrete electromagnetic processes and for electromagnetic (EM) packages an additional base classes were designed to provide common computations [eal09]. Common calculations for discrete EM processes are performed in the class *G4VEnergyLossProcess*. Derived classes (Table 8.1) are concrete processes providing initialisation. The physics models are implemented using the *G4VEmModel* interface. Each process may have one or many models defined to be active over a given energy range and set of *G4Regions*. Models are implementing computation of energy loss, cross section and sampling of final state. The list of EM processes and models for gamma incident is shown in Table 8.1.

Table 8.1: List of process and model classes for charged particles.

EM process	EM model	Ref.
G4eIonisation	G4MollerBhabhaModel	Section 11.1
	G4LivermoreIonisationModel	Section 11.1.6
	G4PenelopeIonisationModel	Section 11.1.5
	G4PAIModel	Section 8.6
	G4PAIPhotModel	Section 8.6
G4ePolarizedIonisation	G4PolarizedMollerBhabhaModel	Section 14.2
G4MuIonisation	G4MuBetheBlochModel	Section 12.1
	G4PAIModel	Section 8.6
	G4PAIPhotModel	Section 8.6
G4hIonisation	G4BetheBlochModel	Section 13.1
	G4BraggModel	Section 13.1
	G4ICRU73QOModel	Section 13.2.1
	G4PAIModel	Section 8.6
	G4PAIPhotModel	Section 8.6
G4ionIonisation	G4BetheBlochModel	Section 13.1
	G4BetheBlochIonGasModel	Section 13.1
	G4BraggIonModel	Section 13.1
	G4BraggIonGasModel	Section 13.1
	G4IonParametrisedLossModel	Section 13.2.4
	G4AtimaEnergyLossModel	Section 8.7
	G4LindhardSorensenIonModel	
G4NuclearStopping	G4ICRU49NuclearStoppingModel	Section 13.1.3
G4mplIonisation	G4mplIonisationWithDeltaModel	
G4eBremsstrahlung	G4SeltzerBergerModel	Section 11.2.1
	G4eBremsstrahlungRelModel	Section 11.2.2
	G4LivermoreBremsstrahlungModel	Section 11.2.4
	G4PenelopeBremsstrahlungModel	Section 11.2.3
G4ePolarizedBremsstrahlung	G4PolarizedBremsstrahlungModel	Section 14.5
G4MuBremsstrahlung	G4MuBremsstrahlungModel	Section 12.2
G4hBremsstrahlung	G4hBremsstrahlungModel	Section 12.2
G4ePairProduction	G4MuPairProductionModel	Section 12.3
G4MuPairProduction	G4MuPairProductionModel	Section 12.3
G4hPairProduction	G4hPairProductionModel	Section 12.3

### 8.2.3 Step-size Limit

Continuous energy loss imposes a limit on the step-size because of the energy dependence of the cross sections. It is generally assumed in MC programs (for example, Geant3) that the cross sections are approximately constant along a step, i.e. the step size should be small enough, so that the change in cross section along the step is also small. In principle one must use very small steps in order to insure an accurate simulation, however the computing time increases as the step-size decreases.

For EM processes the exact solution is available (see [Correcting the Cross Section for Energy Variation](#)) but is not implemented yet for all physics processes including hadronics. A good compromise is to limit the step-size by not allowing the stopping range of the particle to decrease by more than  $\sim 20\%$  during the step. This condition works well for particles with kinetic energies  $> 1$  MeV, but for lower energies it gives too short step-sizes, so must be relaxed. To solve this problem a lower limit on the step-size was introduced. A smooth *StepFunction*, with 2 parameters, controls the step size. At high energy the maximum step size is defined by  $\text{Step}/\text{Range} \sim \alpha_R$  (parameter *dRoverRange*). By default  $\alpha_R = 0.2$ . As the particle travels the maximum step size decreases gradually until the range becomes lower than  $\rho_R$  (parameter *finalRange*). Default *finalRange*  $\rho_R = 1$  mm. For the case of a particle range  $R > \rho_R$  the *StepFunction* provides limit for the step size  $\Delta S_{lim}$  by the following formula:

$$\Delta S_{lim} = \alpha_R R + \rho_R (1 - \alpha_R) \left( 2 - \frac{\rho_R}{R} \right). \quad (8.4)$$

In the opposite case of a small range  $\Delta S_{lim} = R$ . The figure below shows the ratio step/range as a function of range if step limitation is determined only by the expression (8.4).

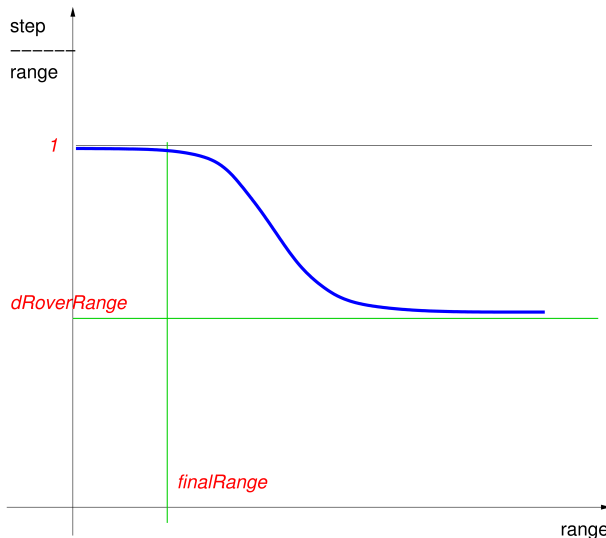


Fig. 8.1: Step limit.

The parameters of *StepFunction* can be overwritten using the UI commands:

```
/process/eLoss/StepFunction 0.2 1 mm
/process/eLoss/StepFunctionMuHad 0.2 1 mm
/process/eLoss/StepFunctionLightIons 0.1 0.01 mm
/process/eLoss/StepFunctionIons 0.1 0.001 mm
```

To provide more accurate simulation of particle ranges in physics constructors *G4EmStandardPhysics\_option3* and *G4EmStandardPhysics\_option4* more strict step limitation is chosen for different particle types.

## 8.2.4 Run Time Energy Loss Computation

The computation of the *mean energy loss* after a given step is done by using the *dE/dx*, *Range*, and *InverseRange* tables. The *dE/dx* table is used if the energy deposition ( $\Delta T$ ) is less than allowed limit  $\Delta T < \xi T_0$ , where  $\xi$  is *linearLossLimit* parameter (by default  $\xi = 0.01$ ),  $T_0$  is the kinetic energy of the particle. In that case

$$\Delta T = \frac{dE}{dx} \Delta s,$$

where  $\Delta T$  is the energy loss,  $\Delta s$  is the *true step length*. When a larger percentage of energy is lost, the mean loss can be written as

$$\Delta T = T_0 - f_T(r_0 - \Delta s)$$

where  $r_0$  the range at the beginning of the step, the function  $f_T(r)$  is the inverse of the *Range* table (i.e. it gives the kinetic energy of the particle for a range value of  $r$ ). By default spline approximation is used to retrieve a value from *dE/dx*, *Range*, and *InverseRange* tables. The spline flag can be changed using an UI command:

```
/process/em/spline false
```

After the mean energy loss has been calculated, the process computes the *actual energy loss*, i.e. the loss with fluctuations. The fluctuation models are described in [Energy Loss Fluctuations](#).

If deexcitation module (see [Atomic relaxation](#)) is enabled then simulation of atomic deexcitation is performed using information on step length and ionisation cross section. Fluorescence gamma and Auger electrons are produced above the same threshold energy as  $\delta$ -electrons and bremsstrahlung gammas. The following UI commands can be used to enable atomic relaxation:

```
/process/em/deexcitation myregion true true true
/process/em/fluo true
/process/em/auger true
/process/em/pixe true
/process/em/deexcitationIgnoreCut true
```

The last command means that production threshold for electrons and gammas are not checked, so full atomic deexcitation decay chain is simulated.

After the step a kinetic energy of a charged particle is compared with the *lowestEnergy*. In the case if final kinetic energy is below the particle is stopped and remaining kinetic energy is assigned to the local energy deposit. The default value of the limit is 1 keV. It may be changed separately for electron/positron and muon/hadron using UI commands:

```
/process/em/lowestElectronEnergy 100 eV
/process/em/lowestMuHadEnergy 50 eV
```

These values may be set to zero.

## 8.2.5 Energy Loss by Heavy Charged Particles

To save memory in the case of positively charged hadrons and ions energy loss, *dE/dx*, *Range* and *InverseRange* tables are constructed only for *proton*, *antiproton*, *muons*, *pions*, *kaons*, and *Generic Ion*. The energy loss for other particles is computed from these tables at the *scaled kinetic energy*  $T_{scaled}$ :

$$T_{scaled} = T \frac{M_{base}}{M_{particle}}, \quad (8.5)$$

where  $T$  is the kinetic energy of the particle,  $M_{base}$  and  $M_{particle}$  are the masses of the base particle (*proton or kaon*) and particle. For positively charged hadrons with non-zero spin *proton* is used as a based particle, for negatively

charged hadrons with non-zero spin - *antiproton*, for charged particles with zero spin -  $K^+$  or  $K^-$  correspondingly. The virtual particle *Generic Ion* is used as a base particle for all ions with  $Z > 2$ . It has mass, charge and other quantum numbers of the *proton*. The energy loss can be defined via scaling relation:

$$\frac{dE}{dx}(T) = q_{eff}^2(F_1(T)\frac{dE}{dx}_{base}(T_{scaled}) + F_2(T, q_{eff})),$$

where  $q_{eff}$  is particle effective charge in units of positron charge,  $F_1$  and  $F_2$  are correction function taking into account Birks effect, Block correction, low-energy corrections based on data from evaluated data bases ICRU90 [eal14], ICRU73 [eal05], NIST PSTAR and ASTAR [ABB+]. For a hadron  $q_{eff}$  is equal to the hadron charge, for a slow ion effective charge is different from the charge of the ion's nucleus, because of electron exchange between transporting ion and the media. The effective charge approach is used to describe this effect [ZM88]. The scaling relation (8.5) is valid for any combination of two heavy charged particles with accuracy corresponding to high order mass, charge and spin corrections [eal93].

## 8.3 Energy Loss Fluctuations

The total continuous energy loss of charged particles is a stochastic quantity with a distribution described in terms of a straggling function. The straggling is partially taken into account in the simulation of energy loss by the production of  $\delta$ -electrons with energy  $T > T_{cut}$  ((8.2)). However, continuous energy loss ((8.1)) also has fluctuations. Hence in the current GEANT4 implementation different models of fluctuations implementing the *G4VEmFluctuationModel* interface:

- G4UniversalFluctuation;
- G4IonFluctuations;
- G4AtimaFluctuations;
- G4PAIModel;
- G4PAIPhotModel.

The first model is the default one used in main Physics List and will be described below. Other models have limited applicability and will be described in chapters for *Hadron and Ion Ionisation*, PAI (*Photoabsorption Ionisation Model*) and ATIMA (*ATIMA energy-loss model*) models.

### 8.3.1 Fluctuations in Thick Absorbers

The total continuous energy loss of charged particles is a stochastic quantity with a distribution described in terms of a straggling function. The straggling is partially taken into account in the simulation of energy loss by the production of  $\delta$ -electrons with energy  $T > T_c$ . However, continuous energy loss also has fluctuations. Hence in the current GEANT4 implementation two different models of fluctuations are applied depending on the value of the parameter  $\kappa$  which is the lower limit of the number of interactions of the particle in a step. The default value chosen is  $\kappa = 10$ . In the case of a high range cut (i.e. energy loss without delta ray production) for thick absorbers the following condition should be fulfilled:

$$\Delta E > \kappa T_{max}$$

where  $\Delta E$  is the mean continuous energy loss in a track segment of length  $s$ , and  $T_{max}$  is the maximum kinetic energy that can be transferred to the atomic electron. If this condition holds the fluctuation of the total (unrestricted) energy loss follows a Gaussian distribution. It is worth noting that this condition can be true only for heavy particles, because for electrons,  $T_{max} = T/2$ , and for positrons,  $T_{max} = T$ , where  $T$  is the kinetic energy of the particle. In order to simulate the fluctuation of the continuous (restricted) energy loss, the condition should be modified. After a study, the following conditions have been chosen:

$$\Delta E > \kappa T_c \tag{8.6}$$

$$T_{max} \leq 2 T_c \quad (8.7)$$

where  $T_c$  is the cut kinetic energy of  $\delta$ -electrons. For thick absorbers the straggling function approaches the Gaussian distribution with Bohr's variance [eal93]:

$$\Omega^2 = 2\pi r_e^2 m_e c^2 N_{el} \frac{Z_h^2}{\beta^2} T_{max} s \left( 1 - \frac{\beta^2}{2} \frac{T_c}{T_{max}} \right), \quad (8.8)$$

where  $r_e$  is the classical electron radius,  $N_{el}$  is the electron density of the medium,  $Z_h$  is the charge of the incident particle in units of positron charge, and  $\beta$  is the relativistic velocity.

### 8.3.2 Fluctuations in Thin Absorbers

If the conditions (8.6) and (8.7) are not satisfied the model of energy fluctuations in thin absorbers is applied. The formulas used to compute the energy loss fluctuation (straggling) are based on a very simple physics model of the atom. It is assumed that the atoms have only two energy levels with binding energies  $E_1$  and  $E_2$ . The particle-atom interaction can be an excitation with energy loss  $E_1$  or  $E_2$ , or ionisation with energy loss distributed according to a function  $g(E) \sim 1/E^2$ :

$$\int_{E_0}^{T_{up}} g(E) dE = 1 \implies g(E) = \frac{E_0 T_{up}}{T_{up} - E_0} \frac{1}{E^2}. \quad (8.9)$$

The macroscopic cross section for excitation ( $i = 1, 2$ ) is

$$\Sigma_i = C \frac{f_i}{E_i} \frac{\ln[2mc^2(\beta\gamma)^2/E_i] - \beta^2}{\ln[2mc^2(\beta\gamma)^2/I] - \beta^2} (1 - r) \quad (8.10)$$

and the ionisation cross section is

$$\Sigma_3 = C \frac{T_{up} - E_0}{E_0 T_{up} \ln(\frac{T_{up}}{E_0})} r \quad (8.11)$$

where  $E_0$  denotes the ionisation energy of the atom,  $I$  is the mean ionisation energy,  $T_{up}$  is the production threshold for delta ray production (or the maximum energy transfer if this value smaller than the production threshold),  $E_i$  and  $f_i$  are the energy levels and corresponding oscillator strengths of the atom, and  $C$  and  $r$  are model parameters.

The oscillator strengths  $f_i$  and energy levels  $E_i$  should satisfy the constraints

$$f_1 + f_2 = 1 \quad (8.12)$$

$$f_1 \cdot \ln E_1 + f_2 \cdot \ln E_2 = \ln I. \quad (8.13)$$

The cross section formulas (8.10),(8.11) and the sum rule equations (8.12),(8.13) can be found e.g.in Ref.[Bic88]. The model parameter  $C$  can be defined in the following way. The numbers of collisions ( $n_i$ ,  $i = 1, 2$  for excitation and 3 for ionisation) follow the Poisson distribution with a mean value  $\langle n_i \rangle$ . In a step of length  $\Delta x$  the mean number of collisions is given by

$$\langle n_i \rangle = \Delta x \Sigma_i$$

The mean energy loss in a step is the sum of the excitation and ionisation contributions and can be written as

$$\frac{dE}{dx} \cdot \Delta x = \left\{ \Sigma_1 E_1 + \Sigma_2 E_2 + \int_{E_0}^{T_{up}} E g(E) dE \right\} \Delta x.$$

From this, using Eq. (8.10) - (8.13), one can see that

$$C = dE/dx.$$

The other parameters in the fluctuation model have been chosen in the following way.  $Z \cdot f_1$  and  $Z \cdot f_2$  represent in the model the number of loosely/tightly bound electrons

$$f_2 = 0 \text{ for } Z = 1$$

$$f_2 = 2/Z \text{ for } Z \geq 2$$

$$E_2 = 10 \text{ eV } Z^2$$

$$E_0 = 10 \text{ eV}.$$

Using these parameter values,  $E_2$  corresponds approximately to the K-shell energy of the atoms (and  $Zf_2 = 2$  is the number of K-shell electrons). The parameters  $f_1$  and  $E_1$  can be obtained from Eqs.(8.12) and (8.13). The parameter  $r$  is the only variable in the model which can be tuned. This parameter determines the relative contribution of ionisation and excitation to the energy loss. Based on comparisons of simulated energy loss distributions to experimental data, its value has been fixed as

$$r = 0.55.$$

### 8.3.3 Width Correction Algorithm

This simple parametrization and sampling in the model give good values for the most probable energy loss in thin layers. The width of the energy loss distribution (Full Width at Half Maximum, FWHM) in most of the cases is too small. In order to get good FWHM values a relatively simple width correction algorithm has been applied. This algorithm rescales the energy levels  $E_1$ ,  $E_2$  and the number of excitations  $n_1$ ,  $n_2$  in such a way that the mean energy loss remains the same. Using this width correction scheme the model gives not only good most probable energy loss, but good FWHM value too.

Width correction algorithm is in the model since version 9.2. The updated version in the model (in version 9.4) causes an important change in the behaviour of the model: the results become much more stable, i.e. the results do not change practically when the cuts and/or the stepsizes are changing. Another important change: the (unphysical) second peak or shoulder in the energy loss distribution which can be seen in some cases (energy loss in thin gas layers) in older versions of the model disappeared. Limit of validity of the model for thin targets: the model gives good (reliable) energy loss distribution if the mean energy loss in the target is  $\geq$  (few times) \*  $I_{exc}$ , where  $I_{exc}$  is the mean excitation energy of the target material.

This simple model of energy loss fluctuations is rather fast and can be used for any thickness of material. This has been verified by performing many simulations and comparing the results with experimental data, such as those in Ref. [LPUrban95]. As the limit of validity of Landau's theory is approached, the loss distribution approaches the Landau form smoothly.

### 8.3.4 Sampling of Energy Loss

If the mean energy loss and step are in the range of validity of the Gaussian approximation of the fluctuation (8.6) and (8.7), the Gaussian sampling is used to compute the actual energy loss (8.8). For smaller steps the energy loss is computed in the model under the assumption that the step length (or relative energy loss) is small and, in consequence, the cross section can be considered constant along the step. The loss due to the excitation is

$$\Delta E_{exc} = n_1 E_1 + n_2 E_2$$

where  $n_1$  and  $n_2$  are sampled from a Poisson distribution. The energy loss due to ionisation can be generated from the distribution  $g(E)$  by the inverse transformation method:

$$u = F(E) = \int_{E_0}^E g(x)dx$$

$$E = F^{-1}(u) = \frac{E_0}{1 - u \frac{T_{up} - E_0}{T_{up}}}$$

where  $u$  is a uniformly distributed random number  $\in [0, 1]$ . The contribution coming from the ionisation will then be

$$\Delta E_{ion} = \sum_{j=1}^{n^3} \frac{E_0}{1 - u_j \frac{T_{up} - E_0}{T_{up}}}$$

where  $n^3$  is the number of ionisations sampled from the Poisson distribution. The total energy loss in a step will be  $\Delta E = \Delta E_{exc} + \Delta E_{ion}$  and the energy loss fluctuation comes from fluctuations in the number of collisions  $n_i$  and from the sampling of the ionisation loss.

## 8.4 Correcting the Cross Section for Energy Variation

As described in [Mean Energy Loss](#) and [Determination of the Interaction Point](#) the step size limitation is provided by energy loss processes in order to insure the precise calculation of the probability of particle interaction. It is generally assumed in Monte Carlo programs that the particle cross sections are approximately constant during a step, hence the reaction probability  $p$  at the end of the step can be expressed as

$$p = 1 - \exp(-ns\sigma(E_i)),$$

where  $n$  is the density of atoms in the medium,  $s$  is the step length,  $E_i$  is the energy of the incident particle at the beginning of the step, and  $\sigma(E_i)$  is the reaction cross section at the beginning of the step.

However, it is possible to sample the reaction probability from the exact expression

$$p = 1 - \exp\left(-\int_{E_i}^{E_f} n\sigma(E)ds\right),$$

where  $E_f$  is the energy of the incident particle at the end of the step, by using the integral approach to particle transport. This approach is available for processes implemented via the *G4VEnergyLossProcess* and *G4VEmProcess* interfaces.

The Monte Carlo method of integration is used for sampling the reaction probability [eal92]. It is assumed that during the step the reaction cross section smaller, than some value  $\sigma(E) < \sigma_m$ . The mean free path for the given step is computed using  $\sigma_m$ . If the process is chosen as the process happens at the step, the sampling of the final state is performed only with the probability  $p = \sigma(E_f)/\sigma_m$ , alternatively no interaction happen and tracking of the particle is continued. To estimate the maximum value  $\sigma_m$  for the given tracking step at GEANT4 initialisation the energy  $E_m$  of absolute maximum  $\sigma_{max}$  of the cross section for given material is determined and stored. If at the tracking time particle energy  $E < E_m$ , then  $\sigma_m = \sigma(E)$ . For higher initial energies if  $\xi E > E_m$  then  $\sigma_m = \max(\sigma(E), \sigma(\xi E))$ , in the opposite case,  $\sigma_m = \sigma_{max}$ . Here  $\xi$  is a parameter of the algorithm. Its optimal value is connected with the value of the *dRoverRange* parameter (see [Mean Energy Loss](#)), by default  $\xi = 1 - \alpha_R = 0.8$ . Note, that described method is precise if the cross section has only one maximum, which is a typical case for electromagnetic processes.

The integral variant of step limitation is the default for the *G4eIonisation*, *G4hIonisation*, *G4eBremsstrahlung* and some other processes for charged particles. The integral variant of the energy loss sampling process is less dependent on values of the production cuts [eal09] and allows to have less step limitation, however it should be applied on a case-by-case basis because may require extra CPU.

## 8.5 Conversion from Cut in Range to Energy Threshold

In GEANT4 charged particles are tracked to the end of their range. The differential cross section of  $\delta$ -electron productions and bremsstrahlung grow rapidly when secondary energy decrease. If all secondary particles will be tracked the CPU performance of any Monte Carlo code will be poor. The traditional solution is to use cuts. The specific of GEANT4 [eal03] is that user provides value of cut in term of *cut in range*, which is unique for defined *G4Region* or for the complete geometry [eal16].

Range is used, rather than energy, as a more natural concept for designing a coherent policy for different particles and materials. Definition of the certain value of the *cut in range* means the requirement for precision of spatial radioactive dose deposition. This conception is more strict for a simulation code and provides fewer handles for user to modify final results. At the same time, it ensures that simulation validated in one geometry is valid also for the other geometries.

The value of cut is defined for electrons, positrons, gamma and protons. At the beginning of initialization of GEANT4 physics the conversion is performed from unique *cut in range* to cuts (production thresholds) in kinetic energy for each *G4MaterialCutsCouple* [eal16]. At that moment no energy loss and range of electron and positron are computed using simplified expressions extracted from cBerger-Seltzer energy loss formula ((11.2)). Absolute accuracy of the estimated range is not needed, so the density correction term is omitted. The contribution of the bremsstrahlung is added using empirical parameterized formula. For  $T < 10$  keV the linear dependence of ionisation losses on electron velocity is assumed, bremsstrahlung contribution is neglected. The stopping range is defined as

$$R(T) = \int_0^T \frac{1}{(dE/dx)} dE.$$

The integration has been done analytically for the low energy part and numerically above an energy limit 1 keV. For each *cut in range* the corresponding kinetic energy can be found out. If obtained production threshold in kinetic energy cannot be below the parameter *lowlimit* (default 1 keV) and above *highlimit* (default 10 GeV). If in specific application lower threshold is required, then the allowed energy cut needs to be extended:

```
G4ProductionCutsTable::GetProductionCutsTable() -> SetEnergyRange(lowlimit, highlimit);
```

or via UI commands:

```
/cuts/setMinCutEnergy 100 eV
/cuts/setMaxCutEnergy 100 TeV
```

In contrary to electrons, gammas have no range, so some approximation should be used for range to energy conversion. An approximate empirical formula is used to compute the *absorption cross section* of a photon in an element  $\sigma_{abs}$ . Here, the *absorption cross section* means the sum of the cross sections of the gamma conversion, Compton scattering and photoelectric effect. These processes are the “destructive” processes for photons: they destroy the photon or decrease its energy. The coherent or Rayleigh scattering changes the direction of the gamma only; its cross section is not included in the *absorption cross section*. The AbsorptionLength  $L_{abs}$  vector is calculated for every material as

$$L_{abs} = 5/\sigma_{abs}.$$

The factor 5 comes from the requirement that the probability of having no ‘destructive’ interaction should be small, hence

$$\exp(-L_{abs}\sigma_{abs}) = \exp(-5) = 6.7 \times 10^{-3}.$$

The photon cross section for a material has a minimum at a certain energy  $E_{min}$ . Correspondingly  $L_{abs}$  has a maximum at  $E = E_{min}$ , the value of the maximal  $L_{abs}$  is the biggest “meaningful” cut in absorption length. If the cut given by the user is bigger than this maximum, a warning is printed and the cut in kinetic energy is set to the *highlimit*.

The cut for proton is introduced with GEANT4 v9.3. The main goal of this cut is to limit production of all recoil ions including protons in elastic scattering processes. A simple linear conversion formula is used to compute energy

threshold from the value of cut in range, in particular, the cut in range 1 mm corresponds to the production threshold 100 keV.

The conversion from range to energy can be studied using *G4EmCalculator* class. This class allows access or recalculation of energy loss, ranges and other values. It can be instantiated and at any place of user code and can be used after initialisation of Physics Lists:

```
G4EmCalculator calc;
calc.ComputeEnergyCutFromRangeCut(range, particle, material);
```

here particle and material may be string names or corresponding const pointers to *G4ParticleDefinition* and *G4Material*.

## 8.6 Photoabsorption Ionisation Model

### 8.6.1 Cross Section for Ionising Collisions

The Photoabsorption Ionisation (PAI) model describes the ionisation energy loss of a relativistic charged particle in matter. For such a particle, the differential cross section  $d\sigma_i/d\omega$  for ionising collisions with energy transfer  $\omega$  can be expressed most generally by the following equations [VSVAAel82]:

$$\frac{d\sigma_i}{d\omega} = \frac{2\pi Ze^4}{mv^2} \left\{ \frac{f(\omega)}{\omega |\varepsilon(\omega)|^2} \left[ \ln \frac{2mv^2}{\omega |1 - \beta^2\varepsilon|} - \frac{\varepsilon_1 - \beta^2|\varepsilon|^2}{\varepsilon_2} \arg(1 - \beta^2\varepsilon^*) \right] + \frac{\tilde{F}(\omega)}{\omega^2} \right\}, \quad (8.14)$$

where

$$\begin{aligned} \tilde{F}(\omega) &= \int_0^\omega \frac{f(\omega')}{|\varepsilon(\omega')|^2} d\omega', \\ f(\omega) &= \frac{m\omega\varepsilon_2(\omega)}{2\pi^2 Z N \hbar^2}. \end{aligned}$$

Here  $m$  and  $e$  are the electron mass and charge,  $\hbar$  is Planck's constant,  $\beta = v/c$  is the ratio of the particle's velocity  $v$  to the speed of light  $c$ ,  $Z$  is the effective atomic number,  $N$  is the number of atoms (or molecules) per unit volume, and  $\varepsilon = \varepsilon_1 + i\varepsilon_2$  is the complex dielectric constant of the medium. In an isotropic non-magnetic medium the dielectric constant can be expressed in terms of a complex index of refraction,  $n(\omega) = n_1 + in_2$ ,  $\varepsilon(\omega) = n^2(\omega)$ . In the energy range above the first ionisation potential  $I_1$  for all cases of practical interest, and in particular for all gases,  $n_1 \sim 1$ . Therefore the imaginary part of the dielectric constant can be expressed in terms of the photoabsorption cross section  $\sigma_\gamma(\omega)$ :

$$\varepsilon_2(\omega) = 2n_1n_2 \sim 2n_2 = \frac{N\hbar c}{\omega} \sigma_\gamma(\omega).$$

The real part of the dielectric constant is calculated in turn from the dispersion relation

$$\varepsilon_1(\omega) - 1 = \frac{2N\hbar c}{\pi} V.p. \int_0^\infty \frac{\sigma_\gamma(\omega')}{\omega'^2 - \omega^2} d\omega',$$

where the integral of the pole expression is considered in terms of the principal value. In practice it is convenient to calculate the contribution from the continuous part of the spectrum only. In this case the normalized photoabsorption cross section

$$\tilde{\sigma}_\gamma(\omega) = \frac{2\pi^2\hbar e^2 Z}{mc} \sigma_\gamma(\omega) \left[ \int_{I_1}^{\omega_{max}} \sigma_\gamma(\omega') d\omega' \right]^{-1}, \quad \omega_{max} \sim 100 \text{ keV}$$

is used, which satisfies the quantum mechanical sum rule [FUJW68]:

$$\int_{I_1}^{\omega_{max}} \tilde{\sigma}_\gamma(\omega') d\omega' = \frac{2\pi^2\hbar e^2 Z}{mc}.$$

The differential cross section for ionising collisions is expressed by the photoabsorption cross section in the continuous spectrum region:

$$\frac{d\sigma_i}{d\omega} = \frac{\alpha}{\pi\beta^2} \left\{ \frac{\tilde{\sigma}_\gamma(\omega)}{\omega |\varepsilon(\omega)|^2} \left[ \ln \frac{2mv^2}{\omega |1 - \beta^2\varepsilon|} - \frac{\varepsilon_1 - \beta^2 |\varepsilon|^2}{\varepsilon_2} \arg(1 - \beta^2\varepsilon^*) \right] + \frac{1}{\omega^2} \int_{I_1}^{\omega} \frac{\tilde{\sigma}_\gamma(\omega')}{|\varepsilon(\omega')|^2} d\omega' \right\},$$

where

$$\begin{aligned} \varepsilon_2(\omega) &= \frac{N\hbar c}{\omega} \tilde{\sigma}_\gamma(\omega), \\ \varepsilon_1(\omega) - 1 &= \frac{2N\hbar c}{\pi} V.p. \int_{I_1}^{\omega_{max}} \frac{\tilde{\sigma}_\gamma(\omega')}{\omega'^2 - \omega^2} d\omega'. \end{aligned}$$

For practical calculations using Eq.(8.14) it is convenient to represent the photoabsorption cross section as a polynomial in  $\omega^{-1}$  as was proposed in [BFR90]:

$$\sigma_\gamma(\omega) = \sum_{k=1}^4 a_k^{(i)} \omega^{-k},$$

where the coefficients,  $a_k^{(i)}$  result from a separate least-squares fit to experimental data in each energy interval  $i$ . As a rule the interval borders are equal to the corresponding photoabsorption edges. The dielectric constant can now be calculated analytically with elementary functions for all  $\omega$ , except near the photoabsorption edges where there are breaks in the photoabsorption cross section and the integral for the real part is not defined in the sense of the principal value. The third term in Eq.(8.14), which can only be integrated numerically, results in a complex calculation of  $d\sigma_i/d\omega$ . However, this term is dominant for energy transfers  $\omega > 10$  keV, where the function  $|\varepsilon(\omega)|^2 \sim 1$ . This is clear from physical reasons, because the third term represents the Rutherford cross section on atomic electrons which can be considered as quasifree for a given energy transfer [AWWMJ80]. In addition, for high energy transfers,  $\varepsilon(\omega) = 1 - \omega_p^2/\omega^2 \sim 1$ , where  $\omega_p$  is the plasma energy of the material. Therefore the factor  $|\varepsilon(\omega)|^{-2}$  can be removed from under the integral and the differential cross section of ionising collisions can be expressed as:

$$\frac{d\sigma_i}{d\omega} = \frac{\alpha}{\pi\beta^2 |\varepsilon(\omega)|^2} \left\{ \frac{\tilde{\sigma}_\gamma(\omega)}{\omega} \left[ \ln \frac{2mv^2}{\omega |1 - \beta^2\varepsilon|} - \frac{\varepsilon_1 - \beta^2 |\varepsilon|^2}{\varepsilon_2} \arg(1 - \beta^2\varepsilon^*) \right] + \frac{1}{\omega^2} \int_{I_1}^{\omega} \tilde{\sigma}_\gamma(\omega') d\omega' \right\}.$$

This is especially simple in gases when  $|\varepsilon(\omega)|^{-2} \sim 1$  for all  $\omega > I_1$  [AWWMJ80].

## 8.6.2 Energy Loss Simulation

For a given track length the number of ionising collisions is simulated by a Poisson distribution whose mean is proportional to the total cross section of ionising collisions:

$$\sigma_i = \int_{I_1}^{\omega_{max}} \frac{d\sigma(\omega')}{d\omega'} d\omega'.$$

The energy transfer in each collision is simulated according to a distribution proportional to

$$\sigma_i(>\omega) = \int_{\omega}^{\omega_{max}} \frac{d\sigma(\omega')}{d\omega'} d\omega'.$$

The sum of the energy transfers is equal to the energy loss. PAI ionisation is implemented according to the model approach (class G4PAIModel) allowing a user to select specific models in different regions. Here is an example physics list:

```

const G4RegionStore* theRegionStore = G4RegionStore::GetInstance();
G4Region* gas = theRegionStore->GetRegion("VertexDetector");
...
if (particleName == "e-")
{
    ...
    G4eIonisation* eion = new G4eIonisation();
    G4PAIModel*      pai = new G4PAIModel(particle, "PAIModel");

    // here 0 is the highest priority in region 'gas'
    eion->AddEmModel(0, pai, pai, gas);
    ...
}
...

```

It shows how to select the G4PAIModel to be the preferred ionisation model for electrons in a *G4Region* named *VertexDetector*. The first argument in *AddEmModel* is 0 which means highest priority.

The class *G4PAIPhotonModel* generates both  $\delta$ -electrons and photons as secondaries and can be used for more detailed descriptions of ionisation space distribution around the particle trajectory.

### 8.6.3 Photoabsorption Cross Section at Low Energies

The photoabsorption cross section,  $\sigma_\gamma(\omega)$ , where  $\omega$  is the photon energy, is used in GEANT4 for the description of the photo-electric effect, X-ray transportation and ionisation effects in very thin absorbers. As mentioned in the discussion of photoabsorption ionisation (see *Photoabsorption Ionisation Model*), it is convenient to represent the cross section as a polynomial in  $\omega^{-1}$  [BFR90] :

$$\sigma_\gamma(\omega) = \sum_{k=1}^4 a_k^{(i)} \omega^{-k}.$$

Using cross sections from the original Sandia data tables, calculations of primary ionisation and energy loss distributions produced by relativistic charged particles in gaseous detectors show clear disagreement with experimental data, especially for gas mixtures which include xenon. Therefore a special investigation was performed [VMAPeal94] by fitting the coefficients  $a_k^{(i)}$  to modern data from synchrotron radiation experiments in the energy range of 10-50 eV. The fits were performed for elements typically used in detector gas mixtures: hydrogen, fluorine, carbon, nitrogen and oxygen. Parameters for these elements were extracted from data on molecular gases such as N<sub>2</sub>, O<sub>2</sub>, CO<sub>2</sub>, CH<sub>4</sub>, and CF<sub>4</sub> [eal73, eal77]. Parameters for the noble gases were found using data given in the tables [MW76, WM80].

## 8.7 ATIMA energy-loss model

ATIMA (ATomic Interaction with MATter) classes, *G4AtimaEnergyLossModel* and *G4AtimaFluctuations*, implemented in GEANT4 since version 10.5 predicts the energy loss and energy-loss straggling of ions penetrating matter for kinetic energies ranging from 1 keV/u to 450 GeV/u. The model is developed at GSI Helmholtz Center for Heavy Ion Research GmbH since 1994. In the last two decades the model has been widely validated for ions using experimental data obtained from experiments carried out at the fragment separator FRS [GS98, SG98]. Basically, the model is based on the Bethe formula but including corrections from the theory developed by Lindhard and Soerensen [LS96], which make this model a powerful tool to predict the energy loss and energy-loss straggling of medium and heavy ions accelerated at relativistic energies [eal94, eal96, eal02, eal00]. This section is devoted to explain the main ingredients and equations of ATIMA model in GEANT4.

### 8.7.1 Continuous energy loss

Above kinetic energies of 30 MeV/u, the stopping power is obtained from the theory developed by Lindhard and Soerensen (LS) [LS96] including the following corrections: the shell effects [BB64], a Barkas term [JM72, Lin76] and the Fermi-density effect [SP71a]. Nuclear size effect of projectiles, which are important for ions moving at high relativistic velocities, comes also from the LS theory. The mean charge of the projectiles is parametrized according to ref. [PB68]. For ions with medium and high atomic numbers the LS theory differs substantially from the Bethe formula because the later is based on the first-order Born approximation, while the LS theory is the exact solution for two-body free electron [eal94, eal96, LS96]. In addition, energy transfer in elastic collisions with the whole target atom is also included.

In ATIMA the continuous energy loss per unit of path length is calculated according to

$$\frac{dE}{dx} = \left( \frac{dE}{dx} \right)_{in} + \left( \frac{dE}{dX} \right)_{elastic} \quad (8.15)$$

where the inelastic (in) contribution is calculated as follows

$$\left( \frac{dE}{dx} \right)_{in} = 2\pi r_e^2 mc^2 n_{el} \frac{< q >^2 Z_T}{A_T \beta^2} \left( \left[ \ln \left( \frac{2mc^2 \beta^2 \gamma^2}{I^2} \right) - \beta^2 - \frac{C}{Z_T} \right] B + LS - \delta/2 \right)$$

being

$r_e$  = classical electron radius =  $e^2/(4\pi\epsilon_0 mc^2)$

$mc^2$  = mass-energy of the electron

$n_{el}$  = electron density in the material

$I$  = mean excitation energy of the material

$Z_T$  = atomic number of the material

$< q >$  = average charge of the hadron or ion in units of the electron charge

$\gamma = E/mc^2$

$\beta^2 = 1 - (1/\gamma^2)$

$C$  = Shell correction function

$B$  = Barkas term

$LS$  = LS term including nuclear size effects for ions at relativistic velocities

$\delta$  = density effect function

The *LS term* accounts for nuclear size and scattering corrections to the Bethe formula [eal94]. The values of LS are interpolated between pre-calculated tables obtained by an analysis of partial waves each contributing with different phase shift [LS96]. These partial waves were calculated with a model developed by Soerensen and they were then summed up for the tables used in ATIMA.

The *shell correction term C* accounts for the fact that at projectile velocities comparable or even smaller than the orbital velocities of the bound target electrons the energy transfer is less effective. This correction is considered only at low energies  $\gamma\beta < 0.13$  and is expressed in the form

$$C = 10^{-9} [(422.377\eta^{-2} + 30.4043\eta^{-4} - 0.38106\eta^{-6})I^2 + (3.858019\eta^{-2} - 0.1667989\eta^{-4} + 0.00157955\eta^{-6})I^3]$$

where  $\eta = \gamma\beta$ .

The *Barkas correction term B* accounts for close and distant collisions and is introduced as a polarisation effect. This term is parameterized in the form

$$B = 1 + 2 < q > \frac{\theta}{\sqrt{(Z_T)\Phi}}$$

where  $\theta$  is calculated according to ref. [JM72],  $\Phi$  is defined as

$$\Phi = \frac{\gamma^2 \beta^2}{Z_T \alpha}$$

and  $\langle q \rangle$  represents the average charge of the projectile, which is determined according to the parameterization given by Pierce and Blann [PB68]:

$$\langle q \rangle = Z_P (1 - e^{(-0.95 \frac{\beta}{\alpha Z_P})}) \quad (8.16)$$

The *density correction*  $\delta$  is described according to the formulation given by Sternheimer [SP71b].

Below 10 MeV/u ATIMA uses an older version of Ziegler's SRIM code [JFZL85], in which the continuous energy loss per unit of path length is calculated according to

$$\left( \frac{dE}{dx} \right)_{in} = Se(\gamma_1 Z_P)^2$$

where  $Se$  represents the stopping power per unit of path length of a proton passing through the same material. The effective charge  $\gamma_1$  is parameterized as

$$\gamma_1 = q_1 + 0.5(1 - q_1) \left( \frac{v_0}{v_F} \right)^2 \ln \left[ 1 + \left( \frac{2\Lambda v_F}{a_0 v_0} \right)^2 \right] C_1$$

where  $v_0$  is the Bohr velocity,  $a_0$  is the Bohr radius and  $v_F$  is the target Fermi velocity that depends on  $Z_T$ . Here  $q_1$  is defined according to

$$q_1 = 1 - \exp(0.803y_r^{0.3} - 1.3167y_r^{0.6} - 0.38157y_r - 0.008983y_r^2)$$

where  $y_r$  is a function of the projectile velocity  $v$

$$y_r = v \left( 1 + \frac{v_F^2}{5v_1^2} \right)$$

or

$$y_r = \frac{0.75v_F}{v_0 Z_P^{2/3}} \left( 1 + \frac{2v^2}{3v_F^2} - \frac{v^4}{15v_F^4} \right)$$

if the projectile velocity is lower than the target Fermi velocity.

$\Lambda$  is the screening length defined as

$$\Lambda = \frac{2a_0(1 - q_1)^{2/3}}{Z_P^{1/3}(1 - (1 - q_1)/7)}$$

and  $C_1$  is expressed in the form

$$C_1 = 1 + \frac{1}{Z_P^2} (0.18 + 0.0015Z_T) \exp(-15.2 + 2\ln(E_P))$$

where  $E_P$  is the projectile kinetic energy in units of keV/u.

In the intermediate energy range  $10 < E_P < 30$  MeV/u ATIMA interpolates between the two parameterizations.

Finally, the elastic contribution in eq. (8.15) is obtained according to

$$\left( \frac{dE}{dx} \right)_{elastic} = \frac{846.21 \cdot 10^{-23} Z_P Z_T A_P A_v \chi}{A_T A_{sum} Z_{pow}}$$

where  $Z_P$  is the atomic number of the projectile,  $A_{sum} = A_T + A_P$ ,  $Z_{pow} = Z_T^{0.23} + Z_P^{0.23}$  and

$$\begin{aligned} \chi &= \frac{\ln(\epsilon)}{2\epsilon} && : \text{ for } \epsilon > 30 \\ \chi &= 0.5 \frac{\ln(1+1.01323\epsilon)}{\epsilon+0.01321\epsilon^{0.21226}+0.19593\epsilon^{0.5}} && : \text{ for } \epsilon \leq 30 \end{aligned}$$

where  $\epsilon$  is defined as:  $\epsilon = 32530 A_T A_P E_P / (Z_T Z_P A_{sum} Z_{pow})$  with  $E_P$  in units of keV/u.

## 8.7.2 Fluctuations of energy loss

ATIMA also accounts for the determination of fluctuations of the energy lost by ions penetrating matter. Here, the energy-loss straggling comes also from the Lindhard and Soerensen theory [eal96]. The variance is defined as

$$\Omega^2 = 4\pi N_a m_e c^2 r_e^2 \gamma^2 \chi < q >^2 \frac{Z_T}{A_T}$$

where  $\chi$  is a correction obtained from the Lindhard and Soerensen theory [eal96, LS96] and  $< q >$  is calculated according to eq. (8.16).

## ELASTIC SCATTERING

### 9.1 Multiple Scattering

Elastic scattering of electrons and other charged particles is an important component of any transport code. Elastic cross section is huge when particle energy decreases, so multiple scattering (MSC) approach should be introduced in order to have acceptable CPU performance of the simulation. A universal interface *G4VMultipleScattering* is used by all GEANT4 MSC processes [eal09, VNIU10]:

- *G4eMultipleScattering*;
- *G4hMultipleScattering*;
- *G4MuMultipleScattering*.

For concrete simulation the *G4VMscModel* interface is used, which is an extension of the base *G4VEmModel* interface. The following models are available:

- *G4UrbanMscModel* - it is applicable to all types of particles and is the default model for electrons and positrons below 100 MeV [eal17];
- *G4GoudsmitSaundersonModel* - for electrons and positrons [OKT09], this model was recently rewritten [eal17] and provides the best accuracy of electron transport below 100 MeV [SIN18];
- *G4WentzelVIModel* - is the default model for all charged particles [eal17, eal16, VNIU10] including electrons and positrons above 100 MeV, it is included in Physics List together with *G4CoulombScattering* process, which is responsible for large angle scattering;
- *G4LowEWentzelVIModel* - for all particles with low-energy limit 10 eV - is a less accurate variant of the above mode.

The discussion on GEANT4 MSC models is available in Ref. [VNIU10]. Below we will describe models developed by L. Urban [Urb06], because these models are used in many GEANT4 applications and have general components reused by other models.

#### 9.1.1 Introduction

MSC simulation algorithms can be classified as either *detailed* or *condensed*. In the detailed algorithms, all the collisions/interactions experienced by the particle are simulated. This simulation can be considered as exact, it gives the same results as the solution of the transport equation. However, it can be used only if the number of collisions is not too large, a condition fulfilled only for special geometries (such as thin foils, or low density gas). In solid or liquid media the average number of collisions is very large and the detailed simulation becomes very inefficient. High energy simulation codes use condensed simulation algorithms, in which the global effects of the collisions are simulated at the end of a track segment. The global effects generally computed in these codes are the net energy loss, displacement, and change of direction of the charged particle. The last two quantities are computed from MSC theories used in the codes and the accuracy of the condensed simulations is limited by accuracy of MSC approximation.

Most particle physics simulation codes use the multiple scattering theories of Molière [Moliere48], Goudsmit and Saunderson [GS40] and Lewis [Lew50]. The theories of Molière and Goudsmit-Saunderson give only the angular distribution after a step, while the Lewis theory computes the moments of the spatial distribution as well. None of these MSC theories gives the probability distribution of the spatial displacement. Each of the MSC simulation codes incorporates its own algorithm to determine the angular deflection, true path length correction, and spatial displacement of the charged particle after a given step. These algorithms are not exact, of course, and are responsible for most of the uncertainties of the transport codes. Also due to inaccuracy of MSC the simulation results can depend on the value of the step length and generally user has to select the value of the step length carefully.

A new class of MSC simulation, the *mixed* simulation algorithms (see e.g.[JMFernandezVS93]), appeared in the literature recently. The mixed algorithm simulates the *hard* collisions one by one and uses a MSC theory to treat the effects of the *soft* collisions at the end of a given step. Such algorithms can prevent the number of steps from becoming too large and also reduce the dependence on the step length. GEANT4 original implementation of a similar approach is realized in *G4WentzelVIModel* [VNIU10].

The Urban MSC models used in GEANT4 belongs to the class of condensed simulations. Urban uses model functions to determine the angular and spatial distributions after a step. The functions have been chosen in such a way as to give the same moments of the (angular and spatial) distributions as are given by the Lewis theory [Lew50].

### 9.1.2 Definition of Terms

In simulation, a particle is transported by steps through the detector geometry. The shortest distance between the endpoints of a step is called the *geometrical path length*,  $z$ . In the absence of a magnetic field, this is a straight line. For non-zero fields,  $z$  is the length along a curved trajectory. Constraints on  $z$  are imposed when particle tracks cross volume boundaries. The path length of an actual particle, however, is usually longer than the *geometrical path length*, due to multiple scattering. This distance is called the *true path length*,  $t$ . Constraints on  $t$  are imposed by the physical processes acting on the particle.

The properties of the MSC process are determined by the *transport mean free paths*,  $\lambda_k$ , which are functions of the energy in a given material. The  $k$ -th transport mean free path is defined as

$$\frac{1}{\lambda_k} = 2\pi n_a \int_{-1}^1 [1 - P_k(\cos \chi)] \frac{d\sigma(\chi)}{d\Omega} d(\cos \chi)$$

where  $d\sigma(\chi)/d\Omega$  is the differential cross section of the scattering,  $P_k(\cos \chi)$  is the  $k$ -th Legendre polynomial, and  $n_a$  is the number of atoms per volume.

Most of the mean properties of MSC computed in the simulation codes depend only on the first and second transport mean free paths. The mean value of the geometrical path length (first moment) corresponding to a given true path length  $t$  is given by

$$\langle z \rangle = \lambda_1 \left[ 1 - \exp \left( -\frac{t}{\lambda_1} \right) \right] \quad (9.1)$$

Eq.(9.1) is an exact result for the mean value of  $z$  if the differential cross section has axial symmetry and the energy loss can be neglected. The transformation between true and geometrical path lengths is called the *path length correction*. This formula and other expressions for the first moments of the spatial distribution were taken from either [JMFernandezVS93] or [KB98], but were originally calculated by Goudsmit and Saunderson [GS40] and Lewis [Lew50].

At the end of the true step length,  $t$ , the scattering angle is  $\theta$ . The mean value of  $\cos \theta$  is

$$\langle \cos \theta \rangle = \exp \left[ -\frac{t}{\lambda_1} \right] \quad (9.2)$$

The variance of  $\cos \theta$  can be written as

$$\sigma^2 = \langle \cos^2 \theta \rangle - \langle \cos \theta \rangle^2 = \frac{1 + 2e^{-2\kappa\tau}}{3} - e^{-2\tau} \quad (9.3)$$

where  $\tau = t/\lambda_1$  and  $\kappa = \lambda_1/\lambda_2$ . The mean lateral displacement is given by a more complicated formula [JMFernandezVS93], but this quantity can also be calculated relatively easily and accurately. The square of the *mean lateral displacement* is

$$\langle x^2 + y^2 \rangle = \frac{4\lambda_1^2}{3} \left[ \tau - \frac{\kappa+1}{\kappa} + \frac{\kappa}{\kappa-1} e^{-\tau} - \frac{1}{\kappa(\kappa-1)} e^{-\kappa\tau} \right] \quad (9.4)$$

Here it is assumed that the initial particle direction is parallel to the the  $z$  axis. The lateral correlation is determined by the equation

$$\langle xv_x + yv_y \rangle = \frac{2\lambda_1}{3} \left[ 1 - \frac{\kappa}{\kappa-1} e^{-\tau} + \frac{1}{\kappa-1} e^{-\kappa\tau} \right] \quad (9.5)$$

where  $v_x$  and  $v_y$  are the x and y components of the direction unit vector. This equation gives the correlation strength between the final lateral position and final direction.

The transport mean free path values have been calculated in Refs. [LI87], [eal90] for electrons and positrons in the kinetic energy range in 15 materials. The Urban MSC model in GEANT4 uses these values for kinetic energies below 10 MeV. For high energy particles (above 10 MeV) the transport mean free path values have been taken from a paper of R. Mayol and F. Salvat [MS97]. When necessary, the model linearly interpolates or extrapolates the transport cross section,  $\sigma_1 = 1/\lambda_1$ , in atomic number  $Z$  and in the square of the particle velocity,  $\beta^2$ . The ratio  $\kappa$  is a very slowly varying function of the energy:  $\kappa > 2$  for  $T >$  a few keV, and  $\kappa \rightarrow 3$  for very high energies (see [KB98]). Hence, a constant value of 2.5 is used in the model.

Nuclear size effects are negligible for low energy particles and they are accounted for in the Born approximation in [MS97], so there is no need for extra corrections of this kind in the Urban model.

### 9.1.3 Path Length Correction

As mentioned above, the path length correction refers to the transformation  $t \rightarrow g$  and its inverse. The  $t \rightarrow g$  transformation is given by Eq.(9.1) if the step is small and the energy loss can be neglected. If the step is not small the energy dependence makes the transformation more complicated. For this case Eqs.(9.2),(9.1) should be modified as

$$\langle \cos \theta \rangle = \exp \left[ - \int_0^t \frac{du}{\lambda_1(u)} \right] \quad (9.6)$$

$$\langle z \rangle = \int_0^t \langle \cos \theta \rangle_u du \quad (9.7)$$

where  $\theta$  is the scattering angle,  $t$  and  $z$  are the true and geometrical path lengths, and  $\lambda_1$  is the transport mean free path.

In order to compute Eqs.(9.6),(9.7) the  $t$  dependence of the transport mean free path must be known.  $\lambda_1$  depends on the kinetic energy of the particle which decreases along the step. All computations in the model use a linear approximation for this  $t$  dependence:

$$\lambda_1(t) = \lambda_{10}(1 - \alpha t) \quad (9.8)$$

Here  $\lambda_{10}$  denotes the value of  $\lambda_1$  at the start of the step, and  $\alpha$  is a constant. It is worth noting that Eq.(9.8) is *not* a crude approximation. It is rather good at low ( $< 1$  MeV) energy. At higher energies the step is generally much smaller than the range of the particle, so the change in energy is small and so is the change in  $\lambda_1$ . Using Eqs.(9.6) - (9.8) the explicit formula for  $\langle \cos \theta \rangle$  and  $\langle z \rangle$  are:

$$\langle \cos \theta \rangle = (1 - \alpha t)^{\frac{1}{\alpha \lambda_{10}}} \quad (9.9)$$

$$\langle z \rangle = \frac{1}{\alpha(1 + \frac{1}{\alpha \lambda_{10}})} \left[ 1 - (1 - \alpha t)^{1 + \frac{1}{\alpha \lambda_{10}}} \right] \quad (9.10)$$

The value of the constant  $\alpha$  can be expressed using  $\lambda_{10}$  and  $\lambda_{11}$  where  $\lambda_{11}$  is the value of the transport mean free path at the end of the step

$$\alpha = \frac{\lambda_{10} - \lambda_{11}}{t\lambda_{10}}$$

At low energies ( $T_{kin} < M$ , where  $M$  is the particle mass)  $\alpha$  has a simpler form:

$$\alpha = \frac{1}{r_0}$$

where  $r_0$  denotes the range of the particle at the start of the step. It can easily be seen that for a small step (i.e. for a step with small relative energy loss) the formula of  $\langle z \rangle$  is

$$\langle z \rangle = \lambda_{10} \left[ 1 - \exp \left( -\frac{t}{\lambda_{10}} \right) \right] \quad (9.11)$$

Eq. (9.10) or (9.11) gives the mean value of the geometrical step length for a given true step length. The actual geometrical path length is sampled in the model according to the simple probability density function defined for  $v = z/t \in [0, 1]$ :

$$f(v) = (k+1)(k+2)v^k(1-v)$$

The value of the exponent  $k$  is computed from the requirement that  $f(v)$  must give the same mean value for  $z = vt$  as Eq. (9.10) or (9.11). Hence

$$k = \frac{3\langle z \rangle - t}{t - \langle z \rangle}$$

The value of  $z = vt$  is sampled using  $f(v)$  if  $k > 0$ , otherwise  $z = \langle z \rangle$  is used. The  $g \rightarrow t$  transformation is performed using the mean values. The transformation can be written as

$$t(z) = \langle t \rangle = -\lambda_1 \log \left( 1 - \frac{z}{\lambda_1} \right)$$

if the geometrical step is small and

$$t(z) = \frac{1}{\alpha} \left[ 1 - (1 - \alpha w z)^{\frac{1}{w}} \right]$$

where

$$w = 1 + \frac{1}{\alpha \lambda_{10}}$$

if the step is not small, i.e. the energy loss should be taken into account.

#### 9.1.4 Angular Distribution

The quantity  $u = \cos \theta$  is sampled according to a model function  $g(u)$ . The shape of this function has been chosen such that Eqs. (9.2) and (9.3) are satisfied. The functional form of  $g$  is

$$g(u) = q[p g_1(u) + (1-p) g_2(u)] + (1-q) g_3(u) \quad (9.12)$$

where  $0 \leq p, q \leq 1$ , and the  $g_i$  are simple functions of  $u = \cos \theta$ , normalized over the range  $u \in [-1, 1]$ . The functions  $g_i$  have been chosen as

$$\begin{aligned} g_1(u) &= C_1 e^{-a(1-u)} & -1 \leq u_0 \leq u \leq 1 \\ g_2(u) &= C_2 \frac{1}{(b-u)^d} & -1 \leq u \leq u_0 \leq 1 \\ g_3(u) &= C_3 & -1 \leq u \leq 1 \end{aligned}$$

where  $a > 0$ ,  $b > 0$ ,  $d > 0$  and  $u_0$  are model parameters, and the  $C_i$  are normalization constants. It is worth noting that for small scattering angles,  $\theta$ ,  $g_1(u)$  is nearly Gaussian ( $\exp(-\theta^2/2\theta_0^2)$ ) if  $\theta_0^2 \approx 1/a$ , while  $g_2(u)$  has a Rutherford-like tail for large  $\theta$ , if  $b \approx 1$  and  $d$  is not far from 2.

### 9.1.5 Determination of the Model Parameters

The parameters  $a$ ,  $b$ ,  $d$ ,  $u_0$  and  $p$ ,  $q$  are not independent. The requirement that the angular distribution function  $g(u)$  and its first derivative be continuous at  $u = u_0$  imposes two constraints on the parameters:

$$\begin{aligned} p g_1(u_0) &= (1 - p) g_2(u_0) \\ p a g_1(u_0) &= (1 - p) \frac{d}{b - u_0} g_2(u_0) \end{aligned} \quad (9.13)$$

A third constraint comes from Eq. (9.6) :  $g(u)$  must give the same mean value for  $u$  as the theory. It follows from Eqs. (9.9) and (9.12) that

$$q\{p\langle u \rangle_1 + (1 - p)\langle u \rangle_2\} = [1 - \alpha t]^{\frac{1}{\alpha X_{10}}} \quad (9.14)$$

where  $\langle u \rangle_i$  denotes the mean value of  $u$  computed from the distribution  $g_i(u)$ . The parameter  $a$  was chosen according to a modified Highland-Lynch-Dahl formula for the width of the angular distribution [Hig75], [LD91].

$$a = \frac{0.5}{1 - \cos(\theta_0)}$$

where  $\theta_0$  is

$$\theta_0 = \frac{13.6\text{MeV}}{\beta cp} z_{ch} \sqrt{\frac{t}{X_0}} \left[ 1 + h_c \ln \left( \frac{t}{X_0} \right) \right]$$

when the original Highland-Lynch-Dahl formula is used. Here  $\theta_0 = \theta_{plane}^{rms}$  is the width of the approximate Gaussian projected angle distribution,  $p$ ,  $\beta c$  and  $z_{ch}$  are the momentum, velocity and charge number of the incident particle, and  $t/X_0$  is the true path length in radiation length unit. The correction term  $h_c = 0.038$  in the formula. This value of  $\theta_0$  is from a fit to the Molière distribution for singly charged particles with  $\beta = 1$  for all  $Z$ , and is accurate to 11% or better for  $10^{-3} \leq t/X_0 \leq 100$  (see e.g. Rev. of Particle Properties, section 23.3).

The model uses a slightly modified Highland-Lynch-Dahl formula to compute  $\theta_0$ . For electrons/positrons the modified  $\theta_0$  formula is

$$\theta_0 = \frac{13.6\text{MeV}}{\beta cp} z_{ch} \sqrt{y c}$$

where

$$y = \ln \left( \frac{t}{X_0} \right)$$

The correction term  $c$  and coefficients  $c_i$  are

$$\begin{aligned} c &= c_0(c_1 + c_2y), \\ c_0 &= 0.990395 - 0.168386Z^{1/6} + 0.093286Z^{1/3}, \\ c_1 &= 1 - \frac{0.08778}{Z}, \\ c_2 &= 0.04078 + 0.00017315Z. \end{aligned}$$

This formula gives a much smaller step dependence in the angular distribution than the Highland form. The value of the parameter  $u_0$  has been chosen as

$$u_0 = 1 - \frac{\xi}{a}$$

where

$$\xi = d_1 + d_2v + d_3v^2 + d_4v^3$$

with

$$v = \ln \left( \frac{t}{\lambda_1} \right)$$

The parameters  $d_i$ -s have the form

$$d_i = d_{i0} + d_{i1}Z^{\frac{1}{3}} + d_{i2}Z^{\frac{2}{3}}$$

The numerical values of the  $d_{ij}$  constants can be found in the code.

The tail parameter  $d$  is the same as the parameter  $\xi$ .

This (empirical) expression is obtained comparing the simulation results to the data of the MuScat experiment [eal06]. The remaining three parameters can be computed from Eqs. (9.13) - (9.14). The numerical value of the parameters can be found in the code.

In the case of heavy charged particles ( $\mu$ ,  $\pi$ ,  $p$ , etc.) the mean transport free path is calculated from the electron or positron  $\lambda_1$  values with a 'scaling' applied. This is possible because the transport mean free path  $\lambda_1$  depends only on the variable  $P\beta c$ , where  $P$  is the momentum, and  $\beta c$  is the velocity of the particle.

In its present form the model samples the path length correction and angular distribution from model functions, while for the lateral displacement and the lateral correlation only the mean values are used and all the other correlations are neglected. However, the model is general enough to incorporate other random quantities and correlations in the future.

### 9.1.6 Step Limitation Algorithm

In GEANT4 the boundary crossing is treated by the transportation process. The transportation ensures that the particle does not penetrate in a new volume without stopping at the boundary, it restricts the step size when the particle leaves a volume. However, this step restriction can be rather weak in big volumes and this fact can result a not very good angular distribution after the volume. At the same time, there is no similar step limitation when a particle enters a volume and this fact does not allow a good backscattering simulation for low energy particles. Low energy particles penetrate too deeply into the volume in the first step and then, because of energy loss, they are not able to reach again the boundary in backward direction.

MSC step limitation algorithm has been developed [Urb06] in order to achieve optimal balance between simulation precision and CPU performance of simulation for different applications. At the start of a track or after entering in a new volume, the algorithm restricts the step size to a value

$$f_r \cdot \max\{r, \lambda_1\}$$

where  $r$  is the range of the particle,  $f_r$  is a parameter  $\in [0, 1]$ , taking the max of  $r$  and  $\lambda_1$  is an empirical choice. The value of  $f_r$  is constant for low energy particles while for particles with  $\lambda_1 > \lambda_{lim}$  an effective value is used given by the scaling equation

$$f_{refl} = f_r \cdot \left[ 1 - sc + sc * \frac{\lambda_1}{\lambda_{lim}} \right]$$

(The numerical values  $sc = 0.25$  and  $\lambda_{lim} = 1$  mm are used in the equation.) In order not to use very small - unphysical - step sizes a lower limit is given for the step size as

$$tlimitmin = \max \left[ \frac{\lambda_1}{nstepmax}, \lambda_{elastic} \right]$$

with  $nstepmax = 25$  and  $\lambda_{elastic}$  is the elastic mean free path of the particle (see later). It can be easily seen that this kind of step limitation poses a real constraint only for low energy particles. In order to prevent a particle from crossing

a volume in just one step, an additional limitation is imposed: after entering a volume the step size cannot be bigger than

$$\frac{d_{geom}}{f_g}$$

where  $d_{geom}$  is the distance to the next boundary (in the direction of the particle) and  $f_g$  is a constant parameter. A similar restriction at the start of a track is

$$\frac{2d_{geom}}{f_g}$$

At this point the program also checks whether the particle has entered a new volume. If it has, the particle steps cannot be bigger than  $t_{lim} = f_r \max(r, \lambda)$ . This step limitation is governed by the physics, because  $t_{lim}$  depends on the particle energy and the material.

The choice of the parameters  $f_r$  and  $f_g$  is also related to performance. By default  $f_r = 0.02$  and  $f_g = 2.5$  are used, but these may be set to any other value in a simple way. One can get an approximate simulation of the backscattering with the default value, while if a better backscattering simulation is needed it is possible to get it using a smaller value for  $f_r$ . However, this model is very simple and it can only approximately reproduce the backscattering data.

### 9.1.7 Boundary Crossing Algorithm

A special stepping algorithm has been implemented in order to improve the simulation around interfaces. This algorithm does not allow ‘big’ last steps in a volume and ‘big’ first steps in the next volume. The step length of these steps around a boundary crossing can not be bigger than the mean free path of the elastic scattering of the particle in the given volume (material). After these small steps the particle scattered according to a single scattering law (i.e. there is no multiple scattering very close to the boundary or at the boundary).

The key parameter of the algorithm is the variable called *skin*. The algorithm is not active for  $skin \leq 0$ , while for  $skin > 0$  it is active in layers of thickness  $skin \cdot \lambda_{elastic}$  before boundary crossing and of thickness  $(skin - 1) \cdot \lambda_{elastic}$  after boundary crossing (for  $skin = 1$  there is only one small step just before the boundary). In this active area the particle performs steps of length  $\lambda_{elastic}$  (or smaller if the particle reaches the boundary traversing a smaller distance than this value).

The scattering at the end of a small step is single or plural and for these small steps there are no path length correction and lateral displacement computation. In other words the program works in this thin layer in ‘microscopic mode’. The elastic mean free path can be estimated as

$$\lambda_{elastic} = \lambda_1 \cdot rat(T_{kin})$$

where  $rat(T_{kin})$  a simple empirical function computed from the elastic and first transport cross section values of Mayol and Salvat [MS97]

$$rat(T_{kin}) = \frac{0.001(\text{MeV})^2}{T_{kin}(T_{kin} + 10\text{MeV})}$$

$T_{kin}$  is the kinetic energy of the particle.

At the end of a small step the number of scatterings is sampled according to the Poisson’s distribution with a mean value  $t/\lambda_{elastic}$  and in the case of plural scattering the final scattering angle is computed by summing the contributions of the individual scatterings. The single scattering is determined by the distribution

$$g(u) = C \frac{1}{(2a + 1 - u)^2}$$

where  $u = \cos(\theta)$ ,  $a$  is the screening parameter,  $C$  is a normalization constant. The form of the screening parameter is the same as in the single scattering (see there).

## 9.1.8 Implementation Details

The step length of a particles is determined by the physics processes or the geometry of the detectors. The tracking/stepping algorithm checks all the step lengths demanded by the (continuous or discrete) physics processes and determines the minimum of these step lengths (see [True Step Length](#)). The MSC model should be called to compute step limit after all processes except the transportation process. The following sequence of computations are performed to make the step:

- the minimum of all processes *true step length* limit  $t$  including one of the MSC process is selected;
- The conversion  $t \rightarrow g$  (*geometrical step limit*) is performed;
- the minimum of obtained value  $g$  and the transportation step limit is selected;
- The final conversion  $g \rightarrow t$  is performed.

The reason for this ordering is that the physics processes ‘feel’ the true path length  $t$  traveled by the particle, while the transportation process (geometry) uses the  $z$  step length.

A new optional mechanism was recently introduced allowing sample displacement in the vicinity of geometry boundary. If it is enabled and transportation limits the step due to a geometry boundary, then after initial sampling of the displacement an additional ‘push’ of the track is applied forcing the end point be at the boundary. Corresponding correction to the true step length is applied according to the value of the ‘push’.

After the actual step of the particle is done, the MSC model is responsible for sampling of scattering angle and relocation of the end-point of the step. The scattering angle  $\theta$  of the particle after the step of length  $t$  is sampled according to the model function given in Eq. (9.12). The azimuthal angle  $\phi$  is generated uniformly in the range  $[0, 2\pi]$ .

After the simulation of the scattering angle, the lateral displacement is computed using Eq. (9.4). Then the correlation given by Eq. (9.5) is used to determine the direction of the lateral displacement. Before ‘moving’ the particle according to the displacement a check is performed to ensure that the relocation of the particle with the lateral displacement does not take the particle beyond the volume boundary.

Default MSC parameter values optimized per particle type are shown in [Table 9.1](#). Note, that there are four types of step limitation by multiple scattering process:

- `Minimal` - only  $f_r$  parameter and range are used;
- `UseSafety` -  $f_r$  parameter, range and geometrical safety are used;
- `UseSafetyPlus` -  $f_r$  parameter, range and geometrical safety are used;
- `UseDistanceToBoundary` - uses particle range, geometrical safety and linear distance to geometrical boundary.

Table 9.1: The default values of parameters for different particle type.

particle	$e^+, e^-$	<i>muons, hadrons</i>	<i>ions</i>
<code>StepLimitType</code>	<code>fUseSafety</code>	<code>fMinimal</code>	<code>fMinimal</code>
<code>skin</code>	0	0	0
$f_r$	0.04	0.2	0.2
$f_g$	2.5	0.1	0.1
<code>LateralDisplacement</code>	<code>true</code>	<code>false</code>	<code>false</code>

The parameters of the model can be changed via public functions of the base class `G4VMultipleScattering`. They can be changed for all multiple scattering processes simultaneously via `G4EmParameters` class, `G4EmProcessOptions` class, or via GEANT4 UI commands. The following commands are available:

```
/process/msc/StepLimit UseDistanceToBoundary
/process/msc/LateralDisplacement false
/process/msc/MuHadLateralDisplacement false
/process/msc/DisplacementBeyondSafety true
/process/msc/RangeFactor 0.02
/process/msc/GeomFactor 2.5
/process/msc/Skin 2
```

## 9.2 Single Scattering

Single elastic scattering process is an alternative to the multiple scattering process. The advantage of the single scattering process is in possibility of usage of theory based cross sections, in contrary to the GEANT4 multiple scattering model [Urb06], which uses a number of phenomenological approximations on top of Lewis theory. The process *G4CoulombScattering* was created for simulation of single scattering of muons, it also applicable with some physical limitations to electrons, muons and ions. Because each of elastic collisions are simulated the number of steps of charged particles significantly increasing in comparison with the multiple scattering approach, correspondingly its CPU performance is poor. However, in low-density media (vacuum, low-density gas) multiple scattering may provide wrong results and single scattering processes are more appropriate.

### 9.2.1 Coulomb Scattering

The single scattering model of Wentzel [Wen27] is used in many multiple scattering models including the Penelope code [JM Fernandez VS93]. The Wentzel model for describing elastic scattering of particles with charge  $ze$  ( $z = -1$  for electron) by atomic nucleus with atomic number  $Z$  is based on simplified scattering potential

$$V(r) = \frac{zZe^2}{r} \exp(-r/R),$$

where the exponential factor tries to reproduce the effect of screening. The parameter  $R$  is a screening radius [Bet53]

$$R = 0.885Z^{-1/3}r_B,$$

where  $r_B$  is the Bohr radius. In the first Born approximation the elastic scattering cross section  $\sigma^{(W)}$  can be obtained as

$$\frac{d\sigma^{(W)}(\theta)}{d\Omega} = \frac{(ze^2)^2}{(p\beta c)^2} \frac{Z(Z+1)}{(2A + 1 - \cos\theta)^2}, \quad (9.15)$$

where  $p$  is the momentum and  $\beta$  is the velocity of the projectile particle. The screening parameter  $A$  according to Moliere and Bethe [Bet53]

$$A = \left( \frac{\hbar}{2pR} \right)^2 (1.13 + 3.76(\alpha Z/\beta)^2),$$

where  $\alpha$  is the fine structure constant and the factor in brackets is used to take into account second order corrections to the first Born approximation. The total elastic cross section  $\sigma$  can be expressed via Wentzel cross section (9.15):

$$\frac{d\sigma(\theta)}{d\Omega} = \frac{d\sigma^{(W)}(\theta)}{d\Omega} \left( \frac{Z}{(1 + \frac{(qR_N)^2}{12})^2} + 1 \right) \frac{1}{Z+1}, \quad (9.16)$$

where  $q$  is momentum transfer to the nucleus,  $R_N$  is nuclear radius. This term takes into account nuclear size effect [eal02], the second term takes into account scattering off electrons. The results of simulation with the single scattering model (Fig. 9.1) are competitive with the results of the multiple scattering.

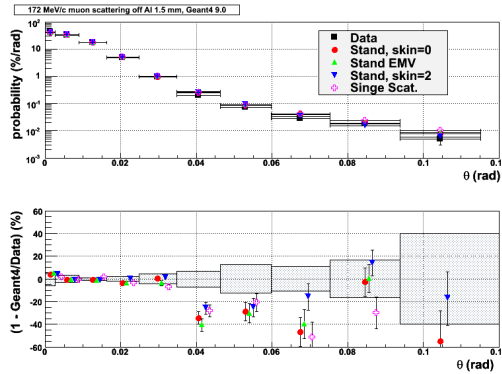


Fig. 9.1: Scattering of muons off 1.5 mm aluminum foil: data [eal06] - black squares; simulation - colored markers corresponding different options of multiple scattering and single scattering model; in the bottom plot - relative difference between the simulation and the data in percents; hashed area demonstrates one standard deviation of the data.

## 9.2.2 Implementation Details

The total cross section of the process is obtained as a result of integration of the differential cross section (9.16). The first term of this cross section is integrated in the interval  $(0, \pi)$ . The second term in the smaller interval  $(0, \theta_m)$ , where  $\theta_m$  is the maximum scattering angle off electrons, which is determined using the cut value for the delta electron production. Before sampling of angular distribution the random choice is performed between scattering off the nucleus and off electrons.

## 9.3 Ion Scattering

The necessity of accurately computing the characteristics of interatomic scattering arises in many disciplines in which energetic ions pass through materials. Traditionally, solutions to this problem not involving hadronic interactions have been dominated by the multiple scattering, which is reasonably successful, but not very flexible. In particular, it is relatively difficult to introduce into such a system a particular screening function which has been measured for a specific atomic pair, rather than the universal functions which are applied. In many problems of current interest, such as the behavior of semiconductor device physics in a space environment, nuclear reactions, particle showers, and other effects are critically important in modeling the full details of ion transport. The process *G4ScreenedNuclearRecoil* provides simulation of ion elastic scattering [MW05]. This process is available with extended electromagnetic example *TestEm7*.

### 9.3.1 Method

The method used in this computation is a variant of a subset of the method described in Ref.[MW91]. A very short recap of the basic material is included here. The scattering of two atoms from each other is assumed to be a completely classical process, subject to an interatomic potential described by a potential function

$$V(r) = \frac{Z_1 Z_2 e^2}{r} \phi\left(\frac{r}{a}\right)$$

where  $Z_1$  and  $Z_2$  are the nuclear proton numbers,  $e^2$  is the electromagnetic coupling constant ( $q_e^2/4\pi\epsilon_0$  in SI units),  $r$  is the inter-nuclear separation,  $\phi$  is the screening function describing the effect of electronic screening of the bare nuclear charges, and  $a$  is a characteristic length scale for this screening. In most cases,  $\phi$  is a universal function used for all ion pairs, and the value of  $a$  is an appropriately adjusted length to give reasonably accurate scattering behavior. In the method described here, there is no particular need for a universal function  $\phi$ , since the method is capable of directly solving the problem for most physically plausible screening functions. It is still useful to define a typical

screening length  $a$  in the calculation described below, to keep the equations in a form directly comparable with our previous work even though, in the end, the actual value is irrelevant as long as the final function  $\phi(r)$  is correct. From this potential  $V(r)$  one can then compute the classical scattering angle from the reduced center-of-mass energy  $\varepsilon \equiv E_c a / Z_1 Z_2 e^2$  (where  $E_c$  is the kinetic energy in the center-of-mass frame) and reduced impact parameter  $\beta \equiv b/a$

$$\theta_c = \pi - 2\beta \int_{x_0}^{\infty} f(z) dz / z^2$$

where

$$f(z) = \left( 1 - \frac{\phi(z)}{z \varepsilon} - \frac{\beta^2}{z^2} \right)^{-1/2}$$

and  $x_0$  is the reduced classical turning radius for the given  $\varepsilon$  and  $\beta$ .

The problem, then, is reduced to the efficient computation of this scattering integral. In our previous work, a great deal of analytical effort was included to proceed from the scattering integral to a full differential cross section calculation, but for application in a Monte-Carlo code, the scattering integral  $\theta_c(Z_1, Z_2, E_c, b)$  and an estimated total cross section  $\sigma_0(Z_1, Z_2, E_c)$  are all that is needed. Thus, we can skip algorithmically forward in the original paper to equations 15-18 and the surrounding discussion to compute the reduced distance of closest approach  $x_0$ . This computation follows that in the previous work exactly, and will not be reintroduced here.

For the sake of ultimate accuracy in this algorithm, and due to the relatively low computational cost of so doing, we compute the actual scattering integral (as described in equations 19-21 of [MW91]) using a Lobatto quadrature of order 6, instead of the 4th order method previously described. This results in the integration accuracy exceeding that of any available interatomic potentials in the range of energies above those at which molecular structure effects dominate, and should allow for future improvements in that area. The integral  $\alpha$  then becomes (following the notation of the previous paper)

$$\alpha \approx \frac{1 + \lambda_0}{30} + \sum_{i=1}^4 w'_i f \left( \frac{x_0}{q_i} \right) \quad (9.17)$$

where

$$\lambda_0 = \left( \frac{1}{2} + \frac{\beta^2}{2x_0^2} - \frac{\phi'(x_0)}{2\varepsilon} \right)^{-1/2} \quad (9.18)$$

$$w'_i \in [0.03472124, 0.1476903, 0.23485003, 0.1860249]$$

$$q_i \in [0.9830235, 0.8465224, 0.5323531, 0.18347974]$$

Then

$$\theta_c = \pi - \frac{\pi \beta \alpha}{x_0}$$

The other quantity required to implement a scattering process is the total scattering cross section  $\sigma_0$  for a given incident ion and a material through which the ion is propagating. This value requires special consideration for a process such as screened scattering. In the limiting case that the screening function is unity, which corresponds to Rutherford scattering, the total cross section is infinite. For various screening functions, the total cross section may or may not be finite. However, one must ask what the intent of defining a total cross section is, and determine from that how to define it.

In GEANT4, the total cross section is used to determine a mean-free-path  $l_\mu$  which is used in turn to generate random transport distances between discrete scattering events for a particle. In reality, where an ion is propagating through, for example, a solid material, scattering is not a discrete process but is continuous. However, it is a useful, and highly accurate, simplification to reduce such scattering to a series of discrete events, by defining some minimum energy transfer of interest, and setting the mean free path to be the path over which statistically one such minimal transfer has

occurred. This approach is identical to the approach developed for the original TRIM code [BH80]. As long as the minimal interesting energy transfer is set small enough that the cumulative effect of all transfers smaller than that is negligible, the approximation is valid. As long as the impact parameter selection is adjusted to be consistent with the selected value of  $l_\mu$ , the physical result isn't particularly sensitive to the value chosen.

Noting, then, that the actual physical result isn't very sensitive to the selection of  $l_\mu$ , one can be relatively free about defining the cross section  $\sigma_0$  from which  $l_\mu$  is computed. The choice used for this implementation is fairly simple. Define a physical cutoff energy  $E_{min}$  which is the smallest energy transfer to be included in the calculation. Then, for a given incident particle with atomic number  $Z_1$ , mass  $m_1$ , and lab energy  $E_{inc}$ , and a target atom with atomic number  $Z_2$  and mass  $m_2$ , compute the scattering angle  $\theta_c$  which will transfer this much energy to the target from the solution of

$$E_{min} = E_{inc} \frac{4 m_1 m_2}{(m_1 + m_2)^2} \sin^2 \frac{\theta_c}{2}.$$

Then, noting that  $\alpha$  from Eq.(9.17) is a number very close to unity, one can solve for an approximate impact parameter  $b$  with a single root-finding operation to find the classical turning point. Then, define the total cross section to be  $\sigma_0 = \pi b^2$ , the area of the disk inside of which the passage of an ion will cause at least the minimum interesting energy transfer. Because this process is relatively expensive, and the result is needed extremely frequently, the values of  $\sigma_0(E_{inc})$  are precomputed for each pairing of incident ion and target atom, and the results cached in a cubic-spline interpolation table. However, since the actual result isn't very critical, the cached results can be stored in a very coarsely sampled table without degrading the calculation at all, as long as the values of the  $l_\mu$  used in the impact parameter selection are rigorously consistent with this table.

The final necessary piece of the scattering integral calculation is the statistical selection of the impact parameter  $b$  to be used in each scattering event. This selection is done following the original algorithm from TRIM, where the cumulative probability distribution for impact parameters is

$$P(b) = 1 - \exp\left(\frac{-\pi b^2}{\sigma_0}\right)$$

where  $N \sigma_0 \equiv 1/l_\mu$  where  $N$  is the total number density of scattering centers in the target material and  $l_\mu$  is the mean free path computed in the conventional way. To produce this distribution from a uniform random variate  $r$  on  $(0,1]$ , the necessary function is

$$b = \sqrt{\frac{-\log r}{\pi N l_\mu}}$$

This choice of sampling function does have the one peculiarity that it can produce values of the impact parameter which are larger than the impact parameter which results in the cutoff energy transfer, as discussed above in the section on the total cross section, with probability  $1/e$ . When this occurs, the scattering event is not processed further, since the energy transfer is below threshold. For this reason, impact parameter selection is carried out very early in the algorithm, so the effort spent on uninteresting events is minimized.

The above choice of impact sampling is modified when the mean-free-path is very short. If  $\sigma_0 > \pi (\frac{l}{2})^2$  where  $l$  is the approximate lattice constant of the material, as defined by  $l = N^{-1/3}$ , the sampling is replaced by uniform sampling on a disk of radius  $l/2$ , so that

$$b = \frac{l}{2} \sqrt{r}$$

This takes into account that impact parameters larger than half the lattice spacing do not occur, since then one is closer to the adjacent atom. This also derives from TRIM.

One extra feature is included in our model, to accelerate the production of relatively rare events such as high-angle scattering. This feature is a cross-section scaling algorithm, which allows the user access to an unphysical control of the algorithm which arbitrarily scales the cross-sections for a selected fraction of interactions. This is implemented as a two-parameter adjustment to the central algorithm. The first parameter is a selection frequency  $f_h$  which sets what

fraction of the interactions will be modified. The second parameter is the scaling factor for the cross-section. This is implemented by, for a fraction  $f_h$  of interactions, scaling the impact parameter by  $b' = b/\sqrt{scale}$ . This feature, if used with care so that it does not provide excess multiple-scattering, can provide between 10 and 100-fold improvements to event rates. If used without checking the validity by comparing to un-adjusted scattering computations, it can also provide utter nonsense.

### 9.3.2 Implementation Details

The coefficients for the summation to approximate the integral for  $\alpha$  in Eq.(9.17) are derived from the values in Abramowitz & Stegun [MA65], altered to make the change-of-variable used for this integral. There are two basic steps to the transformation. First, since the provided abscissas  $x_i$  and weights  $w_i$  are for integration on [-1,1], with only one half of the values provided, and in this work the integration is being carried out on [0,1], the abscissas are transformed as:

$$y_i \in \left\{ \frac{1 \mp x_i}{2} \right\}$$

Then, the primary change-of-variable is applied resulting in:

$$\begin{aligned} q_i &= \cos \frac{\pi y_i}{2} \\ w'_i &= \frac{w_i}{2} \sin \frac{\pi y_i}{2} \end{aligned}$$

except for the first coefficient  $w'_1$  where the  $\sin()$  part of the weight is taken into the limit of  $\lambda_0$  as described in Eq.(9.18). This value is just  $w'_1 = w_1/2$ .

## 9.4 Single Scattering, Screened Coulomb Potential and NIEL

An alternative model of Coulomb scattering of ions have been developed based on [eal11] and references therein. The advantage of this model is the wide applicability range in energy from 50 keV to 100V TeV per nucleon.

### 9.4.1 Nucleus–Nucleus Interactions

As discussed in Ref. [eal11], at small distances from the nucleus, the potential energy is a Coulomb potential, while, at distances larger than the Bohr radius, the nuclear field is screened by the fields of atomic electrons. The interaction between two nuclei is usually described in terms of an interatomic Coulomb potential (e.g., see Section 2.1.4.1 of Ref. [LR09] and Section 4.1 of Ref. [eal93]), which is a function of the radial distance  $r$  between the two nuclei

$$V(r) = \frac{zZe^2}{r} \Psi_I(r_r), \quad (9.19)$$

where  $eZ$  (projectile) and  $eZ$  (target) are the charges of the bare nuclei,  $\Psi_I$  is the *interatomic screening function*, and  $r_r$  is given by

$$r_r = \frac{r}{a_I},$$

with  $a_I$  the *screening length* (also termed *screening radius*). In the framework of the Thomas–Fermi model of the atom (e.g., see Ref. [eal11] and references therein), and thus following the approach of ICRU Report 49 [eal93], a commonly used screening length for  $z = 1$  incoming particles is that from Thomas–Fermi

$$a_{TF} = \frac{C_{TF} a_0}{Z^{1/3}}, \quad (9.20)$$

and, for incoming particles with  $z \geq 2$ , that introduced by Ziegler et al. [JFZL85] (and termed *universal screening length*):

$$a_U = \frac{C_{TF} a_0}{z^{0.23} + Z^{0.23}}, \quad (9.21)$$

where

$$a_0 = \frac{\hbar^2}{me^2}$$

is the Bohr radius,  $m$  is the electron rest mass and

$$C_{TF} = \frac{1}{2} \left( \frac{3\pi}{4} \right)^{2/3} \simeq 0.88534$$

is a constant introduced in the Thomas–Fermi model.

The simple scattering model due to Wentzel [Wen26], with a single exponential screening function  $\Psi_I(r_r)$  (e.g., see Ref. [eal11] and references therein), was repeatedly employed in treating single and multiple Coulomb-scattering with screened potentials. The resulting elastic differential cross section differs from the Rutherford differential cross section by an additional term, the *screening parameter*, which prevents the divergence of the cross section when the angle  $\theta$  of scattered particles approaches  $0^\circ$ . The screening parameter  $A_s$  (e.g., see Eq. (21) of [Bet53]) as derived by Molière [Moliere48, Moliere47] for the single Coulomb scattering using a Thomas–Fermi potential is expressed as

$$A_s = \left( \frac{\hbar}{2 p a_I} \right)^2 \left[ 1.13 + 3.76 \times \left( \frac{\alpha z Z}{\beta} \right)^2 \right]. \quad (9.22)$$

$a_I$  is the screening length from Eqs.(9.20) – (9.21) for particles with  $z = 1$  and  $z \geq 2$ , respectively;  $\alpha$  is the fine-structure constant;  $p \beta c$  is the momentum (velocity) of the incoming particle undergoing the scattering onto a target supposed to be initially at rest;  $c$  and  $\hbar$  are the speed of light and the reduced Planck constant, respectively. When the (relativistic) mass, corresponding to rest mass  $m$ , of the incoming particle is much lower than the rest mass  $M$  of the target nucleus, the differential cross section obtained from the Wentzel–Molière treatment of the single scattering is:

$$\frac{d\sigma^{WM}(\theta)}{d\Omega} = \left( \frac{z Z e^2}{2 p \beta c} \right)^2 \frac{1}{[A_s + \sin^2(\theta/2)]^2}. \quad (9.23)$$

Equation (9.23) differs from Rutherford’s formula, as already mentioned, for the additional term  $A_s$  to  $\sin^2(\theta/2)$ . As discussed in Ref. [eal11], for  $\beta \simeq 1$  (i.e., at very large  $p$ ) and with  $A_s \ll 1$ , one finds that the cross section approaches a constant:

$$\sigma_c^{WM} \simeq \left( \frac{2 z Z e^2 a_I}{\hbar c} \right)^2 \frac{\pi}{1.13 + 3.76 \times (\alpha z Z)^2}. \quad (9.24)$$

As discussed in Ref. [eal11] and references therein, for a scattering under the action of a central potential (for instance that due to a screened Coulomb field), when the rest mass of the target particle is no longer much larger than the relativistic mass of the incoming particle, the expression of the differential cross section must properly be re-written in the center of mass system in terms of an “effective particle” with momentum equal to that of the incoming particle ( $p'_{in}$ ) and rest mass equal to the relativistic reduced mass

$$\mu_{rel} = \frac{mM}{M_{1,2}}. \quad (9.25)$$

$M_{1,2}$  is the invariant mass;  $m$  and  $M$  are the rest masses of the incoming and target particles, respectively. The “effective particle” velocity is given by:

$$\beta_r c = c \sqrt{\left[ 1 + \left( \frac{\mu_{rel} c}{p'_{in}} \right)^2 \right]^{-1}}.$$

Thus, one finds (e.g, see Ref. [eal11]):

$$\frac{d\sigma^{\text{WM}}(\theta')}{d\Omega'} = \left( \frac{zZe^2}{2p'_{in}\beta_r c} \right)^2 \frac{1}{[A_s + \sin^2(\theta'/2)]^2}, \quad (9.26)$$

with

$$A_s = \left( \frac{\hbar}{2p'_{in}a_1} \right)^2 \left[ 1.13 + 3.76 \times \left( \frac{\alpha z Z}{\beta_r} \right)^2 \right] \quad (9.27)$$

and  $\theta'$  the scattering angle in the center of mass system.

The energy  $T$  transferred to the recoil target is related to the scattering angle as  $T = T_{max} \sin^2(\theta'/2)$ , where  $T_{max}$  is the maximum energy which can be transferred in the scattering (e.g., see Section 1.5 of Ref. [LR09]), thus, assuming an isotropic azimuthal distribution one can re-write Eq.(9.26) in terms of the kinetic recoil energy  $T$  of the target

$$\frac{d\sigma^{\text{WM}}(T)}{dT} = \pi \left( \frac{zZe^2}{p'_{in}\beta_r c} \right)^2 \frac{T_{max}}{[T_{max} A_s + T]^2}. \quad (9.28)$$

Furthermore, one can demonstrate that Eq.(9.28) can be re-written as (e.g, see Ref. [eal11]);

$$\frac{d\sigma^{\text{WM}}(T)}{dT} = 2\pi (zZe^2)^2 \frac{E^2}{p^2 Mc^4} \frac{1}{[T_{max} A_s + T]^2} \quad (9.29)$$

with  $p$  and  $E$  the momentum and total energy of the incoming particle in the laboratory. Equation (9.29) expresses, as already mentioned, the differential cross section as a function of the (kinetic) energy  $T$  achieved by the recoil target.

## 9.4.2 Nuclear Stopping Power

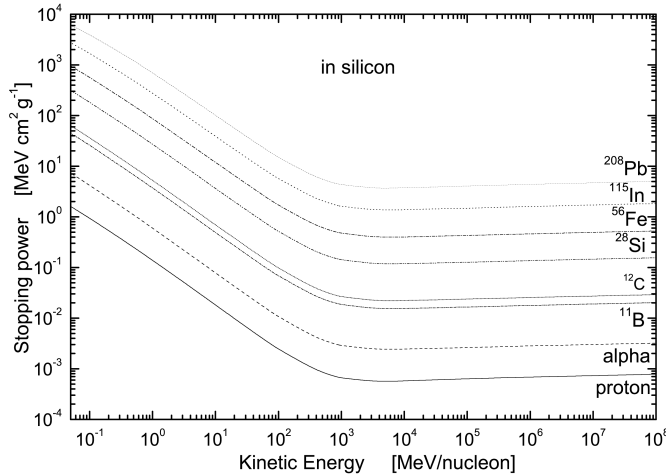


Fig. 9.2: Nuclear stopping power from Ref. [eal11] in  $\text{MeV cm}^2 \text{g}^{-1}$  calculated using Eq.(9.30) in silicon shown as a function of the kinetic energy per nucleon from 50 keV/nucleon up 100 TeV/nucleon for protons,  $\alpha$ -particles and  $^{11}\text{B}$ ,  $^{12}\text{C}$ ,  $^{28}\text{Si}$ ,  $^{56}\text{Fe}$ ,  $^{115}\text{In}$ ,  $^{208}\text{Pb}$  nuclei.

Using Eq. (9.29), the nuclear stopping power in  $\text{MeV cm}^{-1}$  is obtained as

$$-\left( \frac{dE}{dx} \right)_{\text{nuc}} = 2n_A \pi (zZe^2)^2 \frac{E^2}{p^2 Mc^4} \left[ \frac{A_s}{A_s + 1} - 1 + \ln \left( \frac{A_s + 1}{A_s} \right) \right]. \quad (9.30)$$

$n_A$  is the number of nuclei (atoms) per unit of volume and, the negative sign indicates that the energy is lost by the incoming particle. As discussed in Ref. [eal11], a slight increase of the nuclear stopping power with energy is expected because of the decrease of the screening parameter with energy.

For instance, in Fig. 9.2 the nuclear stopping power in silicon is shown as a function of the kinetic energy per nucleon for protons,  $\alpha$ -particles and  $^{11}\text{B}$ ,  $^{12}\text{C}$ ,  $^{28}\text{Si}$ ,  $^{56}\text{Fe}$ ,  $^{115}\text{In}$ ,  $^{208}\text{Pb}$  nuclei.

A comparison of the present treatment with that obtained from Ref. [JFZL85], available in SRIM (2008) [JFZ08], using the *universal screening potential* (see also Ref. [ZBZ08]) is discussed in Ref. [eal11]: a good agreement is achieved down to about 150 keV/nucleon. At large energies, the non-relativistic approach due to Ref. [JFZL85] becomes less appropriate and deviations from stopping powers calculated by means of the universal screening potential are expected and observed.

The non-relativistic approach based on the universal screening potential of [JFZL85] was also used by ICRU (1993) [eal93] to calculate nuclear stopping powers due to protons and  $\alpha$ -particles in materials. ICRU (1993) used as screening lengths those from Eqs.(9.20) for protons and (9.21) for  $\alpha$ -particles, respectively. As discussed in Ref. [eal11], the stopping powers for protons ( $\alpha$ -particles) from Eq.(9.30) are less than  $\approx 5\%$  larger than those reported by ICRU (1993) [eal93] from 50 keV/nucleon up to  $\approx 8\text{MeV}$  (19 MeV/nucleon). At larger energies the stopping powers from Eq.(9.30) differ from those from ICRU, as expected, due to the complete relativistic treatment of the present approach (see Ref. [eal11]).

The simple screening parameter used so far (Eq.(9.27)), derived by Molière [Moliere47]), can be modified by means of a *practical correction*, i.e.,

$$A'_s = \left( \frac{\hbar}{2 p'_{in} a_I} \right)^2 \left[ 1.13 + 3.76 \times C \left( \frac{\alpha z Z}{\beta_r} \right)^2 \right], \quad (9.31)$$

to achieve a better agreement with low energy calculations of [JFZL85]. For instance, as discussed in Ref. [eal11], for  $\alpha$ -particles and heavier ions, with

$$C = (10\pi z Z \alpha)^{0.12} \quad (9.32)$$

the stopping powers obtained from Eq.(9.30) (in which  $A'_s$  replaces  $A_s$ ) differ from the values of SRIM (2008) by less than  $\approx 4.7$  (3.6)% for  $\alpha$ -particles (lead ions) in silicon down to about 50 keV/nucleon. With respect to the tabulated values of ICRU (1993), the agreement for  $\alpha$ -particles is usually better than 4% at low energy down to 50 keV/nucleon. A 5% agreement is achieved at about 50 keV/nucleon in case of a lead medium. At very high energy, the stopping power is slightly affected when  $A'_s$  replaces  $A_s$  (Ref. [eal11]).

### 9.4.3 Non-Ionizing Energy Loss due to Coulomb Scattering

A relevant process which causes permanent damage to the silicon bulk structure is the *displacement damage* (e.g., see Chapter 4 of Ref. [LR09], Ref. [LR07] and references therein). Displacement damage may be inflicted when a *primary knocked-on atom* (PKA) is generated. The interstitial atom and relative vacancy are termed a Frenkel pair (FP). In turn, the displaced atom may have sufficient energy to migrate inside the lattice and, by further collisions, can displace other atoms as in a collision cascade. This displacement process modifies the bulk characteristics of the device and causes its degradation. The total number of FPs can be estimated calculating the energy density deposited from displacement processes. In turn, this energy density is related to the *Non-Ionizing Energy Loss* (NIEL), i.e., the energy per unit path lost by the incident particle due to displacement processes.

In case of Coulomb scattering on nuclei, the non-ionizing energy loss can be calculated using the Wentzel–Molière differential cross section (Eq.(9.29)) discussed in *Single Scattering, Screened Coulomb Potential and NIEL*, i.e.,

$$-\left( \frac{dE}{dx} \right)_{\text{nuc}}^{\text{NIEL}} = n_A \int_{T_d}^{T_{\max}} T L(T) \frac{d\sigma^{\text{WM}}(T)}{dT} dT, \quad (9.33)$$

where  $E$  is the kinetic energy of the incoming particle,  $T$  is the kinetic energy transferred to the target atom,  $L(T)$  is the fraction of  $T$  deposited by means of displacement processes. The expression of  $L(T)$ , denoted the *Lindhard*

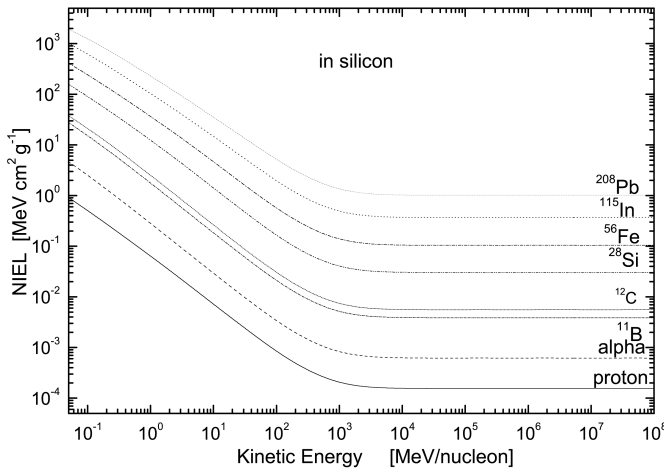


Fig. 9.3: Non-ionizing stopping power from Ref. [eal11] calculated using Eq.(9.33) in silicon is shown as a function of the kinetic energy per nucleon, from 50 keV/nucleon up 100 TeV/nucleon, for protons,  $\alpha$ -particles and  $^{11}\text{B}$ ,  $^{12}\text{C}$ ,  $^{28}\text{Si}$ ,  $^{56}\text{Fe}$ ,  $^{115}\text{In}$ ,  $^{208}\text{Pb}$  nuclei. The threshold energy for displacement is 21 eV in silicon.

*partition function*, can be found, for instance, in Equations (4.94, 4.96) of Section 4.2.1.1 in Ref. [LR09] and references therein.  $T_{de} = T L(T)$  is the *damage energy*, i.e., the energy deposited by a recoil nucleus with kinetic energy  $T$  via displacement damages inside the medium. The integral in Eq.(9.33) is computed from the minimum energy  $T_d$ , denoted the *threshold energy for displacement*, i.e., that energy necessary to displace the atom from its lattice position, up to the maximum energy  $T_{max}$  that can be transferred during a single collision process.  $T_d$  is about 21 eV in silicon. For instance, in Fig. 9.3 the non-ionizing energy loss in silicon is shown as a function of the kinetic energy per nucleon for protons,  $\alpha$ -particles and  $^{11}\text{B}$ ,  $^{12}\text{C}$ ,  $^{28}\text{Si}$ ,  $^{56}\text{Fe}$ ,  $^{115}\text{In}$ ,  $^{208}\text{Pb}$  nuclei.

A further discussion on the agreement with the results obtained by Jun et al. [eal03], using a relativistic treatment of Coulomb scattering of protons with kinetic energies from 50 MeV to 1 GeV on silicon, can be found in Ref. [eal11].

#### 9.4.4 G4IonCoulombScatteringModel

As discussed so far, high energy particles may inflict permanent damage to the electronic devices employed in a radiation environment. In particular the *nuclear energy loss* is important for the formation of defects in semiconductor devices. Nuclear energy loss is also responsible for the displacement damage which is the typical cause of degradation for silicon devices. The electromagnetic model *G4IonCoulombScatteringModel* was created in order to simulate the single scattering of protons, alpha particles and all heavier nuclei incident on all target materials in the energy range from 50–100 keV/nucleon to 10 TeV.

### 9.4.5 The Method

The differential cross section previously described is calculated by means of the class *G4IonCoulombCrossSection* where a modified version of the Wentzel's cross section is used. To solve the scattering problem of heavy ions it is necessary to introduce an effective particle whose mass is equal to the relativistic reduced mass of the system defined as

$$\mu_r \equiv \frac{m_1 m_2 c^2}{E_{cm}}.$$

$m_1$  and  $m_2$  are the incident and target rest masses respectively, and  $E_{cm}$  (in Eq.(9.25),  $M_{1,2} = E_{cm}/c^2$ ) is the total center of mass energy of the two particle system. The effective particle interacts with a fixed scattering center with interacting potential expressed by Eq.(9.19). The momentum of the effective particle is equal to the momentum of the incoming particle calculated in the center of mass system ( $\mathbf{p}_r \equiv \mathbf{p}_{1cm}$ ). Since the target particle is inside the material it can be considered at rest in the laboratory, and as a consequence the magnitude of  $\mathbf{p}_r$  is calculated as

$$p_r \equiv p_{1cm} = p_{1lab} \frac{m_2 c^2}{E_{cm}},$$

with  $E_{cm}$  given by

$$E_{cm} = \sqrt{(m_1 c^2)^2 + (m_2 c^2)^2 + 2 E_{1lab} m_2 c^2}, \quad (9.34)$$

where  $p_{1lab}$  is the momentum, and  $E_{1lab}$  the total energy, of the incoming particle in the laboratory system. The velocity  $\beta_r$  of the effective particle is obtained by the relation

$$\frac{1}{\beta_r^2} = 1 + \left( \frac{\mu_r c^2}{p_r c} \right)^2.$$

The modified Wentzel's cross section is then equal to:

$$\frac{d\sigma(\theta_r)}{d\Omega} = \left( \frac{Z_1 Z_2 e^2}{p_r c \beta_r} \right)^2 \frac{1}{(2A_s + 1 - \cos \theta_r)^2} \quad (9.35)$$

(in Eq.(9.26))  $p'_{in} \equiv p_r$  where  $Z_1$  and  $Z_2$  are the nuclear proton numbers of projectile and of target respectively;  $A_s$  is the screening coefficient (see Eq.(9.27)) and  $\theta_r$  is the scattering angle of the effective particle which is equal to the one in the center of mass system ( $\theta_r \equiv \theta_{1cm}$ ). Knowing the scattering angle, the recoil kinetic energy of the target particle after scattering is calculated by

$$T = m_2 c^2 \left( \frac{p_{1lab} c}{E_{cm}} \right)^2 (1 - \cos \theta_r). \quad (9.36)$$

The momentum and the total energy of the incident particle after scattering in the laboratory system are obtained by the usual Lorentz transformations.

### 9.4.6 Implementation Details

In the *G4IonCoulombScatteringModel* the scattering off electrons is not considered: only scattering off nuclei is simulated. Secondary particles are generated when  $T$  of Eq.(9.36) is greater than a given threshold for displacement  $T_d$ ; it is not cut in range. The user can set this energy threshold  $T_d$  by the method *SetRecoilThreshold(G4double Td)*. The default screening coefficient  $A_s$  is given by Eq.(9.27). If the user wants to use the one given by Eq.(9.31) the condition *SetHeavyIonCorr(I)* must be set. When  $Z_1 = 1$ , the Thomas-Fermi screening length ( $a_{TF}$  of Eq. (9.20)) is used in the calculation of  $A_s$ . For  $Z_1 \geq 2$  the screening length is the universal one ( $a_U$  of Eq. (9.21)). In the

*G4IonCoulombCrossSection* the total differential cross section is obtained by the method *NuclearCrossSection()* where the Eq.(9.35) is integrated in the interval  $(0, \pi)$ :

$$\sigma = \pi \left( \frac{Z_1 Z_2 e^2}{p_r c \beta_r} \right)^2 \frac{1}{A_s (A_s + 1)} \quad (9.37)$$

The cosine of the scattering angle is chosen randomly in the interval  $(-1, 1)$  according to the distribution of the total cross section and it is given by the method *SampleCosineTheta()* which returns  $(1 - \cos \theta_r)$ .

## 9.5 Electron Screened Single Scattering and NIEL

The present treatment [eal12] of electron–nucleus interaction is based on numerical and analytical approximations of the Mott differential cross section. It accounts for effects due to screened Coulomb potentials, finite sizes and finite rest masses of nuclei for electron with kinetic energies above 200 keV and up to ultra high. This treatment allows one to determine both the total and differential cross sections, thus, to calculate the resulting nuclear and non-ionizing stopping powers (NIEL). Above a few hundreds of MeV, neglecting the effects of finite sizes and rest masses of recoil nuclei the stopping power and NIEL result to be largely underestimated, while, above a few tens of MeV prevents a further large increase, thus, resulting in approaching almost constant values at high energies.

The non-ionizing energy loss (NIEL) is the energy lost from a particle traversing a unit length of a medium through physical process resulting in permanent displacement damages (e.g. see Ref.[LR07]). The nuclear stopping power and NIEL deposition due to elastic Coulomb scatterings from protons and light and heavy ions traversing an absorber were previously described [eal11] and are available in GEANT4 (*Single Scattering, Screened Coulomb Potential and NIEL*) (see also Sections 1.6, 1.6.1, 2.1.4–2.1.4.2, 4.2.1.6 of Ref. [LR11]). In the present model included in GEANT4, the nuclear stopping power and NIEL deposition due to elastic Coulomb scatterings of electrons are treated up to ultra relativistic energies.

### 9.5.1 Scattering Cross Section of Electrons on Nuclei

The scattering of electrons by unscreened atomic nuclei was treated by Mott extending a method of Wentzel dealing with incident and scattered waves on point-like nuclei and including effects related to the spin of electrons. The differential cross section (DCS), denoted the *Mott differential cross section* (MDCS), was expressed by Mott as two conditionally convergent infinite series in terms of Legendre expansions. In Mott–Wentzel treatment, the scattering occurs on a field of force generating a radially dependent Coulomb, unscreened (screened) in Mott (Wentzel), potential. Furthermore, the MDCS was derived in the laboratory reference system for infinitely heavy nuclei initially at rest with negligible spin effects and must be numerically evaluated for any specific nuclear target. Effects related to the recoil and finite rest mass of the target nucleus ( $M$ ) were neglected. Thus, in this framework the total energy of electrons has to be smaller or much smaller than  $Mc^2$ .

The MDCS is usually expressed as:

$$\frac{d\sigma^{\text{Mott}}(\theta)}{d\Omega} = \frac{d\sigma^{\text{Rut}}}{d\Omega} \mathcal{R}^{\text{Mott}}, \quad (9.38)$$

where  $\mathcal{R}^{\text{Mott}}$  is the ratio between the MDCS and Rutherford's formula (RDCS, see Equation (1) of Ref. [eal12]). For electrons with kinetic energies from several keV up to 900 MeV and target nuclei with  $1 \leq Z \leq 90$ , Lijian et al. [LQZ95] provided a practical interpolated expression (Eq.(9.48)) for  $\mathcal{R}^{\text{Mott}}$  with an average error less than 1%; in the present treatment, that expression (*Interpolated Expression for*) is the one assumed for  $\mathcal{R}^{\text{Mott}}$  in Eq.(9.38) hereafter. The analytical expression derived by McKinley and Feshbach [MF48] for the ratio with respect to Rutherford's formula (Eq.(7) of Ref. [MF48]) is given by:

$$\mathcal{R}^{\text{McF}} = 1 - \beta^2 \sin^2(\theta/2) + Z \alpha \beta \pi \sin(\theta/2) [1 - \sin(\theta/2)] \quad (9.39)$$

with the corresponding differential cross section (McFDCS)

$$\frac{d\sigma^{\text{McF}}}{d\Omega} = \frac{d\sigma^{\text{Rut}}}{d\Omega} \mathcal{R}^{\text{McF}}. \quad (9.40)$$

Furthermore, for  $Mc^2$  much larger than the total energy of incoming electron energies the distinction between laboratory (i.e., the system in which the target particle is initially at rest) and center-of-mass (CoM) systems disappears (e.g., see discussion in Section 1.6.1 of Ref. [LR11]). Furthermore, in the CoM of the reaction the energy transferred from an electron to a nucleus initially at rest in the laboratory system (i.e., its recoil kinetic energy  $T$ ) is related with the maximum energy transferable  $T_{\max}$  as

$$T = T_{\max} \sin^2(\theta'/2) \quad (9.41)$$

(e.g., see Eqs. (1.27, 1.95) at page 11 and 31, respectively, of Ref. [LR11]), where  $\theta'$  is the scattering angle in the CoM system. In addition, one obtains

$$dT = \frac{T_{\max}}{4\pi} d\Omega'. \quad (9.42)$$

Since for  $Mc^2$  much larger than the electron energy,  $\theta \approx \theta'$ , one finds that Eq.(9.41) can be approximated as

$$T \simeq T_{\max} \sin^2(\theta/2), \quad (9.43)$$

$$\implies \sin^2(\theta/2) = \frac{T}{T_{\max}} \quad (9.44)$$

and

$$dT \simeq \frac{T_{\max}}{4\pi} d\Omega. \quad (9.45)$$

Using Eqs.(9.39), (9.44), (9.45), Rutherford's formula and Eq.(9.40) can be respectively rewritten as:

$$\begin{aligned} &\implies \frac{d\sigma^{\text{Rut}}}{dT} = \left( \frac{Ze^2}{p\beta c} \right)^2 \frac{\pi T_{\max}}{T^2}, \\ &\implies \frac{d\sigma^{\text{McF}}}{T} = \left( \frac{Ze^2}{p\beta c} \right)^2 \frac{\pi T_{\max}}{T^2} \left[ 1 - \beta \frac{T}{T_{\max}} (\beta + Z\alpha\pi) + Z\alpha\beta\pi\sqrt{\frac{T}{T_{\max}}} \right] \\ &= \left( \frac{Ze^2}{p\beta c} \right)^2 \frac{\pi T_{\max}}{T^2} \mathcal{R}^{\text{McF}}(T) \end{aligned} \quad (9.46)$$

with

$$\mathcal{R}^{\text{McF}}(T) = \left[ 1 - \beta \frac{T}{T_{\max}} (\beta + Z\alpha\pi) + Z\alpha\beta\pi\sqrt{\frac{T}{T_{\max}}} \right]. \quad (9.47)$$

Finally, in a similar way the MDCS (Eq.(9.38)) is

$$\begin{aligned} \frac{d\sigma^{\text{Mott}}(T)}{dT} &= \frac{d\sigma^{\text{Rut}}}{dT} \mathcal{R}^{\text{Mott}}(T) \\ &= \left( \frac{Ze^2}{p\beta c} \right)^2 \frac{\pi T_{\max}}{T^2} \mathcal{R}^{\text{Mott}}(T) \end{aligned}$$

with  $\mathcal{R}^{\text{Mott}}(T)$  from Eq.(9.50).

### Interpolated Expression for $\mathcal{R}^{\text{Mott}}$

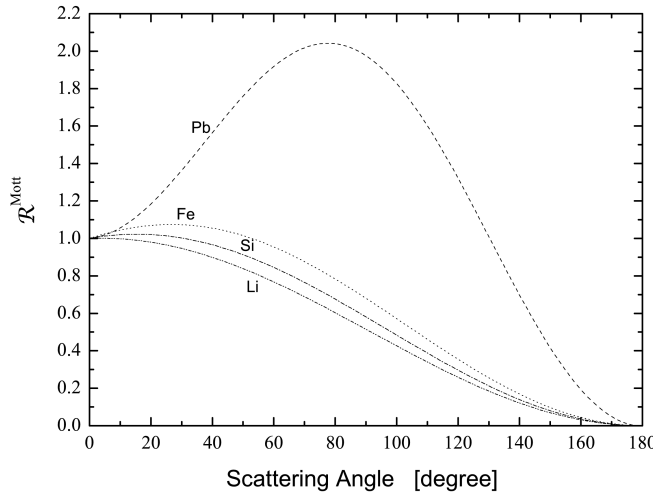


Fig. 9.4:  $\mathcal{R}^{\text{Mott}}$  obtained from Eq.(9.48) at 100 MeV for Li, Si, Fe and Pb nuclei as a function of scattering angle.

Recently, Lijian, Quing and Zhengming [LQZ95] provided a practical interpolated expression (Eq.(9.48)) which is a function of both  $\theta$  and  $\beta$  for electron energies from several keV up to 900 MeV, i.e.,

$$\mathcal{R}^{\text{Mott}} = \sum_{j=0}^4 a_j(Z, \beta)(1 - \cos \theta)^{j/2}, \quad (9.48)$$

where

$$a_j(Z, \beta) = \sum_{k=1}^6 b_{k,j}(Z)(\beta - \bar{\beta})^{k-1}, \quad (9.49)$$

and  $\bar{\beta} c = 0.7181287 c$  is the mean velocity of electrons within the above mentioned energy range. The coefficients  $b_{k,j}(Z)$  are listed in Table 1 of Ref. [LQZ95] for  $1 \leq Z \leq 90$ . Boschini et al. (2013) [eal13] provided an extended numerical solution for the Mott differential cross section on nuclei up to  $Z = 118$  for both electrons and positrons.  $\mathcal{R}^{\text{Mott}}$  obtained from Eq.(9.48) at 100 MeV is shown in Fig. 9.4 for Li, Si, Fe and Pb nuclei as a function of scattering angle. Furthermore, it has to be remarked that the energy dependence of  $\mathcal{R}^{\text{Mott}}$  from Eq.(9.48) was studied and observed to be negligible above  $\approx 10$  MeV (for instance, see Eq.(9.49)).

Finally, from Eqs.(9.41), (9.48) (see also Equation (1.93) at page 31 of Ref.[LR11]), one finds that  $\mathcal{R}^{\text{Mott}}$  can be expressed in terms of the transferred energy  $T$  as

$$\mathcal{R}^{\text{Mott}}(T) = \sum_{j=0}^4 a_j(Z, \beta) \left( \frac{2T}{T_{\max}} \right)^{j/2}. \quad (9.50)$$

## Screened Coulomb Potentials

The simple scattering model due to Wentzel with a single exponential screening function (see Eq. (2.71) of Ref. [LR11]) was repeatedly employed in treating single and multiple Coulomb scattering with screened potentials. Neglecting effects like those related to spin and finite size of nuclei, for proton and nucleus interactions on nuclei it was shown that the resulting elastic differential cross section of a projectile with bare nuclear-charge  $ez$  on a target with bare nuclear-charge  $eZ$  differs from the Rutherford differential cross section (RDCS) by an additional term, the *screening parameter*, which prevents the divergence of the cross section when the angle  $\theta$  of scattered particles approaches  $0^\circ$  (see Section 1.6.1 of Ref. [LR11]). For  $z = 1$  particles the *screening parameter*  $A_{s,M}$  is expressed as

$$A_{s,M} = \left( \frac{\hbar}{2 p a_{TF}} \right)^2 \left[ 1.13 + 3.76 \times \left( \frac{\alpha Z}{\beta} \right)^2 \right] \quad (9.51)$$

where  $\alpha$ ,  $c$  and  $\hbar$  are the fine-structure constant, speed of light and reduced Planck constant, respectively;  $p (\beta c)$  is the momentum (velocity) of the incoming particle undergoing the scattering onto a target supposed to be initially at rest, i.e., in the laboratory system;  $a_{TF}$  is the screening length suggested by Thomas–Fermi

$$a_{TF} = \frac{C_{TF} a_0}{Z^{1/3}}$$

with

$$a_0 = \frac{\hbar^2}{m e^2}$$

the Bohr radius,  $m$  the electron rest mass and

$$C_{TF} = \frac{1}{2} \left( \frac{3\pi}{4} \right)^{2/3} \simeq 0.88534$$

a constant introduced in the Thomas–Fermi model (see Ref. [eal11], Eq.(2.73, 2.82) of Ref. [LR11], and references therein). The modified Rutherford's formula  $d\sigma^{WM}(\theta)/d\Omega$ , i.e., the *differential cross section* obtained from the Wentzel–Molière treatment of the single scattering on screened nuclear potential is given by (see Eq.(2.84) of Ref. [LR11] and Ref. [eal11], and references therein):

$$\begin{aligned} \frac{d\sigma^{WM}(\theta)}{d\Omega} &= \left( \frac{zZe^2}{2 p \beta c} \right)^2 \frac{1}{[A_{s,M} + \sin^2(\theta/2)]^2} \\ &= \frac{d\sigma^{Rut}}{d\Omega} \mathfrak{F}^2(\theta). \end{aligned} \quad (9.52)$$

with

$$\mathfrak{F}(\theta) = \frac{\sin^2(\theta/2)}{A_{s,M} + \sin^2(\theta/2)}. \quad (9.53)$$

$\mathfrak{F}(\theta)$ , the *screening factor*, depends on the scattering angle  $\theta$  and the screening parameter  $A_{s,M}$ . As discussed in *Finite Rest Mass of Target Nucleus*, the term  $A_{s,M}$  (the screening parameter) cannot be neglected in the DCS (Eq.(9.52)) for scattering angles ( $\theta$ ) within a forward (with respect to the electron direction) angular region narrowing with increasing energy from several degrees (for high-Z material) at 200 keV down to less than or much less than a mrad above 200 MeV.

An approximated description of elastic interactions of electrons with screened Coulomb fields of nuclei can be obtained by the factorization of the MDCS, i.e., involving Rutherford's formula  $d\sigma^{Rut}/d\Omega$  for particle with  $z = 1$ , the screening factor  $\mathfrak{F}(\theta)$  and the ratio  $\mathcal{R}^{Mott}$  between the RDCS and MDCS:

$$\frac{d\sigma_{sc}^{Mott}(\theta)}{d\Omega} \simeq \frac{d\sigma^{Rut}}{d\Omega} \mathfrak{F}^2(\theta) \mathcal{R}^{Mott}. \quad (9.54)$$

Thus, the corresponding screened differential cross section derived using the analytical expression from McKinley and Feshbach [MF48] can be approximated with

$$\frac{d\sigma_{sc}^{McF}(\theta)}{d\Omega} \simeq \frac{d\sigma^{Rut}}{d\Omega} \mathfrak{F}^2(\theta) \mathcal{R}^{McF}. \quad (9.55)$$

Zeitler and Olsen [ZO64] suggested that for electron energies above 200 keV the overlap of spin and screening effects is small for all elements and for all energies; for lower energies the overlapping of the spin and screening effects may be appreciable for heavy elements and large angles.

### Finite Nuclear Size

The ratio between the actual measured and that expected from the point-like differential cross section expresses the square of *nuclear form factor*  $|F|$  which, in turn, depends on the momentum transfer  $q$ , i.e., that acquired by the target initially at rest:

$$q = \frac{\sqrt{T(T + 2Mc^2)}}{c}, \quad (9.56)$$

with  $T$  from Eq.(9.41) or for  $Mc^2$  larger or much larger than the electron energy from its approximate expression Eq.(9.43).

The approximated (factorized) differential cross section for elastic interactions of electrons with screened Coulomb fields of nuclei (Eq.(9.54)) accounting for the effects due to the finite nuclear size is given by:

$$\frac{d\sigma_{sc,F}^{Mott}(\theta)}{d\Omega} \simeq \frac{d\sigma^{Rut}}{d\Omega} \mathfrak{F}^2(\theta) \mathcal{R}^{Mott} |F(q)|^2. \quad (9.57)$$

Thus, using the analytical expression derived by [MF48] (Eq.(9.39)) one obtains that the corresponding screened differential cross section (Eq.(9.55)) accounting for the finite nuclear size effects

$$\begin{aligned} \frac{d\sigma_{sc,F}^{McF}(\theta)}{d\Omega} &\simeq \frac{d\sigma^{Rut}}{d\Omega} \mathfrak{F}^2(\theta) \mathcal{R}^{McF} |F(q)|^2 \\ &= \frac{d\sigma^{Rut}}{d\Omega} \mathfrak{F}^2(\theta) |F(q)|^2 \\ &\times \{1 - \beta^2 \sin^2(\theta/2) + Z \alpha \beta \pi \sin(\theta/2) [1 - \sin(\theta/2)]\}. \end{aligned} \quad (9.58)$$

In terms of kinetic energy, one can respectively rewrite Eqs.(9.57), (9.58) as

$$\begin{aligned} \frac{d\sigma_{sc,F}^{Mott}(T)}{dT} &= \frac{d\sigma^{Rut}}{dT} \mathfrak{F}^2(T) \mathcal{R}^{Mott}(T) |F(q)|^2 \\ \frac{d\sigma_{sc,F}^{McF}(T)}{dT} &\simeq \frac{d\sigma^{Rut}(T)}{dT} \mathfrak{F}^2(T) \mathcal{R}^{McF}(T) |F(q)|^2 \end{aligned} \quad (9.59)$$

with  $d\sigma^{Rut}/dT$  from Eq.(9.46),  $\mathcal{R}^{Mott}(T)$  from Eq.(9.50),  $\mathcal{R}^{McF}(T)$  from Eq.(9.47) and, using Eqs.(9.41), (9.43), (9.53),

$$\mathfrak{F}(T) = \frac{T}{T_{\max} A_{s,M} + T}.$$

For instance, the form factor  $F_{\exp}$  is

$$F_{\exp}(q) = \left[ 1 + \frac{1}{12} \left( \frac{qr_n}{\hbar} \right)^2 \right]^{-2}, \quad (9.60)$$

where  $r_n$  is the nuclear radius,  $r_n$  can be parameterized by

$$r_n = 1.27 A^{0.27} \text{ fm} \quad (9.61)$$

with  $A$  the atomic weight. Equation (9.61) provides values of  $r_n$  in agreement up to heavy nuclei (like Pb and U) with those available, for instance, in Table 1 of Ref. [VJV87].

## Finite Rest Mass of Target Nucleus

The DCS treated in *Scattering Cross Section of Electrons on Nuclei to Finite Nuclear Size* is based on the extension of MDCS to include effects due to interactions on screened Coulomb potentials of nuclei and their finite size. However, the electron energies were considered small (or much smaller) with respect to that ( $Mc^2$ ) corresponding to rest mass ( $M$ ) target nuclei.

The Rutherford scattering on screened Coulomb fields, i.e., under the action of a central forces, by massive charged particles at energies large or much larger than  $Mc^2$  was treated by Boschini et al. [ea11] in the CoM system (see also Sections 1.6, 1.6.1, 2.1.4.2 of Ref. [LR11] and references therein). It was shown that the differential cross section ( $d\sigma^{\text{WM}}(\theta')/d\Omega'$  with  $\theta'$  the scattering angle in the CoM system) is that one derived for describing the interaction on a fixed scattering center of a particle with

- momentum  $p'_r$  equal to the momentum of the incoming particle (i.e., the electron in the present treatment) in the CoM system
- rest mass equal to the *relativistic reduced mass*  $\mu_{\text{rel}}$  (see Eqs.(1.80, 1.81) in Ref. [LR11]).

$\mu_{\text{rel}}$  is given by

$$\begin{aligned}\mu_{\text{rel}} &= \frac{mM}{M_{1,2}} \\ &= \frac{mMc}{\sqrt{m^2c^2 + M^2c^2 + 2M\sqrt{m^2c^4 + p^2c^2}}},\end{aligned}$$

where  $p$  is the momentum of the incoming particle (the electron in the present treatment) in the laboratory system;  $m$  is the rest mass of the incoming particle (i.e., the electron rest mass);  $M_{1,2}$  is the invariant mass (Section 1.3.2 of Ref. [LR11] of the two-particle system. Thus, the velocity of the interacting particle is (see Eq.(1.82) at of Ref. [LR11])

$$\beta'_r c = c \sqrt{\left[1 + \left(\frac{\mu_{\text{rel}} c}{p'_r}\right)^2\right]^{-1}}.$$

For an incoming particle with  $z = 1$ ,  $d\sigma^{\text{WM}}(\theta')/d\Omega'$  is given by

$$\frac{d\sigma^{\text{WM}}(\theta')}{d\Omega'} = \left(\frac{Ze^2}{2p'_r \beta'_r c}\right)^2 \frac{1}{[A_s + \sin^2(\theta'/2)]^2}, \quad (9.62)$$

with

$$A_s = \left(\frac{\hbar}{2p'_r a_{\text{TF}}}\right)^2 \left[1.13 + 3.76 \times \left(\frac{\alpha Z}{\beta'_r}\right)^2\right] \quad (9.63)$$

the screening factor (see Eqs.(2.87, 2.88) of Ref. [LR11]). Eq.(9.62) can be rewritten as

$$\frac{d\sigma^{\text{WM}}(\theta')}{d\Omega'} = \frac{d\sigma^{\text{Rut}}(\theta')}{d\Omega'} \mathfrak{F}_{\text{CoM}}^2(\theta') \quad (9.64)$$

with

$$\frac{d\sigma^{\text{Rut}}(\theta')}{d\Omega'} = \left(\frac{Ze^2}{2p'_r \beta'_r c}\right)^2 \frac{1}{\sin^4(\theta'/2)} \quad (9.65)$$

the corresponding RDCS for the reaction in the CoM system (see Eq.(1.79) of Ref. [LR11]) and

$$\mathfrak{F}_{\text{CoM}}(\theta') = \frac{\sin^2(\theta'/2)}{A_s + \sin^2(\theta'/2)} \quad (9.66)$$

the screening factor. Using Eqs.(9.41) and (9.42), one can respectively rewrite Eqs.(9.65), (9.66), (9.64), (9.62) as

$$\frac{d\sigma^{\text{Rut}'} }{dT} = \pi \left( \frac{Ze^2}{p'_r \beta'_r c} \right)^2 \frac{T_{\max}}{T^2} \quad (9.67)$$

$$\mathfrak{F}_{\text{CoM}}(T) = \frac{T}{T_{\max} A_s + T} \quad (9.68)$$

$$\begin{aligned} \frac{d\sigma^{\text{WM}'}(T)}{dT} &= \frac{d\sigma^{\text{Rut}'} }{dT} \mathfrak{F}_{\text{CoM}}(T) \\ \frac{d\sigma^{\text{WM}'}(T)}{dT} &= \pi \left( \frac{Ze^2}{p'_r \beta'_r c} \right)^2 \frac{T_{\max}}{(T_{\max} A_s + T)^2}. \end{aligned}$$

(see Eq.(2.90) of Ref.[LR11] or Eq.(13) of Ref.[eal11]).

To account for the finite rest mass of target nucleus the factorized MDCS (Eq.(9.57)) has to be re-expressed in the CoM system using as:

$$\frac{d\sigma_{\text{sc}, F, \text{CoM}}^{\text{Mott}}(\theta')}{d\Omega'} \simeq \frac{d\sigma^{\text{Rut}'}(\theta')}{d\Omega'} \mathfrak{F}_{\text{CoM}}^2(\theta') \mathcal{R}_{\text{CoM}}^{\text{Mott}}(\theta') |F(q)|^2, \quad (9.69)$$

where  $F(q)$  is the nuclear form factor (*Finite Nuclear Size*) with  $q$ , the momentum transfer to the recoil nucleus (Eq.(9.56)); finally, as discussed in *Interpolated Expression for*,  $\mathcal{R}^{\text{Mott}}$  exhibits almost no dependence on electron energy above  $\approx 10$  MeV, thus, since at low energies  $\theta \simeq \theta'$  and  $\beta \simeq \beta'_r$ ,  $\mathcal{R}_{\text{CoM}}^{\text{Mott}}(\theta')$  is obtained replacing  $\theta$  and  $\beta'_r$  with  $\theta'$  and  $\beta'_r$ , respectively, in Eq.(9.48).

Using the analytical expression derived by McKinley and Feshbach [MF48], one finds that the corresponding screened differential cross section accounting for the finite nuclear size effects (Eqs.(9.58)) can be re-expressed as

$$\frac{d\sigma_{\text{sc}, F, \text{CoM}}^{\text{McF}}(\theta')}{d\Omega'} \simeq \frac{d\sigma^{\text{Rut}'}(\theta')}{d\Omega'} \mathfrak{F}_{\text{CoM}}^2(\theta') \mathcal{R}_{\text{CoM}}^{\text{McF}}(\theta') |F(q)|^2 \quad (9.70)$$

with

$$\mathcal{R}_{\text{CoM}}^{\text{McF}}(\theta') = \{1 - \beta_r^2 \sin^2(\theta'/2) + Z \alpha \beta'_r \pi \sin(\theta'/2) [1 - \sin(\theta'/2)]\}. \quad (9.71)$$

In terms of kinetic energy  $T$ , from Eqs.(9.41) and (9.42), one can respectively rewrite Eqs.(9.69) and (9.70) as

$$\frac{d\sigma_{\text{sc}, F, \text{CoM}}^{\text{Mott}}(T)}{dT} = \frac{d\sigma^{\text{Rut}'} }{dT} \mathfrak{F}_{\text{CoM}}^2(T) \mathcal{R}_{\text{CoM}}^{\text{Mott}}(T) |F(q)|^2 \quad (9.72)$$

$$\frac{d\sigma_{\text{sc}, F, \text{CoM}}^{\text{McF}}(T)}{dT} \simeq \frac{d\sigma^{\text{Rut}'}(T)}{dT} \mathfrak{F}_{\text{CoM}}^2(T) \mathcal{R}_{\text{CoM}}^{\text{McF}}(T) |F(q)|^2 \quad (9.73)$$

with  $d\sigma^{\text{Rut}'} / dT$  from Eq.(9.67),  $\mathfrak{F}_{\text{CoM}}(T)$  from Eq.(9.68) and  $\mathcal{R}_{\text{CoM}}^{\text{McF}}(T)$  replacing  $\beta$  with  $\beta'_r$  in Eq.(9.47), i.e.,

$$\mathcal{R}_{\text{CoM}}^{\text{McF}}(T) = \left[ 1 - \beta'_r \frac{T}{T_{\max}} (\beta'_r + Z \alpha \pi) + Z \alpha \beta'_r \pi \sqrt{\frac{T}{T_{\max}}} \right].$$

Finally, as discussed in *Interpolated Expression for*,  $\mathcal{R}^{\text{Mott}}(T)$  exhibits almost no dependence on electron energy above  $\approx 10$  MeV, thus, since at low energies  $\theta \simeq \theta'$  and  $\beta \simeq \beta'_r$ ,  $\mathcal{R}_{\text{CoM}}^{\text{Mott}}(T)$  is obtained replacing  $\beta$  with  $\beta'_r$  in Eq.(9.50).

## 9.5.2 Nuclear Stopping Power of Electrons

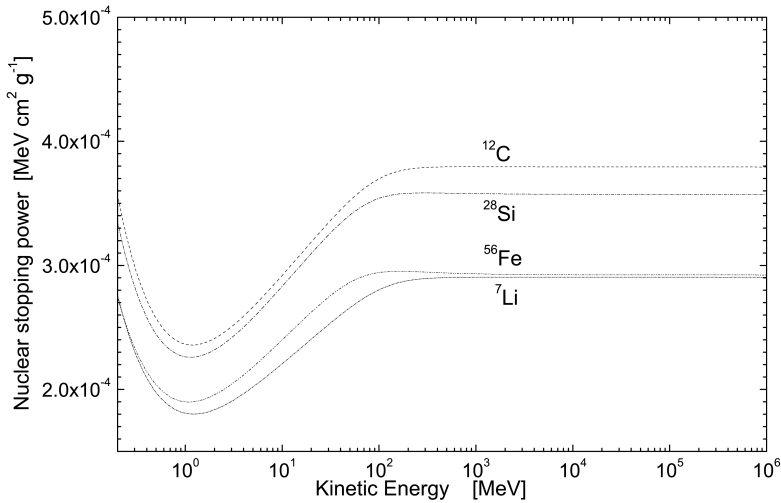


Fig. 9.5: In  $\text{MeV cm}^2/\text{g}$ , nuclear stopping powers in  ${}^7\text{Li}$ ,  ${}^{12}\text{C}$ ,  ${}^{28}\text{Si}$  and  ${}^{56}\text{Fe}$  calculated from Eq.(9.75) and divided by the density of the material as a function of the kinetic energy of electrons from 200 keV up to 1 TeV.

Using Eq.(9.72), the nuclear stopping power in  $\text{MeV cm}^{-1}$  of Coulomb electron–nucleus interaction can be obtained as

$$-\left(\frac{dE}{dx}\right)_{\text{nucl}}^{\text{Mott}} = n_A \int_0^{T_{\max}} \frac{d\sigma_{\text{sc},F,\text{CoM}}^{\text{Mott}}(T)}{dT} T dT \quad (9.74)$$

with  $n_A$  the number of nuclei (atoms) per unit of volume (see Eq.(1.71) of Ref. [LR11]) and, finally, the negative sign indicates that the energy is lost by the electron (thus, achieved by recoil targets). Using the analytical approximation derived by McKinley and Feshbach [MF48], i.e., Eq.(9.73), for the nuclear stopping power one finds

$$-\left(\frac{dE}{dx}\right)_{\text{nucl}}^{\text{McF}} = n_A \int_0^{T_{\max}} \frac{d\sigma_{\text{sc},F,\text{CoM}}^{\text{McF}}(T)}{dT} T dT. \quad (9.75)$$

As already mentioned in *Finite Rest Mass of Target Nucleus*, the large momentum transfers corresponding to large scattering angles are disfavored by effects due to the finite nuclear size accounted for by means of the nuclear form factor (*Finite Nuclear Size*). For instance, the ratios of nuclear stopping powers of electrons in silicon are shown in Ref. [eal12] as a function of the kinetic energies of electrons from 200 keV up to 1 TeV. These ratios are the nuclear stopping powers calculated neglecting

- nuclear size effects (i.e., for  $|F_{\text{exp}}|^2 = 1$ )
- effects due to the finite rest mass of the target nucleus (i.e., in Eq.(9.75) replacing  $d\sigma_{\text{sc},F,\text{CoM}}^{\text{McF}}(T)/dT$  with  $d\sigma_{\text{sc},F}^{\text{McF}}(T)/dT$  from Eq. (9.59) both divided by that one obtained using Eq.(9.75)).

Above a few tens of MeV, a larger stopping power is found assuming  $|F_{\text{exp}}|^2 = 1$  and, in addition, above a few hundreds of MeV the stopping power largely decreases when the effects of nuclear rest mass are not accounted for.

In Fig. 9.5, the nuclear stopping powers in  ${}^7\text{Li}$ ,  ${}^{12}\text{C}$ ,  ${}^{28}\text{Si}$  and  ${}^{56}\text{Fe}$  are shown as a function of the kinetic energy of electrons from 200 keV up to 1 TeV. These nuclear stopping powers are calculated from Eq.(9.75) and divided by the density of the medium.

### 9.5.3 Non-Ionizing Energy-Loss of Electrons

In case of Coulomb scattering of electrons on nuclei, the non-ionizing energy loss can be calculated using (as discussed in [Scattering Cross Section of Electrons on Nuclei](#) to [Nuclear Stopping Power of Electrons](#)) the MDCRS or its approximate expression McFDCS (e.g., Eqs.(9.72), (9.73), respectively), once the screened Coulomb fields, finite sizes and rest masses of nuclei are accounted for, i.e., in MeV/cm

$$-\left(\frac{dE}{dx}\right)_{n,Mott}^{\text{NIEL}} = n_A \int_{T_d}^{T_{max}} T L(T) \frac{d\sigma_{sc,F,\text{CoM}}^{\text{Mott}}(T)}{dT} dT \quad (9.76)$$

or

$$-\left(\frac{dE}{dx}\right)_{n,McF}^{\text{NIEL}} = n_A \int_{T_d}^{T_{max}} T L(T) \frac{d\sigma_{sc,F,\text{CoM}}^{\text{McF}}(T)}{dT} dT \quad (9.77)$$

(see Eq.(4.113) and Sections 4.2.1–4.2.1.2 of Ref. [LR11]), where  $T$  is the kinetic energy transferred to the target nucleus,  $L(T)$  is the fraction of  $T$  deposited by means of displacement processes. The *Lindhard partition function*,  $L(T)$ , can be approximated using the *Norgett–Robintson–Torrens expression* (see Eqs.(4.121, 4.123) of Ref. [LR11] and references therein).  $T_{de} = T L(T)$  is the *damage energy*, i.e., the energy deposited by a recoil nucleus with kinetic energy  $T$  via displacement damages inside the medium. In Eqs.(9.76) and (9.77), the integral is computed from the minimum energy  $T_d$ , the *threshold energy for displacement*, i.e., that energy necessary to displace the atom from its lattice position up to the maximum energy  $T_{max}$  that can be transferred during a single collision process. For instance,  $T_d$  is about 21 eV in silicon requiring electrons with kinetic energies above  $\approx 220$  keV. As already discussed with respect to nuclear stopping powers in [Nuclear Stopping Power of Electrons](#), the large momentum transfers (corresponding to large scattering angles) are disfavored by effects due to the finite nuclear size accounted for by the nuclear form factor. For instance, the ratios of NIELs for electrons in silicon are shown in Ref. [eal12] as a function of the kinetic energy of electrons from 220 keV up to 1 TeV. These ratios are the NIELs calculated neglecting

- nuclear size effects (i.e., for  $|F_{\text{exp}}|^2 = 1$ )
- effects due to the finite rest mass of the target nucleus (i.e., in Eq.(9.77) replacing  $d\sigma_{sc,F,\text{CoM}}^{\text{McF}}(T)/dT$  with  $d\sigma_{sc,F}^{\text{McF}}(T)/dT$  from Eq. (9.59) both divided by that one obtained using Eq.(9.77)).

Above  $\sim 10$  MeV, the NIEL is  $\sim 20\%$  larger assuming  $|F_{\text{exp}}|^2 = 1$  and, in addition, above 100–200 MeV the calculated NIEL largely decreases when the effects of nuclear rest mass are not accounted for.

## 9.6 G4eSingleScatteringModel

The *G4eSingleScatteringModel* performs the single scattering interaction of electrons on nuclei. The differential cross section (DCS) for the energy transferred is define in the *G4ScreeningMottCrossSection* class. In this class the M.Boschini's et al. [eal13] Mott differential cross Section approximation is implemented. This CDS is modified by the introduction of the Moliere's [Moliere48] screening coefficient. In addition the exponential charge distribution Nuclear Form Factor is applied [BKMM02]. This treatment is fully performed in the center of mass system and the usual Lorentz transformations are applied to obtained the energy and momentum quantities in the laboratory system after scattering. This model well simulates the interacting process for low scattering angles and it is suitable for high energy electrons (from 200 keV) incident on medium light target nuclei. The nuclear energy loss (i.e. nuclear stopping power) is calculated for every single interaction. In addition the production of secondary scattered nuclei is simulated from a threshold kinetic energy which can be decided by the user (threshold energy for displacement).

### 9.6.1 The method

In the *G4eSingleScatteringModel* the method *ComputeCrossSectionPerAtom()* performs the total cross section computation. The *SetupParticle()* and the *DefineMaterial()* methods are called to defined the incident and target particles. Before the total cross section computation, the *SetupKinematic()* method of the *G4ScreeningMottCrossSection* class calculates all the physical quantities in the center of mass system (CM). The scattering in the CM system is equivalent to the one of an effective particle which interacts with a fixed scattering center. The effective particle rest mass is equal to the relativistic reduced mass of the system  $\mu$  whose expression is calculated by:

$$\mu = m \frac{Mc^2}{E_{cm}}$$

where  $m$  and  $M$  are rest masses of the electron and of the target nuclei respectively.  $E_{cm}$  is the total center of mass energy and, since the target is at rest before scattering, its expression is calculated by:

$$E_{cm} = \sqrt{(mc^2)^2 + (Mc^2)^2 + 2E' Mc^2}$$

where  $E = \gamma' mc^2$  is the total energy of the electron before scattering in the laboratory system. The momentum and the scattering angle of the effective particle are equal to the corresponding quantities calculated in the center of mass system ( $p \equiv p_{cm}$ ,  $\theta \equiv \theta_{cm}$ ) of the incident electron:

$$pc = p' c \frac{Mc^2}{E_{cm}}$$

where  $p'$  is the momentum of the incident electron calculated in the laboratory system. The velocity of the effective particle is related with its momentum by the following expression:

$$\frac{1}{\beta^2} = 1 + \left( \frac{\mu c^2}{pc} \right)^2$$

The integration of the DCS is performed by the *NuclearCrossSection()* method of the *G4ScreeningMottCrossSection*:

$$\sigma_{tot} = 2\pi \int_{\theta_{min}}^{\theta_{max}} \frac{d\sigma(\theta)}{d\Omega} \sin \theta d\theta$$

The integration is performed in the scattering range  $[0 ; \pi]$  but the user can decide to vary the minimum ( $\theta_{min}$ ) and the maximum ( $\theta_{max}$ ) scattering angles. The DCS is then given by:

$$\frac{d\sigma(\theta)}{d\Omega} = \left( \frac{Ze^2}{\mu c^2 \beta^2 \gamma} \right)^2 \frac{R_{McF} |F_N(q)|^2}{(2A_s + 2 \sin^2(\theta/2))^2}$$

where  $Z$  is the atomic number of the nucleus,  $A_s$  is the screening coefficient whose expression has been given by Moliere [Moliere48] :

$$A_s = \left( \frac{\hbar}{2p a_{TF}} \right)^2 \left[ 1.13 + 3.76 \left( \frac{\alpha Z}{\beta} \right)^2 \right] \quad (9.78)$$

where  $a_{TF}$  is the Thomas-Fermi screening length given by:

$$a_{TF} = \frac{0.88534 a_0}{Z^{1/3}}$$

and  $a_0$  is the Bohr radius.  $R_{McF}$  is the ratio of the Mott to the Rutherford DCS given by McKinley and Feshbach approximation [MF48]:

$$R_{McF} = \left[ 1 - \beta^2 \sin^2(\theta/2) + Z\alpha\beta\pi \sin(\theta/2)(1 - \sin(\theta/2)) \right]$$

The nuclear form factor for the exponential charge distribution is given by [BKMM02]:

$$F_N(q) = \left[ 1 + \frac{(qR_N)^2}{12\hbar^2} \right]^{-2}$$

where  $R_N$  is the nuclear radius that is parameterized by:

$$R_N = 1.27A^{0.27} \text{ fm.}$$

$q$  is the momentum transferred to the nucleus and it is calculated as:

$$qc = \sqrt{T(T + 2Mc^2)}$$

where  $T$  is the kinetic energy transferred to the nucleus. This kinetic energy is calculated in the *GetNewDirection()* method as:

$$T = \frac{2Mc^2(p'c)^2}{E_{cm}^2} \sin^2 \theta / 2.$$

The scattering angle  $\theta$  calculation is performed in the *GetScatteringAngle()* method of *G4ScreeningMottCrossSection* class. By means of *AngleDistribution()* function the scattering angle is chosen randomly according to the total cross section distribution (p.d.f. probability density function) by means of the inverse transform method.

In the *SampleSecondary()* method of *G4eSingleScatteringModel* the kinetic energy of the incident particle after scattering is then calculated as  $E'_{new} = E' - T$  where  $E'$  is the electron incident kinetic energy (in lab.); in addition the new particle direction and momentum are obtained from the scattering angle information.

## 9.6.2 Implementation Details

The scattering angle probability density function  $f(\theta)$  (p.d.f.) is performed by the *AngleDistribution()* of *G4ScreeningMottCrossSection* class where the inverse transform method is applied. The normalized cumulative function of the cross section is calculated as a function of the scattering angle in this way:

$$\sigma_n(\theta) \equiv \int f(\theta) d\theta = \frac{2\pi}{\sigma_{tot}} \int_0^\theta \frac{d\sigma(t)}{d\Omega} \sin t dt$$

The normalized cumulative function  $\sigma_n(\theta)$  depends on the DCS and its values range in the interval [0;1]. After this calculation a random number  $r$ , uniformly distributed in the same interval [0;1], is chosen in order to fix the cumulative function value (i.e.  $r \equiv \sigma_n(\theta)$ ). This number is the probability to find the scattering angle in the interval  $[\theta; \theta + d\theta]$ . The scattering angle  $\theta$  is then given by the inverse function of  $\sigma_n(\theta)$ . The threshold energy for displacement Th can be set by the user in her/his own *Physics* class by adding the electromagnetic model:

```
G4eSingleCoulombScatteringModel* mod =
    new G4eSingleCoulombScatteringModel();
mod->SetRecoilThreshold(Th);
```

If the energy lost by the incident particle is greater than this threshold value a new secondary particle is created for transportation processes. The energy lost is added to *ProposeNonIonizingEnergyDeposit()*. NIEL calculation is available in test58.



## ATOMIC RELAXATION

### 10.1 Atomic relaxation

Atomic relaxation processes can be induced by any ionisation process that leaves the interested atom in an excited state (i.e. with a vacancy in its electronic structure). Processes inducing atomic relaxation in GEANT4 are photoelectric effect, Compton and ionisation (both Standard and Lowenergy).

GEANT4 uses by default the Livermore Evaluation Atomic Data Library EADL [[PCeal](#)], that contains data to describe the relaxation of atoms back to neutrality after they are ionised. It is assumed that the binding energy of all subshells (from now on shells are the same for neutral ground state atoms as for ionised atoms [[PCeal](#)]).

Data in EADL includes the radiative and non-radiative transition probabilities for each sub-shell of each element, for  $Z = 1$  to 100. The atom has been ionised by a process that has caused an electron to be ejected from an atom, leaving a vacancy or “hole” in a given subshell. The EADL data are then used to calculate the complete radiative and non-radiative spectrum of X-rays and electrons emitted as the atom relaxes back to neutrality.

Non-radiative de-excitation can occur via the Auger effect (the initial and secondary vacancies are in different shells) or Coster-Kronig effect (transitions within the same shell).

Please see further detailed information on atomic deexcitation [here](#).

#### 10.1.1 Fluorescence

The simulation procedure for the fluorescence process is the following:

1. If the vacancy shell is not included in the data, energy equal to the binding energy of the shell is deposited locally
2. If the vacancy subshell is included in the data, an outer subshell is randomly selected taking into account the relative transition probabilities for all possible outer subshells.
3. In the case where the energy corresponding to the selected transition is larger than a user defined cut value (equal to zero by default), a photon particle is created and emitted in a random direction in  $4\pi$ , with an energy equal to the transition energy, provided by EADL.
4. the procedure is repeated from step 1, for the new vacancy subshell.

The final local energy deposit is the difference between the binding energy of the initial vacancy subshell and the sum of all transition energies which were taken by fluorescence photons. The atom is assumed to be initially ionised with an electric charge of  $+1e$ .

Sub-shell data are provided in the EADL data bank [[PCeal](#)] for  $Z = 1$  through 100. However, transition probabilities are only explicitly included for  $Z = 6$  through 100, from the subshells of the K, L, M, N shells and some O subshells. For subshells O,P,Q: transition probabilities are negligible (of the order of 0.1%) and smaller than the precision with which they are known. Therefore, for the time being, for  $Z = 1$  through 5, only a local energy deposit corresponding

to the binding energy  $B$  of an electron in the ionised subshell is simulated. For subshells of the O, P, and Q shells, a photon is emitted with that energy  $B$ .

Since G4EMLOW8.0 a new X-ray fluorescence data library has been included with X-ray fluorescence transition probabilities calculated within the Hartree-Fock approach [Sco74], which is recognised to better reproduce PIXE experimental values when compared to the Hartree-Slater approach, adopted in the EADL data library [DDJS15]. This approach is called fluoANSTO in Geant4 and the transition probabilities are provided for  $Z < 93$ . For higher atomic numbers the EADL data libraries are used. The binding energies of all the subshells are derived from the EADL. This approach can be adopted to describe X-ray fluorescence in any application scenario, however, it is particularly recommended for PIXE applications. For more information the reader is referred to Bakr et al 2021 [BDCohenS+21].

### 10.1.2 Auger process

The Auger effect is complementary to fluorescence, hence the simulation process is the same as for the fluorescence, with the exception that two random shells are selected, one for the transition electron that fills the original vacancy, and the other for selecting the shell generating the Auger electron.

Subshell data are provided in the EADL data bank [PCEal] for  $Z = 6$  through 100. Since in EADL no data for elements with  $Z < 5$  are provided, Auger effects are only considered for  $5 < Z < 100$  and always due to the EADL data tables, only for those transitions which have a probability to occur  $> 0.1\%$  of the total non-radiative transition probability. EADL probability data used are, however, normalized to one for Fluorescence + Auger.

### 10.1.3 PIXE

PIXE (Particle Induced X-Ray Emission) can be simulated for ionisation continuous processes performed by ions. Ionised shells are selected randomly according the ionisation cross section of each shell once known the (continuous) energy loss along the step *Mean Energy Loss*.

Different shell ionisation cross sections models are available in different energy ranges:

- ECPSSR [BL79, WBrandtGLapicki81] internal GEANT4 calculation for K and L shells.
- ECPSSR calculations from Factor Form according to Reis [eal11b] for K and L shells from 0.1 to 100 MeV and for M shells from 0.1 to 100 MeV.
- ECPSSR calculations based on state of the art recommendations documented in Cohen et al. 2015 [DDJS15], called ANSTO ECPSSR. This approach provides the ionisation cross section of the K, L and M shells for incident protons and alpha particles up to  $5\text{MeV}/\text{amu}$ , in targets with  $Z < 93$ . The proposed cross sections have been extensively validated against PIXE experimental measurements by many PIXE labs. For more information the reader is referred to [BDCohenS+18].
- empirical “reference” K-shell values from Paul for protons [HP89] and for *alpha* [HP93]. Energies ranges are 0.1 - 10 MeV/amu circa, depending on the atomic number that varies between 4 and 32.
- semi-empirical L-subshell values from Orlic [OST94]. Energy Range 0.1-10 MeV for  $Z$  between 41 and 92.

Outside  $Z$  and energy of limited shell ionisation cross sections, the ECPSSR internal calculation method is applied.

Please refer to Ref.[eal11a] and original papers to have detailed information of every model.

## 10.2 Alternative models for impact ionisation by hadrons and PIXE

Early developments of proton and  $\alpha$  particle impact ionisation cross sections in GEANT4 are reviewed in a detailed paper devoted to PIXE simulation with GEANT4 [eal09]. This article also presents alternative developments for PIXE simulation, their validation with respect to experimental data and the first GEANT4-based simulation involving PIXE in a concrete experimental use case: the optimization of the graded shielding of the X-ray detectors of the eROSITA [eal07] mission. The new developments described in [eal09] are released in GEANT4 in the *pii* package (in *source/processes/electromagnetic/pii*).

The developments for PIXE simulation described in [eal09] provide a variety of proton and  $\alpha$  particle cross sections for the ionisation of K, L and M shells:

- theoretical calculations based on the ECPSSR [BL81] model and its variants (with Hartree-Slater corrections [Lap05], with the “united atom” approximation [Cip07b] and specialized for high energies [Lap08]),
- theoretical calculations based on plane wave Born approximation (PWBA),
- empirical models based on fits to experimental data collected by Paul and Sacher [PS89] (for protons, K shell), Paul and Bolik [PB93] (for  $\alpha$ , K shell), Kahoul et al. [KND08]) (for protons, K, shell), Miyagawa et al. [MNM88], Orlic et al. [OST94] and Sow et al. [SOLT93] for L shell.

The cross section models available in GEANT4 are listed in Table 10.1.

Table 10.1: Cross Section Models in GEANT4

Particle, shell	Model	Z range
<b>Protons, K shell</b>		
	ECPSSR	6-92
	ECPSSR High Energy	6-92
	ECPSSR Hartree-Slater	6-92
	ECPSSR United Atom	6-92
	ECPSSR reference [PS89]	6-92
	PWBA	6-92
	Paul and Sacher	6-92
	Kahoul et al.	6-92
<b>Protons, L shell</b>		
	ECPSSR	6-92
	ECPSSR United Atom	6-92
	PWBA	6-92
	Miyagawa et al.	40-92
	Orlic et al.	43-92
	Sow et al.	43-92
<b>Protons, M shell</b>		
	ECPSSR	6-92
	PWBA	6-92
<b><math>\alpha</math>, K shell</b>		
	ECPSSR	6-92
	ECPSSR Hartree-Slater	6-92
	ECPSSR reference [PB93]	6-92
	PWBA	6-92
<b><math>\alpha</math>, L and M shell</b>		
	ECPSSR	6-92
	PWBA	6-92

The calculation of cross sections in the course of the simulation is based on the interpolation of tabulated values, which are collected in a data library. The tabulations corresponding to theoretical calculations span the energy range between

10 keV and 10 GeV; empirical models are tabulated consistently with the energy range of validity documented by their authors, that corresponds to the range of the data used in the empirical fits and varies along with the atomic number and sub-shell.

ECPSSR tabulations have been produced using the ISICS software [Cip07a, LC96], 2006 version; an extended version, kindly provided by ISICS author S. Cipolla [Cip08], has been exploited to produce tabulations associated with recent high energy modelling developments [Lap08].

An example of the characteristics of different cross section models is illustrated in Fig. 10.1. Fig. 10.2 shows various cross section models for the ionisation of carbon K shell by proton, compared to experimental data reported in [PS89].

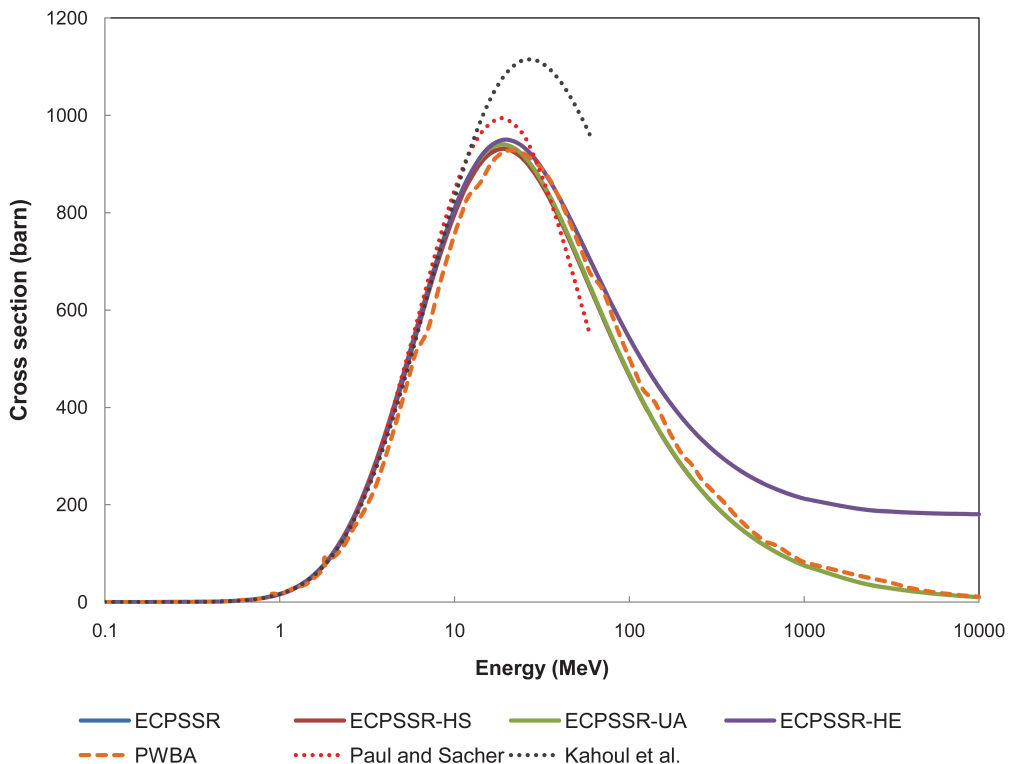


Fig. 10.1: Cross section for the ionisation of copper K shell by proton impact according to the various implemented modeling options: ECPSSR model, ECPSSR model with “united atom” (UA) approximation, Hartree-Slater (HS) corrections and specialized for high energies (HE); plane wave Born approximation (PWBA); empirical models by Paul and Sacher and Kahoul et al. The curves reproducing some of the model implementations can be hardly distinguished in the plot due to their similarity.

The implemented cross section models have been subject to rigorous statistical analysis to evaluate their compatibility with experimental measurements reported in [PS89], [OSaSMT94], [SC84] and to compare the relative accuracy of the various modelling options.

The validation process involved two stages: first goodness-of-fit analysis based on the  $\chi^2$  test to evaluate the hypothesis of compatibility with experimental data, then categorical analysis exploiting contingency tables to determine whether the various modelling options differ significantly in accuracy. Contingency tables were analyzed with the  $\chi^2$  test and with Fisher’s exact test.

The complete set of validation results is documented in [eal09]. Only the main ones are summarized here; GEANT4 users interested in detailed results, like the accuracy of different cross section models for specific target elements, should refer to [eal09] for detailed information.

Regarding the K shell, the statistical analysis identified the ECPSSR model with Hartree-Slater correction as the

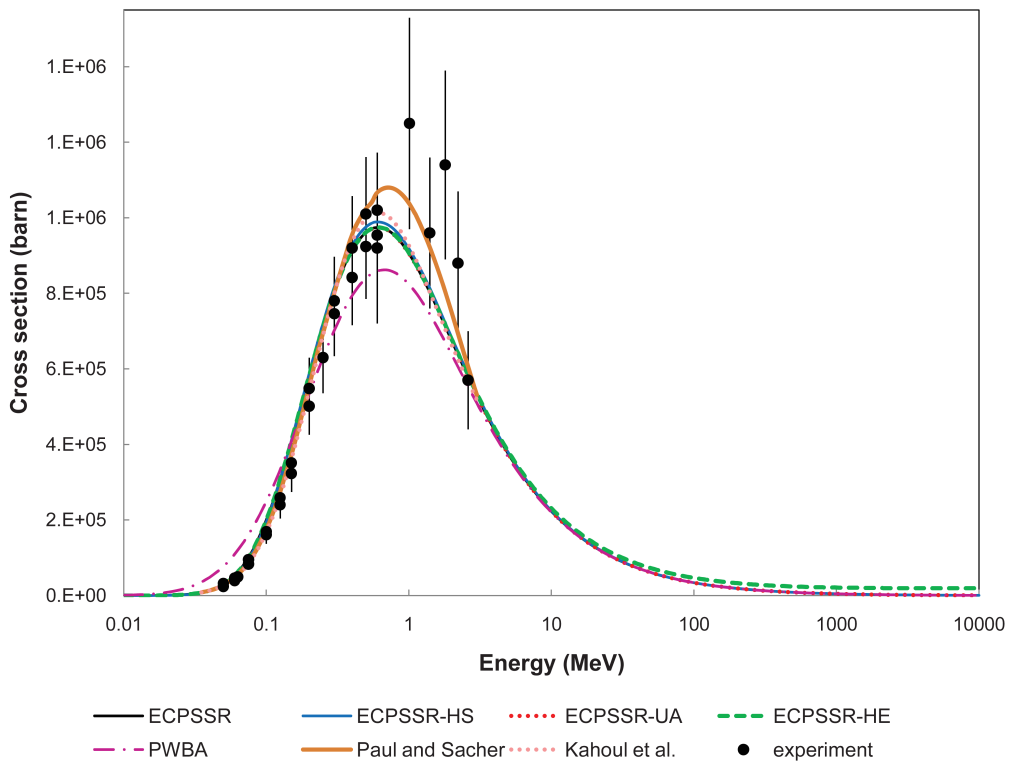


Fig. 10.2: Cross section for the ionisation of carbon K shell by proton impact according to the various implemented modeling options, and comparison with experimental data [PS89]: ECPSSR model, ECPSSR model with “united atom” (UA) approximation, Hartree-Slater (HS) corrections and specialized for high energies (HE); plane wave Born approximation (PWBA); empirical models by Paul and Sacher and Kahoul et al. The curves reproducing some of the model implementations can be hardly distinguished in the plot due to their similarity.

most accurate in the energy range up to approximately 10 MeV; at higher energies the ECPSSR model in its plain formulation or the empirical Paul and Sacher one (within its range of applicability) exhibit the best performance. The scarceness of high energy data prevents a definitive appraisal of the ECPSSR specialization for high energies.

Regarding the L shell, the ECPSSR model with “united atom” approximation exhibits the best accuracy among the various implemented models; its compatibility with experimental measurements at 95% confidence level ranges from approximately 90% of the test cases for the L<sub>3</sub> sub-shell to approximately 65% for the L<sub>1</sub> sub-shell. According to the results of the categorical analysis, the ECPSSR model in its original formulation can be considered an equivalently accurate alternative. The Orlic et al. model exhibits the worst accuracy with respect to experimental data; its accuracy is significantly different from the one of the ECPSSR model in the “united atom” variant.

The implementation of these models for the hadron impact ionisation process is included in the G4hImpactIonisation class, which is largely based on the original G4hLowEnergyIonisation process.

## ELECTRON AND POSITRON INCIDENT

### 11.1 Ionisation

#### 11.1.1 Method

The *G4eIonisation* class provides the continuous and discrete energy losses of electrons and positrons due to ionisation in a material according to the approach described in [Mean Energy Loss](#). The value of the maximum energy transferable to a free electron  $T_{max}$  is given by the following relation:

$$T_{max} = \begin{cases} E - mc^2 & \text{for } e^+ \\ (E - mc^2)/2 & \text{for } e^- \end{cases} \quad (11.1)$$

where  $mc^2$  is the electron mass. Above a given threshold energy the energy loss is simulated by the explicit production of delta rays by Möller scattering ( $e^-e^-$ ), or Bhabha scattering ( $e^+e^-$ ). Below the threshold the soft electrons ejected are simulated as continuous energy loss by the incident  $e^\pm$ .

#### 11.1.2 Continuous Energy Loss

The integration of (8.1) leads to the Berger-Seltzer formula [MC70]:

$$\frac{dE}{dx} \Big|_{T < T_{cut}} = 2\pi r_e^2 mc^2 n_{el} \frac{1}{\beta^2} \left[ \ln \frac{2(\gamma + 1)}{(I/mc^2)^2} + F^\pm(\tau, \tau_{up}) - \delta \right] \quad (11.2)$$

with

- $r_e$  = classical electron radius:  $e^2/(4\pi\epsilon_0 mc^2)$
- $mc^2$  = mass energy of the electron
- $n_{el}$  = electron density in the material
- $I$  = mean excitation energy in the material
- $\gamma = E/mc^2$
- $\beta^2 = 1 - (1/\gamma^2)$
- $\tau = \gamma - 1$
- $T_{cut}$  = minimum energy cut for  $\delta$ -ray production
- $\tau_c = T_{cut}/mc^2$
- $\tau_{max}$  = maximum energy transfer:  $\tau$  for  $e^+$ ,  $\tau/2$  for  $e^-$
- $\tau_{up} = \min(\tau_c, \tau_{max})$
- $\delta$  = density effect function.

In an elemental material the electron density is

$$n_{el} = Z n_{at} = Z \frac{\mathcal{N}_{av} \rho}{A}.$$

$\mathcal{N}_{av}$  is Avogadro's number,  $\rho$  is the material density, and  $A$  is the mass of a mole. In a compound material

$$n_{el} = \sum_i Z_i n_{ati} = \sum_i Z_i \frac{\mathcal{N}_{av} w_i \rho}{A_i},$$

where  $w_i$  is the proportion by mass of the  $i^{th}$  element, with molar mass  $A_i$ .

The mean excitation energies  $I$  for all elements are taken from [eal84].

The functions  $F^\pm$  are given by :

$$\begin{aligned} F^+(\tau, \tau_{up}) &= \ln(\tau\tau_{up}) - \frac{\tau_{up}^2}{\tau} \left[ \tau + 2\tau_{up} - \frac{3\tau_{up}^2 y}{2} - \left( \tau_{up} - \frac{\tau_{up}^3}{3} \right) y^2 - \left( \frac{\tau_{up}^2}{2} - \tau \frac{\tau_{up}^3}{3} + \frac{\tau_{up}^4}{4} \right) y^3 \right] \\ F^-(\tau, \tau_{up}) &= -1 - \beta^2 + \ln[(\tau - \tau_{up})\tau_{up}] + \frac{\tau}{\tau - \tau_{up}} + \frac{1}{\gamma^2} \left[ \frac{\tau_{up}^2}{2} + (2\tau + 1) \ln \left( 1 - \frac{\tau_{up}}{\tau} \right) \right] \end{aligned}$$

where  $y = 1/(\gamma + 1)$ .

The density effect correction is calculated according to the formalism of Sternheimer [SP71b]:

$x$  is a kinetic variable of the particle :  $x = \log_{10}(\gamma\beta) = \ln(\gamma^2\beta^2)/4.606$ , and  $\delta(x)$  is defined by

$$\begin{aligned} \text{for } x < x_0 : \quad \delta(x) &= 0 \\ \text{for } x \in [x_0, x_1] : \quad \delta(x) &= 4.606x - C + a(x_1 - x)^m \\ \text{for } x > x_1 : \quad \delta(x) &= 4.606x - C \end{aligned}$$

where the matter-dependent constants are calculated as follows:

$$\begin{aligned} h\nu_p &= \text{plasma energy of the medium} = \sqrt{4\pi n_{el} r_e^3} mc^2 / \alpha = \sqrt{4\pi n_{el} r_e} \hbar c \\ C &= 1 + 2 \ln(I/h\nu_p) \\ x_a &= C/4.606 \\ a &= 4.606(x_a - x_0)/(x_1 - x_0)^m \\ m &= 3. \end{aligned}$$

For condensed media

$$\begin{aligned} I < 100 \text{ eV} &\quad \left\{ \begin{array}{lll} \text{for } C \leq 3.681 & x_0 = 0.2 & x_1 = 2 \\ \text{for } C > 3.681 & x_0 = 0.326C - 1.0 & x_1 = 2 \end{array} \right. \\ I \geq 100 \text{ eV} &\quad \left\{ \begin{array}{lll} \text{for } C \leq 5.215 & x_0 = 0.2 & x_1 = 3 \\ \text{for } C > 5.215 & x_0 = 0.326C - 1.5 & x_1 = 3 \end{array} \right. \end{aligned}$$

and for gaseous media

$$\begin{aligned} \text{for } C < 10. &\quad x_0 = 1.6 \quad x_1 = 4 \\ \text{for } C \in [10.0, 10.5[ &\quad x_0 = 1.7 \quad x_1 = 4 \\ \text{for } C \in [10.5, 11.0[ &\quad x_0 = 1.8 \quad x_1 = 4 \\ \text{for } C \in [11.0, 11.5[ &\quad x_0 = 1.9 \quad x_1 = 4 \\ \text{for } C \in [11.5, 12.25[ &\quad x_0 = 2. \quad x_1 = 4 \\ \text{for } C \in [12.25, 13.804[ &\quad x_0 = 2. \quad x_1 = 5 \\ \text{for } C \geq 13.804 &\quad x_0 = 0.326C - 2.5 \quad x_1 = 5. \end{aligned}$$

### 11.1.3 Total Cross Section per Atom and Mean Free Path

The total cross section per atom for Möller scattering ( $e^-e^-$ ) and Bhabha scattering ( $e^+e^-$ ) is obtained by integrating Eq. (8.2). In GEANT4  $T_{cut}$  is always 1 keV or larger. For delta ray energies much larger than the excitation energy of the material ( $T \gg I$ ), the total cross section becomes [MC70] for Möller scattering,

$$\sigma(Z, E, T_{cut}) = \frac{2\pi r_e^2 Z}{\beta^2(\gamma - 1)} \left[ \frac{(\gamma - 1)^2}{\gamma^2} \left( \frac{1}{2} - x \right) + \frac{1}{x} - \frac{1}{1-x} - \frac{2\gamma - 1}{\gamma^2} \ln \frac{1-x}{x} \right],$$

and for Bhabha scattering ( $e^+e^-$ ),

$$\sigma(Z, E, T_{cut}) = \frac{2\pi r_e^2 Z}{(\gamma - 1)} \left[ \frac{1}{\beta^2} \left( \frac{1}{x} - 1 \right) + B_1 \ln x + B_2(1-x) - \frac{B_3}{2}(1-x^2) + \frac{B_4}{3}(1-x^3) \right].$$

Here

$$\begin{aligned} \gamma &= E/mc^2 & B_1 &= 2 - y^2 \\ \beta^2 &= 1 - (1/\gamma^2) & B_2 &= (1-2y)(3+y^2) \\ x &= T_{cut}/(E - mc^2) & B_3 &= (1-2y)^2 + (1-2y)^3 \\ y &= 1/(\gamma + 1) & B_4 &= (1-2y)^3. \end{aligned}$$

The above formulas give the total cross section for scattering above the threshold energies

$$T_{Moller}^{thr} = 2T_{cut} \quad \text{and} \quad T_{Bhabha}^{thr} = T_{cut}.$$

In a given material the mean free path is then

$$\lambda = (n_{at} \cdot \sigma)^{-1} \quad \text{or} \quad \lambda = (\sum_i n_{ati} \cdot \sigma_i)^{-1}.$$

### 11.1.4 Simulation of Delta-ray Production

#### Differential Cross Section

For  $T \gg I$  the differential cross section per atom becomes [MC70] for Möller scattering,

$$\frac{d\sigma}{d\epsilon} = \frac{2\pi r_e^2 Z}{\beta^2(\gamma - 1)} \left[ \frac{(\gamma - 1)^2}{\gamma^2} + \frac{1}{\epsilon} \left( \frac{1}{\epsilon} - \frac{2\gamma - 1}{\gamma^2} \right) + \frac{1}{1-\epsilon} \left( \frac{1}{1-\epsilon} - \frac{2\gamma - 1}{\gamma^2} \right) \right] \quad (11.3)$$

and for Bhabha scattering,

$$\frac{d\sigma}{d\epsilon} = \frac{2\pi r_e^2 Z}{(\gamma - 1)} \left[ \frac{1}{\beta^2 \epsilon^2} - \frac{B_1}{\epsilon} + B_2 - B_3 \epsilon + B_4 \epsilon^2 \right]. \quad (11.4)$$

Here  $\epsilon = T/(E - mc^2)$ . The kinematical limits of  $\epsilon$  are

$$\epsilon_0 = \frac{T_{cut}}{E - mc^2} \leq \epsilon \leq \frac{1}{2} \quad \text{for } e^-e^- \quad \epsilon_0 = \frac{T_{cut}}{E - mc^2} \leq \epsilon \leq 1 \quad \text{for } e^+e^-.$$

#### Sampling

The delta ray energy is sampled according to methods discussed in Section 2. Apart from normalization, the cross section can be factorized as

$$\frac{d\sigma}{d\epsilon} = f(\epsilon)g(\epsilon).$$

For  $e^-e^-$  scattering

$$f(\epsilon) = \frac{1}{\epsilon^2} \frac{\epsilon_0}{1 - 2\epsilon_0}$$

$$g(\epsilon) = \frac{4}{9\gamma^2 - 10\gamma + 5} \left[ (\gamma - 1)^2 \epsilon^2 - (2\gamma^2 + 2\gamma - 1) \frac{\epsilon}{1 - \epsilon} + \frac{\gamma^2}{(1 - \epsilon)^2} \right]$$

and for  $e^+e^-$  scattering

$$f(\epsilon) = \frac{1}{\epsilon^2} \frac{\epsilon_0}{1 - \epsilon_0}$$

$$g(\epsilon) = \frac{B_0 - B_1\epsilon + B_2\epsilon^2 - B_3\epsilon^3 + B_4\epsilon^4}{B_0 - B_1\epsilon_0 + B_2\epsilon_0^2 - B_3\epsilon_0^3 + B_4\epsilon_0^4}.$$

Here  $B_0 = \gamma^2 / (\gamma^2 - 1)$  and all other quantities have been defined above.

To choose  $\epsilon$ , and hence the delta ray energy,

1.  $\epsilon$  is sampled from  $f(\epsilon)$
2. the rejection function  $g(\epsilon)$  is calculated using the sampled value of  $\epsilon$
3.  $\epsilon$  is accepted with probability  $g(\epsilon)$ .

After the successful sampling of  $\epsilon$ , the direction of the ejected electron is generated with respect to the direction of the incident particle. The azimuthal angle  $\phi$  is generated isotropically and the polar angle  $\theta$  is calculated from energy-momentum conservation. This information is used to calculate the energy and momentum of both the scattered incident particle and the ejected electron, and to transform them to the global coordinate system.

### 11.1.5 Penelope Model

The *G4PenelopeIonisation* class calculates the continuous energy loss due to electron and positron ionisation and simulates the  $\delta$ -ray production by electrons and positrons. The electron production threshold  $T_c$  for a given material is used to separate the continuous and the discrete parts of the process. The simulation of inelastic collisions of electrons and positrons is performed on the basis of a Generalized Oscillation Strength (GOS) model (see Ref. [eal01] for a complete description). It is assumed that GOS splits into contributions from the different atomic electron shells.

#### Electrons

The total cross section  $\sigma^-(E)$  for the inelastic collision of electrons of energy  $E$  is calculated analytically. It can be split into contributions from distant longitudinal, distant transverse and close interactions,

$$\sigma^-(E) = \sigma_{dis,l} + \sigma_{dis,t} + \sigma_{clo}^-.$$

The contributions from distant longitudinal and transverse interactions are

$$\sigma_{dis,l} = \frac{2\pi e^4}{m_e v^2} \sum_{shells} f_k \frac{1}{W_k} \ln \left( \frac{W_k}{Q_k^{min}} \frac{Q_k^{min} + 2m_e c^2}{W_k + 2m_e c^2} \right) \Theta(E - W_k) \quad (11.5)$$

and

$$\sigma_{dis,t} = \frac{2\pi e^4}{m_e v^2} \sum_{shells} f_k \frac{1}{W_k} \left[ \ln \left( \frac{1}{1 - \beta^2} \right) - \beta^2 - \delta_F \right] \Theta(E - W_k) \quad (11.6)$$

respectively, where:

- $m_e$  = mass of the electron;
- $v$  = velocity of the electron;
- $\beta$  = velocity of the electron in units of  $c$ ;
- $f_k$  = number of electrons in the  $k$ -th atomic shell;
- $\Theta$  = Heaviside step function;
- $W_k$  = resonance energy of the  $k$ -th atomic shell oscillator;

$$Q_k^{\min} = \text{minimum kinematically allowed recoil energy for energy transfer } W_k$$

$$= \sqrt{\left[ \sqrt{E(E + 2m_e c^2)} - \sqrt{(E - W_k)(E - W_k + 2m_e c^2)} \right]^2 + m_e^2 c^4 - m_e^2 c^2};$$

$\delta_F$  = Fermi density effect correction.

$\delta_F$  is computed as described in Ref. [Fan63].

The value of  $W_k$  is calculated from the ionisation energy  $U_k$  of the  $k$ -th shell as  $W_k = 1.65 U_k$ . This relation is derived from the hydrogenic model, which is valid for the innermost shells. In this model, the shell ionisation cross sections are only roughly approximated; nevertheless the ionisation of inner shells is a low probability process and the approximation has a weak effect on the global transport properties<sup>1</sup>.

The integrated cross section for close collisions is the Møller cross section

$$\sigma_{clo}^- = \frac{2\pi e^4}{m_e v^2} \sum_{shells} f_k \int_{W_k}^{\frac{E}{2}} \frac{1}{W^2} F^-(E, W) dW, \quad (11.7)$$

where

$$F^-(E, W) = 1 + \left( \frac{W}{E - W} \right)^2 - \frac{W}{E - W} + \left( \frac{E}{E + m_e c^2} \right)^2 \left( \frac{W}{E - W} + \frac{W^2}{E^2} \right).$$

The integral of Eq.(11.7) can be evaluated analytically. In the final state there are two indistinguishable free electrons and the fastest one is considered as the “primary”; accordingly, the maximum allowed energy transfer in close collisions is  $E/2$ . The GOS model also allows evaluation of the spectrum  $d\sigma^-/dW$  of the energy  $W$  lost by the primary electron as the sum of distant longitudinal, distant transverse and close interaction contributions,

$$\frac{d\sigma^-}{dW} = \frac{d\sigma_{clo}^-}{dW} + \frac{d\sigma_{dis,l}}{dW} + \frac{d\sigma_{dis,t}}{dW}. \quad (11.8)$$

In particular,

$$\frac{d\sigma_{dis,l}}{dW} = \frac{2\pi e^4}{m_e v^2} \sum_{shells} f_k \frac{1}{W_k} \ln \left( \frac{W_k}{Q_-} \frac{Q_- + 2m_e c^2}{W_k + 2m_e c^2} \right) \delta(W - W_k) \Theta(E - W_k), \quad (11.9)$$

where

$$Q_- = \sqrt{\left[ \sqrt{E(E + 2m_e c^2)} - \sqrt{(E - W)(E - W + 2m_e c^2)} \right]^2 + m_e^2 c^4 - m_e^2 c^2},$$

$$\frac{d\sigma_{dis,t}}{dW} = \frac{2\pi e^4}{m_e v^2} \sum_{shells} f_k \frac{1}{W_k} \left[ \ln \left( \frac{1}{1 - \beta^2} \right) - \beta^2 - \delta_F \right] \Theta(E - W_k) \delta(W - W_k) \quad (11.10)$$

and

$$\frac{d\sigma_{clo}^-}{dW} = \frac{2\pi e^4}{m_e v^2} \sum_{shells} f_k \frac{1}{W^2} F^-(E, W) \Theta(W - W_k). \quad (11.11)$$

<sup>1</sup> In cases where inner-shell ionisation is directly observed, a more accurate description of the process should be used.

Eqs.(11.5), (11.6) and (11.7) derive respectively from the integration in  $dW$  of Eqs.(11.9), (11.10) and (11.11) in the interval  $[0, W_{max}]$ , where  $W_{max} = E$  for distant interactions and  $W_{max} = E/2$  for close. The analytical GOS model provides an accurate *average* description of inelastic collisions. However, the continuous energy loss spectrum associated with single distant excitations of a given atomic shell is approximated as a single resonance (a  $\delta$  distribution). As a consequence, the simulated energy loss spectra show unphysical narrow peaks at energy losses that are multiples of the resonance energies. These spurious peaks are automatically smoothed out after multiple inelastic collisions. The explicit expression of  $d\sigma^-/dW$ , Eq.(11.8), allows the analytic calculation of the partial cross sections for soft and hard ionisation events, i.e.

$$\sigma_{soft}^- = \int_0^{T_c} \frac{d\sigma^-}{dW} dW \quad \text{and} \quad \sigma_{hard}^- = \int_{T_c}^{W_{max}} \frac{d\sigma^-}{dW} dW.$$

The first stage of the simulation is the selection of the active oscillator  $k$  and the oscillator branch (distant or close). In distant interactions with the  $k$ -th oscillator, the energy loss  $W$  of the primary electron corresponds to the excitation energy  $W_k$ , i.e.  $W=W_k$ . If the interaction is transverse, the angular deflection of the projectile is neglected, i.e.  $\cos\theta = 1$ . For longitudinal collisions, the distribution of the recoil energy  $Q$  is given by

$$P_k(Q) = \begin{cases} \frac{1}{Q[1+Q/(2m_e c^2)]} & \text{if } Q_- < Q < W_{max} \\ 0 & \text{otherwise} \end{cases}$$

Once the energy loss  $W$  and the recoil energy  $Q$  have been sampled, the polar scattering angle is determined as

$$\cos\theta = \frac{E(E + 2m_e c^2) + (E - W)(E - W + 2m_e c^2) - Q(Q + 2m_e c^2)}{2\sqrt{E(E + 2m_e c^2)(E - W)(E - W + 2m_e c^2)}}.$$

The azimuthal scattering angle  $\phi$  is sampled uniformly in the interval  $(0, 2\pi)$ . For close interactions, the distributions for the reduced energy loss  $\kappa \equiv W/E$  for electrons are

$$P_k^-(\kappa) = \left[ \frac{1}{\kappa^2} + \frac{1}{(1-\kappa)^2} - \frac{1}{\kappa(1-\kappa)} + \left( \frac{E}{E + m_e c^2} \right)^2 \left( 1 + \frac{1}{\kappa(1-\kappa)} \right) \right] \Theta(\kappa - \kappa_c) \Theta(\frac{1}{2} - \kappa)$$

with  $\kappa_c = \max(W_k, T_c)/E$ . The maximum allowed value of  $\kappa$  is  $1/2$ , consistent with the indistinguishability of the electrons in the final state. After the sampling of the energy loss  $W = \kappa E$ , the polar scattering angle  $\theta$  is obtained as

$$\cos^2 \theta = \frac{E - W}{E} \frac{E + 2m_e c^2}{E - W + 2m_e c^2}.$$

The azimuthal scattering angle  $\phi$  is sampled uniformly in the interval  $(0, 2\pi)$ . According to the GOS model, each oscillator  $W_k$  corresponds to an atomic shell with  $f_k$  electrons and ionisation energy  $U_k$ . In the case of ionisation of an inner shell  $i$  (K or L), a secondary electron ( $\delta$ -ray) is emitted with energy  $E_s = W - U_i$  and the residual ion is left with a vacancy in the shell (which is then filled with the emission of fluorescence x-rays and/or Auger electrons). In the case of ionisation of outer shells, the simulated  $\delta$ -ray is emitted with kinetic energy  $E_s = W$  and the target atom is assumed to remain in its ground state. The polar angle of emission of the secondary electron is calculated as

$$\cos^2 \theta_s = \frac{W^2/\beta^2}{Q(Q + 2m_e c^2)} \left[ 1 + \frac{Q(Q + 2m_e c^2) - W^2}{2W(E + m_e c^2)} \right]^2$$

(for close collisions  $Q = W$ ), while the azimuthal angle is  $\phi_s = \phi + \pi$ . In this model, the Doppler effects on the angular distribution of the  $\delta$  rays are neglected. The stopping power due to soft interactions of electrons, which is used for the computation of the continuous part of the process, is analytically calculated as

$$S_{in}^- = N \int_0^{T_c} W \frac{d\sigma^-}{dW} dW$$

from the expression (11.8), where  $N$  is the number of scattering centers (atoms or molecules) per unit volume.

## Positrons

The total cross section  $\sigma^+(E)$  for the inelastic collision of positrons of energy  $E$  is calculated analytically. As in the case of electrons, it can be split into contributions from distant longitudinal, distant transverse and close interactions,

$$\sigma^+(E) = \sigma_{dis,l} + \sigma_{dis,t} + \sigma_{clo}^+.$$

The contributions from distant longitudinal and transverse interactions are the same as for electrons, Eq.(11.5) and (11.6), while the integrated cross section for close collisions is the Bhabha cross section

$$\sigma_{clo}^+ = \frac{2\pi e^4}{m_e v^2} \sum_{shells} f_k \int_{W_k}^E \frac{1}{W^2} F^+(E, W) dW, \quad (11.12)$$

where

$$F^+(E, W) = 1 - b_1 \frac{W}{E} + b_2 \frac{W^2}{E^2} - b_3 \frac{W^3}{E^3} + b_4 \frac{W^4}{E^4};$$

the Bhabha factors are

$$\begin{aligned} b_1 &= \left(\frac{\gamma-1}{\gamma}\right)^2 \frac{2(\gamma+1)^2 - 1}{\gamma^2 - 1}, \\ b_2 &= \left(\frac{\gamma-1}{\gamma}\right)^2 \frac{3(\gamma+1)^2 + 1}{(\gamma+1)^2}, \\ b_3 &= \left(\frac{\gamma-1}{\gamma}\right)^2 \frac{2(\gamma-1)\gamma}{(\gamma+1)^2}, \\ b_4 &= \left(\frac{\gamma-1}{\gamma}\right)^2 \frac{(\gamma-1)^2}{(\gamma+1)^2}, \end{aligned}$$

and  $\gamma$  is the Lorentz factor of the positron. The integral of Eq.(11.12) can be evaluated analytically. The particles in the final state are not indistinguishable so the maximum energy transfer  $W_{max}$  in close collisions is  $E$ . As for electrons, the GOS model allows the evaluation of the spectrum  $d\sigma^+/dW$  of the energy  $W$  lost by the primary positron as the sum of distant longitudinal, distant transverse and close interaction contributions,

$$\frac{d\sigma^+}{dW} = \frac{d\sigma_{clo}^+}{dW} + \frac{d\sigma_{dis,l}}{dW} + \frac{d\sigma_{dis,t}}{dW}, \quad (11.13)$$

where the distant terms  $\frac{d\sigma_{dis,l}}{dW}$  and  $\frac{d\sigma_{dis,t}}{dW}$  are those from Eqs.(11.9) and (11.10), while the close contribution is

$$\frac{d\sigma_{clo}^+}{dW} = \frac{2\pi e^4}{m_e v^2} \sum_{shells} f_k \frac{1}{W^2} F^+(E, W) \Theta(W - W_k).$$

Also in this case, the explicit expression of  $d\sigma^+/dW$ , Eq.(11.13), allows an analytic calculation of the partial cross sections for soft and hard ionisation events, i.e.

$$\sigma_{soft}^+ = \int_0^{T_c} \frac{d\sigma^+}{dW} dW \quad \text{and} \quad \sigma_{hard}^+ = \int_{T_c}^E \frac{d\sigma^+}{dW} dW.$$

The sampling of the final state in the case of distant interactions (transverse or longitudinal) is performed in the same way as for primary electrons, see [Electrons](#). For close positron interactions with the  $k$ -th oscillator, the distribution for the reduced energy loss  $\kappa \equiv W/E$  is

$$P_k^+(\kappa) = \left[ \frac{1}{\kappa^2} - \frac{b_1}{\kappa} + b_2 - b_3\kappa + b_4\kappa^2 \right] \Theta(\kappa - \kappa_c) \Theta(1 - \kappa)$$

with  $\kappa_c = \max(W_k, T_c)/E$ . In this case, the maximum allowed reduced energy loss  $\kappa$  is 1. After sampling the energy loss  $W = \kappa E$ , the polar angle  $\theta$  and the azimuthal angle  $\phi$  are obtained using the equations introduced for electrons

in *Electrons*. Similarly, the generation of  $\delta$  rays is performed in the same way as for electrons. Finally, the stopping power due to soft interactions of positrons, which is used for the computation of the continuous part of the process, is analytically calculated as

$$S_{in}^+ = N \int_0^{T_c} W \frac{d\sigma^+}{dW} dW$$

from the expression (11.13), where  $N$  is the number of scattering centers per unit volume.

### 11.1.6 Livermore Model

The class *G4LivermoreIonisationModel* calculates the continuous energy loss due to electron ionisation and simulates  $\delta$ -ray production by electrons. The  $\delta$ -electron production threshold for a given material,  $T_c$ , is used to separate the continuous and the discrete parts of the process. The energy loss of an electron with the incident energy,  $T$ , is expressed via the sum over all atomic shells,  $s$ , and the integral over the energy,  $t$ , of  $\delta$ -electrons:

$$\frac{dE}{dx} = \sum_s \left( \sigma_s(T) \frac{\int_{0.1eV}^{T_c} t \frac{d\sigma}{dt} dt}{\int_{0.1eV}^{T_{max}} \frac{d\sigma}{dt} dt} \right),$$

where  $T_{max} = 0.5T$  is the maximum energy transferred to a  $\delta$ -electron,  $\sigma_s(T)$  is the total cross-section for the shell,  $s$ , at a given incident kinetic energy,  $T$ , and 0.1 eV is the low energy limit of the EEDL data. The  $\delta$ -electron production cross-section is a complementary function:

$$\sigma(T) = \sum_s \left( \sigma_s(T) \frac{\int_{T_c}^{T_{max}} \frac{d\sigma}{dt} dt}{\int_{0.1eV}^{T_{max}} \frac{d\sigma}{dt} dt} \right).$$

The partial sub-shell cross-sections,  $\sigma_s$ , are obtained from an interpolation of the evaluated cross-section data in the EEDL library [STPerkins89], according to the formula (6.1) in *Generic Calculation of Total Cross Sections*.

The probability of emission of a  $\delta$ -electron with kinetic energy,  $t$ , from a sub-shell,  $s$ , of binding energy,  $B_s$ , as the result of the interaction of an incoming electron with kinetic energy,  $T$ , is described by:

$$\frac{d\sigma}{dt} = \frac{P(x)}{x^2}, \quad \text{with } x = \frac{t + B_s}{T + B_s},$$

where the parameter  $x$  is varied from  $x_{min} = (0.1eV + B_s)/(T + B_s)$  to 0.5. The function,  $P(x)$ , is parametrised differently in 3 regions of  $x$ : from  $x_{min}$  to  $x_1$  the linear interpolation with linear scale of 4 points is used; from  $x_1$  to  $x_2$  the linear interpolation with logarithmic scale of 16 points is used; from  $x_2$  to 0.5 the following interpolation is applied:

$$P(x) = 1 - gx + (1 - g)x^2 + \frac{x^2}{1 - x} \left( \frac{1}{1 - x} - g \right) + A * (0.5 - x)/x, \quad (11.14)$$

where  $A$  is a fit coefficient,  $g$  is expressed via the gamma factor of the incoming electron:

$$g = (2\gamma - 1)/\gamma^2. \quad (11.15)$$

For the high energy case ( $x \gg 1$ ) the formula ((11.14)) is transformed to the Möller electron-electron scattering formula [MC70, eal93].

The value of the coefficient,  $A$ , for each element is obtained as a result of the fit on the spectrum from the EEDL data for those energies which are available in the database. The values of  $x_1$  and  $x_2$  are chosen for each atomic shell according to the spectrum of  $\delta$ -electrons in this shell. Note that  $x_1$  corresponds to the maximum of the spectrum, if the maximum does not coincide with  $x_{min}$ . The dependence of all 24 parameters on the incident energy,  $T$ , is evaluated from a logarithmic interpolation (6.1).

The sampling of the final state proceeds in three steps. First a shell is randomly selected, then the energy of the  $\delta$ -electron is sampled, finally the angle of emission of the scattered electron and of the  $\delta$ -ray is determined by energy-momentum conservation taken into account electron motion on the atomic orbit.

The interaction leaves the atom in an excited state. The deexcitation of the atom is simulated as described in [Atomic relaxation](#). Sampling of the excitations is carried out for both the continuous and the discrete parts of the process.

## 11.2 Bremsstrahlung

The class *G4eBremsstrahlung* provides the energy loss of electrons and positrons due to the radiation of photons in the field of a nucleus according to the approach described in [Mean Energy Loss](#). Above a given threshold energy the energy loss is simulated by the explicit production of photons. Below the threshold the emission of soft photons is treated as a continuous energy loss.

Below electron/positron energies of 1 GeV, the cross section evaluation is based on a dedicated parameterization, above this limit an analytic cross section is used. In GEANT4 the Landau-Pomeranchuk-Migdal effect has also been implemented.

### 11.2.1 Seltzer-Berger bremsstrahlung model

In order to improve accuracy of the model described above a new model *G4SeltzerBergerModel* have been design which implementing cross section based on interpolation of published tables [SB85, SB86]. Single-differential cross section can be written as a sum of a contribution of bremsstrahlung produced in the field of the screened atomic nucleus  $d\sigma_n/dk$ , and the part  $Z d\sigma_e/dk$  corresponding to bremsstrahlung produced in the field of the Z atomic electrons,

$$\frac{d\sigma}{dk} = \frac{d\sigma_n}{dk} + Z \frac{d\sigma_e}{dk}.$$

The differential cross section depends on the energy  $k$  of the emitted photon, the kinetic energy  $T_1$  of the incident electron and the atomic number  $Z$  of the target atom.

Seltzer and Berger have published extensive tables for the differential cross section  $d\sigma_n/dk$  and  $d\sigma_e/dk$  [SB85, SB86], covering electron energies from 1 keV up to 10 GeV, substantially extending previous publications [eal77]. The results are in good agreement with experimental data, and provided also the basis of bremsstrahlung implementations in many Monte Carlo programs (e.g. Penelope, EGS). The estimated uncertainties for  $d\sigma/dk$  are:

- 3% to 5% in the high energy region ( $T_1 \geq 50$  MeV),
- 5% to 10% in the intermediate energy region ( $2 \leq T_1 \leq 50$  MeV),
- and 10% at low energies region compared with Pratt results. ( $T_1 \leq 2$  MeV).

The restricted cross section (8.2) and the energy loss (8.3) are obtained by numerical integration performed at initialisation stage of GEANT4. This method guarantees consistent description independent of the energy cutoff. The current version uses an interpolation in tables for 52 available electron energy points versus 31 photon energy points, and for atomic number  $Z$  ranging from 1 to 99. It is the default bremsstrahlung model in GEANT4 since version 9.5. Fig. 11.1 shows a comparison of the total bremsstrahlung cross sections with the previous implementation, and with the relativistic model.

After the successful sampling of  $\epsilon$ , the polar angles of the radiated photon are generated with respect to the parent electron's momentum. It is difficult to find simple formulae for this angle in the literature. For example the double

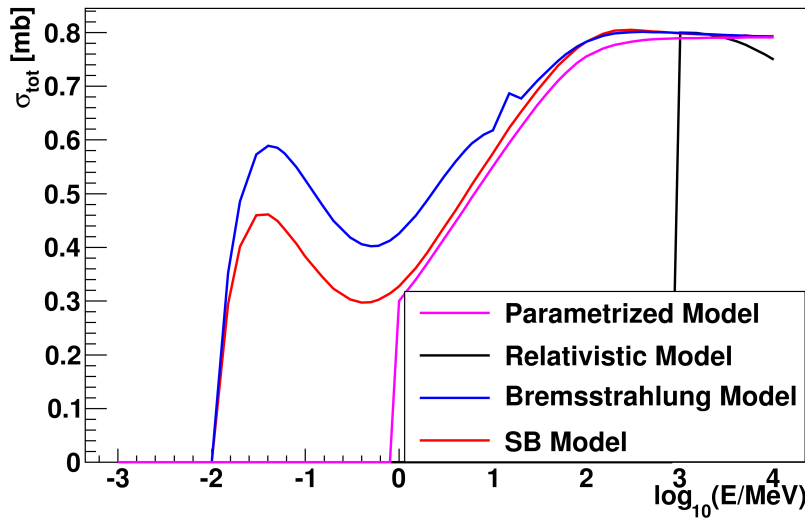


Fig. 11.1: Total cross section comparison between models for  $Z = 29$ : Parametrized Bremsstrahlung Model, Relativistic Model, Bremsstrahlung Model (GEANT4 9.4) and Seltzer-Berger Model. The discontinuities in the Parametrized Model and the Relativistic Model at 1 Mev and 1 GeV, respectively, mark the validity range of these models.

differential cross section reported by Tsai [Tsa74, Tsa77] is

$$\begin{aligned} \frac{d\sigma}{dkd\Omega} &= \frac{2\alpha^2 e^2}{\pi km^4} \left\{ \left[ \frac{2\epsilon - 2}{(1+u^2)^2} + \frac{12u^2(1-\epsilon)}{(1+u^2)^4} \right] Z(Z+1) \right. \\ &\quad \left. + \left[ \frac{2-2\epsilon-\epsilon^2}{(1+u^2)^2} - \frac{4u^2(1-\epsilon)}{(1+u^2)^4} \right] [X - 2Z^2 f_c((\alpha Z)^2)] \right\} \\ u &= \frac{E\theta}{m} \\ X &= \int_{t_{min}}^{m^2(1+u^2)^2} [G_Z^{el}(t) + G_Z^{in}(t)] \frac{t - t_{min}}{t^2} dt \\ G_Z^{el,in}(t) &: \text{atomic form factors} \\ t_{min} &= \left[ \frac{km^2(1+u^2)}{2E(E-k)} \right]^2 = \left[ \frac{\epsilon m^2(1+u^2)}{2E(1-\epsilon)} \right]^2. \end{aligned}$$

The sampling of this distribution is complicated. It is also only an approximation to within a few percent, due at least to the presence of the atomic form factors. The angular dependence is contained in the variable  $u = E\theta m^{-1}$ . For a given value of  $u$  the dependence of the shape of the function on  $Z$ ,  $E$  and  $\epsilon = k/E$  is very weak. Thus, the distribution can be approximated by a function

$$f(u) = C (ue^{-au} + due^{-3au})$$

where

$$C = \frac{9a^2}{9+d} \quad a = 0.625 \quad d = 27$$

where  $E$  is in GeV. While this approximation is good at high energies, it becomes less accurate around a few MeV. However in that region the ionisation losses dominate over the radiative losses. The sampling of the function  $f(u)$  can be done with three random numbers  $r_i$ , uniformly distributed on the interval  $[0,1]$ :

1. choose between  $ue^{-au}$  and  $due^{-3au}$ :

$$b = \begin{cases} a & \text{if } r_1 < 9/(9+d) \\ 3a & \text{if } r_1 \geq 9/(9+d) \end{cases}$$

2. sample  $ue^{-bu}$ :

$$u = -\frac{\log(r_2 r_3)}{b}$$

3. check that:

$$u \leq u_{max} = \frac{E\pi}{m}$$

otherwise go back to 1.

The probability of failing the last test is reported in [Table 11.1](#).

Table 11.1: Probability of failing test.

E (MeV)	P(%)
0.511	3.4
0.6	2.2
0.8	1.2
1.0	0.7
2.0	< 0.1

The function  $f(u)$  can also be used to describe the angular distribution of the photon in  $\mu$  bremsstrahlung and to describe the angular distribution in photon pair production. The azimuthal angle  $\phi$  is generated isotropically. Along with  $\theta$ , this information is used to calculate the momentum vectors of the radiated photon and parent recoiled electron, and to transform them to the global coordinate system. The momentum transfer to the atomic nucleus is neglected.

### 11.2.2 Bremsstrahlung of high-energy electrons

Above an electron energy of 1 GeV an analytic differential cross section representation is used [Per94], which was modified to account for the density effect and the Landau-Pomeranchuk-Migdal (LPM) effect [eal82, Kle99].

#### Relativistic Bremsstrahlung cross section

The basis of the implementation is the well known high energy limit of the Bremsstrahlung process [Per94],

$$\frac{d\sigma}{dk} = \frac{4\alpha r_e^2}{3k} \left[ \{y^2 + 2[1 + (1-y)^2]\}[Z^2(F_{el} - f) + ZF_{inel}] + (1-y)\frac{Z^2 + Z}{3} \right] \quad (11.16)$$

The *elastic form factor*  $F_{el}$  and *inelastic form factor*  $F_{inel}$ , describe the scattering on the nucleus and on the shell electrons, respectively, and for  $Z > 4$  are given by [eal08]

$$F_{el} = \log\left(\frac{184.15}{Z^{\frac{1}{3}}}\right)$$

$$F_{inel} = \log\left(\frac{1194.}{Z^{\frac{2}{3}}}\right).$$

This corresponds to the complete screening approximation. The Coulomb correction is defined as [eal08]

$$f = \alpha^2 Z^2 \sum_{n=1}^{\infty} \frac{1}{n(n^2 + \alpha^2 Z^2)}$$

This approach provides an analytic differential cross section for an efficient evaluation in a Monte Carlo computer code. Note that in this approximation the differential cross section  $d\sigma/dk$  is independent of the energy of the initial electron and is also valid for positrons.

The total integrated cross section  $\int d\sigma/dk dk$  is divergent, but the energy loss integral  $\int k d\sigma/dk dk$  is finite. This allows the usual separation into continuous energy loss, and discrete photon production according to Eqs. (8.3) and (8.2).

### Landau Pomeranchuk Migdal (LPM) effect

At higher energies matter effects become more and more important. In GEANT4 the two leading matter effects, the LPM effect and the dielectric suppression (or Ter-Mikaelian effect), are considered. The analytic cross section representation, (11.16), provides the basis for the incorporation of these matter effects.

The LPM effect (see for example [eal04, eal97, GG64]) is the suppression of photon production due to the multiple scattering of the electron. If an electron undergoes multiple scattering while traversing the so called “formation zone”, the bremsstrahlung amplitudes from before and after the scattering can interfere, reducing the probability of bremsstrahlung photon emission (a similar suppression occurs for pair production). The suppression becomes significant for photon energies below a certain value, given by

$$\frac{k}{E} < \frac{E}{E_{LPM}},$$

where

$k$	photon energy
$E$	electron energy
$E_{LPM}$	characteristic energy for LPM effect (depend on the medium).

The value of the LPM characteristic energy can be written as

$$E_{LPM} = \frac{\alpha m^2 X_0}{4hc}, \quad (11.17)$$

where

$\alpha$	fine structure constant
$m$	electron mass
$X_0$	radiation length in the material
$h$	Planck constant
$c$	velocity of light in vacuum.

At high energies (approximately above 1 GeV) the differential cross section including the Landau-Pomeranchuk-Migdal effect, can be expressed using an evaluation based on [eal82, Kle99, Mig56]

$$\begin{aligned} \frac{d\sigma}{dk} = & \frac{4\alpha r_e^2}{3k} \left[ \xi(s) \{y^2 G(s) + 2[1 + (1 - y)^2] \phi(s)\} \right. \\ & \times [Z^2(F_{el} - f) + Z F_{inel}] + (1 - y) \frac{Z^2 + Z}{3} \left. \right] \end{aligned} \quad (11.18)$$

where LPM suppression functions are defined by [Mig56]

$$G(s) = 24s^2 \left( \frac{\pi}{2} - \int_0^\infty e^{-st} \frac{\sin(st)}{\sinh(\frac{t}{2})} dt \right)$$

and

$$\phi(s) = 12s^2 \left( -\frac{\pi}{2} + \int_0^\infty e^{-st} \sin(st) \sinh\left(\frac{t}{2}\right) dt \right)$$

They can be piecewise approximated with simple analytic functions, see e.g. [eal82]. The suppression function  $\xi(s)$  is recursively defined via

$$s = \sqrt{\frac{k E_{\text{LPM}}}{8E(E-k)\xi(s)}}$$

but can be well approximated using an algorithm introduced by [eal82]. The material dependent characteristic energy  $E_{\text{LPM}}$  is defined in Eq.(11.17) according to [eal97]. Note that this definition differs from other definition (e.g. [Kle99]) by a factor  $\frac{1}{2}$ .

An additional multiplicative factor governs the dielectric suppression effect (Ter-Mikaelian effect) [TER54].

$$S(k) = \frac{k^2}{k^2 + k_p^2}$$

The characteristic photon energy scale  $k_p$  is given by the plasma frequency of the media, defined as

$$k_p = \hbar\omega_p \frac{E_e}{m_e c^2} = \frac{\hbar E_e}{m_e c^2} \cdot \sqrt{\frac{n_e e^2}{\epsilon_0 m_e}}.$$

Both suppression effects, dielectric suppression and LPM effect, reduce the effective formation length of the photon, so the suppressions *do not simply multiply*. A consistent treatment of the overlap region, where both suppression mechanism, was suggested by [TM72]. The algorithm guarantees that the LPM suppression is turned off as the density effect becomes important. This is achieved by defining a modified suppression variable  $\hat{s}$  via

$$\hat{s} = s \cdot \left( 1 + \frac{k_p^2}{k^2} \right)$$

and using  $\hat{s}$  in the LPM suppression functions  $G(s)$  and  $\phi(s)$  instead of  $s$  in Eq.(11.18).

### 11.2.3 Penelope Model

#### Introduction

The class *G4PenelopeBremsstrahlung* calculates the continuous energy loss due to soft  $\gamma$  emission and simulates the photon production by electrons and positrons. As usual, the gamma production threshold  $T_c$  for a given material is used to separate the continuous and the discrete parts of the process.

#### Electrons

The total cross sections are calculated from the data [STPerkins89], as described in *Generic Calculation of Total Cross Sections* and *Livermore Model*. The energy distribution  $\frac{d\sigma}{dW}(E)$ , i.e. the probability of the emission of a photon with energy  $W$  given an incident electron of kinetic energy  $E$ , is generated according to the formula

$$\frac{d\sigma}{dW}(E) = \frac{F(\kappa)}{\kappa}, \quad \kappa = \frac{W}{E}.$$

The functions  $F(\kappa)$  describing the energy spectra of the outgoing photons are taken from Ref.[SB86]. For each element  $Z$  from 1 to 92, 32 points in  $\kappa$ , ranging from  $10^{-12}$  to 1, are used for the linear interpolation of this function.

$F(\kappa)$  is normalized using the condition  $F(10^{-12}) = 1$ . The energy distribution of the emitted photons is available in the library [SB86] for 57 energies of the incident electron between 1 keV and 100 GeV. For other primary energies, logarithmic interpolation is used to obtain the values of the function  $F(\kappa)$ . The direction of the emitted bremsstrahlung photon is determined by the polar angle  $\theta$  and the azimuthal angle  $\phi$ . For isotropic media, with randomly oriented atoms, the bremsstrahlung differential cross section is independent of  $\phi$  and can be expressed as

$$\frac{d^2\sigma}{dW d\cos\theta} = \frac{d\sigma}{dW} p(Z, E, \kappa; \cos\theta).$$

Numerical values of the “shape function”  $p(Z, E, \kappa; \cos\theta)$ , calculated by partial-wave methods, have been published in Ref. [KQP83] for the following benchmark cases:  $Z = 2, 8, 13, 47, 79$  and  $92$ ;  $E = 1, 5, 10, 50, 100$  and  $500$  keV;  $\kappa = 0, 0.6, 0.8$  and  $0.95$ . It was found in Ref. [eal01] that the benchmark partial-wave shape function of Ref. [KQP83] can be closely approximated by the analytical form (obtained in the Lorentz-dipole approximation)

$$p(\cos\theta) = A \frac{3}{8} \left[ 1 + \left( \frac{\cos\theta - \beta'}{1 - \beta'\cos\theta} \right)^2 \right] \frac{1 - \beta'^2}{(1 - \beta'\cos\theta)^2} + (1 - A) \frac{3}{4} \left[ 1 - \left( \frac{\cos\theta - \beta'}{1 - \beta'\cos\theta} m \right)^2 \right] \frac{1 - \beta'^2}{(1 - \beta'\cos\theta)^2},$$

with  $\beta' = \beta(1 + B)$ , if one considers  $A$  and  $B$  as adjustable parameters. The parameters  $A$  and  $B$  have been determined, by least squares fitting, for the 144 combinations of atomic numbers, electron energies and reduced photon energies corresponding to the benchmark shape functions tabulated in [KQP83]. The quantities  $\ln(AZ\beta)$  and  $B\beta$  vary smoothly with  $Z$ ,  $\beta$  and  $\kappa$  and can be obtained by cubic spline interpolation of their values for the benchmark cases. This permits the fast evaluation of the shape function  $p(Z, E, \kappa; \cos\theta)$  for any combination of  $Z$ ,  $\beta$  and  $\kappa$ . The stopping power  $dE/dx$  due to soft bremsstrahlung is calculated by interpolating in  $E$  and  $\kappa$  the numerical data of scaled cross sections of Ref. [BS82]. The energy and the direction of the outgoing electron are determined by using energy-momentum balance.

## Positrons

The radiative differential cross section  $d\sigma^+(E)/dW$  for positrons reduces to that for electrons in the high-energy limit, but is smaller for intermediate and low energies. Owing to the lack of more accurate calculations, the differential cross section for positrons is obtained by multiplying the electron differential cross section  $d\sigma^-(E)/dW$  by a  $\kappa$ -independent factor, i.e.

$$\frac{d\sigma^+}{dW} = F_p(Z, E) \frac{d\sigma^-}{dW}.$$

The factor  $F_p(Z, E)$  is set equal to the ratio of the radiative stopping powers for positrons and electrons, which has been calculated in Ref. [eal86]. For the actual calculation, the following analytical approximation is used:

$$F_p(Z, E) = 1 - \exp(-1.2359 \cdot 10^{-1}t + 6.1274 \cdot 10^{-2}t^2 - 3.1516 \cdot 10^{-2}t^3 + 7.7446 \cdot 10^{-3}t^4 - 1.0595 \cdot 10^{-3}t^5 + 7.0568 \cdot 10^{-5}t^6 - 1.8080 \cdot 10^{-6}t^7),$$

where

$$t = \ln \left( 1 + \frac{10^6}{Z^2} \frac{E}{m_e c^2} \right).$$

Because the factor  $F_p(Z, E)$  is independent on  $\kappa$ , the energy distribution of the secondary  $\gamma$ 's has the same shape as electron bremsstrahlung. Similarly, owing to the lack of numerical data for positrons, it is assumed that the shape of the angular distribution  $p(Z, E, \kappa; \cos\theta)$  of the bremsstrahlung photons for positrons is the same as for the electrons. The energy and direction of the outgoing positron are determined from energy-momentum balance.

### 11.2.4 Livermore Model

The class *G4LivermoreBremsstrahlungModel* calculates the continuous energy loss due to low energy gamma emission and simulates the gamma production by electrons. The gamma production threshold for a given material  $\omega_c$  is used to separate the continuous and the discrete parts of the process. The energy loss of an electron with the incident energy  $T$  are expressed via the integrand over energy of the gammas:

$$\frac{dE}{dx} = \sigma(T) \frac{\int_{0.1\text{eV}}^{\omega_c} t \frac{d\sigma}{d\omega} d\omega}{\int_{0.1\text{eV}}^T \frac{d\sigma}{d\omega} d\omega},$$

where  $\sigma(T)$  is the total cross-section at a given incident kinetic energy,  $T$ , 0.1 eV is the low energy limit of the EEDL data. The production cross-section is a complementary function:

$$\sigma = \sigma(T) \frac{\int_{\omega_c}^T \frac{d\sigma}{d\omega} d\omega}{\int_{0.1\text{eV}}^T \frac{d\sigma}{d\omega} d\omega}.$$

The total cross-section,  $\sigma_s$ , is obtained from an interpolation of the evaluated cross-section data in the EEDL library [STPerkins89].

The EEDL data [eal99] of total cross-sections are parametrised [STPerkins89] according to (6.1). The probability of the emission of a photon with energy,  $\omega$ , considering an electron of incident kinetic energy,  $T$ , is generated according to the formula:

$$\frac{d\sigma}{d\omega} = \frac{F(x)}{x}, \quad \text{with } x = \frac{\omega}{T}.$$

The function,  $F(x)$ , describing energy spectra of the outgoing photons is taken from the EEDL library. For each element 15 points in  $x$  from 0.01 to 1 are used for the linear interpolation of this function. The function  $F$  is normalised by the condition  $F(0.01) = 1$ . The energy distributions of the emitted photons available in the EEDL library are for only a few incident electron energies (about 10 energy points between 10 eV and 100 GeV). For other energies a logarithmic interpolation formula (6.1) is used to obtain values for the function,  $F(x)$ . For high energies, the spectral function is very close to:

$$F(x) = 1 - x + 0.75x^2.$$

#### Bremsstrahlung angular distributions

The angular distribution of the emitted photons with respect to the incident electron can be sampled according to three alternative generators described below. The direction of the outgoing electron is determined from the energy-momentum balance. These generators are currently implemented in *G4ModifiedTsai*, *G4Generator2BS* and *G4Generator2BN* classes.

#### G4ModifiedTsai

The angular distribution of the emitted photons is obtained from a simplified [eal93] formula based on the Tsai cross-section [Tsa74, Tsa77], which is expected to become isotropic in the low energy limit.

## G4Generator2BS

In G4Generator2BS generator, the angular distribution of the emitted photons is obtained from the 2BS Koch and Motz bremsstrahlung double differential cross-section [KM59]:

$$d\sigma_{k,\theta} = \frac{4Z^2 r_0^2}{137} \frac{dk}{k} y dy \left\{ \frac{16y^2 E}{(y^2 + 1)^4 E_0} - \frac{(E_0 + E)^2}{(y^2 + 1)^2 E_0^2} + \left[ \frac{E_0^2 + E^2}{(y^2 + 1)^2 E_0^2} - \frac{4y^2 E}{(y^2 + 1)^4 E_0} \right] \ln M(y) \right\}$$

where  $k$  the photon energy,  $\theta$  the emission angle,  $E_0$  and  $E$  are the initial and final electron energy in units of  $m_e c^2$ ,  $r_0$  is the classical electron radius and  $Z$  the atomic number of the material.  $y$  and  $M(y)$  are defined as:

$$\begin{aligned} y &= E_0 \theta \\ \frac{1}{M(y)} &= \left( \frac{k}{2E_0 E} \right)^2 + \left( \frac{Z^{1/3}}{111(y^2 + 1)} \right)^2 \end{aligned}$$

The adopted sampling algorithm is based on the sampling scheme developed by A. F. Bielajew et al. [AFBC89], and later implemented in EGS4. In this sampling algorithm only the angular part of 2BS is used, with the emitted photon energy,  $k$ , determined by GEANT4  $d\sigma/dk$  differential cross-section.

## G4Generator2BN

The angular distribution of the emitted photons is obtained from the 2BN Koch and Motz bremsstrahlung double differential cross-section [KM59] that can be written as:

$$\begin{aligned} d\sigma_{k,\theta} = \frac{Z^2 r_0^2}{8\pi 137} \frac{dk}{k} \frac{p}{p_0} d\Omega_k \left\{ \frac{8 \sin^2 \theta (2E_0^2 + 1)}{p_0^2 \Delta_0^4} - \right. \\ \frac{2(5E_0^2 + 2EE_0 + 3)}{p_0^2 \Delta_0^2} - \frac{2(p_0^2 - k^2)}{Q^2 \Delta_0} + \frac{4E}{p_0^2 \Delta_0} + \frac{L}{pp_0} \\ \left[ \frac{4E_0 \sin^2 \theta (3k - p_0^2 E)}{p_0^2 \Delta_0^4} + \frac{4E_0^2 (E_0^2 + E^2)}{p_0^2 \Delta_0^2} + \right. \\ \frac{2 - 2(7E_0^2 - 3EE_0 + E^2)}{p_0^2 \Delta_0^2} + \frac{2k(E_0^2 + EE_0 - 1)}{p_0^2 \Delta_0} \\ \left. - \left( \frac{4\epsilon}{p\Delta_0} \right) + \left( \frac{\epsilon^Q}{pQ} \right) \left[ \frac{4}{\Delta_0^2} - \frac{6k}{\Delta_0} - \frac{2k(p_0^2 - k^2)}{Q^2 \Delta_0} \right] \right\} \end{aligned}$$

in which:

$$\begin{aligned} L &= \ln \left[ \frac{EE_0 - 1 + pp_0}{EE_0 - 1 - pp_0} \right] \\ \Delta_0 &= E_0 - p_0 \cos \theta \\ Q^2 &= p_0^2 + k^2 - 2p_0 k \cos \theta \\ \epsilon &= \ln \left[ \frac{E + p}{E - p} \right] \quad \epsilon^Q = \ln \left[ \frac{Q + p}{Q - p} \right] \end{aligned}$$

where  $k$  is the photon energy,  $\theta$  the emission angle and  $(E_0, p_0)$  and  $(E, p)$  are the total (energy, momentum) of the electron before and after the radiative emission, all in units of  $m_e c^2$ .

Since the 2BN cross-section is a 2-dimensional non-factorized distribution an acceptance-rejection technique was the adopted. For the 2BN distribution, two functions  $g_1(k)$  and  $g_2(\theta)$  were defined:

$$g_1(k) = k^{-b} \quad g_2(\theta) = \frac{\theta}{1 + c\theta^2}$$

such that:

$$Ag_1(k)g_2(\theta) \geq \frac{d\sigma}{dkd\theta}$$

where  $A$  is a global constant to be completed. Both functions have an analytical integral  $G$  and an analytical inverse  $G^{-1}$ . The  $b$  parameter of  $g_1(k)$  was empirically tuned and set to 1.2. For positive  $\theta$  values,  $g_2(\theta)$  has a maximum at  $1/\sqrt(c)$ .  $c$  parameter controls the function global shape and it was used to tune  $g_2(\theta)$  according to the electron kinetic energy.

To generate photon energy  $k$  according to  $g_1$  and  $\theta$  according to  $g_2$  the inverse-transform method was used. The integration of these functions gives

$$\begin{aligned} G_1 &= C_1 \int_{k_{min}}^{k_{max}} k'^{-b} dk' = C_1 \frac{k^{1-b} - k_{min}^{1-b}}{1-b} \\ G_2 &= C_2 \int_0^\theta \frac{\theta'}{1+c\theta'^2} d\theta' = C_2 \frac{\log(1+c\theta^2)}{2c} \end{aligned}$$

where  $C_1$  and  $C_2$  are two global constants chosen to normalize the integral in the overall range to the unit. The photon momentum  $k$  will range from a minimum cut value  $k_{min}$  (required to avoid infrared divergence) to a maximum value equal to the electron kinetic energy  $E_k$ , while the polar angle ranges from 0 to  $\pi$ , resulting for  $C_1$  and  $C_2$ :

$$C_1 = \frac{1-b}{E_k^{1-b}} \quad C_2 = \frac{2c}{\log(1+c\pi^2)}$$

$k$  and  $\theta$  are then sampled according to:

$$k = \left[ \frac{1-b}{C_1} \xi_1 + k_{min}^{1-b} \right] \quad \theta = \sqrt{\frac{\exp\left(\frac{2c\xi_2}{C_1}\right)}{2c}}$$

where  $\xi_1$  and  $\xi_2$  are uniformly sampled in the interval (0,1). The event is accepted if:

$$uAg_1(k)g_2(\theta) \leq \frac{d\sigma}{dkd\theta}$$

where  $u$  is a random number with uniform distribution in (0,1). The  $A$  and  $c$  parameters were computed in a logarithmic grid, ranging from 1 keV to 1.5 MeV with 100 points per decade. Since the  $g_2(\theta)$  function has a maximum at  $\theta = \frac{1}{\sqrt{c}}$ , the  $c$  parameter was computed using the relation  $c = \frac{1}{\theta_{max}^2}$ . At the point  $(k_{min}, \theta_{max})$  where  $k_{min}$  is the  $k$  cut value, the double differential cross-section has its maximum value, since it is monotonically decreasing in  $k$  and thus the global normalization parameter  $A$  is estimated from the relation:

$$Ag_1(k_{min})g_2(\theta_{max}) = \left( \frac{d^2\sigma}{dkd\theta} \right)_{max}$$

where  $g_1(k_{min})g_2(\theta_{max}) = \frac{k_{min}^{-b}}{2\sqrt{c}}$ . Since  $A$  and  $c$  can only be retrieved for a fixed number of electron kinetic energies there exists the possibility that  $Ag_1(k_{min})g_2(\theta_{max}) \leq \left( \frac{d^2\sigma}{dkd\theta} \right)_{max}$  for a given  $E_k$ . This is a small violation that can be corrected introducing an additional multiplicative factor to the  $A$  parameter, which was empirically determined to be 1.04 for the entire energy range.

## Comparisons between Tsai, 2BS and 2BN generators

The currently available generators can be used according to the user required precision and timing requirements. Regarding the energy range, validation results indicate that for lower energies ( $\leq 100$  keV) there is a significant deviation on the most probable emission angle between Tsai/2BS generators and the 2BN generator - Fig. 11.2 to Fig. 11.4. The 2BN generator maintains however a good agreement with Kissel data [LKP83], derived from the work of Tseng and co-workers [HKTL79], and it should be used for energies between 1 keV and 100 keV [ea03]. As the electron kinetic energy increases, the different distributions tend to overlap and all generators present a good agreement with Kissel data.

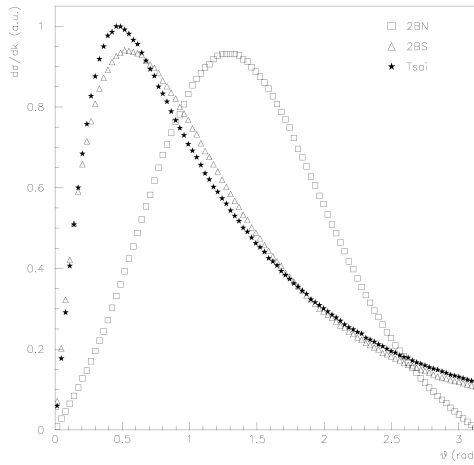


Fig. 11.2: Comparison of polar angle distribution of bremsstrahlung photons ( $k/T = 0.5$ ) for 10 keV electrons in silver, obtained with Tsai, 2BS and 2BN generator

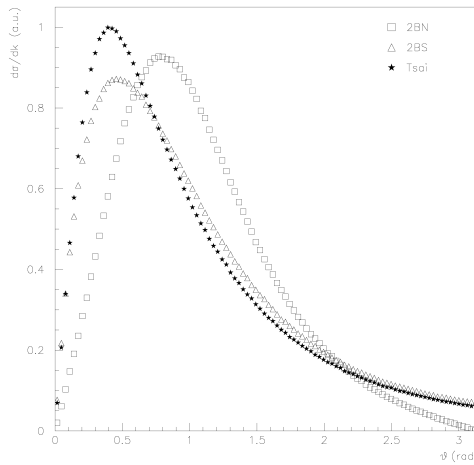


Fig. 11.3: Comparison of polar angle distribution of bremsstrahlung photons ( $k/T = 0.5$ ) for 100 keV electrons in silver, obtained with Tsai, 2BS and 2BN generator

In Fig. 11.5 the sampling efficiency for the different generators are presented. The sampling generation efficiency was defined as the ratio between the number of generated events and the total number of trials. As energies increases

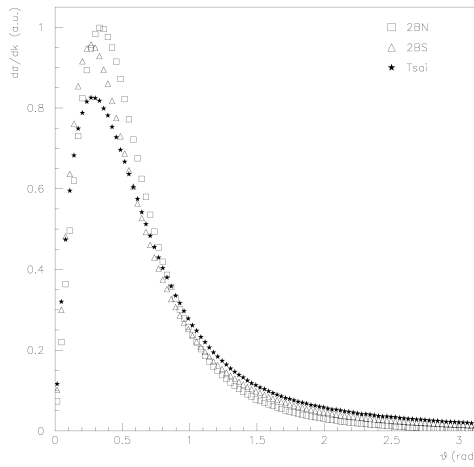


Fig. 11.4: Comparison of polar angle distribution of bremsstrahlung photons ( $k/T = 0.5$ ) for 500 keV electrons in silver, obtained with Tsai, 2BS and 2BN generator

the sampling efficiency of the 2BN algorithm decreases from 0.65 at 1 keV electron kinetic energy down to almost 0.35 at 1 MeV. For energies up to 10 keV the 2BN sampling efficiency is superior or equivalent to the one of the 2BS generator. These results are an indication that precision simulation of low energy bremsstrahlung can be obtained with little performance degradation. For energies above 500 keV, Tsai generator can be used, retaining a good physics accuracy and a sampling efficiency superior to the 2BS generator.

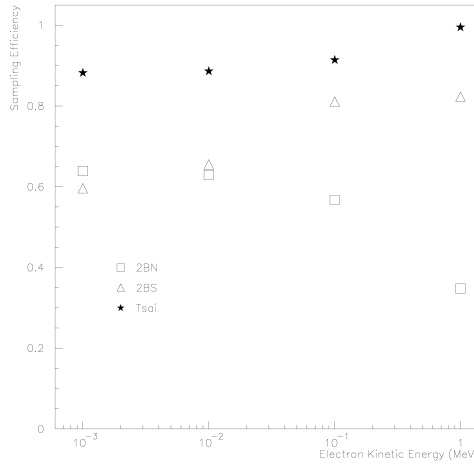


Fig. 11.5: Sampling efficiency for Tsai generator, 2BS and 2BN Koch and Motz generators.

## 11.3 Positron - Electron Annihilation

### 11.3.1 Introduction

The process G4eplusAnnihilation simulates the in-flight annihilation of a positron with an atomic electron. As is usually done in shower programs [NHR85], it is assumed here that the atomic electron is initially free and at rest. Also, annihilation processes producing one, or three or more, photons are ignored because these processes are negligible compared to the annihilation into two photons [MC70, NHR85].

### 11.3.2 Cross Section

The annihilation in flight of a positron and electron is described by the cross section formula of Heitler [Hei54, NHR85]:

$$\sigma(Z, E) = \frac{Z\pi r_e^2}{\gamma + 1} \left[ \frac{\gamma^2 + 4\gamma + 1}{\gamma^2 - 1} \ln \left( \gamma + \sqrt{\gamma^2 - 1} \right) - \frac{\gamma + 3}{\sqrt{\gamma^2 - 1}} \right]$$

where

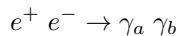
$E$  = total energy of the incident positron

$\gamma = E/mc^2$

$r_e$  = classical electron radius

### 11.3.3 Sampling the final state

The final state of the  $e + e^-$  annihilation process



is simulated by first determining the kinematic limits of the photon energy and then sampling the photon energy within those limits using the differential cross section. Conservation of energy-momentum is then used to determine the directions of the final state photons.

If the incident  $e^+$  has a kinetic energy  $T$ , then the total energy is  $E_e = T + mc^2$  and the momentum is  $P_c = \sqrt{T(T + 2mc^2)}$ . The total available energy is  $E_{tot} = E_e + mc^2 = E_a + E_b$  and momentum conservation requires  $\vec{P} = \vec{P}_{\gamma_a} + \vec{P}_{\gamma_b}$ . The fraction of the total energy transferred to one photon (say  $\gamma_a$ ) is

$$\epsilon = \frac{E_a}{E_{tot}} \equiv \frac{E_a}{T + 2mc^2}.$$

The energy transferred to  $\gamma_a$  is largest when  $\gamma_a$  is emitted in the direction of the incident  $e^+$ . In that case  $E_{a,max} = (E_{tot} + P_c)/2$ . The energy transferred to  $\gamma_a$  is smallest when  $\gamma_a$  is emitted in the opposite direction of the incident  $e^+$ . Then  $E_{a,min} = (E_{tot} - P_c)/2$ . Hence,

$$\epsilon_{max} = \frac{E_{a,max}}{E_{tot}} = \frac{1}{2} \left[ 1 + \sqrt{\frac{\gamma - 1}{\gamma + 1}} \right]$$

$$\epsilon_{min} = \frac{E_{a,min}}{E_{tot}} = \frac{1}{2} \left[ 1 - \sqrt{\frac{\gamma - 1}{\gamma + 1}} \right]$$

where  $\gamma = (T + mc^2)/mc^2$ . Therefore the range of  $\epsilon$  is  $[\epsilon_{min}; \epsilon_{max}] (\equiv [\epsilon_{min}; 1 - \epsilon_{min}])$ .

### 11.3.4 Sampling the Gamma Energy

A short overview of the sampling method is given in Section 2. The differential cross section of the two-photon positron-electron annihilation can be written as [Hei54, NHR85]:

$$\frac{d\sigma(Z, \epsilon)}{d\epsilon} = \frac{Z\pi r_e^2}{\gamma - 1} \frac{1}{\epsilon} \left[ 1 + \frac{2\gamma}{(\gamma + 1)^2} - \epsilon - \frac{1}{(\gamma + 1)^2} \frac{1}{\epsilon} \right]$$

where  $Z$  is the atomic number of the material,  $r_e$  the classical electron radius, and  $\epsilon \in [\epsilon_{min}; \epsilon_{max}]$ . The differential cross section can be decomposed as

$$\frac{d\sigma(Z, \epsilon)}{d\epsilon} = \frac{Z\pi r_e^2}{\gamma - 1} \alpha f(\epsilon) g(\epsilon)$$

where

$$\begin{aligned}\alpha &= \ln(\epsilon_{max}/\epsilon_{min}) \\ f(\epsilon) &= \frac{1}{\alpha\epsilon} \\ g(\epsilon) &= \left[ 1 + \frac{2\gamma}{(\gamma + 1)^2} - \epsilon - \frac{1}{(\gamma + 1)^2} \frac{1}{\epsilon} \right] \equiv 1 - \epsilon + \frac{2\gamma\epsilon - 1}{\epsilon(\gamma + 1)^2}\end{aligned}$$

Given two random numbers  $r, r' \in [0, 1]$ , the photon energies are chosen as follows:

1. sample  $\epsilon$  from  $f(\epsilon)$ :  $\epsilon = \epsilon_{min} \left( \frac{\epsilon_{max}}{\epsilon_{min}} \right)^r$
2. test the rejection function: if  $g(\epsilon) \geq r'$  accept  $\epsilon$ , otherwise return to step 1.

Then the photon energies are  $E_a = \epsilon E_{tot}$       $E_b = (1 - \epsilon) E_{tot}$ .

### Computing the Final State Kinematics

If  $\theta$  is the angle between the incident  $e^+$  and  $\gamma_a$ , then from energy-momentum conservation,

$$\cos \theta = \frac{1}{P_c} \left[ T + mc^2 \frac{2\epsilon - 1}{\epsilon} \right] = \frac{\epsilon(\gamma + 1) - 1}{\epsilon\sqrt{\gamma^2 - 1}}.$$

The azimuthal angle,  $\phi$ , is generated isotropically and the photon momentum vectors,  $\vec{P}_{\gamma_a}$  and  $\vec{P}_{\gamma_b}$ , are computed from energy-momentum conservation and transformed into the lab coordinate system.

### Annihilation at Rest

The method AtRestDoIt treats the special case when a positron comes to rest before annihilating. It generates two photons, each with energy  $k = mc^2$  and an isotropic angular distribution.

### 11.3.5 Penelope Model for positron-electron annihilation

#### Total Cross Section

The total cross section (per target electron) for the annihilation of a positron of energy  $E$  into two photons is evaluated from the analytical formula [Hei54, NHR85]

$$\sigma(E) = \frac{\pi r_e^2}{(\gamma + 1)(\gamma^2 - 1)} \times \left\{ (\gamma^2 + 4\gamma + 1) \ln \left[ \gamma + \sqrt{\gamma^2 - 1} \right] - (3 + \gamma) \sqrt{\gamma^2 - 1} \right\}.$$

where  $r_e$  = classical radius of the electron, and  $\gamma$  = Lorentz factor of the positron.

## Sampling of the Final State

The target electrons are assumed to be free and at rest: binding effects, that enable one-photon annihilation [Hei54], are neglected. When the annihilation occurs in flight, the two photons may have different energies, say  $E_-$  and  $E_+$  (the photon with lower energy is denoted by the superscript “-”), whose sum is  $E + 2m_e c^2$ . Each annihilation event is completely characterized by the quantity

$$\zeta = \frac{E_-}{E + 2m_e c^2},$$

which is in the interval  $\zeta_{min} \leq \zeta \leq \frac{1}{2}$ , with

$$\zeta_{min} = \frac{1}{\gamma + 1 + \sqrt{\gamma^2 - 1}}.$$

The parameter  $\zeta$  is sampled from the differential distribution

$$P(\zeta) = \frac{\pi r_e^2}{(\gamma + 1)(\gamma^2 - 1)} [S(\zeta) + S(1 - \zeta)],$$

where  $\gamma$  is the Lorentz factor and

$$S(\zeta) = -(\gamma + 1)^2 + (\gamma^2 + 4\gamma + 1) \frac{1}{\zeta} - \frac{1}{\zeta^2}.$$

From conservation of energy and momentum, it follows that the two photons are emitted in directions with polar angles

$$\cos \theta_- = \frac{1}{\sqrt{\gamma^2 - 1}} \left( \gamma + 1 - \frac{1}{\zeta} \right)$$

and

$$\cos \theta_+ = \frac{1}{\sqrt{\gamma^2 - 1}} \left( \gamma + 1 - \frac{1}{1 - \zeta} \right)$$

that are completely determined by  $\zeta$ ; in particular, when  $\zeta = \zeta_{min}$ ,  $\cos \theta_- = -1$ . The azimuthal angles are  $\phi_-$  and  $\phi_+ = \phi_- + \pi$ ; owing to the axial symmetry of the process, the angle  $\phi_-$  is uniformly distributed in  $(0, 2\pi)$ .

## 11.4 Positron Annihilation into $\mu^+\mu^-$ Pair in Media

The class G4AnnihiToMuPair simulates the electromagnetic production of muon pairs by the annihilation of high-energy positrons with atomic electrons [eal06]. Details of the implementation are given below and can also be found in Ref. [HBK03].

### 11.4.1 Total Cross Section

The annihilation of positrons and target electrons producing muon pairs in the final state ( $e^+e^- \rightarrow \mu^+\mu^-$ ) may give an appreciable contribution to the total number of muons produced in high-energy electromagnetic cascades. The threshold positron energy in the laboratory system for this process with the target electron at rest is

$$E_{th} = 2m_\mu^2/m_e - m_e \approx 43.69 \text{ GeV}, \quad (11.19)$$

where  $m_\mu$  and  $m_e$  are the muon and electron masses, respectively. Taking into account that the electron is much lighter than the muon, the lowest order cross section can be written in excellent approximation as

$$\sigma = \frac{\pi r_\mu^2}{3} \xi \left( 1 + \frac{\xi}{2} \right) \sqrt{1 - \xi}, \quad (11.20)$$

where  $r_\mu = r_e m_e/m_\mu$  is the classical muon radius,  $\xi = E_{\text{th}}/E$ , and  $E$  is the total positron energy in the laboratory frame.

We take into account, that the cross section gets increased by the Sommerfeld-Schwinger-Sakharov (SSS) threshold Coulomb re-summation factor [BL09]:

$$S(\beta) = \frac{X(\beta)}{1 - e^{-X(\beta)}}$$

where

$$X(\beta) = \frac{\pi\alpha}{\beta\gamma} = \pi\alpha \frac{\sqrt{1-\beta^2}}{\beta}$$

The SSS-corrected cross section can be written in good approximation at all energies above threshold as

$$\sigma_{\text{SSS}} = \frac{\pi r_f^2}{3} \xi \left(1 + \frac{\xi}{2}\right) \frac{\pi\alpha\sqrt{\xi}}{1 - e^{-\frac{\pi\alpha\sqrt{\xi}}{\sqrt{1-\xi}}}}. \quad (11.21)$$

These expressions are used in the simulation of this process since Geant4 10.5beta. The final factor in the expression is replaced by its asymptotic value of unity very close to threshold to avoid numerical instabilities.

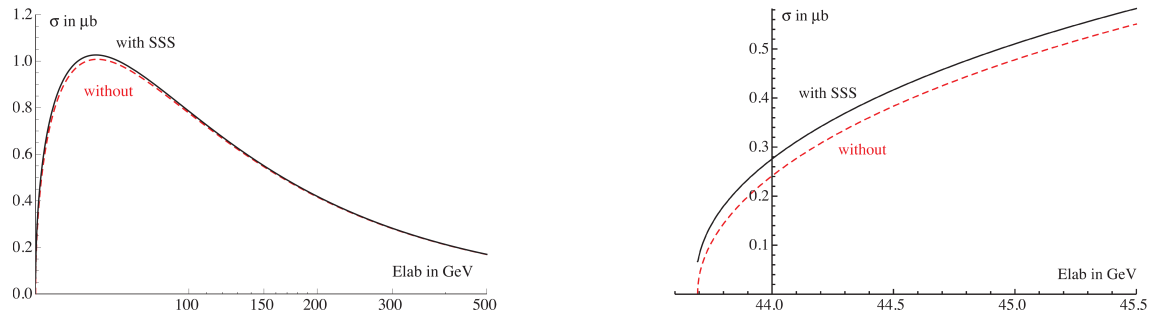


Fig. 11.6: Total cross section for the process  $e^+e^- \rightarrow \mu^+\mu^-$  as a function of the positron energy  $E$  in the laboratory system. With (solid line) and without (dashed red line) SSS Coulomb re-summation factor, zoomed close to the threshold (left), and using a wider energy range (right)

The cross section as a function of the positron energy  $E$  is shown in Fig. 11.6. The noticeable increase of the cross section close to threshold by the SSS-factor is of practical interest for the low emittance production of muons, as proposed in reference [BABGarcia+18].

### 11.4.2 Sampling of Energies and Angles

It is convenient to simulate the muon kinematic parameters in the center-of-mass (c.m.) system, and then to convert into the laboratory frame.

The energies of all particles are the same in the c.m. frame and equal to

$$E_{\text{cm}} = \sqrt{\frac{1}{2} m_e (E + m_e)}. \quad (11.22)$$

The muon momenta in the c.m. frame are  $P_{\text{cm}} = \sqrt{E_{\text{cm}}^2 - m_\mu^2}$ . In what follows, let the cosine of the angle between the c.m. momenta of the  $\mu^+$  and  $e^+$  be denoted as  $x = \cos\theta_{\text{cm}}$ .

From the differential cross section it is easy to derive that, apart from normalization, the distribution in  $x$  is described by

$$f(x) dx = (1 + \xi + x^2 (1 - \xi)) dx, \quad -1 \leq x \leq 1. \quad (11.23)$$

The value of this function is contained in the interval  $(1 + \xi) \leq f(x) \leq 2$  and the generation of  $x$  is straightforward using the rejection technique. Fig. 11.7 shows both generated and analytic distributions.

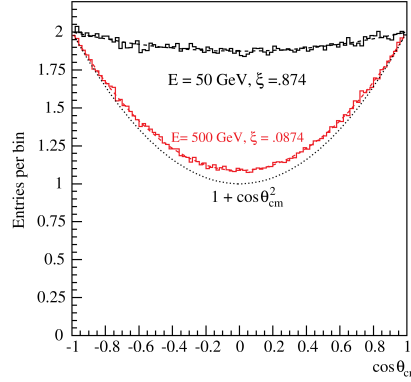


Fig. 11.7: Generated histograms with  $10^6$  entries each and the expected  $\cos \theta_{\text{cm}}$  distributions (dashed lines) at  $E = 50$  and 500 GeV positron energy in the lab frame. The asymptotic  $1 + \cos \theta_{\text{cm}}^2$  distribution valid for  $E \rightarrow \infty$  is shown as dotted line.

The transverse momenta of the  $\mu^+$  and  $\mu^-$  particles are the same, both in the c.m. and the lab frame, and their absolute values are equal to

$$P_\perp = P_{\text{cm}} \sin \theta_{\text{cm}} = P_{\text{cm}} \sqrt{1 - x^2}. \quad (11.24)$$

The energies and longitudinal components of the muon momenta in the lab system may be obtained by means of a Lorentz transformation. The velocity and Lorentz factor of the center-of-mass in the lab frame may be written as

$$\beta = \sqrt{\frac{E - m_e}{E + m_e}}, \quad \gamma \equiv \frac{1}{\sqrt{1 - \beta^2}} = \sqrt{\frac{E + m_e}{2m_e}} = \frac{E_{\text{cm}}}{m_e}. \quad (11.25)$$

The laboratory energies and longitudinal components of the momenta of the positive and negative muons may then be obtained:

$$\begin{aligned} E_+ &= \gamma(E_{\text{cm}} + x\beta P_{\text{cm}}), & P_{+||} &= \gamma(\beta E_{\text{cm}} + x P_{\text{cm}}), \\ E_- &= \gamma(E_{\text{cm}} - x\beta P_{\text{cm}}), & P_{-||} &= \gamma(\beta E_{\text{cm}} - x P_{\text{cm}}). \end{aligned}$$

Finally, for the vectors of the muon momenta one obtains:

$$\begin{aligned} \mathbf{P}_+ &= (+P_\perp \cos \varphi, +P_\perp \sin \varphi, P_{+||}), \\ \mathbf{P}_- &= (-P_\perp \cos \varphi, -P_\perp \sin \varphi, P_{-||}), \end{aligned} \quad (11.26)$$

where  $\varphi$  is a random azimuthal angle chosen between 0 and  $2\pi$ . The  $z$ -axis is directed along the momentum of the initial positron in the lab frame.

The maximum and minimum energies of the muons are given by

$$\begin{aligned} E_{\max} &\approx \frac{1}{2} E \left( 1 + \sqrt{1 - \xi} \right), \\ E_{\min} &\approx \frac{1}{2} E \left( 1 - \sqrt{1 - \xi} \right) = \frac{E_{\text{th}}}{2 \left( 1 + \sqrt{1 - \xi} \right)}. \end{aligned} \quad (11.27)$$

The fly-out polar angles of the muons are approximately

$$\theta_+ \approx P_\perp / P_{+||}, \quad \theta_- \approx P_\perp / P_{-||}; \quad (11.28)$$

the maximal angle  $\theta_{\max} \approx \frac{m_e}{m_\mu} \sqrt{1 - \xi}$  is always small compared to 1.

### 11.4.3 Validity

The process described is assumed to be purely electromagnetic. It is based on virtual  $\gamma$  exchange, and the  $Z$ -boson exchange and  $\gamma - Z$  interference processes are neglected. The  $Z$ -pole corresponds to a positron energy of  $E = M_Z^2/2m_e = 8136$  TeV. The validity of the current implementation is therefore restricted to initial positron energies of less than about 1000 TeV.

## 11.5 Positron Annihilation into Hadrons in Media

### 11.5.1 Introduction

The process G4eeToHadrons simulates the in-flight annihilation of a positron with an atomic electron into hadrons [eal06]. It is assumed here that the atomic electron is initially free and at rest. Currently accurate cross section is available with a validity range up to 1 TeV.

### 11.5.2 Cross Section

The annihilation of positrons and target electrons producing pion pairs in the final state ( $e^+e^- \rightarrow \pi^+\pi^-$ ) may give an appreciable contribution to electron-jet conversion at the LHC, and for the increasing total number of muons produced in the beam pipe of the linear collider [eal06]. The threshold positron energy in the laboratory system for this process with the target electron at rest is

$$E_{\text{th}} = 2m_\pi^2/m_e - m_e \approx 70.35 \text{ GeV}, \quad (11.29)$$

where  $m_\pi$  and  $m_e$  are the pion and electron masses, respectively. The total cross section is dominated by the reaction

$$e^+e^- \rightarrow \rho\gamma \rightarrow \pi^+\pi^-\gamma, \quad (11.30)$$

where  $\gamma$  is a radiative photon and  $\rho(770)$  is a well known vector meson. This radiative correction is essential, because it significantly modifies the shape of the resonance. Details of the theory are described in [BEIS99], in which the main term and the leading  $\alpha^2$  corrections are taken into account.

Additional contribution to the hadron production cross section come from  $\omega(783)$  and  $\phi(1020)$  resonances with  $\pi^+\pi^-\pi^0$ ,  $K^+K^-$ ,  $K_L K_S$ ,  $\eta\gamma$ , and  $\pi^0\gamma$  final states.

### 11.5.3 Sampling the final state

The final state of the  $e^+e^-$  annihilation process is simulated by first sampling of radiative gamma using a sum of all hadronic cross sections in the center of mass system. Photon energy is used to define new differential cross section. After that, hadronic channel is randomly selected according to its partial cross section. Final state is sampled and final particles transformed to the laboratory system.



## MUON INCIDENT

### 12.1 Muon Ionisation

The class *G4MuIonisation* provides the continuous energy loss due to ionisation and simulates the ‘discrete’ part of the ionisation, that is, delta rays produced by muons. Inside this class the following models are used:

- *G4BraggModel* (valid for protons with  $T < 0.2$  MeV)
- *G4BetheBlochModel* (valid for protons with  $0.2$  MeV  $< T < 1$  GeV)
- *G4MuBetheBlochModel* (valid for protons with  $T > 1$  GeV)

The limit energy 0.2 MeV is equivalent to the proton limit energy 2 MeV because of scaling relation (8.5), which allows simulation for muons with energy below 1 GeV in the same way as for point-like hadrons with spin 1/2 described in *Mean Energy Loss*.

For higher energies the *G4MuBetheBlochModel* is applied, in which leading radiative corrections are taken into account [SRKP97]. Simple analytical formula for the cross section, derived with the logarithmic are used. Calculation results appreciably differ from usual elastic  $\mu - e$  scattering in the region of high energy transfers  $m_e \ll T < T_{max}$  and give non-negligible correction to the total average energy loss of high-energy muons. The total cross section is written as following:

$$\sigma(E, \epsilon) = \sigma_{BB}(E, \epsilon) \left[ 1 + \frac{\alpha}{2\pi} \ln \left( 1 + \frac{2\epsilon}{m_e} \right) \ln \left( \frac{4m_e E(E - \epsilon)}{m_\mu^2(2\epsilon + m_e)} \right) \right], \quad (12.1)$$

here  $\sigma(E, \epsilon)$  is the differential cross sections,  $\sigma(E, \epsilon)_{BB}$  is the Bethe-Bloch cross section (13.8),  $m_e$  is the electron mass,  $m_\mu$  is the muon mass,  $E$  is the muon energy,  $\epsilon$  is the energy transfer,  $\epsilon = \omega + T$ , where  $T$  is the electron kinetic energy and  $\omega$  is the energy of radiative gamma.

For computation of the truncated mean energy loss (8.1) the partial integration of the expression (12.1) is performed

$$S(E, \epsilon_{up}) = S_{BB}(E, \epsilon_{up}) + S_{RC}(E, \epsilon_{up}), \quad \epsilon_{up} = \min(\epsilon_{max}, \epsilon_{cut}),$$

where term  $S_{BB}$  is the Bethe-Bloch truncated energy loss (13.2) for the interval of energy transfer  $(0 - \epsilon_{up})$  and term  $S_{RC}$  is a correction due to radiative effects. The function become smooth after log-substitution and is computed by numerical integration

$$S_{RC}(E, \epsilon_{up}) = \int_{\ln \epsilon_1}^{\ln \epsilon_{up}} \epsilon^2 (\sigma(E, \epsilon) - \sigma_{BB}(E, \epsilon)) d(\ln \epsilon),$$

where lower limit  $\epsilon_1$  does not effect result of integration in first order and in the class *G4MuBetheBlochModel* the default value  $\epsilon_1 = 100$  keV is used.

For computation of the discrete cross section (8.2) another substitution is used in order to perform numerical integration of a smooth function

$$\sigma(E) = \int_{1/\epsilon_{max}}^{1/\epsilon_{up}} \epsilon^2 \sigma(E, \epsilon) d(1/\epsilon).$$

The sampling of energy transfer is performed between  $1/\epsilon_{up}$  and  $1/\epsilon_{max}$  using rejection constant for the function  $\epsilon^2\sigma(E, \epsilon)$ . After the successful sampling of the energy transfer, the direction of the scattered electron is generated with respect to the direction of the incident particle. The energy of radiative gamma is neglected. The azimuthal electron angle  $\phi$  is generated isotropically. The polar angle  $\theta$  is calculated from energy-momentum conservation. This information is used to calculate the energy and momentum of both scattered particles and to transform them into the *global* coordinate system.

## 12.2 Bremsstrahlung

Bremsstrahlung dominates other muon interaction processes in the region of catastrophic collisions ( $v \geq 0.1$ ), that is at “moderate” muon energies above the kinematic limit for knock-on electron production. At high energies ( $E \geq 1$  TeV) this process contributes about 40% of the average muon energy loss.

### 12.2.1 Differential Cross Section

The differential cross section for muon bremsstrahlung (in units of  $\text{cm}^2/(\text{g GeV})$ ) can be written as

$$\frac{d\sigma(E, \epsilon, Z, A)}{d\epsilon} = \frac{16}{3} \alpha N_A \left( \frac{m}{\mu} r_e \right)^2 \frac{1}{\epsilon A} Z (Z\Phi_n + \Phi_e) \left( 1 - v + \frac{3}{4} v^2 \right)$$

$$= 0 \quad \text{if } \epsilon \geq \epsilon_{max} = E - \mu,$$

where  $\mu$  and  $m$  are the muon and electron masses,  $Z$  and  $A$  are the atomic number and atomic weight of the material, and  $N_A$  is Avogadro’s number. If  $E$  and  $T$  are the initial total and kinetic energy of the muon, and  $\epsilon$  is the emitted photon energy, then  $\epsilon = E - E'$  and the relative energy transfer  $v = \epsilon/E$ .

$\Phi_n$  represents the contribution of the nucleus and can be expressed as

$$\Phi_n = \ln \frac{B Z^{-1/3} (\mu + \delta(D'_n \sqrt{\epsilon} - 2))}{D'_n (m + \delta \sqrt{\epsilon} B Z^{-1/3})};$$

$$= 0 \quad \text{if negative.}$$

$\Phi_e$  represents the contribution of the electrons and can be expressed as

$$\Phi_e = \ln \frac{B' Z^{-2/3} \mu}{\left( 1 + \frac{\delta \mu}{m^2 \sqrt{\epsilon}} \right) (m + \delta \sqrt{\epsilon} B' Z^{-2/3})};$$

$$= 0 \quad \text{if } \epsilon \geq \epsilon'_{max} = E/(1 + \mu^2/2mE);$$

$$= 0 \quad \text{if negative.}$$

In  $\Phi_n$  and  $\Phi_e$ , for all nuclei except hydrogen,

$$\delta = \mu^2 \epsilon / 2EE' = \mu^2 v / 2(E - \epsilon);$$

$$D'_n = D_n^{(1-1/Z)}, \quad D_n = 1.54A^{0.27};$$

$$B = 183,$$

$$B' = 1429,$$

$$\sqrt{\epsilon} = 1.648(721271).$$

For hydrogen ( $Z=1$ )  $B = 202.4$ ,  $B' = 446$ ,  $D'_n = D_n$ .

These formulae are taken mostly from Refs. [KKP95] and [SRKP97]. They include improved nuclear size corrections in comparison with Ref. [PS68] in the region  $v \sim 1$  and low  $Z$ . Bremsstrahlung on atomic electrons (taking into account target recoil and atomic binding) is introduced instead of a rough substitution  $Z(Z+1)$ . A correction for processes with nucleus excitation is also included [ABB94].

## Applicability and Restrictions of the Method

The above formulae assume that:

1.  $E \gg \mu$ , hence the ultrarelativistic approximation is used;
2.  $E \leq 10^{20}$  eV; above this energy, LPM suppression can be expected;
3.  $v \geq 10^{-6}$ ; below  $10^{-6}$  Ter-Mikaelyan suppression takes place. However, in the latter region the cross section of muon bremsstrahlung is several orders of magnitude less than that of other processes.

The Coulomb correction (for high  $Z$ ) is not included. However, existing calculations [AB97] show that for muon bremsstrahlung this correction is small.

### 12.2.2 Continuous Energy Loss

The restricted energy loss for muon bremsstrahlung  $(dE/dx)_{\text{rest}}$  with relative transfers  $v = \epsilon/(T + \mu) \leq v_{\text{cut}}$  can be calculated as follows :

$$\left( \frac{dE}{dx} \right)_{\text{rest}} = \int_0^{\epsilon_{\text{cut}}} \epsilon \sigma(E, \epsilon) d\epsilon = (T + \mu) \int_0^{v_{\text{cut}}} \epsilon \sigma(E, \epsilon) dv .$$

If the user cut  $v_{\text{cut}} \geq v_{\text{max}} = T/(T + \mu)$ , the total average energy loss is calculated. Integration is done using Gaussian quadratures, and binning provides an accuracy better than about 0.03% for  $T = 1$  GeV,  $Z = 1$ . This rapidly improves with increasing  $T$  and  $Z$ .

### 12.2.3 Total Cross Section

The integration of the differential cross section over  $d\epsilon$  gives the total cross section for muon bremsstrahlung:

$$\sigma_{\text{tot}}(E, \epsilon_{\text{cut}}) = \int_{\epsilon_{\text{cut}}}^{\epsilon_{\text{max}}} \sigma(E, \epsilon) d\epsilon = \int_{\ln v_{\text{cut}}}^{\ln v_{\text{max}}} \epsilon \sigma(E, \epsilon) d(\ln v),$$

where  $v_{\text{max}} = T/(T + \mu)$ . If  $v_{\text{cut}} \geq v_{\text{max}}$ ,  $\sigma_{\text{tot}} = 0$ .

### 12.2.4 Sampling

The photon energy  $\epsilon_p$  is found by numerically solving the equation :

$$P = \int_{\epsilon_p}^{\epsilon_{\text{max}}} \sigma(E, \epsilon, Z, A) d\epsilon / \int_{\epsilon_{\text{cut}}}^{\epsilon_{\text{max}}} \sigma(E, \epsilon, Z, A) d\epsilon .$$

Here  $P$  is the random uniform probability,  $\epsilon_{\text{max}} = T$ , and  $\epsilon_{\text{cut}} = (T + \mu) \cdot v_{\text{cut}}$ .  $v_{\text{min.cut}} = 10^{-5}$  is the minimal relative energy transfer adopted in the algorithm.

For fast sampling, the solution of the above equation is tabulated at initialization time for selected  $Z$ ,  $T$  and  $P$ . During simulation, this table is interpolated in order to find the value of  $\epsilon_p$  corresponding to the probability  $P$ .

The tabulation routine uses accurate functions for the differential cross section. The table contains values of

$$x_p = \ln(v_p/v_{\text{max}}) / \ln(v_{\text{max}}/v_{\text{cut}}), \quad (12.2)$$

where  $v_p = \epsilon_p/(T + \mu)$  and  $v_{\text{max}} = T/(T + \mu)$ . Tabulation is performed in the range  $1 \leq Z \leq 128$ ,  $1 \leq T \leq 1000$  PeV,  $10^{-5} \leq P \leq 1$  with constant logarithmic steps. Atomic weight (which is a required parameter in the cross section) is estimated here with an iterative solution of the approximate relation:

$$A = Z (2 + 0.015 A^{2/3}).$$

For  $Z = 1$ ,  $A = 1$  is used.

To find  $x_p$  (and thus  $\epsilon_p$ ) corresponding to a given probability  $P$ , the sampling method performs a linear interpolation in  $\ln Z$  and  $\ln T$ , and a cubic, 4 point Lagrangian interpolation in  $\ln P$ . For  $P \leq P_{\min}$ , a linear interpolation in  $(P, x)$  coordinates is used, with  $x = 0$  at  $P = 0$ . Then the energy  $\epsilon_p$  is obtained from the inverse transformation of (12.2) :

$$\epsilon_p = (T + \mu)v_{\max}(v_{\max}/v_{\text{cut}})^{x_p}$$

The algorithm with the parameters described above has been tested for various  $Z$  and  $T$ . It reproduces the differential cross section to within  $0.2 - 0.7\%$  for  $T \geq 10$  GeV. The average total energy loss is accurate to within 0.5%. While accuracy improves with increasing  $T$ , satisfactory results are also obtained for  $1 \leq T \leq 10$  GeV.

It is important to note that this sampling scheme allows the generation of  $\epsilon_p$  for different user cuts on  $v$  which are above  $v_{\min.\text{cut}}$ . To perform such a simulation, it is sufficient to define a new probability variable

$$P' = P \sigma_{\text{tot}}(v_{\text{user.cut}})/\sigma_{\text{tot}}(v_{\min.\text{cut}})$$

and use it in the sampling method. Time consuming re-calculation of the 3-dimensional table is therefore not required because only the tabulation of  $\sigma_{\text{tot}}(v_{\text{user.cut}})$  is needed.

The small-angle, ultrarelativistic approximation is used for the simulation (with about 20% accuracy at  $\theta \leq \theta^* \approx 1$ ) of the angular distribution of the final state muon and photon. Since the target recoil is small, the muon and photon are directed symmetrically (with equal transverse momenta and coplanar with the initial muon):

$$p_{\perp\mu} = p_{\perp\gamma}, \quad \text{where} \quad p_{\perp\mu} = E'\theta_\mu, \quad p_{\perp\gamma} = \epsilon\theta_\gamma.$$

$\theta_\mu$  and  $\theta_\gamma$  are muon and photon emission angles. The distribution in the variable  $r = E\theta_\gamma/\mu$  is given by

$$f(r)dr \sim rdr/(1+r^2)^2.$$

Random angles are sampled as follows:

$$\theta_\gamma = \frac{\mu}{E}r \quad \theta_\mu = \frac{\epsilon}{E'}\theta_\gamma,$$

where

$$r = \sqrt{\frac{a}{1-a}}, \quad a = \xi \frac{r_{\max}^2}{1+r_{\max}^2}, \quad r_{\max} = \min(1, E'/\epsilon) \cdot E \theta^*/\mu,$$

and  $\xi$  is a random number uniformly distributed between 0 and 1.

## 12.3 Positron - Electron Pair Production by Muons

Direct electron pair production is one of the most important muon interaction processes. At TeV muon energies, the pair production cross section exceeds those of other muon interaction processes over a range of energy transfers between 100 MeV and  $0.1E_\mu$ . The average energy loss for pair production increases linearly with muon energy, and in the TeV region this process contributes more than half the total energy loss rate.

To adequately describe the number of pairs produced, the average energy loss and the stochastic energy loss distribution, the differential cross section behavior over an energy transfer range of  $5 \text{ MeV} \leq \epsilon \leq 0.1 \cdot E_\mu$  must be accurately reproduced. This is because the main contribution to the total cross section is given by transferred energies  $5 \text{ MeV} \leq \epsilon \leq 0.01 \cdot E_\mu$ , and because the contribution to the average muon energy loss is determined mostly in the region  $0.001 \cdot E_\mu \leq \epsilon \leq 0.1 \cdot E_\mu$ .

For a theoretical description of the cross section, the formulae of Ref. [KP70] are used, along with a correction for finite nuclear size [KP71]. To take into account electron pair production in the field of atomic electrons, the inelastic atomic form factor contribution of Ref. [Kel98] is also applied.

### 12.3.1 Differential Cross Section

#### Definitions and Applicability

In the following discussion, these definitions are used:

- $m$  and  $\mu$  are the electron and muon masses, respectively
- $E \equiv E_\mu$  is the total muon energy,  $E = T + \mu$
- $Z$  and  $A$  are the atomic number and weight of the material
- $\epsilon$  is the total pair energy or, approximately, the muon energy loss ( $E - E'$ )
- $v = \epsilon/E$
- $e = 2.718\dots$
- $A^* = 183$ .

The formula for the differential cross section applies when:

- $E_\mu \gg \mu$  ( $E \geq 2 - 5$  GeV) and  $E_\mu \leq 10^{15} - 10^{17}$  eV. If muon energies exceed this limit, the LPM (Landau Pomeranchuk Migdal) effect may become important, depending on the material
- the muon energy transfer  $\epsilon$  lies between  $\epsilon_{\min} = 4m$  and  $\epsilon_{\max} = E_\mu - \frac{3\sqrt{e}}{4}\mu Z^{1/3}$ , although the formal lower limit is  $\epsilon \gg 2m$ , and the formal upper limit requires  $E'_\mu \gg \mu$ .
- $Z \leq 40 - 50$ . For higher  $Z$ , the Coulomb correction is important but has not been sufficiently studied theoretically.

#### Formulae

The differential cross section for electron pair production by muons  $\sigma(Z, A, E, \epsilon)$  can be written as :

$$\sigma(Z, A, E, \epsilon) = \frac{4}{3\pi} \frac{Z(Z + \zeta)}{A} N_A (\alpha r_0)^2 \frac{1-v}{\epsilon} \int_0^{\rho_{\max}} G(Z, E, v, \rho) d\rho, \quad (12.3)$$

where

$$G(Z, E, v, \rho) = \Phi_e + (m/\mu)^2 \Phi_\mu,$$

$$\Phi_{e,\mu} = B_{e,\mu} L'_{e,\mu}$$

and

$$\Phi_{e,\mu} = 0 \quad \text{whenever} \quad \Phi_{e,\mu} < 0.$$

$B_e$  and  $B_\mu$  do not depend on  $Z, A$ , and are given by

$$\begin{aligned} B_e &= [(2 + \rho^2)(1 + \beta) + \xi(3 + \rho^2)] \ln \left( 1 + \frac{1}{\xi} \right) + \frac{1 - \rho^2 - \beta}{1 + \xi} - (3 + \rho^2); \\ &\approx \frac{1}{2\xi} [(3 - \rho^2) + 2\beta(1 + \rho^2)] \quad \text{for} \quad \xi \geq 10^3; \end{aligned}$$

$$\begin{aligned} B_\mu &= \left[ (1 + \rho^2) \left( 1 + \frac{3\beta}{2} \right) - \frac{1}{\xi} (1 + 2\beta)(1 - \rho^2) \right] \ln(1 + \xi) + \frac{\xi(1 - \rho^2 - \beta)}{1 + \xi} + (1 + 2\beta)(1 - \rho^2); \\ &\approx \frac{\xi}{2} [(5 - \rho^2) + \beta(3 + \rho^2)] \quad \text{for} \quad \xi \leq 10^{-3}; \end{aligned}$$

Also,

$$\xi = \frac{\mu^2 v^2}{4m^2} \frac{(1 - \rho^2)}{(1 - v)}; \quad \beta = \frac{v^2}{2(1 - v)};$$

$$L'_e = \ln \frac{A^* Z^{-1/3} \sqrt{(1 + \xi)(1 + Y_e)}}{1 + \frac{2m\sqrt{e}A^* Z^{-1/3}(1+\xi)(1+Y_e)}{Ev(1-\rho^2)}} - \frac{1}{2} \ln \left[ 1 + \left( \frac{3mZ^{1/3}}{2\mu} \right)^2 (1 + \xi)(1 + Y_e) \right];$$

$$L'_\mu = \ln \frac{(\mu/m) A^* Z^{-1/3} \sqrt{(1 + 1/\xi)(1 + Y_\mu)}}{1 + \frac{2m\sqrt{e}A^* Z^{-1/3}(1+\xi)(1+Y_\mu)}{Ev(1-\rho^2)}} - \ln \left[ \frac{3}{2} Z^{1/3} \sqrt{(1 + 1/\xi)(1 + Y_\mu)} \right].$$

For faster computing, the expressions for  $L'_{e,\mu}$  are further algebraically transformed. The functions  $L'_{e,\mu}$  include the nuclear size correction [KP71] in comparison with parameterization [KP70] :

$$Y_e = \frac{5 - \rho^2 + 4\beta(1 + \rho^2)}{2(1 + 3\beta)\ln(3 + 1/\xi) - \rho^2 - 2\beta(2 - \rho^2)};$$

$$Y_\mu = \frac{4 + \rho^2 + 3\beta(1 + \rho^2)}{(1 + \rho^2)(\frac{3}{2} + 2\beta)\ln(3 + \xi) + 1 - \frac{3}{2}\rho^2};$$

$$\rho_{\max} = [1 - 6\mu^2/E^2(1 - v)]\sqrt{1 - 4m/Ev}.$$

### Comment on the Calculation of the Integral $\int d\rho$ in Eq.(12.3)

The integral  $\int_0^{\rho_{\max}} G(Z, E, v, \rho) d\rho$  is computed with the substitutions:

$$t = \ln(1 - \rho),$$

$$1 - \rho = \exp(t),$$

$$1 + \rho = 2 - \exp(t),$$

$$1 - \rho^2 = e^t (2 - e^t).$$

After that,

$$\int_0^{\rho_{\max}} G(Z, E, v, \rho) d\rho = \int_{t_{\min}}^0 G(Z, E, v, \rho) e^t dt, \quad (12.4)$$

where

$$t_{\min} = \ln \frac{\frac{4m}{\epsilon} + \frac{12\mu^2}{EE'} \left( 1 - \frac{4m}{\epsilon} \right)}{1 + \left( 1 - \frac{6\mu^2}{EE'} \right) \sqrt{1 - \frac{4m}{\epsilon}}}.$$

To compute the integral of Eq.(12.4) with an accuracy better than 0.5%, Gaussian quadrature with  $N = 8$  points is sufficient.

The function  $\zeta(E, Z)$  in Eq.(12.3) serves to take into account the process on atomic electrons (inelastic atomic form factor contribution). To treat the energy loss balance correctly, the following approximation, which is an algebraic transformation of the expression in Ref. [Kel98], is used:

$$\zeta(E, Z) = \frac{0.073 \ln \frac{E/\mu}{1 + \gamma_1 Z^{2/3} E/\mu} - 0.26}{0.058 \ln \frac{E/\mu}{1 + \gamma_2 Z^{1/3} E/\mu} - 0.14};$$

$$= 0 \quad \text{if the numerator is negative.}$$

For  $E \leq 35 \mu$ ,  $\zeta(E, Z) = 0$ . Also  $\gamma_1 = 1.95 \cdot 10^{-5}$  and  $\gamma_2 = 5.30 \cdot 10^{-5}$ .

The above formulae make use of the Thomas-Fermi model which is not good enough for light elements. For hydrogen ( $Z = 1$ ) the following parameters must be changed:

- $A^* = 183 \Rightarrow 202.4$ ;
- $\gamma_1 = 1.95 \cdot 10^{-5} \Rightarrow 4.4 \cdot 10^{-5}$ ;
- $\gamma_2 = 5.30 \cdot 10^{-5} \Rightarrow 4.8 \cdot 10^{-5}$ .

### 12.3.2 Total Cross Section and Restricted Energy Loss

If the user's cut for the energy transfer  $\epsilon_{\text{cut}}$  is greater than  $\epsilon_{\text{min}}$ , the process is represented by continuous restricted energy loss for interactions with  $\epsilon \leq \epsilon_{\text{cut}}$ , and discrete collisions with  $\epsilon > \epsilon_{\text{cut}}$ . Respective values of the total cross section and restricted energy loss rate are defined as:

$$\sigma_{\text{tot}} = \int_{\epsilon_{\text{cut}}}^{\epsilon_{\text{max}}} \sigma(E, \epsilon) d\epsilon; \quad (dE/dx)_{\text{restr}} = \int_{\epsilon_{\text{min}}}^{\epsilon_{\text{cut}}} \epsilon \sigma(E, \epsilon) d\epsilon.$$

For faster computing,  $\ln \epsilon$  substitution and Gaussian quadratures are used.

### 12.3.3 Sampling of Positron - Electron Pair Production

The  $e^+e^-$  pair energy  $\epsilon_P$ , is found numerically by solving the equation

$$P = \int_{\epsilon_P}^{\epsilon_{\text{max}}} \sigma(Z, A, T, \epsilon) d\epsilon \quad / \int_{\text{cut}}^{\epsilon_{\text{max}}} \sigma(Z, A, T, \epsilon) d\epsilon \quad (12.5)$$

or

$$1 - P = \int_{\text{cut}}^{\epsilon_P} \sigma(Z, A, T, \epsilon) d\epsilon \quad / \int_{\text{cut}}^{\epsilon_{\text{max}}} \sigma(Z, A, T, \epsilon) d\epsilon \quad (12.6)$$

To reach high sampling speed, solutions of Eqs.(12.5), (12.6) are tabulated at initialization time. Two 3-dimensional tables (referred to here as A and B) of  $\epsilon_P(P, T, Z)$  are created, and then interpolation is used to sample  $\epsilon_P$ .

The number and spacing of entries in the table are chosen as follows:

- a constant increment in  $\ln T$  is chosen such that there are four points per decade in the range  $T_{\text{min}} - T_{\text{max}}$ . The default range of muon kinetic energies in GEANT4 is  $T = 1 \text{ GeV} - 1000 \text{ PeV}$ .
- a constant increment in  $\ln Z$  is chosen. The shape of the sampling distribution does depend on  $Z$ , but very weakly, so that eight points in the range  $1 \leq Z \leq 128$  are sufficient. There is practically no dependence on the atomic weight  $A$ .
- for probabilities  $P \leq 0.5$ , Eq.(12.5) is used and Table A is computed with a constant increment in  $\ln P$  in the range  $10^{-7} \leq P \leq 0.5$ . The number of points in  $\ln P$  for Table A is about 100.
- for  $P \geq 0.5$ , Eq.(12.6) is used and Table B is computed with a constant increment in  $\ln(1 - P)$  in the range  $10^{-5} \leq (1 - P) \leq 0.5$ . In this case 50 points are sufficient.

The values of  $\ln(\epsilon_P - \text{cut})$  are stored in both Table A and Table B.

To create the “probability tables” for each  $(T, Z)$  pair, the following procedure is used:

- a temporary table of  $\sim 2000$  values of  $\epsilon \cdot \sigma(Z, A, T, \epsilon)$  is constructed with a constant increment ( $\sim 0.02$ ) in  $\ln \epsilon$  in the range  $(\text{cut}, \epsilon_{\text{max}})$ .  $\epsilon$  is taken in the middle of the corresponding bin in  $\ln \epsilon$ .
- the accumulated cross sections

$$\sigma_1 = \int_{\ln \epsilon}^{\ln \epsilon_{\text{max}}} \epsilon \sigma(Z, A, T, \epsilon) d(\ln \epsilon)$$

and

$$\sigma_2 = \int_{\ln(cut)}^{\ln \epsilon} \epsilon \sigma(Z, A, T, \epsilon) d(\ln \epsilon)$$

are calculated by summing the temporary table over the values above  $\ln \epsilon$  (for  $\sigma_1$ ) and below  $\ln \epsilon$  (for  $\sigma_2$ ) and then normalizing to obtain the accumulated probability functions.

- finally, values of  $\ln(\epsilon_P - cut)$  for corresponding values of  $\ln P$  and  $\ln(1 - P)$  are calculated by linear interpolation of the above accumulated probabilities to form Tables A and B. The monotonic behavior of the accumulated cross sections is very useful in speeding up the interpolation procedure.

The random transferred energy corresponding to a probability  $P$ , is then found by linear interpolation in  $\ln Z$  and  $\ln T$ , and a cubic interpolation in  $\ln P$  for Table A or in  $\ln(1 - P)$  for Table B. For  $P \leq 10^{-7}$  and  $(1 - P) \leq 10^{-5}$ , linear extrapolation using the entries at the edges of the tables may be safely used. Electron pair energy is related to the auxiliary variable  $x = \ln(\epsilon_P - cut)$  found by the trivial interpolation  $\epsilon_P = e^x + cut$ .

Similar to muon bremsstrahlung (*Bremsstrahlung*), this sampling algorithm does not re-initialize the tables for user cuts greater than  $cut_{min}$ . Instead, the probability variable is redefined as

$$P' = P \sigma_{tot}(cut_{user}) / \sigma_{tot}(cut_{min}),$$

and  $P'$  is used for sampling.

In the simulation of the final state, the muon deflection angle (which is of the order of  $m/E$ ) is neglected. The procedure for sampling the energy partition between  $e^+$  and  $e^-$  and their emission angles is similar to that used for the  $\gamma \rightarrow e^+ e^-$  conversion.

## 12.4 Muon Photonuclear Interaction

The inelastic interaction of muons with nuclei is important at high muon energies ( $E \geq 10$  GeV), and at relatively high energy transfers  $\nu$  ( $\nu/E \geq 10^{-2}$ ). It is especially important for light materials and for the study of detector response to high energy muons, muon propagation and muon-induced hadronic background. The average energy loss for this process increases almost linearly with energy, and at TeV muon energies constitutes about 10% of the energy loss rate.

The main contribution to the cross section  $\sigma(E, \nu)$  and energy loss comes from the low  $Q^2$ -region ( $Q^2 \ll 1$  GeV $^2$ ). In this domain, many simplifications can be made in the theoretical consideration of the process in order to obtain convenient and simple formulae for the cross section. Most widely used are the expressions given by Borog and Petrukhin [BP75], and Bezrukov and Bugaev [BB81]. Results from these authors agree within 10% for the differential cross section and within about 5% for the average energy loss, provided the same photonuclear cross section,  $\sigma_{\gamma N}$ , is used in the calculations.

### 12.4.1 Differential Cross Section

The Borog and Petrukhin formula for the cross section is based on:

- Hand's formalism [Han63] for inelastic muon scattering,
- a semi-phenomenological inelastic form factor, which is a Vector Dominance Model with parameters estimated from experimental data, and
- nuclear shadowing effects with a reasonable theoretical parameterization [BCG72].

For  $E \geq 10$  GeV, the Borog and Petrukhin cross section, differential in transferred energy, is

$$\sigma(E, \nu) = \Psi(\nu) \Phi(E, v), \quad (12.7)$$

$$\Psi(\nu) = \frac{\alpha}{\pi} \frac{A_{\text{eff}} N_{AV}}{A} \sigma_{\gamma N}(\nu) \frac{1}{\nu}, \quad (12.8)$$

$$\Phi(E, v) = v - 1 + \left[ 1 - v + \frac{v^2}{2} \left( 1 + \frac{2\mu^2}{\Lambda^2} \right) \right] \ln \frac{\frac{E^2(1-v)}{\mu^2} \left( 1 + \frac{\mu^2 v^2}{\Lambda^2(1-v)} \right)}{1 + \frac{Ev}{\Lambda} \left( 1 + \frac{\Lambda}{2M} + \frac{Ev}{\Lambda} \right)}, \quad (12.9)$$

where  $\nu$  is the energy lost by the muon,  $v = \nu/E$ , and  $\mu$  and  $M$  are the muon and nucleon (proton) masses, respectively.  $\Lambda$  is a Vector Dominance Model parameter in the inelastic form factor which is estimated to be  $\Lambda^2 = 0.4$  GeV<sup>2</sup>.

For  $A_{\text{eff}}$ , which includes the effect of nuclear shadowing, the parameterization [BCG72]

$$A_{\text{eff}} = 0.22A + 0.78A^{0.89}$$

is chosen.

A reasonable choice for the photonuclear cross section,  $\sigma_{\gamma N}$ , is the parameterization obtained by Caldwell et al. [eal79] based on the experimental data on photoproduction by real photons:

$$\sigma_{\gamma N} = (49.2 + 11.1 \ln K + 151.8/\sqrt{K}) \cdot 10^{-30} \text{ cm}^2, \quad K \text{ in GeV}. \quad (12.10)$$

The upper limit of the transferred energy is taken to be  $\nu_{\text{max}} = E - M/2$ . The choice of the lower limit  $\nu_{\text{min}}$  is less certain since the formula (12.7), (12.8), (12.9) is not valid in this domain. Fortunately,  $\nu_{\text{min}}$  influences the total cross section only logarithmically and has no practical effect on the average energy loss for high energy muons. Hence, a reasonable choice for  $\nu_{\text{min}}$  is 0.2 GeV.

In Eq.(12.8),  $A_{\text{eff}}$  and  $\sigma_{\gamma N}$  appear as factors. A more rigorous theoretical approach may lead to some dependence of the shadowing effect on  $\nu$  and  $E$ ; therefore in the differential cross section and in the sampling procedure, this possibility is foreseen and the atomic weight  $A$  of the element is kept as an explicit parameter.

The total cross section is obtained by integration of Eq.(12.7) between  $\nu_{\text{min}}$  and  $\nu_{\text{max}}$ ; to facilitate the computation, a  $\ln(\nu)$  substitution is used.

## 12.4.2 Sampling

### Sampling the Transferred Energy

The muon photonuclear interaction is always treated as a discrete process with its mean free path determined by the total cross section. The total cross section is obtained by the numerical integration of Eq.(12.7) within the limits  $\nu_{\text{min}}$  and  $\nu_{\text{max}}$ . The process is considered for muon energies  $1 \text{ GeV} \leq T \leq 1000 \text{ PeV}$ , though it should be noted that above 100 TeV the extrapolation (Eq.(12.10)) of  $\sigma_{\gamma N}$  may be too crude. The random transferred energy,  $\nu_p$ , is found from the numerical solution of the equation :

$$P = \int_{\nu_p}^{\nu_{\text{max}}} \sigma(E, \nu) d\nu / \int_{\nu_{\text{min}}}^{\nu_{\text{max}}} \sigma(E, \nu) d\nu. \quad (12.11)$$

Here  $P$  is the random uniform probability, with  $\nu_{\text{max}} = E - M/2$  and  $\nu_{\text{min}} = 0.2$  GeV. For fast sampling, the solution of Eq.(12.11) is tabulated at initialization time. During simulation, the sampling method returns a value of  $\nu_p$  corresponding to the probability  $P$ , by interpolating the table. The tabulation routine uses Eq.(12.7) for the differential cross section. The table contains values of

$$x_p = \ln(\nu_p/\nu_{\text{max}})/\ln(\nu_{\text{max}}/\nu_{\text{min}}), \quad (12.12)$$

calculated at each point on a three-dimensional grid with constant spacings in  $\ln(T)$ ,  $\ln(A)$  and  $\ln(P)$ . The sampling uses linear interpolations in  $\ln(T)$  and  $\ln(A)$ , and a cubic interpolation in  $\ln(P)$ . Then the transferred energy is calculated from the inverse transformation of Eq.(12.12),  $\nu_p = \nu_{\text{max}} (\nu_{\text{max}}/\nu_{\text{min}})^{x_p}$ . Tabulated parameters reproduce the theoretical dependence to better than 2% for  $T > 1$  GeV and better than 1% for  $T > 10$  GeV.

## Sampling the Muon Scattering Angle

According to Refs. [BKUP77, BP75], in the region where the four-momentum transfer is not very large ( $Q^2 \leq 3\text{GeV}^2$ ), the  $t$ -dependence of the cross section may be described as:

$$\frac{d\sigma}{dt} \sim \frac{(1-t/t_{\max})}{t(1+t/\nu^2)(1+t/m_0^2)} [(1-y)(1-t_{\min}/t) + y^2/2], \quad (12.13)$$

where  $t$  is the square of the four-momentum transfer,  $Q^2 = 2(EE' - PP' \cos \theta - \mu^2)$ . Also,  $t_{\min} = (\mu y)^2 / (1-y)$ ,  $y = \nu/E$  and  $t_{\max} = 2M\nu$ .  $\nu = E - E'$  is the energy lost by the muon and  $E$  is the total initial muon energy.  $M$  is the nucleon (proton) mass and  $m_0^2 \equiv \Lambda^2 \simeq 0.4 \text{ GeV}^2$  is a phenomenological parameter determining the behavior of the inelastic form factor. Factors which depend weakly, or not at all, on  $t$  are omitted.

To simulate random  $t$  and hence the random muon deflection angle, it is convenient to represent Eq.(12.13) in the form :

$$\sigma(t) \sim f(t)g(t),$$

where

$$\begin{aligned} f(t) &= \frac{1}{t(1+t/t_1)}, \\ g(t) &= \frac{1-t/t_{\max}}{1+t/t_2} \cdot \frac{(1-y)(1-t_{\min}/t) + y^2/2}{(1-y) + y^2/2}, \end{aligned} \quad (12.14)$$

and

$$t_1 = \min(\nu^2, m_0^2) \quad t_2 = \max(\nu^2, m_0^2). \quad (12.15)$$

$t_P$  is found analytically from Eq.(12.14) :

$$t_P = \frac{t_{\max}t_1}{(t_{\max} + t_1) \left[ \frac{t_{\max}(t_{\min}+t_1)}{t_{\min}(t_{\max}+t_1)} \right]^P - t_{\max}},$$

where  $P$  is a random uniform number between 0 and 1, which is accepted with probability  $g(t)$ . The conditions of Eq.(12.15) make use of the symmetry between  $\nu^2$  and  $m_0^2$  in Eq.(12.13) and allow increased selection efficiency, which is typically  $\geq 0.7$ . The polar muon deflection angle  $\theta$  can easily be found from<sup>1</sup>.

$$\sin^2(\theta/2) = \frac{t_P - t_{\min}}{4(EE' - \mu^2) - 2t_{\min}}.$$

The hadronic vertex is generated by the hadronic processes taking into account the four-momentum transfer.

---

<sup>1</sup> This convenient formula has been shown to the authors by D.A. Timashkov.

## CHARGED HADRON INCIDENT

### 13.1 Hadron and Ion Ionisation

#### 13.1.1 Method

The class *G4hIonisation* provides the continuous energy loss due to ionisation and simulates the ‘discrete’ part of the ionisation, that is,  $\delta$ -rays produced by charged hadrons. The class *G4ionIonisation* is intended for the simulation of energy loss by positive ions with charge greater than unit. Inside these classes the following models are used:

- *G4BetheBlochModel*, valid for protons with  $T > 2$  MeV
- *G4BraggModel*, valid for protons with  $T < 2$  MeV
- *G4BraggIonModel*, valid for protons with  $T < 2$  MeV
- *G4ICRU73QOModel*, valid for anti-protons with  $T < 2$  MeV

The scaling relation (8.5) is a basic conception for the description of ionisation of heavy charged particles. It is used both in energy loss calculation and in determination of the validity range of models. Namely the  $T_p = 2$  MeV limit for protons is scaled for a particle with mass  $M_i$  by the ratio of the particle mass to the proton mass  $T_i = T_p M_p / M_i$ .

For all ionisation models the value of the maximum energy transferable to a free electron  $T_{max}$  is given by the following relation [ea06]:

$$T_{max} = \frac{2m_e c^2 (\gamma^2 - 1)}{1 + 2\gamma(m_e/M) + (m_e/M)^2}, \quad (13.1)$$

where  $m_e$  is the electron mass and  $M$  is the mass of the incident particle. The method of calculation of the continuous energy loss and the total cross-section are explained below.

#### 13.1.2 Continuous Energy Loss

The integration of (8.1) leads to the Bethe-Bloch restricted energy loss ( $T < T_{cut}$ ) formula [ea06], which is modified taking into account various corrections [Ahl80]:

$$\frac{dE}{dx} = 2\pi r_e^2 mc^2 n_{el} \frac{z^2}{\beta^2} \left[ \ln \left( \frac{2mc^2 \beta^2 \gamma^2 T_{up}}{I^2} \right) - \beta^2 \left( 1 + \frac{T_{up}}{T_{max}} \right) - \delta - \frac{2C_e}{Z} + S + F \right] \quad (13.2)$$

where

$$\begin{aligned}
 r_e &= \text{classical electron radius} = e^2/(4\pi\epsilon_0 mc^2) \\
 mc^2 &= \text{mass-energy of the electron} \\
 n_{el} &= \text{electron density in the material} \\
 I &= \text{mean excitation energy in the material} \\
 Z &= \text{atomic number of the material} \\
 z &= \text{charge of the hadron in units of the electron charge} \\
 \gamma &= E/mc^2 \\
 \beta^2 &= 1 - (1/\gamma^2) \\
 T_{up} &= \min(T_{cut}, T_{max}) \\
 \delta &= \text{density effect function} \\
 C_e &= \text{shell correction function} \\
 S &= \text{spin term} = 0 \text{ for } s=0, \left(\frac{0.5T_{up}}{E}\right)^2 \text{ for } s=1/2 \\
 E &= \text{primary energy} \\
 F &= \text{high order corrections}
 \end{aligned}$$

For spin large than 1/2 the same S term is used in the current model. In a single element the electron density is

$$n_{el} = Z n_{at} = Z \frac{\mathcal{N}_{av} \rho}{A}$$

( $\mathcal{N}_{av}$ : Avogadro number,  $\rho$ : density of the material,  $A$ : mass of a mole). In a compound material

$$n_{el} = \sum_i Z_i n_{ati} = \sum_i Z_i \frac{\mathcal{N}_{av} w_i \rho}{A_i}.$$

$w_i$  is the proportion by mass of the  $i^{th}$  element, with molar mass  $A_i$ .

The mean excitation energy  $I$  for all elements is tabulated according to the NIST recommended values for GEANT4 NIST materials, for other materials ICRU recommended values [eal84] are used.

## Shell Correction

$2C_e/Z$  is the so-called *shell correction term* which accounts for the fact of interaction of atomic electrons with atomic nucleus. This term more visible at low energies and for heavy atoms. The classical expression for the term [eal93] is used

$$C = \sum \nu C_\nu(\theta_\nu, \eta_\nu), \quad \nu = K, L, M, \dots, \quad \theta = \frac{J_\nu}{\epsilon_\nu}, \quad \eta_\nu = \frac{\beta^2}{\alpha^2 Z_\nu^2}, \quad (13.3)$$

where  $\alpha$  is the fine structure constant,  $\beta$  is the hadron velocity,  $J_\nu$  is the ionisation energy of the shell  $\nu$ ,  $\epsilon_\nu$  is Bohr ionisation energy of the shell  $\nu$ ,  $Z_\nu$  is the effective charge of the shell  $\nu$ . First terms  $C_K$  and  $C_L$  can be analytically computed in using an assumption non-relativistic hydrogenic wave functions [Wal52, Wal56]. The results [Kha68] of tabulation of these computations in the interval of parameters  $\eta_\nu = 0.005\text{--}10$  and  $\theta_\nu = 0.25\text{--}0.95$  are used directly. For higher values of  $\eta_\nu$  the parameterization [Kha68] is applied:

$$C_\nu = \frac{K_1}{\eta} + \frac{K_2}{\eta^2} + \frac{K_3}{\eta^3},$$

where coefficients  $K_i$  provide smooth shape of the function. The effective nuclear charge for the  $L$ -shell can be reproduced as  $Z_L = Z - d$ ,  $d$  is a parameter shown in Table 13.1.

Table 13.1: Effective nuclear charge for the  $L$ -shell [eal93].

$Z$	3	4	5	6	7	8	9	$>9$
$d$	1.72	2.09	2.48	2.82	3.16	3.53	3.84	4.15

For outer shells the calculations are not available, so  $L$ -shell parameterization is used and the following scaling relation [eal93, Bic92] is applied:

$$C_\nu = V_\nu C_L(\theta_L, H_\nu \eta_L), \quad V_\nu = \frac{n_\nu}{n_L}, \quad H_\nu = \frac{J_\nu}{J_L}, \quad (13.4)$$

where  $V_\nu$  is a vertical scaling factor proportional to number of electrons at the shell  $n_\nu$ . The contribution of the shell correction term is about 10% for protons at  $T = 2$  MeV.

### Density Correction

$\delta$  is a correction term which takes into account the reduction in energy loss due to the so-called *density effect*. This becomes important at high energies because media have a tendency to become polarized as the incident particle velocity increases. As a consequence, the atoms in a medium can no longer be considered as isolated. To correct for this effect the formulation of Sternheimer [SP71b] is used:

$x$  is a kinetic variable of the particle :  $x = \log_{10}(\gamma\beta) = \ln(\gamma^2\beta^2)/4.606$ , and  $\delta(x)$  is defined by

$$\begin{aligned} \text{for } x < x_0 : \quad \delta(x) &= 0 \\ \text{for } x \in [x_0, x_1] : \quad \delta(x) &= 4.606x - C + a(x_1 - x)^m \\ \text{for } x > x_1 : \quad \delta(x) &= 4.606x - C \end{aligned} \quad (13.5)$$

where the matter-dependent constants are calculated as follows:

$$\begin{aligned} h\nu_p &= \text{plasma energy of the medium} = \sqrt{4\pi n_{el} r_e^3 m c^2 / \alpha} = \sqrt{4\pi n_{el} r_e} \hbar c \\ C &= 1 + 2 \ln(I/h\nu_p) \\ x_a &= C/4.606 \\ a &= 4.606(x_a - x_0)/(x_1 - x_0)^m \\ m &= 3. \end{aligned} \quad (13.6)$$

For condensed media

$$\begin{cases} I < 100 \text{ eV} & \left\{ \begin{array}{lll} \text{for } C \leq 3.681 & x_0 = 0.2 & x_1 = 2 \\ \text{for } C > 3.681 & x_0 = 0.326C - 1.0 & x_1 = 2 \end{array} \right. \\ I \geq 100 \text{ eV} & \left\{ \begin{array}{lll} \text{for } C \leq 5.215 & x_0 = 0.2 & x_1 = 3 \\ \text{for } C > 5.215 & x_0 = 0.326C - 1.5 & x_1 = 3 \end{array} \right. \end{cases}$$

and for gaseous media

$$\begin{aligned} \text{for } C < 10. & \quad x_0 = 1.6 \quad x_1 = 4 \\ \text{for } C \in [10.0, 10.5[ & \quad x_0 = 1.7 \quad x_1 = 4 \\ \text{for } C \in [10.5, 11.0[ & \quad x_0 = 1.8 \quad x_1 = 4 \\ \text{for } C \in [11.0, 11.5[ & \quad x_0 = 1.9 \quad x_1 = 4 \\ \text{for } C \in [11.5, 12.25[ & \quad x_0 = 2. \quad x_1 = 4 \\ \text{for } C \in [12.25, 13.804[ & \quad x_0 = 2. \quad x_1 = 5 \\ \text{for } C \geq 13.804 & \quad x_0 = 0.326C - 2.5 \quad x_1 = 5. \end{aligned}$$

## High Order Corrections

High order corrections term to Bethe-Bloch formula (13.2) can be expressed as

$$F = G - S + 2(zL_1 + z^2L_2), \quad (13.7)$$

where  $G$  is the Mott correction term,  $S$  is the finite size correction term,  $L_1$  is the Barkas correction,  $L_2$  is the Bloch correction. The Mott term [Ahl80] describes the close-collision corrections tend to become more important at large velocities and higher charge of projectile. The Fermi result is used:

$$G = \pi\alpha z\beta.$$

The Barkas correction term describes distant collisions. The parameterization is expressed in the form:

$$L_1 = \frac{1.29F_A(b/x^{1/2})}{Z^{1/2}x^{3/2}}, \quad x = \frac{\beta^2}{Z\alpha^2},$$

where  $F_A$  is tabulated function [ARB73],  $b$  is scaled minimum impact parameter shown in Table 13.2 [eal93]. This and other corrections depending on atomic properties are assumed to be additive for mixtures and compounds.

Table 13.2: Scaled minimum impact parameter  $b$ .

$Z$	1 ( $H_2$ gas)	1	2	3 - 10	11 - 17	18	19 - 25	26 - 50	> 50
$d$	0.6	1.8	0.6	1.8	1.4	1.8	1.4	1.35	1.3

For the Bloch correction term the classical expression [eal93] is following:

$$z^2L_2 = -y^2 \sum_{n=1}^{\infty} \frac{1}{n(n^2 + y^2)}, \quad y = \frac{z\alpha}{\beta}.$$

The finite size correction term takes into account the space distribution of charge of the projectile particle. For muon it is zero, for hadrons this term become visible at energies above few hundred GeV and the following parameterization [Ahl80] is used:

$$S = \ln(1 + q), \quad q = \frac{2m_e T_{max}}{\varepsilon^2},$$

where  $T_{max}$  is given in relation (13.1),  $\varepsilon$  is proportional to the inverse effective radius of the projectile (Table 13.3).

Table 13.3: The values of the  $\varepsilon$  parameter for different particle types.

mesons, spin = 0 ( $\pi^\pm, K^\pm$ )	0.736 GeV
baryons, spin = 1/2	0.843 GeV
ions	$0.843 A^{1/3}$ GeV

All these terms break scaling relation (8.5) if the projectile particle charge differs from  $\pm 1$ . To take this circumstance into account in *G4ionIonisation* process at initialisation time the term  $F$  is ignored for the computation of the  $dE/dx$  table. At run time this term is taken into account by adding to the mean energy loss a value

$$\Delta T' = 2\pi r_e^2 mc^2 n_{el} \frac{z^2}{\beta^2} F \Delta s,$$

where  $\Delta s$  is the *true step length* and  $F$  is the high order correction term (13.7).

## Parameterizations at Low Energies

For scaled energies below  $T_{lim} = 2$  MeV shell correction becomes very large and precision of the Bethe-Bloch formula degrades, so parameterisation of evaluated data for stopping powers at low energies is required. These parameterisations for all atoms is available from ICRU'49 report [ea193]. The proton parametrisation is used in *G4BraggModel*, which is included by default in the process *G4hIonisation*. The alpha particle parameterisation is used in the *G4BraggIonModel*, which is included by default in the process *G4ionIonisation*. To provide a smooth transition between low-energy and high-energy models the modified energy loss expression is used for high energy

$$S(T) = S_H(T) + (S_L(T_{lim}) - S_H(T_{lim})) \frac{T_{lim}}{T}, \quad T > T_{lim},$$

where  $S$  is smoothed stopping power,  $S_H$  is stopping power from formula (13.2) and  $S_L$  is the low-energy parameterisation.

The precision of Bethe-Bloch formula for  $T > 10$  MeV is within 2%, below the precision degrades and at 1 keV only 20% may be guaranteed. In the energy interval 1–10 MeV the quality of description of the stopping power varied from atom to atom. To provide more stable and precise parameterisation the data from the NIST databases are included inside the standard package. These data are provided for 316 predefined materials (98 elemental and 180 compounds). Note that 278 are “real” NIST materials taken from [NISa, NISb, SBS84] and the remainder are based on their chemical formulae (16 HEP Materials, 3 Space Science Materials and 19 Biomedical Materials). The data from the PSTAR database are included into *G4BraggModel*. The data from the ASTAR database are included into *G4BraggIonModel*. So, if GEANT4 material is defined as a NIST material, than NIST data are used for low-energy parameterisation of stopping power. If material is not from the NIST database, then the ICRU'49 parameterisation is used. It is suggested to refer to the class *G4NistMaterialBuilder* to determine the correct nomenclature and composition for each material.

### 13.1.3 Nuclear Stopping

Nuclear stopping due to elastic ion-ion scattering since GEANT4 v9.3 can be simulated with the continuous process *G4NuclearStopping*. By default this correction is active and the ICRU'49 parameterisation [ea193] is used, which is implemented in the model class *G4ICRU49NuclearStoppingModel*.

### 13.1.4 Total Cross Section per Atom

For  $T \gg I$  the differential cross section can be written as

$$\frac{d\sigma}{dT} = 2\pi r_e^2 mc^2 Z \frac{z_p^2}{\beta^2} \frac{1}{T^2} \left[ 1 - \beta^2 \frac{T}{T_{max}} + s \frac{T^2}{2E^2} \right] \quad (13.8)$$

[ea06], where  $s = 0$  for spinless particles and  $s = 1$  for others. The correction for spin 1/2 is exact and it is not for other values of spin. In described models there is an internal limit  $T_{cut} \geq I$ . Integrating from  $T_{cut}$  to  $T_{max}$  gives the total cross section per atom :

$$\sigma(Z, E, T_{cut}) = \frac{2\pi r_e^2 Z z_p^2}{\beta^2} mc^2 \times \left[ \left( \frac{1}{T_{cut}} - \frac{1}{T_{max}} \right) - \frac{\beta^2}{T_{max}} \ln \frac{T_{max}}{T_{cut}} + s \frac{T_{max} - T_{cut}}{2E^2} \right] \quad (13.9)$$

In a given material the mean free path is:

$$\lambda = (n_{at} \cdot \sigma)^{-1} \quad \text{or} \quad \lambda = (\sum_i n_{ati} \cdot \sigma_i)^{-1}$$

The mean free path is tabulated during initialization as a function of the material and of the energy for all kinds of charged particles.

### 13.1.5 Simulating Delta-ray Production

A short overview of the sampling method is given in [Section 2](#). Apart from the normalization, the cross section (13.8) can be factorized:

$$\frac{d\sigma}{dT} = C f(T) g(T) \text{ with } T \in [T_{cut}, T_{max}]$$

where

$$f(T) = \frac{1}{T^2}$$

$$g(T) = 1 - \beta^2 \frac{T}{T_{max}} + s \frac{T^2}{2E^2}.$$

The energy  $T$  is chosen by

1. sampling  $T$  from  $f(T)$
2. calculating the rejection function  $g(T)$  and accepting the sampled  $T$  with a probability of  $g(T)$ .

After the successful sampling of the energy, the direction of the scattered electron is generated with respect to the direction of the incident particle. The azimuthal angle  $\phi$  is generated isotropically. The polar angle  $\theta$  is calculated from energy-momentum conservation. This information is used to calculate the energy and momentum of both scattered particles and to transform them into the *global* coordinate system.

### 13.1.6 Ion Effective Charge

As ions penetrate matter they exchange electrons with the medium. In the implementation of *G4ionIonisation* the effective charge approach is used [[ZBL85](#)]. A state of equilibrium between the ion and the medium is assumed, so that the ion's effective charge can be calculated as a function of its kinetic energy in a given material. Before and after each step the dynamic charge of the ion is recalculated and saved in *G4DynamicParticle*, where it can be used not only for energy loss calculations but also for the sampling of transportation in an electromagnetic field.

The ion effective charge is expressed via the ion charge  $z_i$  and the fractional effective charge of ion  $\gamma_i$ :

$$z_{eff} = \gamma_i z_i. \quad (13.10)$$

For helium ions fractional effective charge is parameterized for all elements

$$(\gamma_{He})^2 = \left( 1 - \exp \left[ - \sum_{j=0}^5 C_j Q^j \right] \right) \left( 1 + \frac{7 + 0.05Z}{1000} \exp(-(7.6 - Q)^2) \right)^2, \quad (13.11)$$

$$Q = \max(0, \ln T),$$

where the coefficients  $C_j$  are the same for all elements, and the helium ion kinetic energy  $T$  is in keV/amu.

The following expression is used for heavy ions [[BK82](#)]:

$$\gamma_i = \left( q + \frac{1-q}{2} \left( \frac{v_0}{v_F} \right)^2 \ln(1 + \Lambda^2) \right) \left( 1 + \frac{(0.18 + 0.0015Z) \exp(-(7.6 - Q)^2)}{Z_i^2} \right), \quad (13.12)$$

where  $q$  is the fractional average charge of the ion,  $v_0$  is the Bohr velocity,  $v_F$  is the Fermi velocity of the electrons in the target medium, and  $\Lambda$  is the term taking into account the screening effect:

$$\Lambda = 10 \frac{v_F}{v_0} \frac{(1-q)^{2/3}}{Z_i^{1/3} (6+q)}. \quad (13.13)$$

The Fermi velocity of the medium is of the same order as the Bohr velocity, and its exact value depends on the detailed electronic structure of the medium. The expression for the fractional average charge of the ion is the following:

$$q = [1 - \exp(0.803y^{0.3} - 1.3167y^{0.6} - 0.38157y - 0.008983y^2)], \quad (13.14)$$

where  $y$  is a parameter that depends on the ion velocity  $v_i$

$$y = \frac{v_i}{v_0 Z^{2/3}} \left( 1 + \frac{v_F^2}{5v_i^2} \right). \quad (13.15)$$

The parametrisation of the effective charge of the ion applied if the kinetic energy is below limit value

$$T < 10z_i \frac{M_i}{M_p} \text{ MeV}, \quad (13.16)$$

where  $M_i$  is the ion mass and  $M_p$  is the proton mass.

## 13.2 Low energy extensions

### 13.2.1 Energy losses of slow negative particles

At low energies, e.g. below a few MeV for protons/antiprotons, the Bethe-Bloch formula is no longer accurate in describing the energy loss of charged hadrons and higher  $Z$  terms should be taken in account. Odd terms in  $Z$  lead to a significant difference between energy loss of positively and negatively charged particles. The energy loss of negative hadrons is scaled from that of antiprotons. The antiproton energy loss is calculated according to the quantum harmonic oscillator model is used, as described in [eal05] and references therein. The lower limit of applicability of the model is chosen for all materials at 10 keV. Below this value stopping power is set to constant equal to the  $dE/dx$  at 10 keV.

### 13.2.2 Energy losses of hadrons in compounds

To obtain energy losses in a mixture or compound, the absorber can be thought of as made up of thin layers of pure elements with weights proportional to the electron density of the element in the absorber (Bragg's rule):

$$\frac{dE}{dx} = \sum_i \left( \frac{dE}{dx} \right)_i, \quad (13.17)$$

where the sum is taken over all elements of the absorber,  $i$  is the number of the element,  $(dE/dx)_i$  is energy loss in the pure  $i$ -th element.

Bragg's rule is very accurate for relativistic particles when the interaction of electrons with a nucleus is negligible. But at low energies the accuracy of Bragg's rule is limited because the energy loss to the electrons in any material depends on the detailed orbital and excitation structure of the material. In the description of GEANT4 materials there is a special attribute: the chemical formula. It is used in the following way:

- if the data on the stopping power for a compound as a function of the proton kinetic energy is available (Table 13.4), then the direct parametrisation of the data for this material is performed;
- if the data on the stopping power for a compound is available for only one incident energy (Table 13.5), then the computation is performed based on Bragg's rule and the chemical factor for the compound is taken into account;
- if there are no data for the compound, the computation is performed based on Bragg's rule.

In the review [ZM88] the parametrisation stopping power data are presented as

$$S_e(T_p) = S_{Bragg}(T_p) \left[ 1 + \frac{f(T_p)}{f(125 \text{ keV})} \left( \frac{S_{exp}(125 \text{ keV})}{S_{Bragg}(125 \text{ keV})} - 1 \right) \right], \quad (13.18)$$

where  $S_{exp}(125 \text{ keV})$  is the experimental value of the energy loss for the compound for 125 keV protons or the reduced experimental value for He ions,  $S_{Bragg}(T_p)$  is a value of energy loss calculated according to Bragg's rule, and  $f(T_p)$  is a universal function, which describes the disappearance of deviations from Bragg's rule for higher kinetic energies according to:

$$f(T_p) = \frac{1}{1 + \exp \left[ 1.48 \left( \frac{\beta(T_p)}{\beta(25 \text{ keV})} - 7.0 \right) \right]}, \quad (13.19)$$

where  $\beta(T_p)$  is the relative velocity of the proton with kinetic energy  $T_p$ .

Table 13.4: Stopping Power Compounds Parameterized vs. Energy

Number	Chemical formula
1	AlO
2	C <sub>2</sub> O
3	CH <sub>4</sub>
4	(C <sub>2</sub> H <sub>4</sub> ) <sub>N</sub> -Polyethylene
5	(C <sub>2</sub> H <sub>4</sub> ) <sub>N</sub> -Polypropylene
6	C <sub>8</sub> H <sub>8</sub> ) <sub>N</sub>
7	C <sub>3</sub> H <sub>8</sub>
8	SiO <sub>2</sub>
9	H <sub>2</sub> O
10	H <sub>2</sub> O-Gas
11	Graphite

Table 13.5: Stopping Power Compounds Data for Fixed Energy

Number	Chemical formula	Number	Chemical formula
1	H <sub>2</sub> O	28	C <sub>2</sub> H <sub>6</sub>
2	C <sub>2</sub> H <sub>4</sub> O	29	C <sub>2</sub> F <sub>6</sub>
3	C <sub>3</sub> H <sub>6</sub> O	30	C <sub>2</sub> H <sub>6</sub> O
4	C <sub>2</sub> H <sub>2</sub>	31	C <sub>3</sub> H <sub>6</sub> O
5	CH <sub>3</sub> OH	32	C <sub>4</sub> H <sub>10</sub> O
6	C <sub>2</sub> H <sub>5</sub> OH	33	C <sub>2</sub> H <sub>4</sub>
7	C <sub>3</sub> H <sub>7</sub> OH	34	C <sub>2</sub> H <sub>4</sub> O
8	C <sub>3</sub> H <sub>4</sub>	35	C <sub>2</sub> H <sub>4</sub> S
9	NH <sub>3</sub>	36	SH <sub>2</sub>
10	C <sub>14</sub> H <sub>10</sub>	37	CH <sub>4</sub>
11	C <sub>6</sub> H <sub>6</sub>	38	CCLF <sub>3</sub>
12	C <sub>4</sub> H <sub>10</sub>	39	CCl <sub>2</sub> F <sub>2</sub>
13	C <sub>4</sub> H <sub>6</sub>	40	CHCl <sub>2</sub> F
14	C <sub>4</sub> H <sub>8</sub> O	41	(CH <sub>3</sub> ) <sub>2</sub> S
15	CCl <sub>4</sub>	42	N <sub>2</sub> O
16	CF <sub>4</sub>	43	C <sub>5</sub> H <sub>10</sub> O
17	C <sub>6</sub> H <sub>8</sub>	44	C <sub>8</sub> H <sub>6</sub>
18	C <sub>6</sub> H <sub>12</sub>	45	(CH <sub>2</sub> ) <sub>N</sub>
19	C <sub>6</sub> H <sub>10</sub> O	46	(C <sub>3</sub> H <sub>6</sub> ) <sub>N</sub>
20	C <sub>6</sub> H <sub>10</sub>	47	(C <sub>8</sub> H <sub>8</sub> ) <sub>N</sub>
21	C <sub>8</sub> H <sub>16</sub>	48	C <sub>3</sub> H <sub>8</sub> C_3H_8
22	C <sub>5</sub> H <sub>10</sub>	49	C <sub>3</sub> H <sub>6</sub> -Propylene
23	C <sub>5</sub> H <sub>8</sub>	50	C <sub>3</sub> H <sub>6</sub> O
24	C <sub>3</sub> H <sub>6</sub> -Cyclopropane	51	C <sub>3</sub> H <sub>6</sub> S
25	C <sub>2</sub> H <sub>4</sub> F <sub>2</sub>	52	C <sub>4</sub> H <sub>4</sub> S
26	C <sub>2</sub> H <sub>2</sub> F <sub>2</sub>	53	C <sub>7</sub> H <sub>8</sub>
27	C <sub>4</sub> H <sub>8</sub> O <sub>2</sub>		

### 13.2.3 Fluctuations of energy losses of hadrons

The total continuous energy loss of charged particles is a stochastic quantity with a distribution described in terms of a straggling function. The straggling is partially taken into account by the simulation of energy loss by the production of  $\delta$ -electrons with energy  $T > T_c$ . However, continuous energy loss also has fluctuations. Hence in the current GEANT4 implementation two different models of fluctuations are applied depending on the value of the parameter  $\kappa$  which is the lower limit of the number of interactions of the particle in the step. The default value chosen is  $\kappa = 10$ . To select a model for thick absorbers the following boundary conditions are used:

$$\Delta E > T_c \kappa \text{ or } T_c < I \kappa, \quad (13.20)$$

where  $\Delta E$  is the mean continuous energy loss in a track segment of length  $s$ ,  $T_c$  is the kinetic energy cut of  $\delta$ -electrons, and  $I$  is the average ionisation potential of the atom.

For long path lengths the straggling function approaches the Gaussian distribution with Bohr's variance [eal93]:

$$\Omega^2 = K N_{el} \frac{Z_h^2}{\beta^2} T_c s f \left( 1 - \frac{\beta^2}{2} \right), \quad (13.21)$$

where  $f$  is a screening factor, which is equal to unity for fast particles, whereas for slow positively charged ions with  $\beta^2 < 3Z(v_0/c)^2$   $f = a + b/Z_{eff}^2$ , where parameters  $a$  and  $b$  are parametrised for all atoms [QY91, WKC77].

For short path lengths, when the condition (13.20) is not satisfied, the model described in *Energy Loss Fluctuations* is applied.

### 13.2.4 ICRU 73-based energy loss model

The ICRU 73 [eal05] report contains stopping power tables for ions with atomic numbers 3–18 and 26, covering a range of different elemental and compound target materials. The stopping powers derive from calculations with the PASS code [SS02], which implements the binary stopping theory described in [SS00, SS02]. Tables in ICRU 73 extend over an energy range up to 1 GeV/nucleon. All stopping powers were incorporated into GEANT4 and are available through a parameterisation model (*G4IonParametrisedLossModel*). For a few materials revised stopping powers were included (water, water vapor, nylon type 6 and 6/6 from P. Sigmund et al. [PSP09] and copper from P. Sigmund [PSigmund09]), which replace the corresponding tables of the original ICRU 73 report.

To account for secondary electron production above  $T_c$ , the continuous energy loss per unit path length is calculated according to

$$\left. \frac{dE}{dx} \right|_{T < T_c} = \left( \frac{dE}{dx} \right)_{ICRU73} - \left( \frac{dE}{dx} \right)_\delta \quad (13.22)$$

where  $(dE/dx)_{ICRU73}$  refers to stopping powers obtained by interpolating ICRU 73 tables and  $(dE/dx)_\delta$  is the mean energy transferred to  $\delta$ -electrons per path length given by

$$\left( \frac{dE}{dx} \right)_\delta = \sum_i n_{at,i} \int_{T_c}^{T_{max}} \frac{d\sigma_i(T)}{dT} T dT \quad (13.23)$$

where the index  $i$  runs over all elements composing the material,  $n_{at,i}$  is the number of atoms of the element  $i$  per volume,  $T_{max}$  is the maximum energy transferable to an electron according to formula and  $d\sigma_i/dT$  specifies the differential cross section per atom for producing an  $\delta$ -electron.

For compound targets not considered in the ICRU 73 report, the first term on the right hand side in Eq.(13.22) is computed by applying Bragg's additivity rule [eal93] if tables for all elemental components are available in ICRU 73.

---

CHAPTER  
FOURTEEN

---

## POLARIZED ELECTRON/POSITRON/GAMMA INCIDENT

### 14.1 Introduction

With the EM polarization extension it is possible to track polarized particles (leptons and photons). Special emphasis will be put in the proper treatment of polarized matter and its interaction with longitudinal polarized electrons/positrons or circularly polarized photons, which is for instance essential for the simulation of positron polarimetry. The implementation is base on Stokes vectors [McM61]. Further details can be found in [Lai08].

In its current state, the following polarization dependent processes are considered:

- Bhabha/Møller scattering,
- Positron Annihilation,
- Compton scattering,
- Pair creation,
- Bremsstrahlung.

Several simulation packages for the realistic description of the development of electromagnetic showers in matter have been developed. A prominent example of such codes is EGS (Electron Gamma Shower) [NHR85]. For this simulation framework extensions with the treatment of polarized particles exist [Flöttmann93a, LKNS, NBH93]; the most complete has been developed by K. Flöttmann [Flöttmann93a]. It is based on the matrix formalism [McM61], which enables a very general treatment of polarization. However, the Flöttmann extension concentrates on evaluation of polarization transfer, i.e. the effects of polarization induced asymmetries are neglected, and interactions with polarized media are not considered.

Another important simulation tool for detector studies is Geant3 [eal85]. Here also some effort has been made to include polarization [aal, Hoo97], but these extensions are not publicly available.

In general the implementation of polarization in this EM polarization library follows very closely the approach by K. Flöttmann [Flöttmann93a]. The basic principle is to associate a *Stokes vector* to each particle and track the mean polarization from one interaction to another. The basics for this approach is the matrix formalism as introduced in [McM61].

### 14.1.1 Stokes vector

The *Stokes vector* [McM61, Sto52] is a rather simple object (in comparison to e.g. the spin density matrix), three real numbers are sufficient for the characterization of the polarization state of any single electron, positron or photon. Using *Stokes vectors* all possible polarization states can be described, i.e. circular and linear polarized photons can be handled with the same formalism as longitudinal and transverse polarized electron/positrons.

The *Stokes vector* can be used also for beams, in the sense that it defines a mean polarization.

In the EM polarization library the Stokes vector is defined as follows:

	Photons	Electrons
$\xi_1$	linear polarization	polarization in x direction
$\xi_2$	linear polarization but $\pi/4$ to right	polarization in y direction
$\xi_3$	circular polarization	polarization in z direction

This definition is assumed in the *particle reference frame*, i.e. with the momentum of the particle pointing to the z direction, cf. also next section about coordinate transformations. Correspondingly a 100% longitudinally polarized electron or positron is characterized by

$$\xi = \begin{pmatrix} 0 \\ 0 \\ \pm 1 \end{pmatrix},$$

where  $\pm 1$  corresponds to spin parallel (anti parallel) to particle's momentum. Note that this definition is similar, but not identical to the definition used in McMaster [McM61].

Many scattering cross sections of polarized processes using Stokes vectors for the characterization of initial and final states are available in [McM61]. In general a differential cross section has the form

$$\frac{d\sigma(\zeta^{(1)}, \zeta^{(2)}, \xi^{(1)}, \xi^{(2)})}{d\Omega},$$

i.e. it is a function of the polarization states of the initial particles  $\zeta^{(1)}$  and  $\zeta^{(2)}$ , as well as of the polarization states of the final state particles  $\xi^{(1)}$  and  $\xi^{(2)}$  (in addition to the kinematic variables  $E$ ,  $\theta$ , and  $\phi$ ).

Consequently, in a simulation we have to account for

- Asymmetries:
- Polarization of beam ( $\zeta^{(1)}$ ) and target ( $\zeta^{(2)}$ ) can induce azimuthal and polar asymmetries, and may also influence on the total cross section (GEANT4: `GetMeanFreePath()`).
- Polarization transfer / depolarization effects
- The dependence on the final state polarizations defines a possible transfer from initial polarization to final state particles.

### 14.1.2 Transfer matrix

Using the formalism of McMaster, differential cross section and polarization transfer from the initial state ( $\zeta^{(1)}$ ) to one final state particle ( $\xi^{(1)}$ ) are combined in an interaction matrix  $T$ :

$$\begin{pmatrix} O \\ \xi^{(1)} \end{pmatrix} = T \begin{pmatrix} I \\ \zeta^{(1)} \end{pmatrix},$$

where  $I$  and  $O$  are the incoming and outgoing currents, respectively. In general the  $4 \times 4$  matrix  $T$  depends on the target polarization  $\zeta^{(2)}$  (and of course on the kinematic variables  $E, \theta, \phi$ ). Similarly one can define a matrix defining the polarization transfer to second final state particle like

$$\begin{pmatrix} O \\ \xi^{(2)} \end{pmatrix} = T' \begin{pmatrix} I \\ \zeta^{(1)} \end{pmatrix}.$$

In this framework the transfer matrix  $T$  is of the form

$$T = \begin{pmatrix} S & A_1 & A_2 & A_3 \\ P_1 & M_{11} & M_{21} & M_{31} \\ P_2 & M_{12} & M_{22} & M_{32} \\ P_3 & M_{13} & M_{23} & M_{33} \end{pmatrix}.$$

The matrix elements  $T_{ij}$  can be identified as (unpolarized) differential cross section ( $S$ ), polarized differential cross section ( $A_j$ ), polarization transfer ( $M_{ij}$ ), and (de)polarization ( $P_i$ ). In the Flöttmann extension the elements  $A_j$  and  $P_i$  have been neglected, thus concentrating on polarization transfer only. Using the full matrix takes now all polarization effects into account.

The transformation matrix, i.e. the dependence of the mean polarization of final state particles, can be derived from the asymmetry of the differential cross section w.r.t. this particular polarization. Where the asymmetry is defined as usual by

$$A = \frac{\sigma(+1) - \sigma(-1)}{\sigma(+1) + \sigma(-1)}.$$

The mean final state polarizations can be determined coefficient by coefficient. In general, the differential cross section is a linear function of the polarizations, i.e.

$$\frac{d\sigma(\zeta^{(1)}, \zeta^{(2)}, \xi^{(1)}, \xi^{(2)})}{d\Omega} = \Phi_{(\zeta^{(1)}, \zeta^{(2)})} + \mathbf{A}_{(\zeta^{(1)}, \zeta^{(2)})} \cdot \xi^{(1)} + \mathbf{B}_{(\zeta^{(1)}, \zeta^{(2)})} \cdot \xi^{(2)} + \xi^{(1)T} M_{(\zeta^{(1)}, \zeta^{(2)})} \xi^{(2)}$$

In this form, the mean polarization of the final state can be read off easily, and one obtains

$$\begin{aligned} \langle \xi^{(1)} \rangle &= \frac{1}{\Phi_{(\zeta^{(1)}, \zeta^{(2)})}} \mathbf{A}_{(\zeta^{(1)}, \zeta^{(2)})} \text{ and} \\ \langle \xi^{(2)} \rangle &= \frac{1}{\Phi_{(\zeta^{(1)}, \zeta^{(2)})}} \mathbf{B}_{(\zeta^{(1)}, \zeta^{(2)})}. \end{aligned}$$

Note that the *mean* polarization states do not depend on the correlation matrix  $M_{(\zeta^{(1)}, \zeta^{(2)})}$ . In order to account for correlation one has to generate *single* particle Stokes vector explicitly, i.e. on an event by event basis. However, this implementation generates *mean* polarization states, and neglects correlation effects.

### 14.1.3 Coordinate transformations

Three different coordinate systems are used in the evaluation of polarization states:

- **World frame** The geometry of the target, and the momenta of all particles in GEANT4 are noted in the world frame  $X, Y, Z$  (the *global reference frame*, GRF). It is the basis of the calculation of any other coordinate system.
- **Particle frame** Each particle is carrying its own coordinate system. In this system the direction of motion coincides with the  $z$ -direction. GEANT4 provides a transformation from any particle frame to the World frame by the method `G4ThreeMomentum::rotateUz()`. Thus, the  $y$ -axis of the *particle reference frame* (PRF) lies in the  $X$ - $Y$ -plane of the world frame.

The Stokes vector of any moving particle is defined w.r.t. the corresponding particle frame. Particles at rest (e.g. electrons of a media) use the world frame as particle frame.

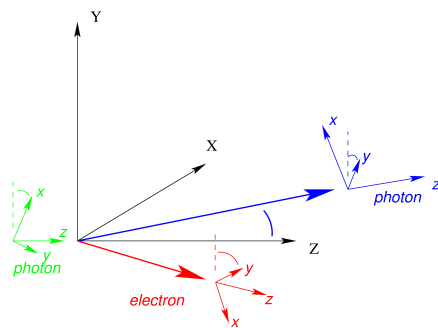


Fig. 14.1: The *interaction frame* and the *particle frames* for the example of Compton scattering. The momenta of all participating particle lie in the  $x$ - $z$ -plane, the scattering plane. The incoming photon gives the  $z$  direction. The outgoing photon is defined as *particle 1* and gives the  $x$ -direction, perpendicular to the  $z$ -axis. The  $y$ -axis is then perpendicular to the scattering plane and completes the definition of a right handed coordinate system called *interaction frame*. The *particle frame* is defined by the GEANT4 routine `G4ThreeMomentum::rotateUz()`.

- **Interaction frame** For the evaluation of the polarization transfer another coordinate system is used, defined by the scattering plane, cf. Fig. 14.1. There the  $z$ -axis is defined by the direction of motion of the incoming particle. The scattering plane is spanned by the  $z$ -axis and the  $x$ -axis, in a way, that the direction of *particle 1* has a positive  $x$  component. The definition of *particle 1* depends on the process, for instance in Compton scattering, the outgoing photon is referred as *particle 1*<sup>1</sup>.

All frames are right handed.

#### 14.1.4 Polarized beam and material

Polarization of beam particles is well established. It can be used for simulating low-energy Compton scattering of linear polarized photons. The interpretation as Stokes vector allows now the usage in a more general framework. The polarization state of a (initial) beam particle can be fixed using the standard *ParticleGunMessenger class*. For example, the class *G4ParticleGun* provides the method `SetParticlePolarization()`, which is usually accessible via:

```
/gun/polarization <Sz> <Sy> <Sz>
```

in a macro file.

In addition for the simulation of polarized media, a possibility to assign Stokes vectors to physical volumes is provided by a new class, the so-called *G4PolarizationManager*. The procedure to assign a polarization vector to a media, is done during the *detector construction*. There the *logical volumes* with certain polarization are made known to *polarization manager*. One example *DetectorConstruction* might look like follows:

```
G4double Targetthickness = .010*mm;
G4double Targetradius      = 2.5*mm;

G4Tubs* solidTarget =
  new G4Tubs("solidTarget",
    0.0,
    Targetradius,
    Targetthickness/2,
    0.0*deg,
    360.0*deg );
```

(continues on next page)

<sup>1</sup> Note, for an incoming particle travelling on the  $Z$ -axis (of GRF), the  $y$ -axis of the PRF of both outgoing particles is parallel to the  $y$ -axis of the *interaction frame*.

(continued from previous page)

```

G4LogicalVolume * logicalTarget =
  new G4LogicalVolume(solidTarget,
                      iron,
                      "logicalTarget",
                      0,0,0);

G4VPhysicalVolume * physicalTarget =
  new G4PVPlacement(0,G4ThreeVector(0.*mm, 0.*mm, 0.*mm),
                    logicalTarget,
                    "physicalTarget",
                    worldLogical,
                    false,
                    0);

G4PolarizationManager * polMgr = G4PolarizationManager::GetInstance();
polMgr->SetVolumePolarization(logicalTarget,G4ThreeVector(0.,0.,0.08));

```

Once a logical volume is known to the G4PolarizationManager, its polarization vector can be accessed from a macro file by its name, e.g. the polarization of the logical volume called “logicalTarget” can be changed via:

```
/polarization/volume/set logicalTarget 0. 0. -0.08
```

Note, the polarization of a material is stated in the world frame.

## 14.2 Ionisation

### 14.2.1 Method

The class *G4ePolarizedIonization* provides continuous and discrete energy losses of polarized electrons and positrons in a material. It evaluates polarization transfer and – if the material is polarized – asymmetries in the explicit delta rays production. The implementation baseline follows the approach derived for the class *G4eIonization* described in *Mean Energy Loss* and *Ionisation*. For continuous energy losses the effects of a polarized beam or target are negligible provided the separation cut  $T_{\text{cut}}$  is small, and are therefore not considered separately. On the other hand, in the explicit production of delta rays by Møller or Bhabha scattering, the effects of polarization on total cross section and mean free path, on distribution of final state particles and the average polarization of final state particles are taken into account.

### 14.2.2 Total cross section and mean free path

Kinematics of Bhabha and Møller scattering is fixed by initial energy

$$\gamma = \frac{E_{k_1}}{mc^2}$$

and variable

$$\epsilon = \frac{E_{p_2} - mc^2}{E_{k_1} - mc^2},$$

which is the part of kinetic energy of initial particle carried out by scatter. Lower kinematic limit for  $\epsilon$  is 0, but in order to avoid divergences in both total and differential cross sections one sets

$$\epsilon_{\min} = x = \frac{T_{\min}}{E_{k_1} - mc^2},$$

where  $T_{\min}$  has meaning of minimal kinetic energy of secondary electron. And,  $\epsilon_{\max} = 1(1/2)$  for Bhabha(Møller) scatterings.

## Total Møller cross section

The total cross section of the polarized Møller scattering can be expressed as follows

$$\sigma_{pol}^M = \frac{2\pi\gamma^2 r_e^2}{(\gamma - 1)^2(\gamma + 1)} \left[ \sigma_0^M + \zeta_3^{(1)} \zeta_3^{(2)} \sigma_L^M + \left( \zeta_1^{(1)} \zeta_1^{(2)} + \zeta_2^{(1)} \zeta_2^{(2)} \right) \sigma_T^M \right],$$

where the  $r_e$  is classical electron radius, and

$$\begin{aligned}\sigma_0^M &= -\frac{1}{1-x} + \frac{1}{x} - \frac{(\gamma - 1)^2}{\gamma^2} \left( \frac{1}{2} - x \right) + \frac{2 - 4\gamma}{2\gamma^2} \ln \left( \frac{1-x}{x} \right) \\ \sigma_L^M &= \frac{(-3 + 2\gamma + \gamma^2)(1 - 2x)}{2\gamma^2} + \frac{2\gamma(-1 + 2\gamma)}{2\gamma^2} \ln \left( \frac{1-x}{x} \right) \\ \sigma_T^M &= \frac{2(\gamma - 1)(2x - 1)}{2\gamma^2} + \frac{(1 - 3\gamma)}{2\gamma^2} \ln \left( \frac{1-x}{x} \right)\end{aligned}$$

## Total Bhabha cross section

The total cross section of the polarized Bhabha scattering can be expressed as follows

$$\sigma_{pol}^B = \frac{2\pi r_e^2}{\gamma - 1} \left[ \sigma_0^B + \zeta_3^{(1)} \zeta_3^{(2)} \sigma_L^B + \left( \zeta_1^{(1)} \zeta_1^{(2)} + \zeta_2^{(1)} \zeta_2^{(2)} \right) \sigma_T^B \right],$$

where

$$\begin{aligned}\sigma_0^B &= \frac{1-x}{2(\gamma - 1)x} + \frac{2(-1 + 3x - 6x^2 + 4x^3)}{3(1+\gamma)^3} \\ &+ \frac{-1 - 5x + 12x^2 - 10x^3 + 4x^4}{2(1+\gamma)x} + \frac{-3 - x + 8x^2 - 4x^3 - \ln(x)}{(1+\gamma)^2} \\ &+ \frac{3 + 4x - 9x^2 + 3x^3 - x^4 + 6x \ln(x)}{3x} \\ \sigma_L^B &= \frac{2(1 - 3x + 6x^2 - 4x^3)}{3(1+\gamma)^3} + \frac{-14 + 15x - 3x^2 + 2x^3 - 9\ln(x)}{3(1+\gamma)} \\ &+ \frac{5 + 3x - 12x^2 + 4x^3 + 3\ln(x)}{3(1+\gamma)^2} + \frac{7 - 9x + 3x^2 - x^3 + 6\ln(x)}{3} \\ \sigma_T^B &= \frac{2(-1 + 3x - 6x^2 + 4x^3)}{3(1+\gamma)^3} + \frac{-7 - 3x + 18x^2 - 8x^3 - 3\ln(x)}{3(1+\gamma)^2} \\ &+ \frac{5 + 3x - 12x^2 + 4x^3 + 9\ln(x)}{6(1+\gamma)}\end{aligned}$$

## Mean free path

With the help of the total polarized Møller cross section one can define a longitudinal asymmetry  $A_L^M$  and the transverse asymmetry  $A_T^M$ , by

$$A_L^M = \frac{\sigma_L^M}{\sigma_0^M}$$

and

$$A_T^M = \frac{\sigma_T^M}{\sigma_0^M}.$$

Similarly, using the polarized Bhabha cross section one can introduce a longitudinal asymmetry  $A_L^B$  and the transverse asymmetry  $A_T^B$  via

$$A_L^B = \frac{\sigma_L^B}{\sigma_0^B}$$

and

$$A_T^B = \frac{\sigma_T^B}{\sigma_0^B}$$

These asymmetries are depicted in Fig. 14.2, Fig. 14.3 for Møller and Fig. 14.4, Fig. 14.5 for Bhabha.

If both beam and target are polarized the mean free path as defined in *Ionisation* has to be modified. In the class *G4ePolarizedIonization* the polarized mean free path  $\lambda^{\text{pol}}$  is derived from the unpolarized mean free path  $\lambda^{\text{unpol}}$  via

$$\lambda^{\text{pol}} = \frac{\lambda^{\text{unpol}}}{1 + \zeta_3^{(1)} \zeta_3^{(2)} A_L + (\zeta_1^{(1)} \zeta_1^{(2)} + \zeta_2^{(1)} \zeta_2^{(2)}) A_T}$$

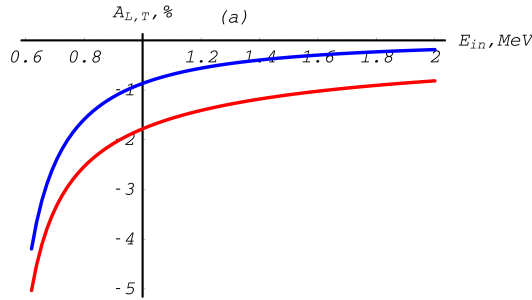


Fig. 14.2: Møller total cross section asymmetries depending on the total energy of the incoming electron, with a cut-off  $T_{\text{cut}} = 1$  keV. Transverse asymmetry is plotted in blue, longitudinal asymmetry in red. Between 0.5 MeV and 2 MeV.

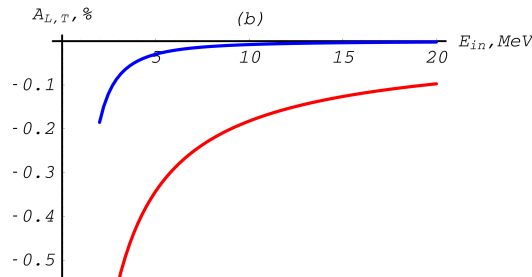


Fig. 14.3: Møller total cross section asymmetries depending on the total energy of the incoming electron, with a cut-off  $T_{\text{cut}} = 1$  keV. Transverse asymmetry is plotted in blue, longitudinal asymmetry in red. Up to 10 MeV.

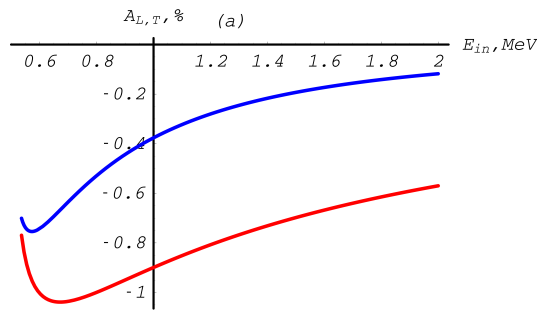


Fig. 14.4: Bhabha total cross section asymmetries depending on the total energy of the incoming positron, with a cut-off  $T_{\text{cut}} = 1\text{keV}$ . Transverse asymmetry is plotted in blue, longitudinal asymmetry in red. Between 0.5 MeV and 2 MeV.

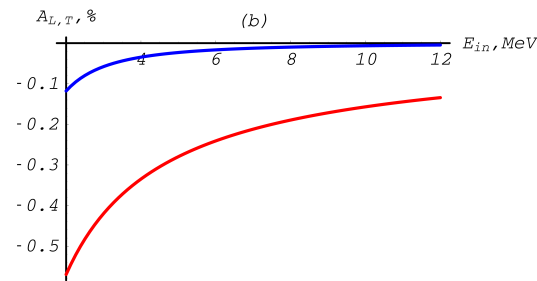


Fig. 14.5: Bhabha total cross section asymmetries depending on the total energy of the incoming positron, with a cut-off  $T_{\text{cut}} = 1\text{keV}$ . Transverse asymmetry is plotted in blue, longitudinal asymmetry in red. Up to 10 MeV.

### 14.2.3 Sampling the final state

#### Differential cross section

The polarized differential cross section is rather complicated. The full result can be found in [eal, FM57, Ste58]. In *G4PolarizedMollerCrossSection* the complete result is available taking all mass effects into account, with only binding effects neglected. Here we state only the ultra-relativistic approximation (URA), to show the general dependencies.

$$\frac{d\sigma_{URA}^M}{d\epsilon d\varphi} = \frac{r_e^2}{\gamma + 1} \times \left[ \frac{(1 - \epsilon + \epsilon^2)^2}{4(\epsilon - 1)^2 \epsilon^2} + \zeta_3^{(1)} \zeta_3^{(2)} \frac{2 - \epsilon + \epsilon^2}{-4\epsilon(1 - \epsilon)} + (\zeta_2^{(1)} \zeta_2^{(2)} - \zeta_1^{(1)} \zeta_1^{(2)}) \frac{1}{4} \right. \\ \left. + (\xi_3^{(1)} \zeta_3^{(1)} - \xi_3^{(2)} \zeta_3^{(2)}) \frac{1 - \epsilon + 2\epsilon^2}{4(1 - \epsilon) \epsilon^2} + (\xi_3^{(2)} \zeta_3^{(1)} - \xi_3^{(1)} \zeta_3^{(2)}) \frac{2 - 3\epsilon + 2\epsilon^2}{4(1 - \epsilon)^2 \epsilon} \right]$$

The corresponding cross section for Bhabha cross section is implemented in *G4PolarizedBhabhaCrossSection*. In the ultra-relativistic approximation it reads

$$\frac{d\sigma_{URA}^B}{d\epsilon d\varphi} = \frac{r_e^2}{\gamma - 1} \times \left[ \frac{(1 - \epsilon + \epsilon^2)^2}{4\epsilon^2} + \zeta_3^{(1)} \zeta_3^{(2)} \frac{(\epsilon - 1)(2 - \epsilon + \epsilon^2)}{4\epsilon} + (\zeta_2^{(1)} \zeta_2^{(2)} - \zeta_1^{(1)} \zeta_1^{(2)}) \frac{(1 - \epsilon)^2}{4} \right. \\ \left. + (\xi_3^{(1)} \zeta_3^{(1)} - \xi_3^{(2)} \zeta_3^{(2)}) \frac{1 - 2\epsilon + 3\epsilon^2 - 2\epsilon^3}{4\epsilon^2} + (\xi_3^{(2)} \zeta_3^{(1)} - \xi_3^{(1)} \zeta_3^{(2)}) \frac{2 - 3\epsilon + 2\epsilon^2}{4\epsilon} \right]$$

where

$r_e$	classical electron radius
$\gamma$	$E_{k_1}/m_e c^2$
$\epsilon$	$(E_{p_1} - m_e c^2)/(E_{k_1} - m_e c^2)$
$E_{k_1}$	energy of the incident electron/positron
$E_{p_1}$	energy of the scattered electron/positron
$m_e c^2$	electron mass
$\zeta^{(1)}$	Stokes vector of the incoming electron/positron
$\zeta^{(2)}$	Stokes vector of the target electron
$\xi^{(1)}$	Stokes vector of the outgoing electron/positron
$\xi^{(2)}$	Stokes vector of the outgoing (2nd) electron .

#### Sampling

The delta ray is sampled according to methods discussed in Section 2. After exploitation of the symmetry in the Møller cross section under exchanging  $\epsilon$  versus  $(1 - \epsilon)$ , the differential cross section can be approximated by a simple function  $f^M(\epsilon)$ :

$$f^M(\epsilon) = \frac{1}{\epsilon^2} \frac{\epsilon_0}{1 - 2\epsilon_0}$$

with the kinematic limits given by

$$\epsilon_0 = \frac{T_{cut}}{E_{k_1} - m_e c^2} \leq \epsilon \leq \frac{1}{2}$$

A similar function  $f^B(\epsilon)$  can be found for Bhabha scattering:

$$f^B(\epsilon) = \frac{1}{\epsilon^2} \frac{\epsilon_0}{1 - \epsilon_0}$$

with the kinematic limits given by

$$\epsilon_0 = \frac{T_{\text{cut}}}{E_{k_1} - m_e c^2} \leq \epsilon \leq 1$$

The kinematic of the delta ray production is constructed by the following steps:

1.  $\epsilon$  is sampled from  $f(\epsilon)$
2. calculate the differential cross section, depending on the initial polarizations  $\zeta^{(1)}$  and  $\zeta^{(2)}$ .
3.  $\epsilon$  is accepted with the probability defined by ratio of the differential cross section over the approximation function.
4. The  $\varphi$  is diced uniformly.
5.  $\varphi$  is determined from the differential cross section, depending on the initial polarizations  $\zeta^{(1)}$  and  $\zeta^{(2)}$

Note, for initial states without transverse polarization components, the  $\varphi$  distribution is always uniform. In Fig. 14.6 and Fig. 14.7 the asymmetries indicate the influence of polarization. In general the effect is largest around  $\epsilon = 1/2$ .

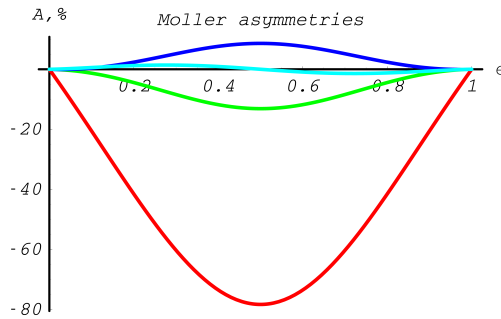


Fig. 14.6: Differential cross section asymmetries in % for Møller scattering (red -  $A_{ZZ}(\epsilon)$ , green -  $A_{XX}(\epsilon)$ , blue -  $A_{YY}(\epsilon)$ , light blue -  $A_{ZX}(\epsilon)$ )

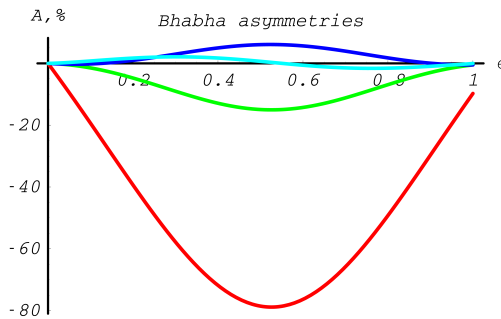


Fig. 14.7: Differential cross section asymmetries in % for Bhabha scattering (red -  $A_{ZZ}(\epsilon)$ , green -  $A_{XX}(\epsilon)$ , blue -  $A_{YY}(\epsilon)$ , light blue -  $A_{ZX}(\epsilon)$ )

After both  $\phi$  and  $\epsilon$  are known, the kinematic can be constructed fully. Using momentum conservation the momenta of the scattered incident particle and the ejected electron are constructed in global coordinate system.

## Polarization transfer

After the kinematics is fixed the polarization properties of the outgoing particles are determined. Using the dependence of the differential cross section on the final state polarization a mean polarization is calculated according to method described in [Introduction](#).

The resulting polarization transfer functions  $\xi_3^{(1,2)}(\epsilon)$  are depicted in Fig. 14.8, Fig. 14.9, and Fig. 14.10, Fig. 14.11.

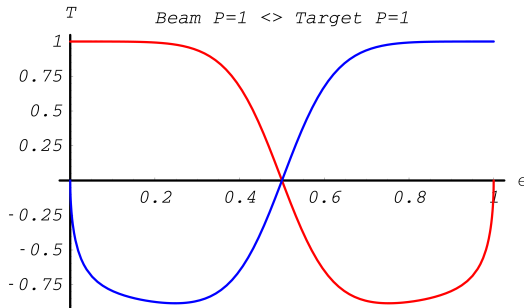


Fig. 14.8: Polarization transfer functions in Møller scattering. Longitudinal polarization  $\xi_3^{(2)}$  of electron with energy  $E_{p2}$  in blue; longitudinal polarization  $\xi_3^{(1)}$  of second electron in red. Kinetic energy of incoming electron  $T_{k_1} = 10\text{MeV}$

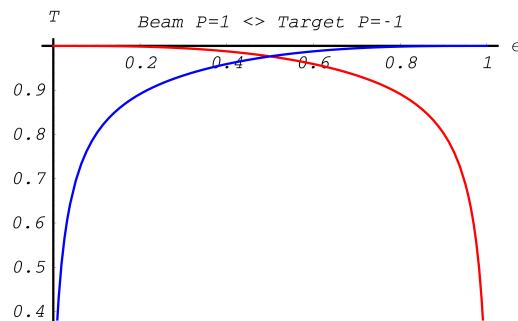


Fig. 14.9: Polarization transfer functions in Møller scattering. Longitudinal polarization  $\xi_3^{(2)}$  of electron with energy  $E_{p2}$  in blue; longitudinal polarization  $\xi_3^{(1)}$  of second electron in red. Kinetic energy of incoming electron  $T_{k_1} = 10\text{MeV}$

## 14.3 Positron - Electron Annihilation

### 14.3.1 Method

The class *G4eplusPolarizedAnnihilation* simulates annihilation of polarized positrons with electrons in a material. The implementation baseline follows the approach derived for the class *G4eplusAnnihilation* described in [Positron - Electron Annihilation](#). It evaluates polarization transfer and – if the material is polarized – asymmetries in the produced photons. Thus, it takes the effects of polarization on total cross section and mean free path, on distribution of final state photons into account. And calculates the average polarization of these generated photons. The material electrons are assumed to be free and at rest.

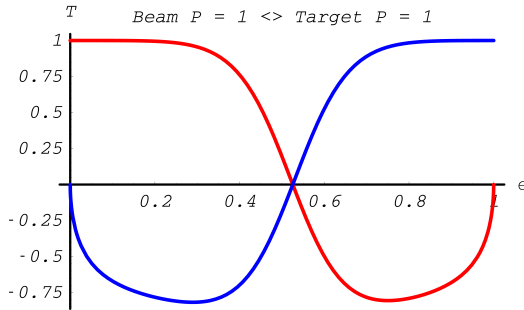


Fig. 14.10: Polarization Transfer in Bhabha scattering. Longitudinal polarization  $\xi_3^{(2)}$  of electron with energy  $E_{p2}$  in blue; longitudinal polarization  $\xi_3^{(1)}$  of scattered positron. Kinetic energy of incoming positron  $T_{k_1} = 10\text{MeV}$

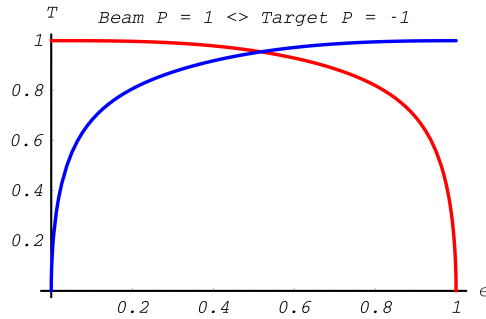


Fig. 14.11: Polarization Transfer in Bhabha scattering. Longitudinal polarization  $\xi_3^{(2)}$  of electron with energy  $E_{p2}$  in blue; longitudinal polarization  $\xi_3^{(1)}$  of scattered positron. Kinetic energy of incoming positron  $T_{k_1} = 10\text{MeV}$

### 14.3.2 Total cross section and mean free path

Kinematics of annihilation process is fixed by initial energy

$$\gamma = \frac{E_{k_1}}{mc^2}$$

and variable

$$\epsilon = \frac{E_{p1}}{E_{k_1} + mc^2},$$

which is the part of total energy available in initial state carried out by first photon. This variable has the following kinematical limits

$$\frac{1}{2} \left( 1 - \sqrt{\frac{\gamma - 1}{\gamma + 1}} \right) < \epsilon < \frac{1}{2} \left( 1 + \sqrt{\frac{\gamma - 1}{\gamma + 1}} \right).$$

## Total Cross Section

The total cross section of the annihilation of a polarized  $e^+e^-$  pair into two photons could be expressed as follows

$$\sigma_{pol}^A = \frac{\pi r_e^2}{\gamma + 1} \left[ \sigma_0^A + \zeta_3^{(1)} \zeta_3^{(2)} \sigma_L^A + \left( \zeta_1^{(1)} \zeta_1^{(2)} + \zeta_2^{(1)} \zeta_2^{(2)} \right) \sigma_T^A \right],$$

where

$$\begin{aligned}\sigma_0^A &= \frac{-(3 + \gamma) \sqrt{-1 + \gamma^2} + (1 + \gamma (4 + \gamma)) \ln(\gamma + \sqrt{-1 + \gamma^2})}{4 (\gamma^2 - 1)} \\ \sigma_L^A &= \frac{-\sqrt{-1 + \gamma^2} (5 + \gamma (4 + 3\gamma)) + (3 + \gamma (7 + \gamma + \gamma^2)) \ln(\gamma + \sqrt{\gamma^2 - 1})}{4 (\gamma - 1)^2 (1 + \gamma)} \\ \sigma_T^A &= \frac{(5 + \gamma) \sqrt{-1 + \gamma^2} - (1 + 5\gamma) \ln(\gamma + \sqrt{-1 + \gamma^2})}{4 (-1 + \gamma)^2 (1 + \gamma)}\end{aligned}$$

## Mean free path

With the help of the total polarized annihilation cross section one can define a longitudinal asymmetry  $A_L^A$  and the transverse asymmetry  $A_T^A$ , by

$$A_L^A = \frac{\sigma_L^A}{\sigma_0^A}$$

and

$$A_T^A = \frac{\sigma_T^A}{\sigma_0^A}.$$

These asymmetries are depicted in Fig. 14.12, Fig. 14.13.

If both incident positron and target electron are polarized the mean free path as defined in section *Positron - Electron Annihilation* has to be modified. The polarized mean free path  $\lambda^{pol}$  is derived from the unpolarized mean free path  $\lambda^{unpol}$  via

$$\lambda^{pol} = \frac{\lambda^{unpol}}{1 + \zeta_3^{(1)} \zeta_3^{(2)} A_L + \left( \zeta_1^{(1)} \zeta_1^{(2)} + \zeta_2^{(1)} \zeta_2^{(2)} \right) A_T}$$

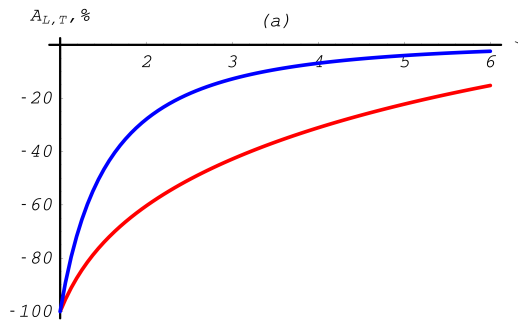


Fig. 14.12: Annihilation total cross section asymmetries depending on the total energy of the incoming positron  $E_{k_1}$ . The transverse asymmetry is shown in blue, the longitudinal asymmetry in red.

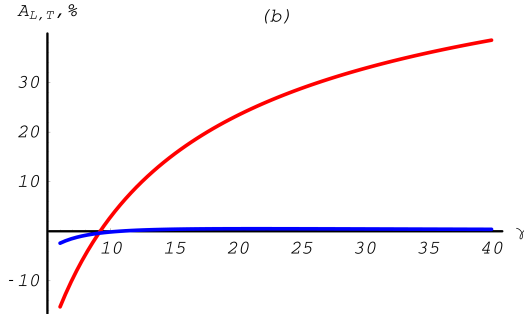


Fig. 14.13: Annihilation total cross section asymmetries depending on the total energy of the incoming positron  $E_{k_1}$ . The transverse asymmetry is shown in blue, the longitudinal asymmetry in red.

### 14.3.3 Sampling the final state

#### Differential Cross Section

The fully polarized differential cross section is implemented in the class *G4PolarizedAnnihilationCrossSection*, which takes all mass effects into account, but binding effects are neglected [eal, Pag57]. In the ultra-relativistic approximation (URA) and concentrating on longitudinal polarization states only the cross section is rather simple:

$$\frac{d\sigma_{URA}^A}{d\epsilon d\varphi} = \frac{r_e^2}{\gamma - 1} \times \left( \frac{1 - 2\epsilon + 2\epsilon^2}{8\epsilon - 8\epsilon^2} \left( 1 + \zeta_3^{(1)} \zeta_3^{(2)} \right) + \frac{(1 - 2\epsilon) (\zeta_3^{(1)} + \zeta_3^{(2)}) (\xi_3^{(1)} - \xi_3^{(2)})}{8(\epsilon - 1)\epsilon} \right)$$

where

$r_e$	classical electron radius
$\gamma$	$E_{k_1}/m_e c^2$
$E_{k_1}$	energy of the incident positron
$m_e c^2$	electron mass
$\zeta^{(1)}$	Stokes vector of the incoming positron
$\zeta^{(2)}$	Stokes vector of the target electron
$\xi^{(1)}$	Stokes vector of the 1st photon
$\xi^{(2)}$	Stokes vector of the 2nd photon .

#### Sampling

The photon energy is sampled according to methods discussed in Section 2. After exploitation of the symmetry in the Annihilation cross section under exchanging  $\epsilon$  versus  $(1 - \epsilon)$ , the differential cross section can be approximated by a simple function  $f(\epsilon)$ :

$$f(\epsilon) = \frac{1}{\epsilon} \ln^{-1} \left( \frac{\epsilon_{\max}}{\epsilon_{\min}} \right)$$

with the kinematic limits given by

$$\epsilon_{\min} = \frac{1}{2} \left( 1 - \sqrt{\frac{\gamma - 1}{\gamma + 1}} \right) ,$$

$$\epsilon_{\max} = \frac{1}{2} \left( 1 + \sqrt{\frac{\gamma - 1}{\gamma + 1}} \right) .$$

The kinematic of the two photon final state is constructed by the following steps:

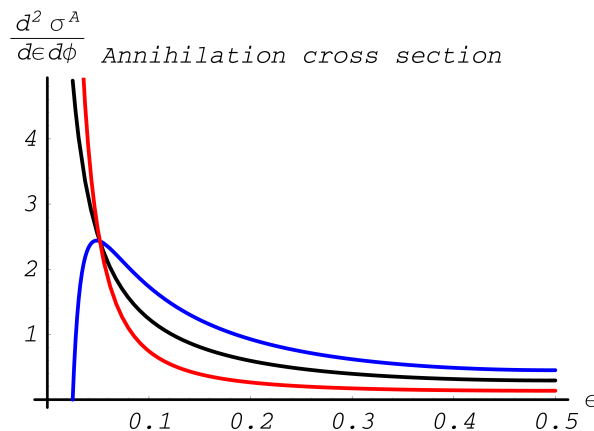


Fig. 14.14: Annihilation differential cross section in arbitrary units. Black line corresponds to unpolarized cross section; red line – to the antiparallel spins of initial particles, and blue line – to the parallel spins. Kinetic energy of the incoming positron  $T_{k_1} = 10\text{MeV}$ .

1.  $\epsilon$  is sampled from  $f(\epsilon)$
2. calculate the differential cross section, depending on the initial polarizations  $\zeta^{(1)}$  and  $\zeta^{(2)}$ .
3.  $\epsilon$  is accepted with the probability defined by the ratio of the differential cross section over the approximation function  $f(\epsilon)$ .
4. The  $\varphi$  is diced uniformly.
5.  $\varphi$  is determined from the differential cross section, depending on the initial polarizations  $\zeta^{(1)}$  and  $\zeta^{(2)}$ .

A short overview over the sampling method is given in [Section 2](#). In [Fig. 14.15](#) the asymmetries indicate the influence of polarization for an 10MeV incoming positron. The actual behavior is very sensitive to the energy of the incoming positron.

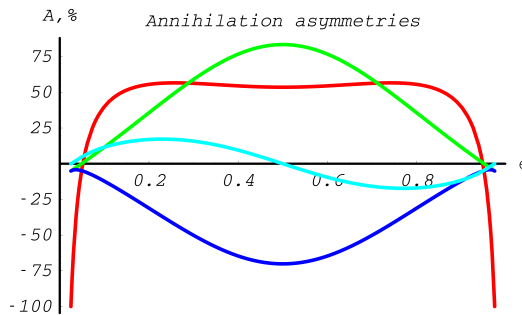


Fig. 14.15: Annihilation differential cross section asymmetries in %. Red line corresponds to  $A_{ZZ}(\epsilon)$ , green line –  $A_{XX}(\epsilon)$ , blue line –  $A_{YY}(\epsilon)$ , lightblue line –  $A_{ZX}(\epsilon)$ ). Kinetic energy of the incoming positron  $T_{k_1} = 10\text{MeV}$ .

## Polarization transfer

After the kinematics is fixed the polarization of the outgoing photon is determined. Using the dependence of the differential cross section on the final state polarizations a mean polarization is calculated for each photon according to method described in section [Introduction](#).

The resulting polarization transfer functions  $\xi^{(1,2)}(\epsilon)$  are depicted in Fig. 14.16, Fig. 14.17.

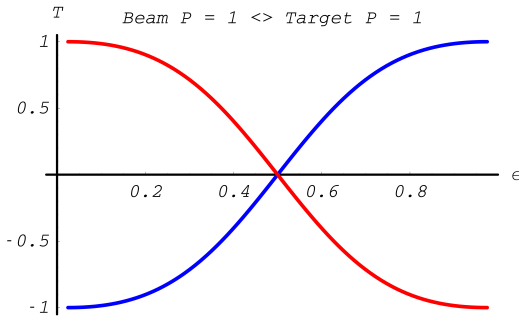


Fig. 14.16: Polarization Transfer in annihilation process. Blue line corresponds to the circular polarization  $\xi_3^{(1)}$  of the photon with energy  $m(\gamma + 1)\epsilon$ ; red line – circular polarization  $\xi_3^{(2)}$  of the photon with energy  $m(\gamma + 1)(1 - \epsilon)$ .

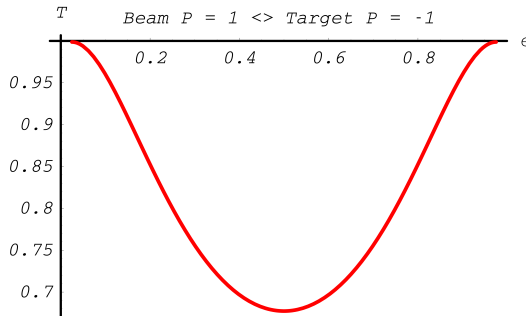


Fig. 14.17: Polarization Transfer in annihilation process. Blue line corresponds to the circular polarization  $\xi_3^{(1)}$  of the photon with energy  $m(\gamma + 1)\epsilon$ ; red line – circular polarization  $\xi_3^{(2)}$  of the photon with energy  $m(\gamma + 1)(1 - \epsilon)$ .

### 14.3.4 Annihilation at Rest

The method `AtRestDoIT` treats the special case where a positron comes to rest before annihilating. It generates two photons, each with energy  $E_{p_{1/2}} = mc^2$  and an isotropic angular distribution. Starting with the differential cross section for annihilation with positron and electron spins opposed and parallel, respectively, [Pag57]

$$d\sigma_1 = \sim \frac{(1 - \beta^2) + \beta^2(1 - \beta^2)(1 - \cos^2 \theta)^2}{(1 - \beta^2 \cos^2 \theta)^2} d\cos \theta$$

$$d\sigma_2 = \sim \frac{\beta^2(1 - \cos^4 \theta)}{(1 - \beta^2 \cos^2 \theta)^2} d\cos \theta$$

In the limit  $\beta \rightarrow 0$  the cross section  $d\sigma_1$  becomes one, and the cross section  $d\sigma_2$  vanishes. For the opposed spin state, the total angular momentum is zero and we have a uniform photon distribution. For the parallel case the total angular momentum is 1. Here the two photon final state is forbidden by angular momentum conservation, and it can be assumed that higher order processes (e.g. three photon final state) play a dominant role. However, in reality 100% polarized electron targets do not exist, consequently there are always electrons with opposite spin, where the positron can annihilate with. Final state polarization does not play a role for the decay products of a spin zero state, and can be safely neglected (is set to zero).

## 14.4 Polarized Compton scattering

### 14.4.1 Method

The class *G4PolarizedCompton* simulates Compton scattering of polarized photons with (possibly polarized) electrons in a material. The implementation follows the approach described for the class *G4ComptonScattering* introduced in [Compton scattering](#). Here the explicit production of a Compton scattered photon and the ejected electron is considered taking the effects of polarization on total cross section and mean free path as well as on the distribution of final state particles into account. Further the average polarizations of the scattered photon and electron are calculated. The material electrons are assumed to be free and at rest.

### 14.4.2 Total cross section and mean free path

Kinematics of the Compton process is fixed by the initial energy

$$X = \frac{E_{k_1}}{mc^2}$$

and the variable

$$\epsilon = \frac{E_{p_1}}{E_{k_1}},$$

which is the part of total energy available in initial state carried out by scattered photon, and the scattering angle

$$\cos \theta = 1 - \frac{1}{X} \left( \frac{1}{\epsilon} - 1 \right)$$

The variable  $\epsilon$  has the following limits:

$$\frac{1}{1 + 2X} < \epsilon < 1$$

#### Total Cross Section

The total cross section of Compton scattering reads

$$\sigma_{pol}^C = \frac{\pi r_e^2}{X^2 (1 + 2X)^2} \left[ \sigma_0^C + \zeta_3^{(1)} \zeta_3^{(2)} \sigma_L^C \right]$$

where

$$\sigma_0^C = \frac{2X (2 + X (1 + X) (8 + X)) - (1 + 2X)^2 (2 + (2 - X) X) \ln(1 + 2X)}{X}$$

and

$$\sigma_L^C = 2X (1 + X (4 + 5X)) - (1 + X) (1 + 2X)^2 \ln(1 + 2X)$$

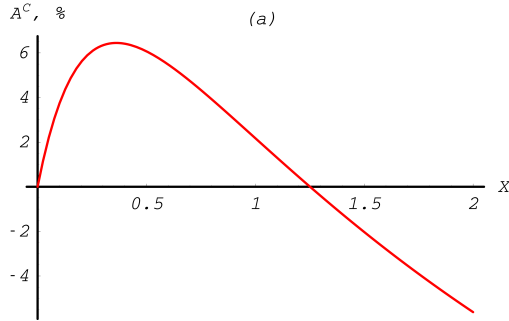


Fig. 14.18: Compton total cross section asymmetry depending on the energy of incoming photon. Between 0 and  $\sim 1$  MeV.

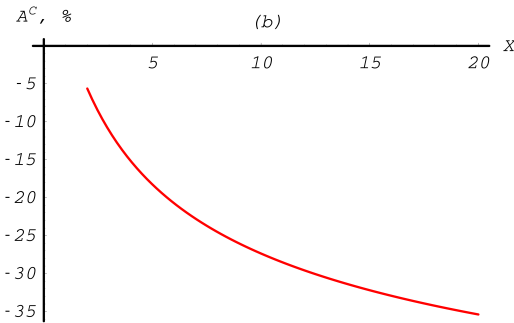


Fig. 14.19: Compton total cross section asymmetry depending on the energy of incoming photon. Up to 10MeV.

### Mean free path

When simulating the Compton scattering of a photon with an atomic electron, an empirical cross section formula is used, which reproduces the cross section data down to 10 keV (see [Compton scattering](#)). If both beam and target are polarized this mean free path has to be corrected.

In the class *G4ComptonScattering* the polarized mean free path  $\lambda^{\text{pol}}$  is defined on the basis of the unpolarized mean free path  $\lambda^{\text{unpol}}$  via

$$\lambda^{\text{pol}} = \frac{\lambda^{\text{unpol}}}{1 + \zeta_3^{(1)} \zeta_3^{(2)} A_L^C}$$

where

$$A_L^C = \frac{\sigma_L^A}{\sigma_0^A}$$

is the expected asymmetry from the total polarized Compton cross section given above. This asymmetry is depicted in Fig. 14.18, Fig. 14.19.

### 14.4.3 Sampling the final state

#### Differential Compton Cross Section

In the ultra-relativistic approximation the dependence of the differential cross section on the longitudinal/circular degree of polarization is very simple. It reads

$$\frac{d\sigma_{URA}^C}{d\epsilon d\phi} = \frac{r_e^2}{X} \left( \frac{\epsilon^2 + 1}{2\epsilon} + \frac{\epsilon^2 - 1}{2\epsilon} (\zeta_3^{(1)} \zeta_3^{(2)} + \zeta_3^{(2)} \xi_3^{(1)} - \zeta_3^{(1)} \xi_3^{(2)}) + \frac{\epsilon^2 + 1}{2\epsilon} (\zeta_3^{(1)} \xi_3^{(1)} - \zeta_3^{(2)} \xi_3^{(2)}) \right)$$

where

$r_e$	classical electron radius
$X$	$E_{k_1}/m_e c^2$
$E_{k_1}$	energy of the incident photon
$m_e c^2$	electron mass

The fully polarized differential cross section is available in the class *G4PolarizedComptonCrossSection*. It takes all mass effects into account, but binding effects are neglected [eal, LT54a, LT54b]. The cross section dependence on  $\epsilon$  for right handed circularly polarized photons and longitudinally polarized electrons is plotted in Fig. 14.20, Fig. 14.21.

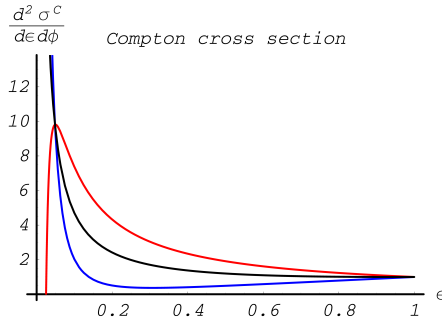


Fig. 14.20: Compton scattering differential cross section in arbitrary units. Black line corresponds to the unpolarized cross section; red line – to the antiparallel spins of initial particles, and blue line – to the parallel spins. Energy of the incoming photon  $E_{k_1} = 10\text{MeV}$ .

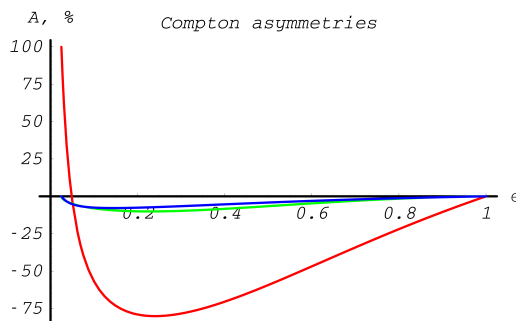


Fig. 14.21: Compton scattering differential cross section asymmetries in %. Red line corresponds to the asymmetry due to circular photon and longitudinal electron initial state polarization, green line – due to circular photon and transverse electron initial state polarization, blue line – due to linear photon and transverse electron initial state polarization.

## Sampling

The photon energy is sampled according to methods discussed in Section 2. The differential cross section can be approximated by a simple function  $\Phi(\epsilon)$ :

$$\Phi(\epsilon) = \frac{1}{\epsilon} + \epsilon$$

with the kinematic limits given by

$$\begin{aligned}\epsilon_{\min} &= \frac{1}{1+2X} \\ \epsilon_{\max} &= 1\end{aligned}$$

The kinematic of the scattered photon is constructed by the following steps:

1.  $\epsilon$  is sampled from  $\Phi(\epsilon)$
2. calculate the differential cross section, depending on the initial polarizations  $\zeta^{(1)}$  and  $\zeta^{(2)}$ , which the correct normalization.
3.  $\epsilon$  is accepted with the probability defined by ratio of the differential cross section over the approximation function.
4. The  $\varphi$  is diced uniformly.
5.  $\varphi$  is determined from the differential cross section, depending on the initial polarizations  $\zeta^{(1)}$  and  $\zeta^{(2)}$ .

In Fig. 14.20, Fig. 14.21 the asymmetries indicate the influence of polarization for an 10 MeV incoming positron. The actual behavior is very sensitive to energy of the incoming positron.

## Polarization transfer

After the kinematics is fixed the polarization of the outgoing photon is determined. Using the dependence of the differential cross section on the final state polarizations a mean polarization is calculated for each photon according to the method described in section [Introduction](#).

The resulting polarization transfer functions  $\xi^{(1,2)}(\epsilon)$  are depicted in Fig. 14.22, Fig. 14.23.

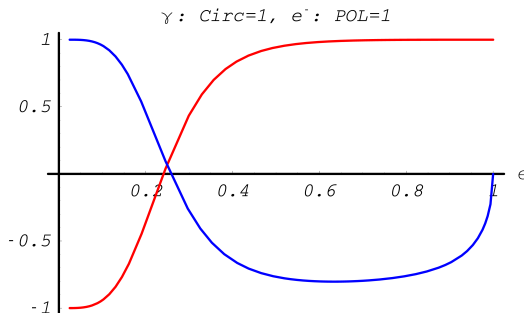


Fig. 14.22: Polarization Transfer in Compton scattering. Blue line corresponds to the longitudinal polarization  $\xi_3^{(2)}$  of the electron, red line – circular polarization  $\xi_3^{(1)}$  of the photon.

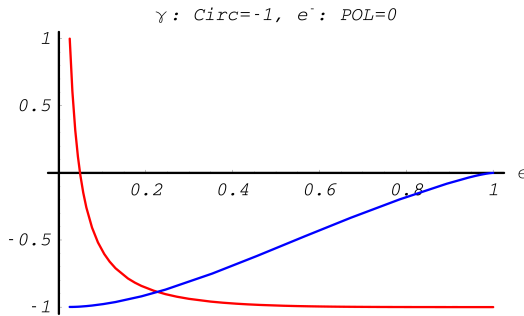


Fig. 14.23: Polarization Transfer in Compton scattering. Blue line corresponds to the longitudinal polarization  $\xi_3^{(2)}$  of the electron, red line – circular polarization  $\xi_3^{(1)}$  of the photon.

## 14.5 Polarized Bremsstrahlung for electron and positron

### 14.5.1 Method

The polarized version of Bremsstrahlung is based on the unpolarized cross section. Energy loss, mean free path, and distribution of explicitly generated final state particles are treated by the unpolarized version *G4eBremsstrahlung*. For details consult [Bremsstrahlung](#).

The remaining task is to attribute polarization vectors to the generated final state particles, which is discussed in the following.

### 14.5.2 Polarization in gamma conversion and bremsstrahlung

Gamma conversion and bremsstrahlung are cross-symmetric processes (i.e. the Feynman diagram for electron bremsstrahlung can be obtained from the gamma conversion diagram by flipping the incoming photon and outgoing positron lines) and their cross sections closely related. For both processes, the interaction occurs in the field of the nucleus and the total and differential cross section are polarization independent. Therefore, only the polarization transfer from the polarized incoming particle to the outgoing particles is taken into account.

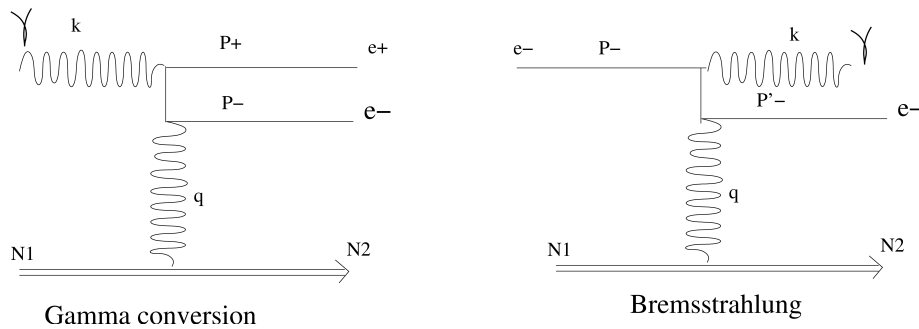


Fig. 14.24: Feynman diagrams of Gamma conversion and bremsstrahlung processes.

For both processes, the scattering can be formulated by:

$$\mathcal{K}_1(k_1, \zeta^{(1)}) + \mathcal{N}_1(k_{\mathcal{N}_1}, \zeta^{(\mathcal{N}_1)}) \rightarrow \mathcal{P}_1(p_1, \xi^{(1)}) + \mathcal{P}_2(p_2, \xi^{(2)}) + \mathcal{N}_2(p_{\mathcal{N}_2}, \xi^{(\mathcal{N}_2)})$$

Where  $\mathcal{N}_1(k_{\mathcal{N}_1}, \zeta^{(\mathcal{N}_1)})$  and  $\mathcal{N}_2(p_{\mathcal{N}_2}, \xi^{(\mathcal{N}_2)})$  are the initial and final state of the field of the nucleus respectively assumed to be unchanged, at rest and unpolarized. This leads to  $k_{\mathcal{N}_1} = k_{\mathcal{N}_2} = 0$  and  $\zeta^{(\mathcal{N}_1)} = \xi^{(\mathcal{N}_2)} = 0$ .

**In the case of gamma conversion process:**  $\mathcal{K}_1(k_1, \zeta^{(1)})$  is the incoming photon initial state with momentum  $k_1$  and polarization state  $\zeta^{(1)}$ .  $\mathcal{P}_1(p_1, \xi^{(1)})$  and  $\mathcal{P}_2(p_2, \xi^{(2)})$  are the two photons final states with momenta  $p_1$  and  $p_2$  and polarization states  $\xi^{(1)}$  and  $\xi^{(2)}$ .

**In the case of bremsstrahlung process:**  $\mathcal{K}_1(k_1, \zeta^{(1)})$  is the incoming lepton  $e^-(e^+)$  initial state with momentum  $k_1$  and polarization state  $\zeta^{(1)}$ .  $\mathcal{P}_1(p_1, \xi^{(1)})$  is the lepton  $e^-(e^+)$  final state with momentum  $p_1$  and polarization state  $\xi^{(1)}$ .  $\mathcal{P}_2(p_2, \xi^{(2)})$  is the bremsstrahlung photon in final state with momentum  $p_2$  and polarization state  $\xi^{(2)}$ .

### 14.5.3 Polarization transfer from the lepton $e^+e^-$ to a photon

The polarization transfer from an electron (positron) to a photon in a bremsstrahlung process was first calculated by Olsen and Maximon [OM59] taking into account both Coulomb and screening effects. In the Stokes vector formalism, the  $e^-(e^+)$  polarization state can be transformed to a photon polarization final state by means of interaction matrix  $T_\gamma^b$ . It is defined via

$$\begin{pmatrix} O \\ \xi^{(2)} \end{pmatrix} = T_\gamma^b \begin{pmatrix} 1 \\ \zeta^{(1)} \end{pmatrix}, \quad (14.1)$$

and

$$T_\gamma^b \approx \begin{pmatrix} 1 & 0 & 0 & 0 \\ D & 0 & 0 & 0 \\ 0 & 0 & 0 & 0 \\ 0 & T & 0 & L \end{pmatrix}, \quad (14.2)$$

where

$$\begin{aligned} I &= (\epsilon_1^2 + \epsilon_2^2)(3 + 2\Gamma) - 2\epsilon_1\epsilon_2(1 + 4u^2\hat{\xi}^2\Gamma) \\ D &= \left\{ 8\epsilon_1\epsilon_2u^2\hat{\xi}^2\Gamma \right\} / I \\ T &= \left\{ -4k\epsilon_2\hat{\xi}(1 - 2\hat{\xi})u\Gamma \right\} / I \\ L &= k\{(\epsilon_1 + \epsilon_2)(3 + 2\Gamma) - 2\epsilon_2(1 + 4u^2\hat{\xi}^2\Gamma)\} / I \end{aligned} \quad (14.3)$$

and

$\epsilon_1$	Total energy of the incoming lepton $e^+(e^-)$ in units $mc^2$
$\epsilon_2$	Total energy of the outgoing lepton $e^+(e^-)$ in units $mc^2$
$k$	$= (\epsilon_1 - \epsilon_2)$ , the energy of the bremsstrahlung photon in units of $mc^2$
$p$	Electron (positron) initial momentum in units $mc$
$k$	Bremsstrahlung photon momentum in units $mc$
$u$	Component of $p$ perpendicular to $k$ in units $mc$ and $u =  \mathbf{u} $
$\hat{\xi}$	$= 1/(1 + u^2)$

Coulomb and screening effects are contained in  $\Gamma$ , defined as follows

$$\begin{aligned} \Gamma &= \ln \left( \frac{1}{\delta} \right) - 2 - f(Z) + \mathcal{F} \left( \frac{\hat{\xi}}{\delta} \right) \quad \text{for } \Delta \leq 120 \\ \Gamma &= \ln \left( \frac{111}{\hat{\xi}Z^{\frac{1}{3}}} \right) - 2 - f(z) \quad \text{for } \Delta \geq 120 \end{aligned}$$

with

$$\Delta = \frac{12Z^{\frac{1}{3}}\epsilon_1\epsilon_2\hat{\xi}}{121k} \quad \text{with } Z \text{ the atomic number and } \delta = \frac{k}{2\epsilon_1\epsilon_2}$$

$f(Z)$  is the Coulomb correction term derived by Davies, Bethe and Maximon [eal54].  $\mathcal{F}(\hat{\xi}/\delta)$  contains the screening effects and is zero for  $\Delta \leq 0.5$  (No screening effects). For  $0.5 \leq \Delta \leq 120$  (intermediate screening) it is a slowly decreasing function. The  $\mathcal{F}(\hat{\xi}/\delta)$  values versus  $\Delta$  are given in Table 14.1 [KM59] and used with a linear interpolation in between.

The polarization vector of the incoming  $e^- (e^+)$  must be rotated into the frame defined by the scattering plane (x-z-plane) and the direction of the outgoing photon (z-axis). The resulting polarization vector of the bremsstrahlung photon is also given in this frame.

Table 14.1:  $\mathcal{F}(\hat{\xi}/\delta)$  for intermediate values of the screening factor.

$\Delta$	$-\mathcal{F}(\hat{\xi}/\delta) \mid \Delta$	$-\mathcal{F}(\hat{\xi}/\delta)$
0.5	0.0145	40.0
1.0	0.0490	45.0
2.0	0.1400	50.0
4.0	0.3312	60.0
8.0	0.6758	70.0
15.0	1.126	80.0
20.0	1.367	90.0
25.0	1.564	100.0
30.0	1.731	120.0
35.0	1.875	

Using Eq.(14.1) and the transfer matrix given by Eq.(14.2) the bremsstrahlung photon polarization state in the Stokes formalism [McM61, McM54] is given by

$$\xi^{(2)} = \begin{pmatrix} \xi_1^{(2)} \\ \xi_2^{(2)} \\ \xi_3^{(2)} \end{pmatrix} \approx \begin{pmatrix} D \\ 0 \\ \zeta_1^{(1)}L + \zeta_2^{(1)}T \end{pmatrix}$$

#### 14.5.4 Remaining polarization of the lepton after emitting a bremsstrahlung photon

The  $e^- (e^+)$  polarization final state after emitting a bremsstrahlung photon can be calculated using the interaction matrix  $T_l^b$  which describes the lepton depolarization. The polarization vector for the outgoing  $e^- (e^+)$  is not given by Olsen and Maximon. However, their results can be used to calculate the following transfer matrix [Flottmann93b, Hoo97].

$$\begin{pmatrix} O \\ \xi^{(1)} \end{pmatrix} = T_l^b \begin{pmatrix} 1 \\ \zeta^{(1)} \end{pmatrix} \quad (14.4)$$

$$T_l^b \approx \begin{pmatrix} 1 & 0 & 0 & 0 \\ D & M & 0 & E \\ 0 & 0 & M & 0 \\ 0 & F & 0 & M + P \end{pmatrix} \quad (14.5)$$

where

$$\begin{aligned} I &= (\epsilon_1^2 + \epsilon_2^2)(3 + 2\Gamma) - 2\epsilon_1\epsilon_2(1 + 4u^2\hat{\xi}^2\Gamma) \\ F &= \epsilon_2 \left\{ 4k\hat{\xi}u(1 - 2\hat{\xi})\Gamma \right\} / I \\ E &= \epsilon_1 \left\{ 4k\hat{\xi}u(2\hat{\xi} - 1)\Gamma \right\} / I \\ M &= \left\{ 4k\epsilon_1\epsilon_2(1 + \Gamma - 2u^2\hat{\xi}^2\Gamma) \right\} / I \\ P &= \left\{ k^2(1 + 8\Gamma(\hat{\xi} - 0.5)^2) \right\} / I \end{aligned}$$

and

$\epsilon_1$	Total energy of the incoming $e^+/e^-$ in units $mc^2$
$\epsilon_2$	Total energy of the outgoing $e^+/e^-$ in units $mc^2$
$k$	$= (\epsilon_1 - \epsilon_2)$ , energy of the photon in units of $mc^2$
$p$	Electron (positron) initial momentum in units $mc$
$k$	Photon momentum in units $mc$
$u$	Component of $p$ perpendicular to $k$ in units $mc$ and $u =  \mathbf{u} $

Using Eq.(14.4) and the transfer matrix given by Eq.(14.5) the  $e^-(e^+)$  polarization state after emitting a bremsstrahlung photon is given in the Stokes formalism by

$$\xi^{(1)} = \begin{pmatrix} \xi_1^{(1)} \\ \xi_2^{(1)} \\ \xi_3^{(1)} \end{pmatrix} \approx \begin{pmatrix} \zeta_1^{(1)} M + \zeta_3^{(1)} E \\ \zeta_2^{(1)} M \\ \zeta_3^{(1)} (M + P) + \zeta_1^{(1)} F \end{pmatrix}.$$

## 14.6 Polarized Gamma conversion into an electron–positron pair

### 14.6.1 Method

The polarized version of gamma conversion is based on the EM standard process *G4GammaConversion*. Mean free path and the distribution of explicitly generated final state particles are treated by this version. For details consult *Gamma Conversion into e+e- Pair*.

The remaining task is to attribute polarization vectors to the generated final state leptons, which is discussed in the following.

### 14.6.2 Polarization transfer from the photon to the two leptons

Gamma conversion process is essentially the inverse process of bremsstrahlung and the interaction matrix is obtained by inverting the rows and columns of the bremsstrahlung matrix and changing the sign of  $\epsilon_2$ , cf. *Polarized Bremsstrahlung for electron and positron*. It follows from the work by Olsen and Maximon [OM59] that the polarization state  $\xi^{(1)}$  of an electron or positron after pair production is obtained by

$$\begin{pmatrix} O \\ \xi^{(1)} \end{pmatrix} = T_l^p \begin{pmatrix} 1 \\ \zeta^{(1)} \end{pmatrix} \quad (14.6)$$

and

$$T_l^p \approx \begin{pmatrix} 1 & D & 0 & 0 \\ 0 & 0 & 0 & T \\ 0 & 0 & 0 & 0 \\ 0 & 0 & 0 & L \end{pmatrix}, \quad (14.7)$$

where

$$\begin{aligned} I &= (\epsilon_1^2 + \epsilon_2^2)(3 + 2\Gamma) + 2\epsilon_1\epsilon_2(1 + 4u^2\hat{\xi}^2\Gamma) \\ D &= \left\{ -8\epsilon_1\epsilon_2u^2\hat{\xi}^2\Gamma \right\} / I \\ T &= \left\{ -4k\epsilon_2\hat{\xi}(1 - 2\hat{\xi})u\Gamma \right\} / I \\ L &= k\{(\epsilon_1 - \epsilon_2)(3 + 2\Gamma) + 2\epsilon_2(1 + 4u^2\hat{\xi}^2\Gamma)\} / I \end{aligned} \quad (14.8)$$

and

$\epsilon_1$	total energy of the first lepton $e^+(e^-)$ in units $mc^2$
$\epsilon_2$	total energy of the second lepton $e^-(e^+)$ in units $mc^2$
$k = (\epsilon_1 + \epsilon_2)$	energy of the incoming photon in units of $mc^2$
$\mathbf{p}$	electron=positron initial momentum in units $mc$
$\mathbf{k}$	photon momentum in units $mc$
$\mathbf{u}$	electron/positron initial momentum in units $mc$
$u$	$=  \mathbf{u} $

Coulomb and screening effects are contained in  $\Gamma$ , defined in section [Polarized Bremsstrahlung for electron and positron](#).

Using Eq.(14.6) and the transfer matrix given by Eq.(14.7) the polarization state of the produced  $e^-(e^+)$  is given in the Stokes formalism by:

$$\xi^{(1)} = \begin{pmatrix} \xi_1^{(1)} \\ \xi_2^{(1)} \\ \xi_3^{(1)} \end{pmatrix} \approx \begin{pmatrix} \zeta_3^{(1)} T \\ 0 \\ \zeta_3^{(1)} L \end{pmatrix}$$

## 14.7 Polarized Photoelectric Effect

### 14.7.1 Method

This section describes the basic formulas of polarization transfer in the photoelectric effect class (*G4PolarizedPhotoElectricEffect*). The photoelectric effect is the emission of electrons from matter upon the absorption of electromagnetic radiation, such as ultraviolet radiation or x-rays. The energy of the photon is completely absorbed by the electron and, if sufficient, the electron can escape from the material with a finite kinetic energy. A single photon can only eject a single electron, as the energy of one photon is only absorbed by one electron. The electrons that are emitted are often called photoelectrons. If the photon energy is higher than the binding energy the remaining energy is transferred to the electron as a kinetic energy

$$E_{kin}^{e^-} = k - B_{shell}$$

In GEANT4 the photoelectric effect process is taken into account if:

$$k > B_{shell}$$

Where  $k$  is the incoming photon energy and  $B_{shell}$  the electron binding energy provided by the class *G4AtomicShells*.

The polarized version of the photoelectric effect is based on the EM standard process *G4PhotoElectricEffect*. Mean free path and the distribution of explicitly generated final state particles are treated by this version. For details consult section [PhotoElectric Effect](#).

The remaining task is to attribute polarization vectors to the generated final state electron, which is discussed in the following.

## 14.7.2 Polarization transfer

The polarization state of an incoming polarized photon is described by the Stokes vector  $\vec{\zeta}^{(1)}$ . The polarization transfer to the photoelectron can be described in the Stokes formalism using the same approach as for the bremsstrahlung and gamma conversion processes, cf. [Polarized Bremsstrahlung for electron and positron](#) and [Polarized Gamma conversion into an electron–positron pair](#). The relation between the photoelectron’s Stokes parameters and the incoming photon’s Stokes parameters is described by the interaction matrix  $T_l^p$  derived from H. Olsen [[OV58](#)] and reviewed by H.W McMaster [[McM61](#)]:

$$\begin{pmatrix} I' \\ \vec{\zeta}^{(1)} \end{pmatrix} = T_l^p \begin{pmatrix} I_0 \\ \vec{\zeta}^{(1)} \end{pmatrix} \quad (14.9)$$

In general, for the photoelectric effect as a two-body scattering, the cross section should be correlated with the spin states of the incoming photon and the target electron. In our implementation the target electron is not polarized and only the polarization transfer from the photon to the photoelectron is taken into account. In this case the cross section of the process remains polarization independent. To compute the matrix elements we take advantage of the available kinematic variables provided by the generic *G4PhotoelectricEffect* class. To compute the photoelectron spin state (Stokes parameters), four main parameters are needed:

- The incoming photon Stokes vector  $\vec{\zeta}^{(1)}$
- The incoming photon’s energy  $k$ .
- the photoelectron’s kinetic energy  $E_{kin}^{e^-}$  or the Lorentz factors  $\beta$  and  $\gamma$ .
- The photoelectron’s polar angle  $\theta$  or  $\cos \theta$ .

The interaction matrix derived by H. Olsen [[OV58](#)] is given by:

$$T_l^P = \begin{pmatrix} 1+D & -D & 0 & 0 \\ 0 & 0 & 0 & B \\ 0 & 0 & 0 & 0 \\ 0 & 0 & 0 & A \end{pmatrix} \quad (14.10)$$

where

$$\begin{aligned} D &= \frac{1}{k} \left[ \frac{2}{k\epsilon(1-\beta \cos \theta)} - 1 \right] \\ A &= \frac{\epsilon}{\epsilon+1} \left[ \frac{2}{k\epsilon} + \beta \cos \theta + \frac{2}{k\epsilon^2(1-\beta \cos \theta)} \right] \\ B &= \frac{\epsilon}{\epsilon+1} \beta \sin \theta \left[ \frac{2}{k\epsilon(1-\beta \cos \theta)} - 1 \right] \end{aligned}$$

Using Eq.(14.9) and the transfer matrix given by Eq.(14.10) the polarization state of the produced  $e^-$  is given in the Stokes formalism by:

$$\vec{\xi}^{(1)} = \begin{pmatrix} \xi_1^{(1)} \\ \xi_2^{(1)} \\ \xi_3^{(1)} \end{pmatrix} = \begin{pmatrix} \zeta_3^{(1)} B \\ 0 \\ \zeta_3^{(1)} A \end{pmatrix} \quad (14.11)$$

From equation (14.11) one can see that a longitudinally (transversally) polarized photoelectron can only be produced if the incoming photon is circularly polarized.

## 14.8 Compton Scattering by Linearly Polarized Gamma Rays - Livermore Model

### 14.8.1 The Cross Section

The quantum mechanical Klein-Nishina differential cross section for polarized photons is [Hei54]:

$$\frac{d\sigma}{d\Omega} = \frac{1}{2} r_0^2 \frac{h\nu^2}{h\nu_o^2} \left[ \frac{h\nu_o}{h\nu} + \frac{h\nu}{h\nu_o} - \sin^2 \Theta \right]$$

where  $\Theta$  is the angle between the two polarization vectors. In terms of the polar and azimuthal angles ( $\theta, \phi$ ) this cross section can be written as

$$\frac{d\sigma}{d\Omega} = \frac{1}{2} r_0^2 \frac{h\nu^2}{h\nu_o^2} \left[ \frac{h\nu_o}{h\nu} + \frac{h\nu}{h\nu_o} - 2 \cos^2 \phi \sin^2 \theta \right].$$

### 14.8.2 Angular Distribution

The integration of this cross section over the azimuthal angle produces the standard cross section. The angular and energy distribution are then obtained in the same way as for the standard process. Using these values for the polar angle and the energy, the azimuthal angle is sampled from the following distribution [Dep03]:

$$P(\phi) = 1 - 2 \frac{a}{b} \cos^2 \phi$$

where  $a = \sin^2 \theta$  and  $b = \epsilon + 1/\epsilon$ .  $\epsilon$  is the ratio between the scattered photon energy and the incident photon energy.

### 14.8.3 Polarization Vector

The components of the vector polarization of the scattered photon are calculated from [Dep03]:

$$\begin{aligned} \vec{\epsilon}_\perp &= \frac{1}{N} \left( \hat{j} \cos \theta - \hat{k} \sin \theta \sin \phi \right) \sin \beta \\ \vec{\epsilon}_\parallel &= \left[ N \hat{i} - \frac{1}{N} \hat{j} \sin^2 \theta \sin \phi \cos \phi - \frac{1}{N} \hat{k} \sin \theta \cos \theta \cos \phi \right] \cos \beta \end{aligned}$$

where

$$N = \sqrt{1 - \sin^2 \theta \cos^2 \phi}.$$

$\cos \beta$  is calculated from  $\cos \theta = N \cos \beta$ , while  $\cos \theta$  is sampled from the Klein-Nishina distribution.

The binding effects and the Compton profile are neglected. The kinetic energy and momentum of the recoil electron are then

$$\begin{aligned} T_{el} &= E - E' \\ \vec{P}_{el} &= \vec{P}_\gamma - \vec{P}'_\gamma. \end{aligned}$$

The momentum vector of the scattered photon  $\vec{P}_\gamma$  and its polarization vector are transformed into the World coordinate system. The polarization and the direction of the scattered gamma in the final state are calculated in the reference frame in which the incoming photon is along the  $z$ -axis and has its polarization vector along the  $x$ -axis. The transformation to the World coordinate system performs a linear combination of the initial direction, the initial polarization and the cross product between them, using the projections of the calculated quantities along these axes.

#### 14.8.4 Unpolarized Photons

A special treatment is devoted to unpolarized photons. In this case a random polarization in the plane perpendicular to the incident photon is selected.

### 14.9 Pair production by Linearly Polarized Gamma Rays - Livermore Model

A method to study the pair production interaction of linearly polarized gamma rays at energies 50 MeV was discussed in [DKT99]. The study of the differential cross section for pair production shows that the polarization information is coded in the azimuthal distribution of the electron - positron pair created by polarized photons (Fig. 14.25).

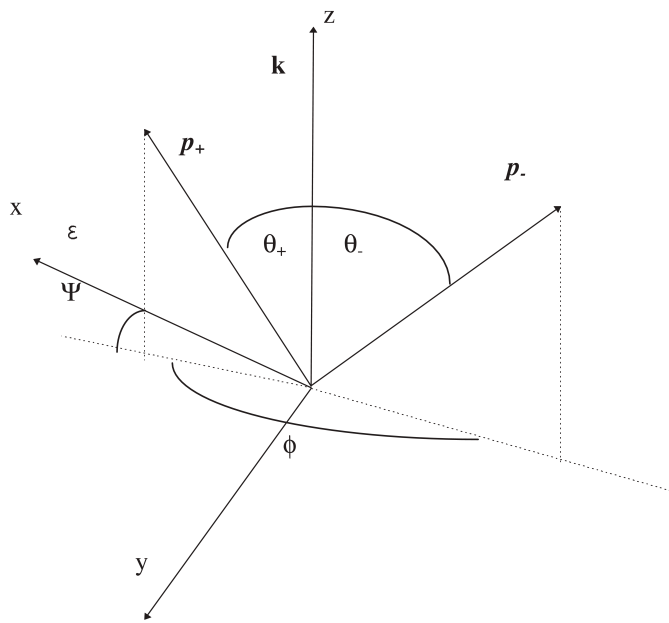


Fig. 14.25: Angles occurring in the pair creation

#### 14.9.1 Relativistic cross section for linearly polarized gamma ray

The cross section for pair production by linearly polarized gamma rays in the high energy limit using natural units with  $h/2\pi = c = 1$  is

$$d\sigma = \frac{-2\alpha Z^2 r_0 m^2}{(2\pi)^2 \omega^3} dE d\Omega_+ d\Omega_- \frac{E(\omega - E)}{|\vec{q}|^4} \left\{ 4 \left[ E \frac{\sin \theta_- \cos \Psi}{1 - \cos \theta_-} + (\omega - E) \frac{\sin \theta_+ \cos (\Psi + \phi)}{1 - \cos \theta_+} \right]^2 - |\vec{q}|^2 \left[ \frac{\sin \theta_- \cos \Psi}{1 - \cos \theta_-} - \frac{\sin \theta_+ \cos (\Psi + \phi)}{1 - \cos \theta_+} \right]^2 - \omega^2 \frac{\sin \theta_- \sin \theta_+}{(1 - \cos \theta_-)(1 - \cos \theta_+)} \left[ \frac{E \sin \theta_+}{(\omega_E) \sin \theta_-} + \frac{(\omega - E) \sin \theta_-}{E \sin \theta_+} + 2 \cos \phi \right] \right\},$$

with

$$|\vec{q}|^2 = -2 [E(\omega - E)(1 - \sin \theta_+ \sin \theta_- \cos \phi - \cos \theta_+ \cos \theta_-) + \omega E(\cos \theta_+ - 1) + \omega(\omega - E)(\cos \theta_- - 1) + m^2].$$

$E$  is the positron energy and we have assumed that the polarization direction is along the  $x$  axis (see Fig. 14.25).

### 14.9.2 Spatial azimuthal distribution

Integrating this cross section over energy and polar angles yields the spatial azimuthal distribution, that was calculated in [DKT99] using a Monte Carlo procedure.

Fig. 14.26 shows an example of this distribution for 100 MeV gamma-ray. In this figure the range of the  $\phi$  axis is restricted between 3.0 and  $\pi$  since it gives the most interesting part of the distribution. For angles smaller than 3.0 this distribution monotonically decreases to zero.

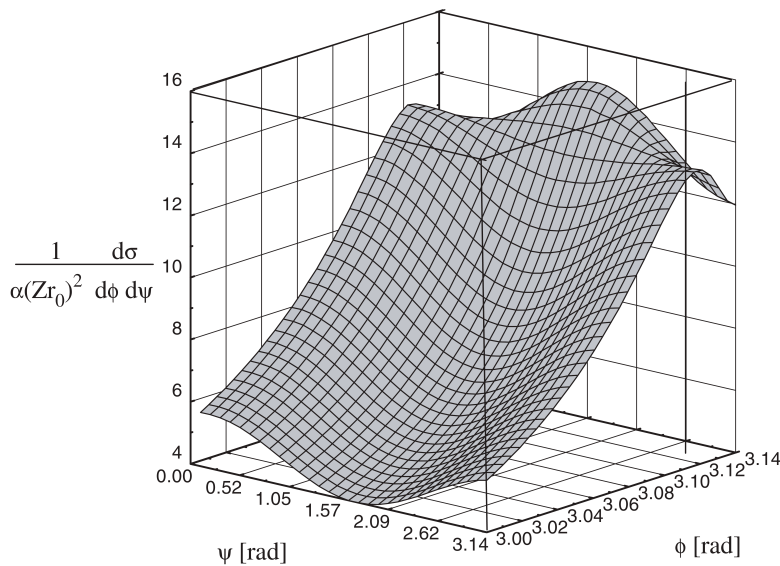


Fig. 14.26: Spatial azimuthal distribution of a pair created by 100 MeV photon

In GEANT4 the azimuthal distribution surface is parametrized in terms of smooth functions of  $(\phi, \psi)$ .

$$f(\phi, \psi) = f_{\pi/2}(\phi) \sin^2 \psi + f_0(\phi) \cos^2 \psi .$$

Since both  $f_0(\phi)$  and  $f_{\pi/2}(\phi)$  are functions that rapidly vary when  $\phi$  approaches  $\pi$ , it was necessary to adjust the functions in two ranges of  $\phi$ :

1.  $0 \leq \phi \leq 3.05$  rad.
2.  $3.06 \text{ rad} \leq \phi \leq \pi$ ,

whereas in the small range  $3.05 \leq \phi \leq 3.06$  we extrapolate the two fitting functions until the intersection point is reached.

In region 2 we used Lorentzian functions of the form

$$f(\phi) = y_0 + \frac{2A\omega}{\pi[\omega^2 + 4(\phi - x_c)^2]} ,$$

whereas for region 1 the best fitting function was found to adopt the form:

$$f(\phi) = a + d \tan(b\phi + c) .$$

The paper [DKT99] reports the coefficients obtained in different energy regions to fit the angular distribution and their function form as function of gamma-ray as energy reported in the Table 14.2 and Table 14.3 below.

Table 14.2: Fit for the parameter of  $f_0(\phi)$  function.

Parameter	Function	a	b	c
$y_0$	$a \ln E - b$	$2.98 \pm 0.06$	$7.7 \pm 0.4$	–
$A$	$a \ln E - b$	$1.41 \pm 0.08$	$5.6 \pm 0.5$	–
$\omega$	$a + b/E + c/E^3$	$0.015 \pm 0.001$	$9.5 \pm 0.6$	$(-2.2 \pm 0.1)10^4$
$x_c$	$a + b/E + c/E^3$	$3.143 \pm 0.001$	$-2.7 \pm 0.2$	$(2 \pm 1)10^3$

Table 14.3: Fit for the parameter of  $f_{\pi/2}(\phi)$  function.

Parameter	Function	a	b	c
$y_0$	$a \ln E - b$	$1.85 \pm 0.07$	$5.1 \pm 0.4$	–
$A$	$a \ln E - b$	$1.3 \pm 0.1$	$(6.6 \pm 0.2)10^{-3}$	–
$\omega$	$a + b/E + c/E^3$	$0.008 \pm 0.002$	$12.1 \pm 0.9$	$(-2.8 \pm 0.8)10^4$
$x_c$	3.149	–	–	–

### 14.9.3 Unpolarized Photons

A special treatment is devoted to unpolarized photons. In this case a random polarization in the plane perpendicular to the incident photon is selected.

## 14.10 Pair production by Linearly Polarized Gamma Rays - Five-dimensional (5D) Bethe-Heitler Model

The *G4BetheHeitler5DModel* described in [Five-dimensional \(5D\) Bethe-Heitler gamma Conversion to e+e-](#) can generate the conversion of either linearly polarized photons or non-polarized photons. The performance is compared to that of other models in [GB17b]. If the optimal estimate of the event azimuthal angle is used, that is, the bisector  $\phi_{+-} \equiv (\phi_+ + \phi_-)/2$  of the electron azimuthal angle  $\phi_-$  and of the positron azimuthal angle  $\phi_+$  [GB17a], the *G4BetheHeitler5DModel* is the only physics model with which the polarization asymmetry of nuclear conversion is verified to be compatible with the low-energy [GB17a] and with the high-energy [BP71] asymptotic expressions, that have been obtained from partial integration of the Bethe-Heitler differential cross section.

As expected (eg. from [May51, OM59]), the electron and the positron are preferentially emitted in the polarization plane (if azimuthal angles are measured from the polarization plane, the single-lepton azimuthal angles  $\phi_-$  and  $\phi_+$  take their maximum at zero). Accordingly, the bisector  $\phi_{+-}$  and the recoil azimuthal angle  $\phi_r$  take their maximum at  $\pm\pi/2$ .

The polarization asymmetry is optimally extracted from the average value of a weight computed from the azimuthal angle of the event [Ber13, GB17a].

See also the extended electromagnetic example *TestEm15*.

## X-RAY PRODUCTION

### 15.1 Transition radiation

#### 15.1.1 The Relationship of Transition Radiation to X-ray Čerenkov Radiation

X-ray transition radiation (XTR) occurs when a relativistic charged particle passes from one medium to another of a different dielectric permittivity. In order to describe this process it is useful to begin with an explanation of X-ray Čerenkov radiation, which is closely related.

The mean number of X-ray Čerenkov radiation (XCR) photons of frequency  $\omega$  emitted into an angle  $\theta$  per unit distance along a particle trajectory is [Gri02b]:

$$\frac{d^3 \bar{N}_{xcr}}{\hbar d\omega dx d\theta^2} = \frac{\alpha}{\pi \hbar c} \frac{\omega}{c} \theta^2 \text{Im}\{Z\}. \quad (15.1)$$

Here the quantity  $Z$  is introduced as the *complex formation zone* of XCR in the medium:

$$Z = \frac{L}{1 - i \frac{L}{l}}, \quad L = \frac{c}{\omega} \left[ \gamma^{-2} + \frac{\omega_p^2}{\omega^2} + \theta^2 \right]^{-1}, \quad \gamma^{-2} = 1 - \beta^2. \quad (15.2)$$

with  $l$  and  $\omega_p$  the photon absorption length and the plasma frequency, respectively, in the medium. For the case of a transparent medium,  $l \rightarrow \infty$  and the complex formation zone reduces to the *coherence length*  $L$  of XCR. The coherence length roughly corresponds to that part of the trajectory in which an XCR photon can be created.

Introducing a complex quantity  $Z$  with its imaginary part proportional to the absorption cross-section ( $\sim l^{-1}$ ) is required in order to account for absorption in the medium. Usually,  $\omega_p^2/\omega^2 \gg c/\omega l$ . Then it can be seen from Eqs. (15.1) and (15.2) that the number of emitted XCR photons is considerably suppressed and disappears in the limit of a transparent medium. This is caused by the destructive interference between the photons emitted from different parts of the particle trajectory.

The destructive interference of X-ray Čerenkov radiation is removed if the particle crosses a boundary between two media with different dielectric permittivities,  $\epsilon$ , where

$$\epsilon = 1 - \frac{\omega_p^2}{\omega^2} + i \frac{c}{\omega l}.$$

Here the standard high-frequency approximation for the dielectric permittivity has been used. This is valid for energy transfers larger than the  $K$ -shell excitation potential.

If layers of media are alternated with spacings of order  $L$ , the X-ray radiation yield from a trajectory of unit length can be increased by roughly  $l/L$  times. The radiation produced in this case is called X-ray transition radiation (XTR).

### 15.1.2 Calculating the X-ray Transition Radiation Yield

Using the methods developed in Ref.[Gri02b] one can derive the relation describing the mean number of XTR photons generated per unit photon frequency and  $\theta^2$  *inside* the radiator for a general XTR radiator consisting of  $n$  different absorbing media with fluctuating thicknesses:

$$\frac{d^2\bar{N}_{in}}{\hbar d\omega d\theta^2} = \frac{\alpha}{\pi\hbar c^2}\omega\theta^2\text{Re} \left\{ \sum_{i=1}^{n-1}(Z_i - Z_{i+1})^2 + 2\sum_{k=1}^{n-1}\sum_{i=1}^{k-1}(Z_i - Z_{i+1}) \left[ \prod_{j=i+1}^k F_j \right] (Z_k - Z_{k+1}) \right\},$$

$$F_j = \exp \left[ -\frac{t_j}{2Z_j} \right].$$

In the case of gamma distributed gap thicknesses (foam or fiber radiators) the values  $F_j$ , ( $j = 1, 2$ ) can be estimated as:

$$F_j = \int_0^\infty dt_j \left( \frac{\nu_j}{\bar{t}_j} \right)^{\nu_j} \frac{t_j^{\nu_j-1}}{\Gamma(\nu_j)} \exp \left[ -\frac{\nu_j t_j}{\bar{t}_j} - i\frac{t_j}{2Z_j} \right] = \left[ 1 + i\frac{\bar{t}_j}{2Z_j \nu_j} \right]^{-\nu_j},$$

where  $Z_j$  is the complex formation zone of XTR (similar to relation (15.2) for XCR) in the  $j$ -th medium [eal00, Gri02a].  $\Gamma$  is the Euler gamma function,  $\bar{t}_j$  is the mean thickness of the  $j$ -th medium in the radiator and  $\nu_j > 0$  is the parameter roughly describing the relative fluctuations of  $t_j$ . In fact, the relative fluctuation is  $\delta t_j / \bar{t}_j \sim 1/\sqrt{\nu_j}$ .

In the particular case of  $n$  foils of the first medium ( $Z_1, F_1$ ) interspersed with gas gaps of the second medium ( $Z_2, F_2$ ), one obtains:

$$\frac{d^2\bar{N}_{in}}{\hbar d\omega d\theta^2} = \frac{2\alpha}{\pi\hbar c^2}\omega\theta^2\text{Re} \left\{ \langle R^{(n)} \rangle \right\}, \quad F = F_1 F_2, \quad (15.3)$$

$$\langle R^{(n)} \rangle = (Z_1 - Z_2)^2 \left\{ n \frac{(1 - F_1)(1 - F_2)}{1 - F} + \frac{(1 - F_1)^2 F_2 [1 - F^n]}{(1 - F)^2} \right\}. \quad (15.4)$$

Here  $\langle R^{(n)} \rangle$  is the stack factor reflecting the radiator geometry. The integration of ((15.3)) with respect to  $\theta^2$  can be simplified for the case of a regular radiator ( $\nu_{1,2} \rightarrow \infty$ ), transparent in terms of XTR generation media, and  $n \gg 1$  [Gar71]. The frequency spectrum of emitted XTR photons is given by:

$$\frac{d\bar{N}_{in}}{\hbar d\omega} = \int_0^{\sim 10\gamma^{-2}} d\theta^2 \frac{d^2\bar{N}_{in}}{\hbar d\omega d\theta^2} = \frac{4\alpha n}{\pi\hbar\omega} (C_1 + C_2)^2 \cdot \sum_{k=k_{min}}^{k_{max}} \frac{(k - C_{min})}{(k - C_1)^2(k + C_2)^2} \sin^2 \left[ \frac{\pi t_1}{t_1 + t_2} (k + C_2) \right], \quad (15.5)$$

$$C_{1,2} = \frac{t_{1,2}(\omega_1^2 - \omega_2^2)}{4\pi c\omega}, \quad C_{min} = \frac{1}{4\pi c} \left[ \frac{\omega(t_1 + t_2)}{\gamma^2} + \frac{t_1\omega_1^2 + t_2\omega_2^2}{\omega} \right].$$

The sum in (15.5) is defined by terms with  $k \geq k_{min}$  corresponding to the region of  $\theta \geq 0$ . Therefore  $k_{min}$  should be the nearest to  $C_{min}$  integer  $k_{min} \geq C_{min}$ . The value of  $k_{max}$  is defined by the maximum emission angle  $\theta_{max}^2 \sim 10\gamma^{-2}$ . It can be evaluated as the integer part of

$$C_{max} = C_{min} + \frac{\omega(t_1 + t_2)}{4\pi c} \frac{10}{\gamma^2}, \quad k_{max} - k_{min} \sim 10^2 - 10^3 \gg 1.$$

Numerically, however, only a few tens of terms contribute substantially to the sum, that is, one can choose  $k_{max} \sim k_{min} + 20$ . Eq.(15.5) corresponds to the spectrum of the total number of photons emitted inside a regular transparent radiator. Therefore the mean interaction length,  $\lambda_{XTR}$ , of the XTR process in this kind of radiator can be introduced as:

$$\lambda_{XTR} = n(t_1 + t_2) \left[ \int_{\hbar\omega_{min}}^{\hbar\omega_{max}} \hbar d\omega \frac{d\bar{N}_{in}}{\hbar d\omega} \right]^{-1},$$

where  $\hbar\omega_{min} \sim 1$  keV, and  $\hbar\omega_{max} \sim 100$  keV for the majority of high energy physics experiments. Its value is constant along the particle trajectory in the approximation of a transparent regular radiator. The spectrum of the total number of XTR photons *after* regular transparent radiator is defined by (15.5) with:

$$n \rightarrow n_{eff} = \sum_{k=0}^{n-1} \exp[-k(\sigma_1 t_1 + \sigma_2 t_2)] = \frac{1 - \exp[-n(\sigma_1 t_1 + \sigma_2 t_2)]}{1 - \exp[-(\sigma_1 t_1 + \sigma_2 t_2)]},$$

where  $\sigma_1$  and  $\sigma_2$  are the photo-absorption cross-sections corresponding to the photon frequency  $\omega$  in the first and the second medium, respectively. With this correction taken into account the XTR absorption in the radiator ((15.5)) corresponds to the results of [FS75]. In the more general case of the flux of XTR photons *after* a radiator, the XTR absorption can be taken into account with a calculation based on the stack factor derived in [GMGY75]:

$$\langle R_{flux}^{(n)} \rangle = (L_1 - L_2)^2 \left\{ \frac{1 - Q^n}{1 - Q} \frac{(1 + Q_1)(1 + F) - 2F_1 - 2Q_1 F_2}{2(1 - F)} \frac{(1 - F_1)(Q_1 - F_1)F_2(Q^n - F^n)}{(1 - F)(Q - F)} \right\}, \quad (15.6)$$

$$Q = Q_1 \cdot Q_2, \quad Q_j = \exp[-t_j/l_j] = \exp[-\sigma_j t_j], \quad j = 1, 2.$$

Both XTR energy loss (15.4) and flux (15.6) models can be implemented as a discrete electromagnetic process (see below).

### 15.1.3 Simulating X-ray Transition Radiation Production

A typical XTR radiator consists of many ( $\sim 100$ ) boundaries between different materials. To improve the tracking performance in such a volume one can introduce an artificial material [eal00], which is the geometrical mixture of foil and gas contents. Here is an example:

```
// In DetectorConstruction of an application
// Preparation of mixed radiator material
foilGasRatio = fRadThickness/(fRadThickness+fGasGap);
foilDensity = 1.39*g/cm3; // Mylar
gasDensity = 1.2928*mg/cm3 ; // Air
totDensity = foilDensity*foilGasRatio +
             gasDensity*(1.0-foilGasRatio);
fractionFoil = foilDensity*foilGasRatio/totDensity;
fractionGas = gasDensity*(1.0-foilGasRatio)/totDensity;
G4Material* radiatorMat = new G4Material("radiatorMat",
                                         totDensity,
                                         ncomponents = 2 );
radiatorMat->AddMaterial( Mylar, fractionFoil );
radiatorMat->AddMaterial( Air, fractionGas );
G4cout << *(G4Material::GetMaterialTable()) << G4endl;
// materials of the TR radiator
fRadiatorMat = radiatorMat; // artificial for geometry
fFoilMat     = Mylar;
fGasMat      = Air;
```

This artificial material will be assigned to the logical volume in which XTR will be generated:

```
solidRadiator = new G4Box("Radiator",
                           1.1*AbsorberRadius ,
                           1.1*AbsorberRadius,
                           0.5*radThick );
logicRadiator = new G4LogicalVolume( solidRadiator,
                                     fRadiatorMat, // !!!
                                     "Radiator");
physiRadiator = new G4PVPlacement(0,
```

(continues on next page)

(continued from previous page)

```
G4ThreeVector(0,0,zRad),
"Radiator", logicRadiator,
physiWorld, false, 0 );
```

XTR photons generated by a relativistic charged particle intersecting a radiator with  $2n$  interfaces between different media can be simulated by using the following algorithm. First the total number of XTR photons is estimated using a Poisson distribution about the mean number of photons given by the following expression:

$$\bar{N}^{(n)} = \int_{\omega_1}^{\omega_2} d\omega \int_0^{\theta_{max}^2} d\theta^2 \frac{d^2 \bar{N}^{(n)}}{d\omega d\theta^2} = \frac{2\alpha}{\pi c^2} \int_{\omega_1}^{\omega_2} \omega d\omega \int_0^{\theta_{max}^2} \theta^2 d\theta^2 \text{Re} \left\{ \langle R^{(n)} \rangle \right\}.$$

Here  $\theta_{max}^2 \sim 10\gamma^{-2}$ ,  $\hbar\omega_1 \sim 1$  keV,  $\hbar\omega_2 \sim 100$  keV, and  $\langle R^{(n)} \rangle$  correspond to the geometry of the experiment. For events in which the number of XTR photons is not equal to zero, the energy and angle of each XTR quantum is sampled from the integral distributions obtained by the numerical integration of expression (15.3). For example, the integral energy spectrum of emitted XTR photons,  $\bar{N}_{>\omega}^{(n)}$ , is defined from the following integral distribution:

$$\bar{N}_{>\omega}^{(n)} = \frac{2\alpha}{\pi c^2} \int_{\omega}^{\omega_2} \omega d\omega \int_0^{\theta_{max}^2} \theta^2 d\theta^2 \text{Re} \left\{ \langle R^{(n)} \rangle \right\}.$$

In GEANT4 XTR generation *inside* or *after* radiators is described as a discrete electromagnetic process. It is convenient for the description of tracks in magnetic fields and can be used for the cases when the radiating charge experiences a scattering inside the radiator. The base class G4VXTRenergyLoss is responsible for the creation of tables with integral energy and angular distributions of XTR photons. It also contains the PostDoIt function providing XTR photon generation and motion (if fExitFlux=true) through a XTR radiator to its boundary. Particular models like G4RegularXTRadiation implement the pure virtual function GetStackFactor, which calculates the response of the XTR radiator reflecting its geometry. Included below are some comments for the declaration of XTR in a user application.

In the physics list one should pass to the XTR process additional details of the XTR radiator involved:

```
// In PhysicsList of an application
else if (particleName == "e-") // Construct processes for electron with XTR
{
    pmanager->AddProcess(new G4MultipleScattering, -1, 1, 1 );
    pmanager->AddProcess(new G4eBremsstrahlung(), -1, -1, 1 );
    pmanager->AddProcess(new Em10StepCut(), -1, -1, 1 );
// in regular radiators:
    pmanager->AddDiscreteProcess(
        new G4RegularXTRadiation // XTR dEdx in general regular radiator
// new G4XTRRegularRadModel - XTR flux after general regular radiator
// new G4TransparentRegXTRadiation - XTR dEdx in transparent
// regular radiator
// new G4XTRTransparentRegRadModel - XTR flux after transparent
// regular radiator
        (pDet->GetLogicalRadiator(), // XTR radiator
         pDet->GetFoilMaterial(), // real foil
         pDet->GetGasMaterial(), // real gas
         pDet->GetFoilThick(), // real geometry
         pDet->GetGasThick(),
         pDet->GetFoilNumber(),
         "RegularXTRadiation"));
// or for foam/fiber radiators:
    pmanager->AddDiscreteProcess(
        new G4GammaXTRadiation // - XTR dEdx in general foam/fiber radiator
// new G4XTRGammaRadModel - XTR flux after general foam/fiber radiator
        ( pDet->GetLogicalRadiator(),
```

(continues on next page)

(continued from previous page)

```

1000.,
100.,
pDet->GetFoilMaterial(),
pDet->GetGasMaterial(),
pDet->GetFoilThick(),
pDet->GetGasThick(),
pDet->GetFoilNumber(),
"GammaXTRadiator"));
}

```

Here for the foam/fiber radiators the values 1000 and 100 are the  $\nu$  parameters (which can be varied) of the Gamma distribution for the foil and gas gaps, respectively. Classes G4TransparentRegXTRadiator and G4XTRTransparentRegRadModel correspond (15.5) to  $n$  and  $n_{eff}$ , respectively.

## 15.2 Scintillation

Every scintillating material has a characteristic light yield,  $Y$ , [photons/MeV], and an intrinsic resolution which generally broadens the statistical distribution,  $\sigma_i/\sigma_s > 1$ , due to impurities which are typical for doped crystals like NaI(Tl) and CsI(Tl). The average yield can have a non-linear dependence on the local energy deposition. Scintillators also have a time distribution spectrum with one or more exponential decay time constants,  $\tau_i$ , with each decay component having its intrinsic photon emission spectrum. These are empirical parameters typical for each material.

The generation of scintillation light can be simulated by sampling the number of photons from a Poisson distribution. This distribution is based on the energy lost during a step in a material and on the scintillation properties of that material. The frequency of each photon is sampled from the empirical spectra. The photons are generated evenly along the track segment and are emitted uniformly into  $4\pi$  with a random linear polarization.

## 15.3 Čerenkov Effect

The radiation of Čerenkov light occurs when a charged particle moves through a dispersive medium faster than the speed of light in that medium. A dispersive medium is one whose index of refraction is an increasing function of photon energy. Two things happen when such a particle slows down:

1. a cone of Čerenkov photons is emitted, with the cone angle (measured with respect to the particle momentum) decreasing as the particle loses energy;
2. the momentum of the photons produced increases, while the number of photons produced decreases.

When the particle velocity drops below the local speed of light, photons are no longer emitted. At that point, the Čerenkov cone collapses to zero. In order to simulate Čerenkov radiation the number of photons per track length must be calculated. The formulae used for this calculation can be found below and in [JDJackson98, eal00]. Let  $n$  be the refractive index of the dielectric material acting as a radiator. Here  $n = c/c'$  where  $c'$  is the group velocity of light in the material, hence  $1 \leq n$ . In a dispersive material  $n$  is an increasing function of the photon energy  $\epsilon$  ( $dn/d\epsilon \geq 0$ ). A particle traveling with speed  $\beta = v/c$  will emit photons at an angle  $\theta$  with respect to its direction, where  $\theta$  is given by

$$\cos \theta = \frac{1}{\beta n}.$$

From this follows the limitation for the momentum of the emitted photons:

$$n(\epsilon_{min}) = \frac{1}{\beta}.$$

Photons emitted with an energy beyond a certain value are immediately re-absorbed by the material; this is the window of transparency of the radiator. As a consequence, all photons are contained in a cone of opening angle  $\cos \theta_{max} = 1/(\beta n(\epsilon_{max}))$ . The average number of photons produced is given by the relations:

$$\begin{aligned} dN &= \frac{\alpha z^2}{\hbar c} \sin^2 \theta d\epsilon dx = \frac{\alpha z^2}{\hbar c} \left(1 - \frac{1}{n^2 \beta^2}\right) d\epsilon dx \\ &\approx 370 z^2 \frac{\text{photons}}{\text{eV cm}} \left(1 - \frac{1}{n^2 \beta^2}\right) d\epsilon dx \end{aligned}$$

and the number of photons generated per track length is

$$\frac{dN}{dx} \approx 370 z^2 \int_{\epsilon_{min}}^{\epsilon_{max}} d\epsilon \left(1 - \frac{1}{n^2 \beta^2}\right) = 370 z^2 \left[ \epsilon_{max} - \epsilon_{min} - \frac{1}{\beta^2} \int_{\epsilon_{min}}^{\epsilon_{max}} \frac{d\epsilon}{n^2(\epsilon)} \right].$$

The number of photons produced is calculated from a Poisson distribution with a mean of  $\langle n \rangle = \text{StepLength } dN/dx$ . The energy distribution of the photon is then sampled from the density function

$$f(\epsilon) = \left[1 - \frac{1}{n^2(\epsilon) \beta^2}\right].$$

## 15.4 Synchrotron Radiation

### 15.4.1 Photon spectrum

Synchrotron radiation photons are emitted by relativistic charged particles traveling in magnetic fields. The properties of synchrotron radiation are well understood and described in textbooks [Hof04, JDJackson98, ST86].

In the simplest case, we have an electron of momentum  $p$  moving perpendicular to a homogeneous magnetic field  $B$ . The magnetic field will keep the particle on a circular path, with radius

$$\rho = \frac{p}{eB} = \frac{m\gamma\beta c}{eB}. \quad \text{Numerically we have} \quad \rho[\text{m}] = p[\text{GeV}/c] \frac{3.336 \text{ m}}{B[\text{T}]}. \quad (15.7)$$

In general, there will be an arbitrary angle  $\theta$  between the local magnetic field  $\mathbf{B}$  and momentum vector  $\mathbf{p}$  of the particle. The motion has a circular component in the plane perpendicular to the magnetic field, and in addition a constant momentum component parallel to the magnetic field. For a constant homogeneous field, the resulting trajectory is a helix.

The critical energy of the synchrotron radiation can be calculated using the radius  $\rho$  of Eq.(15.7) and angle  $\theta$  or the magnetic field perpendicular to the particle direction  $B_\perp = B \sin \theta$  according to

$$E_c = \frac{3}{2} \hbar c \frac{\gamma^3 \sin \theta}{\rho} = \frac{3 \hbar}{2m} \gamma^2 e B_\perp. \quad (15.8)$$

Half of the synchrotron radiation power is radiated by photons above the critical energy.

With  $x$  we denote the photon energy  $E_\gamma$ , expressed in units of the critical energy  $E_c$

$$x = \frac{E_\gamma}{E_c}. \quad (15.9)$$

The photon spectrum (number of photons emitted per path length  $s$  and relative energy  $x$ ) can be written as

$$\frac{d^2 N}{ds dx} = \frac{\sqrt{3} \alpha}{2\pi} \frac{e B_\perp}{mc} \int_x^\infty K_{5/3}(\xi) d\xi \quad (15.10)$$

where  $\alpha = e^2 / 4\pi\epsilon_0\hbar c$  is the dimensionless electromagnetic coupling (or fine structure) constant and  $K_{5/3}$  is the modified Bessel function of the third kind.

The number of photons emitted per unit length and the mean free path  $\lambda$  between two photon emissions is obtained by integration over all photon energies. Using

$$\int_0^\infty dx \int_x^\infty K_{5/3}(\xi) d\xi = \frac{5\pi}{3}$$

we find that

$$\frac{dN}{ds} = \frac{5\alpha}{2\sqrt{3}} \frac{eB_\perp}{m\beta c} = \frac{1}{\lambda}.$$

Here we are only interested in ultra-relativistic ( $\beta \approx 1$ ) particles, for which  $\lambda$  only depends on the field  $B$  and not on the particle energy. We define a constant  $\lambda_B$  such that

$$\lambda = \frac{\lambda_B}{B_\perp} \quad \text{where} \quad \lambda_B = \frac{2\sqrt{3}}{5} \frac{mc}{\alpha e} = 0.16183 \text{ Tm}.$$

As an example, consider a 10 GeV electron, travelling perpendicular to a 1T field. It moves along a circular path of radius  $\rho = 33.356$  m. For the Lorentz factor we have  $\gamma = 19569.5$  and  $\beta = 1 - 1.4 \times 10^{-9}$ . The critical energy is  $E_c = 66.5$  keV and the mean free path between two photon emissions is  $\lambda = 0.16183$  m.

## 15.4.2 Validity

The spectrum given in Eq.(15.10) can generally be expected to provide a very accurate description for the synchrotron radiation spectrum generated by GeV electrons in magnetic fields.

Here we discuss some known limitations and possible extensions.

For particles traveling on a circular path, the spectrum observed in one location will in fact not be a continuous spectrum, but a discrete spectrum, consisting only of harmonics or modes  $n$  of the revolution frequency. In practice, the mode numbers will generally be too high to make this a visible effect. The critical mode number corresponding to the critical energy is  $n_c = 3/2\gamma^3$ . 10GeV electrons for example have  $n_c \approx 10^{13}$ .

Synchrotron radiation can be neglected for slower particles and only becomes relevant for ultra-relativistic particles with  $\gamma > 10^3$ . Using  $\beta = 1$  introduces an uncertainty of about  $1/2\gamma^2$  or less than  $5 \times 10^{-7}$ .

The implementation of synchrotron radiation is not restricted to electrons and applies to any long lived charged particle including ions. The number of photons generated scales with the charge squared [Bur98]. The effects of synchrotron radiation from protons and ions are visible in the LHC and have been considered as source of background in FCC-hh studies [CBBK17]. The number of photons and the power scales with the square of the charge.

The standard synchrotron spectrum of Eq.(15.10) is only valid as long as the photon energy remains small compared to the particle energy [eal71, TEL82]. This is a very safe assumption for GeV electrons and standard magnets with fields of order of Tesla.

An extension of synchrotron radiation to fields exceeding several hundred Tesla, such as those present in the beam-beam interaction in linear-colliders, is also known as beamstrahlung. For an introduction see [Che86].

The standard photon spectrum applies to homogeneous fields and remains a good approximation for magnetic fields which remain approximately constant over a the length  $\rho/\gamma$ , also known as the formation length for synchrotron radiation. Short magnets and edge fields will result instead in more energetic photons than predicted by the standard spectrum.

We also note that short bunches of many particles will start to radiate coherently like a single particle of the equivalent charge at wavelengths which are longer than the bunch dimensions.

Low energy, long-wavelength synchrotron radiation may destructively interfere with conducting surfaces [JBMG97].

The soft part of the synchrotron radiation spectrum emitted by charged particles travelling through a medium will be modified for frequencies close to and lower than the plasma frequency [Gri02].

### 15.4.3 Direct inversion and generation of the photon energy spectrum

The task is to find an algorithm that effectively transforms the flat distribution given by standard pseudo-random generators into the desired distribution proportional to the expressions given in Eqs.(15.10),(15.11). The transformation is obtained from the inverse  $F^{-1}$  of the cumulative distribution function  $F(x) = \int_0^x f(t)dt$ .

Leaving aside constant factors, the probability density function relevant for the photon energy spectrum is

$$\text{SynRad}(x) = \int_x^\infty K_{5/3}(t)dt . \quad (15.11)$$

Numerical methods to evaluate  $K_{5/3}$  are discussed in [Luk75]. An efficient algorithm to evaluate the integral SynRad using Chebyshev polynomials is described in [HHUUmstatter81]. This has been used in an earlier version of the Monte Carlo generator for synchrotron radiation using approximate transformations and the rejection method [Bur90].

The cumulative distribution function is the integral of the probability density function. Here we have

$$\text{SynRadInt}(z) = \int_z^\infty \text{SynRad}(x) dx , \quad (15.12)$$

with normalization

$$\text{SynRadInt}(0) = \int_0^\infty \text{SynRad}(x) dx = \frac{5\pi}{3} ,$$

such that  $\frac{3}{5\pi}\text{SynRadInt}(x)$  gives the fraction of photons above  $x$ .

It is possible to directly obtain the desired distribution with a fast and accurate algorithm using an analytical description based on simple transformations and Chebyshev polynomials. This approach is used here.

We now describe in some detail how the analytical description was obtained. For more details see [Bur].

It turned out to be convenient to start from the normalized complement rather than Eq.(15.12) directly, that is

$$\text{SynFracInt}(x) = \frac{3}{5\pi} \int_0^x \int_x^\infty K_{5/3}(t)dt dx = 1 - \frac{3}{5\pi} \text{SynRadInt}(x) ,$$

which gives the fraction of photons below  $x$ .

Fig. 15.1 shows  $y = \text{SynFracInt}(x)$  and Fig. 15.2 the inverse  $x = \text{InvSynFracInt}(y)$  together with simple approximate functions. We can see, that SynFracInt can be approximated by  $x^{1/3}$  for small arguments, and by  $1 - e^{-x}$  for large  $x$ . Consequently, we have for the inverse, InvSynFracInt( $y$ ), which can be approximated for small  $y$  by  $y^3$  and for large  $y$  by  $-\log(1 - y)$ .

Good convergence for InvSynFracInt( $y$ ) was obtained using Chebyshev polynomials combined with the approximate expressions for small and large arguments. For intermediate values, a Chebyshev polynomial can be used directly. Table 15.1 summarizes the expressions used in the different intervals.

Table 15.1: Expressions used in calculation of InvSynFracInt for different intervals.

$y$	$x = \text{InvSynFracInt}(y)$
$y < 0.7$	$y^3 P_{\text{Ch}}(y)$
$0.7 \leq y \leq 0.9999$	$P_{\text{Ch}}(y)$
$y > 0.9999$	$-\log(1 - y)P_{\text{Ch}}(-\log(1 - y))$

The procedure for Monte Carlo simulation is to generate  $y$  at random uniformly distributed between 0 at 1, as provided by standard random generators, and then to calculate the energy  $x$  in units of the critical energy according to  $x = \text{InvSynFracInt}(y)$ .

The numerical accuracy of the energy spectrum presented here is about 14 decimal places, close to the machine precision. Fig. 15.3 shows a comparison of generated and expected spectra.

A GEANT4 display of an electron moving in a magnetic field radiating synchrotron photons is presented in Fig. 15.4.

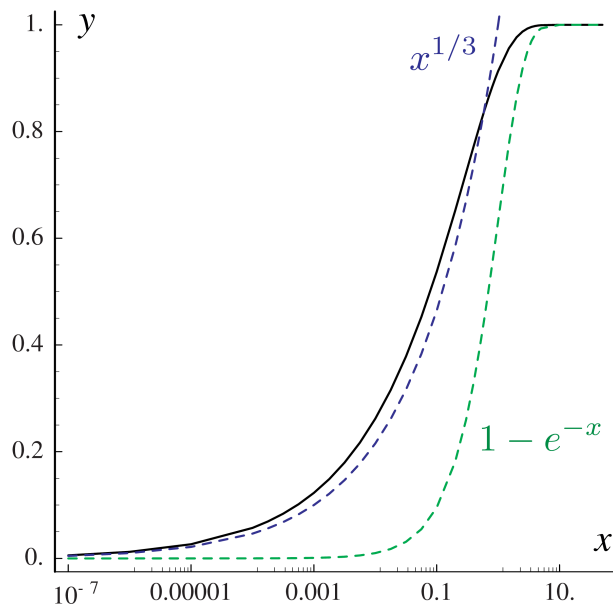


Fig. 15.1: SynFracInt on a log  $x$  scale. The functions  $x^{1/3}$ ,  $y^3$  and  $1 - e^{-x}$ ,  $-\log(1 - y)$  are shown as dashed lines.

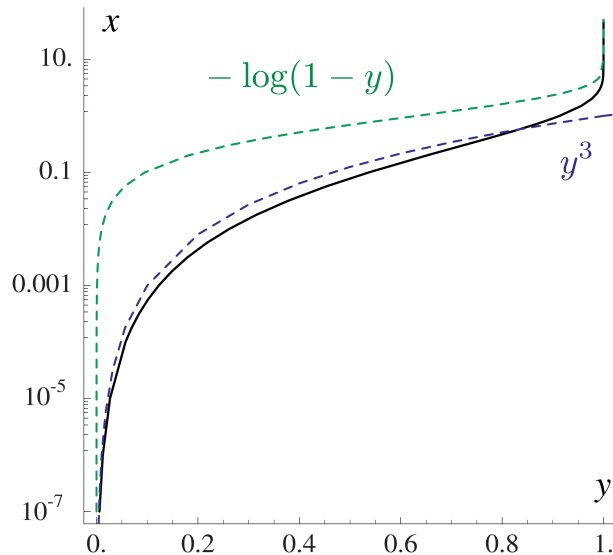


Fig. 15.2: InvSynFracInt on a log  $x$  scale. The functions  $x^{1/3}$ ,  $y^3$  and  $1 - e^{-x}$ ,  $-\log(1 - y)$  are shown as dashed lines.

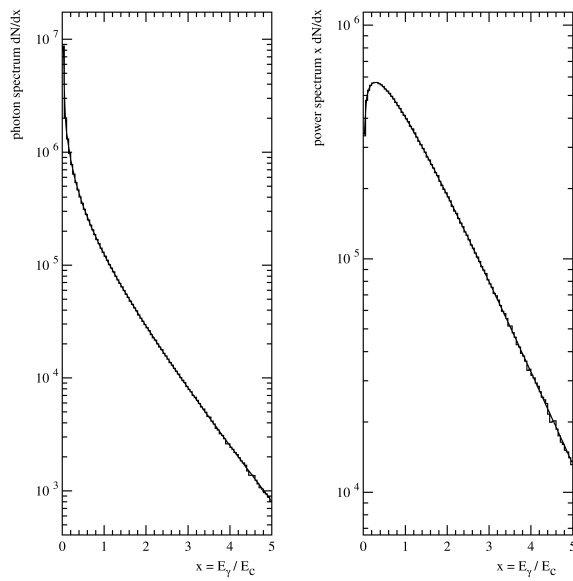


Fig. 15.3: Comparison of the exact (smooth curve) and generated (histogram) spectra for  $2 \times 10^7$  events. The photon spectrum is shown on the left and the power spectrum on the right side.

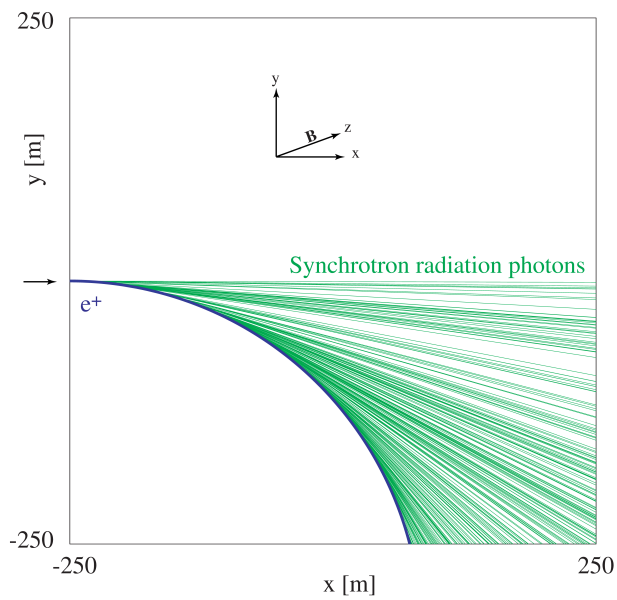


Fig. 15.4: GEANT4 display. 10 GeV  $e^+$  moving initially in  $x$ -direction, bends downwards on a circular path by a 0.1T magnetic field in  $z$ -direction.

#### 15.4.4 Properties of the Power Spectra

The normalised probability function describing the photon energy spectrum is

$$n_\gamma(x) = \frac{3}{5\pi} \int_x^\infty K_{5/3}(t) dt . \quad (15.13)$$

$n_\gamma(x)$  gives the fraction of photons in the interval  $x$  to  $x + dx$ , where  $x$  is the photon energy in units of the critical energy. The first moment or mean value is

$$\mu = \int_0^\infty x n_\gamma(x) dx = \frac{8}{15\sqrt{3}} .$$

implying that the mean photon energy is  $\frac{8}{15\sqrt{3}} = 0.30792$  of the critical energy. The second moment about the mean, or variance, is

$$\sigma^2 = \int_0^\infty (x - \mu)^2 n_\gamma(x) dx = \frac{211}{675} ,$$

and the r.m.s. value of the photon energy spectrum is  $\sigma = \sqrt{\frac{211}{675}} = 0.5591$ .

The normalised power spectrum is

$$P_\gamma(x) = \frac{9\sqrt{3}}{8\pi} x \int_x^\infty K_{5/3}(t) dt .$$

$P_\gamma(x)$  gives the fraction of the power which is radiated in the interval  $x$  to  $x + dx$ .

Half of the power is radiated below the critical energy

$$\int_0^1 P_\gamma(x) dx = 0.5000$$

The mean value of the power spectrum is

$$\mu = \int_0^\infty x P_\gamma(x) dx = \frac{55}{24\sqrt{3}} = 1.32309 .$$

The variance is

$$\sigma^2 = \int_0^\infty (x - \mu)^2 P_\gamma(x) dx = \frac{2351}{1728} ,$$

and the r.m.s. width is  $\sigma = \sqrt{\frac{2351}{1728}} = 1.16642$ .



---

CHAPTER  
SIXTEEN

---

## OPTICAL PHOTONS

### 16.1 Interactions of optical photons

Optical photons are produced when a charged particle traverses:

1. a dielectric material with velocity above the Čerenkov threshold;
2. a scintillating material.

#### 16.1.1 Physics processes for optical photons

A photon is called optical when its wavelength is much greater than the typical atomic spacing, for instance when  $\lambda \geq 10 \text{ nm}$  which corresponds to an energy  $E \leq 100 \text{ eV}$ . Production of an optical photon in a HEP detector is primarily due to:

1. Čerenkov effect;
2. Scintillation.

Optical photons undergo three kinds of interactions:

1. Elastic (Rayleigh) scattering;
2. Absorption;
3. Medium boundary interactions.

#### Rayleigh scattering

For optical photons Rayleigh scattering is usually unimportant. For  $\lambda = .2 \mu\text{m}$  we have  $\sigma_{Rayleigh} \approx .2b$  for  $N_2$  or  $O_2$  which gives a mean free path of  $\approx 1.7 \text{ km}$  in air and  $\approx 1 \text{ m}$  in quartz. Two important exceptions are aerogel, which is used as a Čerenkov radiator for some special applications and large water Čerenkov detectors for neutrino detection.

The differential cross section in Rayleigh scattering,  $d\sigma/d\Omega$ , is proportional to  $1 + \cos^2 \theta$ , where  $\theta$  is the polar angle of the new polarization with respect to the old polarization.

## Absorption

Absorption is important for optical photons because it determines the lower  $\lambda$  limit in the window of transparency of the radiator. Absorption competes with photo-ionisation in producing the signal in the detector, so it must be treated properly in the tracking of optical photons.

## Medium boundary effects

When a photon arrives at the boundary of a dielectric medium, its behaviour depends on the nature of the two materials which join at that boundary:

**Case dielectric → dielectric.** The photon can be transmitted (refracted ray) or reflected (reflected ray). In case where the photon can only be reflected, total internal reflection takes place.

**Case dielectric → metal.** The photon can be absorbed by the metal or reflected back into the dielectric. If the photon is absorbed it can be detected according to the photoelectron efficiency of the metal.

**Case dielectric → black material.** A black material is a tracking medium for which the user has not defined any optical property. In this case the photon is immediately absorbed undetected.

### 16.1.2 Photon polarization

The photon polarization is defined as a two component vector normal to the direction of the photon:

$$\begin{pmatrix} a_1 e^{i\Phi_1} \\ a_2 e^{i\Phi_2} \end{pmatrix} = e^{\Phi_o} \begin{pmatrix} a_1 e^{i\Phi_c} \\ a_2 e^{-i\Phi_c} \end{pmatrix}$$

where  $\Phi_c = (\Phi_1 - \Phi_2)/2$  is called circularity and  $\Phi_o = (\Phi_1 + \Phi_2)/2$  is called overall phase. Circularit gives the left- or right-polarization characteristic of the photon. RICH materials usually do not distinguish between the two polarizations and photons produced by the Čerenkov effect and scintillation are linearly polarized, that is  $\Phi_c = 0$ .

The overall phase is important in determining interference effects between coherent waves. These are important only in layers of thickness comparable with the wavelength, such as interference filters on mirrors. The effects of such coatings can be accounted for by the empirical reflectivity factor for the surface, and do not require a microscopic simulation. GEANT4 does not keep track of the overall phase.

Vector polarization is described by the polarization angle  $\tan \Psi = a_2/a_1$ . Reflection/transmission probabilities are sensitive to the state of linear polarization, so this has to be taken into account. One parameter is sufficient to describe vector polarization, but to avoid too many trigonometrical transformations, a unit vector perpendicular to the direction of the photon is used in GEANT4. The polarization vector is a data member of *G4DynamicParticle*.

### 16.1.3 Tracking of the photons

Optical photons are subject to in flight absorption, Rayleigh scattering and boundary action. As explained above, the status of the photon is defined by two vectors, the photon momentum ( $\vec{p} = \hbar\vec{k}$ ) and photon polarization ( $\vec{e}$ ). By convention the direction of the polarization vector is that of the electric field. Let also  $\vec{u}$  be the normal to the material boundary at the point of intersection, pointing out of the material which the photon is leaving and toward the one which the photon is entering. The behaviour of a photon at the surface boundary is determined by three quantities:

1. refraction or reflection angle, this represents the kinematics of the effect;
2. amplitude of the reflected and refracted waves, this is the dynamics of the effect;
3. probability of the photon to be refracted or reflected, this is the quantum mechanical effect which we have to take into account if we want to describe the photon as a particle and not as a wave.

As said above, we distinguish three kinds of boundary action, dielectric → black material, dielectric → metal, dielectric → dielectric. The first case is trivial, in the sense that the photon is immediately absorbed and it goes undetected.

To determine the behaviour of the photon at the boundary, we will at first treat it as an homogeneous monochromatic plane wave:

$$\vec{E} = \vec{E}_0 e^{i\vec{k} \cdot \vec{x} - i\omega t}$$

$$\vec{B} = \sqrt{\mu\epsilon} \frac{\vec{k} \times \vec{E}}{k}$$

### Case dielectric → dielectric

In the classical description the incoming wave splits into a reflected wave (quantities with a double prime) and a refracted wave (quantities with a single prime). Our problem is solved if we find the following quantities:

$$\vec{E}' = \vec{E}'_0 e^{i\vec{k}' \cdot \vec{x} - i\omega t}$$

$$\vec{E}'' = \vec{E}''_0 e^{i\vec{k}'' \cdot \vec{x} - i\omega t}$$

For the wave numbers the following relations hold:

$$|\vec{k}| = |\vec{k}''| = k = \frac{\omega}{c} \sqrt{\mu\epsilon}$$

$$|\vec{k}'| = k' = \frac{\omega}{c} \sqrt{\mu'\epsilon'}$$

Where the speed of the wave in the medium is  $v = c/\sqrt{\mu\epsilon}$  and the quantity  $n = c/v = \sqrt{\mu\epsilon}$  is called refractive index of the medium. The condition that the three waves, refracted, reflected and incident have the same phase at the surface of the medium, gives us the well known Fresnel law:

$$(\vec{k} \cdot \vec{x})_{surf} = (\vec{k}' \cdot \vec{x})_{surf} = (\vec{k}'' \cdot \vec{x})_{surf}$$

$$k \sin i = k' \sin r = k'' \sin r'$$

where  $i, r, r'$  are, respectively, the angle of the incident, refracted and reflected ray with the normal to the surface. From this formula the well known condition emerges:

$$i = r'$$

$$\frac{\sin i}{\sin r} = \sqrt{\frac{\mu'\epsilon'}{\mu\epsilon}} = \frac{n'}{n}$$

The dynamic properties of the wave at the boundary are derived from Maxwell's equations which impose the continuity of the normal components of  $\vec{D}$  and  $\vec{B}$  and of the tangential components of  $\vec{E}$  and  $\vec{H}$  at the surface boundary. The resulting ratios between the amplitudes of the the generated waves with respect to the incoming one are expressed in the two following cases:

1. a plane wave with the electric field (polarization vector) perpendicular to the plane defined by the photon direction and the normal to the boundary:

$$\frac{E'_0}{E_0} = \frac{2n \cos i}{n \cos i - \frac{\mu}{\mu'} n' \cos r} = \frac{2n \cos i}{n \cos i + n' \cos r}$$

$$\frac{E''_0}{E_0} = \frac{n \cos i - \frac{\mu}{\mu'} n' \cos r}{n \cos i + \frac{\mu}{\mu'} n' \cos r} = \frac{n \cos i - n' \cos r}{n \cos i + n' \cos r}$$

where we suppose, as it is legitimate for visible or near-visible light, that  $\mu/\mu' \approx 1$ ;

2. a plane wave with the electric field parallel to the above surface:

$$\frac{E'_0}{E_0} = \frac{2n \cos i}{\frac{\mu}{\mu'} n' \cos i + n \cos r} = \frac{2n \cos i}{n' \cos i + n \cos r}$$

$$\frac{E''_0}{E_0} = \frac{\frac{\mu}{\mu'} n' \cos i - n \cos r}{\frac{\mu}{\mu'} n' \cos i + n \cos r} = \frac{n' \cos i - n \cos r}{n' \cos i + n \cos r}$$

with the same approximation as above.

We note that in case of photon perpendicular to the surface, the following relations hold:

$$\frac{E'_0}{E_0} = \frac{2n}{n' + n}, \quad \frac{E''_0}{E_0} = \frac{n' - n}{n' + n}$$

where the sign convention for the parallel field has been adopted. This means that if  $n' > n$  there is a phase inversion for the reflected wave.

Any incoming wave can be separated into one piece polarized parallel to the plane and one polarized perpendicular, and the two components treated accordingly.

To maintain the particle description of the photon, the probability to have a refracted or reflected photon must be calculated. The constraint is that the number of photons be conserved, and this can be imposed via the conservation of the energy flux at the boundary, as the number of photons is proportional to the energy. The energy current is given by the expression:

$$\vec{S} = \frac{1}{2} \frac{c}{4\pi} \sqrt{\mu\epsilon} \vec{E} \times \vec{H} = \frac{c}{8\pi} \sqrt{\frac{\epsilon}{\mu}} E_0^2 \hat{k}$$

and the energy balance on a unit area of the boundary requires that:

$$\vec{S} \cdot \vec{u} = \vec{S}' \cdot \vec{u} - \vec{S}'' \cdot \vec{u}$$

$$S \cos i = S' \cos r + S'' \cos i$$

$$\frac{c}{8\pi} \frac{1}{\mu} n E_0^2 \cos i = \frac{c}{8\pi} \frac{1}{\mu'} n' E_0'^2 \cos r + \frac{c}{8\pi} \frac{1}{\mu} n E_0''^2 \cos i$$

If we set again  $\mu/\mu' \approx 1$ , then the transmission probability for the photon will be:

$$T = \left( \frac{E'_0}{E_0} \right)^2 \frac{n' \cos r}{n \cos i}$$

and the corresponding probability to be reflected will be  $R = 1 - T$ .

In case of reflection, the relation between the incoming photon  $(\vec{k}, \vec{e})$ , the refracted one  $(\vec{k}', \vec{e}')$  and the reflected one  $(\vec{k}'', \vec{e}'')$  is given by the following relations:

$$\vec{q} = \vec{k} \times \vec{u}$$

$$\vec{e}_\perp = \left( \frac{\vec{e} \cdot \vec{q}}{|\vec{q}|} \right) \frac{\vec{q}}{|\vec{q}|}$$

$$\vec{e}_\parallel = \vec{e} - \vec{e}_\perp$$

$$e'_\parallel = e_\parallel \frac{2n \cos i}{n' \cos i + n \cos r}$$

$$e'_{\perp\parallel} = e_\perp \frac{2n \cos i}{n \cos i + n' \cos r}$$

$$e''_\parallel = \frac{n'}{n} e'_\parallel - e_\parallel$$

$$e''_{\perp} = e'_{\perp} - e_{\perp}$$

After transmission or reflection of the photon, the polarization vector is re-normalized to 1. In the case where  $\sin r = n \sin i / n' > 1$  then there cannot be a refracted wave, and in this case we have a total internal reflection according to the following formulas:

$$\vec{k}'' = \vec{k} - 2(\vec{k} \cdot \vec{u})\vec{u}$$

$$\vec{e}'' = -\vec{e} + 2(\vec{e} \cdot \vec{u})\vec{u}$$

### Case dielectric → metal

In this case the photon cannot be transmitted. So the probability for the photon to be absorbed by the metal is estimated according to the table provided by the user. If the photon is not absorbed, it is reflected.

#### 16.1.4 Mie Scattering in Henyey-Greenstein Approximation

(Author: X. Qian, 2010-07-04)

Mie Scattering (or Mie solution) is an analytical solution of Maxwell's equations for the scattering of optical photon by spherical particles. The general introduction of Mie scattering can be found in Ref. [wik17]. The analytical express of Mie Scattering are very complicated since they are a series sum of Bessel functions [Fit14]. Therefore, the exact expression of Mie scattering is not suitable to be included in the Monte Carlo simulation.

One common approximation made is called “Henyey-Greenstein” [ZS10]. It has been used by Vlasios Vasileiou in GEANT4 simulation of Milagro experiment [Col07]. In the HG approximation,

$$\frac{d\sigma}{d\Omega} \sim \frac{1-g^2}{(1+g^2-2g\cos(\theta))^{3/2}}$$

where

$$d\Omega = d\cos(\theta)d\phi$$

and  $g = \langle \cos(\theta) \rangle$  can be viewed as a free constant labeling the angular distribution.

Therefore, the normalized density function of HG approximation can be expressed as:

$$P(\cos(\theta_0)) = \frac{\int_{-1}^{\cos(\theta_0)} \frac{d\sigma}{d\Omega} d\cos(\theta)}{\int_{-1}^1 \frac{d\sigma}{d\Omega} d\cos(\theta)} = \frac{1-g^2}{2g} \left( \frac{1}{(1+g^2-2g\cos(\theta_0))} - \frac{1}{1+g} \right)$$

Therefore,

$$\cos(\theta) = \frac{1}{2g} \cdot \left( 1 + g^2 - \left( \frac{1-g^2}{1-g+2gp} \right)^2 \right) = 2p \frac{(1+g)^2(1-g+gp)}{(1-g+2gp)^2} - 1$$

where  $p$  is a uniform random number between 0 and 1.

Similarly, the backward angle where  $\theta_b = \pi - \theta_f$  can also be simulated by replacing  $\theta_f$  to  $\theta_b$ . Therefore the final differential cross section can be viewed as:

$$\frac{d\sigma}{d\Omega} = r \frac{d\sigma}{d\Omega}(\theta_f, g_f) + (1-r) \frac{d\sigma}{d\Omega}(\theta_b, g_b)$$

This is the exact approach used in Ref. [Vas]. Here  $r$  is the ratio factor between the forward angle and backward angle.

In implementing the above MC method into GEANT4, the treatment of polarization and momentum are similar to that of Rayleigh scattering. We require the final polarization direction to be perpendicular to the momentum direction. We also require the final momentum, initial polarization and final polarization to be in the same plane.



---

CHAPTER  
**SEVENTEEN**

---

## **GEANT4-DNA**

### **17.1 GEANT4-DNA physics processes and models**

The GEANT4-DNA physics processes and models are adapted for track structure simulations in liquid water and other materials down to the eV scale.

Water radiolysis can also be simulated with GEANT4-DNA using specific physico-chemical and chemical processes.

They are all described on a dedicated web site: <http://geant4-dna.org>, which includes a full list of publications.

Please also consult the *Book For Application Developers, Tracking and Physics* section.

Any report or published results obtained using the GEANT4-DNA software shall cite the following reference publications:

- *The Geant4-DNA project*, S. Incerti et al., Int. J. Model. Simul. Sci. Comput. 1 (2010) 157–178 - <http://dx.doi.org/10.1142/S1793962310000122>
- *Comparison of Geant4 very low energy cross section models with experimental data in water*, S. Incerti et al., Med. Phys. 37 (2010) 4692-4708 - <http://dx.doi.org/10.1118/1.3476457>
- *Track structure modeling in liquid water: A review of the Geant4-DNA very low energy extension of the Geant4 Monte Carlo simulation toolkit*, M. A. Bernal et al., Phys. Med. 31 (2015) 861-874 - <http://dx.doi.org/10.1016/j.ejmp.2015.10.087>
- *Geant4-DNA example applications for track structure simulations in liquid water: a report from the Geant4-DNA Project*, S. Incerti et al., Med. Phys. 45 (2018) e722-e739 - <https://doi.org/10.1002/mp.13048>
- *Review of chemical models and applications in Geant4-DNA: Report from the ESA BioRad III Project*, H. N. Tran et al., Med. Phys. 51 (2024) 5873–5889 - <https://doi.org/10.1002/mp.17256>



---

CHAPTER  
**EIGHTEEN**

---

## MICROELECTRONICS

### 18.1 The MicroElec extension for microelectronics applications

The GEANT4-MicroElec<sup>1</sup> extension [Inc], developed by CEA, aims at modeling the effect of ionizing radiation in highly integrated microelectronic components. It describes the transport and generation of very low energy electrons by incident electrons, protons and heavy ions in silicon.

All GEANT4-MicroElec physics processes and models simulate step-by-step interactions of particles in silicon down to the eV scale; they are pure discrete processes. Table 18.1 summarizes the list of physical interactions per particle type that can be modeled using the GEANT4-MicroElec extension, along with the corresponding process classes, model classes, low energy limit applicability of models, high energy applicability of models and energy threshold below which the incident particle is killed (stopped and the kinetic energy is locally deposited, because of the low energy limit applicability of the inelastic model). All models are interpolated. For now, they are valid for silicon only (use the G4\_Si GEANT4-NIST material).

Table 18.1: List of G4MicroElec physical interactions

Particle	Interaction	Process	Model	Range	Kill
Electron	Elastic scattering	G4MicroElastic	G4MicroElecElasticModel	5 eV–100 MeV	16.7 eV
Electron	Ionisation	G4MicroElecInelastic	G4MicroElecInelasticModel	16.7 eV–100 MeV	–
Protons, ions	Ionisation	G4MicroElecInelastic	G4MicroElecInelasticModel	50 keV/u–10 MeV/u	–

All details regarding the physics and formula used for these processes and models and available in [AV12] for incident electrons and in [AVP12] for incident protons and heavy ions.

---

<sup>1</sup> Previously called MuElec.



## SHOWER PARAMETERIZATIONS

### 19.1 Gflash Shower Parameterizations

The computing time needed for the simulation of high energy electromagnetic showers can become very large, since it increases approximately linearly with the energy absorbed in the detector. Using parameterizations instead of individual particle tracking for electromagnetic (sub)showers can speed up the simulations considerably without sacrificing much precision. The Gflash package allows the parameterization of electron and positron showers in homogeneous (for the time being) calorimeters and is based on the parameterization described in Ref. [GP93] .

#### 19.1.1 Parameterization Ansatz

The spatial energy distribution of electromagnetic showers is given by three probability density functions (pdf),

$$dE(\vec{r}) = E f(t) dt f(r) dr f(\phi) d\phi,$$

describing the longitudinal, radial, and azimuthal energy distributions. Here  $t$  denotes the longitudinal shower depth in units of radiation length,  $r$  measures the radial distance from the shower axis in Molière units, and  $\phi$  is the azimuthal angle. The start of the shower is defined by the space point where the electron or positron enters the calorimeter, which is different from the original Gflash. A gamma distribution is used for the parameterization of the longitudinal shower profile,  $f(t)$ . The radial distribution  $f(r)$ , is described by a two-component ansatz. In  $\phi$ , it is assumed that the energy is distributed uniformly:  $f(\phi) = 1/2\pi$ .

#### 19.1.2 Longitudinal Shower Profiles

The average longitudinal shower profiles can be described by a gamma distribution [LS75]:

$$\left\langle \frac{1}{E} \frac{dE(t)}{dt} \right\rangle = f(t) = \frac{(\beta t)^{\alpha-1} \beta \exp(-\beta t)}{\Gamma(\alpha)}.$$

The center of gravity,  $\langle t \rangle$ , and the depth of the maximum,  $T$ , are calculated from the shape parameter  $\alpha$  and the scaling parameter  $\beta$  according to:

$$\begin{aligned} \langle t \rangle &= \frac{\alpha}{\beta} \\ T &= \frac{\alpha - 1}{\beta}. \end{aligned} \tag{19.1}$$

In the parameterization all lengths are measured in units of radiation length ( $X_0$ ), and energies in units of the critical energy ( $E_c = 2.66 (X_0 \frac{Z}{A})^{1.1}$ ). This allows material independence, since the longitudinal shower moments are equal

in different materials, according to Ref. [Ros52]. The following equations are used for the energy dependence of  $T_{hom}$  and  $(\alpha_{hom})$ , with  $y = E/E_c$  and  $t = x/X_0$ ,  $x$  being the longitudinal shower depth:

$$T_{hom} = \ln y + t_1$$

$$\alpha_{hom} = a_1 + (a_2 + a_3/Z) \ln y.$$

The  $y$ -dependence of the fluctuations can be described by:

$$\sigma = (s_1 + s_2 \ln y)^{-1}. \quad (19.2)$$

The correlation between  $\ln T_{hom}$  and  $\ln \alpha_{hom}$  is given by:

$$\rho(\ln T_{hom}, \ln \alpha_{hom}) \equiv \rho = r_1 + r_2 \ln y. \quad (19.3)$$

From these formulae, correlated and varying parameters  $\alpha_i$  and  $\beta_i$  are generated according to

$$\begin{pmatrix} \ln T_i \\ \ln \alpha_i \end{pmatrix} = \begin{pmatrix} \langle \ln T \rangle \\ \langle \ln \alpha \rangle \end{pmatrix} + C \begin{pmatrix} z_1 \\ z_2 \end{pmatrix}$$

with

$$C = \begin{pmatrix} \sigma(\ln T) & 0 \\ 0 & \sigma(\ln \alpha) \end{pmatrix} \begin{pmatrix} \sqrt{\frac{1+\rho}{2}} & \sqrt{\frac{1-\rho}{2}} \\ \sqrt{\frac{1+\rho}{2}} & -\sqrt{\frac{1-\rho}{2}} \end{pmatrix}$$

$\sigma(\ln \alpha)$  and  $\sigma(\ln T)$  are the fluctuations of  $T_{hom}$  and  $(\alpha_{hom})$ . The values of the coefficients can be found in Ref.[GP93].

### 19.1.3 Radial Shower Profiles

For the description of average radial energy profiles,

$$f(r) = \frac{1}{dE(t)} \frac{dE(t, r)}{dr},$$

a variety of different functions can be found in the literature. In Gflash the following two-component ansatz, an extension of that in Ref. [GRP90], was used:

$$f(r) = p f_C(r) + (1-p) f_T(r)$$

$$= p \frac{2r R_C^2}{(r^2 + R_C^2)^2} + (1-p) \frac{2r R_T^2}{(r^2 + R_T^2)^2}$$

with

$$0 \leq p \leq 1.$$

Here  $R_C$  ( $R_T$ ) is the median of the core (tail) component and  $p$  is a probability giving the relative weight of the core component. The variable  $\tau = t/T$ , which measures the shower depth in units of the depth of the shower maximum, is used in order to generalize the radial profiles. This makes the parameterization more convenient and separates the energy and material dependence of various parameters. The median of the core distribution,  $R_C$ , increases linearly with  $\tau$ . The weight of the core,  $p$ , is maximal around the shower maximum, and the width of the tail,  $R_T$ , is minimal at  $\tau \approx 1$ .

The following formulae are used to parameterize the radial energy density distribution for a given energy and material:

$$R_{C,hom}(\tau) = z_1 + z_2 \tau$$

$$R_{T,hom}(\tau) = k_1 \{ \exp(k_3(\tau - k_2)) + \exp(k_4(\tau - k_2)) \}$$

$$p_{hom}(\tau) = p_1 \exp \left\{ \frac{p_2 - \tau}{p_3} - \exp \left( \frac{p_2 - \tau}{p_3} \right) \right\}$$

The parameters  $z_1 \dots p_3$  are either constant or simple functions of  $\ln E$  or  $Z$ .

Radial shape fluctuations are also taken into account. A detailed explanation of this procedure, as well as a list of all the parameters used in Gflash, can be found in Ref. [GP93].

### 19.1.4 Gflash Performance

The parameters used in this Gflash implementation were extracted from full simulation studies with Geant 3. They also give good results inside the GEANT4 fast shower framework when compared with the full electromagnetic shower simulation. However, if more precision or higher particle energies are required, retuning may be necessary. For the longitudinal profiles the difference between full simulation and Gflash parameterization is at the level of a few percent. Because the radial profiles are slightly broader in Geant3 than in GEANT4, the differences may reach >10%. The gain in speed, on the other hand, is impressive. The simulation of a 1 TeV electron in a PbWO<sub>4</sub> cube is 160 times faster with Gflash. Gflash can also be used to parameterize electromagnetic showers in sampling calorimeters. So far, however, only homogeneous materials are supported.



## BIBLIOGRAPHY

- [eal16] J. Allison et al. Recent developments in geant4. *Nucl. Instr. and Meth. in Phys. Research Section A*, 835:186–225, nov 2016. URL: <https://doi.org/10.1016/j.nima.2016.06.125>, doi:10.1016/j.nima.2016.06.125.
- [eal09] J. Apostolakis et al. Geometry and physics of the geant4 toolkit for high and medium energy applications. *Radiation Physics and Chemistry*, 78(10):859–873, oct 2009. URL: <https://doi.org/10.1016/j.radphyschem.2009.04.026>, doi:10.1016/j.radphyschem.2009.04.026.
- [eal14] M. Karamitros et al. Diffusion-controlled reactions modeling in geant4-DNA. *Journal of Computational Physics*, 274:841–882, oct 2014. URL: <https://doi.org/10.1016/j.jcp.2014.06.011>, doi:10.1016/j.jcp.2014.06.011.
- [eal03] S. Agostinelli et al. Geant4—a simulation toolkit. *Nucl. Instr. and Meth. in Phys. Research Section A*, 506(3):250–303, jul 2003. URL: [https://doi.org/10.1016/S0168-9002\(03\)01368-8](https://doi.org/10.1016/S0168-9002(03)01368-8), doi:10.1016/s0168-9002(03)01368-8.
- [eal11] V.Ivantchenko et al. Recent improvements in geant4 electromagnetic physics models and interfaces. *Progress in Nuclear Science and Technology*, 2:898–903, 2011. URL: <http://dx.doi.org/10.15669/pnst.2.898>.
- [CHK89] D. Cullen, J.H. Hubbell, and L. Kissel. Epdl97: the evaluated photon data library, '97 version. *UCRL-50400*, 6(Rev.5):, 1989. <https://www-nds.iaea.org/epics/DOCUMENTS/EPDL97.pdf>.
- [eal99] J. Apostolakis et al. Geant4 low energy electromagnetic models for electrons and photons. Technical Report, CERN, CERN/INFN, 1999. CERN-OPEN-99-034(1999), INFN/AE-99/18.
- [NEAa] NEA:. Electron photon interaction cross section library. <https://www.oecd-nea.org/tools/abstract/detail/iaea1435/>. [Online; accessed 26-october-2017].
- [NEAb] NEA:. Evaluated nuclear reaction data. <http://www.oecd-nea.org/dbdata/data/evaluated.htm>. [Online; accessed 26-october-2017].
- [PCEal] S.T. Perkins, D.E. Cullen, and M.H. Chen et al. Tables and graphs of atomic subshell and relaxation data derived from the llnl evaluated atomic data library (eadl), z=1-100. Technical Report UCRL-50400 Vol.30.
- [STPerkins89] S.M.Seltzer S.T.Perkins, D.E.Cullen. Tables and graphs of electron-interaction cross-sections from 10 ev to 100 gev derived from the llnl evaluated electron data library (eedl), z=1-100. Technical Report UCRL-50400 Vol.31, Lawrence Livermore National Laboratory, 1989.
- [Sco75] J.H. Scofield. *Radiative Transitions in Atomic Inner-Shell Processes* B.Crasemann ed. Academic Press, New York, 1975.
- [eal01] F. Salvat et al. Penelope - a code system for monte carlo simulation of electron and photon transport. Technical Report, Workshop Proceedings Issy-les-Moulineaux, France; AEN-NEA, 5-7 November 2001.

- [SFernandezVAS03] J. Sempau, J.M. Fernández-Varea, E. Acosta, and F. Salvat. Experimental benchmarks of the monte carlo code penelope. *Nuclear Instruments and Methods in Physics Research Section B: Beam Interactions with Materials and Atoms*, 207(2):107–123, jun 2003. URL: [https://doi.org/10.1016/s0168-583x\(03\)00453-1](https://doi.org/10.1016/s0168-583x(03)00453-1), doi:10.1016/s0168-583x(03)00453-1.
- [Ste03] Jiri Stepanek. Electron and positron atomic elastic scattering cross sections. *Radiation Physics and Chemistry*, 66(2):99–116, feb 2003. URL: [https://doi.org/10.1016/s0969-806x\(02\)00386-9](https://doi.org/10.1016/s0969-806x(02)00386-9), doi:10.1016/s0969-806x(02)00386-9.
- [eal09] J. Apostolakis et al. Geometry and physics of the geant4 toolkit for high and medium energy applications. *Radiation Physics and Chemistry*, 78(10):859–873, oct 2009. URL: <https://doi.org/10.1016/j.radphyschem.2009.04.026>, doi:10.1016/j.radphyschem.2009.04.026.
- [Bor69] M. Born. *Atomic physics*. Ed. Blackie and Sons, edition, 1969.
- [eal01] F. Salvat et al. Penelope - a code system for monte carlo simulation of electron and photon transport. Technical Report, Workshop Proceedings Issy-les-Moulineaux, France; AEN-NEA, 5-7 November 2001.
- [eal94] J.Baró et al. Analytical cross sections for monte carlo simulation of photon transport. *Radiat. Phys. Chem.*, 44():531, 1994.
- [eal75] J.H. Hubbel et al. Atomic form factors, incoherent scattering functions and photon scattering cross sections. *Phys. Chem. Ref. Data*, 4():471, 1975. Erratum: ibid. 6,615 (1977).
- [PaternoCC+18] G. Paternò, P. Cardarelli, A. Contillo, M. Gambaccini, and A. Taibi. Geant4 implementation of inter-atomic interference effect in small-angle coherent x-ray scattering for materials of medical interest. *Physica Medica*, 51:64–70, jul 2018. URL: <https://doi.org/10.1016/j.ejmp.2018.04.395>, doi:10.1016/j.ejmp.2018.04.395.
- [PaternoCGT20] Gianfranco Paternò, Paolo Cardarelli, Mauro Gambaccini, and Angelo Taibi. Comprehensive data set to include interference effects in monte carlo models of x-ray coherent scattering inside biological tissues. *Physics in Medicine & Biology*, jul 2020. URL: <https://doi.org/10.1088/1361-6560/aba7d2>, doi:10.1088/1361-6560/aba7d2.
- [Cul95] D.E. Cullen. A simple model of photon transport. *Nucl. Instr. Meth. in Phys. Res. B*, 101():499–510, 1995.
- [eal79] J.H. Hubbell et al. Relativistic atom form factors and photon coherent scattering cross sections. *J. Phys. Chem. Ref. Data*, 8():69, 1979.
- [OH17] Mohamed Omer and Ryoichi Hajima. Including delbrück scattering in geant4. *Nucl. Instrum. Methods Phys. Res., Sect. B*, 405:43 – 49, 2017. URL: <http://www.sciencedirect.com/science/article/pii/S0168583X17306092>, doi:<https://doi.org/10.1016/j.nimb.2017.05.028>.
- [OH18] Mohamed Omer and Ryoichi Hajima. Geant4 physics process for elastic scattering of  $\gamma$ -rays. Technical Report 2018-007, Japan Atomic Energy Agency, June 2018. URL: <https://jopss.jaea.go.jp/search/servlet/search?5059687>, doi:<http://dx.doi.org/10.11484/jaea-data-code-2018-007>.
- [AGU+00] J Apostolakis, S Giani, L Urban, M Maire, A.V Bagulya, and V.M Grichine. An implementation of ionisation energy loss in very thin absorbers for the geant4 simulation package. *Nuclear Instruments and Methods in Physics Research Section A: Accelerators, Spectrometers, Detectors and Associated Equipment*, 453(3):597 – 605, 2000. URL: <http://www.sciencedirect.com/science/article/pii/S0168900200004575>, doi:[https://doi.org/10.1016/S0168-9002\(00\)00457-5](https://doi.org/10.1016/S0168-9002(00)00457-5).
- [BL88] F Biggs and R Lighthill. Analytical approximations for x-ray cross sections III. Technical Report, Sandia Lab, aug 1988. Preprint Sandia Laboratory, SAND 87-0070. URL: <https://doi.org/10.2172/7124946>, doi:10.2172/7124946.
- [eal82] B.L. Henke et al. Low-energy x-ray interaction coefficients:photoabsorption, scattering, and reflection. *Atom. Data Nucl. Data Tabl.*, 27:1–144, 1982.

- [eal88] Gallagher et al. *J.Phys.Chem.Ref.Data*, 1988.
- [eal77] Lee L.C. et al. *Journ. of Chem. Phys.*, 67:1237, 1977.
- [Gav59] Mihai Gavrila. Relativistic K-shell photoeffect. *Physical Review*, 113(2):514–526, jan 1959. URL: <https://doi.org/10.1103/PhysRev.113.514>, doi:10.1103/physrev.113.514.
- [MW76] G.V. Marr and J.B. West. Absolute photoionization cross-section tables for helium, neon, argon, and krypton in the vuv spectral regions. *Atom. Data Nucl. Data Tabl.*, 18:497–508, 1976.
- [Rub85] S. Ruben. *Handbook of the Elements*. Open Court, La Salle, IL, 3rd ed. edition, 1985.
- [VMAPeal94] Grichine V.M., Kostin A.P., and Kotelnikov S.K. et al. *Bulletin of the Lebedev Institute*, 1994.
- [WM78] J.B. West and J. Morton. Absolute photoionization cross-sections tables for xenon in the vuv and the soft x-ray regions. *Atom. Data Nucl. Data Tabl.*, 22:103–107, 1978.
- [CHK89] D. Cullen, J.H. Hubbell, and L. Kissel. Epdl97: the evaluated photon data library, '97 version. *UCRL-50400*, 6(Rev.5);, 1989. <https://www-nds.iaea.org/epics/DOCUMENTS/EPDL97.pdf>.
- [eal69] J.W. Motz et al. Pair production by photons. *Rev. Mod. Phys.*, 41():581, 1969.
- [DL06] G.O. Depaola and F. Longo. Measuring polarization in the x-ray range: new simulation method for gaseous detectors. *NIMA*, 566():590, 2006.
- [Gav59] M. Gavrila. Relativistic k-shell photoeffect. *Phys. Rev.*, 113(2):, 1959.
- [Gav61] M. Gavrila. Relativistic l-shell photoeffect. *Phys. Rev.*, 124(4):, 1961.
- [LP03] A. Trindade L. Peralta, P. Rodrigues. Monte carlo generation of 2bnbremsstrahlung distribution. *CERN EXT-2004-039*, (039):, July 2003.
- [RHPA64] R L Paxton R H Pratt, R D Levee and W Aron. K-shell photoelectric cross sections from 200 kev to 2 mev. *Phys. Rev.*, 134(4A):, 1964.
- [Sau31] Fritz Sauter. Über den atomaren photoeffekt bei großer härte der anregenden strahlung. *Annalen der Physik*, 401(2):217–248, 1931. URL: <https://doi.org/10.1002/andp.19314010205>, doi:10.1002/andp.19314010205.
- [BM60] J.C. Butcher and H. Messel. *Nucl. Phys.*, 20(15):, 1960.
- [JHHOverbo80] J.H. Hubbell, H.A. Gimm and I. Øverbø. Pair, Triplet, and Total Atomic Cross Sections (and Mass Attenuation Coefficients) for 1 MeV-100 GeV Photons in Elements Z=1 to 100. *Journal of Physical and Chemical Reference Data*, 9:1023–1148, October 1980. doi:10.1063/1.555629.
- [KN29] O. Klein and Y. Nishina. *Z. Physik*, 52:853, 1929.
- [MC70] H. Messel and D. Crawford. *Electron-Photon shower distribution*. Pergamon Press, 1970.
- [NHR85] W.R. Nelson, H. Hirayama, and D.W.O. Rogers. *EGS4 code system*. SLAC, Dec 1985. SLAC-265, UC-32.
- [SI70] H. Storm and H.I. Israel. *Nucl. Data Tables*, A7:565, 1970.
- [eal96] D. Brusa et al. Fast sampling algorithm for the simulation of photon compton scattering. *NIM A*, 379():167, 1996.
- [eal01] F. Salvat et al. Penelope - a code system for monte carlo simulation of electron and photon transport. Technical Report, Workshop Proceedings Issy-les-Moulineaux, France; AEN-NEA, 5-7 November 2001.
- [eal75] F. Biggs et al. Hartree-fock compton profiles for the elements. *At. Data Nucl. Data Tables*, 16():201, 1975.
- [BM60] J.C. Butcher and H. Messel. *Nucl. Phys.*, 20(15):, 1960.

- [Cul95] D.E. Cullen. A simple model of photon transport. *Nucl. Instr. Meth. in Phys. Res. B*, 101():499–510, 1995.
- [Hub97] J.H. Hubbell. Summary of existing information on the incoherent scattering of photons, particularly on the validity of the use of the incoherent scattering function. *Radiation Physics and Chemistry*, 50(1):113–124, jul 1997. URL: [https://doi.org/10.1016/S0969-806X\(97\)00049-2](https://doi.org/10.1016/S0969-806X(97)00049-2), doi:10.1016/s0969-806x(97)00049-2.
- [MC70] H. Messel and D. Crawford. *Electron-Photon shower distribution*. Pergamon Press, 1970.
- [NSJC04] C. Negreanu, J. Stepanek, O.P. Joneja, and R. Chawla. Validation of new electron and positron data libraries. *Nuclear Instruments and Methods in Physics Research Section B: Beam Interactions with Materials and Atoms*, 213:55–59, jan 2004. URL: [https://doi.org/10.1016/s0168-583x\(03\)01533-7](https://doi.org/10.1016/s0168-583x(03)01533-7), doi:10.1016/s0168-583x(03)01533-7.
- [NHR85] W.R. Nelson, H. Hirayama, and D.W.O. Rogers. *EGS4 code system*. SLAC, Dec 1985. SLAC-265, UC-32.
- [Ste03] Jiri Stepanek. Electron and positron atomic elastic scattering cross sections. *Radiation Physics and Chemistry*, 66(2):99–116, feb 2003. URL: [https://doi.org/10.1016/s0969-806x\(02\)00386-9](https://doi.org/10.1016/s0969-806x(02)00386-9), doi:10.1016/s0969-806x(02)00386-9.
- [eal96] D. Brusa et al. *Nucl. Instrum. Methods Phys. Res. A*, 379():167–175, 1996.
- [eal01] F. Salvat et al. Penelope, a code system for monte carlo simulation of electron and photon transport. Technical Report Proceedings of a Workshop/Training Course, OECD/NEA, 5-7 November 2001.
- [eal14] J.M.C. Brown et al. *Nucl. Instrum. Methods Phys. Res. B*, 338():77–88, 2014.
- [Kip04] R.M. Kippen. *New Astro. Reviews*, 48():221–225, 2004.
- [Mon29] J.W.M. Du Mond. *Phys. Rev.*, 33():643–658, 1929.
- [Rib75] R. Ribberfors. *Phys. Rev. B*, 12():2067–2074, 1975.
- [BM60] J.C. Butcher and H. Messel. *Nucl. Phys.*, 20(15):, 1960.
- [eal93] René Brun et al. *GEANT: Detector Description and Simulation Tool; Oct 1994*. CERN Program Library. CERN, Geneva, 1993. Long Writeup W5013. URL: <https://cds.cern.ch/record/1082634>.
- [FN78] Richard L. Ford and W. Ralph Nelson. The egs code system: computer programs for the monte carlo simulation of electromagnetic cascade showers (version 3). Technical Report, SLAC, 1978.
- [Hei54] W. Heitler. *The Quantum Theory of Radiation*. Oxford Clarendon Press, edition, 1954.
- [JHHOverbo80] J.H. Hubbell, H.A. Gimm and I. Øverbø. Pair, Triplet, and Total Atomic Cross Sections (and Mass Attenuation Coefficients) for 1 MeV-100 GeV Photons in Elements Z=1 to 100. *Journal of Physical and Chemical Reference Data*, 9:1023–1148, October 1980. doi:10.1063/1.555629.
- [MC70] H. Messel and D. Crawford. *Electron-Photon shower distribution*. Pergamon Press, 1970.
- [Tsa74] Y. Tsai. Pair production and bremsstrahlung of charged leptons. *Rev. Mod. Phys.*, 46():815, 1974.
- [Tsa77] Y. Tsai. Pair production and bremsstrahlung of charged leptons. *Rev. Mod. Phys.*, 49():421, 1977.
- [BM50] T. H. Berlin and L. Madansky. On the detection of gamma-ray polarization by pair production. *Phys. Rev.*, (78):623, 1950.
- [Ber13a] D. Bernard. Polarimetry of cosmic gamma-ray sources above e+e- pair creation threshold. *Nucl. Instrum. Meth.*, A729:765–780, 2013.
- [Ber13b] D. Bernard. TPC in gamma-ray astronomy above pair-creation threshold. *Nucl. Instrum. Meth.*, A701:225–230, 2013. [Erratum: Nucl. Instrum. Meth. A713, 76(2013)]. arXiv:1211.1534.

- [Ber18] D. Bernard. A 5d, polarised, bethe-heitler event generator for  $\gamma \rightarrow e^+e^-$  conversion. *Nuclear Instruments and Methods in Physics Research Section A: Accelerators, Spectrometers, Detectors and Associated Equipment*, 899:85–93, aug 2018. URL: <https://doi.org/10.1016/j.nima.2018.05.021>, doi:10.1016/j.nima.2018.05.021.
- [BH34] H. Bethe and W. Heitler. On the stopping of fast particles and on the creation of positive electrons. *Proceedings of the Royal Society of London A*, (146):83, 1934.
- [GB17] P. Gros and D. Bernard. gamma-ray telescopes using conversions to  $e^+e^-$  pairs: event generators, angular resolution and polarimetry. *Astropart. Phys.*, 88:60–67, 2017.
- [Gro16] Particle Data Group. Review of particle physics. *Chin. Phys. C*, (40):100001, 2016.
- [JR76] Jauch and Rohrlich. *The theory of photons and electrons*. Springer Verlag, 1976.
- [JLS50] R. Jost, J. M. Luttinger, and M. Slotnick. Distribution of Recoil Nucleus in Pair Production by Photons. *Phys. Rev.*, 80:189–196, 1950.
- [May51] M. M. May. On the polarization of high energy bremsstrahlung and of high energy pairs. *Phys. Rev.*, (84):265, 1951.
- [Mor67] K. J. Mork. Pair production by photons on electrons. *Phys. Rev.*, (160):1065, 1967.
- [NFM34] H.S.W. Massey N.F. Mott. *The Theory of Atomic Collisions*. University Press, Oxford, 1934.
- [Ols63] Haakon Olsen. Opening Angles of Electron-Positron Pairs. *Phys. Rev.*, 131:406–415, 1963.
- [SB19] I. Semeniouk and D. Bernard. C++ implementation of bethe-heitler, 5d, polarized,  $\gamma \rightarrow e^+e^-$  pair conversion event generator. *Nuclear Instruments and Methods in Physics Research Section A: Accelerators, Spectrometers, Detectors and Associated Equipment*, 936:290–291, aug 2019. URL: <https://doi.org/10.1016/j.nima.2018.09.154>, doi:10.1016/j.nima.2018.09.154.
- [WL39] J.A. Wheeler and W.E. Lamb. Influence of atomic electrons on radiation and pair production. *Phys. Rev.*, ():858, 1939. (errata in 101 (1956) 1836).
- [BH87] M.J. Berger and J.H. Hubbel. Xcom: photom cross sections on a personal computer. Technical Report Report NBSIR 87-3597, National Bureau of Standards, 1987.
- [eal01] F. Salvat et al. Penelope - a code system for monte carlo simulation of electron and photon transport. Technical Report, Workshop Proceedings Issy-les-Moulineaux, France; AEN-NEA, 5-7 November 2001.
- [eal54] H. Davies et al. Theory of bremsstrahlung and pair production. ii. integral cross section for pair production. *Phys. Rev.*, 93(4):788–795, 1954.
- [eal94] J.Baró et al. Analytical cross sections for monte carlo simulation of photon transport. *Radiat. Phys. Chem.*, 44():531, 1994.
- [eal69] J.W. Motz et al. Pair production by photons. *Rev. Mod. Phys.*, 41():581, 1969.
- [JHHOverbo80] J.H. Hubbell, H.A. Gimm and I. Øverbø. Pair, Triplet, and Total Atomic Cross Sections (and Mass Attenuation Coefficients) for 1 MeV-100 GeV Photons in Elements Z=1 to 100. *Journal of Physical and Chemical Reference Data*, 9:1023–1148, October 1980. doi:10.1063/1.555629.
- [BM60] J.C. Butcher and H. Messel. *Nucl. Phys.*, 20(15):, 1960.
- [eal93] René Brun et al. *GEANT: Detector Description and Simulation Tool; Oct 1994*. CERN Program Library. CERN, Geneva, 1993. Long Writeup W5013. URL: <https://cds.cern.ch/record/1082634>.
- [FN78] Richard L. Ford and W. Ralph Nelson. The egs code system: computer programs for the monte carlo simulation of electromagnetic cascade showers (version 3). Technical Report, SLAC, 1978.
- [MC70] H. Messel and D. Crawford. *Electron-Photon shower distribution*. Pergamon Press, 1970.
- [Tsa74] Y. Tsai. Pair production and bremsstrahlung of charged leptons. *Rev. Mod. Phys.*, 46():815, 1974.

- [Tsa77] Y. Tsai. Pair production and bremsstrahlung of charged leptons. *Rev. Mod. Phys.*, 49():421, 1977.
- [DI09] G.O. Depaola and M.L. Iparraguirre. *Nucl. Instr. Meth. A*, 611():84, 2009.
- [MLI11] G.O. Depaola M.L. Iparraguirre. *The European Physical Journal C*, 71():1778, 2011.
- [VFBP94] N.P. Merenkov V.F. Boldyshev, E.A. Vinokurov and Yu.P. Peresunko. *Phys. Part. Nucl.*, 25():292, 1994.
- [VK72] E.A. Vinokurov and E.A. Kuraev. *Zh. Eksp. Teor. Fiz.*, 63():1142, 1972. in Russian.
- [VK73] E.A. Vinokurov and E.A. Kuraev. *Sov. Phys. JETP*, 36:602, 1973. in Russian.
- [Ber19] Denis Bernard. A 5D, polarised, Bethe-Heitler event generator for  $\gamma$  to  $\mu^+\mu^-$  conversion. 2019. [arXiv:1910.12501](https://arxiv.org/abs/1910.12501).
- [BKK02] H Burkhardt, S R Kelner, and R P Kokoulin. Monte carlo generator for muon pair production. Technical Report CERN-SL-2002-016-AP. CLIC-Note-511, CERN, Geneva, May 2002. URL: <https://cds.cern.ch/record/558831>.
- [KKP95] SR Kelner, RP Kokoulin, and AA Petrukhin. About cross section for high-energy muon bremsstrahlung. Technical Report, MEPhI, 1995. Preprint MEPhI 024-95, Moscow, 1995, CERN SCAN-9510048.
- [Ols63] Haakon Olsen. Opening Angles of Electron-Positron Pairs. *Phys. Rev.*, 131:406–415, 1963.
- [Bur25] H. Burkhardt. Technical Report, CERN, Geneva, 2025. To be published. URL: [arXiv\\_nnnn.nnnnn](https://arxiv.org/abs/nnnn.nnnnn).
- [HGD93] B.L. Henke, E.M. Gullikson, and J.C. Davis. X-ray interactions: photoabsorption, scattering, transmission, and reflection at  $e = 50\text{--}30,000 \text{ eV}$ ,  $z = 1\text{--}92$ . *Atomic Data and Nuclear Data Tables*, 54(2):181–342, July 1993. URL: <http://dx.doi.org/10.1006/adnd.1993.1013>, doi:10.1006/adnd.1993.1013.
- [NC80] L. Nérot and P. Croce. Caractérisation des surfaces par réflexion rasante de rayons x. application à l'étude du polissage de quelques verres silicates. *Revue de Physique Appliquée*, 15(3):761–779, 1980. URL: <http://dx.doi.org/10.1051/rphysap:01980001503076100>, doi:10.1051/rphysap:01980001503076100.
- [ABB+] H. H. Anderson, M. J. Berger, H. Bichsel, J. A. Dennis, M. Inokuti, D. Powers, S. M. Seltzer, D. Thwaites, J. E. Turner, and D. E. Watt. Estar, pstar, and astar databases. Technical Report, National Institute of Standards and Technology. URL: <https://physics.nist.gov/PhysRefData/Star/Text/intro.html>.
- [eal09] J. Apostolakis et al. Geometry and physics of the geant4 toolkit for high and medium energy applications. *Radiation Physics and Chemistry*, 78(10):859–873, oct 2009. URL: <https://doi.org/10.1016/j.radphyschem.2009.04.026>, doi:10.1016/j.radphyschem.2009.04.026.
- [eal93] M.J. Berger et al. Report 49. *Journal of the International Commission on Radiation Units and Measurements*, os25(2):NP–NP, may 1993. ICRU Report 49. URL: [https://doi.org/10.1093/jicru/os25.2.report49](https://doi.org/10.1093/jicru/os25.2.Report49), doi:10.1093/jicru/os25.2.report49.
- [eal05] P. Sigmund et al. Stopping of ions heavier than helium. *Journal of the International Commission on Radiation Units and Measurements*, jun 2005. ICRU Report 73. URL: <https://doi.org/10.1093/jicru/ndi001>, doi:10.1093/jicru/ndi001.
- [eal03] S. Agostinelli et al. Geant4—a simulation toolkit. *Nucl. Instr. and Meth. in Phys. Research Section A*, 506(3):250–303, jul 2003. URL: [https://doi.org/10.1016/S0168-9002\(03\)01368-8](https://doi.org/10.1016/S0168-9002(03)01368-8), doi:10.1016/s0168-9002(03)01368-8.
- [eal14] S.M. Seltzer et al. Report 90: key data for ionizing-radiation dosimetry: measurement standards and applications. *Journal of the International Commission on Radiation Units and Measurements*, apr 2014. ICRU Report 90. URL: <https://doi.org/10.1093/jicru/ndi001>, doi:10.1093/jicru\_ndi001.
- [ZM88] J.F. Ziegler and J.M. Manoyan. *Nucl. Instr. and Meth. B*, 35():215, 1988.
- [Bic88] H. Bichsel. *Rev. Mod. Phys.*, 60:663, 1988.

- [eal93] M.J. Berger et al. Report 49. *Journal of the International Commission on Radiation Units and Measurements*, os25(2):NP–NP, may 1993. ICRU Report 49. URL: <https://doi.org/10.1093/jicru/os25.2.49>, doi:10.1093/jicru/os25.2.report49.
- [LPUrban95] K. Lassila-Perini and L. Urbán. *Nucl. Inst. Meth. A*, 362:416, 1995.
- [eal09] J. Apostolakis et al. Geometry and physics of the geant4 toolkit for high and medium energy applications. *Radiation Physics and Chemistry*, 78(10):859–873, oct 2009. URL: <https://doi.org/10.1016/j.radphyschem.2009.04.026>, doi:10.1016/j.radphyschem.2009.04.026.
- [eal92] V.N.Ivanchenko et al. In *Proc. of Int. Conf. MC91: Detector and event simulation in high energy physics, 1991*, HEP INDEX 30 (1992) No. 3237, 79–85. Amsterdam, 1992.
- [eal16] J. Allison et al. Recent developments in geant4. *Nucl. Instr. and Meth. in Phys. Research Section A*, 835:186–225, nov 2016. URL: <https://doi.org/10.1016/j.nima.2016.06.125>, doi:10.1016/j.nima.2016.06.125.
- [eal03] S. Agostinelli et al. Geant4—a simulation toolkit. *Nucl. Instr. and Meth. in Phys. Research Section A*, 506(3):250–303, jul 2003. URL: [https://doi.org/10.1016/S0168-9002\(03\)01368-8](https://doi.org/10.1016/S0168-9002(03)01368-8), doi:10.1016/s0168-9002(03)01368-8.
- [AWWMJ80] Allison W.W.M. and Cobb J. *Ann. Rev. Nucl. Part. Sci.*, 30:253, 1980.
- [BFR90] Biggs F. and Lighthill R. Technical Report SAND 87-0070, Preprint Sandia Laboratory, 1990.
- [eal73] Lee L.C. et al. *J.Q.S.R.T.*, 13:1023, 1973.
- [eal77] Lee L.C. et al. *Journ. of Chem. Phys.*, 67:1237, 1977.
- [FUJW68] Fano U. and Cooper J.W. *Rev. Mod. Phys.*, 40:441, 1968.
- [MW76] G.V. Marr and J.B. West. Absolute photoionization cross-section tables for helium, neon, argon, and krypton in the vuv spectral regions. *Atom. Data Nucl. Data Tabl.*, 18:497–508, 1976.
- [VMAPeal94] Grichine V.M., Kostin A.P., and Kotelnikov S.K. et al. *Bulletin of the Lebedev Institute*, 1994.
- [VSVAael82] Asoskov V.S., Chechin V.A., and Grichine V.M. et al. Technical Report 140, Lebedev Institute annual report, 1982. p.3.
- [WM80] J.B. West and J. Morton. *Atom. Data Nucl. Data Tabl.*, 30:253, 1980.
- [BB64] W.H. Barkas and M.J. Berger. Nasa report sp-3013. Technical Report, NASA, USA, 1964.
- [eal94] C. Scheidenberger et al. *Phys. Rev. Lett.*, 73(50):, 1994.
- [eal96] C. Scheidenberger et al. *Phys. Rev. Lett.*, 77(3987):, 1996.
- [eal02] H. Geissel et al. *Nucl. Instr. and Meth. B*, 195(3):, 2002.
- [eal00] H. Weick et al. *Nucl. Instr. and Meth. B*, 164-165(168):, 2000.
- [GS98] H. Geissel and C. Scheidenberger. *Nucl. Instr. and Meth. B*, 136(114):, 1998.
- [JFZL85] J.B. Biersack J.F. Ziegler and U. Littmark. *The Stopping and Range of Ions in Solids*. Pergamon Press, first edition, 1985.
- [JM72] J.D. Jackson and R.L. McCarthy. *Phys. Rev. B*, 6(4131):, 1972.
- [Lin76] J. Lindhard. *Nucl. Instr. and Meth.*, 132(1):, 1976.
- [LS96] J. Lindhard and A.H. Soerensen. *Phys. Rev. A*, 53(2443):, 1996.
- [PB68] T.E. Pierce and M. Blann. *Phys. Rev.*, 173(390):, 1968.
- [SG98] C. Scheidenberger and H. Geissel. *Nucl. Instr. and Meth. B*, 135(25):, 1998.
- [SP71a] R.M. Sternheimer and R.F. Peierls. *Phys. Rev. B*, 3(3681):, 1971.

- [SP71b] R.M. Sternheimer and R.F. Peierls. General expression for the density effect for the ionization loss of charged particles. *Physical Review B*, 3(11):3681–3692, jun 1971. URL: <https://doi.org/10.1103/PhysRevB.3.3681>, doi:10.1103/physrevb.3.3681.
- [eal17] A. Bagulya et al. Recent progress of geant4 electromagnetic physics for lhc and other applications. *Journal of Physics: Conference Series*, 898():042032, 2017. URL: <https://doi.org/10.1088/1742-6596/898/4/042032>, doi:10.1088/1742-6596/898/4/042032.
- [eal06] D. Attwood et al. The scattering of muons in low-z materials. *Nucl. Instr. and Meth. in Phys. Research B*, 251(1):41–55, sep 2006. URL: <https://doi.org/10.1016/j.nimb.2006.05.006>, doi:10.1016/j.nimb.2006.05.006.
- [eal90] D. Liljequist et al. Transport mean free path tabulated for the multiple elastic scattering of electrons and positrons at energies  $\leq 20$  mev. *Journal of Applied Physics*, 68(7):3061–3065, oct 1990. URL: <https://doi.org/10.1063/1.346399>, doi:10.1063/1.346399.
- [eal16] J. Allison et al. Recent developments in geant4. *Nucl. Instr. and Meth. in Phys. Research Section A*, 835:186–225, nov 2016. URL: <https://doi.org/10.1016/j.nima.2016.06.125>, doi:10.1016/j.nima.2016.06.125.
- [eal09] J. Apostolakis et al. Geometry and physics of the geant4 toolkit for high and medium energy applications. *Radiation Physics and Chemistry*, 78(10):859–873, oct 2009. URL: <https://doi.org/10.1016/j.radphyschem.2009.04.026>, doi:10.1016/j.radphyschem.2009.04.026.
- [GS40] S. Goudsmit and J. L. Saunderson. Multiple scattering of electrons. *Physical Review*, 57(1):24–29, jan 1940. URL: <https://doi.org/10.1103/PhysRev.57.24>, doi:10.1103/physrev.57.24.
- [Hig75] V.L. Highland. Some practical remarks on multiple scattering. *Nuclear Instruments and Methods*, 129:497–499, November 1975. doi:10.1016/0029-554X(75)90743-0.
- [JM Fernandez VS93] J. Baró J.M. Fernández-Varea, R. Mayol and F. Salvat. On the theory and simulation of multiple elastic scattering of electrons. *Nucl. Instrum. and Meth. in Phys. Research B*, 73:447–473, apr 1993. doi:10.1016/0168-583X(93)95827-R.
- [KB98] I. Kawrakow and A.F. Bielajew. On the condensed history technique for electron transport. *Nucl. Instr. and Meth. in Phys. Research Section B*, 142(3):253–280, jul 1998. URL: [https://doi.org/10.1016/S0168-583X\(98\)00274-2](https://doi.org/10.1016/S0168-583X(98)00274-2), doi:10.1016/s0168-583x(98)00274-2.
- [Lew50] H. W. Lewis. Multiple scattering in an infinite medium. *Physical Review*, 78(5):526–529, jun 1950. URL: <https://doi.org/10.1103/PhysRev.78.526>, doi:10.1103/physrev.78.526.
- [LI87] D. Liljequist and M. Ismail. Transport mean free path related to trajectory patterns: comparison of nonrelativistic and highly relativistic electron penetration through matter. *Journal of Applied Physics*, 62(2):342–350, jul 1987. URL: <http://doi.org/10.1063/1.339802>, doi:10.1063/1.339802.
- [LD91] G.R. Lynch and O.I. Dahl. Approximations to multiple Coulomb scattering. *Nucl. Instr. and Meth. in Phys. Research B*, 58:6–10, May 1991. doi:10.1016/0168-583X(91)95671-Y.
- [MS97] Ricard Mayol and Francesc Salvat. Total and Transport Cross Sections for Elastic Scattering of Electrons by Atoms. *Atomic Data and Nuclear Data Tables*, 65(1):55–154, jan 1997. URL: <https://doi.org/10.1006/adnd.1997.0734>, doi:10.1006/adnd.1997.0734.
- [Moliere48] G. Molière. Theorie der Streuung schneller geladener Teilchen II. Mehrfach- und Vielfachstreuung. *Zeitschrift Naturforschung Teil A*, 3:78–97, February 1948. doi:10.1515/zna-1948-0203.
- [OKT09] F. Gharbi O. Kadri, V. Ivanchenko and A. Trabelsi. Incorporation of the goudsmit-saunderson electron transport theory in the geant4 monte carlo code. *Nucl. Instr. and Meth. in Phys. Research Section B*, 267(23-24):3624–3632, dec 2009. URL: <https://doi.org/10.1016/j.nimb.2009.09.015>, doi:10.1016/j.nimb.2009.09.015.

- [SIN18] V Ivanchenko S Incerti and M Novak. Recent progress of geant4 electromagnetic physics for calorimeter simulation. *Journal of Instrumentation*, 13():C02054, feb 2018. URL: <https://doi.org/10.1088/1748-0221/13/02/C02054>, doi:10.1088/1748-0221/13/02/C02054.
- [Urb06] László Urbán. A model for multiple scattering in GEANT4. Technical Report, CERN, Geneva, Dec 2006. URL: <http://cds.cern.ch/record/1004190>.
- [VNIU10] M. Maire V.N. Ivanchenko, O. Kadri and L. Urban. Geant4 models for simulation of multiple scattering. *Journal of Physics: Conference Series*, 219(3):032045, apr 2010. URL: <https://doi.org/10.1088/1742-6596/219/3/032045>, doi:10.1088/1742-6596/219/3/032045.
- [Bet53] H.A. Bethe. *Phys. Rev.*, 89:1256, 1953.
- [eal02] A.V. Butkevich et al. *Nuclear Instruments and Methods in Physics Research A*, 488:282, 2002.
- [eal06] D. Attwood et al. *Nuclear Instruments and Methods in Physics Research B*, 251:41, 2006.
- [JMFernandezVS93] J. Baró J.M. Fernández-Varea, R. Mayol and F. Salvat. On the theory and simulation of multiple elastic scattering of electrons. *Nucl. Instrum. and Meth. in Phys. Research B*, 73:447–473, apr 1993. doi:10.1016/0168-583X(93)95827-R.
- [Urb06] L. Urban. A multiple scattering model. Technical Report CERN-OPEN-2006-077, CERN, Dec 2006. 18 pp.
- [Wen27] G. Wentzel. *Z. Phys.*, 40:590, 1927.
- [BH80] J.P. Biersack and L.G. Haggmark. A monte carlo computer program for the transport of energetic ions in amorphous targets. *Nucl. Instr. and Meth. in Phys. Research*, 174():257, 1980.
- [MA65] I. Stegun (Eds.) M. Abramowitz. *Handbook of Mathematical Functions*. Dover, New York, edition, 1965.
- [MW91] M.H. Mendenhall and R.A. Weller. Algorithms for the rapid computation of classical cross sections for screened coulomb collisions. *Nucl. Instr. and Meth. in Phys. Research B*, 58():11, 1991.
- [MW05] M.H. Mendenhall and R.A. Weller. An algorithm for computing screened coulomb scattering in geant4. *Nuclear Instruments and Methods in Physics Research B*, 227():420, 2005.
- [Bet53] H.A. Bethe. *Phys. Rev.*, 89:1256, 1953.
- [eal03] Insoo Jun et al. Proton nonionizing energy loss (niel) for device applications. *IEEE Transactions on Nuclear Science*, 50(6):1924–1928, dec 2003. URL: <https://doi.org/10.1109/TNS.2003.820760>, doi:10.1109/tns.2003.820760.
- [eal93] M.J. Berger et al. Report 49. *Journal of the International Commission on Radiation Units and Measurements*, os25(2):NP–NP, may 1993. ICRU Report 49. URL: [https://doi.org/10.1093/jicru/os25.2.report49](https://doi.org/10.1093/jicru/os25.2.Report49), doi:10.1093/jicru/os25.2.report49.
- [eal11] M.J. Boschini et al. Nuclear and non-ionizing energy-loss for coulomb scattered particles from low energy up to relativistic regime in space radiation environment. In *Cosmic Rays for Particle and Astroparticle Physics*, 9–23. WORLD SCIENTIFIC, jun 2011. ISBN: 978-981-4329-02-6; arXiv 1011.4822. URL: [https://doi.org/10.1142/9789814329033\\_0002](https://doi.org/10.1142/9789814329033_0002), doi:10.1142/9789814329033\_0002.
- [JFZL85] J.P. Biersack J.F. Ziegler and U. Littmark. *The Stopping Range of Ions in Solids*. Pergamon Press (New York), vol. 1 edition, 1985.
- [JFZ08] J.P. Biersack J.F. Ziegler, M.D. Ziegler. The stopping and range of ions in matter, \em SRIM version 2008.03 (2008). <http://www.srim.org/>, 2008. [Online; accessed 26-october-2017].
- [LR07] C. Leroy and P.-G. Rancoita. Particle interaction and displacement damage in silicon devices operated in radiation environments. *Reports on Progress in Physics*, 70(4):493–625, mar 2007. URL: <https://doi.org/10.1088/0034-4885/70/4/R01>, doi:10.1088/0034-4885/70/4/r01.

- [LR09] C. Leroy and P.G. Rancoita. *Principles of Radiation Interaction in Matter and Detection*. World Scientific (Singapore), 2nd edition edition, 2009.
- [Moliere47] G. Molière. *Zeitschrift Naturforschung Teil A*, 2:133–145, 1947.
- [Moliere48] G. Molière. Theorie der Streuung schneller geladener Teilchen II. Mehrfach- und Vielfachstreuung. *Zeitschrift Naturforschung Teil A*, 3:78–97, February 1948. doi:10.1515/zna-1948-0203.
- [Wen26] G. Wentzel. Zwei bemerkungen über die zerstreuung korpuskularer strahlen als beugungserscheinung. *Zeitschrift für Physik*, 40(8):590–593, aug 1926. URL: <https://doi.org/10.1007/BF01390457>, doi:10.1007/bf01390457.
- [ZBZ08] James F Ziegler, Jochen P Biersack, and Matthias D Ziegler. *SRIM: the stopping and range of ions in matter*. Cadence Design Systems, Raleigh, NC, 2008. URL: <https://cds.cern.ch/record/1525729>.
- [BKMM02] A.V. Butkevich, R.P. Kokoulin, G.V. Matushko, and S.P. Mikheyev. Comments on multiple scattering of high-energy muons in thick layers. *Nuclear Instruments and Methods in Physics Research Section A: Accelerators, Spectrometers, Detectors and Associated Equipment*, 488(1-2):282–294, aug 2002. URL: [https://doi.org/10.1016/S0168-9002\(02\)00478-3](https://doi.org/10.1016/S0168-9002(02)00478-3), doi:10.1016/s0168-9002(02)00478-3.
- [eal12] M. J. Boschini et al. NUCLEAR AND NON-IONIZING ENERGY-LOSS OF ELECTRONS WITH LOW AND RELATIVISTIC ENERGIES IN MATERIALS AND SPACE ENVIRONMENT. In *Astroparticle, Particle, Space Physics, Radiation Interaction, Detectors and Medical Physics Applications*, pages 961–982. WORLD SCIENTIFIC, sep 2012. URL: [https://doi.org/10.1142/9789814405072\\_0147](https://doi.org/10.1142/9789814405072_0147), doi:10.1142/9789814405072\_0147.
- [eal11] M.J. Boschini et al. Nuclear and non-ionizing energy-loss for coulomb scattered particles from low energy up to relativistic regime in space radiation environment. In *Cosmic Rays for Particle and Astroparticle Physics*, 9–23. WORLD SCIENTIFIC, jun 2011. ISBN: 978-981-4329-02-6; arXiv 1011.4822. URL: [https://doi.org/10.1142/9789814329033\\_0002](https://doi.org/10.1142/9789814329033_0002), doi:10.1142/9789814329033\_0002.
- [eal13] M.J. Boschini et al. An expression for the mott cross section of electrons and positrons on nuclei with z up to 118. *Radiation Physics and Chemistry*, 90:39–66, sep 2013. URL: <https://doi.org/10.1016/j.radphyschem.2013.04.020>, doi:10.1016/j.radphyschem.2013.04.020.
- [LR07] C. Leroy and P.-G. Rancoita. Particle interaction and displacement damage in silicon devices operated in radiation environments. *Reports on Progress in Physics*, 70(4):493–625, mar 2007. URL: <https://doi.org/10.1088/0034-4885/70/4/R01>, doi:10.1088/0034-4885/70/4/r01.
- [LR11] C. Leroy and P.G. Rancoita. *Principles of Radiation Interaction in Matter and Detection*. World Scientific (Singapore), 3rd edition edition, 2011.
- [LQZ95] Teng Lijian, Hou Qing, and Luo Zhengming. Analytic fitting to the mott cross section of electrons. *Radiation Physics and Chemistry*, 45(2):235–245, feb 1995. URL: [https://doi.org/10.1016/0969-806X\(94\)00063-8](https://doi.org/10.1016/0969-806X(94)00063-8), doi:10.1016/0969-806x(94)00063-8.
- [MF48] William A. McKinley and Herman Feshbach. The coulomb scattering of relativistic electrons by nuclei. *Physical Review*, 74(12):1759–1763, dec 1948. URL: <https://doi.org/10.1103/PhysRev.74.1759>, doi:10.1103/physrev.74.1759.
- [Moliere48] G. Molière. Theorie der Streuung schneller geladener Teilchen II. Mehrfach- und Vielfachstreuung. *Zeitschrift Naturforschung Teil A*, 3:78–97, February 1948. doi:10.1515/zna-1948-0203.
- [VJV87] H. De Vries, C.W. De Jager, and C. De Vries. Nuclear charge-density-distribution parameters from elastic electron scattering. *Atomic Data and Nuclear Data Tables*, 36(3):495–536, may 1987. URL: [https://doi.org/10.1016/0092-640X\(87\)90013-1](https://doi.org/10.1016/0092-640X(87)90013-1), doi:10.1016/0092-640x(87)90013-1.
- [ZO64] Elmar Zeitler and Haakon Olsen. Screening effects in elastic electron scattering. *Physical Review*, 136(6A):A1546–A1552, dec 1964. URL: <https://doi.org/10.1103/PhysRev.136.A1546>, doi:10.1103/physrev.136.a1546.

- [BDCohenS+21] Samer Bakr, David D.Cohen, Rainer Siegele, Jay W. Archer, Sebastien Incerti, Vladimir Ivanchenko, Alfonso Mantero, Anatoly Rosenfeld, and Susanna Guatelli. Geant4 x-ray fluorescence with updated libraries. *Nuclear Instruments and Methods in Physics Research, Section B: Beam Interactions with Materials and Atoms*, 507:11–19, 2021. URL: <https://doi.org/10.1016/j.nimb.2021.09.009>.
- [BDCohenS+18] Samer Bakr, David D.Cohen, Rainer Siegele, Sebastien Incerti, Vladimir Ivanchenko, Alfonso Mantero, Anatoly Rosenfeld, and Susanna Guatelli. Latest geant4 developments for pixe applications. *Nuclear Instruments and Methods in Physics Research, Section B: Beam Interactions with Materials and Atoms*, 436:285–291, 2018. URL: <https://doi.org/10.1016/j.nimb.2018.10.004>.
- [BL79] W. Brandt and G. Lapicki. *Phys. Rev. A*, 20(N2):, 1979.
- [DDJS15] Cohen D.D., Crawford J., and R. Siegele. K, l, and m shell datasets for pixe spectrum fitting and analysis. *Nuclear Instruments and Methods in Physics Research, Section B: Beam Interactions with Materials and Atoms*, 363:7–18, 2015. URL: <https://doi.org/10.1016/j.nimb.2015.08.012>.
- [eal11a] A. Mantero et al. *X-Ray Spec.*, 40():135–140, 2011.
- [eal11b] A. Taborda et al. *X-Ray Spec.*, 40():127–134, 2011.
- [HP89] J. Sacher H. Paul. *Atom. Dat. and Nucl. Dat. Tabl.*, 42(1):105–156, May 1989.
- [HP93] O. Bolik H. Paul. *Atom. Dat. and Nucl. Dat. Tabl.*, 54(1):75–131, May 1993.
- [OST94] I. Orlic, C. H. Sow, and S. M. Tang. Semiempirical formulas for calculation of l subshell ionization cross sections. *International Journal of PIXE*, 4(4):217–230, 1994.
- [PCEal] S.T. Perkins, D.E. Cullen, and M.H. Chen et al. Tables and graphs of atomic subshell and relaxation data derived from the llnl evaluated atomic data library (eadl), z=1-100. Technical Report UCRL-50400 Vol.30.
- [Sco74] J. H. Scofield. Relativistic hartree-slater values for k and l x-ray emission rates. *At. Data Nucl. Data Tables*, 14(2):121–137, 1974. URL: [https://doi.org/10.1016/S0092-640X\(74\)80019-7](https://doi.org/10.1016/S0092-640X(74)80019-7).
- [WBrandtGLapicki81] W.Brandt and G.Lapicki. *Phys. Rev. A*, 23():, 1981.
- [BL81] W. Brandt and G. Lapicki. Energy-loss effect in inner-shell coulomb ionization by heavy charged particles. *Phys. Rev. A*, 23:1717–1729, 1981.
- [Cip08] S. Cipolla. Isics, 2008 version. 2008. Private communication: S Cipolla, Creighton Univ., Omaha NE 68178.
- [Cip07a] S. J. Cipolla. An improved version of isics: a program for calculating k-, l-, and m-shell cross sections from pwba and ecpsr theory using a personal computer. *Comp. Phys. Comm.*, 176:157–159, 2007.
- [Cip07b] S. J. Cipolla. The united atom approximation option in the isics program to calculate k-, l-, and m-shell cross sections from pwba and ecpsr theory. *Nucl. Instrum. Meth. B*, 261():142–144, 2007.
- [eal09] M. G. Pia et al. Pixe simulation with geant4. *IEEE Trans. Nucl. Sci.*, 56(6):3614–3649, 2009.
- [eal07] P. Predehl et al. Erosita. In *Proc. of the SPIE*, volume 6686, 668617–9. 2007.
- [KND08] A. Kahoul, M. Nekkab, and B. Deghfel. Empirical k-shell ionization cross-sections of elements from  ${}^4\text{Be}$  to  ${}^{92}\text{U}$  by proton impact. *Nucl. Instrum. Meth. B*, 266():4969–4975, 2008.
- [Lap05] G. Lapicki. The status of theoretical k-shell ionization cross sections by protons. *X-Ray Spectrom.*, 34:269–278, 2005.
- [Lap08] G. Lapicki. Scaling of analytical cross sections for k-shell ionization by nonrelativistic protons to cross sections by protons at relativistic velocities. *J. Phys. B*, 41:115201–115213, 2008.
- [LC96] Z. Liu and S. J. Cipolla. Isics: a program for calculating k-, l-, and m-shell cross sections from ecpsr theory using a personal computer. *Comp. Phys. Comm.*, 97:315–330, 1996.

- [MNM88] Y. Miyagawa, S. Nakamura, and S. Miyagawa. Analytical formulas for ionization cross sections and coster-kronig corrected fluorescence yields of the 1l, 12, and 13 subshells. *Nucl. Instrum. Meth. B*, 30:115–122, 1988.
- [OST94] I. Orlic, C. H. Sow, and S. M. Tang. Semiempirical formulas for calculation of 1 subshell ionization cross sections. *International Journal of PIXE*, 4(4):217–230, 1994.
- [OSaSMT94] I. Orlic, J. Sow, and S. M. Tang. Experimental l-shell x-ray production and ionization cross sections for proton impact. *At. Data Nucl. Data Tab.*, 56:159–210, 1994.
- [PB93] H. Paul and O. Bolik. Fitted empirical reference cross sections for k-shell ionization by alpha particles. *At. Data Nucl. Data Tab.*, 54:75–131, 1993.
- [PS89] H. Paul and J. Sacher. Fitted empirical reference cross sections for k-shell ionization by protons. *At. Data Nucl. Data Tab.*, 42:105–156, 1989.
- [SC84] R. S. Sokhi and D. Crumpton. Experimental l-shell x-ray production and ionization cross sections for proton impact. *At. Data Nucl. Data Tab.*, 30:49–124, 1984.
- [SOLT93] C. H. Sow, I. Orlic, K. K. Lob, and S. M. Tang. New parameters for the calculation of 1 subshell ionization cross sections. *Nucl. Instrum. Meth. B*, 75:58–62, 1993.
- [eal84] M.J. Berger et al. Icru report 37. *Journal of the International Commission on Radiation Units and Measurements*, os19(2):, dec 1984. URL: <https://doi.org/10.1093/jicru/os19.2.Report37>, doi:10.1093/jicru/os19.2.report37.
- [MC70] H. Messel and D. Crawford. *Electron-Photon shower distribution*. Pergamon Press, 1970.
- [SP71] R.M. Sternheimer and R.F. Peierls. General expression for the density effect for the ionization loss of charged particles. *Physical Review B*, 3(11):3681–3692, jun 1971. URL: <https://doi.org/10.1103/PhysRevB.3.3681>, doi:10.1103/physrevb.3.3681.
- [eal01] F. Salvat et al. Penelope - a code system for monte carlo simulation of electron and photon transport. Technical Report, Workshop Proceedings Issy-les-Moulineaux, France; AEN-NEA, 5-7 November 2001.
- [Fan63] U. Fano. Penetration of protons, alpha particles and mesons. *Ann. Rev. Nucl. Sci.*, 13():1, 1963.
- [eal93] René Brun et al. *GEANT: Detector Description and Simulation Tool; Oct 1994*. CERN Program Library. CERN, Geneva, 1993. Long Writeup W5013. URL: <https://cds.cern.ch/record/1082634>.
- [MC70] H. Messel and D. Crawford. *Electron-Photon shower distribution*. Pergamon Press, 1970.
- [STPerkins89] S.M.Seltzer S.T.Perkins, D.E.Cullen. Tables and graphs of electron-interaction cross-sections from 10 ev to 100 gev derived from the llnl evaluated electron data library (eedl), z=1-100. Technical Report UCRL-50400 Vol.31, Lawrence Livermore National Laboratory, 1989.
- [eal08] C. Amsler et al. Review of particle physics. *Physics Letters B*, 667(1-5):1–6, sep 2008. URL: <https://doi.org/10.1016/j.physletb.2008.07.018>, doi:10.1016/j.physletb.2008.07.018.
- [eal04] H.D. Hansen et al. Landau-pomeranchuk-migdal effect for multihundred gev electrons. *Physical Review D*, feb 2004. URL: <https://doi.org/10.1103/PhysRevD.69.032001>, doi:10.1103/physrevd.69.032001.
- [eal97] P. L. Anthony et al. Bremsstrahlung suppression due to the landau-pomeranchuk-migdal and dielectric effects in a variety of materials. *Physical Review D*, 56(3):1373–1390, aug 1997. URL: <https://doi.org/10.1103/PhysRevD.56.1373>, doi:10.1103/physrevd.56.1373.
- [eal77] R.H. Pratt et al. Bremsstrahlung energy spectra from electrons of kinetic energy  $1 \text{ keV} \leq t1 \leq 2000 \text{ keV}$  incident on neutral atoms  $2 \leq z \leq 92$ . *Atomic Data and Nuclear Data Tables*, 20(2):175–209, aug 1977. URL: [https://doi.org/10.1016/0092-640X\(77\)90045-6](https://doi.org/10.1016/0092-640X(77)90045-6), doi:10.1016/0092-640X(77)90045-6.

- [eal82] T. Stanev et al. Development of ultrahigh-energy electromagnetic cascades in water and lead including the landau-pomeranchuk-migdal effect. *Physical Review D*, 25(5):1291–1304, mar 1982. URL: <https://doi.org/10.1103/PhysRevD.25.1291>, doi:10.1103/physrevd.25.1291.
- [GG64] V.M. Galitsky and I.I. Gurevich. Coherence effects in ultra-relativistic electron bremsstrahlung. *Il Nuovo Cimento (1955-1965)*, 32(2):396–407, Apr 1964. URL: <https://doi.org/10.1007/BF02733969>, doi:10.1007/BF02733969.
- [Kle99] Spencer Klein. Suppression of bremsstrahlung and pair production due to environmental factors. *Reviews of Modern Physics*, 71(5):1501–1538, oct 1999. URL: <https://doi.org/10.1103/RevModPhys.71.1501>, doi:10.1103/revmodphys.71.1501.
- [Mig56] A.B. Migdal. Bremsstrahlung and pair production in condensed media at high energies. *Physical Review*, 103(6):1811–1820, sep 1956. URL: <https://doi.org/10.1103/PhysRev.103.1811>, doi:10.1103/physrev.103.1811.
- [Per94] M.L. Perl. Notes on the Landau, Pomeranchuk, Migdal effect: Experiment and theory. In *8th Les Rencontres de Physique de la Vallee d'Aoste: Results and Perspectives in Particle Physics La Thuile, Italy, March 6-12, 1994*. 1994. URL: <http://www-public.slac.stanford.edu/sciDoc/docMeta.aspx?slacPubNumber=SLAC-PUB-6514>.
- [SB85] S.M. Seltzer and M.J. Berger. Bremsstrahlung spectra from electron interactions with screened atomic nuclei and orbital electrons. *Nucl. Instr. and Meth. in Phys. Research B*, 12(1):95–134, aug 1985. URL: [https://doi.org/10.1016/0168-583X\(85\)90707-4](https://doi.org/10.1016/0168-583X(85)90707-4), doi:10.1016/0168-583x(85)90707-4.
- [SB86] S.M. Seltzer and M.J. Berger. Bremsstrahlung energy spectra from electrons with kinetic energy 1 kev - 100 gev incident on screened nuclei and orbital electrons of neutral atoms with z = 1–100. *Atomic Data and Nuclear Data Tables*, 35():345, 1986.
- [TM72] M.L. Ter-Mikaelian. *High-energy Electromagnetic Processes in Condensed Media*. Wiley, 1972.
- [TER54] ML TERMIKAELYAN. Spektr tormoznogo izlucheniya v srede. *DOKLADY AKADEMII NAUK SSSR*, 94(6):1033–1036, 1954.
- [Tsa74] Y. Tsai. Pair production and bremsstrahlung of charged leptons. *Rev. Mod. Phys.*, 46():815, 1974.
- [Tsa77] Y. Tsai. Pair production and bremsstrahlung of charged leptons. *Rev. Mod. Phys.*, 49():421, 1977.
- [BS82] M.J. Berger and S.M. Seltzer. Stopping power of electrons and positrons. Technical Report Report NB-SIR 82-2550, National Bureau of Standards, 1982.
- [eal01] F. Salvat et al. Penelope - a code system for monte carlo simulation of electron and photon transport. Technical Report, Workshop Proceedings Issy-les-Moulineaux, France; AEN-NEA, 5-7 November 2001.
- [eal86] L.Kim et al. Ratio of positron to electron bremsstrahlung energy loss: an approximate scaling law. *Phys. Rev. A*, 33():2002, 1986.
- [KQP83] L. Kissel, C.A. Quarles, and R.H. Pratt. Shape functions for atomic-field bremsstrahlung from electrons of kinetic energy 1–500 keV on selected neutral atoms  $1 \leq z \leq 92$ . *Atomic Data and Nuclear Data Tables*, 28(3):381–460, May 1983. URL: [https://doi.org/10.1016/0092-640X\(83\)90001-3](https://doi.org/10.1016/0092-640X(83)90001-3), doi:10.1016/0092-640x(83)90001-3.
- [STPerkins89] S.M.Seltzer S.T.Perkins, D.E.Cullen. Tables and graphs of electron-interaction cross-sections from 10 ev to 100 gev derived from the llnl evaluated electron data library (eedl), z=1-100. Technical Report UCRL-50400 Vol.31, Lawrence Livermore National Laboratory, 1989.
- [SB86] S.M. Seltzer and M.J. Berger. Bremsstrahlung energy spectra from electrons with kinetic energy 1 kev - 100 gev incident on screened nuclei and orbital electrons of neutral atoms with z = 1–100. *Atomic Data and Nuclear Data Tables*, 35():345, 1986.

- [AFBC89] R. Mohan A. F. Bielajew and C.-S. Chui. Improved bremsstrahlung photon angular sampling in the egs4 code system. Technical Report, 1989. Report NRCC/PIRS-0203.
- [ea03] P. Rodrigues et al. Geant4 applications and developments for medical physics experiments. *IEEE NSS/MIC Conference Record*, ():, 2003.
- [eal99] J. Apostolakis et al. Geant4 low energy electromagnetic models for electrons and photons. Technical Report, CERN, CERN/INFN, 1999. CERN-OPEN-99-034(1999), INFN/AE-99/18.
- [eal93] René Brun et al. *GEANT: Detector Description and Simulation Tool; Oct 1994*. CERN Program Library. CERN, Geneva, 1993. Long Writeup W5013. URL: <https://cds.cern.ch/record/1082634>.
- [HKTL79] R. H. Pratt H. K. Tseng and C. M. Lee. Electron bremsstrahlung angular distributions in the 1-500 kev energy range. *Phys. Rev. A*, 19():187, 1979.
- [KM59] H. W. Koch and J. W. Motz. Bremsstrahlung cross-section formulas and related data. *Rev. Mod. Phys.*, 31(4):920–955, 1959.
- [LKP83] C. A. Quarls L. Kissel and R. H. Pratt. Bremsstrahlung from electron collisions with neutral atoms. *Atom. Data Nucl. Data Tables*, 28():382, 1983.
- [STPerkins89] S.M.Seltzer S.T.Perkins, D.E.Cullen. Tables and graphs of electron-interaction cross-sections from 10 ev to 100 gev derived from the llnl evaluated electron data library (eedl), z=1-100. Technical Report UCRL-50400 Vol.31, Lawrence Livermore National Laboratory, 1989.
- [Tsa74] Y. Tsai. Pair production and bremsstrahlung of charged leptons. *Rev. Mod. Phys.*, 46():815, 1974.
- [Tsa77] Y. Tsai. Pair production and bremsstrahlung of charged leptons. *Rev. Mod. Phys.*, 49():421, 1977.
- [Hei54] W. Heitler. *The Quantum Theory of Radiation*. Oxford Clarendon Press, edition, 1954.
- [MC70] H. Messel and D. Crawford. *Electron-Photon shower distribution*. Pergamon Press, 1970.
- [NHR85] W.R. Nelson, H. Hirayama, and D.W.O. Rogers. *EGS4 code system*. SLAC, Dec 1985. SLAC-265, UC-32.
- [BABGarcia+18] M. Boscolo, M. Antonelli, O. Blanco-Garc\'ia, S. Guiducci, S. Liuzzo, P. Raimondi, and F. Collamati. Low emittance muon accelerator studies with production from positrons on target. *Physical Review Accelerators and Beams*, jun 2018. URL: <https://doi.org/10.1103/physrevaccelbeams.21.061005>, doi:10.1103/physrevaccelbeams.21.061005.
- [BL09] Stanley J. Brodsky and Richard F. Lebed. Production of the smallest QED atom: true muonium ( $\mu+\mu-$ ). *Physical Review Letters*, may 2009. URL: <https://doi.org/10.1103/physrevlett.102.213401>, doi:10.1103/physrevlett.102.213401.
- [eal06] A.G. Bogdanov et al. Geant4 simulation of production and interaction of muons. *IEEE Trans. Nucl. Sci.*, 2006. URL: <https://doi.org/10.1109/TNS.2006.872633>.
- [HBK03] H. Burkhardt, S. Kelner and R. Kokoulin. Production of muon pairs in annihilation of high-energy positrons with resting electrons. *CERN-AB-2003-002 (ABP) and CLIC Note 554*, January 2003. URL: <http://cds.cern.ch/record/603739>.
- [BEIS99] M. Benayoun, S. I. Eidelman, V. N. Ivanchenko, and Z. K. Silagadze. Spectroscopy at b-Factories using hard photon emission. *Modern Physics Letters A*, 14(37):2605–2614, dec 1999. URL: <https://doi.org/10.1142/S021773239900273X>, doi:10.1142/s021773239900273x.
- [eal06] A.G. Bogdanov et al. Geant4 simulation of production and interaction of muons. *IEEE Trans. Nucl. Sci.*, 2006. URL: <https://doi.org/10.1109/TNS.2006.872633>.
- [SRKP97] R.P. Kokoulin S.R. Kelner and A.A. Petrukhin. Bremsstrahlung from muons scattered by atomic electrons. *Physics of Atomic Nuclei*, 60:576–583, April 1997.
- [ABB94] Y. M. Andreev, L. B. Bezrukov, and E. V. Bugaev. Excitation of a target in muon bremsstrahlung. *Physics of Atomic Nuclei*, 57:2066–2074, December 1994.

- [AB97] Yu. M. Andreev and E. V. Bugaev. Muon bremsstrahlung on heavy atoms. *Physical Review D*, 55(3):1233–1243, feb 1997. URL: <https://doi.org/10.1103/PhysRevD.55.1233>, doi:10.1103/physrevd.55.1233.
- [KKP95] SR Kelner, RP Kokoulin, and AA Petrukhin. About cross section for high-energy muon bremsstrahlung. Technical Report, MEPhI, 1995. Preprint MEPhI 024-95, Moscow, 1995, CERN SCAN-9510048.
- [PS68] A. A. Petrukhin and V. V. Shestakov. The influence of the nuclear and atomic form factors on the muon bremsstrahlung cross section. *Canadian Journal of Physics*, 46(10):S377–S380, may 1968. URL: <https://doi.org/10.1139/p68-251>, doi:10.1139/p68-251.
- [SRKP97] R.P. Kokoulin S.R. Kelner and A.A. Petrukhin. Bremsstrahlung from muons scattered by atomic electrons. *Physics of Atomic Nuclei*, 60:576–583, April 1997.
- [Kel98] S.R. Kelner. Pair production in collisions between muons and atomic electrons. *Physics of Atomic Nuclei*, 61:448–456, March 1998.
- [KP70] R.P. Kokoulin and A.A. Petrukhin. Analysis of the cross-section of direct pair production by fast muons. *International Cosmic Ray Conference*, 4:277–284, 1970. Proc. 11th International Cosmic Ray Conference, Acta Phys. Acad. Sci. Hung., bf 29, Suppl.4.
- [KP71] R.P. Kokoulin and A.A. Petrukhin. Influence of the nuclear formfactor on the cross-section of electron pair production by high energy muons. In *Cosmic Ray Conference Papers*, volume 6, 2436–2444. Hobart, Tasmania, Australia, 16–25 August 1971. 12th International Conference on Cosmic Rays.
- [BB81] L.B. Bezrukov and E.V. Bugaev. Nucleon shadowing effects in photon nucleus interaction. (in russian). *Yad. Fiz.*, 33:1195–1207, 1981. Sov. J. Nucl. Phys. 33, 635 (1981) - english translation.
- [BKUP77] V. V Borog, V. G. Kirillov-Ugryumov, and A. A Petrukhin. Inelastic Interactions of Muons with Fe Nuclei at Small  $q^{**2}$  in the Energy Region Above 200-GeV. *Yad. Fiz.*, 25:85–93, 1977. Sov. J. Nucl. Phys. 25, 46-51 (1977) - english translation.
- [BP75] V.V. Borog and A.A. Petrukhin. The cross-section of the nuclear interaction of high energy muons. *International Cosmic Ray Conference*, 6:1949–1954, August 1975.
- [BCG72] Stanley J. Brodsky, Francis E. Close, and J. F. Gunion. Phenomenology of photon processes, vector dominance, and crucial tests for parton models. *Physical Review D*, 6(1):177–189, jul 1972. URL: <https://doi.org/10.1103/PhysRevD.6.177>, doi:10.1103/physrevd.6.177.
- [eal79] D. O. Caldwell et al. Measurement of shadowing in photon-nucleus total cross sections from 20 to 185 GeV. *Physical Review Letters*, 42(9):553–556, feb 1979. URL: <https://doi.org/10.1103/PhysRevLett.42.553>, doi:10.1103/physrevlett.42.553.
- [Han63] L. N. Hand. Experimental investigation of pion electroproduction. *Physical Review*, 129(4):1834–1846, feb 1963. URL: <https://doi.org/10.1103/PhysRev.129.1834>, doi:10.1103/physrev.129.1834.
- [Ahl80] Steven P. Ahlen. Theoretical and experimental aspects of the energy loss of relativistic heavily ionizing particles. *Reviews of Modern Physics*, 52(1):121–173, jan 1980. URL: [https://doi.org/10.1103/revmodphys.52.121](https://doi.org/10.1103/RevModPhys.52.121).
- [ARB73] J. C. Ashley, R. H. Ritchie, and Werner Brandt. Z13-dependent stopping power and range contributions. *Physical Review A*, 8(5):2402–2408, nov 1973. URL: <https://doi.org/10.1103/PhysRevA.8.2402>, doi:10.1103/physreva.8.2402.
- [Bic92] Hans Bichsel. Stopping power and ranges of fast ions in heavy elements. *Physical Review A*, 46(9):5761–5773, nov 1992. URL: <https://doi.org/10.1103/PhysRevA.46.5761>, doi:10.1103/physreva.46.5761.
- [BK82] W. Brandt and M. Kitagawa. *Phys. Rev. B*, 25:5631, 1982.

- [ea06] W-M Yao et al. Review of particle physics. *Journal of Physics G: Nuclear and Particle Physics*, 33(1):1–1232, jul 2006. URL: <https://doi.org/10.1088/0954-3899/33/1/001>, doi:10.1088/0954-3899/33/1/001.
- [eal84] M.J. Berger et al. Icru report 37. *Journal of the International Commission on Radiation Units and Measurements*, os19(2):, dec 1984. URL: <https://doi.org/10.1093/jicru/os19.2.Report37>, doi:10.1093/jicru/os19.2.report37.
- [eal93] M.J. Berger et al. Report 49. *Journal of the International Commission on Radiation Units and Measurements*, os25(2):NP–NP, may 1993. ICRU Report 49. URL: <https://doi.org/10.1093/jicru/os25.2.Report49>, doi:10.1093/jicru/os25.2.report49.
- [Kha68] Govind S. Khandelwal. Shell corrections for k- and l-electrons. *Nuclear Physics A*, 116(1):97–111, jul 1968. URL: [https://doi.org/10.1016/0375-9474\(68\)90485-5](https://doi.org/10.1016/0375-9474(68)90485-5), doi:10.1016/0375-9474(68)90485-5.
- [NISa] NIST. Nist database of atomic weight and isotopic composition. <https://www.nist.gov/pml/atomic-weights-and-isotopic-compositions-relative-atomic-masses>. [Online; accessed 11-december-2017].
- [NISb] NIST. Nist material composition database. <https://physics.nist.gov/cgi-bin/Star/compos.pl>. [Online; accessed 11-december-2017].
- [SP71] R.M. Sternheimer and R.F. Peierls. General expression for the density effect for the ionization loss of charged particles. *Physical Review B*, 3(11):3681–3692, jun 1971. URL: <https://doi.org/10.1103/PhysRevB.3.3681>, doi:10.1103/physrevb.3.3681.
- [SBS84] RM Sternheimer, MJ Berger, and Stephen M Seltzer. Density effect for the ionization loss of charged particles in various substances. *Atomic Data and Nuclear Data Tables*, 30(2):261–271, 1984.
- [Wal52] M. C. Walske. The stopping power of K-electrons. *Physical Review*, 88(6):1283–1289, dec 1952. URL: <https://doi.org/10.1103/PhysRev.88.1283>, doi:10.1103/physrev.88.1283.
- [Wal56] M. C. Walske. Stopping power of L-electrons. *Physical Review*, 101(3):940–944, feb 1956. URL: <https://doi.org/10.1103/PhysRev.101.940>, doi:10.1103/physrev.101.940.
- [ZBL85] J.F. Ziegler, J.P. Biersack, and U. Littmark. *The Stopping and Ranges of Ions in Solids*. Pergamon Press, vol.1 edition, 1985.
- [eal93] M.J. Berger et al. Report 49. *Journal of the International Commission on Radiation Units and Measurements*, os25(2):NP–NP, may 1993. ICRU Report 49. URL: <https://doi.org/10.1093/jicru/os25.2.Report49>, doi:10.1093/jicru/os25.2.report49.
- [eal05] P. Sigmund et al. Stopping of ions heavier than helium. *Journal of the International Commission on Radiation Units and Measurements*, jun 2005. ICRU Report 73. URL: <https://doi.org/10.1093/jicru/ndi001>, doi:10.1093/jicru/ndi001.
- [PSP09] A. Schinner P. Sigmund and H. Paul. Stopping of ions heavier than helium. Technical Report Errata and Addenda for ICRU Report 73, 2009.
- [PSigmund09] P.Sigmund. Personal communication. (): 2009.
- [QY91] Z. Wang Q. Yang, D.J. O'Connor. *Nucl. Instr. and Meth. B*, 61():149, 1991.
- [SS00] P. Sigmund and A. Schinner. *Eur. Phys. J. D*, 12():425, 2000.
- [SS02] P. Sigmund and A. Schinner. *Nucl. Instr. Meth. B*, 195():64, 2002.
- [WKC77] in: W.K. Chu. *Ion Beam Handbook for Material Analysis*, edt. J.W. Mayer and E. Rimini. Academic Press, NY, edition, 1977.
- [ZM88] J.F. Ziegler and J.M. Manoyan. *Nucl. Instr. and Meth. B*, 35():215, 1988.
- [aal] G. Alexander et al. Undulator-based production of polarized positrons: a proposal for the 50-gev beam in the fftb. Technical Report SLAC-TN-04-018, SLAC-PROPOSAL-E-166, SLAC.

- [eal54] H. Davies et al. Theory of bremsstrahlung and pair production. ii. integral cross section for pair production. *Phys. Rev.*, 93(4):788–795, 1954.
- [eal] P. Starovoitov et al. *in preparation*.
- [eal85] R. Brun et al. The geant3 electromagnetic shower program and a comparison with the egs3 code. Technical Report CERN-DD/85/1, CERN, 1985.
- [Flottmann93a] K. Flöttmann. DESY-93-161, DESY Hamburg, phd thesis edition, 1993.
- [Flottmann93b] K. Flöttmann. *Investigations toward the development of polarized and unpolarized high intensity positron sources for linear colliders*. Universitat Hamburg, phd thesis edition, 1993.
- [FM57] G. W. Ford and C. J. Mullin. *Phys. Rev.*, 108:477, 1957.
- [Hoo97] Johannes Marinus Hoogduin. *Electron, positron and photon polarimetry*. Rijksuniversiteit Groningen, phd thesis edition, 1997.
- [KM59] H. W. Koch and J. W. Motz. Bremsstrahlung cross-section formulas and related data. *Rev. Mod. Phys.*, 31(4):920–955, 1959.
- [Lai08] K. Laihem. *Measurement of the positron polarization at an helical undulator based positron source for the International Linear Collider ILC*. Humboldt University Berlin, Germany, phd thesis edition, 2008.
- [LT54a] F.W. Lipps and H.A. Tolhoek. Polarization phenomena of electrons and photons i. *Physica*, 20:85, 1954.
- [LT54b] F.W. Lipps and H.A. Tolhoek. Polarization phenomena of electrons and photons ii. *Physica*, 20:395, 1954.
- [LKNS] J. C. Liu, T. Kotseroglou, W. R. Nelson, and D. C. Schultz. Polarization study for nlc positron source using egs4. Technical Report SLAC-PUB-8477, SLAC.
- [McM61] W. H. McMaster. *Rev. Mod. Phys.*, 33():8, 1961.
- [McM54] W.H. McMaster. Polarization and the stokes parameters. *American Journal of Physics*, 22(6):351–362, 1954.
- [NBH93] Y. Namito, S. Ban, and H. Hirayama. Implementation of linearly polarized photon scattering into the egs4 code. *Nucl. Instrum. Meth. A*, 332:277, 1993.
- [NHR85] W.R. Nelson, H. Hirayama, and D.W.O. Rogers. *EGS4 code system*. SLAC, Dec 1985. SLAC-265, UC-32.
- [OM59] H. Olsen and L.C. Maximon. Photon and electron polarization in high- energy bremsstrahlung and pair production with screening. *Physical Review*, 114:887–904, 1959.
- [OV58] H. Olsen and Kgl. N. Videnskab. *Selskabs Forh.*, 1958.
- [Pag57] L. A. Page. Polarization effects in the two-quantum annihilation of positrons. *Phys. Rev.*, 106:394–398, 1957.
- [Ste58] P. Stehle. *Phys. Rev.*, 110:1458, 1958.
- [Sto52] G. Stokes. Trans. Cambridge Phil. Soc., 9 edition, 1852.
- [Dep03] G.O. Depaola. New monte carlo method for compton and rayleigh scattering by polarized gamma rays. *Nucl. Instrum. and Methods A*, 512():619, 2003.
- [Hei54] W. Heitler. *The Quantum Theory of Radiation*. Oxford Clarendon Press, edition, 1954.
- [DKT99] G.O. Depaola, C.N. Kozameh, and M.H. Tiglio. A method to determine the polarization of high energy gamma rays. *Astroparticle Physics*, 10():175, 1999.
- [Ber13] D. Bernard. Polarimetry of cosmic gamma-ray sources above e+e- pair creation threshold. *Nucl. Instrum. Meth.*, A729:765–780, 2013.

- [BP71] V. F. Boldyshev and \relax Yu. P. Peresunko. Electron-positron pair photoproduction on electrons and analysis of photon beam polarization. *Yad. Fiz.*, 14:1027–1032, 1971.
- [GB17a] P. Gros and D. Bernard. gamma-ray polarimetry with conversions to e+e- pairs: polarization asymmetry and the way to measure it. *Astropart. Phys.*, 88:30–37, 2017.
- [GB17b] P. Gros and D. Bernard. gamma-ray telescopes using conversions to e+e- pairs: event generators, angular resolution and polarimetry. *Astropart. Phys.*, 88:60–67, 2017.
- [May51] M. M. May. On the polarization of high energy bremsstrahlung and of high energy pairs. *Phys. Rev.*, (84):265, 1951.
- [OM59] H. Olsen and L.C. Maximon. Photon and electron polarization in high- energy bremsstrahlung and pair production with screening. *Physical Review*, 114:887–904, 1959.
- [eal00] J. Apostolakis et al. *Comput. Phys. Commun.*, 132():241, 2000.
- [FS75] C.W. Fabian and W. Struczinski. *Physics Letters*, B57():483, 1975.
- [GMGY75] G.M. Garibian, L.A. Gevorgian and C. Yang. *Sov. Phys.- JETP*, 39():265, 1975.
- [Gar71] G.M. Garibyan. *Sov. Phys. JETP*, 32():23, 1971.
- [Gri02a] V.M. Grichine. Generation of x-ray transition radiation inside complex radiators. *Physics Letters B*, 525(3-4):225–239, jan 2002. URL: [https://doi.org/10.1016/S0370-2693\(01\)01443-5](https://doi.org/10.1016/S0370-2693(01)01443-5).
- [Gri02b] V.M. Grichine. On the energy-angle distribution of cherenkov radiation in an absorbing medium. *Nuclear Instruments and Methods in Physics Research Section A: Accelerators, Spectrometers, Detectors and Associated Equipment*, 482(3):629–633, apr 2002. URL: [https://doi.org/10.1016/S0168-9002\(01\)01927-1](https://doi.org/10.1016/S0168-9002(01)01927-1).
- [eal00] D.E. Groom et al. Particle data group, rev. of particle properties. *Eur. Phys. J. C15*, 1, 2000. <http://pdg.lbl.gov/>.
- [JDJackson98] J.D.Jackson. *Classical Electrodynamics*. John Wiley and Sons, third edition, 1998.
- [Bur] H. Burkhardt. Monte carlo generation of the energy spectrum of synchrotron radiation. *CERN-AB and EuroTeV report*. CERN-OPEN-2007-018. URL: <http://cds.cern.ch/record/1038899>.
- [Bur98] H. Burkhardt. Reminder of the edge effect in synchrotron radiation. Technical Report 172, CERN, Geneva, 1998. LHC Project Note. URL: <http://cds.cern.ch/record/692027>.
- [Bur90] H. Burkhardt. Monte carlo generator for synchrotron radiation. *LEP Note 632*, CERN, December 1990. URL: <http://cds.cern.ch/record/443490>.
- [Che86] P. Chen. An introduction to beamstrahlung and disruption. *Frontiers of Particle Beams*, pages 481–494, Lecture Notes in Physics 296 1986. M. Month and S. Turner, eds. URL: <http://slac.stanford.edu/pubs/slacpubs/4250/slac-pub-4379.pdf>.
- [CBBK17] F Collamati, M Boscolo, H Burkhardt, and R Kersevan. Synchrotron radiation backgrounds for the FCC-hh experiments. *Journal of Physics: Conference Series*, 874:012004, jul 2017. URL: <https://doi.org/10.1088/1742-6596/874/1/012004>.
- [eal71] F. Herlach et al. Experiments with megagauss targets at slac. *IEEE Trans. Nucl. Sci.*, NS 18(3):809–814, 1971. URL: <https://doi.org/10.1109/TNS.1971.4326194>.
- [Gri02] V.M. Grichine. Radiation of accelerated charge in absorbing medium. *CERN-OPEN-2002-056*, 2002. URL: <http://cds.cern.ch/record/582178>.
- [HHUmstatter81] H.H.Umstätter. *CERN/PS/SM/81-13*, CERN Geneva, 1981.
- [Hof04] A. Hofmann. *The Physics of Synchrotron Radiation*. Cambridge University Press, edition, 2004.
- [JBMG97] J.B. Murphy, S. Krinsky and R.L. Gluckstern. Longitudinal wakefield for an electron moving on a circular orbit. *Part. Acc.* 57, 9, 1997. URL: <http://cds.cern.ch/record/1120287>.

- [JDJackson98] J.D.Jackson. *Classical Electrodynamics*. John Wiley and Sons, third edition, 1998.
- [Luk75] Y. Luke. *The special functions and their approximations*. New York, NY: Academic Press, edition, 1975. 585p.
- [ST86] A.A. Sokolov and I.M. Ternov. *Radiation from Relativistic Electrons*. Amer. Inst of Physics, edition, 1986.
- [TEL82] D. White T. Erber, G.B. Baumgartner and H.G. Latal. Megagauss bremsstrahlung and radiation reaction. *Batavia 1983, proceedings, High Energy Accelerators*, pages 372–374, 1982. URL: <https://inspirehep.net/files/8019a7defef117ad62cb1245ee9208f4>.
- [Col07] Milagro Collaboration. Tev all-sky gamma ray observatory. <http://hawc.umd.edu/>, 2007. [Online; accessed 15-July-2017].
- [Fit14] Richard Fitzpatrick. Mie scattering lectures. <http://farside.ph.utexas.edu/teaching/jk1/lectures/node103.html>, 2014. [Online; accessed 26-october-2017].
- [Vas] Vlasios Vasileiou. Private communication.
- [wik17] wikipedia. Mie scattering. [http://en.wikipedia.org/wiki/Mie\\_scattering](http://en.wikipedia.org/wiki/Mie_scattering), 2017. [Online; accessed 26-october-2017].
- [ZS10] Guangyuan Zhao and Xianming Sun. Error analysis of using henyey-greenstein [sic] in monte carlo radiative transfer simulations. In *Progress In Electromagnetics Research Symposium Proceedings*, 1449–1452. Xi'an, China, March 22nd 2010. web-site: <https://www.piers.org/proceedings/home.html>. URL: <https://www.piers.org/pierspublications/PIERS2010XianProceedings04.pdf>.
- [AV12] J.-E. Sauvestre et al. A. Valentin, M. Raine. Geant4 physics processes for microdosimetry simulation: very low energy electromagnetic models for electrons in silicon. *Nucl. Instr. and Meth. in Phys. Research B*, 288():66–73, 2012.
- [AVP12] M. Gaillardin A. Valentin, M. Raine and P. Paillet. Geant4 physics processes for microdosimetry simulation: very low energy electromagnetic models for protons and heavy ions in silicon. *Nucl. Instr. and Meth. in Phys. Research B*, 287():124–129, 2012.
- [Inc] S. Incerti. Geant4-microelec online available at:. Technical Report. URL: <http://geant4-internal.web.cern.ch/node/1623>.
- [GRP90] G. Grindhammer, M. Rudowicz, and S. Peters. The fast simulation of electromagnetic and hadronic showers. *Nuclear Instruments and Methods in Physics Research Section A: Accelerators, Spectrometers, Detectors and Associated Equipment*, 290(2-3):469–488, may 1990. URL: [https://doi.org/10.1016/0168-9002\(90\)90566-O](https://doi.org/10.1016/0168-9002(90)90566-O), doi:10.1016/0168-9002(90)90566-o.
- [GP93] Guenter Grindhammer and S. Peters. The Parameterized simulation of electromagnetic showers in homogeneous and sampling calorimeters. In *International Conference on Monte Carlo Simulation in High-Energy and Nuclear Physics - MC 93 Tallahassee, Florida, February 22-26, 1993*. 1993. arXiv:hep-ex/0001020.
- [LS75] Egidio Longo and Ignazio Sestili. Monte carlo calculation of photon-initiated electromagnetic showers in lead glass. *Nuclear Instruments and Methods*, 128(2):283–307, oct 1975. URL: [https://doi.org/10.1016/0029-554X\(75\)90679-5](https://doi.org/10.1016/0029-554X(75)90679-5), doi:10.1016/0029-554x(75)90679-5.
- [Ros52] B. Rossi. *High Energy Particles*. Prentice-Hall, edition, 1952.



# **Part IV**

# **Hadronic**



## HADRONIC CROSS SECTIONS IN GEANT4

Total, inelastic and elastic cross sections for hadron-nucleus, nucleus-nucleus and antinucleus-nucleus reactions are provided for all possible energies [eal16]. Coulomb cross sections are implemented within electromagnetic physics libraries as single or multiple scatterings of charged particles, so the main Coulomb term is excluded from hadron cross sections. An interference between electromagnetic and strong amplitudes should be taken into account in hadronic physics but in the main models is ignored so far.

### 20.1 Hadron-nucleus Cross Sections

#### 20.1.1 Hadron-nucleon cross sections

The hadron-nucleon cross section parameterisations were tuned to the PDG-2016 data [ealParticleDGroup16]. Both total and elastic cross sections are parameterized for protons, anti-protons, pions, and kaons. For positively charged projectile a Coulomb barrier factor is applied, for negatively charged particles below laboratory kinetic energy 100 keV cross section is set to const value. For hyperons, charmed and bottom mesons and baryons scaling from proton and pion cross sross sections is applied.

#### 20.1.2 Neutron-Nucleus cross sections

Neutron cross section data for elastic, inelastic, capture, and fission processes are available with the G4NDL4.6 dataset derived from the recent ENDF database. These data are used with all HP models. For fast access to the neutron cross sections for all target nuclei, the dataset G4PARTICLEXS4.0 is used in the default and many other reference Physics Lists.

#### 20.1.3 Other Hadron-Nucleus cross sections

For protons and pions a special combination of cross sections from the Barashenkov interpolations [BT72, NEA] are used below 91 GeV and the Glauber-Gribov cross sections are used above. Glauber-Gribov cross sections are used for all other hadrons and ions.

The simplified Glauber model cross sections assume Gaussian-distributed, point-like nucleons and are given by [Gri09a, Gri09b]:

$$\begin{aligned}\sigma_{tot}^{hA} &= 2\pi R^2 \ln \left[ 1 + \frac{A\sigma_{tot}^{hN}}{2\pi R^2} \right], & \sigma_{in}^{hA} &= \pi R^2 \ln \left[ 1 + \frac{A\sigma_{tot}^{hN}}{\pi R^2} \right], \\ \sigma_{el}^{hA} &= \sigma_{tot}^{hA} - \sigma_{in}^{hA}.\end{aligned}$$

Here  $\sigma_{tot}^{hA}$ ,  $\sigma_{in}^{hA}$ , and  $\sigma_{el}^{hA}$  are the total, inelastic and elastic cross sections, respectively.

The model is reduced to the selection of  $\sigma_{tot}^{hN}$  and  $R(A)$  values. The latest edition of PDG [Groom00] and parameterizations were used for  $\sigma_{tot}^{hN}$ , including the total cross sections of  $p, \bar{p}, n, \pi^\pm, K^\pm$  and  $\Sigma^-$  on protons and neutrons. For known cross sections on protons and neutrons,  $A\sigma_{tot}^{hN} = N_p\sigma_{tot}^{hp} + N_n\sigma_{tot}^{hn}$ , where  $N_p$  and  $N_n$  are the number of protons and neutrons in the nucleus. The nuclear radius (the RMS radius of the nucleon Gaussian distribution), is parametrized as  $R(A) = r_o A^{\frac{1}{3}} f(A)$ ,  $r_o \sim 1.1 \text{ fm}$ , with  $f(A) < 1$  for  $A > 21$ , and  $f(A) > 1$  for the case  $3 < A < 21$ . Fig. 20.1 and Fig. 20.2 show the prediction of the Barashenkov and Glauber-Gribov model for total, inelastic and production cross sections of neutrons and protons on a carbon target. The production cross section is defined to be the difference between the inelastic and charge exchange cross sections.

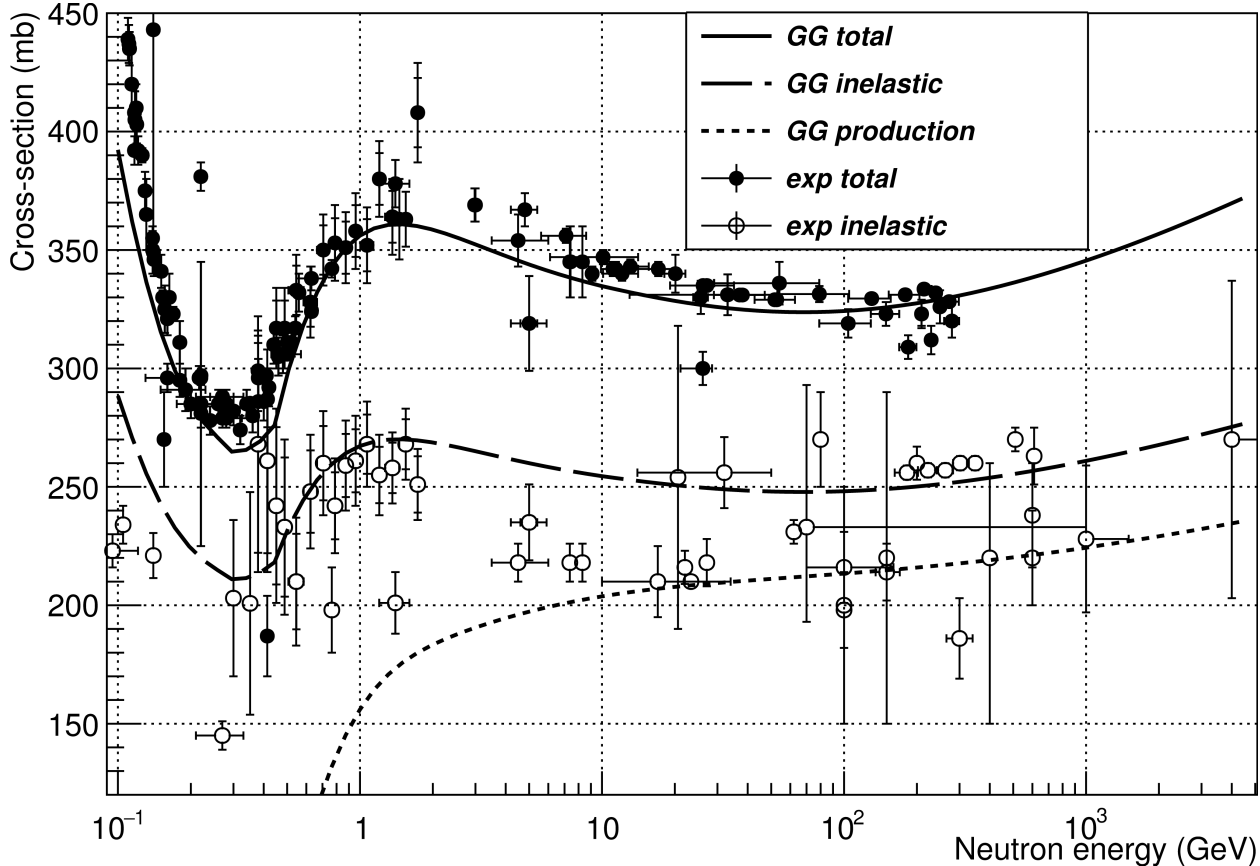


Fig. 20.1: Total, inelastic and production cross-sections of neutrons on a carbon target in the energy range  $10^{-2} - 10^3 \text{ GeV}$ . Experimental data (open and solid points) from [IHEP, NEA], lines correspond to the Glauber-Gribov model.

#### 20.1.4 Extraction of CHIPS kaon and hyperon nuclear cross sections

Alternative cross sections for kaons and hyperons incident upon nuclei are based on the parameterization by Kossov and Degtyarenko who developed them as part of the CHIPS package [DKW00a, DKW00b, DKW00c, Kos02]. This parameterization was developed using extensive data samples and contains a number of parameters which depend on the type of projectile. With 9.6 these cross sections were made independent of the CHIPS package and their interfaces made to conform to the hadronic standard in the toolkit.

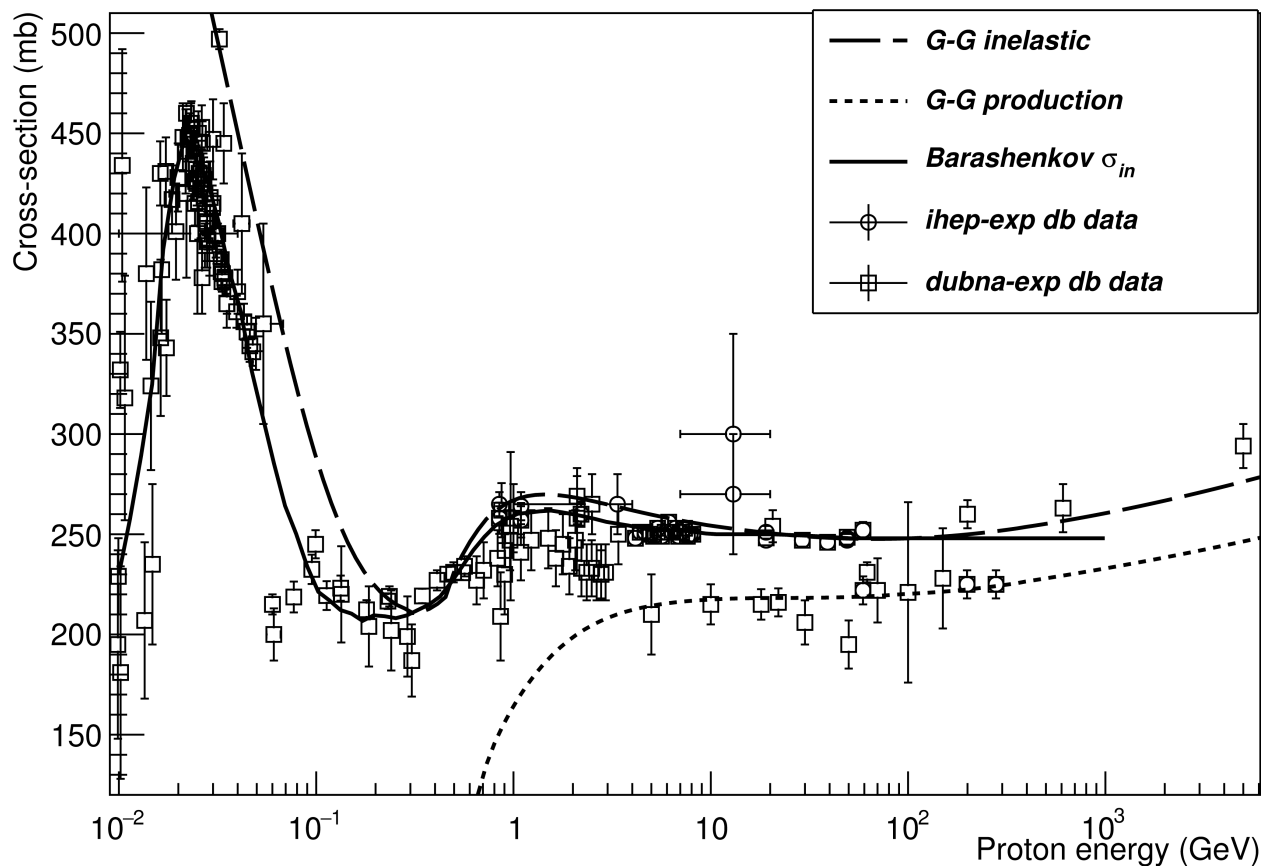


Fig. 20.2: Inelastic and production cross-sections of protons on a carbon target in the energy range  $10^{-2} - 10^3$  GeV. Experimental data (open points and squares) are from [IHEP, NEA]. The solid and dashed lines correspond to the Barashenkov and Glauber-Gribov inelastic models, respectively. The dotted line shows the Glauber-Gribov production model.

## 20.2 Total Reaction Cross Section in Nucleus-nucleus Reactions

### 20.2.1 Nucleus-nucleus cross sections

The simulation of nucleus-nucleus interactions and the corresponding cross sections is required by accelerator experiments, cosmic ray studies and medical applications, and in other applications. An important input for simulations of this process is the total reaction cross section, which is defined as the total ( $\sigma_T$ ) minus the elastic ( $\sigma_{el}$ ) cross section for nucleus-nucleus reactions:

$$\sigma_R = \sigma_T - \sigma_{el}.$$

With increasing energy electromagnetic dissociation (EMD) becomes dominant, especially for the collisions of heavy nuclei. At low and intermediate energies EMD does not play an essential role, while the nuclear break-up and multi-particle productions dominate. Currently, EDM cross section is not used in reference Physics Lists.

The strong interaction cross sections can be calculated in the Glauber approximation [SYuSZ89, Shu03] at high ( $> 1$  GeV) energies. The description of the cross sections at low and intermediate energies is the challenging component.

A first simple expression was proposed in [BP50]:  $\sigma_{1,2} = \pi(R_1 + R_2 - c)^2$ , where  $R_1$  and  $R_2$  are the radii of the two interacting nuclei ( $R = r_0 A^{1/3}$ ),  $r_0 \approx 1.36$  fm, and  $c \sim 0 - 1.5$  fm, depending on a projectile energy (following [SBV74, SBV75] and the further refinements of [STS+93]  $c \propto (A_1^{-1/3} + A_2^{-1/3})$ ).

In order to extend the parameterization to the intermediate energy range [eal87]  $\sigma_{AB} = \pi R_{int}^2 (1 - B/E_{CMS})$  can be used, where  $R_{int}$  is composed of two terms, energy dependent and independent,  $B = Z_A Z_B e^2 / r_C (A^{1/3} + B^{1/3})$  is the Coulomb barrier of the projectile-target system, and  $E_{CMS}$  is center-of-mass system energy.

### 20.2.2 Antinucleus–nucleus cross sections

Production of anti-nuclei, especially anti- ${}^4\text{He}$ , has been observed in nucleus-nucleus and proton-proton collisions by the RHIC and LHC experiments. Contemporary and future experimental studies of anti-nucleus production require a knowledge of anti-nucleus interaction cross sections with matter which are needed to estimate various experimental corrections, especially those due to particle losses which reduce the detected rate. Because only a few measurements of these cross sections exist, they were calculated using the Glauber approach [DK85, Fra68, FG66] and the Monte Carlo averaging method proposed in [AMZS84, SYuSZ89].

Two main considerations are used in the calculations: a parameterization of the amplitude of antinucleon-nucleon elastic scattering in the impact parameter representation and a parameterization of one-particle nuclear densities for various nuclei. The Gaussian form from [DK85, FG66] was used for the amplitude and for the nuclear density the Woods-Saxon distribution for intermediate and heavy nuclei and the Gaussian form for light nuclei was used, with parameters from the paper [WBB09]. Details of the calculations are presented in [eal11].

Resulting calculations agree rather well with experimental data on anti-proton interactions with light and heavy target nuclei ( $\chi^2/\text{NoF} = 258/112$ ) which corresponds to an accuracy of  $\sim 8\%$  [eal11]. Nearly all available experimental data were analyzed to get this result. The predicted antideuteron-nucleus cross sections are in agreement with the corresponding experimental data [eal72].

Direct application of the Glauber approach in software packages like is ineffective due to the large number of numerical integrations required. To overcome this limitation, a parameterization of calculations [Gri09a, Gri09b] was used, with expressions for the total and inelastic cross sections as proposed above in the discussion of the Glauber-Gribov extension. Fitting the calculated Glauber cross sections yields the effective nuclear radii presented in the expressions for  $\bar{p}A$ ,  $\bar{d}A$ ,  $\bar{t}A$  and  $\bar{\alpha}A$  interactions:

$$R_A^{eff} = a A^b + c/A^{1/3}.$$

The quantities  $a$ ,  $b$  and  $c$  are given in [eal11].

As a result of these studies, the toolkit can now simulate anti-nucleus interactions with matter for projectiles with momenta between 100 MeV/c and 1 TeV/c per anti-nucleon.

### 20.2.3 Alternative nucleus-nucleus cross sections

The total reaction cross section has been studied both theoretically and experimentally and several empirical parameterizations of it have been developed. In GEANT4 the Shen[SWF+89] parameterization offers an alternative way to estimate the nucleus-nucleus total cross sections. The Shen approach is based on the strong absorption model. It expresses the total reaction cross section in terms of the interaction radius  $R$ , the nucleus-nucleus interaction barrier  $B$ , and the center-of-mass energy of the colliding system  $E_{CM}$ :

$$\sigma_R = 10\pi R^2 \left[ 1 - \frac{B}{E_{CM}} \right].$$

The interaction radius  $R$  is given by

$$R = r_0 \left[ A_t^{1/3} + A_p^{1/3} + 1.85 \frac{A_t^{1/3} A_p^{1/3}}{A_t^{1/3} + A_p^{1/3}} - C'(KE) \right] + \alpha \frac{5(A_t - Z_t)Z_p}{A_p A_r} + \beta E_{CM}^{-1/3} \frac{A_t^{1/3} A_p^{1/3}}{A_t^{1/3} + A_p^{1/3}}$$

where  $\alpha$ ,  $\beta$  and  $r_0$  are

$$\begin{aligned} \alpha &= 1 \text{ fm} \\ \beta &= 0.176 \text{ MeV}^{1/3} \cdot \text{fm} \\ r_0 &= 1.1 \text{ fm}. \end{aligned}$$

In Ref. [SWF+89] as well, no functional form for  $C'(KE)$  is given. Hence the same simple analytical function is used by GEANT4 to derive  $c$  values.

The second term  $B$  is called the nuclear-nuclear interaction barrier in the Shen formula and is given by

$$B = \frac{1.44 Z_t Z_p}{r} - b \frac{R_t R_p}{R_t + R_p} (\text{MeV})$$

where  $r$ ,  $b$ ,  $R_t$  and  $R_p$  are given by

$$\begin{aligned} r &= R_t + R_p + 3.2 \text{ fm} \\ b &= 1 \text{ MeV} \cdot \text{fm}^{-1} \\ R_i &= 1.12 A_i^{1/3} - 0.94 A_i^{-1/3} \quad (i = t, p) \end{aligned}$$



---

CHAPTER  
**TWENTYONE**

---

## **COHERENT ELASTIC SCATTERING**

### **21.1 Nucleon-Nucleon elastic Scattering**

The classes G4LEpp and G4LEnp provide data-driven models for proton-proton (or neutron-neutron) and neutron-proton elastic scattering over the range 10-1200 MeV. Final states (primary and recoil particle) are derived by sampling from tables of the cumulative distribution function of the centre-of-mass scattering angle, tabulated for a discrete set of lab kinetic energies from 10 MeV to 1200 MeV. The CDF's are tabulated at 1 degree intervals and sampling is done using bi-linear interpolation in energy and CDF values. The data are derived from differential cross sections obtained from the SAID database, R. Arndt, 1998.

In class G4LEpp there are two data sets: one including Coulomb effects (for p-p scattering) and one with no Coulomb effects (for n-n scattering or p-p scattering with Coulomb effects suppressed). The method G4LEpp::SetCoulombEffects can be used to select the desired data set:

- SetCoulombEffects(0): No Coulomb effects (the default)
- SetCoulombEffects(1): Include Coulomb effects

The recoil particle will be generated as a new secondary particle. In class G4LEnp, the possibility of a charge-exchange reaction is included, in which case the incident track will be stopped and both the primary and recoil particles will be generated as secondaries.



---

CHAPTER  
TWENTYTWO

---

## HADRON-NUCLEUS ELASTIC SCATTERING AT MEDIUM AND HIGH ENERGY

### 22.1 Method of Calculation

The Glauber model [Gla70] is used as an alternative method of calculating differential cross sections for elastic and quasi-elastic hadron-nucleus scattering at high and intermediate energies.

For high energies this includes corrections for inelastic screening and for quasi-elastic scattering the excitation of a discrete level or a state in the continuum is considered.

The usual expression for the Glauber model amplitude for multiple scattering was used

$$F(q) = \frac{ik}{2\pi} \int d^2 b e^{i\vec{q} \cdot \vec{b}} M(\vec{b}). \quad (22.1)$$

Here  $M(\vec{b})$  is the hadron-nucleus amplitude in the impact parameter representation

$$M(\vec{b}) = 1 - \left[ 1 - e^{-A \int d^3 r \Gamma(\vec{b} - \vec{s}) \rho(\vec{r})} \right]^A, \quad (22.2)$$

$k$  is the incident particle momentum,  $\vec{q} = \vec{k}' - \vec{k}$  is the momentum transfer, and  $\vec{k}'$  is the scattered particle momentum. Note that  $|\vec{q}|^2 = -t$  - invariant momentum transfer squared in the center of mass system.  $\Gamma(\vec{b})$  is the hadron-nucleon amplitude of elastic scattering in the impact-parameter representation

$$\Gamma(\vec{b}) = \frac{1}{2\pi i k^{hN}} \int d\vec{q} e^{-i\vec{q} \cdot \vec{b}} f(\vec{q}). \quad (22.3)$$

The exponential parameterization of the hadron-nucleon amplitude is usually used:

$$f(\vec{q}) = \frac{ik^{hN} \sigma^{hN}}{2\pi} e^{-0.5q^2 B}. \quad (22.4)$$

Here  $\sigma^{hN} = \sigma_{tot}^{hN}(1-i\alpha)\sigma_{tot}^{hN}$  is the total cross section of a hadron-nucleon scattering,  $B$  is the slope of the diffraction cone and  $\alpha$  is the ratio of the real to imaginary parts of the amplitude at  $q = 0$ . The value  $k^{hN}$  is the hadron momentum in the hadron-nucleon coordinate system.

The important difference of these calculations from the usual ones is that the two-gaussian form of the nuclear density was used

$$\rho(r) = C \left( e^{-(r/R_1)^2} - p e^{-(r/R_2)^2} \right), \quad (22.5)$$

where  $R_1$ ,  $R_2$  and  $p$  are the fitting parameters and  $C$  is a normalization constant.

This density representation allows the expressions for amplitude and differential cross section to be put into analytical form. It was earlier used for light [BW68, BDK+81, Cho68, NGG+78] and medium [EKS81, KS83] nuclei. Described

below is an extension of this method to heavy nuclei. The form (22.5) is not physical for a heavy nucleus, but nevertheless works rather well (see figures below). The reason is that the nucleus absorbs the hadrons very strongly, especially at small impact parameters where the absorption is full. As a result only the peripheral part of the nucleus participates in elastic scattering. Eq. (22.5) therefore describes only the edge of a heavy nucleus.

Substituting Eqs. (22.5) and (22.4) into Eqs. (22.1), (22.2) and (22.3) yields the following formula

$$F(q) = \frac{ik\pi}{2} \sum_{k=1}^A (-1)^k \binom{A}{k} \left[ \frac{\sigma^{hN}}{2\pi(R_1^3 - pR_2^3)} \right]^k \sum_{m=0}^k (-1)^m \binom{k}{m} \left[ \frac{R_1^3}{R_1^2 + 2B} \right]^{k-m} \\ \times \left[ \frac{pR_2^3}{R_2^2 + 2B} \right]^m \left( \frac{m}{R_2^2 + 2B} + \frac{k-m}{R_1^2 + 2B} \right)^{-1} \times \exp \left[ -\frac{-q^2}{4} \left( \frac{m}{R_2^2 + 2B} + \frac{k-m}{R_1^2 + 2B} \right)^{-1} \right]. \quad (22.6)$$

An analogous procedure can be used to get the inelastic screening corrections to the hadron-nucleus amplitude  $\Delta M(\vec{b})$  [NNikolskiiS+77]. In this case an intermediate inelastic diffractive state is created which rescatters on the nucleons of the nucleus and then returns into the initial hadron. Hence it is necessary to integrate the production cross section over the mass distribution of the excited system  $d\sigma^{diff}/dt dM_x^2$ . The expressions for the corresponding amplitude are quite long and so are not presented here. The corrections for the total cross-sections can be found in [NNikolskiiS+77].

The full amplitude is the sum  $M(\vec{b}) + \Delta M(\vec{b})$ .

The differential cross section is connected with the amplitude in the following way

$$\frac{d\sigma}{d\Omega_{CM}} = |F(q)|^2, \quad \frac{d\sigma}{|dt|} = \frac{d\sigma}{dq_{CM}^2} = \frac{\pi}{k_{CM}^2} |F(q)|^2. \quad (22.7)$$

The main energy dependence of the hadron-nucleus elastic scattering cross section comes from the energy dependence of the parameters of hadron-nucleon scattering ( $\sigma_{tot}^{hN} \propto B$  and  $\frac{d\sigma^{diff}}{dt dM_x^2}$ ). At interesting energies these parameters were fixed at their well-known values. The fitting of the nuclear density parameters was performed over a wide range of atomic numbers ( $A = 4 - 208$ ) using experimental data on proton-nuclei elastic scattering at a kinetic energy of  $T_p = 1$  GeV.

The fitting was performed both for individual nuclei and for the entire set of nuclei at once. It is necessary to note that for every nucleus an optimal set of density parameters exists and it differs slightly from the one derived for the full set of nuclei.

A comparison of the phenomenological cross sections [ABV78] with experiment is presented in Fig. 22.1 - Fig. 22.9.

In this comparison, the individual nuclei parameters were used. The experimental data were obtained in Gatchina (Russia) and in Saclay (France) [ABV78]. The horizontal axis is the scattering angle in the center of mass system  $\Theta_{CM}$  and the vertical axis is  $\frac{d\sigma}{d\Omega_{CM}}$  in mb/Ster. Comparisons were also made for  $p^4\text{He}$  elastic scattering at  $T = 1$  GeV [7], 45 GeV and 301 GeV [3]. The resulting cross sections  $\frac{d\sigma}{|dt|}$  are shown in Fig. 22.10 - Fig. 22.12.

In order to generate events the distribution function  $\mathcal{F}$  of a corresponding process must be known. The differential cross section is proportional to the density distribution. Therefore to get the distribution function it is sufficient to integrate the differential cross section and normalize it:

$$\mathcal{F}(q^2) = \frac{\int_0^{q^2} d(q^2) \frac{d\sigma}{d(q^2)}}{\int_0^{q_{max}^2} d(q^2) \frac{d\sigma}{d(q^2)}} \quad (22.8)$$

Expressions (22.6) and (22.7) allow analytic integration in Eq. (22.8) but the result is too long to be given here.

For light and medium nuclei the analytic expression is more convenient for calculations than the numerical integration of Eq. (22.8), but for heavy nuclei the latter is preferred due to the large number of terms in the analytic expression.

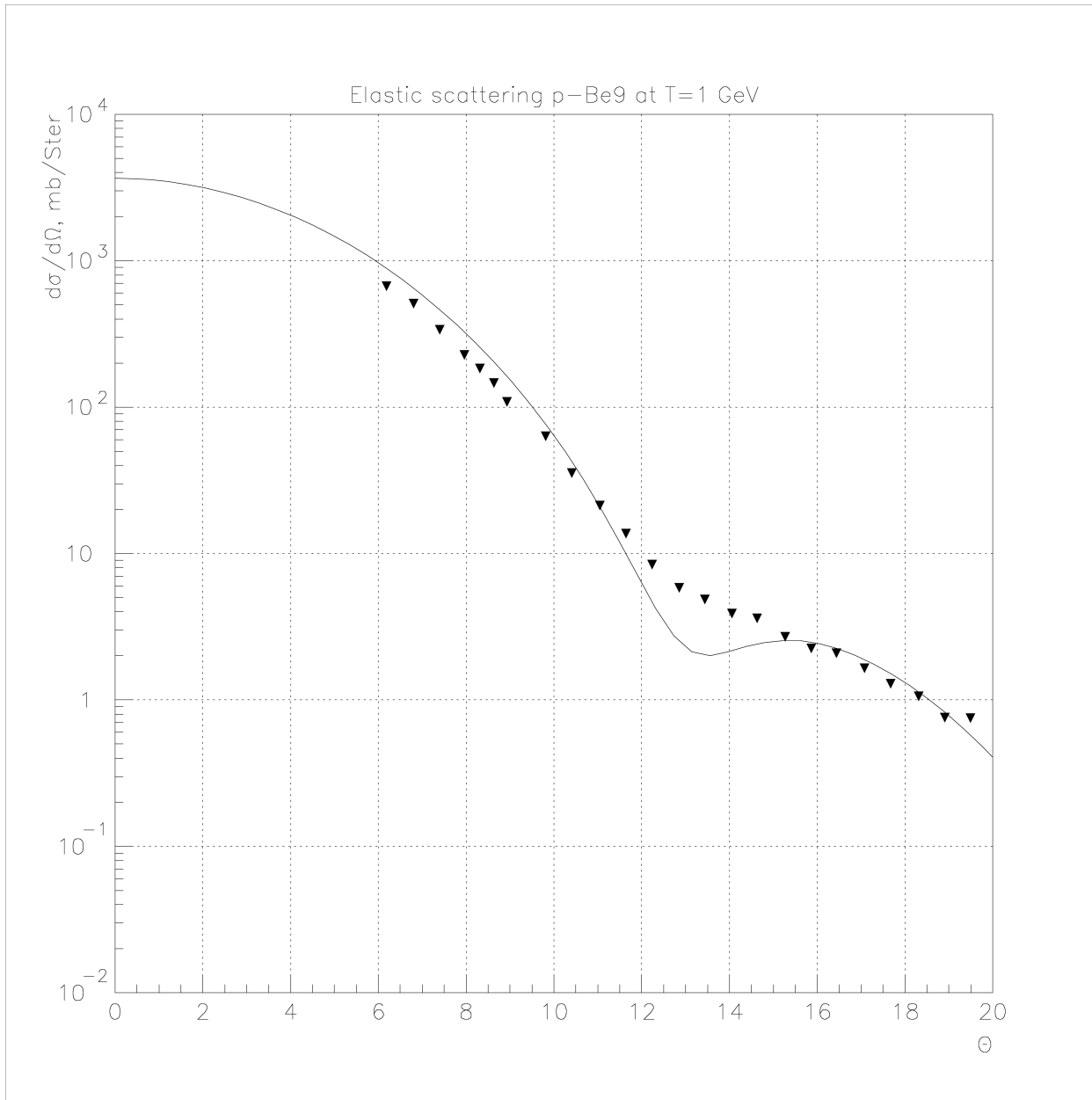
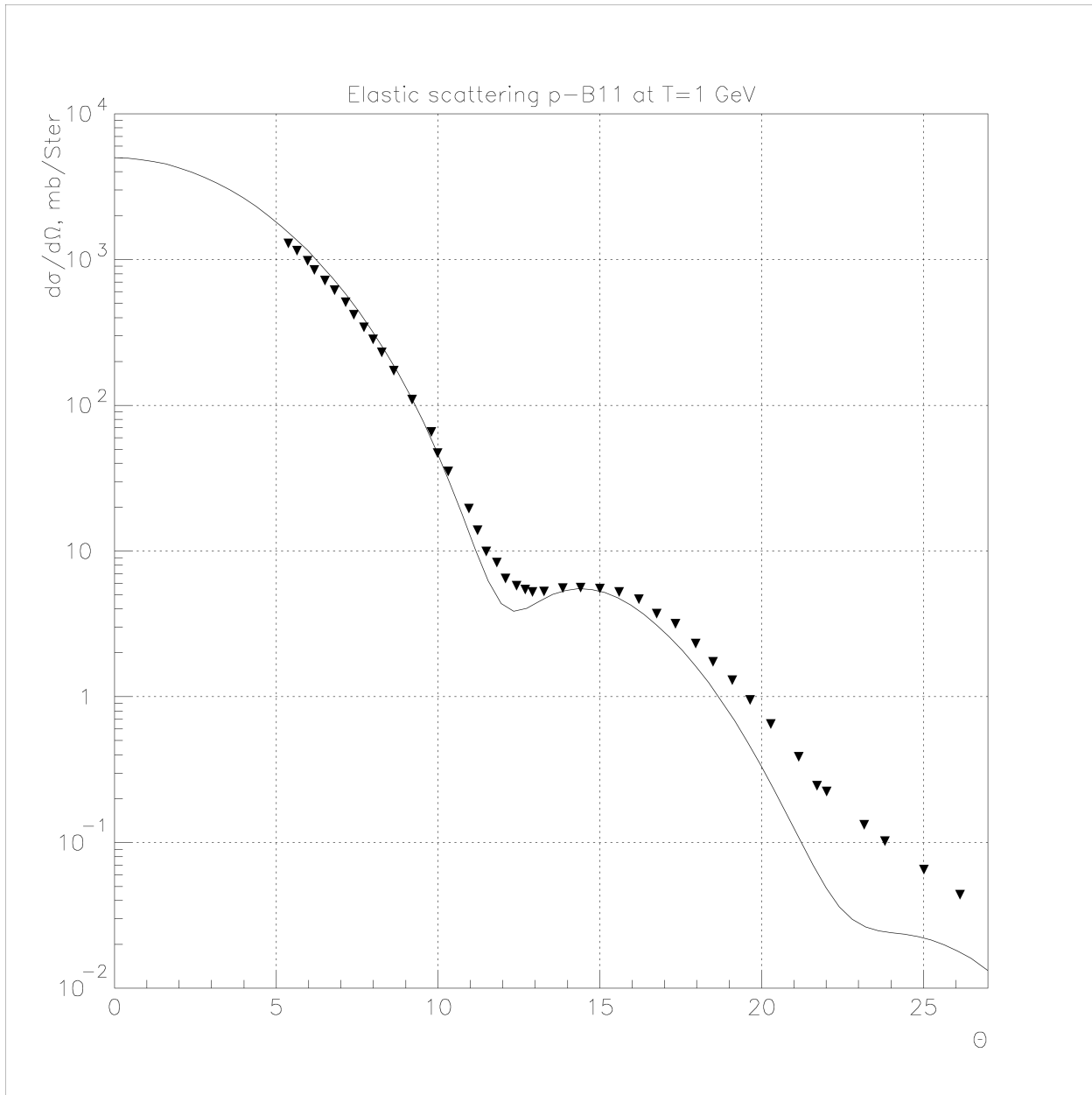


Fig. 22.1: Elastic proton scattering on  ${}^9\text{Be}$  at 1 GeV.

Fig. 22.2: Elastic proton scattering on  $^{11}\text{B}$  at 1 GeV.

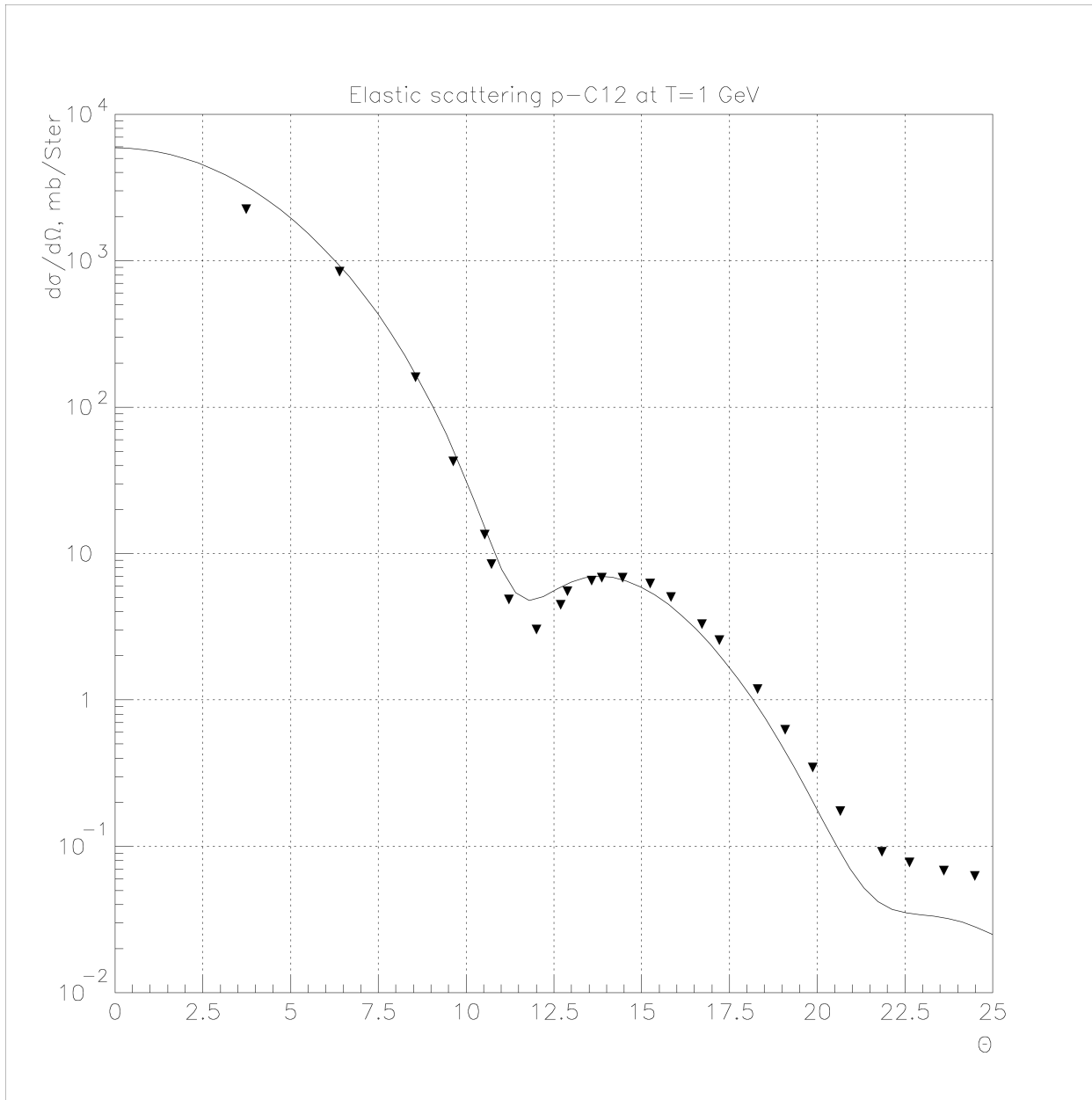
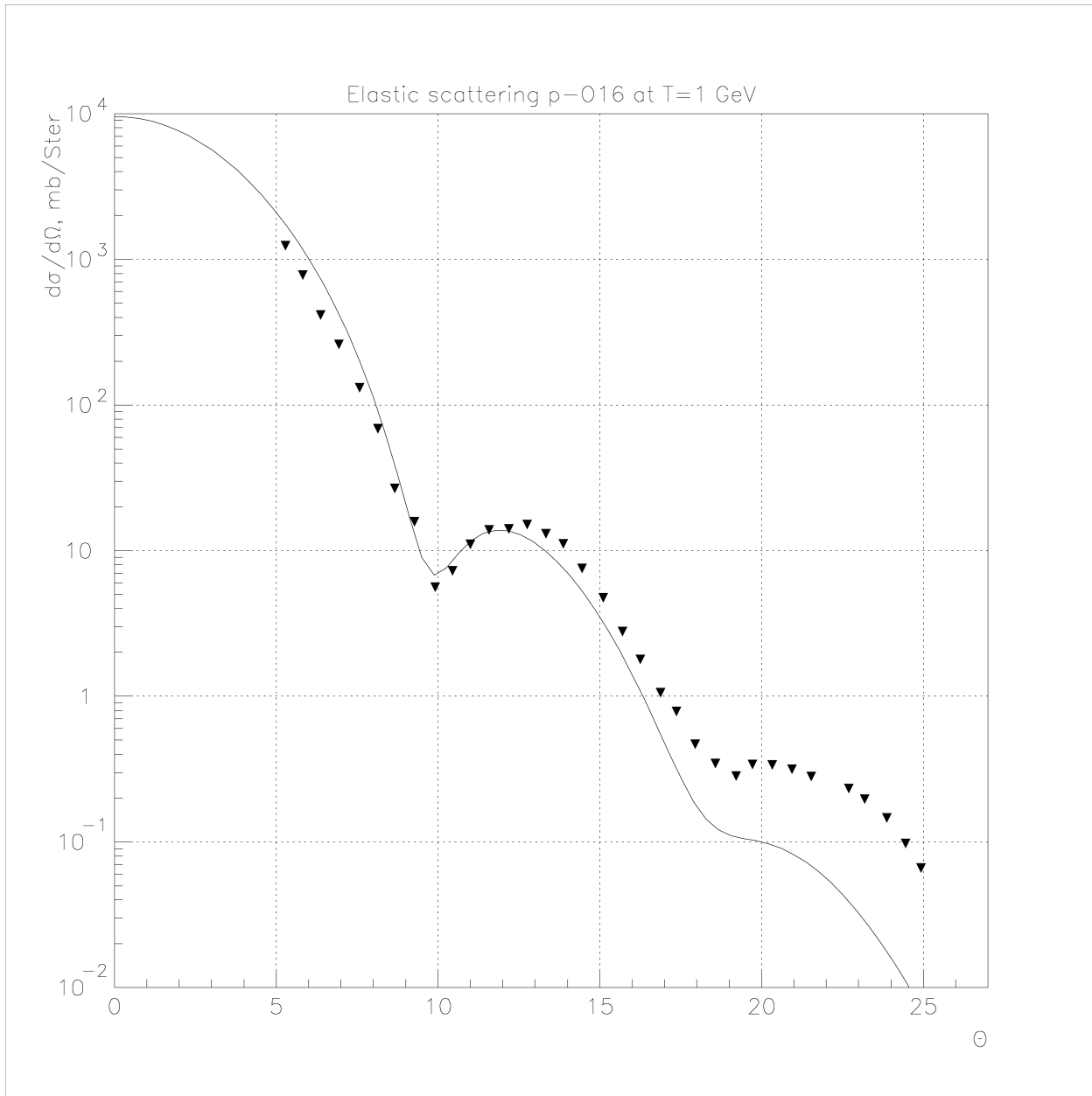


Fig. 22.3: Elastic proton scattering on  $^{12}\text{C}$  at 1 GeV.

Fig. 22.4: Elastic proton scattering on  $^{16}\text{O}$  at 1 GeV.

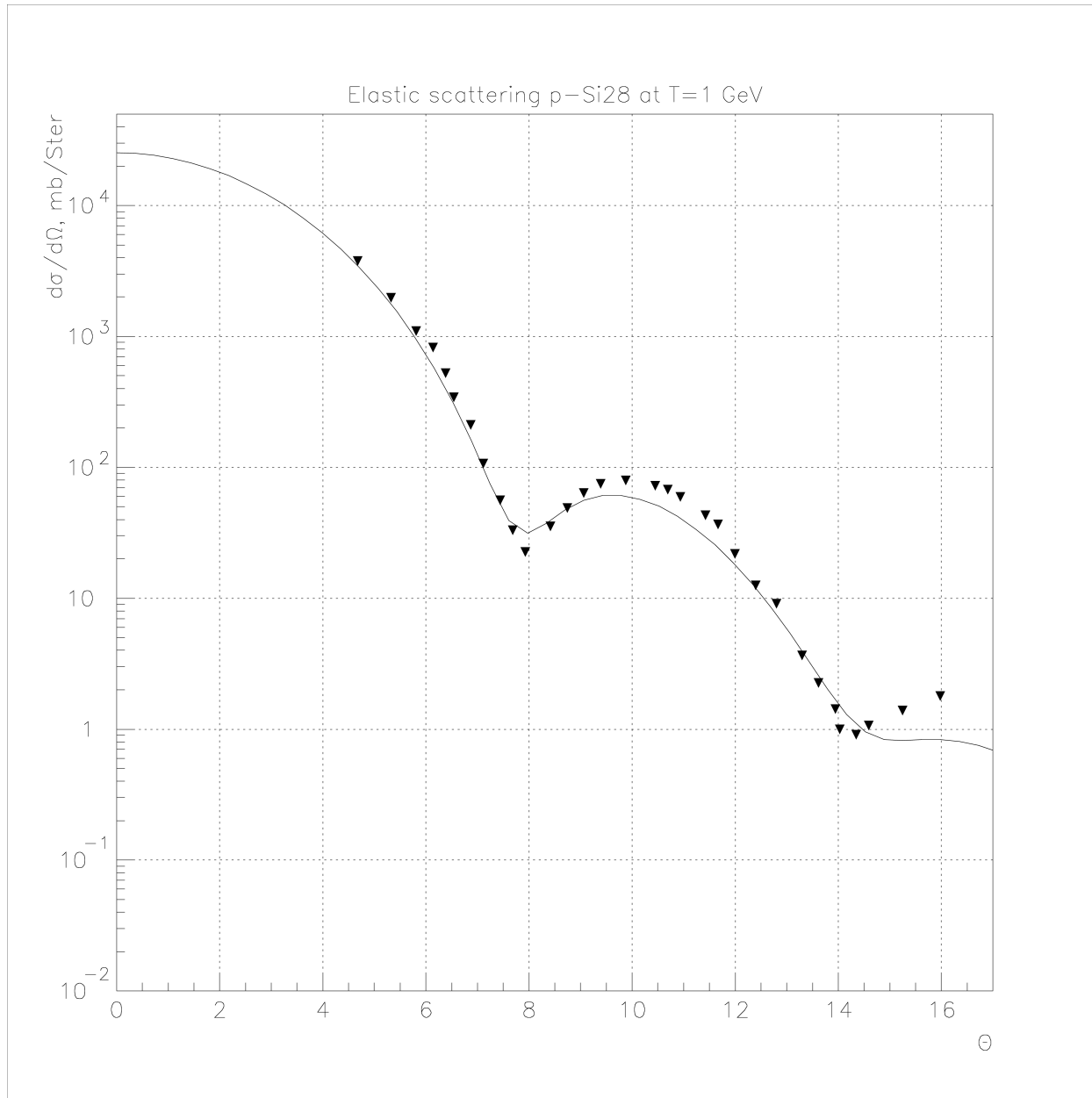
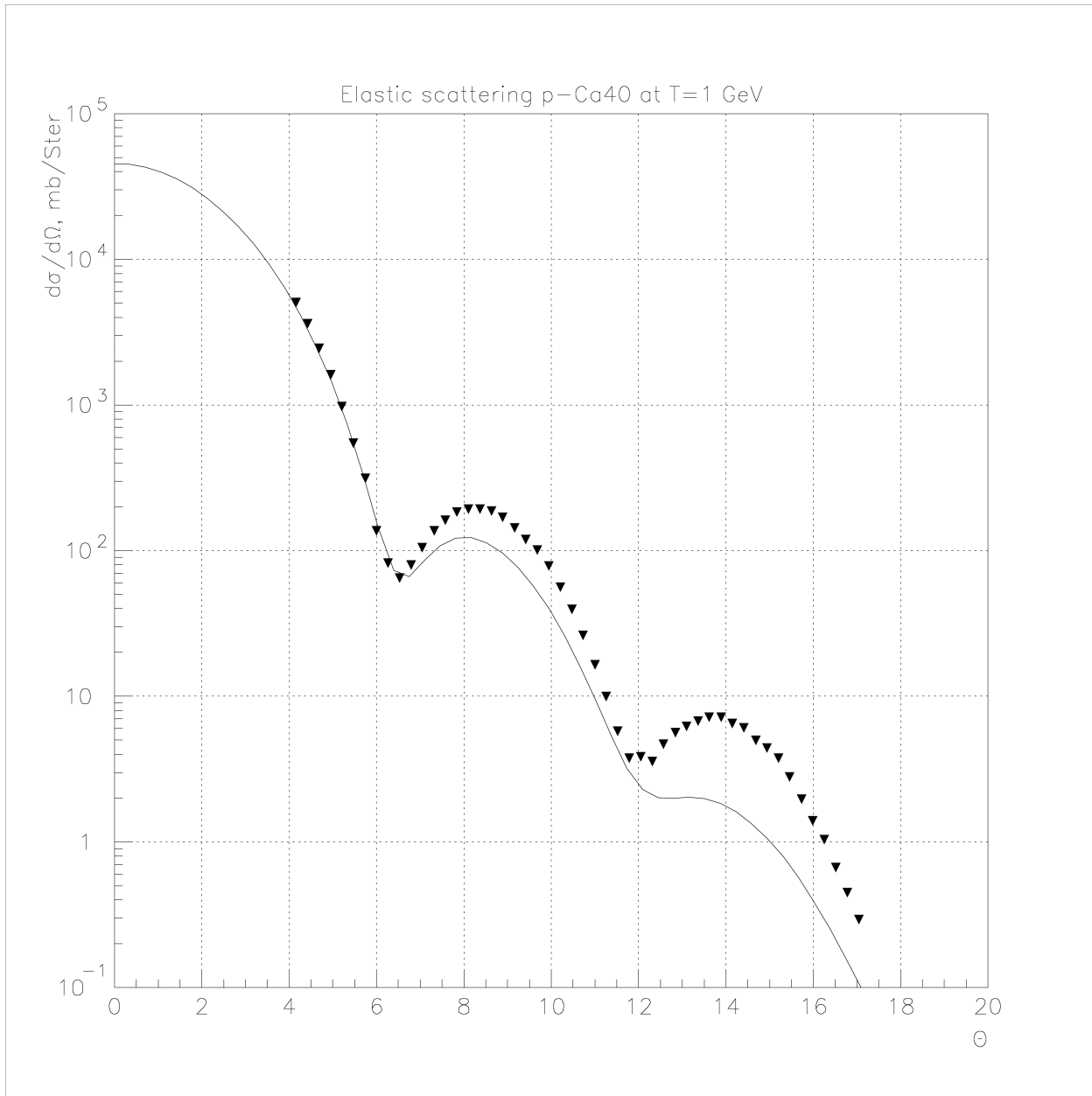
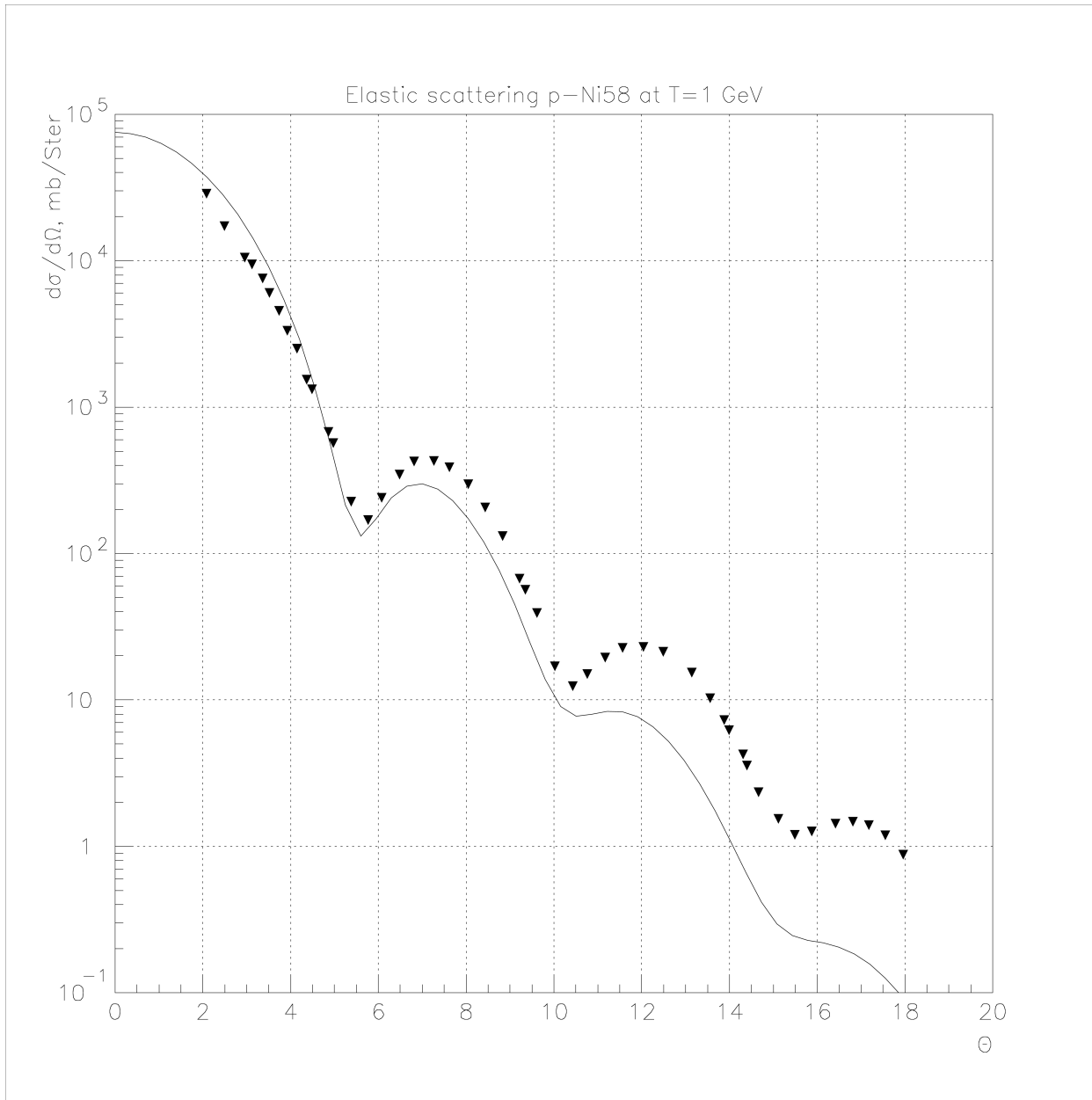
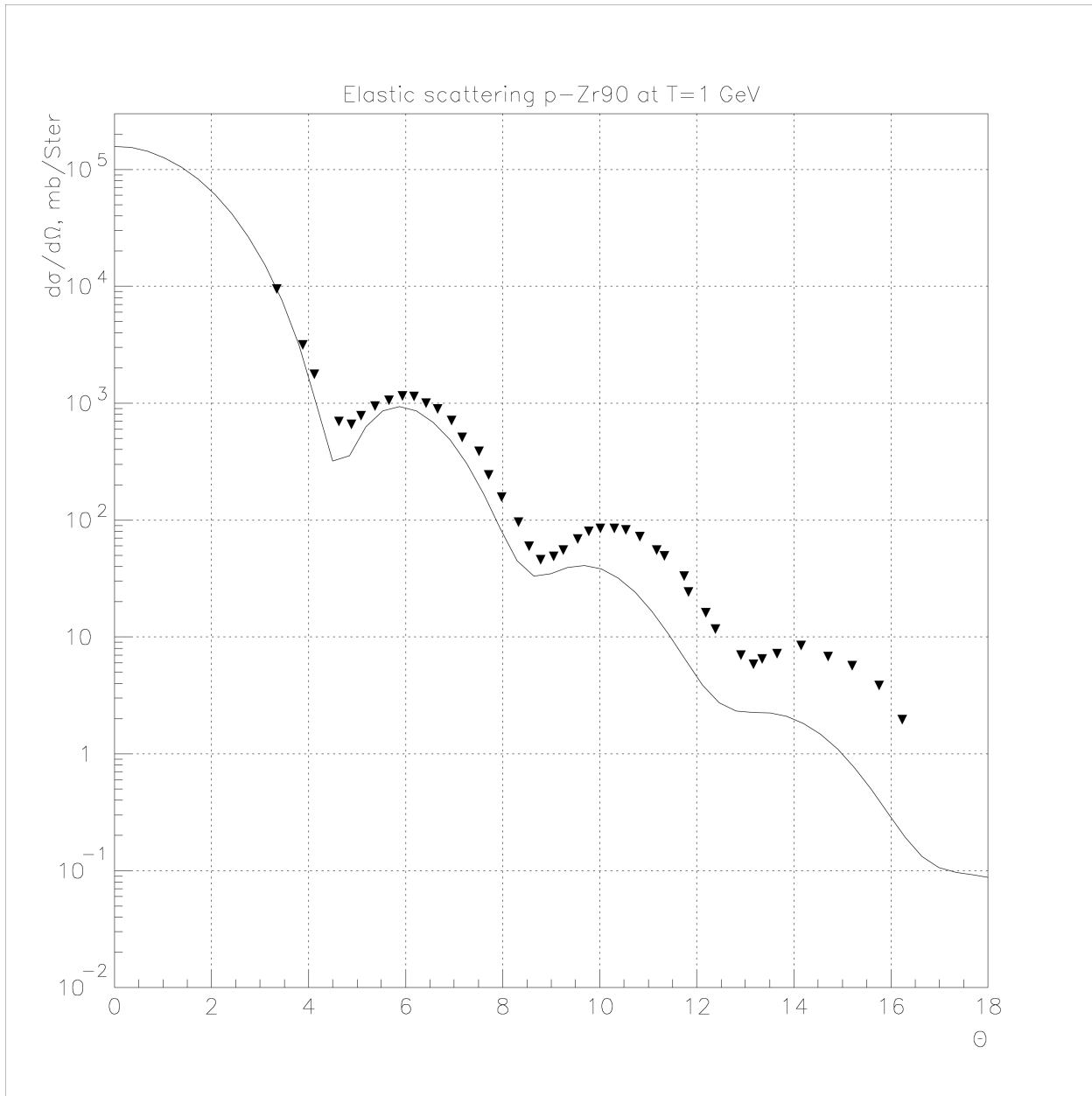
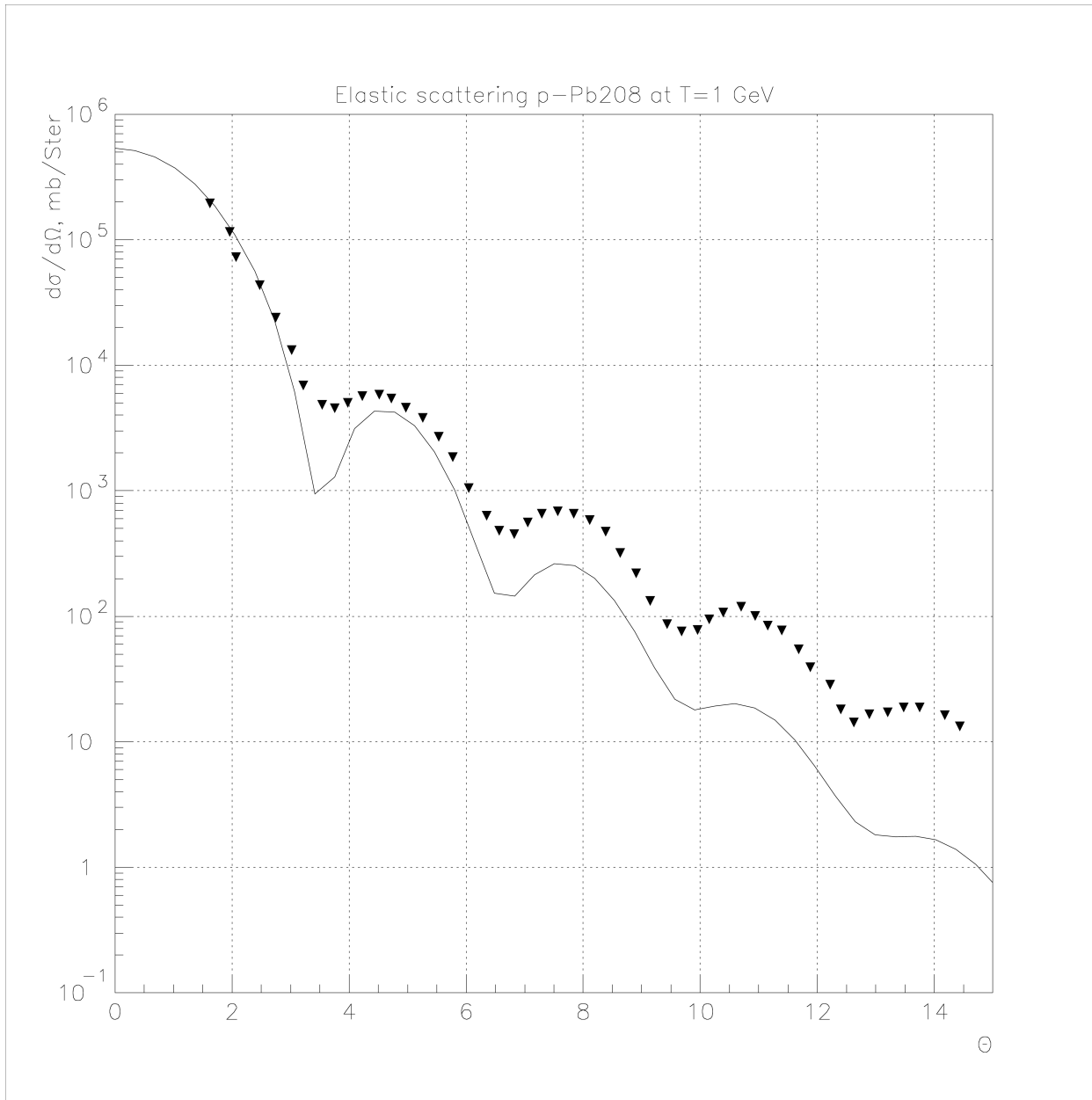


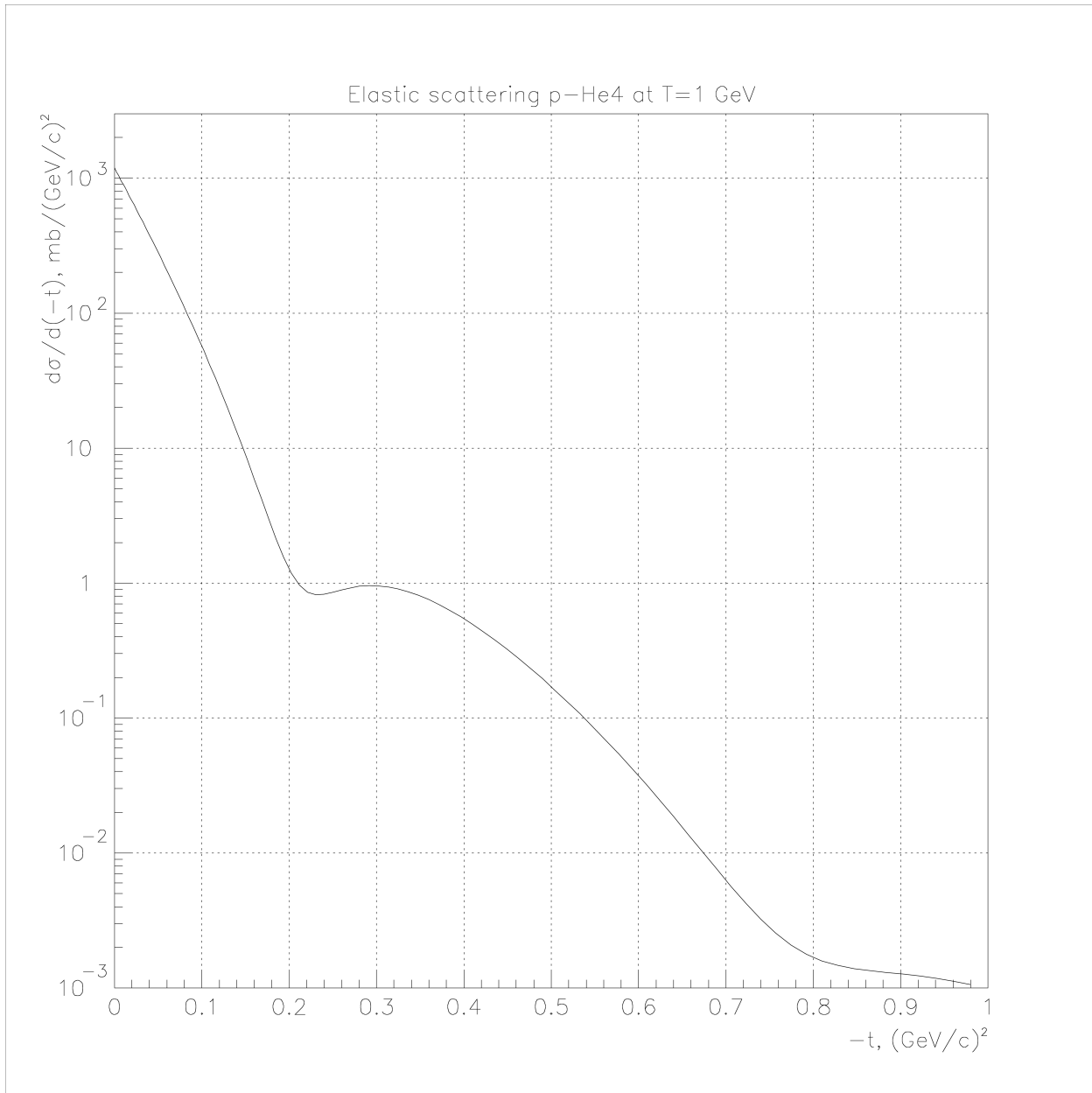
Fig. 22.5: Elastic proton scattering on <sup>28</sup>Si at 1 GeV.

Fig. 22.6: Elastic proton scattering on  ${}^{40}\text{Ca}$  at 1 GeV.

Fig. 22.7: Elastic proton scattering on  ${}^{58}\text{Ni}$  at 1 GeV.

Fig. 22.8: Elastic proton scattering on  $^{90}\text{Zr}$  at 1 GeV.

Fig. 22.9: Elastic proton scattering on  ${}^{208}\text{Pb}$  at 1 GeV.

Fig. 22.10: Elastic proton scattering on  ${}^4\text{He}$  at 1 GeV.

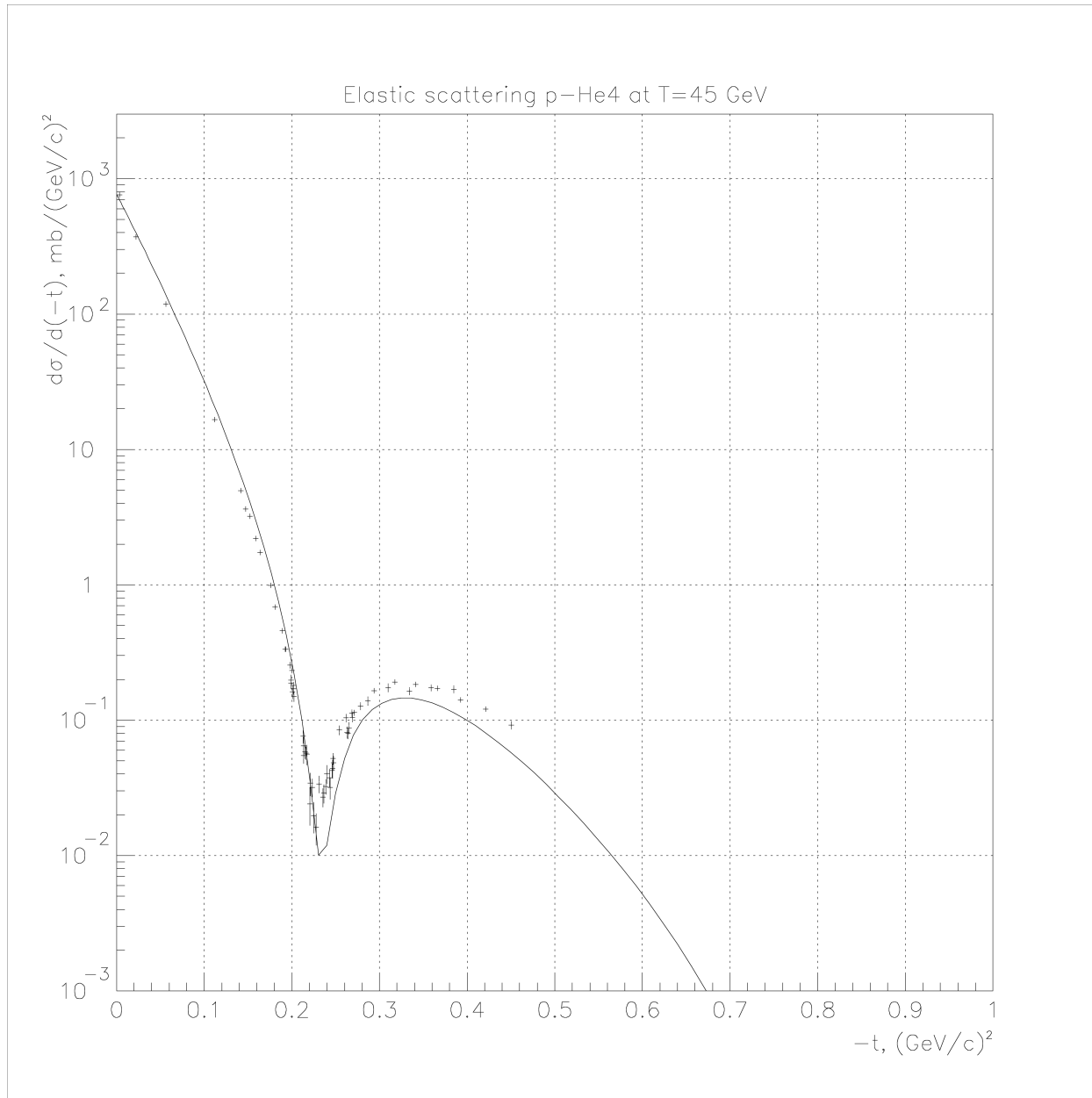
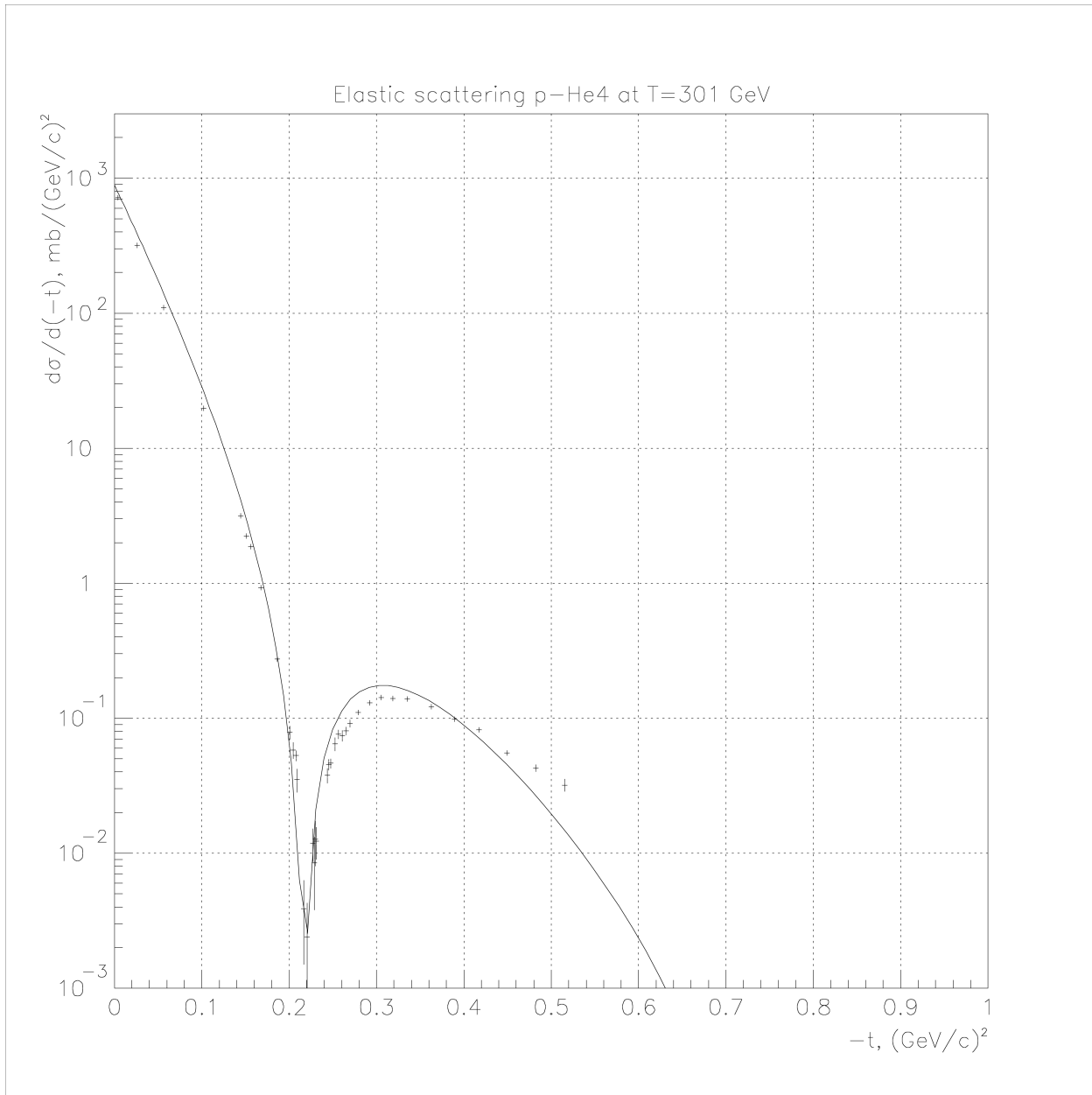


Fig. 22.11: Elastic proton scattering on  ${}^4\text{He}$  at 45 GeV.

Fig. 22.12: Elastic proton scattering on  ${}^4\text{He}$  at 301 GeV.

---

CHAPTER  
TWENTYTHREE

---

## PARTON STRING MODEL

### 23.1 Reaction initial state simulation.

#### 23.1.1 Allowed projectiles and bombarding energy range for interaction with nucleon and nuclear targets

The GEANT4 parton string models are capable to predict final states (produced hadrons which belong to the scalar and vector meson nonets and the baryon (antibaryon) octet and decuplet) of reactions on nucleon and nuclear targets with nucleon, pion and kaon projectiles. The allowed bombarding energy  $\sqrt{s} > 5$  GeV is recommended. Two approaches, based on diffractive excitation or soft scattering with diffractive admixture according to cross-section, are considered. Hadron-nucleus collisions in the both approaches (diffractive and parton exchange) are considered as a set of the independent hadron-nucleon collisions. However, the string excitation procedures in these approaches are rather different.

#### 23.1.2 MC initialization procedure for nucleus

The initialization of each nucleus, consisting from  $A$  nucleons and  $Z$  protons with coordinates  $\mathbf{r}_i$  and momenta  $\mathbf{p}_i$ , where  $i = 1, 2, \dots, A$  is performed. We use the standard initialization Monte Carlo procedure, which is realized in the most of the high energy nuclear interaction models:

- Nucleon radii  $r_i$  are selected randomly in the rest of nucleus according to proton or neutron density  $\rho(r_i)$ . For heavy nuclei with  $A > 16$  [GLMP91] nucleon density is

$$\rho(r_i) = \frac{\rho_0}{1 + \exp[(r_i - R)/a]}$$

where

$$\rho_0 \approx \frac{3}{4\pi R^3} \left(1 + \frac{a^2 \pi^2}{R^2}\right)^{-1}.$$

Here  $R = r_0 A^{1/3}$  fm and  $r_0 = 1.16(1 - 1.16A^{-2/3})$  fm and  $a \approx 0.545$  fm. For light nuclei with  $A < 17$  nucleon density is given by a harmonic oscillator shell model [B61], e. g.

$$\rho(r_i) = (\pi R^2)^{-3/2} \exp(-r_i^2/R^2),$$

where  $R^2 = 2/3\langle r^2 \rangle = 0.8133A^{2/3}$  fm<sup>2</sup>. To take into account nucleon repulsive core it is assumed that internucleon distance  $d > 0.8$  fm;

- The initial momenta of the nucleons are randomly chosen between 0 and  $p_F^{max}$ , where the maximal momenta of nucleons (in the local Thomas-Fermi approximation [DA74]) depends from the proton or neutron density  $\rho$  according to

$$p_F^{max} = \hbar c (3\pi^2 \rho)^{1/3}$$

with  $\hbar c = 0.197327 \text{ GeV fm}$ ;

- To obtain coordinate and momentum components, it is assumed that nucleons are distributed isotropically in configuration and momentum spaces;
- Then perform shifts of nucleon coordinates  $\mathbf{r}'_j = \mathbf{r}_j - 1/A \sum_i \mathbf{r}_i$  and momenta  $\mathbf{p}'_j = \mathbf{p}_j - 1/A \sum_i \mathbf{p}_i$  of nucleon momenta. The nucleus must be centered in configuration space around  $\mathbf{0}$ , i. e.  $\sum_i \mathbf{r}_i = \mathbf{0}$  and the nucleus must be at rest, i. e.  $\sum_i \mathbf{p}_i = \mathbf{0}$ ;
- We compute energy per nucleon  $e = E/A = m_N + B(A, Z)/A$ , where  $m_N$  is nucleon mass and the nucleus binding energy  $B(A, Z)$  is given by the Bethe-Weizsäcker formula [BA69]:

$$B(A, Z) = -0.01587A + 0.01834A^{2/3} + 0.09286(Z - \frac{A}{2})^2 + 0.00071Z^2/A^{1/3},$$

and find the effective mass of each nucleon  $m_i^{eff} = \sqrt{(E/A)^2 - p_i^2}$ .

### 23.1.3 Random choice of the impact parameter

The impact parameter  $0 \leq b \leq R_t$  is randomly selected according to the probability:

$$P(\mathbf{b})d\mathbf{b} = bd\mathbf{b},$$

where  $R_t$  is the target radius, respectively. In the case of nuclear projectile or target the nuclear radius is determined from condition:

$$\frac{\rho(R)}{\rho(0)} = 0.01.$$

## 23.2 Sample of collision participants in nuclear collisions.

### 23.2.1 MC procedure to define collision participants.

The inelastic hadron–nucleus interactions at ultra–relativistic energies are considered as independent hadron–nucleon collisions. It was shown long time ago [AA78] for the hadron–nucleus collision that such a picture can be obtained starting from the Regge–Gribov approach [MA76], when one assumes that the hadron-nucleus elastic scattering amplitude is a result of reggeon exchanges between the initial hadron and nucleons from target–nucleus. This result leads to simple and efficient MC procedure [ANS90, S86] to define the interaction cross sections and the number of the nucleons participating in the inelastic hadron–nucleus collision:

- We should randomly distribute  $B$  nucleons from the target-nucleus on the impact parameter plane according to the weight function  $T([\vec{b}_j^B])$ . This function represents probability density to find sets of the nucleon impact parameters  $[\vec{b}_j^B]$ , where  $j = 1, 2, \dots, B$ .
- For each pair of projectile hadron  $i$  and target nucleon  $j$  with chosen impact parameters  $\vec{b}_i$  and  $\vec{b}_j^B$  we should check whether they interact inelastically or not using the probability  $p_{ij}(\vec{b}_i - \vec{b}_j^B, s)$ , where  $s_{ij} = (p_i + p_j)^2$  is the squared total c.m. energy of the given pair with the 4-momenta  $p_i$  and  $p_j$ , respectively.

In the Regge–Gribov approach [MA76] the probability for an inelastic collision of pair of  $i$  and  $j$  as a function at the squared impact parameter difference  $b_{ij}^2 = (\vec{b}_i - \vec{b}_j^B)^2$  and  $s$  is given by

$$p_{ij}(\vec{b}_i - \vec{b}_j^B, s) = c^{-1}[1 - \exp\{-2u(b_{ij}^2, s)\}] = \sum_{n=1}^{\infty} p_{ij}^{(n)}(\vec{b}_i - \vec{b}_j^B, s), \quad (23.1)$$

where

$$p_{ij}^{(n)}(\vec{b}_i - \vec{b}_j^B, s) = c^{-1} \exp\{-2u(b_{ij}^2, s)\} \frac{[2u(b_{ij}^2, s)]^n}{n!}. \quad (23.2)$$

is the probability to find the  $n$  cut Pomerons or the probability for  $2n$  strings produced in an inelastic hadron-nucleon collision. These probabilities are defined in terms of the (eikonal) amplitude of hadron–nucleon elastic scattering with Pomeron exchange:

$$u(b_{ij}^2, s) = \frac{z(s)}{2} \exp(-b_{ij}^2/4\lambda(s)).$$

The quantities  $z(s)$  and  $\lambda(s)$  are expressed through the parameters of the Pomeron trajectory,  $\alpha'_P = 0.25 \text{ GeV}^{-2}$  and  $\alpha_P(0) = 1.0808$ , and the parameters of the Pomeron-hadron vertex  $R_P$  and  $\gamma_P$ :

$$\begin{aligned} z(s) &= \frac{2c\gamma_P}{\lambda(s)} (s/s_0)^{\alpha_P(0)-1} \\ \lambda(s) &= R_P^2 + \alpha'_P \ln(s/s_0), \end{aligned}$$

respectively, where  $s_0$  is a dimensional parameter.

In Eqs. (23.1),(23.2) the so-called shower enhancement coefficient  $c$  is introduced to determine the contribution of diffractive dissociation [MA76]. Thus, the probability for diffractive dissociation of a pair of nucleons can be computed as

$$p_{ij}^d(\vec{b}_i - \vec{b}_j^B, s) = \frac{c-1}{c} [p_{ij}^{tot}(\vec{b}_i - \vec{b}_j^B, s) - p_{ij}(\vec{b}_i - \vec{b}_j^B, s)],$$

where

$$p_{ij}^{tot}(\vec{b}_i - \vec{b}_j^B, s) = (2/c)[1 - \exp\{-u(b_{ij}^2, s)\}].$$

The Pomeron parameters are found from a global fit of the total, elastic, differential elastic and diffractive cross sections of the hadron–nucleon interaction at different energies.

For the nucleon-nucleon, pion-nucleon and kaon-nucleon collisions the Pomeron vertex parameters and shower enhancement coefficients are found:  $R_P^{2N} = 3.56 \text{ GeV}^{-2}$ ,  $\gamma_P^N = 3.96 \text{ GeV}^{-2}$ ,  $s_0^N = 3.0 \text{ GeV}^2$ ,  $c^N = 1.4$  and  $R_P^{2\pi} = 2.36 \text{ GeV}^{-2}$ ,  $\gamma_P^\pi = 2.17 \text{ GeV}^{-2}$ , and  $R_P^{2K} = 1.96 \text{ GeV}^{-2}$ ,  $\gamma_P^K = 1.92 \text{ GeV}^{-2}$ ,  $s_0^K = 2.3 \text{ GeV}^2$ ,  $c^\pi = 1.8$ .

### 23.2.2 Separation of hadron diffraction excitation.

For each pair of target hadron  $i$  and projectile nucleon  $j$  with chosen impact parameters  $\vec{b}_i$  and  $\vec{b}_j^B$  we should check whether they interact inelastically or not using the probability

$$p_{ij}^{in}(\vec{b}_i - \vec{b}_j^B, s) = p_{ij}(\vec{b}_i - \vec{b}_j^B, s) + p_{ij}^d(\vec{b}_i^A - \vec{b}_j^B, s).$$

If interaction will be realized, then we have to consider it to be diffractive or nondiffractive with probabilities

$$\frac{p_{ij}^d(\vec{b}_i - \vec{b}_j^B, s)}{p_{ij}^{in}(\vec{b}_i^A - \vec{b}_j^B, s)}$$

and

$$\frac{p_{ij}(\vec{b}_i - \vec{b}_j^B, s)}{p_{ij}^{in}(\vec{b}_i^A - \vec{b}_j^B, s)}.$$

## 23.3 Longitudinal string excitation

### 23.3.1 Hadron–nucleon inelastic collision

Let us consider collision of two hadrons with their c. m. momenta  $P_1 = \{E_1^+, m_1^2/E_1^+, \mathbf{0}\}$  and  $P_2 = \{E_2^-, m_2^2/E_2^-, \mathbf{0}\}$ , where the light-cone variables  $E_{1,2}^\pm = E_{1,2} \pm P_{z1,2}$  are defined through hadron energies  $E_{1,2} = \sqrt{m_{1,2}^2 + P_{z1,2}^2}$ , hadron longitudinal momenta  $P_{z1,2}$  and hadron masses  $m_{1,2}$ , respectively. Two hadrons collide by two partons with momenta  $p_1 = \{x^+ E_1^+, 0, \mathbf{0}\}$  and  $p_2 = \{0, x^- E_2^-, \mathbf{0}\}$ , respectively.

### 23.3.2 The diffractive string excitation

In the diffractive string excitation (the Fritiof approach [AB87]) only momentum can be transferred:

$$\begin{aligned} P'_1 &= P_1 + q \\ P'_2 &= P_2 - q, \end{aligned}$$

where

$$q = \{-q_t^2/(x^- E_2^-), q_t^2/(x^+ E_1^+), \mathbf{q}_t\} \quad (23.3)$$

is parton momentum transferred and  $\mathbf{q}_t$  is its transverse component. We use the Fritiof approach to simulate the diffractive excitation of particles.

### 23.3.3 The string excitation by parton exchange

For this case the parton exchange (rearrangement) and the momentum exchange are allowed [AUIJ94, ANS90, KAB82, S86]:

$$\begin{aligned} P'_1 &= P_1 - p_1 + p_2 + q \\ P'_2 &= P_2 + p_1 - p_2 - q, \end{aligned} \quad (23.4)$$

where  $q = \{0, 0, \mathbf{q}_t\}$  is parton momentum transferred, i. e. only its transverse components  $\mathbf{q}_t = 0$  is taken into account.

### 23.3.4 Transverse momentum sampling

The transverse component of the parton momentum transferred is generated according to probability

$$P(\mathbf{q}_t) d\mathbf{q}_t = \sqrt{\frac{a}{\pi}} \exp(-aq_t^2) d\mathbf{q}_t, \quad (23.5)$$

where parameter  $a = 0.6 \text{ GeV}^{-2}$ .

### 23.3.5 Sampling x-plus and x-minus

Light cone parton quantities  $x^+$  and  $x^-$  are generated independently and according to distribution:

$$u(x) \sim x^\alpha (1-x)^\beta, \quad (23.6)$$

where  $x = x^+$  or  $x = x^-$ . Parameters  $\alpha = -1$  and  $\beta = 0$  are chosen for the FRITIOF approach [AB87]. In the case of the QGSM approach [ANS90, S86]  $\alpha = -0.5$  and  $\beta = 1.5$  or  $\beta = 2.5$ . Masses of the excited strings should satisfy the kinematical constraints:

$$P_1'^+ P_1'^- \geq m_{h1}^2 + q_t^2 \quad (23.7)$$

and

$$P_2'^+ P_2'^- \geq m_{h2}^2 + q_t^2, \quad (23.8)$$

where hadronic masses  $m_{h1}$  and  $m_{h2}$  (model parameters) are defined by string quark contents. Thus, the random selection of the values  $x^+$  and  $x^-$  is limited by above constraints.

### 23.3.6 The diffractive string excitation

In the diffractive string excitation (the FRITIOF approach [AB87]) for each inelastic hadron–nucleon collision we have to select randomly the transverse momentum transferred  $\mathbf{q}_t$  (in accordance with the probability given by Eq. (23.5) and select randomly the values of  $x^\pm$  (in accordance with distribution defined by Eq. (23.6). Then we have to calculate the parton momentum transferred  $q$  using Eq. (23.3) and update scattered hadron and nucleon or scattered nucleon and nucleon momenta using Eq. (23.4). For each collision we have to check the constraints (23.7) and (23.8), which can be written more explicitly:

$$\left[ E_1^+ - \frac{q_t^2}{x^- E_2^-} \right] \left[ \frac{m_1^2}{E_1^+} + \frac{q_t^2}{x^+ E_1^+} \right] \geq m_{h1}^2 + q_t^2$$

and

$$\left[ E_2^- + \frac{q_t^2}{x^- E_2^-} \right] \left[ \frac{m_2^2}{E_2^-} - \frac{q_t^2}{x^+ E_1^+} \right] \geq m_{h2}^2 + q_t^2.$$

### 23.3.7 The string excitation by parton rearrangement

In this approach [ANS90, S86] strings (as result of parton rearrangement) should be spanned not only between valence quarks of colliding hadrons, but also between valence and sea quarks and between sea quarks. The each participant hadron or nucleon should be splitted into set of partons: valence quark and antiquark for meson or valence quark (antiquark) and diquark (antidiquark) for baryon (antibaryon) and additionally the  $(n - 1)$  sea quark-antiquark pairs (their flavours are selected according to probability ratios  $u : d : s = 1 : 1 : 0.35$ ), if hadron or nucleon is participating in the  $n$  inelastic collisions. Thus for each participant hadron or nucleon we have to generate a set of light cone variables  $x_{2n}$ , where  $x_{2n} = x_{2n}^+$  or  $x_{2n} = x_{2n}^-$  according to distribution:

$$f^h(x_1, x_2, \dots, x_{2n}) = f_0 \prod_{i=1}^{2n} u_{q_i}^h(x_i) \delta(1 - \sum_{i=1}^{2n} x_i),$$

where  $f_0$  is the normalization constant. Here, the quark structure functions  $u_{q_i}^h(x_i)$  for valence quark (antiquark)  $q_v$ , sea quark and antiquark  $q_s$  and valence diquark (antidiquark)  $qq$  are:

$$u_{q_v}^h(x_v) = x_v^{\alpha_v}, \quad u_{q_s}^h(x_s) = x_s^{\alpha_s}, \quad u_{qq}^h(x_{qq}) = x_{qq}^{\beta_{qq}},$$

where  $\alpha_v = -0.5$  and  $\alpha_s = -0.5$  [KAB82] for the non-strange quarks (antiquarks) and  $\alpha_v = 0$  and  $\alpha_s = 0$  for strange quarks (antiquarks),  $\beta_{uu} = 1.5$  and  $\beta_{ud} = 2.5$  for proton (antiproton) and  $\beta_{dd} = 1.5$  and  $\beta_{ud} = 2.5$  for neutron (antineutron). Usually  $x_i$  are selected between  $x_i^{min} \leq x_i \leq 1$ , where model parameter  $x^{min}$  is a function of initial energy, to prevent from production of strings with low masses (less than hadron masses), when whole selection procedure should be repeated. Then the transverse momenta of partons  $\mathbf{q}_{it}$  are generated according to the Gaussian probability Eq. (23.5) with  $a = 1/4\Lambda(s)$  and under the constraint:  $\sum_{i=1}^{2n} \mathbf{q}_{it} = 0$ . The partons are considered as the off-shell partons, i. e.  $m_i^2 \neq 0$ .

## 23.4 Longitudinal string decay.

### 23.4.1 Hadron production by string fragmentation.

A string is stretched between flying away constituents: quark and antiquark or quark and diquark or diquark and antidiquark or antiquark and antidiquark. From knowledge of the constituents longitudinal  $p_{3i} = p_{zi}$  and transversal  $p_{1i} = p_{xi}$ ,  $p_{2i} = p_{yi}$  momenta as well as their energies  $p_{0i} = E_i$ , where  $i = 1, 2$ , we can calculate string mass squared:

$$M_S^2 = p^\mu p_\mu = p_0^2 - p_1^2 - p_2^2 - p_3^2,$$

where  $p_\mu = p_{\mu 1} + p_{\mu 2}$  is the string four momentum and  $\mu = 0, 1, 2, 3$ .

The fragmentation of a string follows an iterative scheme:

$$\text{string} \Rightarrow \text{hadron} + \text{new string},$$

*i.e.* a quark-antiquark (or diquark-antidiquark) pair is created and placed between leading quark-antiquark (or diquark-quark or diquark-antidiquark or antiquark-antidiquark) pair.

The values of the strangeness suppression and diquark suppression factors are

$$u : d : s : qq = 1 : 1 : 0.35 : 0.1.$$

A hadron is formed randomly on one of the end-points of the string. The quark content of the hadrons determines its species and charge. In the chosen fragmentation scheme we can produce not only the groundstates of baryons and mesons, but also their lowest excited states. If for baryons the quark-content does not determine whether the state belongs to the lowest octet or to the lowest decuplet, then octet or decuplet are choosen with equal probabilities. In the case of mesons the multiplet must also be determined before a type of hadron can be assigned. The probability of choosing a certain multiplet depends on the spin of the multiplet.

The zero transverse momentum of created quark-antiquark (or diquark-antidiquark) pair is defined by the sum of an equal and opposite directed transverse momenta of quark and antiquark.

The transverse momentum of created quark is randomly sampled according to probability (23.5) with the parameter  $a = 0.25 \text{ GeV}^{-2}$ . Then a hadron transverse momentum  $\mathbf{p}_t$  is determined by the sum of the transverse momenta of its constituents.

The fragmentation function  $f^h(z, p_t)$  represents the probability distribution for hadrons with the transverse momenta  $\mathbf{p}_t$  to acquire the light cone momentum fraction  $z = z^\pm = (E^h \pm p_z^h)/(E^q \pm p_z^q)$ , where  $E^h$  and  $E^q$  are the hadron and fragmented quark energies, respectively and  $p_z^h$  and  $p_z^q$  are hadron and fragmented quark longitudinal momenta, respectively, and  $z_{min}^\pm \leq z^\pm \leq z_{max}^\pm$ , from the fragmenting string. The values of  $z_{min,max}^\pm$  are determined by hadron  $m_h$  and constituent transverse masses and the available string mass. One of the most common fragmentation function is used in the LUND model [BGGT83]:

$$f^h(z, p_t) \sim \frac{1}{z} (1-z)^a \exp \left[ -\frac{b(m_h^2 + p_t^2)}{z} \right].$$

One can use this fragmentation function for the decay of the excited string.

One can use also the fragmentation functions are derived in [B87]:

$$f_q^h(z, p_t) = [1 + \alpha_q^h(\langle p_t \rangle)](1-z)^{\alpha_q^h(\langle p_t \rangle)}.$$

The advantage of these functions as compared to the LUND fragmentation function is that they have correct three-reggeon behaviour at  $z \rightarrow 1$  [B87].

### 23.4.2 The hadron formation time and coordinate.

To calculate produced hadron formation times and longitudinal coordinates we consider the  $(1+1)$ -string with mass  $M_S$  and string tension  $\kappa$ , which decays into hadrons at string rest frame. The  $i$ -th produced hadron has energy  $E_i$  and its longitudinal momentum  $p_{zi}$ , respectively. Introducing light cone variables  $p_i^\pm = E_i \pm p_{iz}$  and numbering string breaking points consecutively from right to left we obtain  $p_0^+ = M_S$ ,  $p_i^+ = \kappa(z_{i-1}^+ - z_i^+)$  and  $p_i^- = \kappa x_i^-$ .

We can identify the hadron formation point coordinate and time as the point in space-time, where the quark lines of the quark-antiquark pair forming the hadron meet for the first time (the so-called 'yo-yo' formation point [BGGT83]):

$$t_i = \frac{1}{2\kappa} \left[ M_S - 2 \sum_{j=1}^{i-1} p_{zj} + E_i - p_{zi} \right]$$

and coordinate

$$z_i = \frac{1}{2\kappa} \left[ M_S - 2 \sum_{j=1}^{i-1} E_j + p_{zi} - E_i \right].$$



**FRITIOF (FTF) MODEL**

## 24.1 Introduction

The Fritiof model, or FTF for short, is used in GEANT4 for simulation of the following interactions: hadron-nucleus at  $P_{\text{lab}} > 3\text{--}4 \text{ GeV}/c$ , nucleus-nucleus at  $P_{\text{lab}} > 2\text{--}3 \text{ GeV}/c/\text{nucleon}$ , antibaryon-nucleus at all energies, and antinucleus-nucleus. Because the model does not include multi-jet production in hadron-nucleon interactions, the upper limit of its validity range is estimated to be 1000 GeV/c per hadron or nucleon.

The model assumes that one or two unstable objects (quark-gluon strings) are produced in elementary interactions. If only one object is created, the process is called diffraction dissociation. It is assumed also that the objects can interact with other nucleons in hadron-nucleus and nucleus-nucleus collisions, and can produce other objects. The number of produced objects in these non-diffractive interactions is proportional to the number of participating nucleons. Thus, multiplicities in the hadron-nucleus and nucleus-nucleus interactions are larger than those in elementary ones.

The modeling of hadron-nucleon interactions in the FTF model includes simulations of elastic scattering, binary reactions like  $NN \rightarrow N\Delta, \pi N \rightarrow \pi\Delta$ , single diffractive and non-diffractive events, and annihilation in antibaryon-nucleon interactions. It is assumed that the unstable objects created in hadron-nucleus and nucleus-nucleus collisions can have analogous reactions.

Parameterizations of the CHIPS GEANT4 model are used for calculations of elastic and inelastic hadron-nucleon cross sections. Data-driven parameterizations of the binary reaction cross sections and the diffraction dissociation cross sections in the elementary interactions are implemented in the FTF model. It is assumed in the model that the unstable object cross sections are equal to the cross sections of stable objects having the same quark content.

The LUND string fragmentation model is used for the simulation of unstable object decays. The formation time of hadrons is considered also. Parameters of the fragmentation model were tuned to experimental data. A restriction of the available phase space is taken into account in low mass string fragmentation.

A simplified Glauber model is used for sampling the multiplicity of intra-nuclear collisions. Gribov inelastic screening is not considered. For medium and heavy nuclei a Saxon-Woods parameterization of the one-particle nuclear density is used, while for light nuclei a harmonic oscillator shape is used. Center-of-mass correlations and short range nucleon-nucleon correlations are taken into account.

The reggeon theory inspired model (RTIM) of nuclear destruction is applied for a description of secondary particle intra-nuclear cascading. A new algorithm to simulate “Fermi motion” in nuclear reactions is used.

Excitation energies of residual nuclei are estimated in the wounded nucleon approximation. This allows for a direct coupling of the FTF model to the Precompound model of GEANT4 and hence with the GEM nuclear fragmentation model. The determination of the particle formation time allows one to couple the FTF model with the Binary cascade model of GEANT4 (*The Binary Cascade Model*).

### 24.1.1 Main assumptions of the FTF model

The Fritiof model [BNilssonAEStenlund87, eal87] assumes that all hadron-hadron interactions are binary reactions,  $h_1 + h_2 \rightarrow h'_1 + h'_2$ , where  $h'_1$  and  $h'_2$  are excited states of the hadrons with discrete or continuous mass spectra (see Fig. 24.1). If one of the final hadrons is in its ground state ( $h_1 + h_2 \rightarrow h_1 + h'_2$ ) the reaction is called “single diffraction dissociation”, and if neither hadron is in its ground state it is called a “non-diffractive” interaction. (Notice that, in spite of its name, this definition of “non-diffractive” interaction includes the double diffraction dissociation as well.)

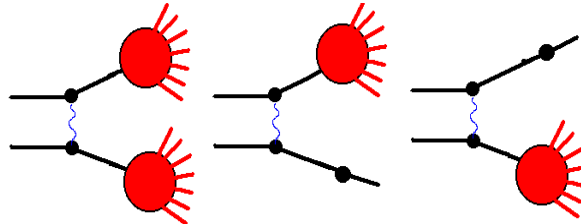


Fig. 24.1: Non-diffractive and diffractive interactions considered in the Fritiof model.

The excited hadrons are considered as QCD-strings, and the corresponding LUND-string fragmentation model is applied in order to simulate their decays.

The key ingredient of the Fritiof model is the sampling of the string masses. In general, the set of final state of interactions can be represented by Fig. 24.2, where samples of possible string masses are shown. There is a point corresponding to elastic scattering, a group of points which represents final states of binary hadron-hadron interactions, lines corresponding to the diffractive interactions, and various intermediate regions. The region populated with the red points is responsible for the non-diffractive interactions. In the model, the mass sampling threshold is set equal to the ground state hadron masses, but in principle the threshold can be lower than these masses. The string masses are sampled in the triangular region restricted by the diagonal line corresponding to the kinematical limit  $M_1 + M_2 = E_{\text{cms}}$  where  $M_1$  and  $M_2$  are the masses of the  $h'_1$  and  $h'_2$  hadrons, and also of the threshold lines. If a point is below the string mass threshold, it is shifted to the nearest diffraction line.

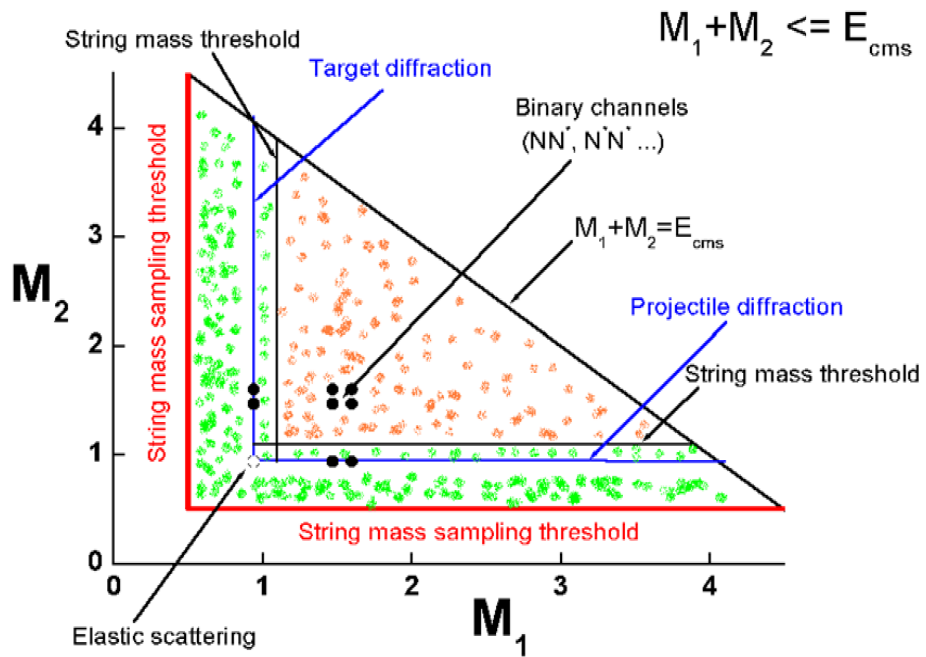


Fig. 24.2: Diagram of the final states of hadron-hadron interactions.

Unlike the original Fritiof model, the final state diagram of the current model is complicated, which leads to a mass sampling algorithm that is not simple. This will be considered below. The original model had no points corresponding to elastic scattering or to the binary final states. As it was known at the time, the mass of an object produced by diffraction dissociation,  $M_x$ , for example from the reaction  $p + p \rightarrow p + X$ , is distributed as  $dM_x/M_x \propto dM_x^2/M_x^2$ , so it was natural to assume that the object mass distributions in all inelastic interactions obeyed the same law. This can be re-written using the light-cone momentum variables,  $P^+$  or  $P^-$ ,

$$P^+ = E + p_z, \quad P^- = E - p_z$$

where  $E$  is an energy of a particle, and  $p_z$  is its longitudinal momentum along the collision axis. At large energy and positive  $p_z$ ,  $P^- \simeq (M^2 + P_T^2)/2p_z$ . At negative  $p_z$ ,  $P^+ \simeq (M^2 + P_T^2)/2|p_z|$ . Usually, the transferred transverse momentum,  $P_T$ , is small and can be neglected. Thus, it was assumed that  $P^-$  and  $P^+$  of a projectile, or target associated hadron, respectively, are distributed as

$$dP^-/P^-, \quad dP^+/P^+$$

A gaussian distribution was used to sample  $P_T$ .

In the case of hadron-nucleus or nucleus-nucleus interactions it was assumed that the created objects can interact further with other nuclear nucleons and create new objects. Assuming equal masses of the objects, the multiplicity of particles produced in these interactions will be proportional to the number of participating nuclear nucleons, or to the multiplicity of intra-nuclear collisions. Due to this, the multiplicity of particles produced in hadron-nucleus or nucleus-nucleus interactions is larger than that in hadron-hadron ones. The probabilities of multiple intra-nuclear collisions were sampled with the help of a simplified Glauber model. Cascading of secondary particles was not considered.

Because the Fermi motion of nuclear nucleons was simulated in a simple manner, the original Fritiof model could not work at  $P_{lab} < 10\text{--}20 \text{ GeV}/c$ .

It was assumed in the model that the created objects are quark-gluon strings with constituent quarks at their ends originating from the primary colliding hadrons. Thus, the LUND-string fragmentation model was applied for a simulation of the object decays. It was assumed also that the strings with sufficiently large masses have “kinks” – additional radiated gluons. This was very important for a correct reproduction of particle multiplicities in the interactions.

All of the above assumptions were reconsidered in the implementation of the GEANT4 Fritiof model, and new features were added. These will be presented below.

### 24.1.2 General properties of hadron–nucleon interactions

Before going into details of the FTF model implementation it would be better to consider briefly the general properties of hadron-nucleon interactions in order to understand what needs to be simulated. These properties include total and elastic cross sections, and cross sections of various other reactions. There is so much data on inclusive spectra that not all of it can be addressed in this work. It is hoped that the remaining data will be the subject of a future paper. Inclusive data present kinematical properties of produced particles. Their description requires additional methods and parameters, which will be considered later.

#### $\pi^- p$ interactions

Total, elastic and reaction cross sections of  $\pi^- p$ -interactions are presented in Fig. 24.3. As seen, there are peaks in the total cross section connected with  $\Delta$ -isobar production ( $\Delta(1232)$ ,  $\Delta(1600)$ ,  $\Delta(1700)$  and so on) in the  $s$ -channel,  $\pi^- + p \rightarrow \Delta^0$ . The main channel of a  $\Delta^0$ -isobar decay is  $\Delta^0 \rightarrow \pi^- + p$ . These resonances are reflected in the elastic cross section. The other important decay channel is  $\Delta^0 \rightarrow \pi^0 + n$ , which is the main inelastic reaction channel at  $P_{lab} < 700 \text{ MeV}/c$ . At higher energy two-meson production channels start to dominate, and at  $P_{lab} > 3 \text{ GeV}/c$  there is practically no structure in the cross sections. Cross sections of final states with defined charged particle multiplicity, so-called prong cross sections according to the old terminology, are presented in the last figure. As seen, real multi-particle production processes ( $n \geq 4$ ) dominate at  $P_{lab} > 5\text{--}7 \text{ GeV}/c$ .

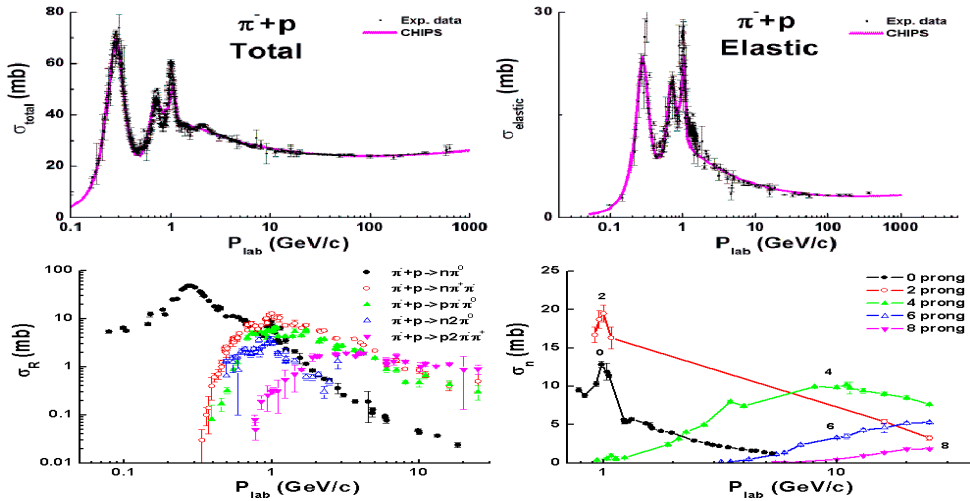


Fig. 24.3: General properties of  $\pi^- p$ -interactions. Points are experimental data: data on total and elastic cross sections from PDG data-base [PDG12], other data from [eal72].

In the constituent quark model of hadrons, the creation of  $s$ -channel  $\Delta$ -isobars is explained by quark–antiquark annihilation (see Fig. 24.4a). The production of two mesons may result from quark exchange (see Fig. 24.4b, Fig. 24.4c). A quark–diquark ( $q-q\bar{q}$ ) system created in the process can be in a resonance state (Fig. 24.4b), or in a state with a continuous mass spectrum (Fig. 24.4c). In the latter case, multi-meson production is possible. Amplitudes of these two channels are connected by crossing symmetry to annihilation in the  $t$ -channel, and with non-vacuum exchanges in the elastic scattering according to the reggeon phenomenology. According to that phenomenology, pomeron exchange must dominate in elastic scattering at high energies. In a simple approach, this corresponds to two-gluon exchange between colliding hadrons. It reflects also one or many non-perturbative gluon exchanges in the inelastic reaction. Due to these exchanges, a state with subdivided colors is created (see Fig. 24.4d). The state can decay into two colorless objects. The quark content of the objects coincides with the quark content of the primary hadrons, according to the FTF model, or it is a mixture of the primary hadron’s quarks, according to the Quark-Gluon-String model (QGSM).

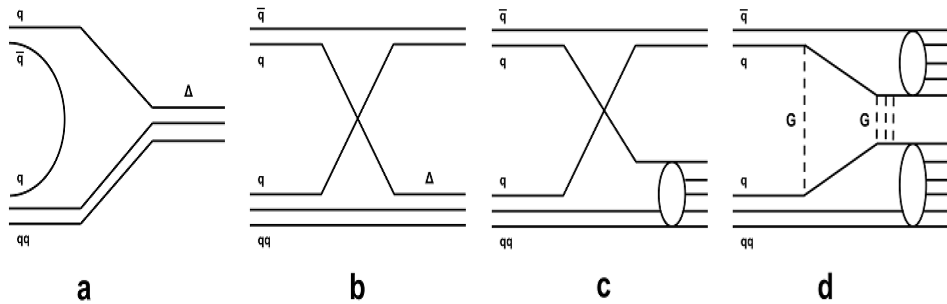


Fig. 24.4: Quark flow diagrams of  $\pi N$ -interactions.

The original Fritiof model contains only the pomeron exchange process shown in Fig. 24.4d. It would be useful to extend the model by adding the exchange processes shown in Fig. 24.4b and Fig. 24.4c, and the annihilation process of Fig. 24.4a. This could probably be done by introducing a restricted set of mesonic and baryonic resonances and a corresponding set of parameters. This procedure was employed in *The Binary Cascade Model* of GEANT4 (BIC) [FIW04] and in the Ultra-Relativistic-Quantum-Molecular-Dynamic model (UrQMD) [eal99, eal98] (see *Quantum Molecular Dynamics for Heavy Ions*). However, it is complicated to use this solution for a simulation of hadron-nucleus and nucleus-nucleus interactions. The problem is that one has to consider resonance propagation in the nuclear medium and take into account their possible decays which enormously increases computing time. Thus, in the

current version of the FTF model only quark exchange processes have been added to account for meson and baryon interactions with nucleons, without considering resonance propagation and decay. This is a reasonable hypothesis at sufficiently high energies.

### $\pi^+ p$ interactions

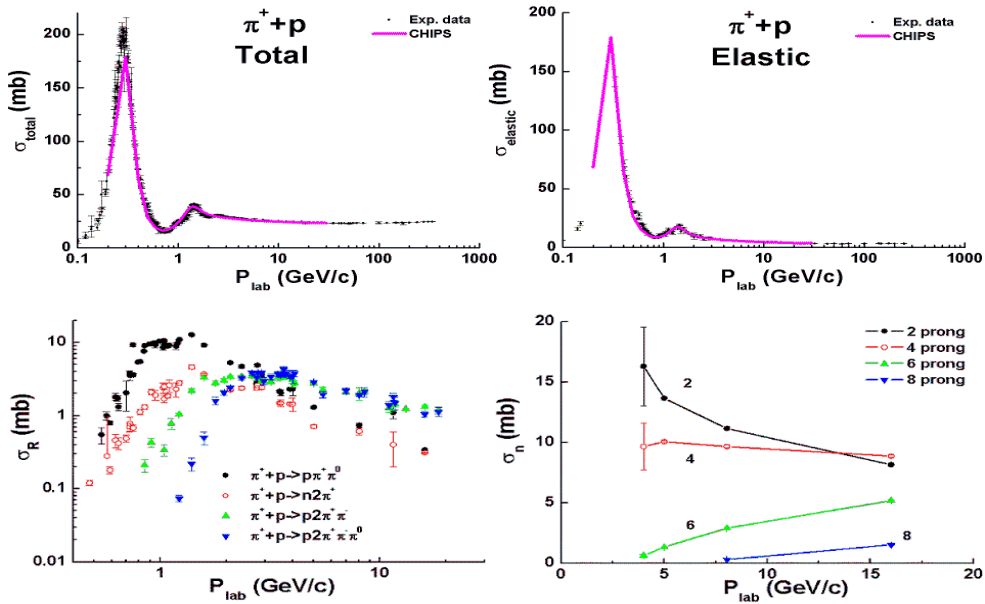


Fig. 24.5: General properties of  $\pi^+ p$ -interactions. Points are experimental data: data on total and elastic cross sections from PDG data-base [PDG12], other data from [eal72].

Total, elastic and reaction cross sections of  $\pi^+ p$ -interactions are presented in Fig. 24.5. As seen, there are fewer peaks in the total cross section than in  $\pi^- p$ -collisions. The creation of  $\Delta^{++}$ -isobars in the  $s$ -channel ( $\pi^+ + p \rightarrow \Delta^{++}$ ) is mainly seen in the elastic cross section because the main channel of  $\Delta^{++}$ -isobar decay is  $\Delta^{++} \rightarrow \pi^+ + p$ . This process is due to quark–antiquark annihilation. At  $P_{lab} > 400$  MeV/c two-meson production channels appear. They can be connected with quark exchange and with the formation of  $\Delta^{++}$  and  $\Delta^+$  isobars at the proton site. The corresponding cross sections of the reactions  $\pi^+ + p \rightarrow \pi^0 + \Delta^{++} \rightarrow \pi^0 + \pi^+ + p$ ,  $\pi^+ + p \rightarrow \pi^+ + \Delta^+ \rightarrow \pi^+ + \pi^0 + p$ ,  $\pi^+ + p \rightarrow \pi^+ + \Delta^+ \rightarrow \pi^+ + \pi^+ + n$  have structures at  $P_{lab} \simeq 1.5$  and  $2.8$  GeV/c. At higher energies there is no structure. The cross sections of other reactions are rather smooth.

### $pp$ interactions

Total, elastic and reaction cross sections of  $pp$ -interactions are presented in Fig. 24.6. The total cross section is seen to decrease with energy below the meson production threshold ( $P_{lab} \leq 800$  MeV/c). Above the threshold the cross section starts to increase and becomes nearly constant. The main reaction channel below 6–8 GeV/c is  $p + p \rightarrow p + n + \pi^+$ . Because there cannot be quark–antiquark annihilation in the interaction, the reaction must be connected to quark exchange. Intermediate states can be  $p + p \rightarrow p + \Delta^+$  and  $p + p \rightarrow n + \Delta^{++}$ . In the first case, quarks of the same flavor in the projectile and the target are exchanged. In the second case quarks with different flavors take part in the exchange. Because the cross section of the  $p + p \rightarrow p + n + \pi^+$  reaction is larger than the that of  $p + p \rightarrow p + p + \pi^0$ , one has to assume that the exchange of quarks with the same flavors is suppressed.

All the reactions shown can also be caused by diffraction dissociation. Although there can be a contribution of the  $p + p \rightarrow \Delta^0 + \Delta^{++}$  reaction into the cross section of the channel  $p + p \rightarrow (p + \pi^-) + (p + \pi^+)$  at  $P_{lab} \sim 2$ – $3$  GeV/c, one can assume that diffraction plays an essential role in these interactions, because there are no defined structures in the cross sections.

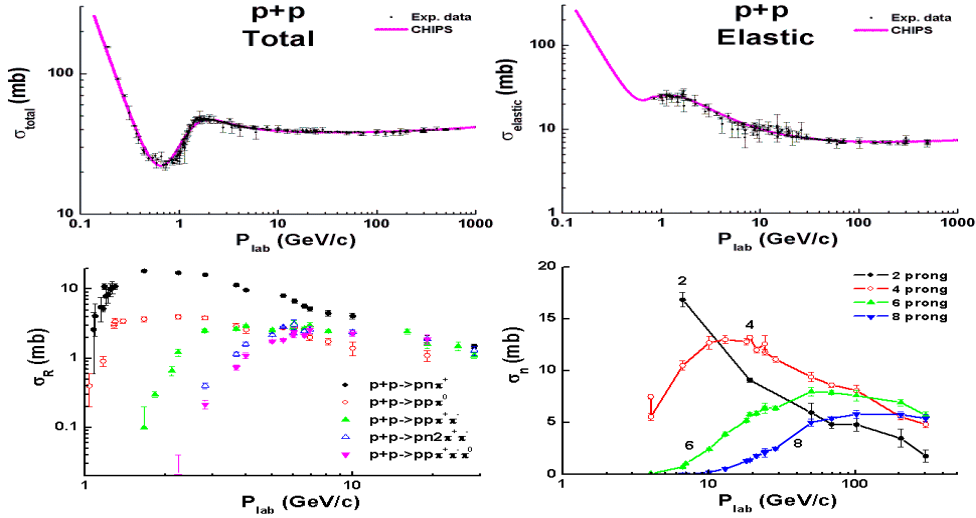


Fig. 24.6: General properties of  $p\bar{p}$ -interactions. Points are experimental data: data on total and elastic cross sections from PDG data-base [PDG12], other data from [eal73a, eal84].

Summing up the consideration of the interactions, one can conclude that the probability of quark exchanges can depend on quark flavors, and that  $p\bar{p}$ -collisions could be a source of information about diffraction.

### $K^+p$ – and $K^-p$ interactions

For completeness, the properties of  $K^+p$ - and  $K^-p$ -interactions are presented. Total and elastic cross sections are shown in Fig. 24.7. As the  $s$ -antiquark in the  $K^+$ -mesons cannot annihilate in the  $K^+p$ -interactions, the structure of the corresponding cross sections is rather simple, and is very like the structure of  $p\bar{p}$  cross sections. The  $u$ -antiquark in the  $K^-$ -mesons can annihilate, and the structure of the cross sections is more complicated. Due to these features, inelastic reactions are very different even though all of them can be connected with various quark flow diagrams like that shown in Fig. 24.4

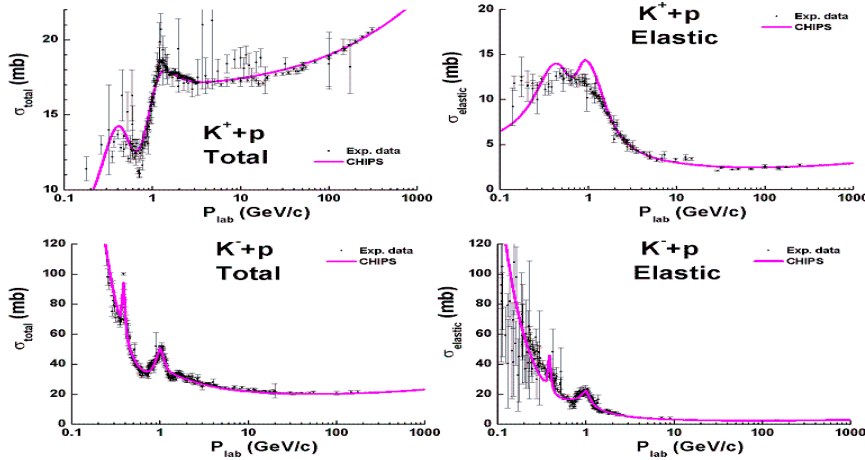


Fig. 24.7: Total and elastic cross sections of  $Kp$ -interactions. Points are experimental data from PDG data-base .

The reactions  $K^- + p \rightarrow \Sigma^- + \pi^+$  and  $K^- + p \rightarrow \Sigma^0 + \pi^0$  can be explained by the annihilation of the  $u$ -antiquark of the  $K^-$  and the formation of  $s$ -channel resonances. The other reactions –  $K^- + p \rightarrow \Sigma^+ + \pi^-$  and  $K^- + p \rightarrow \Lambda + \pi^0$ ,

are connected with quark exchange. As seen, the energy dependence of the cross sections of the two types of processes are different. The  $K^- + p \rightarrow n + K^0$  reaction must be caused by annihilation, but the dependence of its cross section on energy is closer to that of the quark exchange processes. The cross section of the reaction has a resonance structure only at  $P_{lab} < 2 \text{ GeV}/c$ . Above that energy there is no structure. Because the cross section of the reaction is sufficiently small at high energies, one can omit its correct description.

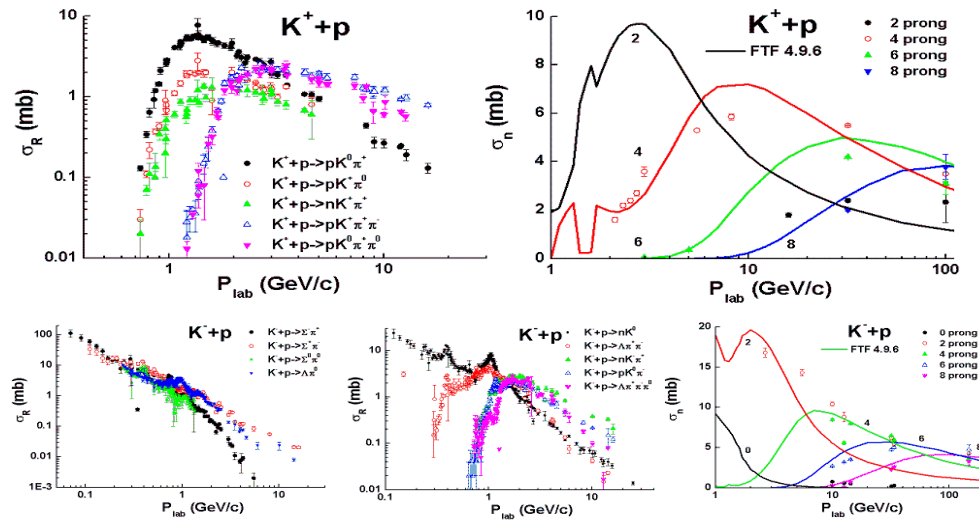


Fig. 24.8: Reaction cross sections of  $Kp$ -interactions. Points are experimental data .

$K^- + p \rightarrow n + K^- + \pi^+$  and  $K^- + p \rightarrow p + K^0 + \pi^-$  reactions are mainly caused by the diffraction dissociation of a projectile or a target hadron. The energy dependence of their cross sections are different from those of annihilation and quark exchange.

The same regularities can be seen in  $K^+p$  reactions. The energy dependence of the cross sections of the  $K^+ + p \rightarrow p + K^0 + \pi^+$ ,  $K^+ + p \rightarrow p + K^+ + \pi^0$  and  $K^+ + p \rightarrow n + K^+ + \pi^+$  reactions are quite different from those of  $K^- + p$ .

In summary, there are three types of energy dependence in the reaction cross sections. The rapidly decreasing one is due to annihilation. The cross sections of the quark exchange processes decrease more slowly. Finally, the diffraction cross sections grow with energy and reach near-constant values.

### $p\bar{p}$ interactions

Proton–antiproton interactions provide the beautiful possibility of studying annihilation processes in detail. The general properties of the interactions are presented in Fig. 24.9. Almost no structure is seen in the cross sections and their energy dependence is very different from the previously described reactions.

Cross sections of the reactions  $\bar{p} + p \rightarrow \pi^+ + \pi^-$  and  $\bar{p} + p \rightarrow K^+ + K^-$ , decrease faster than other cross sections as a functions of energy.  $\bar{p} + p \rightarrow \pi^+ + \pi^- + \pi^0$  and  $\bar{p} + p \rightarrow 2\pi^+ + 2\pi^-$  cross sections decrease less rapidly, nearly in the same manner as cross sections of the reactions  $\bar{p} + p \rightarrow n + \bar{n}$  and  $\bar{p} + p \rightarrow \Lambda + \bar{\Lambda}$ . The cross sections of the reaction  $\bar{p} + p \rightarrow 2\pi^+ + 2\pi^- + \pi^0$ , is a slowly decreasing function. The cross section of the process  $\bar{p} + p \rightarrow 3\pi^+ + 3\pi^- + \pi^0$  varies only a little over the studied energy range. Cross sections of other reactions ( $\bar{p} + p \rightarrow p + \pi^0 + \bar{p}$ ,  $\bar{p} + p \rightarrow p + \pi^+ + \pi^- + \bar{p}$  and so on) show behaviour typical of diffraction cross sections.

The main channel of  $\bar{p}p$  interactions at  $P_{lab} < 4 \text{ GeV}/c$  is  $\bar{p} + p \rightarrow 2\pi^+ + 2\pi^- + \pi^0$ . At higher energies, there is a mixture of various channels. Such variety in the processes is indicative of complicated quark interactions. Possible quark flow diagrams are shown in Fig. 24.10.

As usual, quarks and antiquarks are shown by solid lines. Dashed lines present so-called string junctions. It is assumed

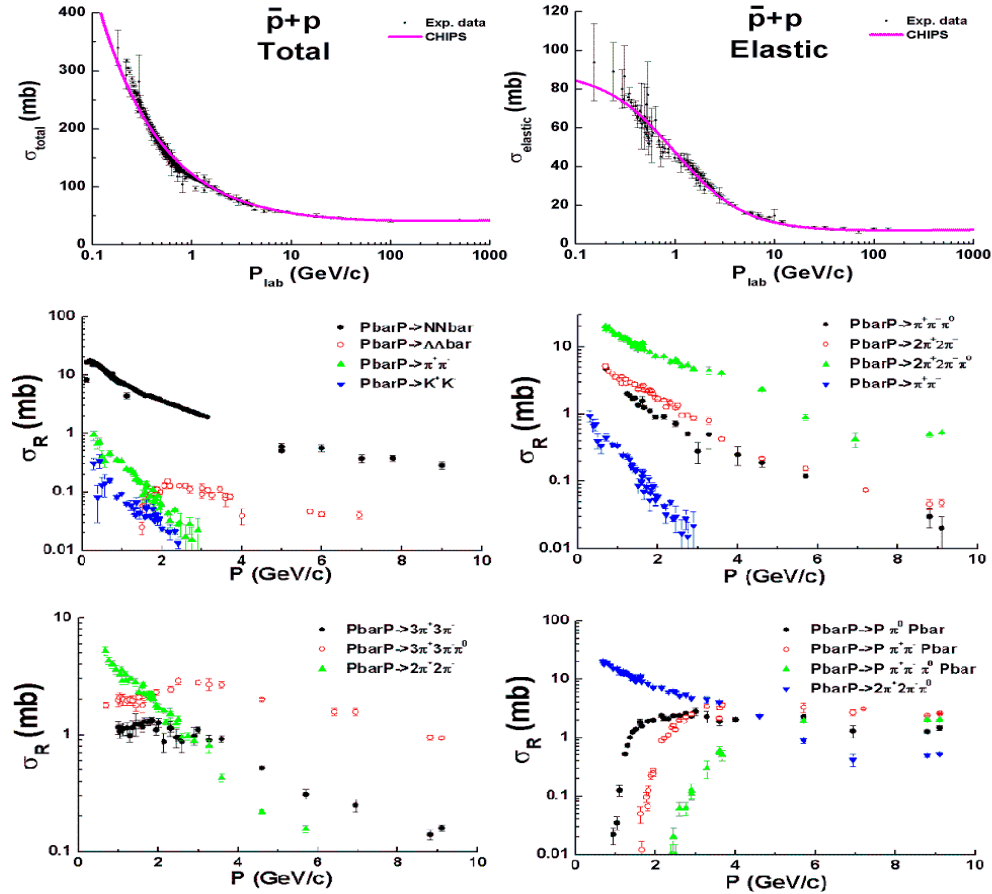
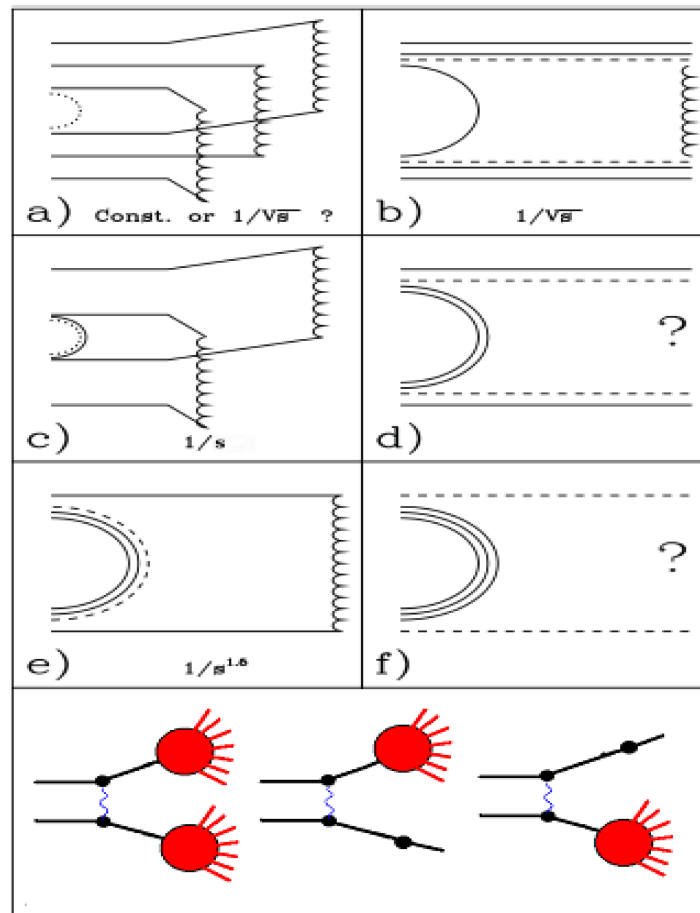


Fig. 24.9: General properties of  $\bar{p}p$ -interactions. Points are experimental data: data on total and elastic cross sections from PDG data-base [PDG12], other data from [eal73a, eal84].

Fig. 24.10: Quark flow diagrams of  $\bar{p}p$ -interactions.

that the gluon field in baryons has a non-trivial topology. This heterogeneity is called a “string junction”. Quark-gluon strings produced in the reaction are shown by wavy lines.

The diagram of Fig. 24.10a represents a process with a string junction annihilation and the creation of three strings. Diagram Fig. 24.10b describes quark-antiquark annihilation and string creation between the diquark and anti-diquark. Quark-antiquark and string junction annihilation is shown in Fig. 24.10c. Finally, one string is created in the process of Fig. 24.10e. Hadrons appear at the fragmentation of the strings in the same way that they appear in  $e^+e^-$ -annihilation. One can assume that excited strings with complicated gluonic field configurations are created in processes Fig. 24.10d and Fig. 24.10f. If the collision energy is sufficiently small glueballs can be formed in the process Fig. 24.10f. Mesons with constituent gluons or with hidden baryon number can be created in process Fig. 24.10d. Of course the standard FTF processes shown in the bottom of the figure are also allowed.

In the simplest approach it is assumed that the energy dependence of the cross sections of these processes vary inversely with a power of  $s$  as depicted in Fig. 24.10. Here  $s$  is center-of-mass energy squared. This is suggested by the reggeon phenomenology (at the leading order). Calculating the cross sections of binary reactions (in the reggeon framework, including higher-order terms) is a rather complicated procedure (see [KV94]) because there can be interactions in the initial and final states. Similar complications appear also in the computation of cross sections of other reactions [UG02].

### 24.1.3 Cross sections of hadron–nucleon processes

#### Total, elastic and inelastic hadron–nucleon cross sections

Parameterizations of the cross sections implemented in the CHIPS model of GEANT4 (authors: M.V. Kossov and P.V. Degtyarenko) are used in the FTF model. The general form of the parameterization is:

$$\sigma = \sigma_{LE} + \sigma_{As}$$

where  $\sigma_{LE}$  is a low energy parameterization depending on the types of colliding particles, and  $\sigma_{As}$  is the asymptotic part of cross sections. The COMPLETE Collaboration proposed a hypothesis [ealCOMPLETEcollab02] that  $\sigma_{As}$  of total cross sections at very high energies does not depend on the types of colliding particles:

$$\sigma_{As}^{tot} = Z_{h_1 h_2} + B (\log(s/s_0))^2$$

$$B = 0.3152, s_0 = 34.0 [(\text{GeV}/c)^2] \quad (\text{COMPLETE}, 2002)$$

$$B = 0.308, s_0 = 28.9 [(\text{GeV}/c)^2] \quad (\text{PDG}, 2006)$$

$$B = 0.304, s_0 = 33.1 [(\text{GeV}/c)^2] \quad (\text{M. Ishida, K.Igi}, 2009)$$

while the pre-asymptotic part does depend on colliding particles ( $h_1, h_2$ ).

The CHIPS model  $\sigma_{As}$  for total and elastic cross sections has the same form:

$$\begin{aligned} \sigma_{As} = & \left\{ A [\ln(P_{lab}) - B]^2 + C + D/P_{lab}^{0.5} + E/P_{lab} + F/P_{lab}^2 \right\} / \\ & (1 + G/P_{lab}^{0.5} + H/P_{lab}^3 + I/P_{lab}^4) \quad [\text{mb}] \end{aligned}$$

where  $P_{lab}$  is in  $[\text{GeV}/c]$ , and the parameters  $A, B$ , etc. are given in the tables Table 24.1 and Table 24.2.

Table 24.1: CHIPS model parameters for total cross sections

$h_1 \ h_2$	$A$	$B$	$C$	$D$	$E$	$F$	$G$	$H$	$I$
$\pi^- p$	0.3	3.5	22.3	12.0	0	0	0	0	0.4
$\pi^+ p$	0.3	3.5	22.3	5.0	0	0	0	0	1.0
$p p$	0.3	3.5	38.2	0	0	0	0	0	0.54
$n p$	0.3	3.5	38.2	0	0	52.7	0	0	2.72
$K^+ p$	0.3	3.5	19.5	0	0	0	0.46	0	1.6
$K^- p$	0.3	3.5	19.5	0	0	0	-0.21	0	0.52
$\bar{p} p$	0.3	3.5	38.2	0	0	0	0	0	0

Table 24.2: CHIPS model parameters for elastic cross sections

$h_1 \ h_2$	$A$	$B$	$C$	$D$	$E$	$F$	$G$	$H$	$I$
$\pi^- p$	0.0557	3.5	2.4	6.0	0	0	0	0	3.0
$\pi^+ p$	0.0557	3.5	2.4	7.0	0	0	0	0	0.7
$pp$	0.0557	3.5	6.72	0	30.0	0	0	0.49	0.0
$np$	0.0557	3.5	6.72	0	32.6	0	0	0	1.0
$K^+ p$	0.0557	3.5	2.23	0	0	0	-0.7	0	0.1
$K^- p$	0.0557	3.5	2.23	0	0	0	-0.7	0	0.075

The low energy parts of the cross sections are very different for various projectiles, and they are not presented here. These can be found in the corresponding classes of GEANT4.

It is obvious that  $\sigma^{in} = \sigma^{tot} - \sigma^{el}$ .

A comparison of the parameterizations with experimental data was presented in the previous figures.

### Cross sections of quark exchange processes

Cross sections of quark exchange processes are parameterized as:

$$\sigma_{qe} = \sigma_{in} A e^{-B y_{lab}} \quad (24.1)$$

where  $y_{lab}$  is a projectile rapidity in a target rest frame.  $A$  and  $B$  are parameters given in Table 24.3.

Table 24.3: Parameters of quark exchange cross sections

$h_1 \ h_2$	$A$	$B$
$pp/pn$	1.85	0.7
$\pi p/\pi n$	240	2
$Kp/Kn$	40	2.25

The parameters were determined from a description of reaction channel cross sections.

### Cross sections of antiproton processes

The annihilation cross section is parameterized as:

$$\sigma_{ann} = \sigma_a + B X_b + C X_c + D X_d \quad (24.2)$$

where:  $X_i$  are the contributions of the diagrams of Fig. 24.10; all cross sections are given in [mb];

$$\begin{aligned}
 \sigma_a &= 25 \sqrt{s}/\lambda^{1/2}(s, m_p^2, m_N^2) \\
 \lambda(s, m_p^2, m_N^2) &= s^2 + m_p^4 + m_N^4 - 2sm_p^2 - 2sm_N^2 - 2m_p^2m_N^2 \\
 X_b &= 3.13 + 140 (s_{th} - s)^{2.5}, \quad s < s_{th} \\
 X_b &= 6.8/\sqrt{s}, \quad s > s_{th} \\
 s_{th} &= (m_p + m_N + 2m_\pi + \delta)^2 \\
 X_c &= 2 \frac{\sqrt{s}}{\lambda^{1/2}(s, m_p^2, m_N^2)} \frac{(m_p + m_N)^2}{s} \\
 X_d &= 23.3/s
 \end{aligned} \quad (24.3)$$

Table 24.4: Coefficients  $B$ ,  $C$ , and  $D$ .

	$\bar{p}p$	$\bar{p}n$	$\bar{n}p$	$\bar{n}n$	$\Lambda p$	$\Lambda n$	$\Sigma^- p$	$\Sigma^- n$	$\Sigma^0 p$	$\Sigma^0 n$	$\Sigma^+ p$	$\Sigma^+ n$
B	5	4	4	5	3	3	2	4	3	3	4	2
C	5	4	4	5	3	3	2	4	3	3	4	2
D	6	4	4	6	3	3	2	2	2	2	2	0

 Table 24.5: Coefficients  $B$ ,  $C$ , and  $D$  (continued).

	$\Xi^- p$	$\Xi^- n$	$\Xi^0 p$	$\Xi^0 n$	$\Omega^- p$	$\Omega^- n$
B	1	2	2	1	0	0
C	1	2	2	1	0	0
D	0	0	0	0	0	0

The coefficients  $B$ ,  $C$  and  $D$  are pure combinatorial coefficients calculated on the assumption that the same conditions apply to all quarks and antiquarks. For example, in  $\bar{p}p$  interactions there are five possibilities to annihilate a quark and an antiquark, and six possibilities to annihilate two quarks and two antiquarks. Thus,  $B = C = 5$  and  $D = 6$ .

Note that final state particles in the process of Fig. 24.10b can coincide with initial state particles. Thus the true elastic cross section is not given by the experimental cross section.

At  $P_{lab} < 40$  MeV/c antiproton-nucleon cross sections are:

$$\sigma^{tot} = 1512.9, \quad \sigma^{el} = 473.2, \quad \sigma_a = 625.1, \quad \sigma_b = 0, \quad \sigma_c = 49.99, \quad \sigma_d = 6.61$$

All cross sections are given in mb.  $\sigma_b = 0$  for  $\bar{p}p$ -interactions because the process  $\bar{p}p \rightarrow \bar{n}n$  is impossible at these energies ( $P_{lab} < 40$  MeV/c).

### Cross sections of diffractive and non-diffractive processes

As mentioned above, three processes are considered in the FTF model at high energies: projectile diffraction (pd), target diffraction (td) and non-diffractive interactions (nd). They are parameterized as:

$$\begin{aligned} \sigma_{pp}^{pd} &= \sigma_{pp}^{td} = 6 + \sigma^{in} \frac{1.5}{s} \text{ (mb)} \\ \sigma_{\bar{p}p}^{pd} &= \sigma_{\bar{p}p}^{td} = 6 + \sigma^{in} \frac{1.5}{s} \text{ (mb)} \\ \sigma_{\pi p}^{pd} &= 6.2 - e^{-\frac{(\sqrt{s}-7)^2}{16}} \\ \sigma_{\pi p}^{td} &= 2 + 22/s \text{ (mb)} \\ \sigma_{Kp}^{pd} &= 4.7, \\ \sigma_{Kp}^{td} &= 1.5 \text{ (mb)} \end{aligned} \tag{24.4}$$

For the determination of these cross sections, inclusive spectra of particles in hadronic interactions were used. In Fig. 24.11 an inclusive spectrum of protons in the reaction  $p + p \rightarrow p + X$  is shown in comparison with model predictions.

As it can be seen, all the models have difficulties in describing the data. In the FTF model this was overcome by tuning the single diffraction dissociation cross section. Tuning was possible by the fact that the height of the proton peak at large rapidities depends on this cross section (see left Fig. 24.11).

The  $2\sigma_{pp}^{pd}$  (the factor of 2 is due to the fact that  $\sigma_{pp}^{pd} = \sigma_{pp}^{td}$ ) predicted by the expression (blue solid curve) is shown at the right of Fig. 24.11 in a comparison with experimental data gathered by K. Goulianos and J. Montanha [GM99]. The values are larger than experimental data. Though taking into account the restriction that the mass of a produced system,  $X$ , cannot be very small or very large ( $M^2/s < 0.05$  and  $M > 1.5$  GeV) brings the predictions closer to the data. So, the accounting of this restriction is very important for a correct reproduction of the data.

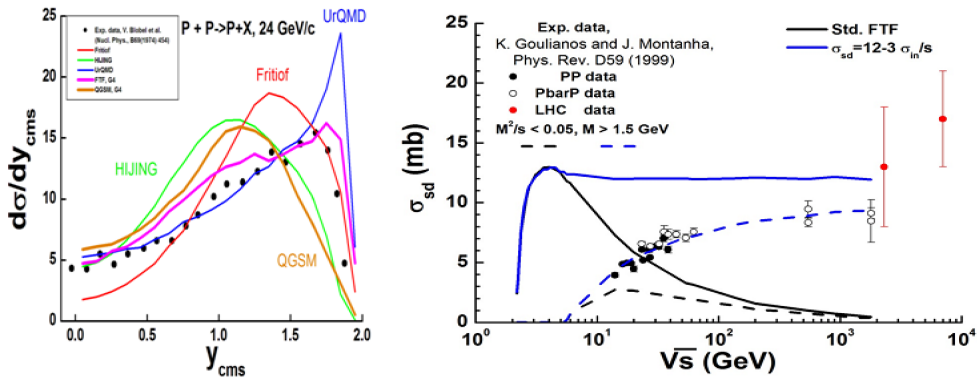


Fig. 24.11: Left: inclusive spectrum of proton in  $p + p$ -interactions at  $P_{lab} = 24 \text{ GeV}/c$ . Points are experimental data [eal74], lines are model calculations. Right: single diffraction dissociation cross section in  $p + p$ -interactions. Points are data gathered by K. Goulianos and J. Montanha [GM99]. Lines are FTF model calculations.

A more complicated situation arises with  $\pi p$ - and  $Kp$ -interactions. The set of experimental data on diffraction cross sections is very restricted. Thus, a refined tuning was used. The FTF processes discussed above contribute in various regions of particle spectra. The target diffraction dissociation,  $\pi + p \rightarrow \pi + X$ , gives its main contribution at large values of  $x_F = 2p_z/\sqrt{s}$  for  $\pi$ -mesons. The projectile diffraction dissociation contribution ( $\pi + p \rightarrow X + p$ ) has a maximum at  $x_F \sim -1$ . Thus, using various experimental data and varying the cross sections of the processes, the points presented in the lower left corner of Fig. 24.12 were obtained. They were parameterized by the expressions in (24.4). A correct reproduction of particle spectra in the central region,  $x_F \sim 0$ , was very important for these. As a result, we have a good description of  $\pi$ -meson spectra in the interactions at various energies.

In  $Kp$ -interactions the projectile diffraction cross sections were determined by tuning on proton spectra from the reactions  $K + p \rightarrow p + X$  (see Fig. 24.13). There are no data on leading  $K$ -meson spectra in the reactions  $K + p \rightarrow K + X$ . Thus,  $\pi^-$ -meson spectra in the central region were tuned. At a given value of a projectile diffraction cross section, the central spectrum depends on a target diffraction. This was used to determine the target diffraction cross sections. The estimated cross sections are shown in the lower left corner of Fig. 24.13. As a result, a satisfactory description of meson spectra was obtained.

## 24.1.4 Simulation of hadron-nucleon interactions

### Simulation of meson–nucleon and nucleon–nucleon interactions

Colliding hadrons may either be on or off the mass shell when they are bound in nuclei. When they are off-shell the total mass of the hadrons is checked. If the sum of the masses is above the center-of-mass energy of the collision, the simulated event is rejected. If below, the event is accepted. It is assumed that due to the interaction the hadrons go on-shell, and the center-of-mass energy of the collision is not changed.

The simulation of an inelastic hadron-nucleon interaction starts with a choice: should a quark exchange or a diffractive/non-diffractive excitation be simulated? The probability of a quark exchange is given by  $W_{qe} = \sigma_{qe}/\sigma^{in}$ . The combined probability of diffractive dissociation and non-diffractive excitation is then  $1 - W_{qe}$ .  $\sigma_{qe}$  depends on the energies and flavors of the colliding hadron (see Eq.(24.1)).

If a quark exchange is sampled, the quark contents of the projectile and target are determined. After that the possibility of a quark exchange is checked. A meson consists of a quark and an antiquark. Thus there is no alternative but to choose a quark. Let it be  $q_M$ . A baryon has three quarks,  $q_1, q_2$  and  $q_3$ . The quark from the meson can be exchanged, in principle, with any of the baryon quarks, but the above description of the experimental data indicates that an exchange of quarks with the same flavor must be suppressed. So, only the exchange of quarks with different flavors is allowed. After the exchange ( $q_M \leftrightarrow q_i$ ), the new contents of the meson and the baryon are determined. The new meson may be either pseudo-scalar or pseudo-vector with a 50% probability. The new baryon may be in its ground state, or in an

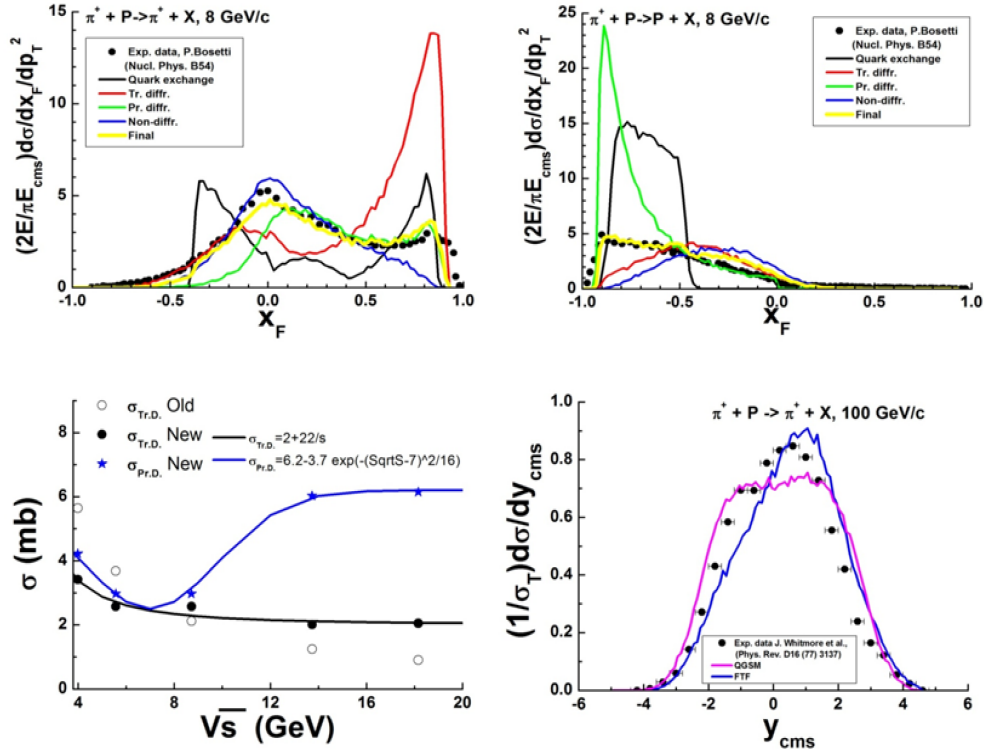


Fig. 24.12: Upper figures: inclusive spectra of protons and  $\pi^+$ -mesons in  $\pi^+ p$ -interactions. Points are experimental data [eal73b]. Lines represent the contributions of the various FTF processes calculated by assuming that the probability of each process is 100 %. Bottom left figure: diffraction dissociation cross sections obtained by tuning (points), and their description (lines) by the expression for  $\pi$  in (24.4). Bottom right figure: rapidity spectrum of  $\pi^+$ -mesons in  $\pi^+ p$ -interactions at  $p_{\text{lab}} = 100 \text{ GeV}/c$ . Points are experimental data [Whi74].

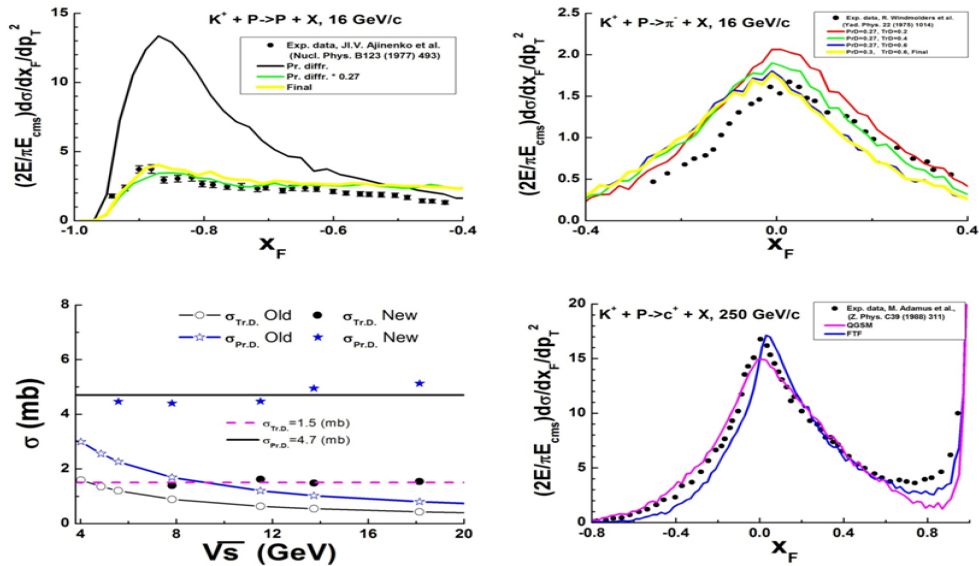


Fig. 24.13: Upper figures: inclusive spectra of protons and  $\pi^-$ -mesons in  $Kp^*$ -interactions. Points are experimental data\* :cite:had-Ajinenko,had-Ajinenko2. Lines are FTF calculations. Bottom left figure: diffraction dissociation cross sections obtained by tuning (points), and their description (lines) by the expression for  $Kp$  in (24.4). Bottom right figure:  $x_F$  spectrum of positive charged particles in  $Kp$ -interactions at  $p_{\text{lab}} = 250 \text{ GeV}/c$ . Points are experimental data [Whi74], lines are model calculations.

excited state. The probability of an excited baryon state is assumed (as common also in other codes) to be 0.5 for both  $\pi N$ -interactions and  $KN$ -interactions. Only  $\Delta(1232)$ 's are considered as excited states. If all quarks of a baryon have the same flavor, the  $\Delta(1232)$  is always created ( $\Delta(1232)^{++}$  or  $\Delta(1232)^{--}$ ).

The same procedure is followed for a projectile baryon, but in this case any quark of the projectile or target may participate in an exchange if they have different flavors. Only the ground state of the new baryon is considered.

In order to generate a transverse momentum between the two final-state hadrons, these final-state hadrons undergo to either an additional elastic scattering with probability  $W_{el} = 2.256 e^{-0.6 y_{lab}}$  (the parameters have been fitted from experimental data), or a diffractive/non-diffractive excitation with probability  $1 - W_{el}$ , where  $y_{lab}$  is the rapidity of the projectile in the target rest frame.

The above procedure is sufficient for a description of hadron-nucleon reaction cross sections at  $p_{lab} < 3 - 5 \text{ GeV}/c$ . At higher energies, diffractive dissociations and non-diffractive excitations must be simulated.

As mentioned above, there can be a projectile diffraction, or a target diffraction, or a non-diffractive interaction. Probabilities of the corresponding processes at high energies are:  $\sigma^{pd}/\sigma^{in}$ ,  $\sigma^{td}/\sigma^{in}$ , and  $(\sigma^{in} - \sigma^{pd} - \sigma^{td})/\sigma^{in}$ . The processes are sampled randomly.

Having sampled a projectile diffraction or a target diffraction, the corresponding light-cone momentum ( $P^-$  or  $P^+$ ) is chosen according to the distribution:  $dP^-/P^-$  or  $dP^+/P^+$ . Boundaries for a sampling have to be determined before.

Let us consider the kinematics of projectile diffraction,  $P + T \rightarrow P' + T$ , for the definition of these boundaries. It is obvious that a mass of the diffractive produced system,  $m_{P'}$ , must satisfy the conditions:

$$m_D \leq m_{P'} \leq \sqrt{s} - m_T$$

where  $m_D$  is the minimal mass of the system,  $s$  is the center-of-mass energy squared,  $m_T$  is the mass of the target. If there is not a transverse momentum transfer, and  $m_{P'}$  reaches the lower boundary then

$$P_{min}^- = \sqrt{m_D^2 + p_z^2} - p_z, \quad p_z = \lambda^{1/2}(s, m_D^2, m_T^2)/2\sqrt{s}$$

(See (24.3) for the definition of  $\lambda()$ .)

When  $m_{P'}$  reaches the upper boundary, the longitudinal momenta of the particles are zeros. Thus,

$$P_{max}^- = \sqrt{s} - m_T$$

Having sampled  $P^-$ , then  $m_{P'}$  and  $P^+$  can be found with the help of the energy-momentum conservation law written in the center-of-mass system:

$$\begin{cases} E_{P'} + E_T = \sqrt{s} \\ P_{z,P'} + P_{z,T} = 0 \end{cases} \quad \begin{cases} P_{P'}^- + P_T^- = \sqrt{s} \\ P_{P'}^+ + P_T^+ = \sqrt{s} \end{cases} \quad \begin{cases} P_T^- = \sqrt{s} - P_{P'}^- \\ P_T^+ = m_T^2/P_T^- \\ m_{P'}^2 = P_{P'}^- \cdot (\sqrt{s} - P_T^+) \end{cases}$$

The transferred transverse momentum is sampled according to the distribution:

$$dW = \frac{1}{\pi \langle P_\perp^2 \rangle} e^{-P_\perp^2/\langle P_\perp^2 \rangle} d^2 P_\perp, \quad \langle P_\perp^2 \rangle = 0.3 \text{ (GeV}/c\text{)}^2$$

To account for it, it is enough to replace the masses with the transverse masses,  $m_\perp = \sqrt{m^2 + P_\perp^2}$ .

The light-cone momenta transferred to the projectile are:

$$Q^+ = P_{T,0}^+ - P_T^+, \quad Q^- = P_{T,0}^- - P_T^-$$

where  $P_{T,0}^+$  and  $P_{T,0}^-$  are the light-cone momenta of the target in the initial state.

In the case of non-diffractive excitation ( $P + T \rightarrow P' + T'$ ),  $P_{P'}^-$  is sampled first of all as it was described above at  $m_T = m_{T,nd}$ , where  $m_{T,nd}$  is the minimal mass of a target-originated particle produced in the non-diffractive

excitation. After that,  $P_{T'}^+$  is independently sampled at  $m_P = m_{P,nd}$ . The minimal light-cone momenta,  $P_P^-$  and  $P_T^+$ , are calculated at  $m_P = m_{P,nd}$  and  $m_T = m_{T,nd}$ . At the last step it is checked that  $m_{P'} \geq m_{P,nd}$  and  $m_{T'} \geq m_{T,nd}$ . In the current version of the FTF model the same values for minimal masses are used in the diffractive and non-diffractive excitation.

Table 24.6: Minimal masses of diffractive produced strings

	$p/n$	$\pi$	$K$
$m_D$ (MeV)	1160	500	600

### Simulation of antibaryon–nucleon interactions

At the beginning of the simulation of an annihilation interaction, the cross sections of the processes (see Fig. 24.10) are calculated (see (24.2)). After that a sampling of the processes takes place.

In the cases of the processes Fig. 24.10b and Fig. 24.10e quarks for the annihilation are chosen randomly. In each of the processes only one string is created. Its mass is equal to the center-of-mass energy of the interaction. After that the string is fragmented. It is required that in the fragmentation of the process Fig. 24.10b there must not be a baryon and an antibaryon in the final state.

At sufficiently high energies the standard FTF processes can be simulated as it was described above.

In the process Fig. 24.10c only 2 strings will be created. If their masses are given, the kinematical properties of the strings can be determined with the help of the energy-momentum conservation law. The masses must be related to the momenta of the quarks and antiquarks.

We assume that in the process all quarks and antiquarks are in the same conditions, thus, their transverse momenta are sampled independently according to the gaussian distribution with  $\langle P_\perp^2 \rangle = 0.04$  (GeV/c)<sup>2</sup>. To guarantee that the sum of the transverse momenta is zero, the transverse momentum of each particle is re-defined as follows:  $\vec{P}_{\perp i} \rightarrow \vec{P}_{\perp i} - \frac{1}{4} \sum_{j=1}^4 \vec{P}_{\perp j}$ .

To find the longitudinal momenta of quarks we use the light-cone momenta: total light-cone momenta of projectile-originated antiquarks and target-originated quarks,

$$P^+ = P_{\bar{q}_1}^+ + P_{\bar{q}_2}^+, \quad P^- = P_{q_1}^- + P_{q_2}^-$$

Let us introduce also the light-cone momentum fractions:

$$\begin{aligned} x_{\bar{q}_1}^+ &= P_{\bar{q}_1}^+/P^+, & x_{\bar{q}_2}^+ &= 1 - x_{\bar{q}_1}^+ \\ x_{\bar{q}_1}^- &= P_{\bar{q}_1}^-/P^-, & x_{\bar{q}_2}^- &= 1 - x_{\bar{q}_1}^- \end{aligned}$$

Using these variables, the energy-momentum conservation law in the center-of-mass system can be written as:

$$\begin{aligned} \frac{P^+}{2} + \frac{\alpha}{2 P^+} + \frac{P^-}{2} + \frac{\beta}{2 P^-} &= \sqrt{s} \\ \frac{P^+}{2} - \frac{\alpha}{2 P^+} - \frac{P^-}{2} + \frac{\beta}{2 P^-} &= 0 \\ \alpha &= \frac{m_{\perp \bar{q}_1}^2}{x_{\bar{q}_1}^+} + \frac{m_{\perp \bar{q}_2}^2}{1 - x_{\bar{q}_1}^+} \\ \beta &= \frac{m_{\perp q_1}^2}{x_{q_1}^-} + \frac{m_{\perp q_2}^2}{1 - x_{q_1}^-} \end{aligned}$$

A solution of the equations at  $\sqrt{\alpha} + \sqrt{\beta} \leq \sqrt{s}$  is:

$$\begin{aligned} P^+ &= \frac{s + \alpha - \beta + \lambda^{1/2}(s, \alpha, \beta)}{2 \sqrt{s}} \\ P^- &= \frac{s - \alpha + \beta + \lambda^{1/2}(s, \alpha, \beta)}{2 \sqrt{s}} \end{aligned}$$

(See (24.3) for the definition of  $\lambda()$ .)

If  $\sqrt{\alpha} + \sqrt{\beta} > \sqrt{s}$ , the transverse momenta and  $x$ s are re-sampled until the inequality is broken.

Because quarks are in the same conditions, the distribution on  $x$  can have the form  $x^a (1 - x)^a$ . A recommended value of  $a$  can be zero or  $-0.5$ . We chose  $a = -0.5$ . We assumed also that the quark masses are zero. Probably, other values could be used, but we have not yet found experimental data sensitive to these parameters.

For the simulation of the process Fig. 24.10a we follow the same approach, and introduce light-cone momentum fractions –  $x_{\bar{q}1}^+$ ,  $x_{\bar{q}2}^+$ ,  $x_{\bar{q}3}^+$  and  $x_{q1}^-$ ,  $x_{q2}^-$ ,  $x_{q3}^-$ . The distribution on  $x$ s is chosen according to the form:

$$dW \propto x_{q1}^a x_{q2}^a x_{q3}^a \delta(1 - x_{q1} - x_{q2} - x_{q3}) dx_{q1} dx_{q2} dx_{q3}, \quad a = -0.5$$

It is obvious that in this case:

$$\alpha = \sum_{i=1}^3 \frac{m_{\perp \bar{q}_i}^2}{x_{\bar{q}_i}^+}, \quad \beta = \sum_{i=1}^3 \frac{m_{\perp q_i}^2}{x_{q_i}^-}$$

### 24.1.5 Flowchart of the FTF model

The simulation of hadron-nucleus or nucleus-nucleus interaction events starts with an initialization (done “on-the-fly” just before simulating the interaction, not at the beginning of the program) of the model variables: calculations of cross sections, setting up slopes, masses and so on. The next step is the determination of intra-nuclear collision multiplicity with the help of Glauber model. If the energy of collisions is sufficiently high, the simulation of secondary particle cascading within the reggeon theory inspired model (RTIM [AWU97, AWU98]) is carried out. After that all involved nuclear nucleons are put on the mass-shell. If the energy is not high enough these steps are skipped. The reason for this will be explained later.

The main job of the FTF algorithm is done in the loop over intra-nuclear collisions. At that moment, the time ordering of the collisions has been determined. For each collision, it is sampled what has to be simulated – elastic scattering, inelastic interaction or annihilation for projectile antibaryons. For each branch, an adjustment of the participating nuclear nucleon is performed at low energy, and the corresponding process is simulated. In the case of the sampling of the inelastic interaction at high energy there is an alternative – to reject the interaction or to process it.

At the end of the loop, the properties of nuclear residuals (mass number, charge, excitation energy and 4-momentum) are transferred to a calling program. The program initiates the fragmentation of created strings and decays the excited residuals.

Simulations of elastic scattering, inelastic interactions and annihilation were considered above. Other steps of the FTF model will be presented below.

### 24.1.6 Simulation of nuclear interactions

#### Sampling of intra-nuclear collisions

##### Classical cascade-type sampling

As it is known, the intra-nuclear cascade models like the ones implemented in GEANT4 – *The Bertini Intranuclear Cascade Model*, *The Binary Cascade Model*, *INCL++: the Liège Intranuclear Cascade Model* – work well for projectile energies below 5 – 10 GeV. The first step in these models is the sampling of the impact parameter,  $b$ . The next step is the sampling of a point where the projectile will interact with nuclear matter (see Fig. 24.15a).

The following consideration is used here: the probability that the projectile reaches a point  $z$  going from minus infinity to the point  $z$  is

$$P = e^{-\sigma^{tot} \int_{-\infty}^z \rho_A(\vec{b}, z') dz'}$$

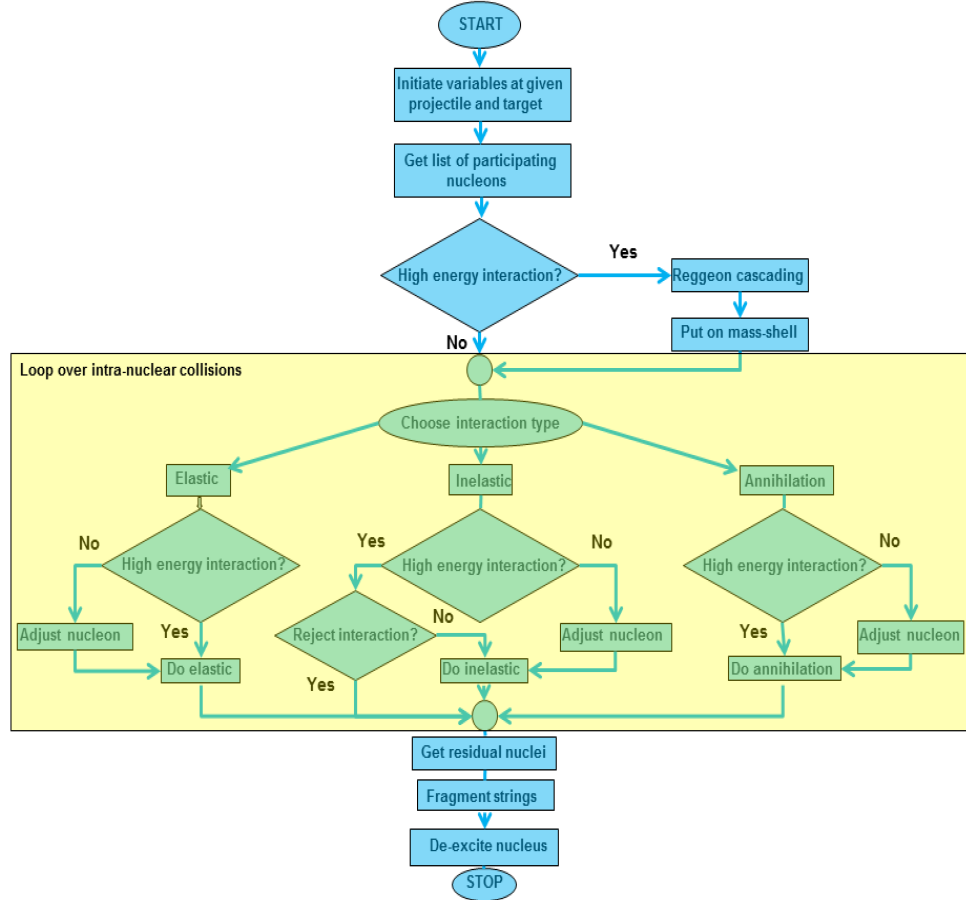


Fig. 24.14: Flowchart of the FTF model.

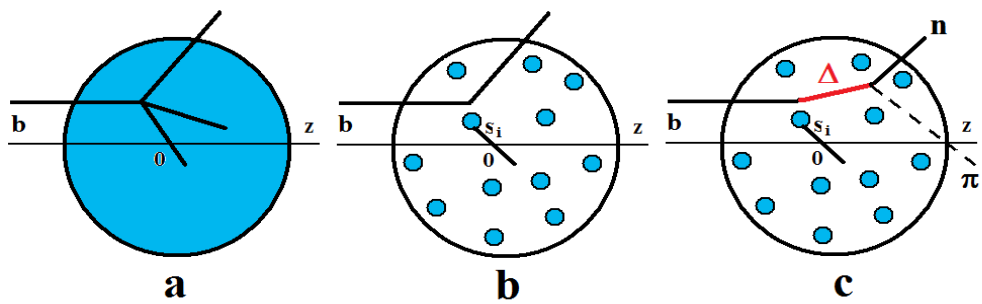


Fig. 24.15: Cascade-type sampling.

where  $\sigma^{tot}$  is the total cross section of the projectile-nucleon interaction,  $\rho_A$  is the density of the nucleus considered as a continuous medium.

The probability that the projectile will have an interaction in the range  $z - z + dz$  is equal to  $\sigma^{tot} \rho_A(\vec{b}, z) dz$ . Thus, the total probability is:

$$P(\vec{b}, z) = \sigma^{tot} \rho_A(\vec{b}, z) e^{-\sigma^{tot} \int_{-\infty}^z \rho_A(\vec{b}, z') dz'} dz$$

$$P(\vec{b}) = \int_{-\infty}^{+\infty} P(\vec{b}, z) dz = 1 - e^{-\sigma^{tot} \int_{-\infty}^{\infty} \rho_A(\vec{b}, z') dz'}$$

Having sampled the interaction point, the choice between an elastic scattering and an inelastic interaction is then implemented.

In the case of the inelastic interaction, a multi-particle production process is simulated. After this, for each produced particle new interaction points are sampled, and so on.

In the case of the elastic scattering, the scattering is simulated, and then new interaction points for the recoil nucleon and the projectile are sampled.

The prescription is changed a little bit by replacing the continuous medium with a collection of  $A$  nucleons located in the points  $\{\vec{s}_i, z_i\}$ ,  $i = 1-A$  where  $\{\vec{s}_i\}$  are coordinates of the nucleons in the impact parameter plane. The projectile can interact with the nearest nuclear nucleon, whose  $\vec{s}_i$  satisfies the condition:  $|\vec{b} - \vec{s}_i| \leq \sqrt{\sigma^{tot}/\pi}$  (see Fig. 24.15b).

In the first versions of the cascade models, only nucleons and pions were considered. When it was recognized that most of inelastic reactions at intermediate energies are going through resonance productions, various baryonic and mesonic resonances were included, and the algorithm changed (see Fig. 24.15c). As energy grows, more and more heavy resonances are produced. Because the properties of resonance-nucleon collisions were not known, the interpretation of the Glauber approximation was very useful.

### Short review of Glauber approximation

The Glauber approach [Gla59, Gla67] was proposed in the framework of the potential theory, before the creation of the intra-nuclear cascade models. Its main assumption is that at sufficiently high energies many partial waves contribute to a particle elastic scattering amplitude,  $f(\vec{q})$ . Thus, a summation on angular momenta can be replaced by an integral:

$$f(\vec{q}) = \frac{iP}{2\pi} \int e^{i\vec{q}\vec{b}} \left[ 1 - e^{i\chi(\vec{b})} \right] d^2b, \quad \frac{d\sigma}{d\Omega} = |f(\vec{q})|^2$$

$$\gamma(\vec{b}) = \frac{1}{2\pi i P} \int e^{-i\vec{q}\vec{b}} f(\vec{q}) d^2q$$

where  $P$  is the projectile momentum,  $q$  is the transferred transverse momentum,  $\vec{b}$  is the impact parameter,  $\chi$  is the phase shift, and  $\gamma$  is the scattering amplitude in the impact parameter representation.

Due to the additivity of potentials, it was natural to assume that the overall phase shift for the projectile scattered on  $A$  centers located in the points  $\{\vec{s}_i, z_i\}$ ,  $i = 1-A$  is the sum of the corresponding shifts on each center:

$$\chi_{hA} = \sum_{i=1}^A \chi(\vec{b} - \vec{s}_i)$$

$$\gamma_{hA}(\vec{b}) = 1 - \prod_{i=1}^A \left[ 1 - \gamma(\vec{b} - \vec{s}_i) \right] \tag{24.5}$$

Because the positions of nucleons in nuclei are not fixed, the Eq. (24.5) has to be averaged, and the hadron-nucleus scattering amplitude takes the form:

$$F_{0 \rightarrow f}^{hA} = \frac{iP}{2\pi} \int d^2b e^{-i\vec{q}\vec{b}} \left\{ 1 - \prod_{i=1}^A \left[ 1 - \gamma(\vec{b} - \vec{s}_i) \right] \right\} \Psi_0(\{r_A\}) \Psi_f^*(\{r_A\}) \prod_{i=1}^A d^3r_i$$

where  $\Psi_0$  and  $\Psi_f$  are wave functions of the nucleus in initial and final states, respectively.

In the case of elastic scattering,  $\Psi_0 = \Psi_f$ , we have:

$$\begin{aligned}
 F_{el}^{hA} &= \frac{iP}{2\pi} \int d^2b e^{-i\vec{q}\vec{b}} \left\{ 1 - \prod_{i=1}^A \left[ 1 - \int \gamma(\vec{b} - \vec{s}_i) \rho_A(\vec{s}_i, z') d^2 s_i dz' \right] \right\} \\
 &\simeq \frac{iP}{2\pi} \int d^2b e^{-i\vec{q}\vec{b}} \left\{ 1 - \left[ 1 - \frac{1}{A} \int \gamma(\vec{b} - \vec{s}) T_A(\vec{s}) d^2 s \right]^A \right\} \\
 &\simeq \frac{iP}{2\pi} \int d^2b e^{-i\vec{q}\vec{b}} \left\{ 1 - e^{-\int \gamma(\vec{b} - \vec{s}) T_A(\vec{s}) d^2 s} \right\} \\
 &\simeq \frac{iP}{2\pi} \int d^2b e^{-i\vec{q}\vec{b}} \left\{ 1 - e^{-\sigma_{hN}^{tot}(1-i\alpha)T_A(\vec{b})/2} \right\}
 \end{aligned} \tag{24.6}$$

Some assumptions and simplifications have been used in the above derivations. First of all, it was assumed that  $|\Psi_0|^2 \simeq \prod_{i=1}^A \rho(\vec{s}_i, z_i)$  where  $\rho$  is the one-particle nuclear density. Because the nucleon coordinates must obey the obvious condition:  $\sum_{i=1}^A \vec{r}_i = 0$ , it would be better to use  $|\Psi_0|^2 \simeq \delta(\sum_{i=1}^A \vec{r}_i) \prod_{i=1}^A \rho(\vec{s}_i, z_i)$ . Considering this  $\delta$ -function corresponds to take into account the center-of-mass correlation. The second assumption is that  $A$  is sufficiently large, thus  $(1 - \frac{x}{A})_{A \rightarrow \infty}^A = e^{-x}$  (optical limit). A thickness function of the nucleus was introduced:

$$T(\vec{b}) = A \int_{-\infty}^{+\infty} \rho(\vec{b}, z) dz$$

It was assumed also that the range of the  $\gamma$ -function is much less than the range of the nuclear density:  $\int \gamma(\vec{b} - \vec{s}) T_A(\vec{s}) d^2 s \simeq \sigma_{hN}^{tot}(1-i\alpha)T_A(\vec{b})/2$ , where  $\sigma_{hN}^{tot}$  is the hadron-nucleon total cross section, and  $\alpha = \text{Re } f(0)/\text{Im } f(0)$  is the ratio of real and imaginary parts of hadron-nucleon elastic scattering amplitude at zero momentum transfer.

There were many applications of the Glauber approach for calculations of elastic scattering cross sections, cross sections of nuclear excitations, coherent particle production and so on. We consider here only its application to inelastic reactions.

If the energy resolution of a scattered projectile is not too high, many nuclear excited states can contribute to the scattering amplitude:  $F^{hA} = \sum_f F_{0 \rightarrow f}^{hA}$ . To find the corresponding cross section, it is usually assumed that a set of final-state wave functions satisfy the completeness relation:  $\sum_f \Psi_f(\{\vec{r}_i\}) \Psi_f^*(\{\vec{r}'_j\}) = \prod_{i=1}^A \delta(\vec{r}_i - \vec{r}'_i)$ .

In the Glauber approach, it is possible to show that the cross section of elastic and quasi-elastic scatterings has the following expression:

$$\sigma_{el.+qel.}^{hA} = \int d^2b \left\{ 1 - 2\text{Re } e^{-\sigma_{hN}^{tot}(1-i\alpha)T_A(\vec{b})/2} + e^{-\sigma_{hN}^{in} T_A(\vec{b})} \right\}$$

Subtracting from it the cross section of the elastic scattering, we have:

$$\begin{aligned}
 \sigma_{qel.}^{hA} &= \int d^2b \left\{ e^{-\sigma_{hN}^{in} T_A(\vec{b})} - e^{-\sigma_{hN}^{tot} T_A(\vec{b})} \right\} \\
 &= \int d^2b e^{-\sigma_{hN}^{tot} T_A(\vec{b})} \left\{ e^{\sigma_{hN}^{el} T_A(\vec{b})} - 1 \right\} \\
 &= \int d^2b e^{-\sigma_{hN}^{tot} T_A(\vec{b})} \sum_{n=1}^{\infty} \frac{[\sigma_{hN}^{el} T_A(\vec{b})]^n}{n!}
 \end{aligned}$$

The last expression shows that the quasi-elastic cross section is a sum of cross sections with various multiplicities of elastic scatterings. It coincides with the prescription of the cascade model if only elastic scatterings of the projectile are considered.

The cross section of multi-particle production processes in the Glauber approach has the form:

$$\begin{aligned}\sigma_{mpp}^{hA} &= \sigma_{tot}^{hA} - \sigma_{el.+qel.}^{hA} = \int d^2b \left\{ 1 - e^{-\sigma_{hN}^{in} T_A(\vec{b})} \right\} \\ &= \int d^2b e^{-\sigma_{hN}^{in} T_A(\vec{b})} \sum_{n=1}^{\infty} \frac{[\sigma_{hN}^{in} T_A(\vec{b})]^n}{n!}\end{aligned}\quad (24.7)$$

This expression coincides with the analogous cascade expression in the case of a projectile particle that can be distinguished from the produced particles. Of course, it cannot be so in the case of projectile pions.

In the FTF model of GEANT4 it is assumed that projectile- and target-originated strings are distinguished. Thus, the cascade-type algorithm of the sampling of the multiplicities and types of interactions in nuclei is used.

A generalization of the Glauber approach for the case of nucleus-nucleus interactions was proposed by V. Franco [Fra68]. In this approach, the cross section of multi-particle production processes is given by the expression:

$$\sigma_{mpp}^{AB} = \int d^2b \left\{ 1 - \prod_{i=1}^A \prod_{j=1}^B \left[ 1 - g(\vec{b} + \tau_j - \vec{s}_i) \right] \right\} \cdot |\Psi_0^A(\{r_A\})|^2 |\Psi_0^B(\{t_B\})|^2 \left[ \prod_{i=1}^A d^3r_i \right] \left[ \prod_{j=1}^B d^3t_i \right] \quad (24.8)$$

where  $g(\vec{b}) = \gamma(\vec{b}) + \gamma^*(\vec{b}) - |\gamma(\vec{b})|^2$ ,  $A$  and  $B$  are mass numbers of colliding nuclei,  $\{\vec{\tau}_j\}$  is a set of impact coordinates of projectile nucleons ( $\vec{t} = (\vec{\tau}, z)$ ).

Considering  $g(\vec{b})$  as a probability that two nucleons separated by the impact parameter  $\vec{b}$  will have an inelastic interaction, a simple interpretation of the Eq. (24.8) can be given. The expression in the curly brackets of Eq. (24.8) is the probability that there will be at least one or more inelastic nucleon-nucleon interactions.  $|\Psi_0^A(\{r_A\})|^2 |\Psi_0^B(\{t_B\})|^2 \left[ \prod_{i=1}^A d^3r_i \right] \left[ \prod_{j=1}^B d^3t_i \right]$  is the probability to find nucleons with coordinates  $\{r_A\}$  and  $\{t_B\}$ . This interpretation allows a simple implementation in a program code, as described in many papers [ABLaPS05, BRaPB09, MRSS07, SUZ89], sometimes with the simplifying assumption that  $g(\vec{b}) = \theta(|\vec{b}| - \sqrt{\sigma_{NN}^{in}}/\pi)$ . This is the so-called Glauber Monte Carlo approach.

Because there is no expression in the Glauber theory that combines elastic and inelastic nucleon-nucleon collisions in nucleus-nucleus interactions, the same cascade-type sampling is used in the FTF model also in the case of these interactions.

### Correction of the number of interactions

The Glauber cross section of multi-particle production processes in hadron-nucleus interactions (Eq. (24.7)) was obtained in the reggeon phenomenology approach [Sha81], applying the asymptotical Abramovski-Gribov-Kancheli cutting rules [AGK74] to the elastic scattering amplitude (Eq. (24.6)). Thus, the summation in Eq. (24.7) is going from one to infinity. But a large number of intra-nuclear collisions cannot be reached in interactions with extra-heavy nuclei (like neutron star), or at low energy. To restrict the number of collisions it is needed to introduce finite-energy corrections to the cutting rules. Because there is no well-defined prescriptions for accounting these corrections, let us take a phenomenological approach, starting with the cascade model.

As it was said above, a simple cascade model considers only pions and nucleons. Due to this it cannot work when resonance production is a dominating process in hadronic interactions. But if energy is sufficiently low the resonances can decay before a next possible collision, and the model can be valid. Let  $p$  be the momentum of a produced resonance ( $\Delta$ ). The average life-time of the resonance in its rest frame is  $1/\Gamma$ . In the laboratory frame the time is  $E_\Delta/\Gamma m_\Delta$ . During the time, the resonance will fly a distance  $\bar{l} = v E_\Delta/\Gamma m_\Delta = p/\Gamma m_\Delta$ . If the distance is less than the average distance between nucleons in nuclei ( $\bar{d} \sim 2$  fm), the model can be applied. From this condition, we have:

$$p \leq \bar{d} \Gamma m_\Delta \sim 1.5 \text{ (GeV/c)}$$

Direct  $\Delta$ -resonance production takes place in  $\pi N$  interactions at low energies. Thus the model cannot work quite well for momentum of pions above 2 GeV/c. In nucleon-nucleon interactions, due to the momentum transfer to a target nucleon, the boundary can be higher.

Returning back to the FTF model, let us assume that the projectile-originated strings have average life-time  $1/\Gamma$ , and an average mass  $m^*$ . The strings can interact on average with  $\bar{l}/\bar{d} = p/\Gamma m^*/\bar{d} = p/p_0$  nucleons. Here  $p_0$  is a new parameter. According to our estimations  $p_0$  has value of about 3–5 GeV/c. Thus, we can assume that at a given energy there is a maximum number of intra-nuclear collisions in the FTF model, given by:  $\nu_{max} = p/p_0$ .

Let us introduce this number in the Glauber expression for the cross section of multi-particle production processes.

$$\begin{aligned}\sigma_{mpp}^{hA} &= \int d^2b \left\{ 1 - \left( 1 - \frac{1}{A} \sigma_{hN}^{in} T_A(\vec{b}) \right)^A \right\} \\ &= \int d^2b \left\{ 1 - \left[ \left( 1 - \frac{1}{A} \sigma_{hN}^{in} T_A(\vec{b}) \right)^{A/\nu_{max}} \right]^{\nu_{max}} \right\} \\ &= \int d^2b \sum_{\nu=1}^{\nu_{max}} \frac{\nu_{max}!}{\nu!(\nu_{max}-\nu)!} \left[ 1 - \left( 1 - \frac{1}{A} \sigma_{hN}^{in} T_A(\vec{b}) \right)^{A/\nu_{max}} \right]^\nu \cdot \left[ \left( 1 - \frac{1}{A} \sigma_{hN}^{in} T_A(\vec{b}) \right)^{A/\nu_{max}} \right]^{\nu_{max}-\nu}\end{aligned}$$

As seen from the expression above, the number of the intra-nuclear collisions is restricted to  $\nu_{max}$ .

The formula looks rather complicated, but a Monte Carlo algorithm for the rejection of the interaction number is quite simple. For example, an algorithm implementing it could look like this: at the beginning, a projectile has the “power”,  $P_w$ , to interact inelastically with  $\nu_{max}$  nucleons ( $P_w = \nu_{max}$ ; you can think about it as a likelihood, or unnormalized probability), thus the probability of an interaction with the first nucleon,  $P_w/\nu_{max}$ , is equal to 1. The power decreases after the first interaction. Thus, the probability of an inelastic interaction with a second nucleon is equal to  $P_w/\nu_{max}$ , where  $P_w = \nu_{max} - 1$ . If the second interaction happens, the power is decreased once more; else it is left at the same level. This is applied for each possible interaction.

The same algorithm is applied in the case of nucleus-nucleus interactions, but the power  $P_w$  is ascribed to each of the projectile or target nucleons.

## Reggeon cascading

As known, the Glauber approximation used in the Fritiof model and in other string models does not provide enough amount of intra-nuclear collisions for a correct description of nuclear destruction. Additional cascading in nuclei is needed. The usage of a standard cascade for secondary particle interactions leads to a too large multiplicity of produced particles. Usually, it is assumed that the inclusion of secondary particle’s formation time can help to solve this problem. Hadrons are not point-like particles: they have finite space sizes. Thus, the production of a hadron cannot be considered as a process taking place in a point, but rather in a space region. To implement this idea in Monte Carlo generators, it is assumed that particles do not appear in the nominal space-time point of production, but after some time interval called the formation time, and at some distance called the formation length. Because these time and length depend on the reference frame, it is assumed that for them standard relativistic formulae can be applied:  $t_F = \tau_0 E/m$ ,  $l_F = \tau_0 p/m$ , where  $E$ ,  $p$  and  $m$  are, respectively, energy, momentum and mass of the particle in the final state;  $\tau_0$  is a parameter. The problem is now: how can one determine the “nominal” point of the production? There is no a well established and accepted solution to this problem. Moreover, reggeon theory experts criticized for long time the concept of the formation time and the “standard” model of particle cascading in nuclei – the approaches do not consider the space-time structure of strong interactions. It was also assumed that the cascading could be correctly treated in the reggeon theory by considering the of so-called enhanced diagrams.

## Reggeon phenomenology of nuclear interactions

According to the phenomenology, an elastic hadron-hadron scattering amplitude is the sum of contributions connected with various exchanges in the  $t$ -channel. Each contribution has the following form in the impact parameter representation:

$$A_{NN}^R(\vec{b}, \xi) = \eta_R g_R^2 e^{\Delta_R \xi} \frac{e^{-\frac{b^2}{4(R^2 + \alpha'_R \xi)}}}{(R_{NN}^2 + \alpha'_R \xi)}$$

Here  $|\vec{b}|$  is the impact parameter,  $\xi = \ln(s)$ ,  $s$  is the squared center-of-mass energy,  $\eta_R$  is the signature factor:  $\eta_R = 1 + i \cot(\pi(1 + \Delta_R)/2)$  for a pole with positive signature, and  $\eta_R = -1 + i \cot(\pi(1 + \Delta_R)/2)$  for a pole with negative signature.  $1 + \Delta_R$  is the intercept of the reggeon trajectory,  $\alpha'_R$  is its slope, and the vertex of reggeon-nucleon interaction is parameterized as  $g(t) = g_R \exp(R_{NN}^2 t/2)$ ,  $t$  is the transferred 4-momentum.

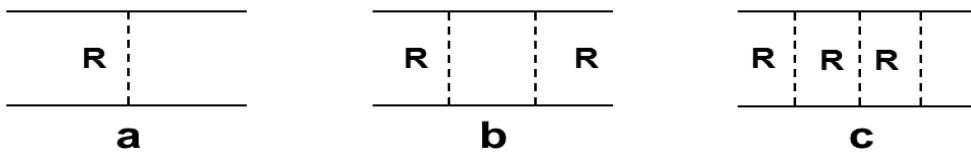


Fig. 24.16: Nonenhanced diagrams of  $NN$ -scattering.

Taking into account the contributions of other diagrams, shown in Fig. 24.16, one can find the  $NN$ -scattering amplitude:

$$\gamma_{NN}(\vec{b}, \xi) = 1 - e^{-A_{NN}^R(\vec{b}, \xi)}$$

The calculation of amplitudes and cross sections for cascade interactions requires to consider the so-called enhanced diagrams, like those shown in Fig. 24.17.

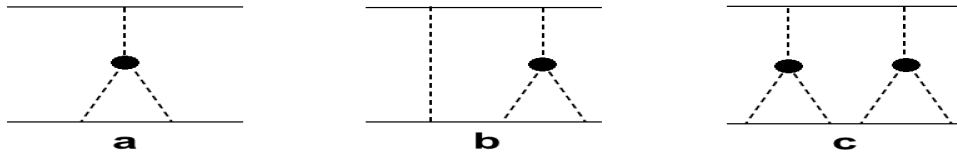


Fig. 24.17: Simplest enhanced diagrams of  $NN$ -scattering.

The contribution of the diagram in Fig. 24.17a to the elastic scattering amplitude is given by the expression:

$$GE_a(\vec{b}, \xi) = -G \int_{\epsilon}^{\xi-\epsilon} d\xi' \int d^2 b' A_{N\pi}^{R_1}(\vec{b} - \vec{b}', \xi - \xi') A_{\pi N}^{R_2}(\vec{b}', \xi') A_{\pi N}^{R_3}(\vec{b}', \xi')$$

where  $A_{\pi N}$  is the amplitude of meson-nucleon scattering due to one-reggeon exchange,  $G$  is the three reggeon's coupling constant,  $\epsilon$  is the cutoff parameter ( $\epsilon \sim 1$ ). Here we use the model of multi-reggeon vertices proposed in [KpTM86], where it was assumed that reggeons are coupled to one another via a created virtual meson (pion) pair.

The simplest enhanced diagrams for hadron-nucleus scattering were evaluated in [JDTreliani76, Sar80]. An effective computational procedure was proposed in papers [CSRJenco76, Sch75], but it was not applied to the analysis of experimental data. The structure of the enhanced diagrams and their analytical properties were studied in [BKKS91].

In the reggeon approach the interaction of secondary particles with a nucleus is described by cuttings of enhanced diagrams. Here the Abramovski-Gribov-Kancheli (AGK) cutting rules [AGK74] are frequently applied. The corrections to them were discussed in [BKKS91] for the problem of particle cascading into the nucleus. It was shown there that

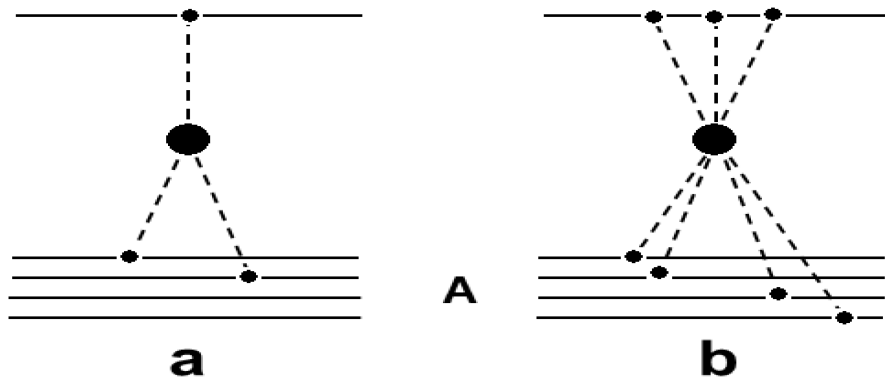


Fig. 24.18: Possible enhanced diagrams of  $hA$ -interactions.

inelastic rescatterings occur for any secondary particle, both slow and fast, and the contributions of enhanced diagrams lead to the enrichment of the spectrum by slow particles in the target fragmentation region.

As in [KpTM86] we shall assume that the reggeon interaction vertices are small. Therefore of the full set of enhanced diagrams the only important ones will be those containing vertices where one of the reggeons split into several, which then interact with different nucleons of the nucleus (Fig. 24.18a). In studying interactions with nuclei, however, it is convenient, in the spirit of the Glauber approach, to deal not with individual reggeons, but with sets of them interacting with a given nucleon of the nucleus (Fig. 24.18b). Unfortunately, the reggeon method of calculating the sum of the contributions of enhanced diagrams in the case of  $hA$ - and  $AA$ -interactions is not developed for practical tasks. Hence we propose a simple model of estimating reggeon cascading in  $hA$ - and  $AA$ -interactions.

Let us consider the contribution of the first diagram of Fig. 24.18a:

$$Y = G \int d\xi' d^2 b' F_{N\pi}(\vec{b} - \vec{b}', \xi - \xi') \times F_{\pi N}(\vec{b}' - \vec{s}_1, \xi') F_{\pi N}(\vec{b}' - \vec{s}_2, \xi')$$

where  $\vec{b}$  is the impact parameter of a projectile hadron,  $\vec{s}_1$  and  $\vec{s}_2$  are impact coordinates of two nuclear nucleons,  $\vec{b}'$  is the position of the reggeon interaction vertex in the impact parameter plane,  $\xi'$  is its rapidity.

Using a gaussian parameterization for  $F_{N\pi}$  ( $F_{\pi N} = \exp(-|\vec{b}|^2/R_{\pi N}^2)$ ) and neglecting its dependence on energy, we have

$$Y \simeq G(\xi_0 - 2\epsilon) \frac{R_{\pi N}^2}{3} \exp(-(\vec{b} - (\vec{s}_1 + \vec{s}_2)/2)^2/3R_{\pi N}^2) \times \exp(-(\vec{s}_1 - \vec{s}_2)^2/2R_{\pi N}^2)$$

where  $R_{\pi N}$  is the pion-nucleon interaction radius. According to this expression, the contribution reaches a maximum when the nucleon coordinates,  $\vec{s}_1$  and  $\vec{s}_2$ , coincide, and decreases very fast with increasing distance between the nucleons.

Cutting the diagram, one can obtain that the probability,  $\phi$ , to involve 2 neighboring nucleons is

$$\phi(|\vec{s}_1 - \vec{s}_2|) \sim \exp\left(-\frac{|\vec{s}_1 - \vec{s}_2|^2}{R_{\pi N}^2}\right)$$

Schematically, the hadron-nucleus interaction process in the impact parameter plane can be represented as in Fig. 24.19, where the position of the projectile hadron is marked by an open circle, the positions of nuclear nucleons by closed circles, reggeon exchanges by dashed lines and the small points are the coordinates of the reggeon interaction vertices.

Let us consider the problem by using the quark-gluon approach. There were some successful attempts to describe the hadron-nucleon elastic scattering at low and intermediate energies (below 1 – 2 GeV) within this approach (see [BESSwanson92, TBarnesESSwanson92, TBarnesESSwansonJWeinstein92, TBarnesSCapstickMDKovarikS93]). In particular, in the paper [BESSwanson92] the theoretical calculations of the amplitudes of  $\pi\pi$ -,  $KK$ - and  $NN$ -scatterings

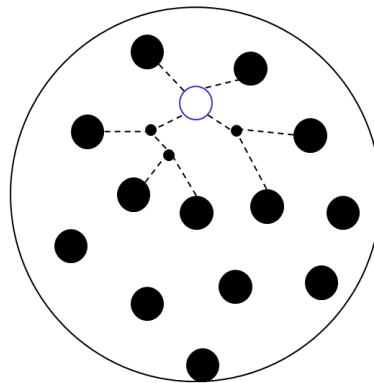


Fig. 24.19: Reggeon “cascade” in  $hA$ -scattering.

were found in agreement with experimental data, assuming that in the elastic hadron scattering one-gluon exchange with following quark interchange between hadrons takes place (see Fig. 24.20a). At high energies, two-gluon exchange approximation (Fig. 24.20b) works quite well (see [GDSoper77, LR81, Low75, Nus76]). What kind of exchanges can dominate in hadron-nucleus and nucleus-nucleus interactions?

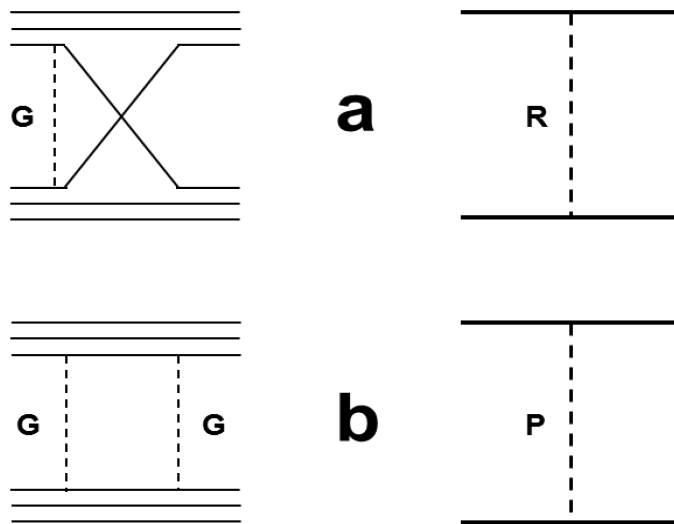


Fig. 24.20: Diagrams of quark-gluon exchanges and corresponding reggeon diagrams for hadron-nucleus interactions.

The simplest possible diagrams of processes with three nucleons are given in Fig. 24.21. A calculation of their amplitudes according to [BESSwanson92] is a serious mathematical problem. It can be simplified if one takes into account an analogy between quark-gluon diagrams and reggeon diagrams: the quark diagram of Fig. 24.20a corresponds to a one-nonvacuum reggeon exchange; the diagram of Fig. 24.20b describes the pomeron exchange in the  $t$ -channel; the diagram of Fig. 24.21a is in correspondence with the enhanced reggeon diagram of the pomeron splitting into two non-vacuum reggeons. The three pomeron diagram (Fig. 24.21d) represents a more complicated process. It is rather difficult to find a correspondence between reggeon diagrams and the diagrams of Fig. 24.21b, Fig. 24.21c.

It seems obvious that the processes like one in Fig. 24.21d cannot dominate in the elastic hadron-nucleus scattering because they are accompanied by a production of high-mass diffractive particles in the intermediate state. Thus, their contributions are damped by a nuclear form-factor. For the same reason, the contributions of processes like the ones in Fig. 24.21a, Fig. 24.21b can be small too. If this is not the case, then one can expect large corrections to Glauber cross sections. The practice shows that the corrections to hadron-nucleus cross sections must be lower than 5–7%.

The diagram Fig. 24.21c can give a correction to the Glauber one-scattering amplitude. Analogous corrections exist for

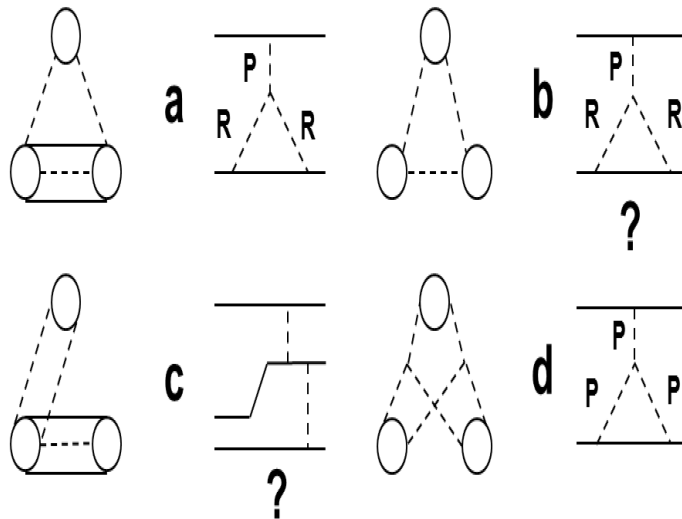


Fig. 24.21: Diagrams of quark-gluon exchanges and corresponding reggeon diagrams for hadron-nucleus interactions.

the other terms of Glauber series. They can re-normalize the nuclear vertex constants. According to [BESSwanson92] the contribution has the form:

$$Y_c \propto \exp [-(\vec{b} - \vec{s}_1)/R_p^2] \exp [-(\vec{s}_1 - \vec{s}_2)/R_c^2]$$

where  $R_p$  is the radius of high-energy nucleon-nucleon interactions, and  $R_c$  is another low-energy radius. Let us note that  $Y_c$  does not depend, as other reggeon diagram contributions, on the longitudinal coordinates of nucleons and the multiplicity of produced particles. This is the main difference between “reggeon cascading” and usual cascading.

As well known, the intra-nuclear cascade models assume that in a hadron-nucleus collision secondary particles are produced in the first inelastic interaction of the projectile with a nuclear nucleon. The produced particles can interact with other target nucleons. The distribution of the distance  $l$  between the first interaction and the second one has the form:

$$W(l)dl \propto \frac{n}{\langle l \rangle} \exp \left( -\frac{n}{\langle l \rangle} l \right)$$

where  $\langle l \rangle = 1/\sigma\rho_A$ ,  $\sigma$  is the hadron-nucleon cross section,  $n$  is the multiplicity of the produced particles, and  $\rho_A \sim 0.15 \text{ (fm)}^{-3}$  is the nuclear density. At the same time, the amplitudes or cross sections of processes like Fig. 24.21 have no dependence on  $l$  or  $n$ . Thus, one can expect that the “cascade” in the quark-gluon approach will be more restricted than in the cascade models. The difference between these approaches can lead to different predictions for hadron interactions with heavy nuclei due to the large multiplicity of the produced particles.

Because it is complicated to calculate the contributions of various diagrams, and to take into account all possibilities, let us formulate a simpler phenomenological model that keeps the main features of the above approaches.

### The model formulation

- As it was said above, the “reggeon” cascade is developed in the impact parameter plane, and has features typical for branching processes. Thus, for its description it is needed to determine the probability to involve a nuclear nucleon into the “cascade”. It is obvious that the probability depends on the difference of the impact coordinates of the new and previous involved nucleons. Looking at the contribution of the diagram Fig. 24.21c, the functional form of the probability is chosen as:

$$P(|\vec{s}_i - \vec{s}_j|) = C_{nd} \exp [-(\vec{s}_i - \vec{s}_j)^2/R_c^2] \quad (24.9)$$

where  $\vec{s}_i$  and  $\vec{s}_j$  are the projections of the radii of the  $i^{th}$  and  $j^{th}$  nucleons on the impact parameter plane.

2. The “cascade” is initiated by the primary involved nucleons. These nucleons are determined with the help of the Glauber approach.
3. All involved nucleons are ejected from the nucleus.

The “cascade” looks like that: a projectile particle interacts with some intra-nuclear nucleons. These nucleons are called “wounded” or “participating” nucleons. These nucleons initiate the “cascade”. A wounded nucleon can involve a “spectator” nucleon into the “cascade” with the probability (24.9). A spectator nucleon can involve another nucleon, which in turn can involve a third one and so on. This algorithm is implemented in the FTF model.

We have tuned  $C_{nd}$  using the HARP-CDP data on proton production in the  $p + Cu$  interactions [eal09]. According to our estimations,

$$C_{nd} = e^{4(y-2.1)} / [1 + e^{4(y-2.1)}], \quad R_c^2 = 1.5 \text{ (fm)}^2$$

where  $y$  is the projectile rapidity. The value of the exponent, 2.1, corresponds to  $P_{lab} \sim 4 \text{ GeV/c}$ .

### “Fermi motion” of nuclear nucleons

In the “standard” approach, a nucleus is considered as a potential well where nucleons are freely moving. A particle falling on the nucleus changes its momentum on the border of the well. Here a question appears: to whom the recoil momentum must be ascribed? If the particle is absorbed by the nucleus, probably, one has to imagine in the final state the potential well with its nucleons moving with a momentum of the particle. If some nucleons are ejected from the nucleus, what conditions have to satisfy the nucleon momenta, and how will the “residual” well be moving to satisfy the energy-momentum conservation law? In the case of a 3-dimensional potential well, how will be changed the momentum components of a particle on the well surface? Will only the component transverse to the surface, or the one parallel to the surface, or both be changed? The list of questions can be extended by considering nucleus-nucleus interactions.

Two approaches are frequently used in practice.

According to the first one, the nucleus is considered as a continuous medium, and nucleons appeared only in points of the projectile interactions with the medium. It seems natural in this approach to sum the momenta of all ejected particles. Then, subtracting it from the initial momentum, one can find the momentum of the residual nucleus. It is unclear, however, what has to be done in the case of nucleus-nucleus interactions.

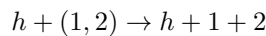
In the second approach, space coordinates and momenta of the nucleons are sampled according to some assumptions. In order to satisfy the energy-momentum conservation law, the projectile momentum does not change, and to each nucleon is ascribed a new mass:

$$m = \sqrt{(m_0 - \epsilon_b)^2 - p^2}$$

where  $m_0$  is the nucleon mass in the free state,  $\epsilon_b$  is the nuclear binding energy per nucleon, and  $p$  is the momentum of the nucleon. In this approach, the nucleus is a collection of off-mass-shell particles. Apparently, in the case of nucleus-nucleus interactions one has to consider two of such collections. The energy-momentum conservation law is satisfied in this approach if it is satisfied in each collision of out-of-mass-shell nucleons. However, there is a problem with the excitation energy of the nuclear residual: in most of the cases, it is too small.

All these questions are absent in the approach proposed in the paper [eal97].

Let us consider it starting from a simple example of a hadron interaction with a bound system of two nucleons, (1, 2). In this approach it is assumed that the process has two stages. At the first one, the system is dissociated:



At the second stage a “hard” collision of the projectile with the first or second nucleon takes place. Neglecting transverse momenta let us write the energy-momentum conservation law in the form:

$$\begin{cases} p_h = p'_h + p_1 + p_2 \\ E_h + E_{(1,2)} = E'_h + E_1 + E_2 \end{cases}$$

In the above expressions, there are three variables and two equations. Thus, only one variable can be chosen as independent. It can be  $p'_h$  – hadron momentum in the final state, or  $p_1$  or  $p_2$  – nucleon momentum in the final state. We choose as the variable the light-cone momentum fraction of one of the final-state nucleons:

$$x_1 = (E_1 - p_1) / (E_1 + E_2 - p_1 - p_2)$$

This variable is invariant under the Lorentz transformation along the collision axis.

Using this variable and the energy-momentum conservation law, one can find:

$$W^- = E_1 + E_2 - p_1 - p_2 = [s - m_h^2 + \beta^2 - \lambda^{1/2}(s, m_h^2, \beta^2)]/2 W_0^+$$

where:

$$\begin{aligned} W_0^+ &= E_h + E_{(1,2)} + p_h, \quad W_0^- = E_h + E_{(1,2)} - p_h \\ s &= W_0^+ W_0^-, \quad \beta^2 = \frac{m_1^2}{x_1} + \frac{m_2^2}{1-x_1} \end{aligned}$$

(See (24.3) for the definition of  $\lambda()$ .)

The other kinematical variables are:

$$\begin{aligned} p_1 &= \frac{m_1^2}{2x_1 W^-} - \frac{x_1 W^-}{2}, \quad E_1 = \frac{m_1^2}{2x_1 W^-} + \frac{x_1 W^-}{2} \\ p_2 &= \frac{m_2^2}{2(1-x_1) W^-} - \frac{(1-x_1) W^-}{2}, \quad E_2 = \frac{m_2^2}{2(1-x_1) W^-} + \frac{(1-x_1) W^-}{2} \\ p'_h &= p_h - p_1 - p_2, \quad E'_h = E_h + E_{(1,2)} - E_1 - E_2 \end{aligned}$$

So, for the simulation of the interactions, one has to determine only one function:  $f(x_1)$  – the distribution of  $x_1$ . Distributions for  $p_1$  and  $p_2$  have interesting properties: at  $p_h \rightarrow \infty$  they become stable (i.e. the distributions remain nearly unchanged when we vary  $p_h$ , for large values of  $p_h$ ), thus reproducing the typical “limiting fragmentation” (according to an old terminology) of bound system; at  $p_h \rightarrow 0$ ,  $E_h + E_{(1,2)} > m_h + m_1 + m_2$  the distributions  $p_1$  and  $p_2$  become narrower and narrower (i.e. similar to a  $\delta$ -Dirac distribution).

It is not complicated to introduce transverse momenta –  $p'_{\perp h}$ ,  $p_{\perp 1}$  and  $p_{\perp 2}$ , such that  $p'_{\perp h} + p_{\perp 1} + p_{\perp 2} = 0$ . It is sufficient to replace the masses with the transverse ones:  $m_i \rightarrow m_{\perp i} = \sqrt{m_i^2 + p_{\perp i}^2}$ .

In the case of interactions of two composed systems,  $A$  and  $B$ , consisting of  $A$  and  $B$  constituents respectively (for brevity, we denote with the same symbol both a composed system and the number of its constituents), let us describe the  $i^{th}$  constituent of  $A$  by the variables:

$$x_i^+ = (E_{Ai} + p_{iz})/W_A^+ \quad \text{and} \quad \vec{p}_{i\perp}$$

and the  $j^{th}$  constituent of  $B$  by the variables:

$$y_j^- = (E_{Bj} - q_{jz})/W_B^- \quad \text{and} \quad \vec{q}_{i\perp}$$

Here  $E_{Ai}$  ( $E_{Bi}$ ) and  $\vec{p}_i$  ( $\vec{q}_i$ ) are energy and momentum of the  $i^{th}$  constituent of the system  $A$  ( $B$ ).

$$W_A^+ = \sum_{i=1}^A (E_{Ai} + p_{iz}), \quad W_B^- = \sum_{i=1}^B (E_{Bi} - q_{jz})$$

Using these variables, the energy-momentum conservation law takes the form:

$$\begin{aligned} \frac{W_A^+}{2} + \frac{1}{2W_A^+} \sum_{i=1}^A \frac{m_{i\perp}^2}{x_i^+} + \frac{W_B^-}{2} + \frac{1}{2W_B^-} \sum_{i=1}^B \frac{\mu_{i\perp}^2}{y_i^-} &= E_A^0 + E_B^0 \\ \frac{W_A^+}{2} - \frac{1}{2W_A^+} \sum_{i=1}^A \frac{m_{i\perp}^2}{x_i^+} - \frac{W_B^-}{2} + \frac{1}{2W_B^-} \sum_{i=1}^B \frac{\mu_{i\perp}^2}{y_i^-} &= P_A^0 + P_B^0 \\ \sum_{i=1}^A \vec{p}_{i\perp} + \sum_{i=1}^B \vec{q}_{i\perp} &= 0 \end{aligned} \quad (24.10)$$

where  $m_{i\perp}^2 = m_i^2 + \vec{p}_{i\perp}^2$ ,  $\mu_{i\perp}^2 = \mu_i^2 + \vec{q}_{i\perp}^2$ , and  $m_i(\mu_i)$  is the mass of  $i^{th}$  constituent of the system  $A$  ( $B$ ).

The system of equations (24.10) allows one to find  $W_A^+$ ,  $W_B^-$  and all kinematical properties of the particles at given  $\{x_i^+, \vec{p}_{i\perp}\}, \{y_i^-, \vec{q}_{i\perp}\}$ .

$$\begin{aligned} W_A^+ &= (W_0^- W_0^+ + \alpha - \beta + \sqrt{\Delta})/2W_0^- \\ W_B^- &= (W_0^- W_0^+ - \alpha + \beta + \sqrt{\Delta})/2W_0^+ \\ W_0^+ &= (E_A^0 + E_B^0) + (P_{Az}^0 + P_{Bz}^0) \\ W_0^- &= (E_A^0 + E_B^0) - (P_{Az}^0 + P_{Bz}^0) \\ \alpha &= \sum_{i=1}^A \frac{m_{i\perp}^2}{x_i^+}, \quad \beta = \sum_{i=1}^B \frac{\mu_{i\perp}^2}{y_i^-} \\ \Delta &= (W_0^- W_0^+)^2 + \alpha^2 + \beta^2 - 2W_0^- W_0^+ \alpha - 2W_0^- W_0^+ \beta - 2\alpha\beta \\ p_{iz} &= (W_A^+ x_i^+ - \frac{m_{i\perp}^2}{x_i^+ W_A^+})/2; \quad q_{iz} = -(W_B^- y_i^- - \frac{\mu_{i\perp}^2}{y_i^- W_B^-})/2 \end{aligned}$$

Consequently, the problem of accounting for the binding energy and Fermi motion in the simulation of interacting composed systems comes to the definition of the distributions for  $x_i^+, y_i^-, \vec{p}_{i\perp}, \vec{q}_{i\perp}$ .

The transverse momentum of an ejected nucleon ( $\vec{p}_\perp$ ) is sampled according to the distribution:

$$\begin{aligned} dW &\propto \exp(-\vec{p}_\perp^2/\langle p_\perp^2 \rangle) d^2 p_\perp \\ \langle p_\perp^2 \rangle &= 0.035 + 0.04 \frac{e^{4(y_{lab}-2.5)}}{1 + e^{4(y_{lab}-2.5)}} \quad (\text{GeV}/c)^2 \end{aligned}$$

where  $y_{lab}$  is the projectile nucleus rapidity in the rest frame of the target nucleus. The sum of the transverse momenta with minus sign is ascribed to the residual of the target nucleus.

$x^+$  (and similarly for  $y^-$ ) is sampled according to the distribution:

$$dW \propto \exp[-(x^+ - 1/A)^2/(d/A)^2] dx^+, \quad d = 0.3$$

$x^+$  of the nuclear residual is determined as  $1 - \sum x_i^+$ .

### Excitation energy of nuclear residuals

According to the approach presented above, the excitation energy of a nuclear residual has to be determined before the simulation of particle production. It seems natural to assume that this excitation energy is connected with the multiplicity of ejected nuclear nucleons, both the participating ones and those involved in the reggeon cascading. Without the involved nucleons, the excitation energy would be proportional to the multiplicity of the participating nucleons as calculated in the Glauber approach. Such approach was followed in the paper [AMWA Friedman J Hufner 86], where

proton-nucleus interactions at intermediate energies were analyzed. There the multiplicity of the nucleons was calculated in the Glauber approach. It was also assumed that each recoil of the participating nucleons contributes to the excitation energy with a value sampled from the following distribution:

$$dW(E) = \frac{1}{\langle E \rangle} e^{-E/\langle E \rangle} dE$$

The sum of these contributions determines the residual excitation energy. The authors of the paper [AMWA Friedman-JHufner86] considered both absorptions and ejections of the nucleons, and took into account the effect of decreasing projectile energy during the interactions. They obtained a good agreement of their calculations with experimental data on neutron production as a function of the residual excitation energy.

Extending this approach, we assume, as a first step, that each participating or involved nucleon adds 100 MeV to the nuclear residual excitation energy. The excited residual is then fragmented by using the Generalized Evaporation Model (GEM) [Fur00].

---

CHAPTER  
TWENTYFIVE

---

## THE GEANT4 BERTINI INTRANUCLEAR CASCADE MODEL

### 25.1 Introduction

This cascade model is a re-engineered version of the INUCL code and includes the Bertini intra-nuclear cascade model with excitons, a pre-equilibrium model, a nucleus explosion model, a fission model, and an evaporation model. It treats nuclear reactions initiated by long-lived hadrons ( $p, n, \pi, K, \Lambda, \Sigma, \Xi, \Omega$ ) and  $\gamma$ s with energies between 0 and 10 GeV. Presented here is an overview of the models and a review of results achieved from simulations and comparisons with experimental data.

The intranuclear cascade model (INC) was first proposed by Serber in 1947 [Ser47]. He noticed that in particle-nuclear collisions the deBroglie wavelength of the incident particle is comparable (or shorter) than the average intra-nucleon distance. Hence, a description of interactions in terms of particle-particle collisions is justified.

The INC has been used successfully in Monte Carlo simulations at intermediate energies since Goldberger made the first hand-calculations in 1947 [Gol48]. The first computer simulations were done by Metropolis et al. in 1958 [MBS58]. Standard methods in INC implementations were developed when Bertini published his results in 1968 [GAB68]. An important addition to INC was the exciton model introduced by Griffin in 1966 [Gri66].

The current presentation describes the implementation of the Bertini INC model within the GEANT4 hadronic physics framework [eal03]. This framework is flexible and allows for the modular implementation of various kinds of hadronic interactions.

### 25.2 The GEANT4 Cascade Model

Inelastic particle-nucleus collisions are characterized by both fast and slow components. The fast ( $10^{-23} - 10^{-22}$  s) intra-nuclear cascade results in a highly excited nucleus which may decay by fission or pre-equilibrium emission. The slower ( $10^{-18} - 10^{-16}$  s) compound nucleus phase follows with evaporation. A Boltzmann equation must be solved to treat the collision process in detail.

The intranuclear cascade (INC) model developed by Bertini [BG71, GAB68] solves the Boltzmann equation on average. This model has been implemented in several codes such as HETC [AAH90]. Our model, which is based on a re-engineering of the INUCL code [eal99], includes the Bertini intranuclear cascade model with excitons, a pre-equilibrium model, a simple nucleus explosion model, a fission model, and an evaporation model.

The target nucleus is modeled by up to six concentric shells of constant density as an approximation to the continuously changing density distribution of nuclear matter within nuclei. The cascade begins when an incident particle strikes a nucleon in the target nucleus and produces secondaries. The secondaries may in turn interact with other nucleons or be absorbed. The cascade ends when all particles, which are kinematically able to do so, escape the nucleus. At that point energy conservation is checked. Relativistic kinematics is applied throughout the cascade.

## 25.2.1 Model Limits

The model is valid for incident  $p, n, \pi, K, \Lambda, \Sigma, \Xi, \Omega$  and  $\gamma$ s with energies between 0 and 10 GeV. All types of nuclear targets are allowed.

The necessary condition of validity of the INC model is  $\lambda_B/v \ll \tau_c \ll \Delta t$ , where  $\delta_B$  is the deBroglie wavelength of the nucleons,  $v$  is the average relative velocity between two nucleons and  $\Delta t$  is the time interval between collisions. At energies below 200 MeV, this condition is no longer strictly valid, and a pre-equilibrium model must be invoked. At energies greater than ~10 GeV the INC picture breaks down. This model has been tested against experimental data at incident kinetic energies between 100 MeV and 10 GeV.

## 25.2.2 Intranuclear Cascade Model

The basic steps of the INC model are summarized as follows:

1. the space point at which the incident particle enters the nucleus is selected uniformly over the projected area of the nucleus,
2. the total particle-particle cross sections and region-dependent nucleon densities are used to select a path length for the projectile,
3. the momentum of the struck nucleon, the type of reaction and the four-momenta of the reaction products are determined, and
4. the exciton model is updated as the cascade proceeds.
5. If the Pauli exclusion principle allows and  $E_{particle} > E_{cutoff} = 2$  MeV, step (2) is performed to transport the products.

After the intra-nuclear cascade, the residual excitation energy of the resulting nucleus is used as input for non-equilibrium model.

## 25.2.3 Nuclear Model

Some of the basic features of the nuclear model are:

- the nucleons are assumed to have a Fermi gas momentum distribution. The Fermi energy is calculated in a local density approximation i.e. the Fermi energy is made radius-dependent with Fermi momentum  $p_F(r) = (\frac{3\pi^2\rho(r)}{2})^{\frac{1}{3}}$ .
- Nucleon binding energies (BE) are calculated using the mass formula. A parameterization of the nuclear binding energy uses a combination of the Kummel mass formula and experimental data. Also, the asymptotic high temperature mass formula is used if it is impossible to use experimental data.

### Initialization

The initialization phase fixes the nuclear radius and momentum according to the Fermi gas model.

If the target is hydrogen ( $A = 1$ ) a direct particle-particle collision is performed, and no nuclear modeling is required.

If  $1 < A < 4$ , a nuclear model consisting of one layer with a radius of 8.0 fm is created.

For  $4 < A < 11$ , the nuclear model is composed of three concentric spheres  $i = \{1, 2, 3\}$  with radius

$$r_i(\alpha_i) = \sqrt{C_1^2 \left(1 - \frac{1}{A}\right) + 6.4\sqrt{-\log(\alpha_i)}}.$$

Here  $\alpha_i = \{0.01, 0.3, 0.7\}$  and  $C_1 = 3.3836A^{1/3}$ .

If  $A > 11$ , a nuclear model with three concentric spheres is also used. The sphere radius is now defined as

$$r_i(\alpha_i) = C_2 \log \left( \frac{1 + e^{-\frac{C_1}{C_2}}}{\alpha_i} - 1 \right) + C_1,$$

where  $C_2 = 1.7234$ .

The potential energy  $V$  for nucleon  $N$  is

$$V_N = \frac{p_F^2}{2m_N} + BE_N(A, Z),$$

where  $p_f$  is the Fermi momentum and  $BE$  is the binding energy.

The momentum distribution in each region follows the Fermi distribution with zero temperature.

$$f(p) = cp^2$$

where

$$\int_0^{p_F} f(p) dp = n_p \text{ or } n_n$$

where  $n_p$  and  $n_n$  are the number of protons or neutrons in the region.  $P_f$  is the momentum corresponding to the Fermi energy

$$E_f = \frac{p_F^2}{2m_N} = \frac{\hbar^2}{2m_N} \left( \frac{3\pi^2}{v} \right)^{2/3},$$

which depends on the density  $n/v$  of particles, and which is different for each particle and each region.

### Pauli Exclusion Principle

The Pauli exclusion principle forbids interactions where the products would be in occupied states. Following the assumption of a completely degenerate Fermi gas, the levels are filled from the lowest level. The minimum energy allowed for the products of a collision correspond to the lowest unfilled level of the system, which is the Fermi energy in the region. So in practice, the Pauli exclusion principle is taken into account by accepting only secondary nucleons which have  $E_N > E_f$ .

### Cross Sections and Kinematics

Path lengths of nucleons in the nucleus are sampled according to the local density and the free  $N - N$  cross sections. Angles after the collision are sampled from experimental differential cross sections. Tabulated total reaction cross sections are calculated by Letaw's formulation [eal83, eal93, Pea89]. For  $N - N$  cross sections the parameterizations are based on the experimental energy and isospin dependent data. The parameterization described in [BT72] is used.

For pions the intra-nuclear cross sections are provided to treat elastic collisions and the following inelastic channels:  $\pi^- p \rightarrow \pi^0 n$ ,  $\pi^0 p \rightarrow \pi^+ n$ ,  $\pi^0 n \rightarrow \pi^- p$ , and  $\pi^+ n \rightarrow \pi^0 p$ . Multiple particle production is also implemented.

The pion absorption channels are  $\pi^+ nn \rightarrow pn$ ,  $\pi^+ pn \rightarrow pp$ ,  $\pi^0 nn \rightarrow nn$ ,  $\pi^0 pn \rightarrow pn$ ,  $\pi^0 pp \rightarrow pp$ ,  $\pi^- pn \rightarrow nn$ , and  $\pi^- pp \rightarrow pn$ .

## 25.2.4 Pre-equilibrium Model

The GEANT4 cascade model implements the exciton model proposed by Griffin [Gri66, Gri67]. In this model, nucleon states are characterized by the number of excited particles and holes (the excitons). Intra-nuclear cascade collisions give rise to a sequence of states characterized by increasing exciton number, eventually leading to an equilibrated nucleus. For a practical implementation of the exciton model we use parameters from [eal73], (level densities) and [Kal78] (matrix elements).

In the exciton model the possible selection rules for particle-hole configurations in the source of the cascade are:  $\Delta p = 0, \pm 1$   $\Delta h = 0, \pm 1$   $\Delta n = 0, \pm 2$ , where  $p$  is the number of particles,  $h$  is number of holes and  $n = p + h$  is the number of excitons.

The cascade pre-equilibrium model uses target excitation data and the exciton configurations for neutrons and protons to produce non-equilibrium evaporation. The angular distribution is isotropic in the rest frame of the exciton system.

Parameterizations of the level density are tabulated as functions of  $A$  and  $Z$ , and with high temperature behavior (the nuclear binding energy using the smooth liquid high energy formula).

## 25.2.5 Break-up models

Fermi break-up is allowed only in some extreme cases, i.e. for light nuclei ( $A < 12$  and  $3(A - Z) < Z < 6$ ) and  $E_{excitation} > 3E_{binding}$ . A simple explosion model decays the nucleus into neutrons and protons and decreases exotic evaporation processes.

The fission model is phenomenological, using potential minimization. A binding energy parameterization is used and some features of the fission statistical model are incorporated [Fon69].

## 25.2.6 Evaporation Model

A statistical theory for particle emission of the excited nucleus remaining after the intra-nuclear cascade was originally developed by Weisskopf [Wei37]. This model assumes complete energy equilibration before particle emission, and re-equilibration of excitation energies between successive evaporations. As a result the angular distribution of emitted particles is isotropic.

The GEANT4 evaporation model for the cascade implementation adapts the often-used computational method developed by Dostrowski [dff59, DFR60]. The emission of particles is computed until the excitation energy falls below some specific cutoff. If a light nucleus is highly excited, the Fermi break-up model is executed. Also, fission is performed if that channel is open. The main chain of evaporation is followed until  $E_{excitation}$  falls below  $E_{cutoff} = 0.1$  MeV. The evaporation model ends with an emission chain which is followed until  $E_{excitation} < E_{cutoff}^{\gamma} = 10^{-15}$  MeV.

An example of Bertini evaporation model in action is shown in Fig. 25.1.

## 25.3 Interfacing Bertini implementation

Typically Bertini models are used through physics lists, with 'BERT' in their name. User should consult these validated physics model collection to understand the inclusion mechanisms before using directly the actual Bertini cascade interfaces:

**G4CascadeInterface** All the Bertini cascade submodels in integrated fashion, can be used collectively through this interface using method *ApplyYourself*. A GEANT4 track (*G4Track*) and a nucleus (*G4Nucleus*) are given as parameters.

**G4ElasticCascadeInterface** provides an access to elastic hadronic scattering. Particle treated are the same as in case for *G4CascadeInterface* but only elastic scattering is modeled.

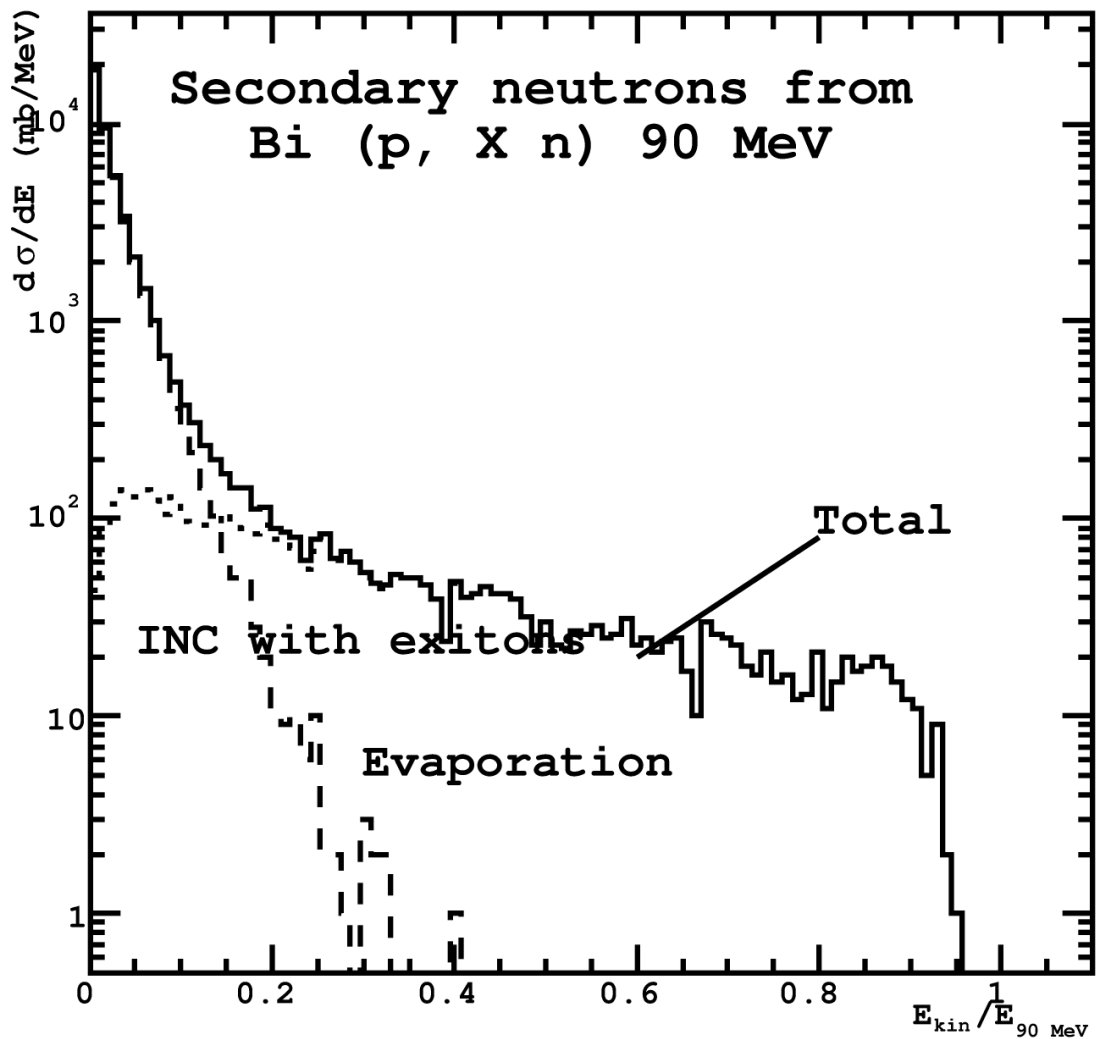


Fig. 25.1: Secondary neutrons generated by Bertini INC with excitons and evaporation model.

**G4PreCompoundCascadeInterface** provides an interface to INUCL intra nuclear cascade with excitons. Subsequent evaporation phase is *not* modeled.

**G4InuclEvaporation** provides an interface to INUCL evaporation model. This interface with method *BreakItUp* inputs an excited nuclei *G4Fragment* to model evaporation phase.

## THE GEANT4 BINARY CASCADE MODEL

### 26.1 Modeling overview

The GEANT4 Binary Cascade is an intranuclear cascade propagating primary and secondary particles in a nucleus [FIW04]. Interactions are between a primary or secondary particle and an individual nucleon of the nucleus, leading to the name Binary Cascade [CVV97a, CVV97b, IBGP92, PBN94, WHQ92]. Cross section data are used to select collisions. Where available, experimental cross sections are used by the simulation. Propagating of particles in the nuclear field is done by numerically solving the equation of motion. The cascade terminates when the average and maximum energy of secondaries is below threshold. The remaining fragment is treated by precompound and de-excitation models documented in the corresponding chapters.

#### 26.1.1 The transport algorithm

For the primary particle an impact parameter is chosen random in a disk outside the nucleus perpendicular to a vector passing through the center of the nucleus coordinate system and being parallel to the momentum direction. Using a straight line trajectory, the distance of closest approach  $d_i^{\min}$  to each target nucleon  $i$  and the corresponding time-of-flight  $t_i^d$  is calculated. In this calculation the momentum of the target nucleons is ignored, i.e. the target nucleons do not move. The interaction cross section  $\sigma_i$  with target nucleons is calculated using total inclusive cross-sections described below. For calculation of the cross-section the momenta of the nucleons are taken into account. The primary particle may interact with those target nucleons where the distance of closest approach  $d_i^{\min}$  is smaller than  $d_i^{\min} < \sqrt{\frac{\sigma_i}{\pi}}$ . These candidate interactions are called collisions, and these collisions are stored ordered by time-of-flight  $t_i^d$ . In the case no collision is found, a new impact parameter is chosen.

The primary particle is tracked the time-step given by the time to the first collision. As long a particle is outside the nucleus, that is a radius of the outermost nucleon plus 3 fm, particles travel along straight line trajectories. Particles entering the nucleus have their energy corrected for Coulomb effects. Inside the nucleus particles are propagated in the scalar nuclear field. The equation of motion in the field is solved for a given time-step using a Runge-Kutta integration method.

At the end of the step, the primary and the nucleon interact using the scattering term. The resulting secondaries are checked for the Fermi exclusion principle. If any of the two particles has a momentum below Fermi momentum, the interaction is suppressed, and the original primary is tracked to the next collision. In case interaction is allowed, the secondaries are treated like the primary, that is, all possible collisions are calculated like above, with the addition that these new primary particles may be short-lived and may decay. A decay is treated like others collisions, the collision time being the time until the decay of the particle. All secondaries are tracked until they leave the nucleus, or until the cascade stops.

### 26.1.2 The description of the target nucleus and fermi motion

The nucleus is constructed from  $A$  nucleons and  $Z$  protons with nucleon coordinates  $\mathbf{r}_i$  and momenta  $\mathbf{p}_i$ , with  $i = 1, 2, \dots, A$ . We use a common initialization Monte Carlo procedure, which is realized in the most of the high energy nuclear interaction models:

- Nucleon radii  $r_i$  are selected randomly in the nucleus rest frame according to nucleon density  $\rho(r_i)$ . For heavy nuclei with  $A > 16$  [GLMP91] nucleon density is

$$\rho(r_i) = \frac{\rho_0}{1 + \exp[(r_i - R)/a]}$$

where

$$\rho_0 \approx \frac{3}{4\pi R^3} \left(1 + \frac{a^2 \pi^2}{R^2}\right)^{-1}.$$

Here  $R = r_0 A^{1/3}$  fm and  $r_0 = 1.16(1 - 1.16A^{-2/3})$  fm and  $a \approx 0.545$  fm. For light nuclei with  $A < 17$  nucleon density is given by a harmonic oscillator shell model [B61], e.g.

$$\rho(r_i) = (\pi R^2)^{-3/2} \exp(-r_i^2/R^2),$$

where  $R^2 = 2/3\langle r^2 \rangle = 0.8133A^{2/3}$  fm<sup>2</sup>. To take into account nucleon repulsive core it is assumed that internucleon distance  $d > 0.8$  fm;

- The nucleus is assumed to be isotropic, i.e. we place each nucleon using a random direction and the previously determined radius  $r_i$ .
- The initial momenta of the nucleons  $p_i$  are randomly chosen between 0 and  $p_F^{max}(r)$ , where the maximal momenta of nucleons (in the local Thomas-Fermi approximation [DA74]) depends from the proton or neutron density  $\rho$  according to

$$p_F^{max}(r) = \hbar c (3\pi^2 \rho(r))^{1/3}$$

- To obtain momentum components, it is assumed that nucleons are distributed isotropic in momentum space; i.e. the momentum direction is chosen at random.
- The nucleus must be centered in momentum space around 0, i. e. the nucleus must be at rest, i. e.  $\sum_i \mathbf{p}_i = \mathbf{0}$ ; To achieve this, we choose one nucleon to compensate the sum the remaining nucleon momenta  $p_{rest} = \sum_{i=1}^{i=A-1} p_i$ . If this sum is larger than maximum momentum  $p_F^{max}(r)$ , we change the direction of the momentum of a few nucleons. If this does not lead to a possible momentum value, than we repeat the procedure with a different nucleon having a larger maximum momentum  $p_F^{max}(r)$ . In the rare case this fails as well, we choose new momenta for all nucleons.

This procedure gives special for hydrogen <sup>1</sup>H, where the proton has momentum  $p = 0$ , and for deuterium <sup>2</sup>H, where the momenta of proton and neutron are equal, and in opposite direction.

- We compute energy per nucleon  $e = E/A = m_N + B(A, Z)/A$ , where  $m_N$  is nucleon mass and the nucleus binding energy  $B(A, Z)$  is given by the tabulation of [rtbcXX] and find the effective mass of each nucleon  $m_i^{eff} = \sqrt{(E/A)^2 - p_i^2}$ .

### 26.1.3 Optical and phenomenological potentials

The effect of collective nuclear elastic interaction upon primary and secondary particles is approximated by a nuclear potential.

For projectile protons and neutrons this scalar potential is given by the local Fermi momentum  $p_F(r)$

$$V(r) = \frac{p_F^2(r)}{2m}$$

where  $m$  is the mass of the neutron  $m_n$  or the mass of proton  $m_p$ .

For pions the potential is given by the lowest order optical potential [SMC79]

$$V(r) = \frac{-2\pi(\hbar c)^2 A}{\bar{m}_\pi} \left(1 + \frac{m_\pi}{M}\right) b_0 \rho(r)$$

where  $A$  is the nuclear mass number,  $m_\pi$ ,  $M$  are the pion and nucleon mass,  $\bar{m}_\pi$  is the reduced pion mass  $\bar{m}_\pi = (m_\pi m_N)/(m_\pi + m_N)$ , with  $m_N$  is the mass of the nucleus, and  $\rho(r)$  is the nucleon density distribution. The parameter  $b_0$  is the effective  $s$ -wave scattering length and is obtained from analysis to pion atomic data to be about -0.042 fm.

### 26.1.4 Pauli blocking simulation

The cross sections used in this model are cross sections for free particles. In the nucleus these cross sections are reduced to effective cross sections by Pauli-blocking due to Fermi statistics.

For nucleons created by a collision, i.e. an inelastic scattering or from decay, we check that all secondary nucleons occupy a state allowed by Fermi statistics. We assume that the nucleus in its ground state and all states below Fermi energy are occupied. All secondary nucleons therefore must have a momentum  $p_i$  above local Fermi momentum  $p_F(r)$ , i.e.

$$p_i > p_F^{max}(r).$$

If any of the nucleons of the collision has a momentum below the local Fermi momentum, then the collision is Pauli blocked. The reaction products are discarded, and the original particles continue the cascade.

### 26.1.5 The scattering term

The basis of the description of the reactive part of the scattering amplitude are two particle binary collisions (hence binary cascade), resonance production, and decay. Based on the cross-section described later in this paper, collisions will occur when the transverse distance  $d_t$  of any projectile target pair becomes smaller than the black disk radius corresponding to the total cross-section  $\sigma_t$

$$\frac{\sigma_t}{\pi} > d_t^2$$

In case of a collision, all particles will be propagated to the estimated time of the collision, i.e. the time of closest approach, and the collision final state is produced.

## 26.1.6 Total inclusive cross-sections

Experimental data are used in the calculation of the total, inelastic and elastic cross-section wherever available.

### Hadron-nucleon scattering

For the case of proton-proton(pp) and proton-neutron(pn) collisions, as well as  $\pi^+$  and  $\pi^-$  nucleon collisions, experimental data are readily available as collected by the Particle Data Group (PDG) for both elastic and inelastic collisions. We use a tabulation based on a sub-set of these data for  $\sqrt{S}$  below 3 GeV. For higher energies, parametrizations from the CERN-HERA collection are included.

### Channel cross-sections

A large fraction of the cross-section in individual channels involving meson nucleon scattering can be modeled as resonance excitation in the s-channel. This kind of interactions show a resonance structure in the energy dependency of the cross-section, and can be modeled using the Breit-Wigner function

$$\sigma_{res}(\sqrt{s}) = \sum_{FS} \frac{2J+1}{(2S_1+1)(2S_2+1)} \frac{\pi}{k^2} \frac{\Gamma_{IS}\Gamma_{FS}}{(\sqrt{s}-M_R)^2 + \Gamma/4},$$

Where  $S_1$  and  $S_2$  are the spins of the two fusing particles,  $J$  is the spin of the resonance,  $\sqrt{s}$  the energy in the center of mass system,  $k$  the momentum of the fusing particles in the center of mass system,  $\Gamma_{IS}$  and  $\Gamma_{FS}$  the partial width of the resonance for the initial and final state respectively.  $M_R$  is the nominal mass of the resonance.

The initial states included in the model are pion and kaon nucleon scattering. The product resonances taken into account are the Delta resonances with masses 1232, 1600, 1620, 1700, 1900, 1905, 1910, 1920, 1930, and 1950 MeV, the excited nucleons with masses of 1440, 1520, 1535, 1650, 1675, 1680, 1700, 1710, 1720, 1900, 1990, 2090, 2190, 2220, and 2250 MeV, the Lambda, and its excited states at 1520, 1600, 1670, 1690, 1800, 1810, 1820, 1830, 1890, 2100, and 2110 MeV, and the Sigma and its excited states at 1660, 1670, 1750, 1775, 1915, 1940, and 2030 MeV.

### Mass dependent resonance width and partial width

During the cascading, the resonances produced are assigned real masses, with values distributed according to the production cross-section described above. The concrete (rather than nominal) masses of these resonances may be small compared to the PDG value, and this implies that some channels may not be open for decay. In general it means, that the partial and total width will depend on the concrete mass of the resonance. We are using the UrQMD [rtbcYY, rtbcZZ] approach for calculating these actual widths,

$$\Gamma_{R \rightarrow 12}(M) = (1+r) \frac{\Gamma_{R \rightarrow 12}(M_R)}{p(M_R)^{(2l+1)}} \frac{M_R}{M} \frac{p(M)^{(2l+1)}}{1+r(p(M)/p(M_R))^{2l}}. \quad (26.1)$$

Here  $M_R$  is the nominal mass of the resonance,  $M$  the actual mass,  $p$  is the momentum in the center of mass system of the particles,  $L$  the angular momentum of the final state, and  $r = 0.2$ .

## Resonance production cross-section in the t-channel

In resonance production in the t-channel, single and double resonance excitation in nucleon-nucleon collisions are taken into account. The resonance production cross-sections are as much as possible based on parametrizations of experimental data [rtbcWW] for proton proton scattering. The basic formula used is motivated from the form of the exclusive production cross-section of the  $\Delta_{1232}$  in proton proton collisions:

$$\sigma_{AB} = 2\alpha_{AB}\beta_{AB} \frac{\sqrt{s} - \sqrt{s_0}}{(\sqrt{s} - \sqrt{s_0})^2 + \beta_{AB}^2} \left( \frac{\sqrt{s_0} + \beta_{AB}}{\sqrt{s}} \right)^{\gamma_{AB}}$$

The parameters of the description for the various channels are given in Table 26.1. For all other channels, the parametrizations were derived from these by adjusting the threshold behavior.

Table 26.1: Values of the parameters of the cross-section formula for the individual channels.

Reaction	$\alpha$	$\beta$	$\gamma$
$pp \rightarrow p\Delta_{1232}$	25 mbarn	0.4 GeV	3
$pp \rightarrow \Delta_{1232}\Delta_{1232}$	1.5 mbarn	1 GeV	1
$pp \rightarrow pp$	0.55 mbarn	1 GeV	1
$pp \rightarrow p\Delta$	0.4 mbarn	1 GeV	1
$pp \rightarrow \Delta_{1232}\Delta$	0.35 mbarn	1 GeV	1
$pp \rightarrow \Delta_{1232}N^*$	0.55 mbarn	1 GeV	1

The remainder of the cross-section are derived from these, applying detailed balance. Iso-spin invariance is assumed. The formalism used to apply detailed balance is

$$\sigma(cd \rightarrow ab) = \sum_{J,M} \frac{\langle j_c m_c j_d m_d \parallel JM \rangle^2}{\langle j_a m_a j_b m_b \parallel JM \rangle^2} \frac{(2S_a + 1)(2S_b + 1)}{(2S_c + 1)(2S_d + 1)} \frac{\langle p_{ab}^2 \rangle}{\langle p_{cd}^2 \rangle} \sigma(ab \rightarrow cd)$$

### 26.1.7 Nucleon Nucleon elastic collisions

Angular distributions for elastic scattering of nucleons are taken as closely as possible from experimental data, i.e. from the result of phase-shift analysis. They are derived from differential cross sections obtained from the SAID database, R. Arndt, 1998.

Final states are derived by sampling from tables of the cumulative distribution function of the centre-of-mass scattering angle, tabulated for a discrete set of lab kinetic energies from 10 MeV to 1200 MeV. The CDF's are tabulated at 1 degree intervals and sampling is done using bi-linear interpolation in energy and CDF values. Coulomb effects are taken into consideration for pp scattering.

### 26.1.8 Generation of transverse momentum

Angular distributions for final states other than nucleon elastic scattering are calculated analytically, derived from the collision term of the in-medium relativistic Boltzmann-Uehling-Uhlenbeck equation, based on the nucleon nucleon elastic scattering cross-sections:

$$\sigma_{NN \rightarrow NN}(s, t) = \frac{1}{(2\pi)^2 s} (D(s, t) + E(s, t) + (invertedt, u))$$

Here  $s, t, u$  are the Mandelstamm variables,  $D(s, t)$  is the direct term, and  $E(s, t)$  is the exchange term, with

$$D(s, t) = \frac{(g_{NN}^\sigma)^4(t - 4m^{*2})^2}{2(t - m_\sigma^2)^2} + \frac{(g_{NN}^\omega)^4(2s^2 + 2st + t^2 - 8m^{*2}s + 8m^{*4})}{(t - m_\omega^2)^2} + \\ + \frac{24(g_{NN}^\pi)^4m^{*2}t^2}{(t - m_\pi^2)^2} - \frac{4(g_{NN}^\sigma g_{NN}^\omega)^2(2s + t - 4m^{*2})m^{*2}}{(t - m_\sigma^2)(t - m_\omega^2)},$$

and

$$E(s, t) = \frac{(g_{NN}^\sigma)^4(t(t + s) + 4m^{*2}(s - t))}{8(t - m_\sigma^2)(u - m_\sigma^2)} + \frac{(g_{NN}^\omega)^4(s - 2m^{*2})(s - 6m^{*2})}{2(t - m_\omega^2)(u - m_\omega^2)} - \\ - \frac{6(g_{NN}^\pi)^4(4m^{*2} - s - t)m^{*4}t}{(t - m_\pi^2)(u - m_\pi^2i^2)} + \frac{3(g_{NN}^\sigma g_{NN}^\pi)^2m^{*2}(4m^{*2} - s - t)(4m^{*2} - t)}{(t - m_\sigma^2)(u - m_\pi^2)} + \\ + \frac{3(g_{NN}^\sigma g_{NN}^\pi)^2t(t + s)m^{*2}}{2(t - m_\pi^2)(u - m_\sigma^2)} + \frac{(g_{NN}^\sigma g_{NN}^\omega)^2t^2 - 4m^{*2}s - 10m^{*2}t + 24m^{*4}}{4(t - m_\sigma^2)(u - m_\omega^2)} + \\ + \frac{(g_{NN}^\sigma g_{NN}^\omega)^2(t + s)^2 - 2m^{*2}s + 2m^{*2}t}{4(t - m_\omega^2)(u - m_\sigma^2)} + \frac{3(g_{NN}^\omega g_{NN}^\pi)^2(t + s - 4m^{*2})(t + s - 2m^{*2})}{(t - m_\omega^2)(u - m_\pi^2)} + \\ + \frac{3(g_{NN}^\omega g_{NN}^\pi)^2m^{*2}(t^2 - 2m^{*2}t)}{(t - m_\pi^2)(u - m_\omega^2)}.$$

Here, in this first release, the in-medium mass was set to the free mass, and the nucleon nucleon coupling constants used were 1.434 for the  $\pi$ , 7.54 for the  $\omega$ , and 6.9 for the  $\sigma$ . This formula was used for elementary hadron-nucleon differential cross-sections by scaling the center of mass energy squared accordingly.

Finite size effects were taken into account at the meson nucleon vertex, using a phenomenological form factor (cut-off) at each vertex.

### 26.1.9 Decay of strong resonances

In the simulation of decay of strong resonances, we use the nominal decay branching ratios from the particle data book. The stochastic mass of a individual resonance created is sampled at creation time from the Breit-Wigner form, under the mass constraints posed by center of mass energy of the scattering, and the mass in the lightest decay channel. The decay width from the particle data book are then adjusted according to Eq. eq:width, to take the stochastic mass value into account.

All decay channels with nominal branching ratios greater than 1% are simulated.

### 26.1.10 The escaping particle and coherent effects

When a nucleon other than the incident particle leaves the nucleus, the ground state of the nucleus changes. The energy of the outgoing particle cannot be such that the total mass of the new nucleus would be below its ground state mass. To avoid this, we reduce the energy of an outgoing nucleons by the mass-difference of old and new nucleus.

Furthermore, the momentum of the final exited nucleus derived from energy momentum balance may be such that its mass is below its ground state mass. In this case, we arbitrarily scale the momenta of all outgoing particles by a factor derived from the mass of the nucleus and the mass of the system of outgoing particles.

### 26.1.11 Light ion reactions

In simulating light ion reactions, the initial state of the cascade is prepared in the form of two nuclei, as described in the above section on the nuclear model.

The lighter of the collision partners is selected to be the projectile. The nucleons in the projectile are then entered, with position and momenta, into the initial state of the cascade. Note that before the first scattering of an individual nucleon, a projectile nucleon's Fermi-momentum is not taken into account in the tracking inside the target nucleus. The nucleon distribution inside the projectile nucleus is taken to be a representative distribution of its nucleons in configuration space, rather than an initial state in the sense of QMD. The Fermi momentum and the local field are taken into account in the calculation of the collision probabilities and final states of the binary collisions.

### 26.1.12 Transition to pre-compound modeling

Eventually, the cascade assumptions will break down at low energies, and the state of affairs has to be treated by means of evaporation and pre-equilibrium decay. This transition is not at present studied in depth, and an interesting approach which uses the tracking time, as in the Liege cascade code, remains to be studied in our context.

For this first release, the following algorithm is used to determine when cascading is stopped, and pre-equilibrium decay is called: As long as there are still particles above the kinetic energy threshold (75 MeV), cascading will continue. Otherwise, when the mean kinetic energy of the participants has dropped below a second threshold (15 MeV), the cascading is stopped.

The residual participants, and the nucleus in its current state are then used to define the initial state, i.e. excitation energy, number of excitons, number of holes, and momentum of the exciton system, for pre-equilibrium decay.

In the case of light ion reactions, the projectile excitation is determined from the binary collision participants (P) using the statistical approach towards excitation energy calculation in an adiabatic abrasion process, as described in [GS91]:

$$E_{ex} = \sum_P (E_{fermi}^P - E^P)$$

Given this excitation energy, the projectile fragment is then treated by the evaporation models described previously.

### 26.1.13 Calculation of excitation energies and residuals

At the end of the cascade, we form a fragment for further treatment in precompound and nuclear de-excitation models ([rtbcVV]).

These models need information about the nuclear fragment created by the cascade. The fragment is characterized by the number of nucleons in the fragment, the charge of the fragment, the number of holes, the number of all excitons, and the number of charged excitons, and the four momentum of the fragment.

The number of holes is given by the difference of the number of nucleons in the original nucleus and the number of non-excited nucleons left in the fragment. An exciton is a nucleon captured in the fragment at the end of the cascade.

The momentum of the fragment calculated by the difference between the momentum of the primary and the outgoing secondary particles must be split in two components. The first is the momentum acquired by coherent elastic effects, and the second is the momentum of the excitons in the nucleus rest frame. Only the later part is passed to the de-excitation models. Secondaries arising from de-excitation models, including the final nucleus, are transformed back the frame of the moving fragment.

## 26.2 Comparison with experiments

We add here a set of preliminary results produced with this code, focusing on neutron and pion production. Given that we are still in the process of writing up the paper, we apologize for the at release time still less than publication quality plots.

## 26.3 Neutrons Comparison with Experimental Data

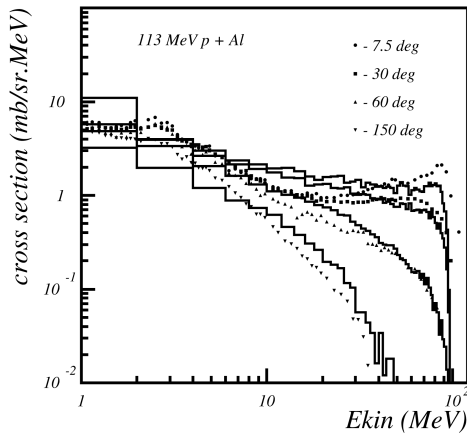


Fig. 26.1: Double differential cross-section for neutrons produced in proton scattering off Aluminum. Proton incident energy was 113 MeV.

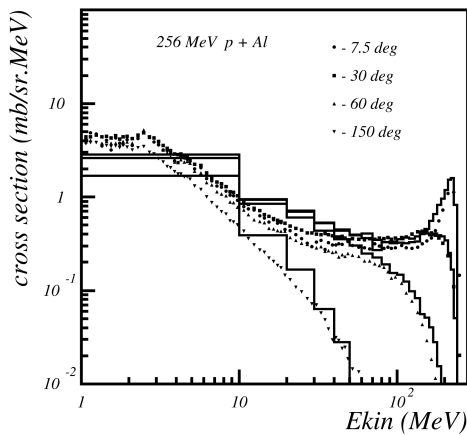


Fig. 26.2: Double differential cross-section for neutrons produced in proton scattering off Aluminum. Proton incident energy was 256 MeV. The points are data, the histogram is Binary Cascade prediction.

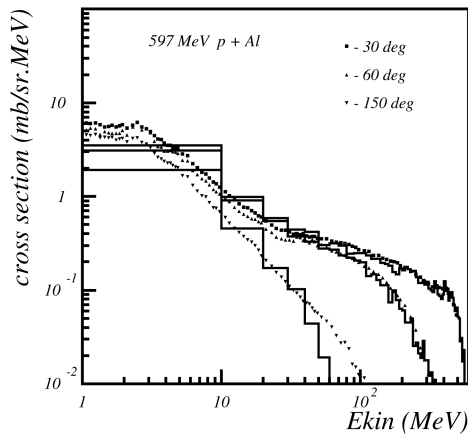


Fig. 26.3: Double differential cross-section for neutrons produced in proton scattering off Aluminum. Proton incident energy was 597 MeV. The points are data, the histogram is Binary Cascade prediction.

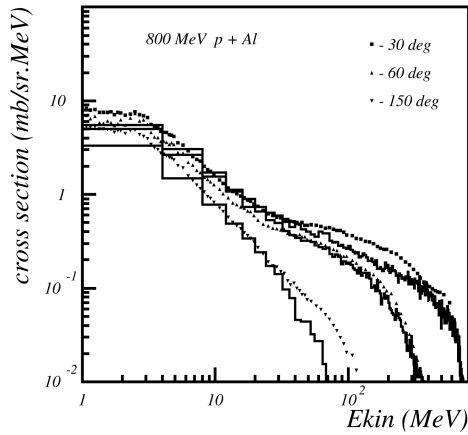


Fig. 26.4: Double differential cross-section for neutrons produced in proton scattering off Aluminum. Proton incident energy was 800 MeV. The points are data, the histogram is Binary Cascade prediction.

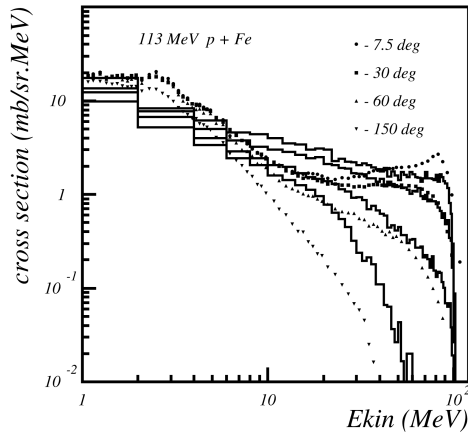


Fig. 26.5: Double differential cross-section for neutrons produced in proton scattering off Iron. Proton incident energy was 113 MeV. The points are data, the histogram is Binary Cascade prediction.

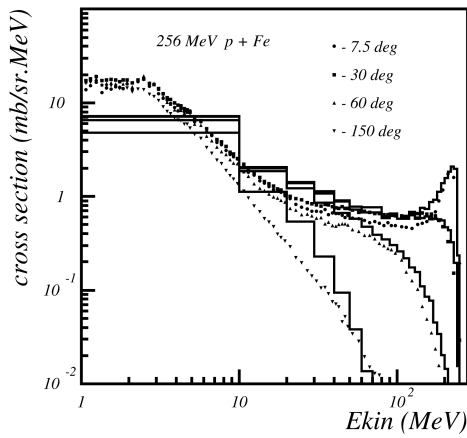


Fig. 26.6: Double differential cross-section for neutrons produced in proton scattering off Iron. Proton incident energy was 256 MeV. The points are data, the histogram is Binary Cascade prediction.

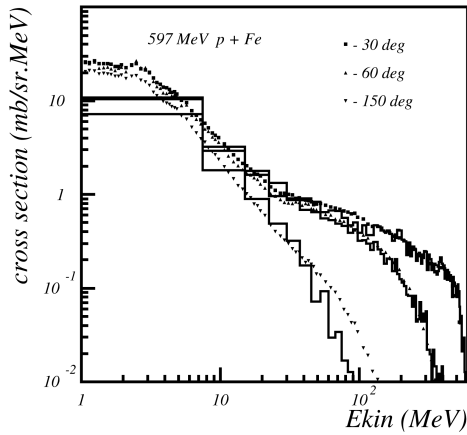


Fig. 26.7: Double differential cross-section for neutrons produced in proton scattering off Iron. Proton incident energy was 597 MeV. The points are data, the histogram is Binary Cascade prediction.

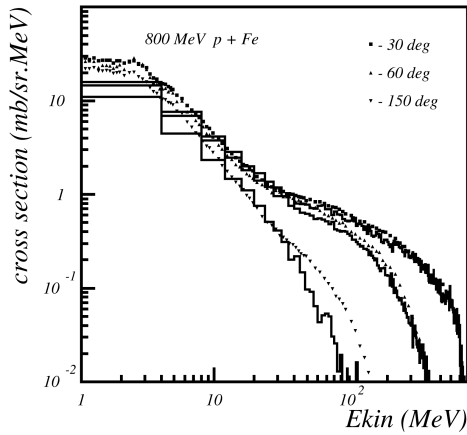


Fig. 26.8: Double differential cross-section for neutrons produced in proton scattering off Iron. Proton incident energy was 800 MeV. The points are data, the histogram is Binary Cascade prediction.

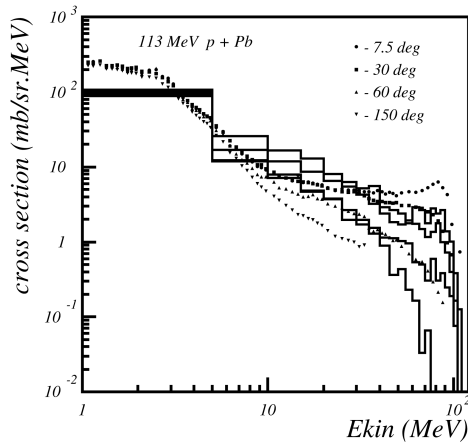


Fig. 26.9: Double differential cross-section for neutrons produced in proton scattering off Lead. Proton incident energy was 113 MeV. The points are data, the histogram is Binary Cascade prediction.

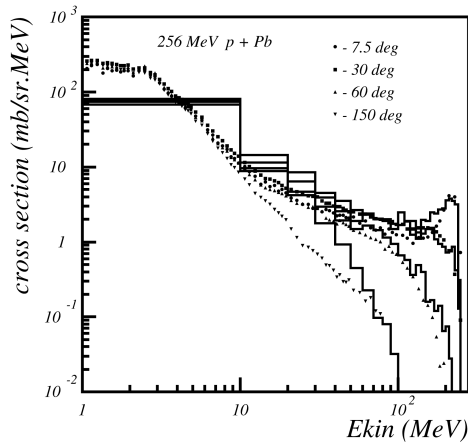


Fig. 26.10: Double differential cross-section for neutrons produced in proton scattering off Lead. Proton incident energy was 256 MeV. The points are data, the histogram is Binary Cascade prediction.

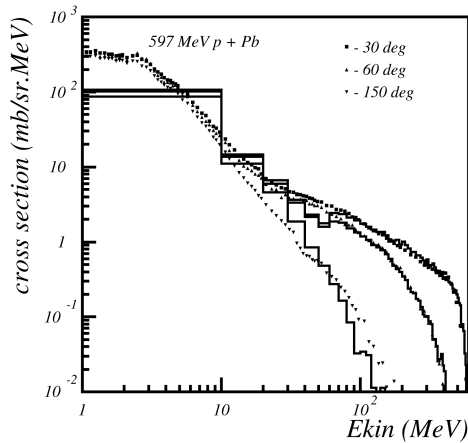


Fig. 26.11: Double differential cross-section for neutrons produced in proton scattering off Lead. Proton incident energy was 597 MeV. The points are data, the histogram is Binary Cascade prediction.

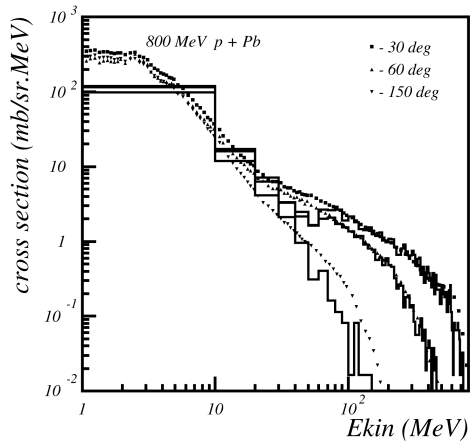


Fig. 26.12: Double differential cross-section for neutrons produced in proton scattering off Lead. Proton incident energy was 800 MeV. The points are data, the histogram is Binary Cascade prediction.

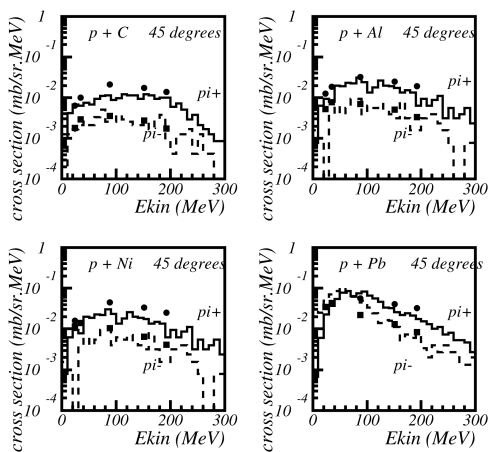


Fig. 26.13: Double differential cross-section for pions produced at  $45^\circ$  in proton scattering off various materials. Proton incident energy was 597 MeV in each case. The points are data, the histogram is Binary Cascade prediction.

---

CHAPTER  
**TWENTYSEVEN**

---

## **INCL++: THE LIÈGE INTRANUCLEAR CASCADE MODEL**

### **27.1 Introduction**

There is a renewed interest in the study of spallation reactions. This is largely due to new technological applications, such as Accelerator-Driven Systems, consisting of sub-critical nuclear reactor coupled to a particle accelerator. These applications require optimized targets as spallation sources. This type of problem typically involves a large number of parameters and thus it cannot be solved by trial and error. One has to rely on simulations, which implies that very accurate tools need to be developed and their validity and accuracy need to be assessed.

Above  $\sim 200$  MeV incident energy it is necessary to use reliable models due to the prohibitive number of open channels. The most appropriate modeling technique in this energy region is intranuclear cascade (INC) combined with evaporation model. One such pair of models is the Liège cascade model `INCL++` [BCD+13, MBC+14] coupled with the `G4ExcitationHandler` statistical de-excitation model. The strategy adopted by the `INCL++` cascade is to improve the quasi-classical treatment of physics without relying on too many free parameters.

This chapter introduces the physics provided by `INCL++` as implemented in GEANT4. Table 27.1 summarizes the key features and provides references to detailed descriptions of the physics.

The `INCL++` model is available through dedicated physics lists (see Table 27.1). The `_HP` variants of the physics lists use the `NeutronHP` model (Chapter *Low Energy Neutron Interactions*) for neutron interactions at low energy; the `QGSP_` and `FTFP_` variants respectively use the `QGSP` and `FTFP` model at high energy. Fig. 27.1 shows a schematic model map of the `INCL++`-based physics lists.

Finally, the `INCL++` model is directly accessible through its interface (`G4INCLXXInterface`).

The reference paper for the `INCL++` model is Ref. [MBC+14]. Please make sure you cite it appropriately if you publish any work based on this model.

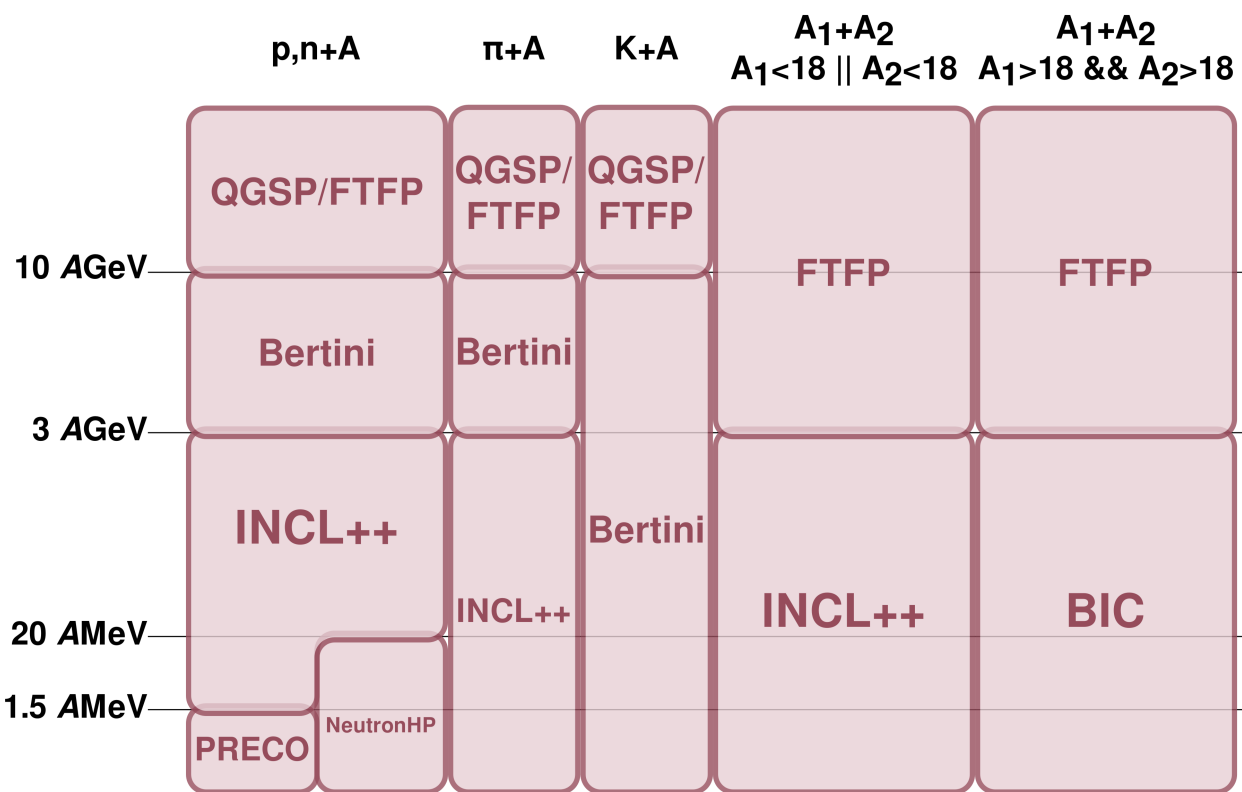


Fig. 27.1: Model map for the `INCL++`-based physics lists. The first two columns represent nucleon- and pion-induced reactions. The third column represents nucleus-nucleus reactions where at least one of the partners is below  $A = 18$ . The fourth column represents other nucleus-nucleus reactions.

Table 27.1: `INCL++` feature summary.

<b>usage</b>	
physics lists	<code>QGSP_INCLXX</code>
	<code>QGSP_INCLXX_HP</code>
	<code>FTFP_INCLXX</code>
	<code>FTFP_INCLXX_HP</code>
<b>interfaces</b>	
<code>G4INCLXXInterface</code>	nucleon-, pion-, kaon- and nucleus-nucleus
<b>projectile particles</b>	
	proton, neutron
	pions ( $\pi^+$ , $\pi^0$ , $\pi^-$ )
	kaons ( $K^+$ , $K^-$ )
	deuteron, triton
	$^3\text{He}$ , $\alpha$
	light ions (up to $A = 18$ )
<b>energy range</b>	1 MeV - 20 GeV
<b>target nuclei</b>	
lightest applicable	deuterium, $^2\text{H}$
heaviest	no limit, tested up to uranium
<b>features</b>	
	no ad-hoc parameters
	realistic nuclear densities
	Coulomb barrier
	non-uniform time-step
	pion and delta production cross sections
	delta decay
	Pauli blocking
	emission of composite particles ( $A \leq 8$ )
	complete-fusion model at low energy
	conservation laws satisfied at the keV level
<b>typical CPU time</b>	$0.5 \lesssim \text{INCL++}/\text{Binary Cascade} \lesssim 2$
<b>code size</b>	75 classes, 14k lines
<b>references</b>	Ref. [ <a href="#">MBC+14</a> ]

### 27.1.1 Suitable application fields

The `INCL++`-dedicated physics lists are suitable for the simulation of any system where spallation reactions or light-ion-induced reactions play a dominant role. As examples, we include here a non-exhaustive list of possible application fields:

- Accelerator-Driven Systems (ADS);
- spallation targets;
- radioprotection close to high-energy accelerators;
- radioprotection in space;
- proton or carbon therapy;
- production of beams of exotic nuclei.

## 27.2 Generalities of the INCL++ cascade

INCL++ is a Monte-Carlo simulation incorporating the aforementioned cascade physics principles. The INCL++ algorithm consists of an initialization stage and the actual data processing stage.

The INCL++ cascade can be used to simulate the collisions between bullet particles and nuclei. The supported bullet particles and the interface classes supporting them are presented in table [Table 27.1](#).

The momenta and positions of the nucleons inside the nuclei are determined at the beginning of the simulation run. The proton and neutron density profiles are based on Hartree-Fock-Bogoliubov calculations (Ref. [[Rodriguez-SanchezDM+17](#)]) and the nucleons move in a static potential well. The cascade is modeled by tracking the nucleons and their collisions.

The possible reactions inside the nucleus are

- $NN \rightarrow NN$  (elastic scattering)
- $NN \rightarrow N\Delta$  and  $N\Delta \rightarrow NN$
- $\Delta \rightarrow \pi N$  and  $\pi N \rightarrow \Delta$
- $NN \rightarrow NN x\pi$  (multiple pion production;  $x \geq 1$ )
- $\pi N \rightarrow \pi N$  (elastic scattering and charge exchange)
- $\pi N \rightarrow N(x+1)\pi$  (multiple pion production;  $x \geq 1$ )
- $NN \rightarrow NNM x\pi$  ( $M = \eta$  or  $\omega$ ;  $x \geq 0$ )
- $\pi N \rightarrow MN$  ( $M = \eta$  or  $\omega$ )
- $MN \rightarrow \pi N, \pi\pi N$  ( $M = \eta$  or  $\omega$ )
- $MN \rightarrow MN$  ( $M = \eta$  or  $\omega$ ; elastic scattering)
- $NN \rightarrow NYK x\pi$  ( $Y = \Lambda$  or  $\Sigma$ ;  $x \geq 0$ )
- $NN \rightarrow NNK\bar{K}$  ( $Y = \Lambda$  or  $\Sigma$ )
- $\pi N \rightarrow YK x\pi$  ( $Y = \Lambda$  or  $\Sigma$ ;  $x \geq 0$ )
- $\pi N \rightarrow NK\bar{K}$
- $N\bar{K} \rightarrow N\bar{K} x\pi$  ( $x = 0, 1, 2$ )
- $N\bar{K} \rightarrow Y x\pi$  ( $Y = \Lambda$  or  $\Sigma$ ;  $x = 1, 2$ )
- $NK \rightarrow NK x\pi$  ( $x = 0, 1, 2$ )
- $NY \rightarrow NY'$  ( $Y, Y' = \Lambda$  or  $\Sigma$ )
- $\Delta N \rightarrow NYK$  ( $Y = \Lambda$  or  $\Sigma$ )
- $\Delta N \rightarrow \Delta YK$  ( $Y = \Lambda$  or  $\Sigma$ )
- $\Delta N \rightarrow NNK\bar{K}$

### 27.2.1 Model limits

The `INCL++` model has certain limitations with respect to the bullet particle energy and type, and target-nucleus type. The supported energy range for incident nucleons and pions is 1 MeV–20 GeV. Any target nucleus from deuterium (<sup>2</sup>H) up is in principle acceptable, but not all areas of the nuclide chart have received equal attention during testing. Heavy nuclei (say above Fe) close to the stability valley have been more thoroughly studied than light or unstable nuclei. The model is anyway expected to accept any existing nucleus as a target.

Light nuclei (from  $A = 2$  to  $A = 18$  included) can also be used as projectiles. The `G4INCLXXInterface` class can be used for collisions between nuclei of any mass, but it will internally rely on the Binary Cascade model (see chapter [The Binary Cascade Model](#)) if both reaction partners have  $A > 18$ . A warning message will be displayed (once) if this happens.

## 27.3 Physics ingredients

The philosophy of the `INCL++` model is to minimize the number of free parameters, which guarantees the predictive power of the model. All `INCL++` parameters are either taken from known phenomenology (e.g. nuclear radii, elementary cross sections, nucleon potentials) or fixed once and for all (stopping time, cluster-coalescence parameters).

The nucleons are modeled from HFB calculations (Ref. [RodriguezSanchezDM+17]) in a static potential well. The radius of the well depends on the nucleon momentum, the  $r$ - $p$  correlation being determined by the desired spatial density distribution  $\rho_r(r)$  according to the following equation:

$$\rho_p(p)p^2dp = -\frac{d\rho_r(r)}{dr} \frac{r^3}{3} dr,$$

where  $\rho_p(p)$  is the momentum-space density (drawn from HFB calculations (Ref. [RodriguezSanchezDM+17])).

After the initialization a projectile particle, or bullet, is shot towards the target nucleus. In the following we assume that the projectile is a nucleon, a pion or a kaon; the special case of composite projectiles will be described in more detail in subsection [Initialisation of composite projectiles](#).

The impact parameter, i.e. the distance between the projectile particle and the center point of the projected nucleus surface is chosen at random. The value of the impact parameter determines the point where the bullet particle will enter the calculation volume. After this the algorithm tracks the nucleons by determining the times at which an event will happen. The possible events are:

- collision
- decay of a delta resonance
- reflection from the nuclear potential well
- transmission through the nuclear potential well

The particles are assumed to propagate along straight-line trajectories. The algorithm calculates the time at which events will happen and propagates the particles directly to their positions at that particular point in time. This means that the length of the time step in simulation is not constant, and that we do not need to perform expensive numerical integration of the particle trajectories.

Particles in the model are labeled either as *participants* (projectile particles and particles that have undergone a collision with a projectile) or *spectators* (target particles that have not undergone any collision). Collisions between spectator particles are neglected.

### 27.3.1 Emission of composite particles

`INCL++` is able to simulate the emission of composite particles (up to  $A = 8$ ) during the cascade stage. Clusters are formed by coalescence of nucleons; when a nucleon (the *leading* particle) reaches the surface and is about to leave the system, the coalescence algorithm looks for other nucleons that are “sufficiently close” in phase space; if any are found, a candidate cluster is formed. If several clusters are formed, the algorithm selects the least excited one. Penetration of the Coulomb barrier is tested for the candidate cluster, which is emitted if the test is successful; otherwise, normal transmission of the leading nucleon is attempted.

There are at least two peculiarities of `INCL++`’s cluster-coalescence algorithm. First, it acts in *phase space*, while many existing algorithms act in momentum space only. Second, it is *dynamical*, in the sense that it acts on the instantaneous phase-space distribution of nucleons in the system, and not on the distribution of the escaping nucleons.

### 27.3.2 Cascade stopping time

Stopping time is defined as the point in time when the cascade phase is finished and the excited remnant is passed to evaporation model. In the `INCL++` model the stopping time,  $t_{\text{stop}}$ , is defined as:

$$t_{\text{stop}} = t_0 (A_{\text{target}}/208)^{0.16}.$$

Here  $A_{\text{target}}$  is the target mass number and  $t_0 = 70 \text{ fm}/c$ . The intranuclear cascade also stops if no participants are left in the nucleus.

### 27.3.3 Conservation laws

The `INCL++` model generally guarantees energy and momentum conservation at the keV level, which is compatible with the numerical accuracy of the code. It uses `G4ParticleTable` and `G4IonTable` for the masses of particles and ions, which means that the energy balance is guaranteed to be consistent with radiation transport. However, `INCL++` can occasionally generate an event such that conservation laws cannot be exactly fulfilled; these corner cases typically happen for very light targets.

Baryon number and charge are always conserved.

### 27.3.4 Initialisation of composite projectiles

In the case of composite projectiles, the projectile nucleons are initialised off their mass shell, to account for their binding in the projectile. The sum of the four-momenta of the projectile nucleons is equal to the nominal four-momentum of the projectile nucleus.

Given a random impact parameter, projectile nucleons are separated in geometrical spectators (those that do not enter the calculation volume) and geometrical participants (those that do). Geometrical participant that traverse the nucleus without undergoing any collision are coalesced with any existing geometrical spectators to form an excited projectile-like pre-fragment. The excitation energy of the pre-fragment is generated by a simple particle-hole model. At the end of the cascade stage, the projectile-like pre-fragment is handed over to `G4ExcitationHandler`.

### 27.3.5 Two meson resonances implemented: $\eta$ and $\omega$

The mesons  $\eta$  and  $\omega$  can be produced and emitted during the intranuclear cascade phase. The cross sections taken into account are listed in section [Generalities of the INCL++ cascade](#). By default in GEANT4 the  $\eta$  meson emitted is not decayed by INCL++, while that is the case for the  $\omega$  meson (then only the decay products ( $\pi$  and  $\gamma$ ) are given to GEANT4). More details will be available in a paper published soon.

### 27.3.6 Strangeness added: $Kaon$ , $\Lambda$ and $\Sigma$

Strangeness degree of freedom is available in INCL++ with production, scattering and absorption of eight new particles (the four kaons, the  $\Lambda$  and the three  $\Sigma$ ). The cross sections taken into account are listed in section [Generalities of the INCL++ cascade](#). In this first version hyperons are forced to decay at the end of the cascade. More details will be available in a paper published soon.

### 27.3.7 De-excitation phase

The INCL++ model simulates only the first part of the nuclear reaction; the de-excitation of the cascade remnant is simulated by default by G4ExcitationHandler. As an alternative, the ABLA++ model (Chapter [ABLA++ evaporation/fission model](#)) can be used instead, by employing the technique described in the Application Developer Guide, section “hadronic interactions”.

## 27.4 Physics performance

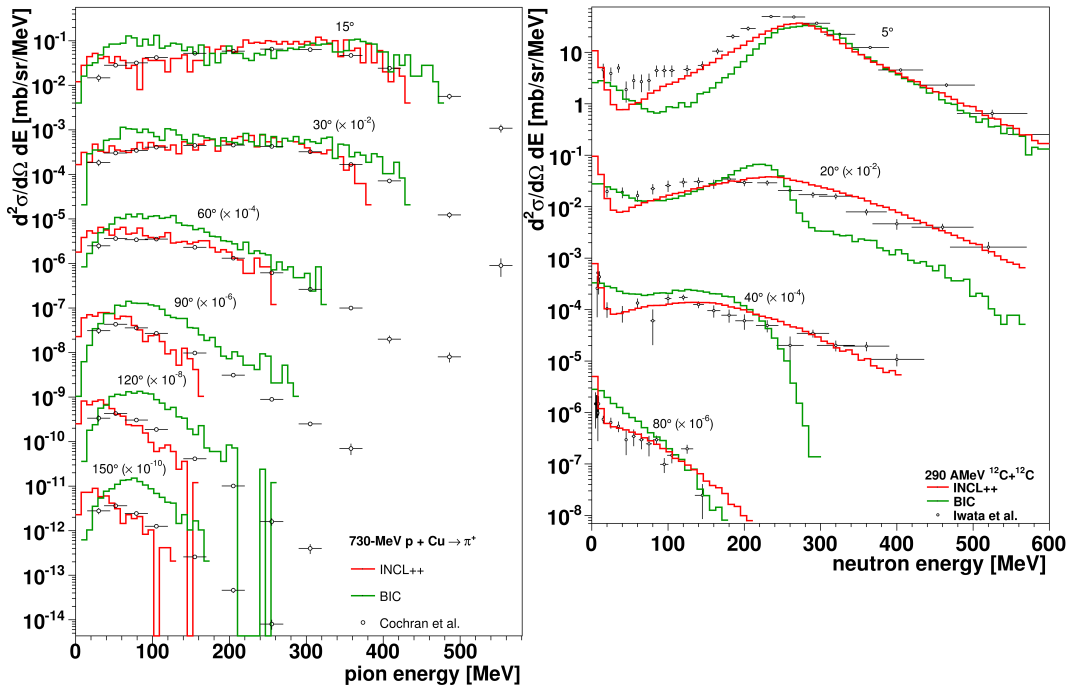


Fig. 27.2: Left: double-differential cross sections for the production of charged pions in 730-MeV  $p+Cu$ . Right: double-differential cross sections for the production of neutrons in 290-AMeV  $^{12}C+^{12}C$ . Predictions of the INCL++ and Binary-Cascade models are compared with experimental data from Refs. [CDG+72] and [IMS+01].

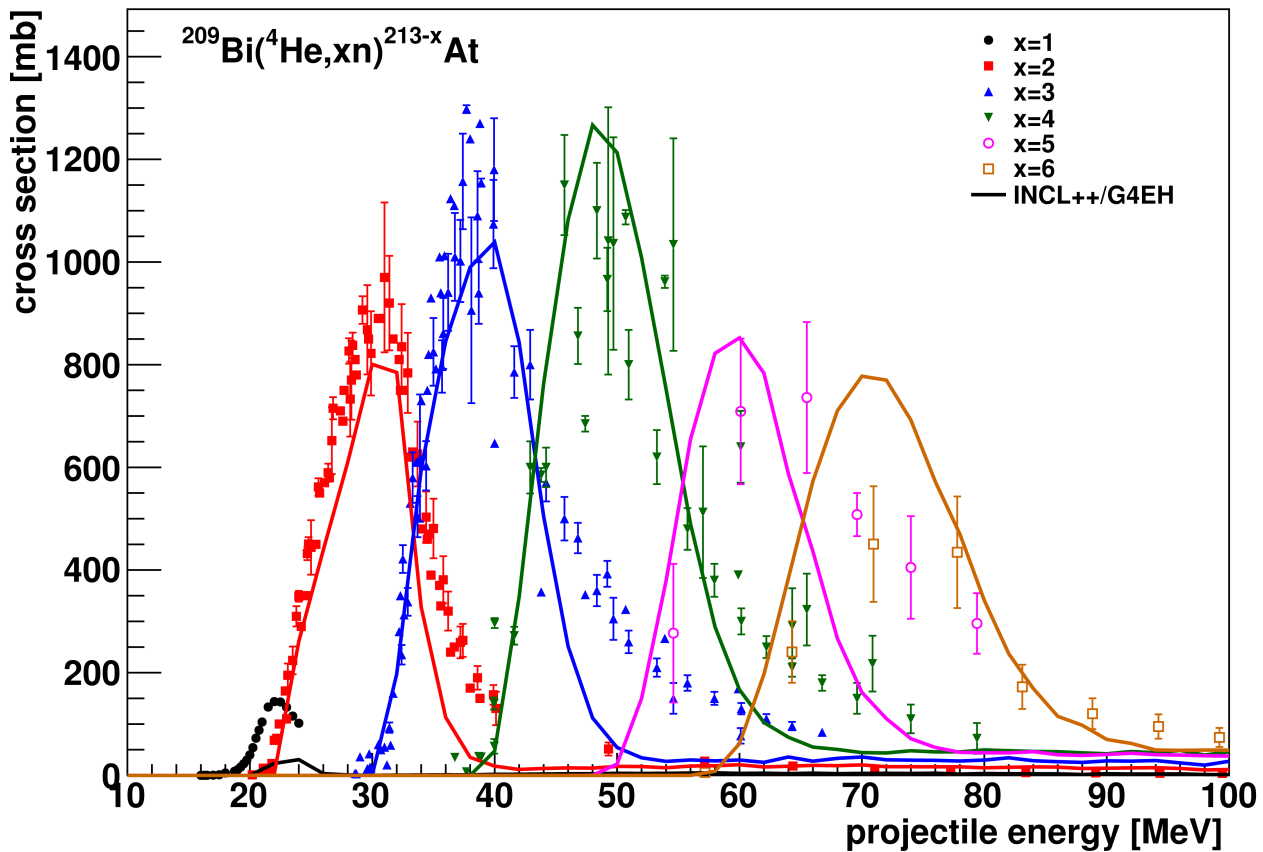


Fig. 27.3: Excitation functions for  $(\alpha, xn)$  cross sections on  $^{209}\text{Bi}$ . The predictions of INCL++-G4ExcitationHandler are represented by the solid line and are compared to experimental data [BL74, DL74, eal05, KSegre49, LM85, RBAC90, SMS94, SH74, PatelShahSingh99].

`INCL++` (coupled with `G4ExcitationHandler`) provides an accurate modeling tool for spallation studies in the tens of MeV–15 GeV energy range. The `INCL++-ABLA07` [KAH08] model was recognized as one of the best on the market by the IAEA Benchmark of Spallation Models [IAE] (note that the `ABLA07` de-excitation model is presently available in `GEANT4` as `ABLA++`).

As a sample of the quality of the model predictions of `INCL++-G4ExcitationHandler` for nucleon-induced reactions, the left panel of Fig. 27.2 presents a comparison of double-differential cross sections for pion production in 730-MeV  $p+Cu$ , compared with the predictions of the Binary-Cascade model (chapter *The Binary Cascade Model*) and with experimental data.

Reactions induced by light-ion projectiles up to  $A = 18$  are also treated by the model. The right panel of Fig. 27.2 shows double-differential cross sections for neutron production in 290-AMeV  $^{12}C+^{12}C$ . Fig. 27.3 shows excitation curves for  $^{209}Bi(\alpha, xn)$  reactions at very low energy. We stress here that intranuclear-cascade models are supposedly not valid below  $\sim 150$  AMeV. The very good agreement presented in Fig. 27.3 is due to the complete-fusion model that smoothly replaces `INCL++` at low energy.

`INCL++` is continuously updated and validated against experimental data.



---

CHAPTER  
**TWENTYEIGHT**

---

## **PRECOMPOUND MODEL**

### **28.1 Reaction initial state.**

The GEANT4 precompound model is considered as an extension of the hadron kinetic model. It gives a possibility to extend the low energy range of the hadron kinetic model for nucleon-nucleus inelastic collision and it provides a “smooth” transition from kinetic stage of reaction described by the hadron kinetic model to the equilibrium stage of reaction described by the equilibrium deexcitation models.

The initial information for calculation of pre-compound nuclear stage consists from the atomic mass number  $A$ , charge  $Z$  of residual nucleus, its four momentum  $P_0$ , excitation energy  $U$  and number of excitons  $n$  equals the sum of number of particles  $p$  (from them  $p_Z$  are charged) and number of holes  $h$ .

At the preequilibrium stage of reaction, we following the [GMT83] approach, take into account all possible nuclear transition the number of excitons  $n$  with  $\Delta n = +2, -2, 0$  [GMT83], which defined by transition probabilities. Only emission of neutrons, protons, deuterons, tritium and helium nuclei are taken into account.

### **28.2 Simulation of pre-compound reaction**

The precompound stage of nuclear reaction is considered until nuclear system is not an equilibrium state. Further emission of nuclear fragments or photons from excited nucleus is simulated using an equilibrium model (see Section *Sampling procedure*).

#### **28.2.1 Statistical equilibrium condition**

In the state of statistical equilibrium, which is characterized by an equilibrium number of excitons  $n_{eq}$ , all three type of transitions are equiprobable. Thus  $n_{eq}$  is fixed by  $\omega_{+2}(n_{eq}, U) = \omega_{-2}(n_{eq}, U)$ . From this condition we can get

$$n_{eq} = \sqrt{2gU}. \quad (28.1)$$

#### **28.2.2 Level density of excited ( $n$ -exciton) states**

To obtain Eq.(28.1) it was assumed an equidistant scheme of single-particle levels with the density  $g \approx 0.595aA$ , where  $a$  is the level density parameter, when we have the level density of the  $n$ -exciton state as

$$\rho_n(U) = \frac{g(gU)^{n-1}}{p!h!(n-1)!}. \quad (28.2)$$

### 28.2.3 Transition probabilities

The partial transition probabilities changing the exciton number by  $\Delta n$  is determined by the squared matrix element averaged over allowed transitions  $\langle |M|^2 \rangle$  and the density of final states  $\rho_{\Delta n}(n, U)$ , which are really accessible in this transition. It can be defined as following:

$$\omega_{\Delta n}(n, U) = \frac{2\pi}{\hbar} \langle |M|^2 \rangle \rho_{\Delta n}(n, U). \quad (28.3)$$

The density of final states  $\rho_{\Delta n}(n, U)$  were derived in paper [Wil70] using the Eq.(28.2) for the level density of the  $n$ -exciton state and later corrected for the Pauli principle and indistinguishability of identical excitons in paper [eal73]:

$$\begin{aligned}\rho_{\Delta n=+2}(n, U) &= \frac{1}{2}g \frac{[gU - F(p+1, h+1)]^2}{n+1} \frac{[gU - F(p+1, h+1)]^{n-1}}{gU - F(p, h)}, \\ \rho_{\Delta n=0}(n, U) &= \frac{1}{2}g \frac{[gU - F(p, h)]}{n} [p(p-1) + 4ph + h(h-1)] \\ \rho_{\Delta n=-2}(n, U) &= \frac{1}{2}gph(n-2),\end{aligned}$$

where  $F(p, h) = (p^2 + h^2 + p - h)/4 - h/2$  and it was taken to be equal zero. To avoid calculation of the averaged squared matrix element  $\langle |M|^2 \rangle$  it was assumed [GMT83] that transition probability  $\omega_{\Delta n=+2}(n, U)$  is the same as the probability for quasi-free scattering of a nucleon above the Fermi level on a nucleon of the target nucleus, i. e.

$$\omega_{\Delta n=+2}(n, U) = \frac{\langle \sigma(v_{rel})v_{rel} \rangle}{V_{int}}. \quad (28.4)$$

In Eq.(28.4) the interaction volume is estimated as  $V_{int} = \frac{4}{3}\pi(2r_c + \lambda/2\pi)^3$ , with the De Broglie wave length  $\lambda/2\pi$  corresponding to the relative velocity  $\langle v_{rel} \rangle = \sqrt{2T_{rel}/m}$ , where  $m$  is nucleon mass and  $r_c = 0.6$  fm.

The averaging in  $\langle \sigma(v_{rel})v_{rel} \rangle$  is further simplified by

$$\langle \sigma(v_{rel})v_{rel} \rangle = \langle \sigma(v_{rel}) \rangle \langle v_{rel} \rangle.$$

For  $\sigma(v_{rel})$  we take approximation:

$$\sigma(v_{rel}) = 0.5[\sigma_{pp}(v_{rel}) + \sigma_{pn}(v_{rel})]P(T_F/T_{rel}),$$

where factor  $P(T_F/T_{rel})$  was introduced to take into account the Pauli principle. It is given by

$$P(T_F/T_{rel}) = 1 - \frac{7}{5} \frac{T_F}{T_{rel}}$$

for  $\frac{T_F}{T_{rel}} \leq 0.5$  and

$$P(T_F/T_{rel}) = 1 - \frac{7}{5} \frac{T_F}{T_{rel}} + \frac{2}{5} \frac{T_F}{T_{rel}} \left(2 - \frac{T_{rel}}{T_F}\right)^{5/2}$$

for  $\frac{T_F}{T_{rel}} > 0.5$ .

The free-particle proton-proton  $\sigma_{pp}(v_{rel})$  and proton-neutron  $\sigma_{pn}(v_{rel})$  interaction cross sections are estimated using the equations [MBS58]:

$$\sigma_{pp}(v_{rel}) = \frac{10.63}{v_{rel}^2} - \frac{29.93}{v_{rel}} + 42.9$$

and

$$\sigma_{pn}(v_{rel}) = \frac{34.10}{v_{rel}^2} - \frac{82.2}{v_{rel}} + 82.2,$$

where cross sections are given in mbarn.

The mean relative kinetic energy  $T_{rel}$  is needed to calculate  $\langle v_{rel} \rangle$  and the factor  $P(T_F/T_{rel})$  was computed as  $T_{rel} = T_p + T_n$ , where mean kinetic energies of projectile nucleons  $T_p = T_F + U/n$  and target nucleons  $T_N = 3T_F/5$ , respectively.

Combining Eqs. (28.3) - (28.4) and assuming that  $\langle |M|^2 \rangle$  are the same for transitions with  $\Delta n = 0$  and  $\Delta n = \pm 2$  we obtain for another transition probabilities:

$$\omega_{\Delta n=0}(n, U) = \frac{\langle \sigma(v_{rel})v_{rel} \rangle}{V_{int}} \frac{n+1}{n} \left[ \frac{gU - F(p, h)}{gU - F(p+1, h+1)} \right]^{n+1} \frac{p(p-1) + 4ph + h(h-1)}{gU - F(p, h)}$$

and

$$\omega_{\Delta n=-2}(n, U) = \frac{\langle \sigma(v_{rel})v_{rel} \rangle}{V_{int}} \left[ \frac{gU - F(p, h)}{gU - F(p+1, h+1)} \right]^{n+1} \frac{ph(n+1)(n-2)}{[gU - F(p, h)]^2}.$$

## 28.2.4 Emission probabilities for nucleons

Emission process probability has been chosen similar as in the classical equilibrium Weisskopf-Ewing model [WE40]. Probability to emit nucleon  $b$  in the energy interval  $(T_b, T_b + dT_b)$  is given

$$W_b(n, U, T_b) = \sigma_b(T_b) \frac{(2s_b + 1)\mu_b}{\pi^2 h^3} R_b(p, h) \frac{\rho_{n-b}(E)}{\rho_n(U)} T_b, \quad (28.5)$$

where  $\sigma_b(T_b)$  is the inverse (absorption of nucleon  $b$ ) reaction cross section,  $s_b$  and  $m_b$  are nucleon spin and reduced mass, the factor  $R_b(p, h)$  takes into account the condition for the exciton to be a proton or neutron,  $\rho_{n-b}(E^*)$  and  $\rho_n(U)$  are level densities of nucleus after and before nucleon emission are defined in the evaporation model, respectively and  $E^* = U - Q_b - T_b$  is the excitation energy of nucleus after fragment emission.

## 28.2.5 Emission probabilities for complex fragments

It was assumed [GMT83] that nucleons inside excited nucleus are able to “condense” forming complex fragment. The “condensation” probability to create fragment consisting from  $N_b$  nucleons inside nucleus with  $A$  nucleons is given by

$$\gamma_{N_b} = N_b^3 (V_b/V)^{N_b-1} = N_b^3 (N_b/A)^{N_b-1},$$

where  $V_b$  and  $V$  are fragment  $b$  and nucleus volumes, respectively. The last equation was estimated [GMT83] as the overlap integral of (constant inside a volume) wave function of independent nucleons with that of the fragment.

During the preequilibrium stage a “condense” fragment can be emitted. The probability to emit a fragment can be written as [GMT83]

$$W_b(n, U, T_b) = \gamma_{N_b} R_b(p, h) \frac{\rho(N_b, 0, T_b + Q_b)}{g_b(T_b)} \sigma_b(T_b) \frac{(2s_b + 1)\mu_b}{\pi^2 h^3} \frac{\rho_{n-b}(E^*)}{\rho_n(U)} T_b, \quad (28.6)$$

where

$$g_b(T_b) = \frac{V_b (2s_b + 1) (2\mu_b)^{3/2}}{4\pi^2 h^3} (T_b + Q_b)^{1/2}$$

is the single-particle density for complex fragment  $b$ , which is obtained by assuming that complex fragment moves inside volume  $V_b$  in the uniform potential well whose depth is equal to be  $Q_b$ , and the factor  $R_b(p, h)$  guarantees correct isotopic composition of a fragment  $b$ .

## 28.2.6 The total probability

This probability is defined as

$$W_{tot}(n, U) = \sum_{\Delta n=+2,0,-2} \omega_{\Delta n}(n, U) + \sum_{b=1}^6 W_b(n, U),$$

where total emission  $W_b(n, U)$  probabilities to emit fragment  $b$  can be obtained from Eqs.(28.5) and (28.6) by integration over  $T_b$ :

$$W_b(n, U) = \int_{V_b}^{U-Q_b} W_b(n, U, T_b) dT_b.$$

## 28.2.7 Calculation of kinetic energies for emitted particle

The equations (28.5) and (28.6) are used to sample kinetic energies of emitted fragment.

## 28.2.8 Parameters of residual nucleus

After fragment emission we update parameter of decaying nucleus:

$$\begin{aligned} A_f &= A - A_b; Z_f = Z - Z_b; P_f = P_0 - p_b; \\ E_f^* &= \sqrt{E_f^2 - \vec{P}_f^2} - M(A_f, Z_f). \end{aligned}$$

Here  $p_b$  is the evaporated fragment four momentum.

---

CHAPTER  
TWENTYNINE

---

## EVAPORATION MODEL

### 29.1 Introduction

At the end of the pre-equilibrium stage, or a thermalizing process, the residual nucleus is supposed to be left in an equilibrium state, in which the excitation energy  $E^*$  is shared by a large number of nucleons. Such an equilibrated compound nucleus is characterized by its mass, charge and excitation energy with no further memory of the steps which led to its formation. If the excitation energy is higher than the separation energy, it can still eject nucleons and fragments ( $d$ ,  $t$ ,  ${}^3\text{He}$ ,  $\alpha$ , others). These constitute the low energy and most abundant part of the emitted particles in the rest system of the residual nucleus. The emission of particles by an excited compound nucleus has been successfully described by comparing the nucleus with the evaporation of molecules from a fluid [Fre36]. The first statistical theory of compound nuclear decay is due to Weisskopf and Ewing [WE40].

### 29.2 Evaporation model

The Weisskopf treatment is an application of the detailed balance principle that relates the probabilities to go from a state  $i$  to another  $d$  and viceversa through the density of states in the two systems:

$$P_{i \rightarrow d} \rho(i) = P_{d \rightarrow i} \rho(d)$$

where  $P_{d \rightarrow i}$  is the probability per unit of time of a nucleus  $d$  captures a particle  $j$  and form a compound nucleus  $i$  which is proportional to the compound nucleus cross section  $\sigma_{\text{inv}}$ . Thus, the probability that a parent nucleus  $i$  with an excitation energy  $E^*$  emits a particle  $j$  in its ground state with kinetic energy  $\varepsilon$  is

$$P_j(\varepsilon) d\varepsilon = g_j \sigma_{\text{inv}}(\varepsilon) \frac{\rho_d(E_{\max} - \varepsilon)}{\rho_i(E^*)} \varepsilon d\varepsilon \quad (29.1)$$

where  $\rho_i(E^*)$  is the level density of the evaporating nucleus,  $\rho_d(E_{\max} - \varepsilon)$  that of the daughter (residual) nucleus after emission of a fragment  $j$  and  $E_{\max}$  is the maximum energy that can be carried by the ejectile. With the spin  $s_j$  and the mass  $m_j$  of the emitted particle,  $g_j$  is expressed as  $g_j = (2s_j + 1)m_j/\pi^2\hbar^2$ .

This formula must be implemented with a suitable form for the level density and inverse reaction cross section. We have followed, like many other implementations, the original work of Dostrovsky *et al.* [DFF59] (which represents the first Monte Carlo code for the evaporation process) with slight modifications. The advantage of the Dostrovsky model is that it leads to a simple expression for equation (29.1) that can be analytically integrated and used for Monte Carlo sampling.

### 29.2.1 Cross sections for inverse reactions

The cross section for inverse reaction is expressed by means of empirical equation [DFF59]

$$\sigma_{\text{inv}}(\varepsilon) = \sigma_g \alpha \left( 1 + \frac{\beta}{\varepsilon} \right) \quad (29.2)$$

where  $\sigma_g = \pi R^2$  is the geometric cross section.

In the case of neutrons,  $\alpha = 0.76 + 2.2A^{-\frac{1}{3}}$  and  $\beta = (2.12A^{-\frac{2}{3}} - 0.050)/\alpha$  MeV. This equation gives a good agreement to those calculated from continuum theory [BW52] for intermediate nuclei down to  $\varepsilon \sim 0.05$  MeV. For lower energies  $\sigma_{\text{inv},n}(\varepsilon)$  tends toward infinity, but this causes no difficulty because only the product  $\sigma_{\text{inv},n}(\varepsilon)\varepsilon$  enters in equation (29.1). It should be noted, that the inverse cross section needed in (29.1) is that between a neutron of kinetic energy  $\varepsilon$  and a nucleus in an excited state.

For charged particles (p, d, t,  ${}^3\text{He}$  and  $\alpha$ ),  $\alpha = (1 + c_j)$  and  $\beta = -V_j$ , where  $c_j$  is a set of parameters calculated by Shapiro [Sha53] in order to provide a good fit to the continuum theory [BW52] cross sections and  $V_j$  is the Coulomb barrier.

### 29.2.2 Coulomb barriers

Coulomb repulsion, as calculated from elementary electrostatics are not directly applicable to the computation of reaction barriers but must be corrected in several ways. The first correction is for the quantum mechanical phenomenon of barrier penetration. The proper quantum mechanical expressions for barrier penetration are far too complex to be used if one wishes to retain equation (29.1) in an integrable form. This can be approximately taken into account by multiplying the electrostatic Coulomb barrier by a coefficient  $k_j$  designed to reproduce the barrier penetration approximately whose values are tabulated [Sha53].

$$V_j = k_j \frac{Z_j Z_d e^2}{R_c}$$

The second correction is for the separation of the centers of the nuclei at contact,  $R_c$ . We have computed this separation as  $R_c = R_j + R_d$  where  $R_{j,d} = r_c A_{j,d}^{1/3}$  and  $r_c$  is given [ASIP94] by

$$r_c = 2.173 \frac{1 + 0.006103 Z_j Z_d}{1 + 0.009443 Z_j Z_d}$$

### 29.2.3 Level densities

The simplest and most widely used level density based on the Fermi gas model are those of Weisskopf [Wei37] for a completely degenerate Fermi gas. We use this approach with the corrections for nucleon pairing proposed by Hurwitz and Bethe [HB51] which takes into account the displacements of the ground state:

$$\rho(E) = C \exp \left( 2\sqrt{a(E - \delta)} \right) \quad (29.3)$$

where  $C$  is considered as constant and does not need to be specified since only ratios of level densities enter in equation (29.1).  $\delta$  is the pairing energy correction of the daughter nucleus evaluated by Cook *et al.* [CFdLM67] and Gilbert and Cameron [GC65] for those values not evaluated by Cook *et al.*. The level density parameter is calculated according to:

$$a(E, A, Z) = \tilde{a}(A) \left\{ 1 + \frac{\delta}{E} [1 - \exp(-\gamma E)] \right\}$$

and the parameters calculated by Iljinov *et al.* [IMB+92] and shell corrections of Truran, Cameron and Hilf [TCH70].

## 29.2.4 Maximum energy available for evaporation

The maximum energy  $\varepsilon_j^{\max}$  available for the evaporation process (*i.e.* the maximum kinetic energy of the outgoing fragment  $j$ ) is computed like

$$\varepsilon_j^{\max} = \frac{(M_i + E^*)^2 + M_j^2 - M_d^2}{2(M_i + E^*)} - M_j$$

where  $M_i$ ,  $M_d$ , and  $M_j$  are the nuclear masses of the compound, residual, and evaporated nuclei respectively. The minimum energy  $\varepsilon_j^{\min}$  of the evaporation fragment depends also on the Coulomb barrier  $Q_j$  and the paring correction  $\delta$  which increasing effective residual mass  $M_f = M_i + E^* - M_j - Q_j - \delta$ :

$$\varepsilon_j^{\max} = \frac{(M_i + E^*)^2 + M_j^2 - M_f^2}{2(M_i + E^*)} - M_j$$

## 29.2.5 Total decay width

The total decay width for evaporation of a fragment  $j$  can be obtained by integrating equation (29.1) over kinetic energy

$$\Gamma_j = \hbar \int_{V_j}^{\varepsilon_j^{\max}} P(\varepsilon_j) d\varepsilon_j$$

This integration can be performed analitically if we use equation (29.3) for level densities and equation (29.2) for inverse reaction cross section. Thus, the total width is given by

$$\Gamma_j = \frac{g_j m_j R_d^2}{2\pi\hbar^2} \frac{\alpha}{a_d^2} \times \left\{ \begin{aligned} & \left\{ (\beta a_d - \frac{3}{2}) + a_d(\varepsilon_j^{\max} - V_j) \right\} \exp \left\{ -\sqrt{a_i(E^* - \delta_i)} \right\} + \\ & \left\{ (2\beta a_d - 3) \sqrt{a_d(\varepsilon_j^{\max} - V_j)} + 2a_d(\varepsilon_j^{\max} - V_j) \right\} \times \\ & \exp \left\{ 2 \left[ \sqrt{a_d(\varepsilon_j^{\max} - V_j)} - \sqrt{a_i(E^* - \delta_i)} \right] \right\} \end{aligned} \right\}$$

where  $a_d = a(A_d, Z_d, \varepsilon_j^{\max})$  and  $a_i = a(A_i, Z_i, E^*)$ .

## 29.3 GEM model

As an alternative model we have implemented the generalized evaporation model (GEM) by Furihata [Fur00]. This model considers emission of fragments heavier than  $\alpha$  particles and uses a more accurate level density function for total decay width instead of the approximation used by Dostrovsky. We use the same set of parameters but for heavy projectiles the parameters determined by Matsuse *et al.* [MAL82] are used.

Based on the Fermi gas model, the level density function is expressed as

$$\rho(E) = \begin{cases} \frac{\sqrt{\pi}}{12} \frac{e^{2\sqrt{a(E-\delta)}}}{a^{1/4}(E-\delta)^{5/4}} & \text{for } E \geq E_x \\ \frac{1}{T} e^{(E-E_0)/T} & \text{for } E < E_x \end{cases} \quad (29.4)$$

where  $E_x = U_x + \delta$  and  $U_x = 150/M_d + 2.5$  ( $M_d$  is the mass of the daughter nucleus). Nuclear temperature  $T$  is given as  $1/T = \sqrt{a/U_x} - 1.5U_x$ , and  $E_0$  is defined as  $E_0 = E_x - T(\log T - \log a/4 - (5/4)\log U_x + 2\sqrt{aU_x})$ .

By substituting equation (29.4) into equation (29.1) and integrating over kinetic energy can be obtained the following expression

$$\Gamma_j = \frac{\sqrt{\pi} g_j \pi R_d^2 \alpha}{12\rho(E^*)} \times \begin{cases} \{I_1(t, t) + (\beta + V)I_0(t)\} & \text{for } \varepsilon_j^{\max} - V_j < E_x \\ \{I_1(t, t_x) + I_3(s, s_x)e^s + \\ (\beta + V)(I_0(t_x) + I_2(s, s_x)e^s)\} & \text{for } \varepsilon_j^{\max} - V_j \geq E_x. \end{cases}$$

$I_0(t)$ ,  $I_1(t, t_x)$ ,  $I_2(s, s_x)$ , and  $I_3(s, s_x)$  are expressed as:

$$\begin{aligned}
 I_0(t) &= e^{-E_0/T}(e^t - 1) \\
 I_1(t, t_x) &= e^{-E_0/T}T\{(t - t_x + 1)e^{t_x} - t - 1\} \\
 I_2(s, s_x) &= 2\sqrt{2}\left\{s^{-3/2} + 1.5s^{-5/2} + 3.75s^{-7/2} - \right. \\
 &\quad \left.(s_x^{-3/2} + 1.5s_x^{-5/2} + 3.75s_x^{-7/2})\right\} \\
 I_3(s, s_x) &= \frac{1}{2\sqrt{2}}\left[2s^{-1/2} + 4s^{-3/2} + 13.5s^{-5/2} + 60.0s^{-7/2} + \right. \\
 &\quad \left.325.125s^{-9/2} - \left\{(s^2 - s_x^2)s_x^{-3/2} + (1.5s^2 + 0.5s_x^2)s_x^{-5/2} + \right.\right. \\
 &\quad \left.\left.(3.75s^2 + 0.25s_x^2)s_x^{-7/2} + (12.875s^2 + 0.625s_x^2)s_x^{-9/2} + \right.\right. \\
 &\quad \left.\left.(59.0625s^2 + 0.9375s_x^2)s_x^{-11/2} + \right.\right. \\
 &\quad \left.\left.(324.8s^2 + 3.28s_x^2)s_x^{-13/2} + \right\}\right]
 \end{aligned}$$

where  $t = (\varepsilon_j^{\max} - V_j)/T$ ,  $t_x = E_x/T$ ,  $s = 2\sqrt{a(\varepsilon_j^{\max} - V_j - \delta_j)}$  and  $s_x = 2\sqrt{a(E_x - \delta)}$ .

Besides light fragments, 60 nuclides up to  $^{28}\text{Mg}$  are considered, not only in their ground states but also in their excited states, are considered. The excited state is assumed to survive if its lifetime  $T_{1/2}$  is longer than the decay time, *i. e.*,  $T_{1/2}/\ln 2 > \hbar/\Gamma_j^*$ , where  $\Gamma_j^*$  is the emission width of the resonance calculated in the same manner as for ground state particle emission. The total emission width of an ejectile  $j$  is summed over its ground state and all its excited states which satisfy the above condition.

## 29.4 Nuclear fission

The fission decay channel (only for nuclei with  $A > 65$ ) is taken into account as a competitor for fragment and photon evaporation channels.

### 29.4.1 The fission total probability

The fission probability (per unit time)  $W_{fis}$  in the Bohr and Wheeler theory of fission [BW39] is proportional to the level density  $\rho_{fis}(T)$  (approximation Eq. (29.3)) is used) at the saddle point, *i.e.*

$$\begin{aligned}
 W_{fis} &= \frac{1}{2\pi\hbar\rho_{fis}(E^*)} \int_0^{E^* - B_{fis}} \rho_{fis}(E^* - B_{fis} - T)dT \\
 &= \frac{1 + (C_f - 1)\exp(C_f)}{4\pi a_{fis} \exp(2\sqrt{aE^*})},
 \end{aligned}$$

where  $B_{fis}$  is the fission barrier height. The value of  $C_f = 2\sqrt{a_{fis}(E^* - B_{fis})}$  and  $a$ ,  $a_{fis}$  are the level density parameters of the compound and of the fission saddle point nuclei, respectively.

The value of the level density parameter is large at the saddle point, when excitation energy is given by initial excitation energy minus the fission barrier height, than in the ground state, *i. e.*  $a_{fis} > a$ .  $a_{fis} = 1.08a$  for  $Z < 85$ ,  $a_{fis} = 1.04a$  for  $Z \geq 89$  and  $a_f = a[1.04 + 0.01(89. - Z)]$  for  $85 \leq Z < 89$  is used.

## 29.4.2 The fission barrier

The fission barrier is determined as difference between the saddle-point and ground state masses.

We use simple semiphenomenological approach was suggested by Barashenkov and Gereghi [BITG73]. In their approach fission barrier  $B_{fis}(A, Z)$  is approximated by

$$B_{fis} = B_{fis}^0 + \Delta_g + \Delta_p.$$

The fission barrier height  $B_{fis}^0(x)$  varies with the fissility parameter  $x = Z^2/A$ .  $B_{fis}^0(x)$  is given by

$$B_{fis}^0(x) = 12.5 + 4.7(33.5 - x)^{0.75}$$

for  $x \leq 33.5$  and

$$B_{fis}^0(x) = 12.5 - 2.7(x - 33.5)^{2/3}$$

for  $x > 33.5$ . The  $\Delta_g = \Delta M(N) + \Delta M(Z)$ , where  $\Delta M(N)$  and  $\Delta M(Z)$  are shell corrections for Cameron's liquid drop mass formula [Cam57, Cam58] and the pairing energy corrections:  $\Delta_p = 1$  for odd-odd nuclei,  $\Delta_p = 0$  for odd-even nuclei,  $\Delta_p = 0.5$  for even-odd nuclei and  $\Delta_p = -0.5$  for even-even nuclei.

## 29.5 Photon evaporation

Photon evaporation may be simulated as a continuum gamma transition using a dipole approximation or via discrete gamma transitions using an evaluated database of nuclear gamma transitions.

### 29.5.1 Computation of probability

As the first approximation we assume that dipole  $E1$ -transitions is the main source of  $\gamma$ -quanta from highly-excited nuclei [IMB+92]. The probability to evaporate  $\gamma$  in the energy interval  $(\epsilon_\gamma, \epsilon_\gamma + d\epsilon_\gamma)$  per unit of time is given

$$W_\gamma(\epsilon_\gamma) = \frac{1}{\pi^2(\hbar c)^3} \sigma_\gamma(\epsilon_\gamma) \frac{\rho(E^* - \epsilon_\gamma)}{\rho(E^*)} \epsilon_\gamma^2, \quad (29.5)$$

where  $\sigma_\gamma(\epsilon_\gamma)$  is the inverse (absorption of  $\gamma$ ) reaction cross section,  $\rho$  is a nucleus level density is defined by Eq.(29.3).

The photoabsorption reaction cross section is given by the expression

$$\sigma_\gamma(\epsilon_\gamma) = \frac{\sigma_0 \epsilon_\gamma^2 \Gamma_R^2}{(\epsilon_\gamma^2 - E_{GDP}^2)^2 + \Gamma_R^2 \epsilon_\gamma^2},$$

where  $\sigma_0 = 2.5A$  mb,  $\Gamma_R = 0.3E_{GDP}$  and  $E_{GDP} = 40.3A^{-1/5}$  MeV are empirical parameters of the giant dipole resonance [IMB+92]. The total radiation probability is

$$W_\gamma = \frac{1}{\pi^2(\hbar c)^3} \int_0^{E^*} \sigma_\gamma(\epsilon_\gamma) \frac{\rho(E^* - \epsilon_\gamma)}{\rho(E^*)} \epsilon_\gamma^2 d\epsilon_\gamma.$$

The integration is performed numerically. The energy of  $\gamma$ -quantum is sampled according to the Eq.(29.5) distribution.

## 29.5.2 Discrete photon evaporation

The last step of evaporation cascade consists of evaporation of photons with discrete energies. The competition between photons and fragments as well as giant resonance photons is neglected at this step. We consider the discrete E0, E1, M1, E2, M2, E3, M3 (including possible mixing) photon transitions from tabulated isotopes. Angular-correlated gamma-emission can be performed (if enabled). There are a large number of isotopes [had] with the experimentally measured excited level energies, spins, parities and relative transitions probabilities. This information is uploaded for each excited state in run time when the corresponding excited state is first created.

Transition information is also included for floating levels when available at [had]. Discrete photon evaporation also takes place between floating states from the same floating band. When the lowest floating state of a band is reached the nucleus is set to its ground state.

The list of isotopes included in the photon evaporation data base has been extended from  $A \leq 250$  to  $A \leq 294$ . The highest atomic number included is  $Z = 117$  (this ensures that Americium sources can now be simulated). For the heaviest of isotopes, in the so-called Super Heavy Elements region, the included files contain only placeholder values.

## 29.5.3 Internal conversion electron emission

An important competitive channel to photon emission is internal conversion. To take this into account, the photon evaporation database was extended to include internal conversion coefficients.

The database employ for this is the same as for *discrete.photon.evaporation*. If total internal conversion coefficient is not 0, partial conversion probabilities for K, L1, L2, L3, M1, M2, M3, M4, M5 and N+ respectively are included in the database. These coefficients are normalised to 1.0.

The calculation of the Internal Conversion Coefficients (ICCs) is done by a cubic spline interpolation of tabulated data for the corresponding transition energy. These ICC tables, which we shall label Band [BT78, BTL76], Rösel [RFAP78] and Hager-Seltzer [HS68], are widely used and were provided in electronic format by staff at LBNL. The reliability of these tabulated data has been reviewed in Ref. [RD00]. From tests carried out on these data we find that the ICCs calculated from all three tables are comparable within a 10% uncertainty, which is better than what experimental measurements are reported to be able to achieve.

The range in atomic number covered by these tables is Band:  $1 \leq Z \leq 80$ ; Rösel:  $30 \leq Z \leq 104$  and Hager-Seltzer:  $3, 6, 10, 14 \leq Z \leq 103$ . For simplicity and taking into account the completeness of the tables, we have used the Band table for  $Z \leq 80$  and Rösel for  $81 \leq Z \leq 98$ .

The Band table provides a higher resolution of the ICC curves used in the interpolation and covers ten multipolarities for all elements up to  $Z = 80$ , but it only includes ICCs for shells up to M5. In order to calculate the ICC of the N+ shell, the ICCs of all available M shells are added together and the total divided by 3. This is the scheme adopted in the LBNL ICC calculation code when using the Band table. The Rösel table includes ICCs for all shells in every atom and for  $Z > 80$  the N+ shell ICC is calculated by adding together the ICCs of all shells above M5. In this table only eight multipolarities have ICCs calculated for.

For the production of an internal conversion electron, the energy of the transition must be at least the binding energy of the shell the electron is being released from. The binding energy corresponding to the various shells in all isotopes used in the ICC calculation has been taken from the GEANT4 file G4AtomicShells.hh.

The ENSDF data provides information on the multipolarity of the transition. The ICCs included in the photon evaporation data base refer to the multipolarity indicated in the ENSDF file for that transition. Only one type of mixed multipolarity is considered (M1+E2) and whenever the mixing ratio is provided in the ENSDF file, it is used to calculate the ICCs corresponding to the mixed multipolarity according to the formula:

- fraction in  $M1 = 1/(1 + \delta^2)$
- fraction in  $E2 = \delta^2/(1 + \delta^2)$

where  $\delta$  is the mixing ratio.

## 29.6 Sampling procedure

The evaporation model algorithm consists from repeating steps on decay channels. The stack of excited nuclear fragments is created and initial excited fragment is stored there. For each fragment from the stack decay chain is sampled via loop of actions:

1. switch to the next excited fragment in the stack;
2. check if Fermi break-up model [FBU] is applicable and apply this model if it is the case;
3. sort out decay products between store of excited fragments and the list of final products;
4. if Fermi break up is not applicable compute probabilities of all evaporation channels;
5. if computed probability of a decay is not zero randomly select of a break-up channel and sample final state for the selected channel;
6. if computed probability of a decay is zero and the fragment is not known in isotope table try to apply a simplified decay method which may provide known isotopes in the final state;
7. if computed probability is zero and simplified decay method is not applicable stop the evaporation loop and store residual fragment in the list of final products
8. sort out decay products between store of excited fragments and the list of final products;
9. continue the main loop from (1).



## FISSION MODEL

### 30.1 Reaction initial state.

The GEANT4 fission model is capable to predict final excited fragments as result of an excited nucleus symmetric or asymmetric fission. The fission process (only for nuclei with atomic number  $A \geq 65$ ) is considered as a competitor for evaporation process, when nucleus transits from an excited state to the ground state. Here we describe the final state generation. The calculation of the relative probability of fission with respect to the evaporation channels are described in the chapter concerning evaporation.

The initial information for calculation of fission decay consists from the atomic mass number  $A$ , charge  $Z$  of excited nucleus, its four momentum  $P_0$  and excitation energy  $U$ .

### 30.2 Fission process simulation.

#### 30.2.1 Atomic number distribution of fission products.

As follows from experimental data [VR73] mass distribution of fission products consists of the symmetric and the asymmetric components:

$$F(A_f) = F_{sym}(A_f) + \omega F_{asym}(A_f),$$

where  $\omega(U, A, Z)$  defines relative contribution of each component and it depends from excitation energy  $U$  and  $A, Z$  of fissioning nucleus. It was found in [eal93] that experimental data can be approximated with a good accuracy, if one take

$$F_{sym}(A_f) = \exp \left[ -\frac{(A_f - A_{sym})^2}{2\sigma_{sym}^2} \right]$$

and

$$\begin{aligned} F_{asym}(A_f) &= \exp \left[ -\frac{(A_f - A_2)^2}{2\sigma_2^2} \right] + \exp \left[ -\frac{A_f - (A - A_2)^2}{2\sigma_2^2} \right] + \\ &+ C_{asym} \left\{ \exp \left[ -\frac{(A_f - A_1)^2}{2\sigma_1^2} \right] + \exp \left[ -\frac{A_f - (A - A_1)^2}{2\sigma_2^2} \right] \right\}, \end{aligned}$$

where  $A_{sym} = A/2$ ,  $A_1$  and  $A_2$  are the mean values and  $\sigma_{sym}^2$ ,  $\sigma_1^2$  and  $\sigma_2^2$  are dispersion of the Gaussians respectively. From an analysis of experimental data [eal93] the parameter  $C_{asym} \approx 0.5$  was defined and the next values for dispersions:

$$\sigma_{sym}^2 = \exp(0.00553U + 2.1386),$$

where  $U$  in MeV,

$$2\sigma_1 = \sigma_2 = 5.6 \text{ MeV}$$

for  $A \leq 235$  and

$$2\sigma_1 = \sigma_2 = 5.6 + 0.096(A - 235) \text{ MeV}$$

for  $A > 235$  were found.

The weight  $\omega(U, A, Z)$  was approximated as follows

$$\omega = \frac{\omega_a - F_{asym}(A_{sym})}{1 - \omega_a F_{sym}((A_1 + A_2)/2)}.$$

The values of  $\omega_a$  for nuclei with  $96 \geq Z \geq 90$  were approximated by

$$\omega_a(U) = \exp(0.538U - 9.9564)$$

for  $U \leq 16.25$  MeV,

$$\omega_a(U) = \exp(0.09197U - 2.7003)$$

for  $U > 16.25$  MeV and

$$\omega_a(U) = \exp(0.09197U - 1.08808)$$

for  $Z = 89$ . For nuclei with  $Z \leq 88$  the authors of [eal93] constructed the following approximation:

$$\omega_a(U) = \exp[0.3(227 - a)] \exp\{0.09197[U - (B_{fis} - 7.5)] - 1.08808\},$$

where for  $A > 227$  and  $U < B_{fis} - 7.5$  the corresponding factors occurring in exponential functions vanish.

### 30.2.2 Charge distribution of fission products.

At given mass of fragment  $A_f$  the experimental data [VR73] on the charge  $Z_f$  distribution of fragments are well approximated by Gaussian with dispersion  $\sigma_z^2 = 0.36$  and the average  $\langle Z_f \rangle$  is described by expression:

$$\langle Z_f \rangle = \frac{A_f}{A} Z + \Delta Z,$$

when parameter  $\Delta Z = -0.45$  for  $A_f \geq 134$ ,  $\Delta Z = -0.45(A_f - A/2)/(134 - A/2)$  for  $A - 134 < A_f < 134$  and  $\Delta Z = 0.45$  for  $A \leq A - 134$ .

After sampling of fragment atomic masses numbers and fragment charges, we have to check that fragment ground state masses do not exceed initial energy and calculate the maximal fragment kinetic energy

$$T^{max} < U + M(A, Z) - M_1(A_{f1}, Z_{f1}) - M_2(A_{f2}, Z_{f2}),$$

where  $U$  and  $M(A, Z)$  are the excitation energy and mass of initial nucleus,  $M_1(A_{f1}, Z_{f1})$ , and  $M_2(A_{f2}, Z_{f2})$  are masses of the first and second fragment, respectively.

### 30.2.3 Kinetic energy distribution of fission products.

We use the empirically defined [EKM85] dependence of the average kinetic energy  $\langle T_{kin} \rangle$  (in MeV) of fission fragments on the mass and the charge of a fissioning nucleus:

$$\langle T_{kin} \rangle = 0.1178Z^2/A^{1/3} + 5.8.$$

This energy is distributed differently in cases of symmetric and asymmetric modes of fission. It follows from the analysis of data [eal93] that in the asymmetric mode, the average kinetic energy of fragments is higher than that in the symmetric one by approximately 12.5 MeV. To approximate the average numbers of kinetic energies  $\langle T_{kin}^{sym} \rangle$  and  $\langle T_{kin}^{asym} \rangle$  for the symmetric and asymmetric modes of fission the authors of [eal93] suggested empirical expressions:

$$\langle T_{kin}^{sym} \rangle = \langle T_{kin} \rangle - 12.5W_{asim},$$

$$\langle T_{kin}^{asym} \rangle = \langle T_{kin} \rangle + 12.5W_{sim},$$

where

$$W_{sim} = \omega \int F_{sim}(A)dA / \int F(A)dA$$

and

$$W_{asim} = \int F_{asim}(A)dA / \int F(A)dA,$$

respectively. In the symmetric fission the experimental data for the ratio of the average kinetic energy of fission fragments  $\langle T_{kin}(A_f) \rangle$  to this maximum energy  $\langle T_{kin}^{max} \rangle$  as a function of the mass of a larger fragment  $A_{max}$  can be approximated by expressions

$$\langle T_{kin}(A_f) \rangle / \langle T_{kin}^{max} \rangle = 1 - k[(A_f - A_{max})/A]^2$$

for  $A_{sim} \leq A_f \leq A_{max} + 10$  and

$$\langle T_{kin}(A_f) \rangle / \langle T_{kin}^{max} \rangle = 1 - k(10/A)^2 - 2(10/A)k(A_f - A_{max} - 10)/A$$

for  $A_f > A_{max} + 10$ , where  $A_{max} = A_{sim}$  and  $k = 5.32$  and  $A_{max} = 134$  and  $k = 23.5$  for symmetric and asymmetric fission respectively. For both modes of fission the distribution over the kinetic energy of fragments  $T_{kin}$  is chosen Gaussian with their own average values  $\langle T_{kin}(A_f) \rangle = \langle T_{kin}^{sym}(A_f) \rangle$  or  $\langle T_{kin}(A_f) \rangle = \langle T_{kin}^{asym}(A_f) \rangle$  and dispersions  $\sigma_{kin}^2$  equal  $8^2$  MeV $^2$  or  $10^2$  MeV $^2$  for symmetrical and asymmetrical modes, respectively.

### 30.2.4 Calculation of the excitation energy of fission products.

The total excitation energy of fragments  $U_{frag}$  can be defined according to equation:

$$U_{frag} = U + M(A, Z) - M_1(A_{f1}, Z_{f1}) - M_2(A_{f2}, Z_{f2}) - T_{kin},$$

where  $U$  and  $M(A, Z)$  are the excitation energy and mass of initial nucleus,  $T_{kin}$  is the fragments kinetic energy,  $M_1(A_{f1}, Z_{f1})$ , and  $M_2(A_{f2}, Z_{f2})$  are masses of the first and second fragment, respectively.

The value of excitation energy of fragment  $U_f$  determines the fragment temperature ( $T = \sqrt{U_f/a_f}$ , where  $a_f \sim A_f$  is the parameter of fragment level density). Assuming that after disintegration fragments have the same temperature as initial nucleus than the total excitation energy will be distributed between fragments in proportion to their mass numbers one obtains

$$U_f = U_{frag} \frac{A_f}{A}.$$

### 30.2.5 Excited fragment momenta.

Assuming that fragment kinetic energy  $T_f = P_f^2 / (2(M(A_f, Z_f) + U_f))$  we are able to calculate the absolute value of fragment c.m. momentum

$$P_f = \frac{(M_1(A_{f1}, Z_{f1}) + U_{f1})(M_2(A_{f2}, Z_{f2}) + U_{f2})}{M_1(A_{f1}, Z_{f1}) + U_{f1} + M_2(A_{f2}, Z_{f2}) + U_{f2}} T_{kin}.$$

and its components, assuming fragment isotropical distribution.

## FERMI BREAK-UP MODEL

### 31.1 Fermi break-up simulation for light nuclei

For light nuclei the values of excitation energy per nucleon are often comparable with nucleon binding energy. Thus a light excited nucleus breaks into two or more fragments with branching given by available phase space. To describe a process of nuclear disassembling the so-called Fermi break-up model is formulated [Fer50], [Kre61], [EGKR69], [EpherreG67], [BBI+95]. This statistical approach was first used by Fermi [Fer50] to describe the multiple production in high energy nucleon collision. The GEANT4 Fermi break-up model is capable to predict final states as result of an excited nucleus with  $Z < 9$  and  $A < 17$  statistical break-up.

#### 31.1.1 Allowed channels

The channel will be allowed for decay, if the total kinetic energy  $E_{kin}$  of all fragments of the given channel at the moment of break-up is positive. This energy can be calculated according to equation:

$$E_{kin} = U + M(A, Z) - E_{Coulomb} - \sum_{b=1}^n (m_b + \epsilon_b), \quad (31.1)$$

$U$  is primary fragment excitation,  $m_b$  and  $\epsilon_b$  are masses and excitation energies of fragments, respectively,  $E_{Coulomb}$  is the Coulomb barrier for a given channel. It is approximated by

$$E_{Coulomb} = \frac{3 e^2}{5 r_0} \left( 1 + \frac{V}{V_0} \right)^{-1/3} \left( \frac{Z^2}{A^{1/3}} - \sum_{b=1}^n \frac{Z^2}{A_b^{1/3}} \right),$$

where  $V_0$  is the volume of the system corresponding to the normal nuclear matter density

$$V_0 = 4\pi R^3 / 3 = 4\pi r_0^3 A / 3,$$

where  $r_0 = 1.3$  fm is used. Free parameter of the model is the ratio of the effective volume  $V$  to the normal volume, currently

$$\kappa = \frac{V}{V_0} = 6.$$

### 31.1.2 Break-up probability

The total probability for nucleus to break-up into  $n$  components (nucleons, neutrons, tritons, alphas etc) in the final state is given by

$$W(E, n) = (V/\Omega)^{n-1} \rho_n(E),$$

where  $\rho_n(E)$  is the density of a number of final states,  $\Omega = (2\pi\hbar)^3$  is the normalization volume. The density  $\rho_n(E)$  can be defined as a product of three factors:

$$\rho_n(E) = M_n(E) S_n G_n.$$

The first one is the phase space factor defined as

$$M_n = \int_{-\infty}^{+\infty} \dots \int_{-\infty}^{+\infty} \delta \left( \sum_{b=1}^n \mathbf{p}_b \right) \delta \left( E - \sum_{b=1}^n \sqrt{p_b^2 + m_b^2} \right) \prod_{b=1}^n d^3 p_b, \quad (31.2)$$

where  $\mathbf{p}_b$  is fragment  $b$  momentum. The second one is the spin factor

$$S_n = \prod_{b=1}^n (2s_b + 1),$$

which gives the number of states with different spin orientations. The last one is the permutation factor

$$G_n = \prod_{j=1}^k \frac{1}{n_j!},$$

which takes into account identity of components in final state.  $n_j$  is a number of components of  $j$ - type particles and  $k$  is defined by  $n = \sum_{j=1}^k n_j$ .

In non-relativistic case (Eq. (31.4) the integration in Eq. (31.2) can be evaluated analitically (see e. g. [BaravsenkovBarbavsevB58]). The probability for a nucleus with energy  $E$  disassembling into  $n$  fragments with masses  $m_b$ , where  $b = 1, 2, 3, \dots, n$  equals

$$W(E_{kin}, n) = S_n G_n \left( \frac{V}{\Omega} \right)^{n-1} \left( \frac{1}{\sum_{b=1}^n m_b} \prod_{b=1}^n m_b \right)^{3/2} \frac{(2\pi)^{3(n-1)/2}}{\Gamma(3(n-1)/2)} E_{kin}^{3n/2-5/2}, \quad (31.3)$$

where  $\Gamma(x)$  is the gamma function.

### 31.1.3 Fragment characteristics

We take into account the formation of fragments in their ground and low-lying excited states, which are stable for nucleon emission. However, several unstable fragments with large lifetimes:  ${}^5\text{He}$ ,  ${}^5\text{Li}$ ,  ${}^8\text{Be}$ ,  ${}^9\text{B}$  etc. are also considered. Fragment characteristics  $A_b$ ,  $Z_b$ ,  $s_b$  and  $\epsilon_b$  are taken from [AS81, AS82, AS83, AS84, AS85, Err83, Err84]. Recently nuclear level energies were changed to be identical with nuclear levels in the gamma evaporation database (see Section [Photon evaporation](#)).

### 31.1.4 Sampling procedure

The nucleus break-up is described by the Monte Carlo (MC) procedure. We randomly (according to probability Eq. (31.3) and condition Eq. (31.1) select decay channel. Then for given channel we calculate kinematical quantities of each fragment according to  $n$ -body phase space distribution:

$$M_n = \int_{-\infty}^{+\infty} \dots \int_{-\infty}^{+\infty} \delta \left( \sum_{b=1}^n \mathbf{p}_b \right) \delta \left( \sum_{b=1}^n \frac{p_b^2}{2m_b} - E_{kin} \right) \prod_{b=1}^n d^3 p_b. \quad (31.4)$$

The Kopylov's sampling procedure [I70, Kop85, Kop73] is applied. The angular distributions for emitted fragments are considered to be isotropical.

---

CHAPTER  
THIRTYTWO

---

## MULTIFRAGMENTATION MODEL

### 32.1 Multifragmentation process simulation

The GEANT4 multifragmentation model is capable of predicting final states as result of an highly excited nucleus statistical break-up.

The initial information for calculation of multifragmentation stage consists from the atomic mass number  $A$ , charge  $Z$  of excited nucleus and its excitation energy  $U$ . At high excitation energies  $U/A > 3$  MeV the multifragmentation mechanism, when nuclear system can eventually breaks down into fragments, becomes the dominant. Later on the excited primary fragments propagate independently in the mutual Coulomb field and undergo de-excitation. Detailed description of multifragmentation mechanism and model can be found in review [BBI+95].

#### 32.1.1 Multifragmentation probability

The probability of a breakup channel  $b$  is given by the expression (in the so-called microcanonical approach [BBI+95, eal87]):

$$W_b(U, A, Z) = \frac{1}{\sum_b \exp[S_b(U, A, Z)]} \exp[S_b(U, A, Z)], \quad (32.1)$$

where  $S_b(U, A, Z)$  is the entropy of a multifragment state corresponding to the breakup channel  $b$ . The channels  $\{b\}$  can be parametrized by set of fragment multiplicities  $N_{A_f, Z_f}$  for fragment with atomic number  $A_f$  and charge  $Z_f$ . All partitions  $\{b\}$  should satisfy constraints on the total mass and charge:

$$\sum_f N_{A_f, Z_f} A_f = A$$

and

$$\sum_f N_{A_f, Z_f} Z_f = Z.$$

It is assumed [eal87] that thermodynamic equilibrium is established in every channel, which can be characterized by the channel temperature  $T_b$ .

The channel temperature  $T_b$  is determined by the equation constraining the average energy  $E_b(T_b, V)$  associated with partition  $b$ :

$$E_b(T_b, V) = U + E_{ground} = U + M(A, Z), \quad (32.2)$$

where  $V$  is the system volume,  $E_{ground}$  is the ground state (at  $T_b = 0$ ) energy of system and  $M(A, Z)$  is the mass of nucleus.

According to the conventional thermodynamical formulae the average energy of a partition  $b$  is expressed through the system free energy  $F_b$  as follows

$$E_b(T_b, V) = F_b(T_b, V) + T_b S_b(T_b, V). \quad (32.3)$$

Thus, if free energy  $F_b$  of a partition  $b$  is known, we can find the channel temperature  $T_b$  from Eqs.(32.2) and (32.3), then the entropy  $S_b = -dF_b/dT_b$  and hence, decay probability  $W_b$  defined by Eq.(32.1) can be calculated.

Calculation of the free energy is based on the use of the liquid-drop description of individual fragments [eal87]. The free energy of a partition  $b$  can be splitted into several terms:

$$F_b(T_b, V) = \sum_f F_f(T_b, V) + E_C(V),$$

where  $F_f(T_b, V)$  is the average energy of an individual fragment including the volume

$$F_f^V = [-E_0 - T_b^2/\epsilon(A_f)]A_f,$$

surface

$$F_f^{Sur} = \beta_0[(T_c^2 - T_b^2)/(T_c^2 + T_b^2)]^{5/4} A_f^{2/3} = \beta(T_b) A_f^{2/3}, \quad (32.4)$$

symmetry

$$F_f^{Sim} = \gamma(A_f - 2Z_f)^2/A_f,$$

Coulomb

$$F_f^C = \frac{3}{5} \frac{Z_f^2 e^2}{r_0 A_f^{1/3}} [1 - (1 + \kappa_C)^{-1/3}]$$

and translational

$$F_f^t = -T_b \ln(g_f V_f / \lambda_{T_b}^3) + T_b \ln(N_{A_f, Z_f}!)/N_{A_f, Z_f}$$

terms and the last term

$$E_C(V) = \frac{3}{5} \frac{Z^2 e^2}{R}$$

is the Coulomb energy of the uniformly charged sphere with charge  $Ze$  and the radius  $R = (3V/4\pi)^{1/3} = r_0 A^{1/3} (1 + \kappa_C)^{1/3}$ , where  $\kappa_C = 2$  [eal87].

Parameters  $E_0 = 16$  MeV,  $\beta_0 = 18$  MeV,  $\gamma = 25$  MeV are the coefficients of the Bethe-Weizsäcker mass formula at  $T_b = 0$ .  $g_f = (2S_f + 1)(2I_f + 1)$  is a spin  $S_f$  and isospin  $I_f$  degeneracy factor for fragment (fragments with  $A_f > 1$  are treated as the Boltzmann particles),  $\lambda_{T_b} = (2\pi h^2/m_N T_b)^{1/2}$  is the thermal wavelength,  $m_N$  is the nucleon mass,  $r_0 = 1.17$  fm,  $T_c = 18$  MeV is the critical temperature, which corresponds to the liquid-gas phase transition.  $\epsilon(A_f) = \epsilon_0[1 + 3/(A_f - 1)]$  is the inverse level density of the mass  $A_f$  fragment and  $\epsilon_0 = 16$  MeV is considered as a variable model parameter, whose value depends on the fraction of energy transferred to the internal degrees of freedom of fragments [eal87]. The free volume  $V_f = \kappa V = \kappa \frac{4}{3} \pi r_0^3 A$  available to the translational motion of fragment, where  $\kappa \approx 1$  and its dependence on the multiplicity of fragments was taken from [eal87]:

$$\kappa = \left[ 1 + \frac{1.44}{r_0 A^{1/3}} (M^{1/3} - 1) \right]^3 - 1.$$

For  $M = 1$   $\kappa = 0$ .

The light fragments with  $A_f < 4$ , which have no excited states, are considered as elementary particles characterized by the empirical masses  $M_f$ , radii  $R_f$ , binding energies  $B_f$ , spin degeneracy factors  $g_f$  of ground states. They contribute to the translation free energy and Coulomb energy.

### 32.1.2 Direct simulation of the low multiplicity multifragment disintegration

At comparatively low excitation energy (temperature) system will disintegrate into a small number of fragments  $M \leq 4$  and number of channel is not huge. For such situation a direct (microcanonical) sorting of all decay channels can be performed. Then, using Eq.(32.1), the average multiplicity value  $\langle M \rangle$  can be found. To check that we really have the situation with the low excitation energy, the obtained value of  $\langle M \rangle$  is examined to obey the inequality  $\langle M \rangle \leq M_0$ , where  $M_0 = 3.3$  and  $M_0 = 2.6$  for  $A \sim 100$  and for  $A \sim 200$ , respectively [eal87]. If the discussed inequality is fulfilled, then the set of channels under consideration is believed to be able for a correct description of the break up. Then using calculated according Eq.(32.1) probabilities we can randomly select a specific channel with given values of  $A_f$  and  $Z_f$ .

### 32.1.3 Fragment multiplicity distribution

The individual fragment multiplicities  $N_{A_f, Z_f}$  in the so-called macrocanonical ensemble [BBI+95] are distributed according to the Poisson distribution:

$$P(N_{A_f, Z_f}) = \exp(-\omega_{A_f, Z_f}) \frac{\omega_{A_f, Z_f}^{N_{A_f, Z_f}}}{N_{A_f, Z_f}!} \quad (32.5)$$

with mean value  $\langle N_{A_f, Z_f} \rangle = \omega_{A_f, Z_f}$  defined as

$$\langle N_{A_f, Z_f} \rangle = g_f A_f^{3/2} \frac{V_f}{\lambda_{T_b}^3} \exp \left[ \frac{1}{T_b} (F_f(T_b, V) - F_f^t(T_b, V) - \mu A_f - \nu Z_f) \right], \quad (32.6)$$

where  $\mu$  and  $\nu$  are chemical potentials. The chemical potential are found by substituting Eq.(32.6) into the system of constraints:

$$\sum_f \langle N_{A_f, Z_f} \rangle A_f = A$$

and

$$\sum_f \langle N_{A_f, Z_f} \rangle Z_f = Z \quad (32.7)$$

and solving it by iteration.

### 32.1.4 Atomic number distribution of fragments

Fragment atomic numbers  $A_f > 1$  are also distributed according to the Poisson distribution [BBI+95] (see Eq.(32.5) with mean value  $\langle N_{A_f} \rangle$  defined as

$$\langle N_{A_f} \rangle = A_f^{3/2} \frac{V_f}{\lambda_{T_b}^3} \exp \left[ \frac{1}{T_b} (F_f(T_b, V) - F_f^t(T_f, V) - \mu A_f - \nu \langle Z_f \rangle) \right],$$

where calculating the internal free energy  $F_f(T_b, V) - F_f^t(T_b, V)$  one has to substitute  $Z_f \rightarrow \langle Z_f \rangle$ . The average charge  $\langle Z_f \rangle$  for fragment having atomic number  $A_f$  is given by

$$\langle Z_f(A_f) \rangle = \frac{(4\gamma + \nu) A_f}{8\gamma + 2[1 - (1 + \kappa)^{-1/3}] A_f^{2/3}}.$$

### 32.1.5 Charge distribution of fragments

At given mass of fragment  $A_f > 1$  the charge  $Z_f$  distribution of fragments are described by Gaussian

$$P(Z_f(A_f)) \sim \exp \left[ -\frac{(Z_f(A_f) - \langle Z_f(A_f) \rangle)^2}{2(\sigma_{Z_f}(A_f))^2} \right]$$

with dispersion

$$\sigma_{Z_f(A_f)} = \sqrt{\frac{A_f T_b}{8\gamma + 2[1 - (1 + \kappa)^{-1/3}]A_f^{2/3}}} \approx \sqrt{\frac{A_f T_b}{8\gamma}}.$$

and the average charge  $\langle Z_f(A_f) \rangle$  defined by Eq. (32.7).

### 32.1.6 Kinetic energy distribution of fragments

It is assumed [eal87] that at the instant of the nucleus break-up the kinetic energy of the fragment  $T_{kin}^f$  in the rest of nucleus obeys the Boltzmann distribution at given temperature  $T_b$ :

$$\frac{dP(T_{kin}^f)}{dT_{kin}^f} \sim \sqrt{T_{kin}^f} \exp(-T_{kin}^f/T_b).$$

Under assumption of thermodynamic equilibrium the fragment have isotropic velocities distribution in the rest frame of nucleus. The total kinetic energy of fragments should be equal  $\frac{3}{2}MT_b$ , where  $M$  is fragment multiplicity, and the total fragment momentum should be equal zero. These conditions are fullfilled by choosing properly the momenta of two last fragments.

The initial conditions for the divergence of the fragment system are determined by random selection of fragment coordinates distributed with equal probabilities over the break-up volume  $V_f = \kappa V$ . It can be a sphere or prolonged ellipsoid. Then Newton's equations of motion are solved for all fragments in the self-consistent time-dependent Coulomb field [eal87]. Thus the asymptotic energies of fragments determined as result of this procedure differ from the initial values by the Coulomb repulsion energy.

### 32.1.7 Calculation of the fragment excitation energies

The temparature  $T_b$  determines the average excitation energy of each fragment:

$$U_f(T_b) = E_f(T_b) - E_f(0) = \frac{T_b^2}{\epsilon_0} A_f + \left[ \beta(T_b) - T_b \frac{d\beta(T_b)}{dT_b} - \beta_0 \right] A_f^{2/3},$$

where  $E_f(T_b)$  is the average fragment energy at given temperature  $T_b$  and  $\beta(T_b)$  is defined in Eq.(32.4). There is no excitation for fragment with  $A_f < 4$ , for  ${}^4\text{He}$  excitation energy was taken as  $U_{}^4\text{He} = 4T_b^2/\epsilon_o$ .

---

CHAPTER  
THIRTYTHREE

---

## ABLA++ EVAPORATION/FISSION MODEL

### 33.1 Introduction

The ABLA++ evaporation model describes the de-excitation of hot remnants by taking their characteristic parameters, such as the excitation energy, mass number, atomic number and nucleus spin, as input. This model is a translation to C++ of the fortran code ABLA07 developed at GSI by Kelic and collaborators [KAH08]. Both codes contain the same physics and input parameters [RSCD+22], even if ABLA++ has been recently extended to the strange sector by including the emission of  $\Lambda$  particles and the formation of hypernuclei, see Refs. [RSDH+18] and [RSCD+23].

### 33.2 Evaporation

These models calculate the probabilities for emitting  $\gamma$ -rays, neutrons, light-charged particles, and intermediate-mass fragments (IMFs) according to Weisskopf's formalism [WE40]. For a more realistic description of the deexcitation, the separation energies and the Coulomb barriers for charged particles are also considered according to the atomic mass evaluation AME 2020 [HWK+21] and the Bass potential [Bas80], respectively. In the case of hyper-remnants, the  $\Lambda$  separation energies are calculated according to the equation found by Samanta [SCB06].

The probabilities for emission of particle type  $j$  are calculated using formula ``:

$$W_j(N, Z, E) = \frac{\Gamma_j(N, Z, E)}{\sum_k \Gamma_k(N, Z, E)}, \quad (33.1)$$

where  $\Gamma_j$  is emission width for particle  $j$ ,  $N$  is neutron number,  $Z$  charge number and  $E$  excitation energy. Possible emitted particles are  $\gamma$ ,  $n$ ,  $\Lambda$ ,  $p$ ,  $d$ ,  $t$ ,  ${}^3He$ ,  $\alpha$  and IMFs. Emission widths are calculated using the following formula:

$$\Gamma_j = \frac{1}{2\pi\rho_c(E)} \frac{4m_j R^2}{\hbar^2} T_j^2 \rho_j(E - S_j - B_j), \quad (33.2)$$

where  $\rho_c(E)$  and  $\rho_j(E - S_j - B_j)$  are the level densities of the compound nucleus and the exit channel, respectively.  $B_j$  is the height of the Coulomb barrier,  $S_j$  the separation energy,  $R$  is the radius and  $T_j$  the temperature of the remnant nucleus after emission and  $m_j$  the mass of the emitted particle. For  $\gamma$  emission, see Ref. [KAH08]. De-excitation by fission is also possible if the excitation energy is higher than the fission barrier height.

The summary of GEANT4 ABLA++ implementation is represented in Table 33.1.

Table 33.1: ABLA++ (located in the GEANT4 directory source/processes/hadronic/models/abla) feature summary.

Requirements	
External data file	G4ABLA3.3 available at GEANT4 site
Environment variable for external data	G4ABLADATA
Usage	
Physics list	No default physics list, see Section <a href="#">How to use ABLA++</a> .
Interfaces	
G4InclAblaCascadeInterface	h-A
G4InclAblaLightIonInterface	A-A
Supported input	Excited nuclei
Output particles	$\gamma$ , $n$ , $\Lambda$ , $p$ , $d$ , $t$ , $^3He$ , $\alpha$ and IMFs ( $2 < Z < 6$ ) fission products residual nuclei multifragmentation products hyper-fission products and hyper-residues
Features	evaporation of $\gamma$ , $n$ , $\Lambda$ , $p$ , $d$ , $t$ , $^3He$ , $\alpha$ intermediate-mass fragments (IMFs) fission and multifragmentation
Misc.	5 classes, $\sim 12k$ lines $0.9 < \text{speed C++/F77} < 1.1$
References	Key reference: <a href="#">[RSCD+22]</a> , see also <a href="#">[KAH08]</a>

### 33.3 Level densities

The nuclear level density is calculated according to the Fermi gas model as a function of the excitation energy  $E^*$  and the angular momentum  $J$ , and is expressed as:

$$\rho(E^*, J) = \frac{J + 1/2}{\sqrt{2\pi}\sigma^3} e^{-\frac{J(J+1)}{2\sigma^2}} \frac{\sqrt{\pi}}{12} \frac{e^S}{\tilde{a}^{1/4} E^{*5/4}} \quad (33.3)$$

where  $\sigma^2$  is the spin cut-off factor given by  $\sigma^2 = \frac{\Im T}{\hbar^2}$  with  $\Im$  as the moment of inertia of the nucleus and  $T$  the nuclear temperture,  $E^*$  is the excitacion energy of the system,  $S$  is the entropy and  $\tilde{a}$  is the level-density parameter in units of  $\text{MeV}^{-1}$ . Generally, this last parameter can be written as:

$$\tilde{a} = \alpha_v A + \alpha_s B_s \cdot A^{2/3} + \alpha_k B_k A^{1/3} \quad (33.4)$$

where  $A$  is the mass of the nucleus and  $\alpha_v$ ,  $\alpha_s$  and  $\alpha_k$  are the coefficients that correspond to the volume, surface and curvature components of the single-particle level densities, respectively. The values of these coefficients were calculated by Ignatyuk [\[Ign00\]](#) ( $\alpha_v = 0.095$ ,  $\alpha_s = 0.073$ , and  $\alpha_k = 0$  in units of  $\text{MeV}^{-1}$ ) and are the most-frequently used in model calculations. In the equation,  $B_s$  represents the ratio between the surface of the deformed nucleus and a spherical nucleus while  $B_k$  corresponds to the ratio between the integrated curvature of the deformed nucleus and a spherical nucleus.

In order to account for the role of collective excitations in the decay of excited compound nuclei, the level density of Eq. (33.3) is corrected using the vibrational and rotational enhancement factors according to:

$$\rho(E, J) = K_{vib} K_{rot} \rho(E, J)_{int} \quad (33.5)$$

where  $\rho(E, J)_{int}$  is given by Eq. (33.3),  $K_{vib}$  represents the vibrational enhancement factor and  $K_{rot}$  corresponds to the rotational factor. Both are calculated according to Ref. [\[JdJC+98\]](#).

## 33.4 Fission

The fission decay width is described by the Bohr-Wheeler transition-state model [BW39] following the formulation given by Moretto [Mor75]:

$$\Gamma_f^{BW} = \frac{T}{2\pi} \frac{\rho_{sp}(E - B_f, J)}{\rho_{gs}(E, J)};$$

where  $\rho_{sp}(E - B_f, J)$  and  $\rho_{gs}(E, J)$  are the level densities at the saddle-point and ground-state configurations, respectively, and  $B_f$  is the fission-barrier height obtained from the finite-range liquid-drop model of Sierk [Sie86] taking into account the influence of angular momentum and considering the ground-state shell effects [MNMS95].

The diffusion process above the fission barrier is described by the Fokker-Planck equation, where the quasi-stationary solution of this equation was introduced by Kramers [Kra40] and provides a reduction of the fission decay width due to dissipation:

$$\Gamma_f^K = \left[ \sqrt{1 + \left( \frac{\beta}{2\omega_0} \right)^2} - \frac{\beta}{2\omega_0} \right] \Gamma_f^{BW}.$$

Here  $\beta$  is the reduced dissipation coefficient and  $\omega_0$  is the frequency of the harmonic oscillator describing the inverted potential at the fission barrier, calculated according to the liquid-drop model. This equation provides the asymptotic value of the fission decay width.

The analytical approximation to the solution of the one-dimensional Fokker-Planck equation for the time-dependent fission-decay width was developed by Jurado and collaborators in Refs. [JSB03, JSS+05], using a Gaussian distribution centred at the spherical shape as initial condition. The mean values and the widths of the initial Gaussian distributions in space and momentum are given by the entrance channel. In this approximation, the time-dependent fission-decay width is defined as:

$$\Gamma_f(t) = \frac{W_n(x = x_b; t, \beta)}{W_n(x = x_b; t \rightarrow \infty, \beta)} \Gamma_f^K;$$

where  $W(x; t, \beta)$  is the normalized probability distribution at the saddle-point deformation  $x_b$ . The saddle-point deformations are calculated according to Ref. [HM88].

The description of the properties of the fission fragments is based on a semi-empirical model developed in Refs. [BGdJ+98, KAB+02]. The fission channels are explained by the macroscopic and microscopic properties of the potential-energy landscape that is determined by the characteristics of the fissioning nucleus at the saddle point. In particular, the stiffness of the macroscopic potential along the mass-asymmetry degree of freedom is obtained from the systematics of the width of mass distributions measured in Ref. [RIO97]. The neutron-to-proton ratio ( $N/Z$ ) of the fission fragments is assumed to be given by the unchanged-charge distribution (UCD). This ( $N/Z$ ) ratio is modified by the charge polarization effect calculated in terms of the liquid-drop model (LDM) by assuming a two touching spheres configuration at the scission point, and by the evaporation of particles during the descent from saddle to scission [RSCD+22]. Finally, at the scission point, the two fission fragments are characterized by their atomic numbers  $Z_{1,2}$ , mass numbers  $A_{1,2}$ , kinetic energies  $E_{kin}^{1,2}$ , and excitation energies  $E_{exc}^{1,2}$ . After the formation of the two fission fragments, their corresponding deexcitation chains are followed until their excitation energies fall below the lowest particle-emission threshold.

According to the statistical model, the widths of the mass and atomic-number distributions of the fission fragments ( $\sigma_A$  and  $\sigma_Z$  respectively) are related to the temperature at the saddle point, following the equations:

$$\sigma_A^2 = \frac{A_{fiss}^2 T_{sad}}{16d^2V/d\nu^2} \quad \text{and} \quad \sigma_Z^2 = \frac{Z_{fiss}^2 T_{sad}}{16d^2V/d\nu^2} \quad (33.6)$$

where  $d^2V/d\nu^2$  is the second derivative of the potential with respect to the mass-asymmetry degree of freedom at the saddle point  $\nu = (4/A_{fiss})/(M - A_{fiss}/2)$ .  $A_{fiss}$  and  $Z_{fiss}$  correspond to the mass and atomic numbers of the fissioning nucleus, respectively, and  $M$  represents the mass number of the corresponding fragment.

The kinetic energies of the fission fragments are calculated according to the semi-statistical scission point model of Wilkins and collaborators [WSC76]. The main contribution to the total kinetic energies released in the fission process comes from the Coulomb repulsion of the two fission fragments at the scission point and, therefore, this total kinetic energy is given by:

$$TKE \sim \frac{Z_1 Z_2}{D} \quad (33.7)$$

where  $Z_1$  and  $Z_2$  refer to the atomic number of the two fission fragments, and  $D$  is the distance between the two uniformly-charged spheroids representing the fission fragments. This distance is parametrized as:

$$D = r_0 A_1^{*1/3} \left( 1 + \frac{2\beta_1}{3} \right) + r_0 A_2^{*1/3} \left( 1 + \frac{2\beta_2}{3} \right) + d \quad (33.8)$$

where  $A_1^*$  and  $A_2^*$  refer to the mass number of the two fission fragments at the scission point,  $\beta_1$  and  $\beta_2$  are their quadrupole deformations at the scission point,  $r_0$  is the fermi radius, and  $d$  is the distance between the tips of the two fission fragments. Here, we take  $d = 2$  fm.

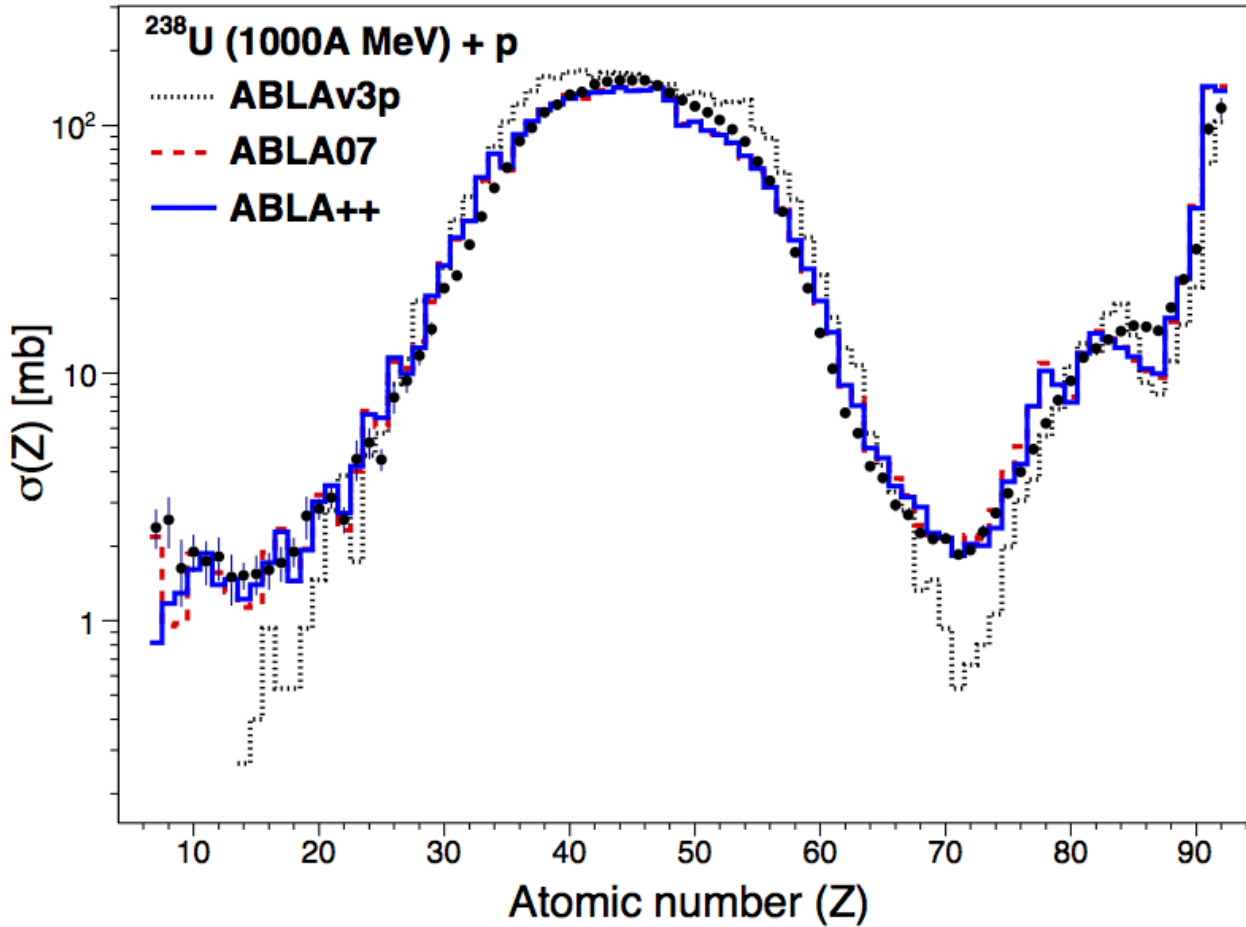


Fig. 33.1: ABLA calculations performed with the fortran version (ABLA07), the new one in C++ (ABLA++) and the previous version (ABLAv3p) are compared with the atomic-number distribution of fission and evaporation residues produced in the reactions  $p + {}^{238}\text{U}$  at 1A GeV.

## 33.5 Multifragmentation

If the excitation energy acquired during the first, collision, stage is high enough, the increase of volume has a dramatic consequence: The nucleus enters the spinodal region [CCR04] characterized by negative incompressibility. In this region, an increase in the system volume due to expansion is connected with the increase in pressure, and, consequently, any local fluctuation in density is strongly amplified leading to a mixed phase consisting of droplets represented by a small amount of light nuclei at normal nuclear density, and the nuclear gas represented by individual nucleons. This process is often called “break-up”. The fragments formed in this process undergo deexcitation process and cool down. What is finally experimentally observed are the cold fragments, normally called IMFs. The entire multifragmentation process is scientifically very interesting for its relation to the equation-of-state of nuclear matter, in particular to the liquid-gas phase transition.

The starting point of the multifragmentation stage in ABLA++ is a hot nuclear system –so-called “spectator”, leftover of the initial collision stage. We assume that, if the excitation energy per nucleon of the spectator exceeds a limiting value [KAH08], the system undergoes the break-up stage; otherwise we assume that it will directly de-excite through sequential evaporation and/or fission.

About the limiting excitation energy per nucleon, two options are possible in ABLA++. The default option is a mass-dependent value of the limiting excitation energy, deduced from the mass dependence of the temperature in the plateau of the caloric curve as pointed out by Natowitz in [NWH+02]. Another possible option is to assume that the limiting excitation energy per nucleon is constant for all nuclei; its value is fixed to 5.5 MeV.

The comparison of the new version of ABLA07 in C++ with the previous versions is shown in Fig. 33.1 for the reaction p +  $^{238}\text{U}$  at 1A GeV. The calculations are also compared with the experimental data obtained at GSI [RAB+06]. This benchmark demonstrates that the new version ABLA++ reproduces the results obtained with the fortran code and confirms also the improvement with respect to the old version ABLAv3p.

## 33.6 External data file required

ABLA++ needs specific data files. These files contain ABLA++ shell corrections and nuclear masses. To enable this data set, the environment variable G4ABLADATA needs to be set, and the relevant data should be installed on your machine. You can download them from the GEANT4 web site or you can have CMake download them for you during installation. For GEANT4 11.2 we use the G4ABLA3.3 data files.

## 33.7 How to use ABLA++

None of the stock physics lists use the ABLA++ model by default. It should also be understood that ABLA++ is a nuclear de-excitation model and must be used as a secondary reaction stage; the first, dynamical reaction stage must be simulated using some other model, typically an intranuclear-cascade (INC) model. The coupling of the ABLA++ to the INCL++ model (Chapter *INCL++: the Liège Intranuclear Cascade Model*) has been somewhat tested and seems to work, but no extensive benchmarking has been realized at the time of writing. Coupling to the Binary-Cascade model (Chapter *The Binary Cascade Model*) should in principle be possible, but has never been tested. The technique to realize the coupling is described in the Application Developer Guide.



---

CHAPTER  
**THIRTYFOUR**

---

## QUANTUM MOLECULAR DYNAMICS FOR HEAVY IONS

QMD is the quantum extension of the classical molecular dynamics model and is widely used to analyze various aspects of heavy ion reactions, especially for many-body processes, and in particular the formation of complex fragments. In the previous section, we mentioned several similar and dissimilar points between Binary Cascade and QMD. There are three major differences between them:

1. The definition of a participant particle,
2. The potential term in the Hamiltonian, and
3. Participant-participant interactions.

At first, we will explain how they are each treated in QMD. The entire nucleons in the target and projectile nucleus are considered as participant particles in the QMD model. Therefore each nucleon has its own wave function, however the total wave function of a system is still assumed as the direct product of them. The potential terms of the Hamiltonian in QMD are calculated from the entire relation of particles in the system, in other words, it can be regarded as self-generating from the system configuration. On the contrary to Binary Cascade which tracks the participant particles sequentially, all particles in the system are tracked simultaneously in QMD. Along with the time evolution of the system, its potential is also dynamically changed. As there is no criterion between participant particle and others in QMD, participant-participant scatterings are naturally included. Therefore QMD accomplishes more detailed treatments of the above three points, however with a cost of computing performance.

### 34.1 Equations of Motion

The basic assumption of QMD is that each nucleon state is represented by a Gaussian wave function of width  $L$ ,

$$\varphi_i(\mathbf{r}) \equiv \frac{1}{(2\pi L)^{3/4}} \exp\left(-\frac{(r - r_i)^2}{4L} + \frac{i}{\hbar} \mathbf{r} \cdot \mathbf{p}_i\right)$$

where  $r_i$  and  $p_i$  represent the center values of position and momentum of the  $i^{\text{th}}$  particle. The total wave function is assumed to be a direct product of them,

$$\Psi(\mathbf{r}_1, \mathbf{r}_2, \dots, \mathbf{r}_N) \equiv \prod_i \varphi_i(r_i).$$

Equations of the motion of particle derived on the basis of the time dependent variation principle as

$$\dot{r}_i = \frac{\partial H}{\partial p_i}, \quad \dot{p}_i = -\frac{\partial H}{\partial r_i}$$

where  $H$  is the Hamiltonian which consists particle energy including mass energy and the energy of the two-body interaction.

However, further details in the prescription of QMD differ from author to author and JAERI QMD (JQMD) [eal95, eal99] is selected as a basis for our model. In this model, the Hamiltonian is

$$H = \sum_i \sqrt{m_i^2 + p_i^2} + \hat{V}$$

A Skyrme type interaction, a Coulomb interaction, and a symmetry term are included in the effective Potential ( $\hat{V}$ ). The relativistic form of the energy expression is introduced in the Hamiltonian. The interaction term is a function of the squared spatial distance:

$$R_{ij} = (R_i - R_j)^2$$

This is not a Lorentz scalar. In Relativistic QMD (RQMD) [SStockerG89], they are replaced by the squared transverse four-dimensional distance,

$$-q_{Tij}^2 = -q_{ij}^2 + \frac{(q_{ij} \cdot p_{ij})^2}{p_{ij}^2}$$

where  $q_{ij}$  is the four-dimensional distance and  $p_{ij}$  is the sum of the four momentum. In JQMD they change the argument by the squared distance in center of mass system of the two particles,

$$\tilde{R} = R_{ij}^2 + \gamma_{ij}^2 (R_{ij} \cdot \beta_{ij})^2$$

with

$$\beta_{ij} = \frac{p_i + p_j}{E_i + E_j}, \quad \gamma_{ij} = \frac{1}{\sqrt{1 - \beta_{ij}}}$$

As a result of this, the interaction term in also depends on momentum.

Recently R-JQMD, the Lorentz covariant version of JQMD, has been proposed [MNMS09]. The covariant version of Hamiltonian is

$$H_C = \sum_i \sqrt{p_i^2 + m_i^2 + 2m_i V_i}$$

where  $V_i$  is the effective potential felt by the  $i^{\text{th}}$  particle.

With on-mass-shell constraints and a simple form of the “time fixations” constraint, the entire particle has the same time coordinate. They justified the latter assumption with the following argument “In high-energy reactions, two-body collisions are dominant; the purpose of the Lorentz-covariant formalism is only to describe relatively low energy phenomena between particles in a fast-moving medium” [MNMS09].

From this assumption, they get following equation of motion together with a big improvement in CPU performance.

$$\begin{aligned} \dot{r}_i &= \frac{p_i}{2p_i^0} + \sum_j \frac{2m_j}{2p_j^0} \frac{\tilde{V}_j}{\partial p_i} \\ &= \frac{\partial}{\partial p_i} \sum_j \sqrt{p_j^2 + m_j^2 + 2m_j \tilde{V}} \\ \dot{p}_i &= - \sum_j \frac{2m_j}{2p_j^0} \frac{\tilde{V}_j}{\partial r_i} \\ &= \frac{\partial}{\partial r_i} \sum_j \sqrt{p_j^2 + m_j^2 + 2m_j \tilde{V}} \end{aligned}$$

The  $i^{\text{th}}$  particle has an effective mass of

$$m_i^* = \sqrt{m_i^2 + 2m_i V_i}.$$

We follow their prescription and also use the same parameter values, such as the width of the Gaussian  $L = 2.0 \text{ fm}^2$  and so on.

## 34.2 Ion-ion Implementation

For the case of two body collisions and resonance decay, we used the same codes which the Binary Cascade uses in GEANT4. However for the relativistic covariant kinematic case, the effective mass of  $i^{\text{th}}$  particle depends on the one-particle effective potential,  $V_i$ , which also depends on the momentum of the entire particle system. Therefore, in R-JQMD, all the effective masses are calculated iteratively for keeping energy conservation of the whole system. We track their treatment for this.

As already mentioned, the Binary cascade model creates detailed  $3r + 3p$  dimensional nucleus at the beginning of each reaction. However, we could not use them in our QMD code, because they are not stable enough in time evolution. Also, a real ground state as an energy minimum state of the nucleus is not available in the framework of QMD, because it does not have fermionic properties. However, a reasonably stable “ground state” nucleus is required for the initial phase space distribution of nucleons in the QMD calculation. JQMD succeeded to create such a “ground state” nucleus. We also follow their prescription of generating the ground state nucleus. And “ground state” nuclei for target and projectile will be Lorentz-boosted (construct) to the center-of-mass system between them. By this Lorentz transformation, additional instabilities are introduced into both nuclei in the case of the non-covariant version.

The time evolution of the QMD system will be calculated until a certain time, typically 100 fm/c. The  $\delta T$  of the evolution is 1 fm/c. The user can modify both values from the Physics List of GEANT4. After the termination of the time evolution, cluster identification is carried out in the phase space distribution of nucleons in the system. Each identified cluster is considered as a fragmented nucleus from the reaction and it usually has more energy than the ground state. Therefore, excitation energy of the nucleus is calculated and then the nucleus is passed on to other GEANT4 models like Binary Cascade. However, unlike Binary Cascade which passes them to Precompound model and Excitation models by calling them inside of the model, the QMD model uses Excitation models directly. There are multiple choices of excitation model and one of them is the GEM model [Fur00] which JQMD and RJQMD use. The default excitation model is currently this GEM model.

Figure [fig:qmd-time] shows an example of time evolution of the reaction of 290 MeV/n  $^{56}\text{Fe}$  ions bombarding a  $^{208}\text{Pb}$  target. Because of the small Lorentz factor ( $\sim 1.3$ ), the Lorentz contractions of both nuclei are not seen clearly.

## 34.3 Cross Sections

Nucleus-Nucleus (NN) cross section is not a fundamental component of either QMD or Binary Light Ions Cascade model. However without the cross section, no meaningful simulation beyond the study of the NN reaction itself can be done. In other words, GEANT4 needs the cross section to decide where an NN reaction will happen in simulation geometry.

Many cross section formulae for NN collisions are included in GEANT4, such as Tripathi[TCW97] and Tripathi Light System[TCW99], Shen[SWF+89], Kox[eal87] and Sihver[STS+93]. These are empirical and parameterized formulae with theoretical insights and give total reaction cross section of wide variety of combination of projectile and target nucleus in fast. These cross sections are also used in the sampling of impact parameter in the QMD model.

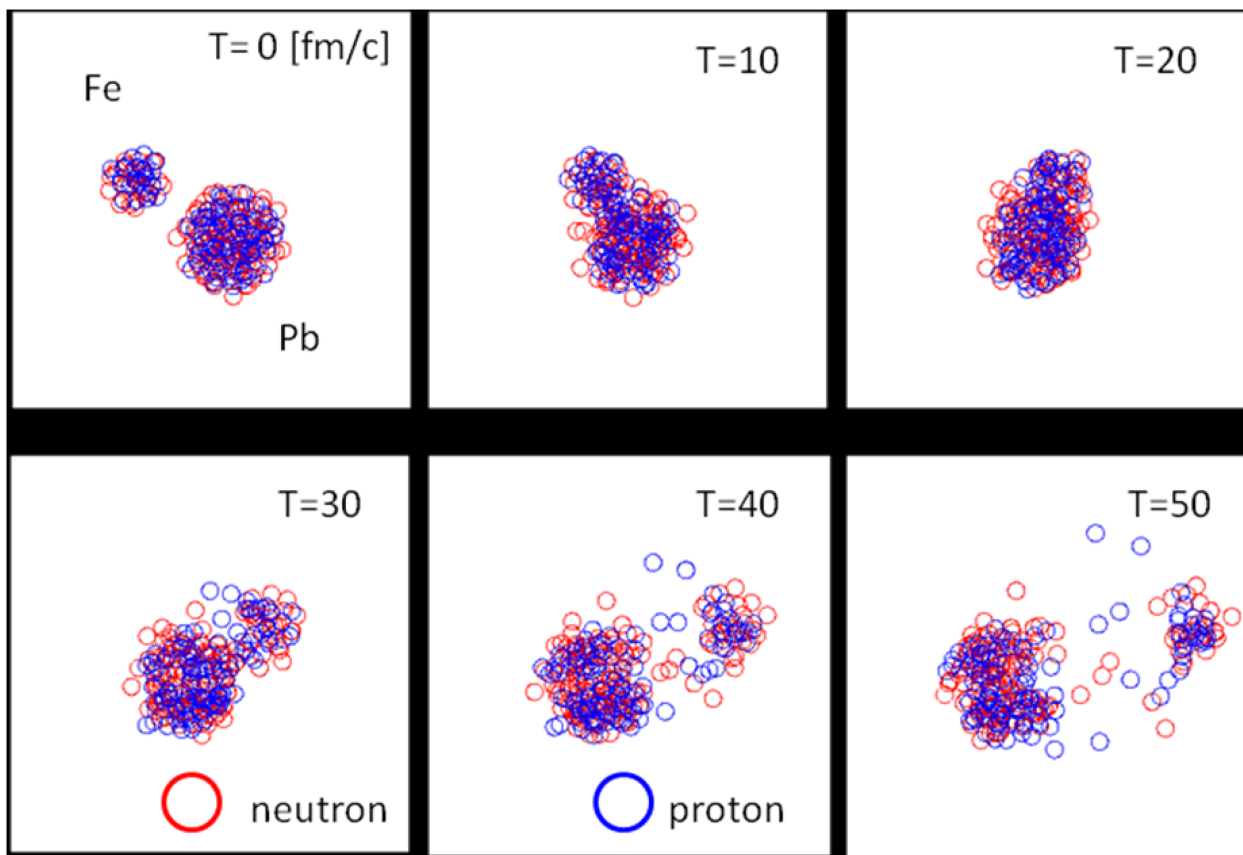


Fig. 34.1: Time evolution of reaction of 290 MeV/n Fe on Pb in position space. Red and Blue circle represents neutron and proton respectively. Full scale of each panel is 50 fm.

## ABRASION-ABLATION MODEL

### 35.1 Introduction

The abrasion model is a simplified macroscopic model for nuclear-nuclear interactions based largely on geometric arguments rather than detailed consideration of nucleon-nucleon collisions. As such the speed of the simulation is found to be faster than models such as G4BinaryCascade, but at the cost of accuracy. The version of the model implemented is interpreted from the so-called abrasion-ablation model described by Wilson *et al.* [TWT+93, WTC+95] together with an algorithm from Cucinotta to approximate the secondary nucleon energy spectrum [Cuc94]. By default, instead of performing an ablation process to simulate the de-excitation of the nuclear pre-fragments, the GEANT4 implementation of the abrasion model makes use of existing and more detailed nuclear de-excitation models within GEANT4 (G4Evaporation, G4FermiBreakup, G4StatMF) to perform this function (see *De-excitation of the projectile and target nuclear pre-fragments by standard de-excitation physics*). However, in some cases cross sections for the production of fragments with large  $\Delta A$  from the pre-abrasion nucleus are more accurately determined using a GEANT4 implementation of the ablation model (see *De-excitation of the projectile and target nuclear pre-fragments by nuclear ablation*).

The abrasion interaction is the initial fast process in which the overlap region between the projectile and target nuclei is sheered-off (see Fig. 35.1) The spectator nucleons in the projectile are assumed to undergo little change in momentum, and likewise for the spectators in the target nucleus. Some of the nucleons in the overlap region do suffer a change in momentum, and are assumed to be part of the original nucleus which then undergoes de-excitation.

Less central impacts give rise to an overlap region in which the nucleons can suffer significant momentum change, and zones in the projectile and target outside of the overlap where the nucleons are considered as spectators to the initial energetic interaction.

The initial description of the interaction must, however, take into consideration changes in the direction of the projectile and target nuclei due to Coulomb effects, which can then modify the distance of closest approach compared with the initial impact parameter. Such effects can be important for low-energy collisions.

### 35.2 Initial nuclear dynamics and impact parameter

For low-energy collisions, we must consider the deflection of the nuclei as a result of the Coulomb force (see Fig. 35.2). Since the dynamics are non-relativistic, the motion is governed by the conservation of energy equation:

$$E_{tot} = \frac{1}{2}\mu\dot{r}^2 + \frac{l^2}{2\mu r^2} + \frac{Z_P Z_T e^2}{r}$$

where:

- $E_{tot}$  = total energy in the centre of mass frame;
- $r, \dot{r}$  = distance between nuclei, and rate of change of distance;
- $l$  = angular momentum;
- $\mu$  = reduced mass of system i.e.  $m_1 m_2 / (m_1 + m_2)$ ;
- $e$  = electric charge (units dependent upon the units for  $E_{tot}$  and  $r$ );
- $Z_P, Z_T$  = charge numbers for the projectile and target nuclei.

The angular momentum is based on the impact parameter between the nuclei when their separation is large, *i.e.*

$$E_{tot} = \frac{1}{2} \frac{l^2}{\mu b^2} \Rightarrow l^2 = 2E_{tot}\mu b^2$$

At the point of closest approach,  $\dot{r} = 0$ , therefore:

$$\begin{aligned} E_{tot} &= \frac{E_{tot}b^2}{r^2} + \frac{Z_P Z_T e^2}{r} \\ r^2 &= b^2 + \frac{Z_P Z_T e^2}{E_{tot}} r \end{aligned}$$

Rearranging this equation results in the expression:

$$b^2 = r(r - r_m)$$

where:

$$r_m = \frac{Z_P Z_T e^2}{E_{tot}}$$

In the implementation of the abrasion process in GEANT4, the square of the far-field impact parameter,  $b$ , is sampled uniformly subject to the distance of closest approach,  $r$ , being no greater than  $r_P + r_T$  (the sum of the projectile and target nuclear radii).

### 35.3 Abrasion process

In the abrasion process, as implemented by Wilson *et al* [WTC+95] it is assumed that the nuclear density for the projectile is constant up to the radius of the projectile ( $r_P$ ) and zero outside. This is also assumed to be the case for the target nucleus. The amount of nuclear material abraded from the projectile is given by the expression:

$$\Delta_{abr} = F A_P \left[ 1 - \exp \left( -\frac{C_T}{\lambda} \right) \right]$$

where  $F$  is the fraction of the projectile in the interaction zone,  $\lambda$  is the nuclear mean-free-path, assumed to be:

$$\lambda = \frac{16.6}{E^{0.26}}$$

$E$  is the energy of the projectile in MeV/nucleon and  $C_T$  is the chord-length at the position in the target nucleus for which the interaction probability is maximum. For cases where the radius of the target nucleus is greater than that of the projectile (*i.e.*  $r_T > r_P$ ):

$$C_T = \begin{cases} 2\sqrt{r_T^2 - x^2} & : x > 0 \\ 2\sqrt{r_T^2 - r^2} & : x \leq 0 \end{cases}$$

where:

$$x = \frac{r_P^2 + r^2 - r_T^2}{2r}$$

In the event that  $r_P > r_T$  then  $C_T$  is:

$$C_T = \begin{cases} 2\sqrt{r_T^2 - x^2} & : x > 0 \\ 2r_T & : x \leq 0 \end{cases}$$

where:

$$x = \frac{r_T^2 + r^2 - r_P^2}{2r}$$

The projectile and target nuclear radii are given by the expression:

$$\begin{aligned} r_P &\approx 1.29 \sqrt{r_{RMS,P}^2 - 0.84^2} \\ r_T &\approx 1.29 \sqrt{r_{RMS,T}^2 - 0.84^2} \end{aligned}$$

The excitation energy of the nuclear fragment formed by the spectators in the projectile is assumed to be determined by the excess surface area, given by:

$$\Delta S = 4\pi r_P^2 \left[ 1 + P - (1 - F)^{2/3} \right]$$

where the functions  $P$  and  $F$  are given in section [PandF]. Wilson *et al* equate this surface area to the excitation to:

$$E_S = 0.95 \Delta S$$

if the collision is peripheral and there is no significant distortion of the nucleus, or

$$\begin{aligned} E_S &= 0.95 \{ 1 + 5F + \Omega F^3 \} \Delta S \\ \Omega &= \begin{cases} 0 & : A_P > 16 \\ 1500 & : A_P < 12 \\ 1500 - 320(A_P - 12) & : 12 \leq A_P \leq 16 \end{cases} \end{aligned}$$

if the impact separation is such that  $r \ll r_P + r_T$ .  $E_S$  is in MeV provided  $\Delta S$  is in  $\text{fm}^2$ .

For the abraded region, Wilson *et al* assume that fragments with a nucleon number of five are unbounded, 90% of fragments with a nucleon number of eight are unbound, and 50% of fragments with a nucleon number of nine are unbound. This was not implemented within the GEANT4 version of the abrasion model, and disintegration of the pre-fragment was only simulated by the subsequent de-excitation physics models in the G4DeexcitationHandler (evaporation, *etc.* or G4WilsonAblationModel) since the yields of lighter fragments were already underestimated compared with experiment.

In addition to energy as a result of the distortion of the fragment, some energy is assumed to be gained from transfer of kinetic energy across the boundaries of the nuclei. This is approximated to the average energy transferred to a nucleon per unit intersection pathlength (assumed to be 13 MeV/fm) and the longest chord-length,  $C_l$ , and for half of the nucleon-nucleon collisions it is assumed that the excitation energy is:

$$E_X^* = \begin{cases} 13 \cdot \left[ 1 + \frac{C_t - 1.5}{3} \right] C_l & : C_t > 1.5 \text{ fm} \\ 13 \cdot C_l & : C_t \leq 1.5 \text{ fm} \end{cases}$$

where:

$$C_l = \begin{cases} 2\sqrt{r_P^2 + 2rr_T - r^2 - r_T^2} & r > r_T \\ 2r_P & r \leq r_T \end{cases}$$

$$C_t = 2\sqrt{r_P^2 - \frac{(r_P^2 + r^2 - r_T^2)^2}{4r^2}}$$

For the remaining events, the projectile energy is assumed to be unchanged. Wilson *et al* assume that the energy required to remove a nucleon is 10 MeV, therefore the number of nucleons removed from the projectile by ablation is:

$$\Delta_{abl} = \frac{E_S + E_X}{10} + \Delta_{spc}$$

where  $\Delta_{spc}$  is the number of loosely-bound spectators in the interaction region, given by:

$$\Delta_{spc} = A_P F \exp\left(-\frac{C_T}{\lambda}\right)$$

Wilson *et al* appear to assume that for half of the events the excitation energy is transferred into one of the nuclei (projectile or target), otherwise the energy is transferred in to the other (target or projectile respectively).

The abrasion process is assumed to occur without preference for the nucleon type, *i.e.* the probability of a proton being abraded from the projectile is proportional to the fraction of protons in the original projectile, therefore:

$$\Delta Z_{abr} = \Delta_{abr} \frac{Z_P}{A_P}$$

In order to calculate the charge distribution of the final fragment, Wilson *et al* assume that the products of the interaction lie near to nuclear stability and therefore can be sampled according to the Rudstam equation (see [De-excitation of the projectile and target nuclear pre-fragments by nuclear ablation](#)). The other obvious condition is that the total charge must remain unchanged.

## 35.4 Abraded nucleon spectrum

Cucinotta has examined different formulae to represent the secondary protons spectrum from heavy ion collisions [[Cuc94](#)]. One of the models (which has been implemented to define the final state of the abrasion process) represents the momentum distribution of the secondaries as:

$$\psi(p) \propto \sum_{i=1}^3 C_i \exp\left(-\frac{p^2}{2p_i^2}\right) + d_0 \frac{\gamma p}{\sinh(\gamma p)}$$

where:

$$\begin{aligned} \psi(p) &= \text{number of secondary protons with momentum } p \\ &\quad \text{per unit of momentum phase space } [c^3/\text{MeV}^3]; \\ p &= \text{magnitude of the proton momentum in the rest frame} \\ &\quad \text{of the nucleus from which the particle is projected } [\text{MeV}/c]; \end{aligned}$$

$$C_1, C_2, C_3 = 1.0, 0.03, \text{ and } 0.0002;$$

$$p_1, p_2, p_3 = \sqrt{2/5}, \sqrt{6/5}p_F, 500 [\text{MeV}/c]$$

$$p_F = \text{Momentum of nucleons in the nuclei at the Fermi surface } [\text{MeV}/c]$$

$$d_0 = 0.1$$

$$\frac{1}{\gamma} = 90 [\text{MeV}/c];$$

G4WilsonAbrasionModel approximates the momentum distribution for the neutrons to that of the protons, and as mentioned above, the nucleon type sampled is proportional to the fraction of protons or neutrons in the original nucleus.

The angular distribution of the abraded nucleons is assumed to be isotropic in the frame of reference of the nucleus, and therefore those particles from the projectile are Lorentz-boosted according to the initial projectile momentum.

## 35.5 De-excitation of the projectile and target nuclear pre-fragments by standard GEANT4 de-excitation physics

Unless specified otherwise, G4WilsonAbrasionModel will instantiate the following de-excitation models to treat subsequent particle emission of the excited nuclear pre-fragments (from both the projectile and the target):

1. G4Evaporation, which will perform nuclear evaporation of ( $\alpha$ -particles,  ${}^3\text{He}$ ,  ${}^3\text{H}$ ,  ${}^2\text{H}$ , protons and neutrons, in competition with photo-evaporation and nuclear fission (if the nucleus has sufficiently high  $A$ ).
2. G4FermiBreakUp, for nuclei with  $A \leq 12$  and  $Z \leq 6$ .
3. G4StatMF, for multi-fragmentation of the nucleus (minimum energy for this process set to 5 MeV).

As an alternative to using this de-excitation scheme, the user may provide to the G4WilsonAbrasionModel a pointer to her own de-excitation handler, or invoke instantiation of the ablation model (G4WilsonAblationModel).

## 35.6 De-excitation of the projectile and target nuclear pre-fragments by nuclear ablation

A nuclear ablation model, based largely on the description provided by Wilson *et al* [WTC+95], has been developed to provide a better approximation for the final nuclear fragment from an abrasion interaction. The algorithm implemented in G4WilsonAblationModel uses the same approach for selecting the final-state nucleus as NUCFRG2 and determining the particles evaporated from the pre-fragment in order to achieve that state. However, use is also made of classes in GEANT4's evaporation physics to determine the energies of the nuclear fragments produced.

The number of nucleons ablated from the nuclear pre-fragment (whether as nucleons or light nuclear fragments) is determined based on the average binding energy, assumed by Wilson *et al* to be 10 MeV, *i.e.*:

$$A_{abl} = \begin{cases} \text{Int}\left(\frac{E_x}{10\text{MeV}}\right) & : A_{PF} > \text{Int}\left(\frac{E_x}{10\text{MeV}}\right) \\ A_{PF} & : \text{otherwise} \end{cases}$$

Obviously, the nucleon number of the final fragment,  $A_F$ , is then determined by the number of remaining nucleons. The proton number of the final nuclear fragment ( $Z_F$ ) is sampled stochastically using the Rudstam equation:

$$\sigma(A_F, Z_F) \propto \exp\left(-R|Z_F - SA_F - TA_F^2|^{3/2}\right)$$

Here  $R = 11.8/AF^{0.45}$ ,  $S = 0.486$ , and  $T = 3.8 \cdot 10^{-4}$ . Once  $Z_F$  and  $A_F$  have been calculated, the species of the ablated (evaporated) particles are determined again using Wilson's algorithm. The number of  $\alpha$ -particles is determined first, on the basis that these have the greatest binding energy:

$$N_\alpha = \begin{cases} \text{Int}\left(\frac{Z_{abl}}{2}\right) & : \text{Int}\left(\frac{Z_{abl}}{2}\right) < \text{Int}\left(\frac{A_{abl}}{4}\right) \\ \text{Int}\left(\frac{A_{abl}}{4}\right) & : \text{Int}\left(\frac{Z_{abl}}{2}\right) \geq \text{Int}\left(\frac{A_{abl}}{4}\right) \end{cases}$$

Calculation of the other ablated nuclear/nucleon species is determined in a similar fashion in order of decreasing binding energy per nucleon of the ablated fragment, and subject to conservation of charge and nucleon number.

Once the ablated particle species are determined, use is made of the GEANT4 evaporation classes to sample the order in which the particles are ejected (from G4AlphaEvaporationProbability, G4He3EvaporationProbability, G4TritonEvaporationProbability, G4DeuteronEvaporationProbability, G4ProtonEvaporationProbability and G4NeutronEvaporationProbability) and the energies and momenta of the evaporated particle and the residual nucleus at each two-body decay (using G4AlphaEvaporationChannel, G4He3EvaporationChannel, G4TritonEvaporationChannel, G4DeuteronEvaporationChannel, G4ProtonEvaporationChannel and G4NeutronEvaporationChannel). If at any stage the probability for evaporation of any of the particles selected by the ablation process is zero, the evaporation is forced, but no significant momentum is imparted to the particle/nucleus. Note, however, that any particles ejected from the projectile will be Lorentz boosted depending upon the initial energy per nucleon of the projectile.

## 35.7 Definition of the functions P and F used in the abrasion model

In the first instance, the form of the functions  $P$  and  $F$  used in the abrasion model are dependent upon the relative radii of the projectile and target and the distance of closest approach of the nuclear centres. Four radius conditions are treated:

- Case 1, where  $r_T > r_P$  and  $r_T - r_P \leq r \leq r_T + r_P$ :

$$P = 0.125\sqrt{\mu\nu} \left( \frac{1}{\mu} - 2 \right) \left( \frac{1-\beta}{\nu} \right)^2 - 0.125 \left[ 0.5\sqrt{\mu\nu} \left( \frac{1}{\mu} - 2 \right) + 1 \right] \left( \frac{1-\beta}{\nu} \right)^3$$

$$F = 0.75\sqrt{\mu\nu} \left( \frac{1-\beta}{\nu} \right)^2 - 0.125 [3\sqrt{\mu\nu} - 1] \left( \frac{1-\beta}{\nu} \right)^3$$

where:

$$\nu = \frac{r_P}{r_P + r_T}$$

$$\beta = \frac{r}{r_P + r_T}$$

$$\mu = \frac{r_T}{r_P}$$

- Case 2, where  $r_T > r_P$  and  $r < r_T - r_P$ :

$$P = -1$$

$$F = 1$$

- Case 3, where  $r_P > r_T$  and  $r_P - r_T \leq r \leq r_P + r_T$ :

$$P = 0.125\sqrt{\mu\nu} \left( \frac{1}{\mu} - 2 \right) \left( \frac{1-\beta}{\nu} \right)^2 - 0.125 \left\{ 0.5\sqrt{\frac{\nu}{\mu}} \left( \frac{1}{\mu} - 2 \right) - \left[ \frac{\sqrt{1-\mu^2}}{\nu} - 1 \right] \sqrt{\frac{2-\mu}{\mu^5}} \right\} \left( \frac{1-\beta}{\nu} \right)^3$$

$$F = 0.75\sqrt{\mu\nu} \left( \frac{1-\beta}{\nu} \right)^2 - 0.125 \left[ 3\sqrt{\frac{\nu}{\mu}} - \frac{[1 - (1-\mu^2)^{3/2}] \sqrt{1-(1-\mu)^2}}{\mu^3} \right] \left( \frac{1-\beta}{\nu} \right)^3$$

- Case 4, where  $r_P > r_T$  and  $r < r_T - r_P$ :

$$P = \left[ \frac{\sqrt{1-\mu^2}}{\nu} - 1 \right] \sqrt{1 - \left( \frac{\beta}{\nu} \right)^2}$$

$$F = \left[ 1 - (1-\mu^2)^{3/2} \right] \sqrt{1 - \left( \frac{\beta}{\nu} \right)^2}$$

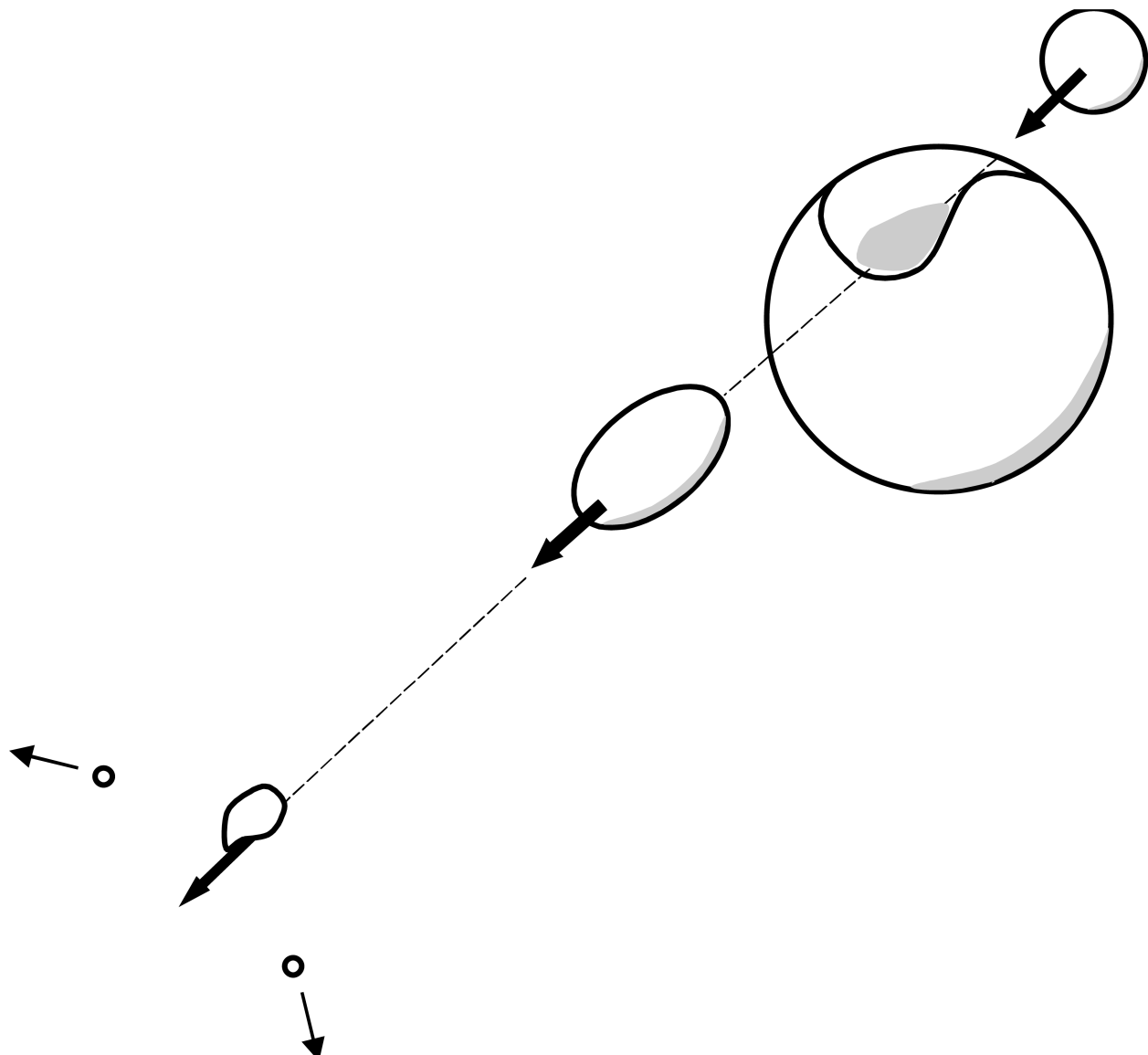


Fig. 35.1: In the abrasion process, a fraction of the nucleons in the projectile and target nucleons interact to form a fireball region with a velocity between that of the projectile and the target. The remaining spectator nucleons in the projectile and target are not initially affected (although they do suffer change as a result of longer-term de-excitation).

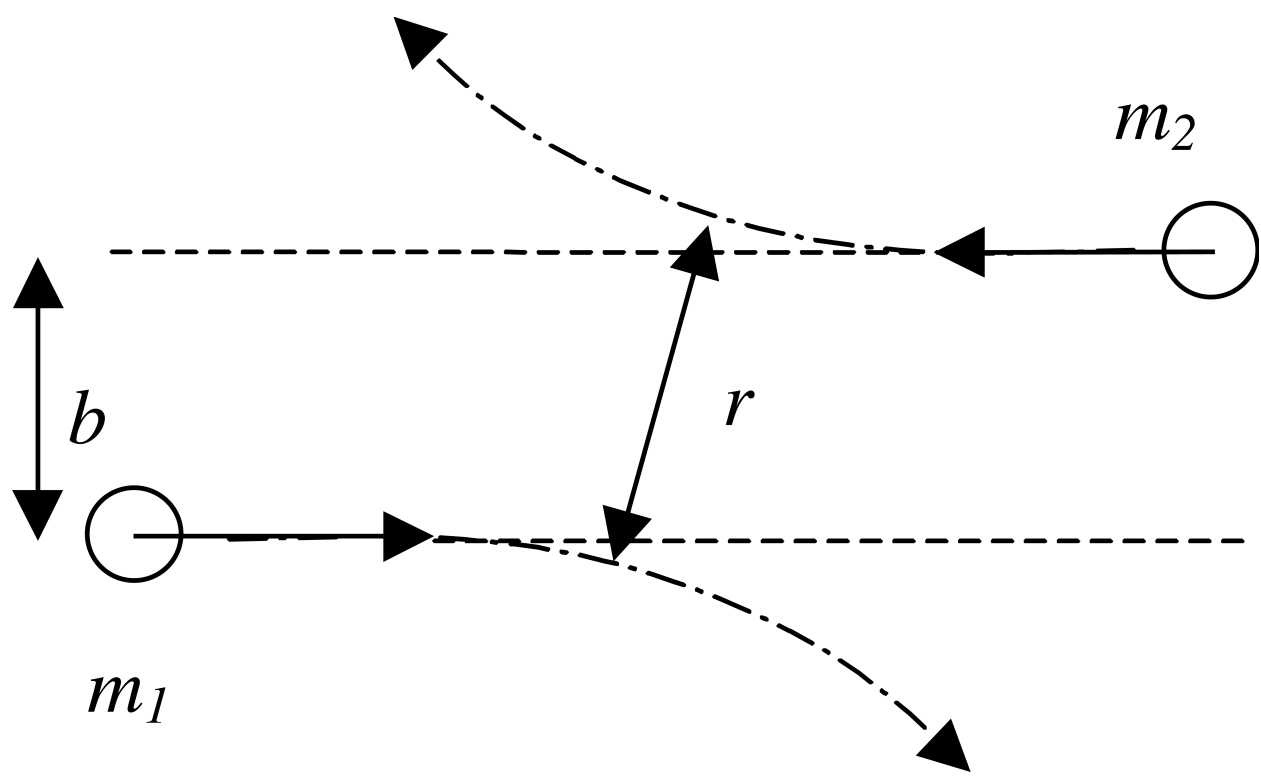


Fig. 35.2: Illustration clarifying impact parameter in the far-field ( $b$ ) and actual impact parameter ( $r$ ).

---

CHAPTER  
THIRTYSIX

---

## ELECTROMAGNETIC DISSOCIATION MODEL

### 36.1 The Model

The relative motion of a projectile nucleus travelling at relativistic speeds with respect to another nucleus can give rise to an increasingly hard spectrum of virtual photons. The excitation energy associated with this energy exchange can result in the liberation of nucleons or heavier nuclei (*i.e.* deuterons,  $\alpha$ -particles, *etc.*). The contribution of this source to the total inelastic cross section can be important, especially where the proton number of the nucleus is large. The electromagnetic dissociation (ED) model is implemented in the classes G4EMDissociation, G4EMDissociationCrossSection and G4EMDissociationSpectrum, with the theory taken from Wilson *et al* [WTC+95], and Bertulani and Baur [BaGB86].

The number of virtual photons  $N(E_\gamma, b)$  per unit area and energy interval experienced by the projectile due to the dipole field of the target is given by the expression [BaGB86]:

$$N(E_\gamma, b) = \frac{\alpha Z_T^2}{\pi^2 \beta^2 b^2 E_\gamma} \left\{ x^2 k_1^2(x) + \left( \frac{x^2}{\gamma^2} \right) k_0^2(x) \right\} \quad (36.1)$$

where  $x$  is a dimensionless quantity defined as:

$$x = \frac{b E_\gamma}{\gamma \beta \hbar c}$$

and:

$\alpha$  = fine structure constant

$\beta$  = ratio of the velocity of the projectile in the laboratory frame to the velocity of light

$\gamma$  = Lorentz factor for the projectile in the laboratory frame

$b$  = impact parameter

$c$  = speed of light

$\hbar$  = quantum constant

$E_\gamma$  = energy of virtual photon

$k_0$  and  $k_1$  = zeroth and first order modified Bessel functions of the second kind

$Z_T$  = atomic number of the target nucleus

Integrating Eq. (36.1) over the impact parameter from  $b_{min}$  to  $\infty$  produces the virtual photon spectrum for the dipole field of:

$$N_{E1}(E_\gamma) = \frac{2\alpha Z_T^2}{\pi \beta^2 E_\gamma} \left\{ \xi k_0(\xi) k_1(\xi) - \frac{\xi^2 \beta^2}{2} (k_1^2(\xi) - k_0^2(\xi)) \right\}$$

where, according to the algorithm implemented by Wilson *et al* in NUCFRG2 [WTC+95]:

$$\begin{aligned}\xi &= \frac{E_\gamma b_{min}}{\gamma \beta \hbar c} \\ b_{min} &= (1 + x_d)b_c + \frac{\pi \alpha_0}{2\gamma} \\ \alpha_0 &= \frac{Z_P Z_T e^2}{\mu \beta^2 c^2} \\ b_c &= 1.34 \left[ A_P^{1/3} + A_T^{1/3} - 0.75 \left( A_P^{-1/3} + A_T^{-1/3} \right) \right]\end{aligned}$$

and  $\mu$  is the reduced mass of the projectile/target system,  $x_d = 0.25$ , and  $A_P$  and  $A_T$  are the projectile and target nucleon numbers. For the last equation, the units of  $b_c$  are fm. Wilson *et al* state that there is an equivalent virtual photon spectrum as a result of the quadrupole field:

$$N_{E2}(E_\gamma) = \frac{2\alpha Z_T^2}{\pi \beta^4 E_\gamma} \left\{ 2(1 - \beta^2)k_1^2(\xi) + \xi(2 - \beta^2)^2 k_0(\xi)k_1(\xi) - \frac{\xi^2 \beta^4}{2} (k_1^2(\xi) - k_0^2(\xi)) \right\}$$

The cross section for the interaction of the dipole and quadrupole fields is given by:

$$\sigma_{ED} = \int N_{E1}(E_\gamma) \sigma_{E1}(E_\gamma) dE_\gamma + \int N_{E2}(E_\gamma) \sigma_{E2}(E_\gamma) dE_\gamma \quad (36.2)$$

Wilson *et al* assume that  $\sigma_{E1}(E_\gamma)$  and  $\sigma_{E2}(E_\gamma)$  are sharply peaked at the giant dipole and quadrupole resonance energies:

$$\begin{aligned}E_{GDR} &= \hbar c \left[ \frac{m^* c^2 R_0^2}{8J} \left( 1 + u - \frac{1 + \varepsilon + 3u}{1 + \varepsilon + u} \varepsilon \right) \right]^{-1/2} \\ E_{GQR} &= \frac{63}{A_P^{1/3}}\end{aligned} \quad (36.3)$$

so that the terms for  $N_{E1}$  and  $N_{E2}$  can be taken out of the integrals in Eq. (36.2) and evaluated at the resonances.

In Eq. (36.3):

$$\begin{aligned}u &= \frac{3J}{Q'} A_P^{-1/3} \\ R_0 &= r_0 A_P^{1/3}\end{aligned}$$

$\epsilon = 0.0768$ ,  $Q' = 17$  MeV,  $J = 36.8$  eV,  $r_0 = 1.18$  fm, and  $m^*$  is 7/10 of the nucleon mass (taken as 938.95 MeV/c<sup>2</sup>). (The dipole and quadrupole energies are expressed in units of MeV.)

The photonuclear cross sections for the dipole and quadrupole resonances are assumed to be given by:

$$\int \sigma_{E1}(E_\gamma) dE_\gamma = 60 \frac{N_P Z_P}{A_P} \quad (36.4)$$

in units of MeV-mb ( $N_P$  being the number of neutrons in the projectile) and:

$$\int \sigma_{E2}(E_\gamma) \frac{dE_\gamma}{E_\gamma^2} = 0.22 f Z_P A_P^{2/3} \quad (36.5)$$

in units of  $\mu\text{b}/\text{MeV}$ . In the latter expression,  $f$  is given by:

$$f = \begin{cases} 0.9 & A_P > 100 \\ 0.6 & 40 < A_P \leq 100 \\ 0.3 & 40 \leq A_P \end{cases}$$

The total cross section for electromagnetic dissociation is therefore given by Eq. (36.2) with the virtual photon spectra for the dipole and quadrupole fields calculated at the resonances:

$$\sigma_{ED} = N_{E1}(E_{GDR}) \int \sigma_{E1}(E_\gamma) dE_\gamma + N_{E2}(E_{GQR}) E_{GQR}^2 \int \frac{\sigma_{E2}(E_\gamma)}{E_\gamma^2} dE_\gamma$$

where the resonance energies are given by Eq. (36.3) and the integrals for the photonuclear cross sections given by Eq. (36.4) and Eq. (36.5).

The selection of proton or neutron emission is made according to the following prescription from Wilson *et al.*

$$\sigma_{ED,p} = \sigma_{ED} \times \begin{cases} 0.5 & Z_P < 6 \\ 0.6 & 6 \leq Z_P \leq 8 \\ 0.7 & 8 < Z_P < 14 \\ \min \left[ \frac{Z_P}{A_P}, 1.95 \exp(-0.075Z_P) \right] & Z_P \geq 14 \end{cases}$$

and

$$\sigma_{ED,n} = \sigma_{ED} - \sigma_{ED,p}$$

Note that this implementation of ED interactions only treats the ejection of single nucleons from the nucleus, and currently does not allow emission of other light nuclear fragments.



## INTERACTIONS OF STOPPING PARTICLES

### 37.1 Complementary parameterised and theoretical treatment

Absorption of negative pions and kaons at rest from a nucleus is described in literature [GE87], [CH81], [AS86], [Wey90] as consisting of two main components:

- a primary absorption process, involving the interaction of the incident stopped hadron with one or more nucleons of the target nucleus;
- the deexcitation of the remnant nucleus, left in an excited state as a result of the occurrence of the primary absorption process.

This interpretation is supported by several experiments [HIE+78], [MVA+82], [SCMZ79], [ODD+80], [PEH+79], [HIP+83], [IZE+83], that have measured various features characterizing these processes. In many cases the experimental measurements are capable to distinguish the final products originating from the primary absorption process and those resulting from the nuclear deexcitation component.

A set of stopped particle absorption processes is implemented in GEANT4, based on this two-component model (PiMinusAbsorptionAtRest and KaonMinusAbsorptionAtRest classes, for  $\pi^-$  and  $K^-$  respectively. Both implementations adopt the same approach: the primary absorption component of the process is parameterised, based on available experimental data; the nuclear deexcitation component is handled through the theoretical models described elsewhere in this Manual.

### 37.2 Pion absorption at rest

The absorption of stopped negative pions in nuclei is interpreted [GE87], [CH81], [AS86], [Wey90] as starting with the absorption of the pion by two or more correlated nucleons; the total energy of the pion is transferred to the absorbing nucleons, which then may leave the nucleus directly, or undergo final-state interactions with the residual nucleus. The remaining nucleus de-excites by evaporation of low energetic particles.

G4HadronicAbsorptionBertini(G4PionMinus::Definition()) generates the primary absorption component of the process through the parameterisation of existing experimental data. In the current implementation only absorption on a nucleon pair is considered, while contributions from absorption on nucleon clusters are neglected; this approximation is supported by experimental results [GE87], [Mac83] showing that it is the dominating contribution.

Several features of stopped pion absorption are known from experimental measurements on various materials [HIE+78], [MVA+82], [SCMZ79], [ODD+80], [PEH+79], [HIP+83], [IZE+83], [eal82]:

- the average number of nucleons emitted, as resulting from the primary absorption process;
- the ratio of nn vs np as nucleon pairs involved in the absorption process;
- the energy spectrum of the resulting nucleons emitted and their opening angle distribution.

The corresponding final state products and related distributions are generated according to a parameterisation of the available experimental measurements listed above. The dependence on the material is handled by a strategy pattern: the features pertaining to material for which experimental data are available are treated in G4PiMinusStopX classes (where X represents an element), inheriting from G4StopMaterial base class. In case of absorption on an element for which experimental data are not available, the experimental distributions for the elements closest in Z are used.

The excitation energy of the residual nucleus is calculated by difference between the initial energy and the energy of the final state products of the primary absorption process.

Another strategy handles the nucleus deexcitation; the current default implementation consists in handling the deexcitation component of the process through the evaporation model described elsewhere in this Manual.

---

CHAPTER  
**THIRTYEIGHT**

---

## LOW ENERGY NEUTRON INTERACTIONS

### 38.1 Introduction

The neutron transport class library described here simulates the interactions of neutrons with kinetic energies from thermal energies up to O(20 MeV). The upper limit is set by the comprehensive evaluated neutron scattering data libraries that the simulation is based on. The result is a set of secondary particles that can be passed on to the tracking sub-system for further geometric tracking within GEANT4.

The interactions of neutrons at low energies are split into four parts in analogy to the other hadronic processes in GEANT4. We consider radiative capture, elastic scattering, fission, and inelastic scattering as separate models. These models comply with the interface for use with the GEANT4 hadronic processes which enables their transparent use within the GEANT4 tool-kit together with all other GEANT4 compliant hadronic shower models.

### 38.2 Physics and Verification

#### 38.2.1 Inclusive Cross-sections

All cross-section data are taken from the JEFF-3.3 [J3AJMP20] evaluated data library.

All inclusive cross-sections are treated as point-wise cross-sections for reasons of performance. For this purpose, the data from the evaluated data library have been processed, to explicitly include all neutron nuclear resonances in the form of point-like cross-sections rather than in the form of parametrisations. The resulting data have been transformed into a linearly interpolable format, such that the error due to linear interpolation between adjacent data points is smaller than a few percent.

The inclusive cross-sections comply with the cross-sections data set interface of the GEANT4 hadronic design. They are, when registered with the tool-kit at initialisation, used to select the basic process. In the case of fission and inelastic scattering, point-wise semi-inclusive cross-sections are also used in order to decide on the active channel for an individual interaction. As an example, in the case of fission this could be first, second, third, or fourth chance fission.

## 38.3 Elastic Scattering

The final state of elastic scattering is described by sampling the differential scattering cross-sections  $d\sigma/d\Omega$ . Two representations are supported for the normalised differential cross-section for elastic scattering. The first is a tabulation of the differential cross-section, as a function of the cosine of the scattering angle  $\theta$  and the kinetic energy  $E$  of the incoming neutron.

$$\frac{d\sigma}{d\Omega} = \frac{d\sigma}{d\Omega}(\cos \theta, E)$$

The tabulations used are normalised by  $\sigma/(2\pi)$  so the integral of the differential cross-sections over the scattering angle yields unity.

In the second representation, the normalised cross-section are represented as a series of legendre polynomials  $P_l(\cos \theta)$ , and the legendre coefficients  $a_l$  are tabulated as a function of the incoming energy of the neutron.

$$\frac{2\pi}{\sigma(E)} \frac{d\sigma}{d\Omega}(\cos \theta, E) = \sum_{l=0}^{n_l} \frac{2l+1}{2} a_l(E) P_l(\cos \theta)$$

Describing the details of the sampling procedures is outside the scope of this paper.

An example of the result we show in Fig. 38.1 for the elastic scattering of 15 MeV neutrons off uranium a comparison of the simulated angular distribution of the scattered neutrons with evaluated data. The points are the evaluated data, the histogram is the Monte Carlo prediction.

In order to provide full test-coverage for the algorithms, similar tests have been performed for  $^{72}\text{Ge}$ ,  $^{126}\text{Sn}$ ,  $^{238}\text{U}$ ,  $^4\text{He}$ , and  $^{27}\text{Al}$  for a set of neutron kinetic energies. The agreement is very good for all values of scattering angle and neutron energy investigated.

## 38.4 Radiative Capture

The final state of radiative capture is described by either photon multiplicities, or photon production cross-sections, and the discrete and continuous contributions to the photon energy spectra, along with the angular distributions of the emitted photons.

For the description of the photon multiplicity there are two supported data representations. It can either be tabulated as a function of the energy of the incoming neutron for each discrete photon as well as the eventual continuum contribution, or the full transition probability array is known, and used to determine the photon yields. If photon production cross-sections are used, only a tabulated form is supported.

The photon energies  $E_\gamma$  are associated to the multiplicities or the cross-sections for all discrete photon emissions. For the continuum contribution, the normalised emission probability  $f$  is broken down into a weighted sum of normalised distributions  $g$ .

$$f(E \rightarrow E_\gamma) = \sum_i p_i(E) g_i(E \rightarrow E_\gamma)$$

The weights  $p_i$  are tabulated as a function of the energy  $E$  of the incoming neutron. For each neutron energy, the distributions  $g$  are tabulated as a function of the photon energy. As in the ENDF/B-VI data formats [Gro91], several interpolation laws are used to minimise the amount of data, and optimise the descriptive power. All data are derived from evaluated data libraries.

The techniques used to describe and sample the angular distributions are identical to the case of elastic scattering, with the difference that there is either a tabulation or a set of legendre coefficients for each photon energy and continuum distribution.

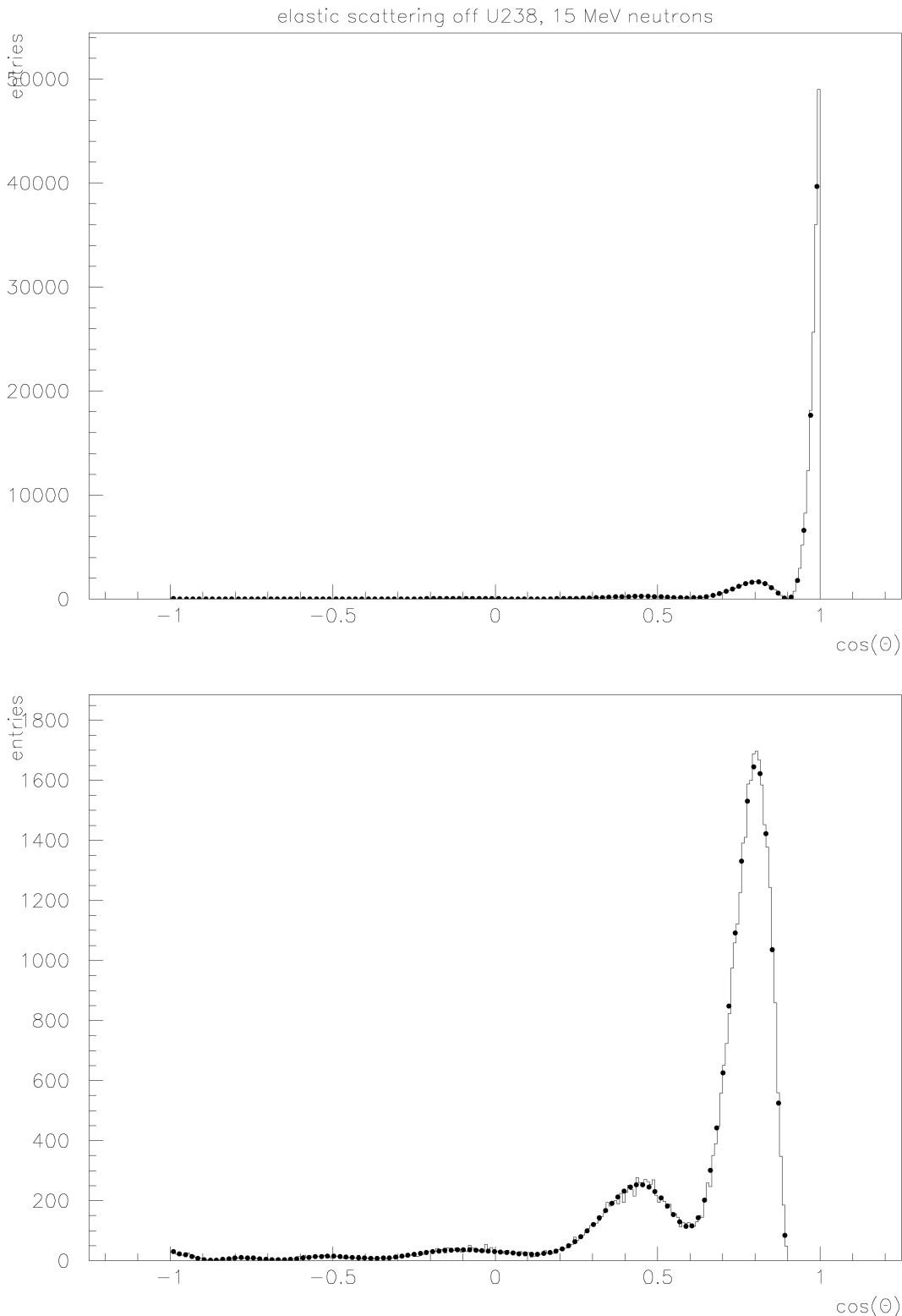


Fig. 38.1: Comparison of data and Monte Carlo for the angular distribution of 15 MeV neutrons scattered elastically off uranium ( $^{238}\text{U}$ ). The points are evaluated data, and the histogram is the Monte Carlo prediction. The lower plot excludes the forward peak, to better show the Frenel structure of the angular distribution of the scattered neutron.

As an example of the results is shown in Fig. 38.2 the energy distribution of the emitted photons for the radiative capture of 15 MeV neutrons on Uranium ( $^{238}\text{U}$ ). Similar comparisons for photon yields, energy and angular distributions have been performed for capture on  $^{238}\text{U}$ ,  $^{235}\text{U}$ ,  $^{23}\text{Na}$ , and  $^{14}\text{N}$  for a set of incoming neutron energies. In all cases investigated the agreement between evaluated data and Monte Carlo is very good.

## 38.5 Fission

For neutron induced fission, we take first chance, second chance, third chance and fourth chance fission into account.

Neutron yields are tabulated as a function of both the incoming and outgoing neutron energy. The neutron angular distributions are either tabulated, or represented in terms of an expansion in legendre polynomials, similar to the angular distributions for neutron elastic scattering. In case no data are available on the angular distribution, isotropic emission in the centre of mass system of the collision is assumed.

There are six different possibilities implemented to represent the neutron energy distributions. The energy distribution of the fission neutrons  $f(E \rightarrow E')$  can be tabulated as a normalised function of the incoming and outgoing neutron energy, again using the ENDF/B-VI interpolation schemes to minimise data volume and maximise precision.

The energy distribution can also be represented as a general evaporation spectrum,

$$f(E \rightarrow E') = f(E'/\Theta(E)).$$

Here  $E$  is the energy of the incoming neutron,  $E'$  is the energy of a fission neutron, and  $\Theta(E)$  is effective temperature used to characterise the secondary neutron energy distribution. Both the effective temperature and the functional behaviour of the energy distribution are taken from tabulations.

Alternatively energy distribution can be represented as a Maxwell spectrum,

$$f(E \rightarrow E') \propto \sqrt{E'} e^{E'/\Theta(E)},$$

or an evaporation spectrum

$$f(E \rightarrow E') \propto E' e^{E'/\Theta(E)}.$$

In both these cases, the temperature is tabulated as a function of the incoming neutron energy.

The last two options are the energy dependent Watt spectrum, and the Madland Nix spectrum. For the energy dependent Watt spectrum, the energy distribution is represented as

$$f(E \rightarrow E') \propto e^{-E'/a(E)} \sinh \sqrt{b(E)E'}.$$

Here both the parameters  $a$  and  $b$  are used from tabulation as function of the incoming neutron energy. In the case of the Madland Nix spectrum, the energy distribution is described as

$$f(E \rightarrow E') = \frac{1}{2} [g(E', \langle K_l \rangle) + g(E', \langle K_h \rangle)].$$

Here

$$\begin{aligned} g(E', \langle K \rangle) &= \frac{1}{3\sqrt{\langle K \rangle}\Theta} \left[ u_2^{3/2} E_1(u_2) - u_1^{3/2} E_1(u_1) + \gamma(3/2, u_2) - \gamma(3/2, u_1) \right], \\ u_1(E', \langle K \rangle) &= \frac{(\sqrt{E'} - \sqrt{\langle K \rangle})^2}{\Theta}, \text{ and} \\ u_2(E', \langle K \rangle) &= \frac{(\sqrt{E'} + \sqrt{\langle K \rangle})^2}{\Theta}. \end{aligned}$$

Here  $K_l$  is the kinetic energy of light fragments and  $K_h$  the kinetic energy of heavy fragments,  $E_1(x)$  is the exponential integral, and  $\gamma(x)$  is the incomplete gamma function. The mean kinetic energies for light and heavy fragments are

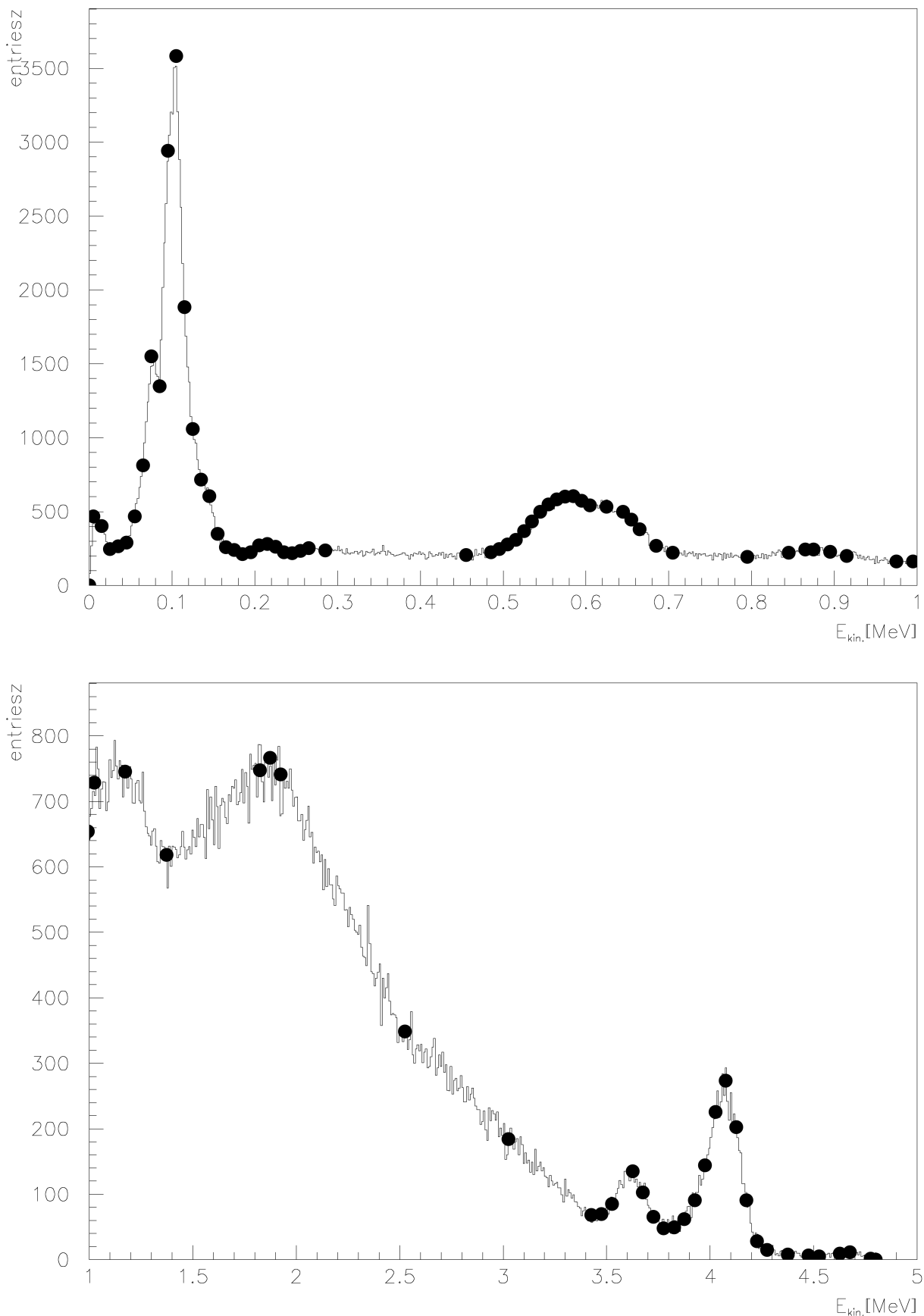


Fig. 38.2: Comparison of data and Monte Carlo for photon energy distributions for radiative capture of 15 MeV neutrons on Uranium ( $^{238}\text{U}$ ). The points are evaluated data, the histogram is the Monte Carlo prediction.

assumed to be energy independent. The temperature  $\Theta$  is tabulated as a function of the kinetic energy of the incoming neutron.

Fission photons are described in analogy to capture photons, where evaluated data are available. The measured nuclear excitation levels and transition probabilities are used otherwise, if available.

As an example of the results is shown in Fig. 38.3 the energy distribution of the fission neutrons in third chance fission of 15 MeV neutrons on uranium ( $^{238}\text{U}$ ). This distribution contains two evaporation spectra and one Watt spectrum. Similar comparisons for neutron yields, energy and angular distributions, and well as fission photon yields, energy and angular distributions have been performed for  $^{238}\text{U}$ ,  $^{235}\text{U}$ ,  $^{234}\text{U}$ , and  $^{241}\text{Am}$  for a set of incoming neutron energies. In all cases the agreement between evaluated data and Monte Carlo is very good.

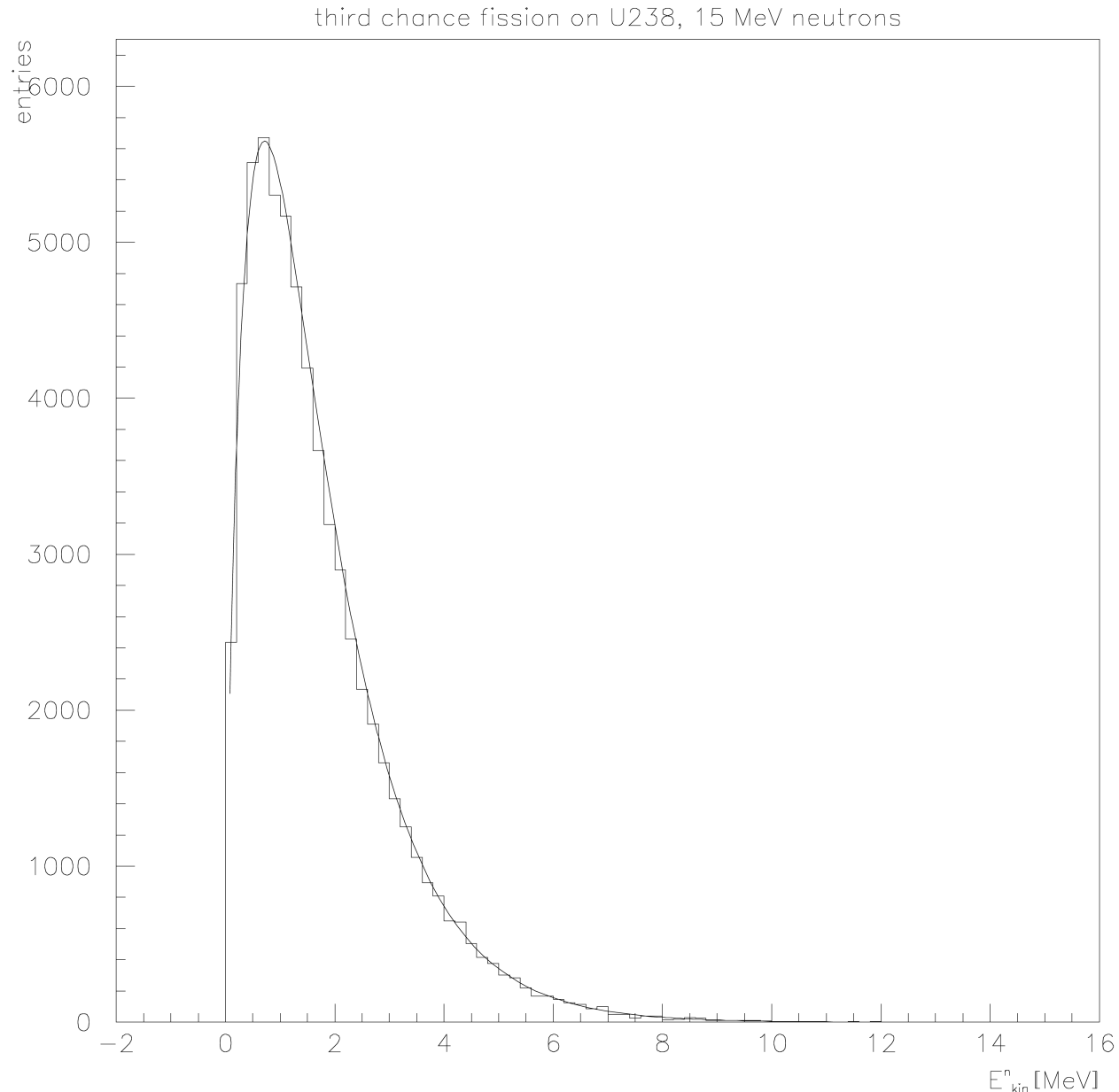


Fig. 38.3: Comparison of data and Monte Carlo for fission neutron energy distributions for induced fission by 15 MeV neutrons on uranium ( $^{238}\text{U}$ ). The curve represents evaluated data and the histogram is the Monte Carlo prediction.

## 38.6 Inelastic Scattering

For inelastic scattering, the currently supported final states are ( $nA \rightarrow n\gamma s$  (discrete and continuum), np, nd, nt,  $n^3He$ ,  $n\alpha$ ,  $nd2\alpha$ ,  $nt2\alpha$ ,  $n2p$ ,  $n2\alpha$ ,  $np\alpha$ ,  $n3\alpha$ , 2n, 2np, 2nd, 2n $\alpha$ , 2n2 $\alpha$ , nX, 3n, 3np, 3n $\alpha$ , 4n, p, pd, p $\alpha$ , 2p d, d $\alpha$ , d2 $\alpha$ , dt, t, t2 $\alpha$ ,  $^3He$ ,  $\alpha$ , 2 $\alpha$ , and 3 $\alpha$ .

The photon distributions are again described as in the case of radiative capture.

The possibility to describe the angular and energy distributions of the final state particles as in the case of fission is maintained, except that normally only the arbitrary tabulation of secondary energies is applicable.

In addition, we support the possibility to describe the energy angular correlations explicitly, in analogy with the ENDF/B-VI data formats. In this case, the production cross-section for reaction product n can be written as

$$\sigma_n(E, E', \cos(\theta)) = \sigma(E)Y_n(E)p(E, E', \cos(\theta)).$$

Here  $Y_n(E)$  is the product multiplicity,  $\sigma(E)$  is the inelastic cross-section, and  $p(E, E', \cos(\theta))$  is the distribution probability. Azimuthal symmetry is assumed.

The representations for the distribution probability supported are isotropic emission, discrete two-body kinematics, N-body phase-space distribution, continuum energy-angle distributions, and continuum angle-energy distributions in the laboratory system.

The description of isotropic emission and discrete two-body kinematics is possible without further information. In the case of N-body phase-space distribution, tabulated values for the number of particles being treated by the law, and the total mass of these particles are used. For the continuum energy-angle distributions, several options for representing the angular dependence are available. Apart from the already introduced methods of expansion in terms of legendre polynomials, and tabulation (here in both the incoming neutron energy, and the secondary energy), the Kalbach-Mann systematic is available. In the case of the continuum angle-energy distributions in the laboratory system, only the tabulated form in incoming neutron energy, product energy, and product angle is implemented.

First comparisons for product yields, energy and angular distributions have been performed for a set of incoming neutron energies, but full test coverage is still to be achieved. In all cases currently investigated, the agreement between evaluated data and Monte Carlo is very good.

## 38.7 Unresolved Resonance Region (URR) description with Probability Tables (PT)

The unresolved resonance region is the energy domain in which nuclear resonances cannot be longer experimentally determined (resolved) because the distance between two resonances becomes small compared to the neutron beam experimental energy resolution and because the resonance widths are such that the resonances begin to overlap each other.

In the URR, the cross section is obtained from adjusted average resonance parameters. The ENDF files compile the distribution and average of the partial widths and spacings of the resonances obtained from this adjustment. The partial width distribution is a Wigner distribution and the spacing distribution is a chi-square law.

In Geant4 the URR can be described either by the smooth cross sections or by using the probability table method to incorporate resonances in a stochastic way with the resonance average parameters (width and mean). By default GEANT4 uses the smooth cross sections. If the probability table method is selected the user has the choice to use probability tables processed either from NJOY [MMB+17] or CALENDF [SRCD11]. This allows the user to test the impact of the treatment performed in the two processing code.

The description of the URR with probability tables can have an impact on shielding and critical calculations.

The implementation of the probability tables has been validated against reference neutron transport code MCNP and Tripoli4 [ZTTD25].

## 38.8 Neutron Data Library (G4NDL) Format

This document describes the format of G4NDL4.5. The previous version of G4NDL does not have entries for data library identification and names of original data libraries, but other formats are same, i.e., the first element of the old version is equivalent to the 3rd element of a new version.

Since G4NDL4.4, files in the data library are compressed by zlib [[zli](#)]. In this section, we will explain the format of G4NDL in its pre-compressed form.

### 38.8.1 Cross Section

Each file in the cross section directories has the following entries:

- the first entry is identification of library (in this case G4NDL)
- the second entry original data library from which the file came
- the third entry is a dummy entry but the value usually corresponds to the MT number of reaction in ENDF formats (2:Elastic, 102:Capture, 18:Fission; files in the directory of inelastic cross section usually have 0 for this entry).<sup>1</sup>
- the fourth entry is also a dummy
- the fifth entry represents the number of (energy, cross section) pairs (in eV, barn) to follow.

This is an example of cross section file format:

```

G4NDL      (1st entry)
ENDF/B-VII.1 (2nd entry)
              (3rd entry)      \\MT
              0 (4th entry)
              682 (5th entry)    \\number of E-XS pairs
              1.000000e-05 2.043634e+01 1.062500e-05 2.043634e+01 ,,,,
              (1st pair of E and XS) (2nd pair of E and XS)
              2.000000e+07 4.827462e-01
              (682th pair of E and XS)
  
```

### 38.8.2 Final State

Unlike the format of the cross section files, the format of the final state files is not straightforward and pretty complicated. Even though each of these files follows the same format rules, the actual length and appearance of each file will depend on the specific data. The format rules of the final state files are a subset of the ENDF-6 format and a deep understanding of the format is required to correctly interpret the content of the files. Because of limited resources, we do not plan to provide a complete documentation on this part in the near future.

<sup>1</sup> MF and MT numbers are used in the ENDF format to indicate the type of data and the type of reaction or products resulting from the reaction. For example, MF3 represents cross section data and MF4 symbolizes angular distribution, also, MT2 represents elastic reaction and MT102 is radiative capture.

### 38.8.3 Thermal Scattering Cross Section

The format of the thermal scattering cross section data is similar to that of the cross section data described above:

- the 1st and 2nd entries have the same meaning
- the 3rd and 4th entries are also dummies and not used in simulation. However the 3rd entry has the value of 3 that represents MF number of ENDF-6 format and the 4th entry has the value of MT numbers of ENDF-6 format.
- the 5th entry is the temperature (in Kelvin)
- the 6th entry represents the number of (energy, cross section) pairs given for the temperature in entry 5.
- If there are multiple temperatures listed, which is typical, then for each temperature there is a corresponding data block which consists of MF, MT, temperature, number of pairs, and paired E and cross section data.

This is an example of thermal scattering cross section file format:

```

G4NDL      (1st entry)
ENDF/B-VII.1 (2nd entry)
            3 (3rd entry)      \\MF
            223 (4th entry)    \\MT
            296 (5th entry)    \\temperature
            2453 (6th entry)   \\number of E-XS pairs
1.000000e-5 3.456415e+2 1.125000e-5 3.272908e+2 ,,,,
(1st pair of E and XS) (2nd pair of E and XS)
4.000040e+0 0.000000e+0 2.000000e+7 0.000000e+0
(2452nd pair of E and XS) (2453rd pair of E and XS)
            3 (MF)
            223 (MT)
            350 (temperature)
            2789 (Number of E-XS pair)
1.000000e-5 4.457232e+2 1.125000e-5 4.220525e+2 ,,,,
(1st pair of E and XS) (2nd pair of E and XS)

```

### 38.8.4 Coherent Final State

The final state files have a similar format:

- the 1st and 2nd entries have the same meaning before
- the 3rd and 4th entries are also dummy entries and not used in simulation. However the 3rd entry has the value of 7 that represents MF number of ENDF-6 format and the 4th entry has the value 2 as MT number of the ENDF-6 format.
- the 5th entry represents temperature
- the 6th entry shows the number of Bragg edges given. This is followed by pairs of Bragg edge energies in eV and structure factors.
- If there are multiple temperatures listed, which is typical, then for each temperature there is a corresponding data block which consists of MF, MT, temperature, number of Bragg edges, and paired energy of Bragg edge and structure factors. However the energies of the Bragg edges only appear in the first data block.

This is an example of thermal scattering coherent final state file:

```

G4NDL      (1st entry)
ENDF/B-VII.1 (2nd entry)
            7 (3rd entry)      // MF

```

(continues on next page)

(continued from previous page)

```

2      (4th entry)          // MT
296    (5th entry)          // temperature
248    (6th entry)          // number of Bragg edges
4.555489e-4 0.000000e+0 1.822196e-3 1.347465e-2 ,,,,
(1st pair of E and S) (2nd pair of E and S)
1.791770e+0 6.259710e-1 5.000000e+0 6.259711e-1
(247th pair of E, S) (248th pair of E, S)
    7      (MF)
    2      (MT)
    400    (temperature)
    248    (# of Bragg edge structure factors without energies)
0.000000e+0 1.342127e-2 ,,,,
(1st pair of E and S)
4.994888e-1 4.994889e-1
(247th pair of E and S)

```

### 38.8.5 Incoherent Final State

The incoherent final state files have a similar format:

- the 1st and 2nd entry has same meaning before
- the 3rd and 4th entries are dummy entries and not used in simulation. However the 3rd entry has the value of 6 that represents the MF number of the ENDF-6 format and the 4th entry is the MT number of the ENDF-6 format.
- the 5th entry is the temperature of this data block
- the 6th entry is the number of isoAngle data sets, described below.
- If there are multiple temperatures listed, which is typical, then for each temperature there is a corresponding data block which consists of MF, MT, temperature, number of isoAngle data sets and the isoAngle data sets.

The format of the isoAngle data set is following.

- Up to the 8th entry, only 2nd and 5th entry has real meaning in simulation and the 2nd entry has energy of incidence neutron and 5th entry is the number of equal probability bins (N) in mu.
- 9th to (9+N-2)th entries are the boundary values of the equal probability bins. The lowest and highest boundary of -1 and 1 are obvious thus they are omitted from entries.

This is an example of isoAngle data set

```

0.000000e+0 1.000000e-5      0      0      10      10
(1st entry) (2nd entry) (3rd entry) (4th entry) (5th entry) (6th entry)
1.000000e-05 1.000000e+00 -8.749199e-01 -6.247887e-01 ,,
(7th entry) (8th entry) (2nd boundary) (3rd boundary)
6.252111e-01 8.750801e-01
(9th boundary) (10th boundary)

```

This is an example of thermal scattering incoherent final state file

G4NDL	(1st entry)
ENDF/B-VII.1	(2nd entry)
6	(3rd entry) \\MF
224	(4th entry) \\MT
296	(5th entry) \\temperature
2452	(6th entry) \\number of isoAngle data sets

(continues on next page)

(continued from previous page)

0.000000e+0	1.000000e-5	0	0	10	10
(1st isoAngle data set)					
1.000000e-05	1.000000e+00	-8.749199e-01	-6.247887e-01	-3.747014e-01	
	-1.246577e-01	1.253423e-01	3.752985e-01	6.252111e-01	8.750801e-01
.....					
0.000000e+0	1.125000e-5	0	0	10	10
(2452st isoAngle data set)					
4.000040e+00	1.000000e+00	9.889886e-01	9.939457e-01	9.958167e-01	
	9.970317e-01	9.979352e-01	9.986553e-01	9.992540e-01	9.997666e-01
	6	(MF)			
	224	(MT)			
	350	(temperature)			
	2788	(sumber of isoAngle data sets)			
0.000000e+0	1.000000e-5	0	0	10	10
1.000000e-05	1.000000e+00	-8.749076e-01	-6.247565e-01	-3.746559e-01	
	-1.246055e-01	1.253944e-01	3.753440e-01	6.252433e-01	8.750923e-01
.....					

### 38.8.6 Inelastic Final State

As before, the top six entries are similar:

- the 1st and 2nd entries have the same meaning.
- the 3rd and 4th entries are dummy entries and not used in simulation. However the 3rd entry has the value of 6 that represents the MF number of ENDF-6 format and the 4th entry corresponding to MT number of ENDF-6 format.
- the 5th entry is the temperature [K] of this data block
- the 6th entry is number of E-(E'-isoAngle) data sets, where E is the energy of the incident neutron and E' is energy of the scattered neutron.
- If there are multiple temperatures listed, which is typical, then for each temperature there is a corresponding data block which consists of MF, MT, temperature, number of E-(E'-isoAngle) data set and E-(E'-isoAngle) data.

The format of E-(E'-isoAngle) is following.

- The 1st, 3rd and 4th entries are dummies and not be used in simulation.
- The 2nd entry is the energy of the incident neutron(E)
- the 5th entry is the number of entries to be found after the 6th entry.
- the 6th entry corresponds to the number of entries of each E'-isoAngle data set. The first entry of E'-isoAngle data set represents energy of scattered neutron(E') and 2nd entry is probability of E->E' scattering. Following entries correspond to boundaries of iso-probability bins in mu. The lowest and highest boundaries are also omitted. The first and last E'-isoAng set should always have all 0 values excepting for energy of scattering neutron.

This is an example of E-(E'-isoAngle) data set

0.000000e+0	1.000000e-5	0	0	2080	10
(1st entry)	(2nd entry)	(3rd entry)	(4th entry)	(5th entry)	(6th entry)
0.000000e+00	0.000000e+00	0.000000e+00	0.000000e+00	0.000000e+00	
	0.000000e+00	0.000000e+00	0.000000e+00	0.000000e+00	0.000000e+00
(1st E'-isoAng data set)					

(continues on next page)

(continued from previous page)

```

6.103500e-10  3.127586e+00 -8.741139e-01 -6.226646e-01 -3.716976e-01
-1.212145e-01  1.287860e-01  3.783033e-01  6.273366e-01  8.758833e-01
(2nd E'-isoAng data set)
.....
7.969600e-01  5.411300e-13 -8.750360e-01 -6.254547e-01 -3.755898e-01
-1.257686e-01  1.241790e-01  3.742614e-01  6.242919e-01  8.753607e-01
(207th E'-isoAng data set)
8.199830e-01  0.000000e+00  0.000000e+00  0.000000e+00  0.000000e+00
0.000000e+00  0.000000e+00  0.000000e+00  0.000000e+00  0.000000e+00
(208th E'-isoAng data set)

```

This is an example of thermal scattering inelastic final state file

```

G4NDL          (1st entry)
ENDF/B-VII.1   (2nd entry)
    6           (3rd entry)      \\MF
    222          (4th entry)     \\MT
    293.6         (5th entry)    \\temperature
    107          (6th entry)    \\number of E-(E'-isoAngle) data sets
0.000000e+0 1.000000e-5      0          0        2080       10
0.000000e+00 0.000000e+00 0.000000e+00 0.000000e+00 0.000000e+00
0.000000e+00 0.000000e+00 0.000000e+00 0.000000e+00 0.000000e+00
6.103500e-10 3.127586e+00 -8.741139e-01 -6.226646e-01 -3.716976e-01
-1.212145e-01 1.287860e-01 3.783033e-01 6.273366e-01 8.758833e-01
1.220700e-09 4.423091e+00 -8.737468e-01 -6.216975e-01 -3.703295e-01
-1.196465e-01 1.303546e-01 3.796722e-01 6.283050e-01 8.762478e-01

```

### 38.8.7 Further Information

A detailed description of the file format has been created by reverse engineering the code by a user, Wesley Ford, who was a masters student at McMaster University [[WFMA ScEP](#)] under the supervision of Prof. Adriaan Buijs and has kindly agreed for its inclusion [here](#).

The link provides a document which describes G4NDL format and as a consequence readers and expert users may obtain useful information from it. Especially detailed descriptions of variable names used in the package and their meanings will be useful to developers who consider extensions of the package.

There is also a more recent full description of the data format which is also application to charged particles available [here](#).

## 38.9 High Precision Models and Low Energy Parameterized Models

The high precision neutron models discussed in the previous section depend on an evaluated neutron data library (G4NDL) for cross sections, angular distributions and final state information. However the library is not complete because there are no data for several key elements. In order to use the high precision models, users must develop their detectors using only elements which exist in the library. In order to avoid this difficulty, alternative models were developed which use the high precision models when data are found in the library, but use the low energy parameterized neutron models when data are missing.

The alternative models cover the same types of interaction as the originals, that is elastic and inelastic scattering, capture and fission. Because the low energy parameterized part of the models is independent of G4NDL, results will not be as precise as they would be if the relevant data existed.

## 38.10 NuDEX

NuDEX is a computer toolkit which allows to generate de-excitation cascades of atomic nuclei. The code is available for download from [MCO], together with a manual describing its performance.

For the moment, it has been incorporated into Geant4 to model the emission of  $\gamma$ -rays and electrons following neutron capture reactions, but in the future it is expected to be extended to other types of nuclear de-excitations.

Most neutron capture reactions that are modeled with Geant4 occur through the mechanism known as compound nucleus. In this mechanism, the neutron is absorbed by the target nucleus ( ${}^A_Z$ ), giving rise to a nucleus with one more neutron ( ${}^{A+1}_{Z+1}$ ) and which is in an excited state with typical energies of 5-10 MeV. In a second step, the compound nucleus decays to the ground state or an isomeric state emitting an electromagnetic cascade, which may be modeled by NuDEX.

To model the de-excitation of a nucleus, NuDEX generates the full level scheme, branching ratios and internal conversion coefficients, in a similar way as it is done by the codes DICEBOX [Bec98] and DEGEN [JAT16]. To do this, it takes the known values from a database based mainly in RIPL-3 [CHO+09] and ENSDF [had], and fills in the missing information with statistical models.

The level scheme of a certain nucleus is supposed to be complete up to a certain excitation energy  $E_{\text{crit}}$ , provided by RIPL-3. Above  $E_{\text{crit}}$ , the level scheme is generated randomly according to level density formulas. The distances between consecutive levels are sampled according to a Wigner distribution. Some of the level density models implemented in the code are the Back-Shifted Fermi Gas Model and the Gilbert-Cameron Model, which depend on some parameters which are taken from RIPL-3.

In order to reduce the computation memory and time, NuDEX has the possibility of grouping the levels into bands. The levels that make up each of these bands all have the same spin and parity. Each of these bands is then characterized by their lower and upper excitation energy, their spin and parity, and the number of levels which contains. The effect of making bands does not have an important impact in the resulting electromagnetic cascades for most practical cases.

Branching ratios not present in the databases are generated according to the so called *extreme statistical model* [Bec98]. The branching ratio of the transition from a level  $a$  to a level  $b$ ,  $\text{BR}_{a \rightarrow b}$ , is computed according to:

$$\text{BR}_{a \rightarrow b} \propto \sum_{X,L} \xi_{a \rightarrow b}^2 E_\gamma^{2L+1} \overleftarrow{f}^{XL}(E_\gamma, E_a)$$

where  $X$  is the type of transition (electric or magnetic);  $L$  is the multipolarity;  $\xi_{a \rightarrow b}$  is a random variable drawn independently from a normal distribution with zero mean and unit variance, which introduce the Porter-Thomas fluctuations;  $E_\gamma$  is the difference between the energy of the level  $a$ ,  $E_a$ , and the energy of the level  $b$ ,  $E_b$ ; and  $\overleftarrow{f}^{XL}(E_\gamma, E_a)$  is the Photon Strength Function (PSF). The branching ratios are normalized so that the sum of all of them starting from the same level equals 1,  $\sum_{i=0}^{n-1} \text{BR}_{n \rightarrow i} = 1$ . For the moment, only  $E1$ ,  $M1$  and  $E2$  transitions are considered.

In addition to the branching ratios from the known part of the level scheme, the NuDEX database contains also lists of primary  $\gamma$ -rays from thermal neutron capture, together with the observed intensities, taken from ENSDF. These data are particularly important for simulating thermal neutron capture  $\gamma$ -rays of light nuclei.

Internal conversion coefficients are obtained from the same RIPL-3 database as the known levels, if present. Otherwise they are obtained from the data tables provided by Band et al. in [BTN+02].

To generate the cascades, NuDEX uses default parameters that are mainly found in its database. Users can change these values, if required, in two possible ways:

1. By editing the file with name GeneralStatNuclParameters.dat, which is located in the NuDEX database. There it is possible to change, for example, the level density or Photon Strength Function models, or the width of the bands where the levels are grouped. Changes can be made for all nuclei ( $Z=0 A=0$ ) or for some specific ones.
2. By editing the files or creating new ones inside the folder SpecialInputs. There each file corresponds to a particular nucleus.

More information concerning the performance of NuDEX can be found in the NuDEX manual [MCO] or in [MACO+23, MCOJ+20].

## 38.11 Summary and Important Remark

By the way of abstraction and code reuse we minimised the amount of code to be written and maintained. The concept of container-sampling lead to abstraction and encapsulation of data representation and the corresponding random number generators. The Object Oriented design allows for easy extension of the cross-section base of the system, and the ENDF-B VI data evaluations have already been supplemented with evaluated data on nuclear excitation levels, thus improving the energy spectra of de-excitation photons. Other established data evaluations have been investigated, and extensions based on the JENDL[eal95], JEF [J2CN94], CENDL[Cen96], and Brond[eal94] data libraries are foreseen for next year.

Followings are important remark of the NeutornHP package. Correlation between final state particles is not included in tabulated data. The method described here does not include necessary correlation or phase space constrains needed to conserve momentum and energy. Such conservation is not guaranteed either in single event or averaged over many events.

## **LOWENERGYCHARGEDPARTICLES**

### **39.1 Low Energy Charged Particle Interactions**

#### **39.1.1 Introduction**

The low energy charged particle transport class library described here simulates the interactions of protons, deuterons, tritons, He-3 and alpha particle with kinetic energies up to 200 MeV. The upper limit is set by the comprehensive evaluated neutron scattering data libraries that the simulation is based on. It reuses the code of the low energy neutron interactions package, with some small modifications to take into account the change of incident particle.

Only the inelastic interactions are included in this model, while the elastic interaction is treated approximately by other GEANT4 models, and the interference between Coulomb and nuclear elastic is neglected.

#### **39.1.2 Physics and Verification**

##### **Inclusive Cross-sections**

Cross-section data is taken from the ENDF/B-VIII.0 [Gro91] and JENDL/DEU-2020 [JENDLDEU2020SNO21] evaluated data libraries for those few elements where data exist. As these isotopes are only a few, most of the isotopes data are taken from the TENDL data library (version TENDL-2019) which uses the TALYS nuclear model. The format is exactly the same as for the low energy neutron data libraries. While the energy of the TENDL files goes up to 200 MeV, in the case of ENDF it only reaches 150 MeV for most isotopes and for some is even less.

The treatment of this data is done with the same code as for the low energy neutron package. It should be mentioned that for all except a few low Z isotopes in the ENDF data library, there is no information about individual decay channels, but only about the total cross section plus particle yields. Therefore the same remark as for the neutron package holds: there is no event-by-event conservation of energy, nor of atomic or mass number.

The absence of treatment of the correlation between inelastic and elastic interactions affects the emission of charged particles, while it does not for neutron and gamma emission. The effect is expected to increase with incident energy and modify the secondary particle spectra.

### 39.1.3 Neutron-induced alpha production reactions on carbon

Some breakup reactions are only partially described or not described at all by *G4ParticleHP*, either because of incomplete or missing information in the evaluated neutron data library, or an incomplete implementation of the model itself.

The base class *G4ParticleHPInelasticBaseFS* and its derived classes in *G4ParticleHP* are devoted to describing reactions that involve more than one particle and a residual nucleus in the final state. These classes use, when available, evaluated energy-angle distributions to sample the final state of the reaction products, otherwise, the n-body phase space distribution. Reactions involving only one particle and a residual nucleus in the final state are described in *G4ParticleHPInelasticCompFS* and its derived classes instead. The description is however incomplete when it comes to breakup reactions proceeding in multiple steps, as they are not considered to their whole extent but only to the first step, leaving an intermediate nucleus in an excited state that is forced to decay to the ground state without any particle emission. This can be the case of the  $^{12}\text{C}(\text{n},\text{n}'3\alpha)$  reactions, which are important in many applications.

*G4ParticleHPInelasticCompFS* incorporates the  $^{12}\text{C}(\text{n},\text{n}'3\alpha)$  multistep breakup model from NRESP7.1: a Monte Carlo simulation code developed at the Physikalisch-Technische Bundesanstalt (PTB), Germany, to study the response of organic scintillation detectors to fast neutrons between 0.02 and 20 MeV [DK82]. Two different mechanisms are considered:

- I)  $\text{n} + ^{12}\text{C} \rightarrow \alpha + ^9\text{Be}^* \mid ^9\text{Be}^* \rightarrow \text{n}' + ^8\text{Be} \mid ^8\text{Be} \rightarrow 2\alpha$
- II)  $\text{n} + ^{12}\text{C} \rightarrow \text{n}' + ^{12}\text{C}^* \mid ^{12}\text{C}^* \rightarrow \alpha + ^8\text{Be} \mid ^8\text{Be} \rightarrow 2\alpha$

Both end up with the  $2\alpha$  decay of  $^8\text{Be}$  from its ground state but differ in the first and intermediate steps. Each mechanism comprises one or more reaction channels associated with excited well-defined or pseudo-states of the intermediate nucleus. The model samples the direction of the outgoing neutron from an isotropic distribution in the center-of-mass system and the alpha particles are emitted conserving energy and momentum. Relativistic kinematics is applied at each step.

Beware that angular distributions for the  $^{12}\text{C}(\text{n},\text{n}'3\alpha)$  reactions in the neutron data library are ignored in this model. The  $^{12}\text{C}(\text{n},\alpha)^9\text{Be}$  reaction, on the other hand, has a strong anisotropy in the center-of-mass system and there is no angular distribution data for this reaction in the neutron data library G4NDL whatsoever. Hence, for a complete description of neutron-induced alpha production reactions on carbon, the angular distributions for the  $^{12}\text{C}(\text{n},\alpha)^9\text{Be}$  reaction in NRESP7.1 are also incorporated (hard coded) in *G4ParticleHPInelasticCompFS*.

To invoke this model, the user needs to use the UI command:

```
/process/had/particle_hp/use_NRESP71_model true
```

A detailed description of the model and its verification and validation are published in A. R. Garcia et al, NIMA 868, 73-81 (2017) [GMCO+17]. The authors would appreciate the citation of their work by users of this model in the publication of their results.

### 39.1.4 Data Format

A detailed description of the data format used for the charged particle files available is described in an extensive note available for download <<https://geant4-userdoc.web.cern.ch/ContributionFromUsers/UsefulNotes/particleHPFormat.pdf>>.

## GEANT4 LOW ENERGY NUCLEAR DATA (LEND) PACKAGE

### 40.1 Low Energy Nuclear Data

GEANT4 Low Energy Nuclear Data (LEND) Package G4LEND is a set of low energy nuclear interaction models in GEANT4. The LEND package uses Generalized Nuclear Data (GND) which is a modern format for storing nuclear data. To use the package, users must download data from <ftp://gdo142.ucllnl.org/> and then **GND\_v1.3.tar.gz** in the directory *GND\_after2013* is the file you need to download and unpack. Please set an environment variable G4LENDDATA pointing the directory which contains unpacked gammas.map and neutrons.map files. The download contains GND-formatted nuclear data for incident neutrons and gammas which are converted from the ENDF/B-VII.r1 library. A total of 421 target nuclides from H to Es are available for the neutron- incident data and 162 nuclides from H to Pt for the gamma-incident data. The cross sections and final state products of the interactions are extracted from the data using the General Interaction Data Interface (GIDI). G4LEND then allow them to be used in GEANT4 hadronic cross section and model. G4LEND is a data-driven model; therefore the data library quality is crucial for its physics performance. Energy range of the package is also a function of data library. In the case of the data which converted from ENDF/B-VII.r1, it can handle neutrons interaction from below thermal energy up to 20 MeV for most target nuclides. The upper limit of the energy enhances up to 150 MeV for some target nuclides. One important limitation of the model is that it does not guarantee conservation laws beyond the 2 body interaction.

The evaluated data applied to this model are particularly suitable for incident gammas below 20 MeV giving higher precision than the default Bertini Cascade model (*The Bertini Intranuclear Cascade Model*).



## RADIOACTIVE DECAY

### 41.1 The Radioactive Decay Module

*G4RadioactiveDecay* and associated classes are used to simulate the decay, either in-flight or at rest, of radioactive nuclei by  $\alpha$ ,  $\beta^+$ , and  $\beta^-$  emission and by electron capture (EC). The simulation model depends on data taken from the Evaluated Nuclear Structure Data File (ENSDF) [Tul96] which provides details on the following properties (with the corresponding Geant4 library storing that property shown in brackets):

- alpha, beta and internal transition half-lives (G4ENSDFSTATE)
- nuclear level structure for the parent or daughter nuclide (PhotonEvaporation, G4ENSDFSTATE, RadioactiveDecay)
- decay branching ratios (RadioactiveDecay)
- the energy of the decay process (RadioactiveDecay)

If the daughter of a nuclear decay is an excited isomer, its prompt nuclear de-excitation is treated using the *G4PhotoEvaporation* class (see Section *Photon evaporation*).

### 41.2 Alpha Decay

The final state of alpha decay consists of an  $\alpha$  and a recoil nucleus with  $(Z - 2, A - 4)$ . The two particles are emitted back-to-back in the center of mass with the energy of the  $\alpha$  taken from the ENSDF data entry for the decaying isotope.

### 41.3 Beta Decay

Beta decay is modeled by the emission of a  $\beta^-$  or  $\beta^+$ , an anti-neutrino or neutrino, and a recoil nucleus of either  $Z + 1$  or  $Z - 1$ . The energy of the  $\beta$  is obtained by sampling either from histogrammed data or from the theoretical three-body phase space spectral shapes. The latter include allowed, first, second and third unique forbidden, and first non-unique forbidden transitions.

The shape of the energy spectrum of the emitted lepton is given by

$$\frac{d^2n}{dE dp_e} = (E_0 - E_e)^2 E_e p_e F(Z, E_e) S(Z, E_0, E_e)$$

where, in units of electron mass,  $E_0$  is the endpoint energy of the decay taken from the ENSDF data,  $E_e$  and  $p_e$  are the emitted electron energy and momentum,  $Z$  is the atomic number,  $F$  is the Fermi function and  $S$  is the shape factor.

The Fermi function  $F$  accounts for the effect of the Coulomb barrier on the probability of  $\beta^\pm$  emission. Its relativistic form is

$$F(Z, E_e) = 2(1 + \gamma)(2p_e R)^{2\gamma - 2} e^{\pm\pi\alpha Z E_e / p_e} \frac{|\Gamma(\gamma + i\alpha Z E_e / p_e)|^2}{\Gamma(2\gamma + 1)^2}$$

where  $R$  is the nuclear radius,  $\gamma = \sqrt{1 - (\alpha Z)^2}$ , and  $\alpha$  is the fine structure constant. The squared modulus of  $\Gamma$  is computed using approximation B of Wilkinson [Wil70].

The factor  $S$  determines whether or not additional corrections are applied to the decay spectrum. When  $S = 1$  the decay spectrum takes on the so-called allowed shape which is just the phase space shape modified by the Fermi function. For this type of transition the emitted lepton carries no angular momentum and the nuclear spin and parity do not change. When the emitted lepton carries angular momentum and nuclear size effects are not negligible, the factor  $S$  is no longer unity and the transitions are called “forbidden”. Corrections are then made to the spectrum shape which take into account the energy dependence of the nuclear matrix element. The form of  $S$  used in the spectrum sampling is that of Konopinski [Kon66].

## 41.4 Electron Capture

Electron capture from the atomic K, L and M shells is simulated by producing a recoil nucleus of  $(Z - 1, A)$  and an electron-neutrino back-to-back in the center of mass. Since this leaves a vacancy in the electron orbitals, the atomic relaxation model (ARM) is triggered in order to produce the resulting x-rays and Auger electrons. More information on the ARM can be found in the Electromagnetic section of this manual.

In the electron capture decay mode, internal conversion is also enabled so that atomic electrons may be ejected when interacting with the nucleus.

## 41.5 Recoil Nucleus Correction

Due to the level of imprecision of the rest-mass energy of the nuclei generated by `G4IonTable::GetNucleusMass`, the mass of the parent nucleus is modified to a minor extent just before performing the two- or three-body decay so that the  $Q$  for the transition process equals that identified in the ENSDF data.

## 41.6 Biasing Methods

By default, sampling of the times of radioactive decay and branching ratios is done according to standard, analogue Monte Carlo modeling. The user may switch on one or more of the following variance reduction schemes, which can provide significant improvement in the modelling efficiency:

1. The decays can be biased to occur more frequently at certain times, for example, corresponding to times when measurements are taken in a real experiment. The statistical weights of the daughter nuclides are reduced according to the probability of survival to the time of the event,  $t$ , which is determined from the decay rate. The decay rate of the  $n^{th}$  nuclide in a decay chain is given by the recursive formulae:

$$R_n(t) = \sum_{i=1}^{n-1} A_{n:i} f(t, \tau_i) + A_{n:n} f(t, \tau_n)$$

where:

$$A_{n:i} = \frac{\tau_i}{\tau_i - \tau_n} A_{n:i} \quad \forall i < n \quad (41.1)$$

$$A_{n:n} = - \sum_{i=1}^{n-1} \frac{\tau_n}{\tau_i - \tau_n} A_{n:i} - y_n$$

$$f(t, \tau_i) = \frac{e^{-\frac{t}{\tau_i}}}{\tau_i} \int_{-\infty}^t F(t') e^{\frac{t'}{\tau_i}} dt'. \quad (41.2)$$

The values  $\tau_i$  are the mean life-times for the nuclei,  $y_i$  is the yield of the  $i^{th}$  nucleus, and  $F(t)$  is a function identifying the time profile of the source. The above expression for decay rate is simplified, since it assumes that the  $i^{th}$  nucleus undergoes 100% of the decays to the  $(i+1)^{th}$  nucleus. Similar expressions which allow for branching and merging of different decay chains can be found in Ref. [Tru96].

A consequence of the form of equations (41.1) and (41.2) is that the user may provide a source time profile so that each decay produced as a result of a simulated source particle incident at time  $t = 0$  is convolved over the source time profile to derive the actual decay rate for that source function.

This form of variance reduction is only appropriate if the radionuclei can be considered to be at rest with respect to the geometry when decay occurs.

2. For a given decay mode ( $\alpha$ ,  $\beta^+$  + EC, or  $\beta^-$ ) the branching ratios to the daughter nuclide can be sampled with equal probability, so that some low probability branches which may have a disproportionately greater effect on the measurement are sampled with increased probability.
3. Each parent nuclide can be split into a user-defined number of nuclides (of proportionally lower statistical weight) prior to treating decay in order to increase the sampling of the effects of the daughter products.



## BIBLIOGRAPHY

- [BT72] V.S. Barashenkov and V.D. Toneev. *High Energy interactions of particles and nuclei (In russian)*. 1972.
- [DKW00a] P. V. Degtyarenko, M. V. Kossov, and H. -P. Wellisch. Chiral invariant phase space event generator, i. nucleon-antinucleon annihilation at rest. *The European Physical Journal A*, 8(2):217–222, Jul 2000. URL: <https://doi.org/10.1007/s100500070108>, doi:10.1007/s100500070108.
- [DKW00b] P.V. Degtyarenko, M.V. Kossov, and H.-P. Wellisch. Chiral invariant phase space event generator, ii. nuclear pion capture at rest. *The European Physical Journal A*, 9(3):411–420, Dec 2000. URL: <https://doi.org/10.1007/s100500070025>, doi:10.1007/s100500070025.
- [DKW00c] P.V. Degtyarenko, M.V. Kossov, and H.-P. Wellisch. Chiral invariant phase space event generator, iii. modeling of real and virtual photon interactions with nuclei below pion production threshold. *The European Physical Journal A*, 9(3):421–424, Dec 2000. URL: <https://doi.org/10.1007/s100500070026>, doi:10.1007/s100500070026.
- [ealParticleDGroup16] C. Patrignani et al. (Particle Data Group). 2016 review of particle physics. *Chin. Phys. C*, 40, 100001, 2016.
- [Gri09a] V. M. Grichine. A simplified glauber model for hadron–nucleus cross sections. *The European Physical Journal C*, 62(2):399–404, May 2009. URL: <https://doi.org/10.1140/epjc/s10052-009-1033-z>, doi:10.1140/epjc/s10052-009-1033-z.
- [Gri09b] V.M. Grichine. A simple model for integral hadron–nucleus and nucleus–nucleus cross-sections. *Nuclear Instruments and Methods in Physics Research Section B: Beam Interactions with Materials and Atoms*, 267(14):2460–2462, Jul 2009. URL: <https://doi.org/10.1016/j.nimb.2009.05.020>, doi:10.1016/j.nimb.2009.05.020.
- [IHEP] IHEP:. Institute for high energy physics database, protvino, russia. <http://wwwppds.ihep.su:8001/ppds.html>. [Online; accessed 15-July-2023].
- [Kos02] M.V. Kossov. *European Physical Journal A*, 14:265, 2002.
- [NEA] NEA:. Barashenkov cross sections from nuclear energy agency, france. <http://www.nea.fr/html/dbdata/bara.html>. [Online; accessed 12-December-2017].
- [Groom00] D.E. et al. Groom. Review of Particle Physics. *The European Physical Journal*, C15:1+, 2000. URL: <http://pdg.lbl.gov>.
- [BP50] H.L. Bradt and B. Peters. *Physical Review*, 77:54, 1950.
- [eal87] S. Kox et al. Trends of total reaction cross sections for heavy ion collisions in the intermediate energy range. *Phys. Rev. C*, 35:1678–1691, 1987.
- [SBV74] C.B. Dover S. Barshay and J.P. Vary. *Physics Letters*, 51B():5, 1974.
- [SBV75] C.B. Dover S. Barshay and J.P. Vary. *Physical Review C*, 11():360, 1975.

- [SYuSZ89] V.V. Uzhinskii S.Yu. Shmakov and A.M. Zadorozhny. *Computer Physics Communications*, 54:125, 1989.
- [Shu03] P. Shukla. *Physical Review C*, 67(0):054607, 2003.
- [STS+93] L. Sihver, C. H. Tsao, R. Silberberg, T. Kanai, and A. F. Barghouty. Total reaction and partial cross section calculations in proton-nucleus ( $Zt \leq 26$ ) and nucleus-nucleus reactions ( $Zp$  and  $Zt \leq 26$ ). *Physical Review C*, 47(3):1225–1236, Mar 1993. URL: <https://doi.org/10.1103%2Fphysrevc.47.1225>, doi:10.1103/physrevc.47.1225.
- [AMZS84] V.V. Uzhinsky A.M. Zadorozhnyi and S.Yu. Shmakov. *Soviet Journal of Nuclear Physics*, 39:729, 1984. Russian original: *Yadernaya Fizika* 39 (1984) 1155.
- [DK85] O.D. Dalkarov and V.A. Karmanov. Scattering of low-energy antiprotons from nuclei. *Nuclear Physics A*, 445(4):579–604, Dec 1985. URL: [https://doi.org/10.1016/0375-9474\(85\)90561-5](https://doi.org/10.1016/0375-9474(85)90561-5), doi:10.1016/0375-9474(85)90561-5.
- [eal72] S.P. Denisov et al. *Nuclear Physics B*, 31:253, 1972.
- [eal11] V. Uzhinsky et al. *Physics Letters B*, 705:235, 2011.
- [Fra68] V. Franco. *Phys. Rev.*, 175:1376, 1968.
- [FG66] V. Franco and R. J. Glauber. High-energy deuteron cross sections. *Physical Review*, 142(4):1195–1214, Feb 1966. URL: <https://doi.org/10.1103/PhysRev.142.1195>, doi:10.1103/physrev.142.1195.
- [Gri09a] V. M. Grichine. A simplified glauber model for hadron–nucleus cross sections. *The European Physical Journal C*, 62(2):399–404, May 2009. URL: <https://doi.org/10.1140/epjc/s10052-009-1033-z>, doi:10.1140/epjc/s10052-009-1033-z.
- [Gri09b] V.M. Grichine. A simple model for integral hadron–nucleus and nucleus–nucleus cross-sections. *Nuclear Instruments and Methods in Physics Research Section B: Beam Interactions with Materials and Atoms*, 267(14):2460–2462, Jul 2009. URL: <https://doi.org/10.1016/j.nimb.2009.05.020>, doi:10.1016/j.nimb.2009.05.020.
- [SYuSZ89] V.V. Uzhinskii S.Yu. Shmakov and A.M. Zadorozhny. *Computer Physics Communications*, 54:125, 1989.
- [SWF+89] W.-Q. Shen, B. Wang, J. Feng, W.-L. Zhan, Y.-T. Zhu, and E.-P. Feng. Total reaction cross section for heavy-ion collisions and its relation to the neutron excess degree of freedom. *Nuclear Physics A*, 491:130–146, 1989.
- [WBB09] M. Rybczynski W. Broniowski and P. Bozek. *Computer Physics Communications*, 180:69, 2009.
- [ABV78] G.D. Alkhazov, S.L. Belostotsky, and A.A. Vorobyov. Scattering of 1 GeV protons on nuclei. *Physics Reports*, 42(2):89–144, Jun 1978. URL: [https://doi.org/10.1016/0370-1573\(78\)90083-2](https://doi.org/10.1016/0370-1573(78)90083-2), doi:10.1016/0370-1573(78)90083-2.
- [BW68] Robert H. Bassel and Colin Wilkin. High-energy proton scattering and the structure of light nuclei. *Physical Review*, 174(4):1179–1199, Oct 1968. URL: <https://doi.org/10.1103/PhysRev.174.1179>, doi:10.1103/physrev.174.1179.
- [BDK+81] A. Bujak, P. Devensky, A. Kuznetsov, B. Morozov, V. Nikitin, P. Nomokonov, Yu. Pilipenko, V. Smirnov, E. Jenkins, E. Malamud, M. Miyajima, and R. Yamada. Proton-helium elastic scattering from 45 to 400 GeV. *Physical Review D*, 23(9):1895–1910, May 1981. URL: <https://doi.org/10.1103/PhysRevD.23.1895>, doi:10.1103/physrevd.23.1895.
- [Cho68] T. T. Chou. Remarks on particle-nucleus scattering. *Physical Review*, 168(5):1594–1597, Apr 1968. URL: <https://doi.org/10.1103/PhysRev.168.1594>, doi:10.1103/physrev.168.1594.
- [EKS81] NT ERMEKOV, VL KOROTKIKH, and NI STARKOV. Estimate of the contribution of excitation of the 2+(1.78 mev) level of silicon to the cross-section for the reaction si-28(pi, 3-pi)si-28'. *Soviet Journal of Nuclear Physics*, 33(6):775–777, 1981.

- [Gla70] R.J. Glauber. *High Energy Physics and Nuclear Structure*. Plenum Press, NY, edited by s. devons edition, 1970.
- [KS83] VL KOROTKIKH and NI STARKOV. Photoproduction of heavy vector-mesons on nuclei with excitation of a discrete level. *Soviet Journal of Nuclear Physics*, 37(4):610–613, 1983.
- [NNikolskiiS+77] R.A. Nam, S.I. Nikol'skii, N.I. Starkov, V.A. Tsarev, A.P. Chubenko, and V.I. Yakovlev. Proton-proton total cross sections from cosmic ray data. *Sov. J. Nucl. Phys. (Engl. Transl.); (United States)*, 26:5:550–555, Nov 1977. *Yad. Fiz.* 26 1038 - Russian.
- [NGG+78] M.A. Nasser, M.M. Gazzaly, J.V. Geaga, B. Höistad, G. Igo, J.B. McClelland, A.L. Sagle, H. Spinka, J.B. Carroll, V. Perez-Mendez, and E.T.B. Whipple. P-4he elastic scattering at 2.68 GeV. *Nuclear Physics A*, 312(3):209–216, Dec 1978. URL: [https://doi.org/10.1016/0375-9474\(78\)90586-9](https://doi.org/10.1016/0375-9474(78)90586-9), doi:10.1016/0375-9474(78)90586-9.
- [B61] Elton L. R. B. *Nuclear Sizes*. Oxford University Press, Oxford, 1961.
- [BA69] Mottelson B. R. Bohr A. *Nuclear Structure*. W. A. Benjamin, New York, vol. 1 edition, 1969.
- [DA74] Feshbach H. DeShalit A. *Theoretical Nuclear Physics*. Wyley, vol. 1: nuclear structure edition, 1974.
- [GLMP91] M E Gryeos, G A Lalazissis, S E Massen, and C P Panos. The 'cosh' or symmetrized woods-saxon nuclear potential. *Journal of Physics G: Nuclear and Particle Physics*, 17(7):1093, 1991. URL: <http://stacks.iop.org/0954-3899/17/i=7/a=008>.
- [AA78] Capella A. and Krzywicki A. *Phys. Rev. D*, 18:4120, 1978.
- [ANS90] Toneev V. D. Amelin N. S., Gudima K. K. *Sov. J. Nucl. Phys.*, 51:327, 1990.
- [MA76] Baker M. and Ter-Martirosyan K. A. *Phys. Rep. C*, 28:1, 1976.
- [S86] Amelin N. S. *JINR Report*, 1986.
- [AUIJ94] Capella A., Sukhatme U., Tan C. I., and Tran Thanh Van. *J. Phys. Rep.*, 236:225, 1994.
- [ANS90] Toneev V. D. Amelin N. S., Gudima K. K. *Sov. J. Nucl. Phys.*, 51:327, 1990.
- [AB87] Nielsson-Almquist Andersson B., Gustafson G. *Nucl. Phys.*, 281:289, 1987.
- [KAB82] Ter-Martirosyan K. A. Kaidalov A. B. *Phys. Lett. B*, 117:247, 1982.
- [S86] Amelin N. S. *JINR Report*, 1986.
- [BGGT83] Andersson B., Gustafson G., Ingelman G., and Sjöstrand T. *Phys. Rep.*, 97:31, 1983.
- [B87] Kaidalov A. B. *Sov. J. Nucl. Phys.*, 45:1452, 1987.
- [AWU97] K. Abdel-Waged and V. V. Uzhinsky. Model of nuclear disintegration in high-energy nucleus nucleus interactions. *Phys. Atom. Nucl.*, 60:828–840, 1997. [Yad. Fiz.60,925(1997)].
- [AWU98] Kh Abdel-Waged and V V Uzhinskii. Estimation of nuclear destruction using ALADIN experimental data. *Journal of Physics G: Nuclear and Particle Physics*, 24(9):1723–1733, Sep 1998. URL: <https://doi.org/10.1088/0954-3899/24/9/006>, doi:10.1088/0954-3899/24/9/006.
- [AGK74] V.A. Abramovsky, V.N. Gribov, and O.V. Kancheli. *Sov. J. Nucl. Phys.*, 18:308, 1974. Russian original: *Yad. Fiz.* \bf 18 595 (1973).
- [AMWAFriedmanJHufner86] A.Y. Abul-Magd, W.A.Friedman, and J.Hufner. *Phys. Rev. C*, 34():113, 1986.
- [ABLAPS05] B. Alver, M. Baker, C. Loizides, and and P. Steinberg. *pre-print*, 2005. arxiv:0805.4411 [nucl-exp].
- [BNilssonAEStenlund87] B.Nilsson-Almquist and E.Stenlund. *Comp. Phys. Comm.*, 43:43, 1987.
- [BESSwanson92] T. Barnes and E.S.Swanson. *Phys. Rev. D*, 46:131, 1992.
- [BKKS91] K.G. Boreskov, A.B. Kaidalov, S.M. Kiselev, and N.Ya. Smorodinskaya. *Sov. J. Nucl. Phys.*, 53():356, 1991. Russian original: *Yad. Fiz.* \bf 53 569 (1991).

- [BRaPB09] W. Broniowski, M. Rybczynski, and and P. Bozek. *Comp. Phys. Commun.*, 180:69, 2009.
- [CSRJenco76] L. Caneschi, A. Schwimmer, and R.Jenco. *Nucl. Phys. B*, 108:82, 1976.
- [eal87] B.Andersson et al. *Nucl. Phys. B*, 281:289, 1987.
- [eal72] E. Bracci et al. Technical Report CERN–HERA 72-1, CERN, 1972.
- [eal73a] E. Bracci et al. Technical Report 73-1, CERN–HERA, 1973.
- [eal99] M. Bleicher et al. *J. Phys. G*, 25:1859, 1999.
- [eal73b] P. Bosettii et al. *Nucl. Phys. B*, 54:141, 1973.
- [eal98] S.A. Bass et al. *Prog. Part. Nucl. Phys.*, 41:225, 1998.
- [eal84] V. Flaminio et al. Technical Report 84-01, CERN–HERA, 1984.
- [ealCOMPLETEcollab02] J.R. Cudell et al. (COMPLETE collab.). *Phys. Rev. D*, 65:074024, 2002.
- [eal74] Bonn-Hamburg-Munich Collab. (V. Blobel et al.). *Nucl. Phys. B*, 69:454, 1974.
- [eal97] EMU-01 Collab. (M.I. Adamovich et al.). *Zeit. fur Phys. A*, 358:337, 1997.
- [eal09] HARP-CDP Collab. (A. Bolshakova et al.). *Eur. Phys. J. C*, 64:181, 2009.
- [FIW04] G. Folger, V. N. Ivanchenko, and J. P. Wellisch. The binary cascade. *The European Physical Journal A*, 21(3):407–417, Sep 2004. URL: <https://doi.org/10.1140/epja/i2003-10219-7>, doi:10.1140/epja/i2003-10219-7.
- [Fra68] V. Franco. *Phys. Rev.*, 175:1376, 1968.
- [Fur00] S. Furihata. *Nuclear Instruments and Methods in Physics Research B*, 171():251, 2000.
- [Gla59] R.J. Glauber. "Lectures in Theoretical Physics", Ed. W.E.Brittin et al. Interscience Publishers, N.Y., vol. 1 edition, 1959.
- [Gla67] R.J. Glauber. In Ed. G.A.Alexander, editor, *Proc. of the 2nd Int. Conf. on High Energy Physics and Nuclear structure*. Rehovoth, 1967. North-Holland, Amsterdam.
- [GM99] K.A. Goulianos and J. Montanha. *Phys. Rev. D*, 59:114017, 1999.
- [GDShoper77] J. Gunion and D.Shoper. *Phys. Rev. D*, 15():2617, 1977.
- [JDTreliani76] R. Jengo and D.Treliani. *Nucl. Phys. B*, 117:433, 1976.
- [KpTM86] A.B. Kaidalov, L.A. ponomarev, and K.A. Ter-Martirosian. *Sov. J. Nucl. Phys.*, 44:468, 1986. Russian original: Yad. Fiz. \bf 44 722 (1986).
- [KV94] A.B. Kaidalov and P.E. Volkovitsky. *Zeit. fur Phys.*, C63:517, 1994.
- [LR81] E.M. Levin and M.G. Ryskin. *Yad. Fiz.*, 34:619, 1981.
- [Low75] F. Low. *Phys. Rev. D*, 12:163, 1975.
- [MRSS07] M.L. Miller, K. Reygers, S.J. Sanders, and P. Steinberg. *Ann. Rev. Nucl. Part. Sci.*, 57:205, 2007.
- [Nus76] S. Nussinov. *Phys. Rev. D*, 14():246, 1976.
- [PDG12] PDG. Pdg 2012 online reference. <http://pdg.lbl.gov/2012/hadronic-xsections/hadron.html>, 2012. [Online; accessed 26-October-2017].
- [Sar80] R.E. Camboa Saravi. *Phys. Rev.*, 21:2021, 1980.
- [Sch75] A. Schwimmer. *Nucl. Phys. B*, 94:445, 1975.
- [Sha81] Yu.M. Shabelski. *Sov. J. Part. Nucl.*, 12:430, 1981.
- [SUZ89] S.Yu. Shmakov, V.V. Uzhinski, and A.M. Zadorojny. *Comp. Phys. Commun.*, 54:125, 1989.

- [TBarnesESSwanson92] T.Barnes and E.S.Swanson. *Phys. Rev. C*, 49:1166, 1992.
- [TBarnesESSwansonJWeinstein92] T.Barnes, E.S.Swanson, and J.Weinstein. *Phys. Rev. D*, 46:4868, 1992.
- [TBarnesSCapstickMDKovarikS93] T.Barnes, S.Capstick, M.D.Kovarik, and E.S. Swanson. *Phys. Rev. C*, 48:539, 1993.
- [UG02] V.V. Uzhinsky and A.S. Galoyan. *pre-print*, 2002.
- [Whi74] J. Whitmore. *Phys. Rep.*, 10:273, 1974.
- [AAH90] R.G. Alsmiller, F.S. Alsmiller, and O.W. Hermann. The high-energy transport code hetc88 and comparisons with experimental data. *Nuclear Instruments and Methods in Physics Research A*, 295():337–343, 1990.
- [BT72] V.S. Barashenkov and V.D. Toneev. *High Energy interactions of particles and nuclei (In russian)*. 1972.
- [BG71] H. W. Bertini and P. Guthrie. Results from medium-energy intranuclear-cascade calculation. *Nucl. Phys. A*, 1971.
- [DFF59] I. Dostrovsky, Z. Fraenkel, and G. Friedlander. Monte carlo calculations of nuclear evaporation processes. III. applications to low-energy reactions. *Physical Review*, 116(3):683–702, Nov 1959. URL: <https://doi.org/10.1103/PhysRev.116.683>, doi:10.1103/physrev.116.683.
- [DFR60] I. Dostrovsky, Z. Fraenkel, and P. Rabinowitz. Monte carlo calculations of nuclear evaporation processes. v. emission of particles heavier than  ${}^4\text{He}$ . *Physical Review*, 118(3):791–793, May 1960. URL: <https://doi.org/10.1103/physrev.118.791>, doi:10.1103/physrev.118.791.
- [eal73] I. Ribansky et al. Pre-equilibrium decay and the exciton model. *Nucl. Phys. A*, 205():545–560, 1973.
- [eal83] J. R. Letaw et al. *The Astrophysical Journal Supplements*, 51:271, 1983.
- [eal93] J. R. Letaw et al. *The Astrophysical Journal*, 414:601, 1993.
- [eal03] S. Agostinelli et al. Geant4—a simulation toolkit. *Nuclear Instruments and Methods in Physics Research Section A: Accelerators, Spectrometers, Detectors and Associated Equipment*, 506(3):250–303, Jul 2003. URL: [https://doi.org/10.1016/S0168-9002\(03\)01368-8](https://doi.org/10.1016/S0168-9002(03)01368-8), doi:10.1016/s0168-9002(03)01368-8.
- [eal99] Yu. E. Titarenko et al. Experimental and computer simulations study of radionuclide production in heavy materials irradiated by intermediate energy protons. Technical Report nucl-ex/9908012, pre-print, 1999.
- [Fon69] P. Fong. *Statistical Theory of Fission*. Gordon and Breach, New York, 1969.
- [Gol48] M. Goldberger. The interaction of high energy neutrons and hevy nuclei. *Phys. Rev.*, 74:1269, 1948.
- [Gri66] J. J. Griffin. Statistical model of intermediate structure. *Physical Review Letters*, 17():478–481, 1966.
- [Gri67] J. J. Griffin. Statistical model of intermediate structure. *Physical Letters*, 24B(1):5–7, 1967.
- [GAB68] M. P. Guthrie, R. G. Alsmiller, and H. W. Bertini. *Nucl. Instr. Meth.*, 66:29, 1968.
- [Kal78] C. Kalbach. Exciton number dependence of the griffin model two-body matrix element. *Z. Physik A*, 287:319–322, 1978.
- [MBS58] N. Metropolis, R. Bibins, and M. Storm. Monte carlo calculations on intranuclear cascades. i. low-energy studies. *Physical Review*, 110:185, 1958.
- [Pea89] S. Pearlstein. Medium-energy nuclear data libraries: a case study, neutron- and proton-induced reactions in  ${}^{56}\text{Fe}$ . *The Astrophysical Journal*, 346():1049–1060, 1989.
- [Ser47] R. Serber. Nuclear reactions at high energies. *Phys. Rev.*, 72:1114, 1947.
- [Wei37] V. Weisskopf. Statistics and nuclear reactions. *Physical Review*, 52(4):295–303, Aug 1937. URL: <https://doi.org/10.1103/PhysRev.52.295>, doi:10.1103/physrev.52.295.

- [B61] Elton L. R. B. *Nuclear Sizes*. Oxford University Press, Oxford, 1961.
- [CVV97a] J. Cugnon, C. Volant, and S. Vuillier. Improved intranuclear cascade model for nucleon-nucleus interactions. *Nuclear Physics A*, 620(4):475–509, Jul 1997. URL: [https://doi.org/10.1016/S0375-9474\(97\)00186-3](https://doi.org/10.1016/S0375-9474(97)00186-3), doi:10.1016/s0375-9474(97)00186-3.
- [CVV97b] J. Cugnon, C. Volant, and S. Vuillier. Nucleon and deuteron induced spallation reactions. *Nuclear Physics A*, 625(4):729–757, Nov 1997. URL: [https://doi.org/10.1016/S0375-9474\(97\)00602-7](https://doi.org/10.1016/S0375-9474(97)00602-7), doi:10.1016/s0375-9474(97)00602-7.
- [DA74] Feshbach H. DeShalit A. *Theoretical Nuclear Physics*. Wley, vol. 1: nuclear structure edition, 1974.
- [FIW04] G. Folger, V. N. Ivanchenko, and J. P. Wellisch. The binary cascade. *The European Physical Journal A*, 21(3):407–417, Sep 2004. URL: <https://doi.org/10.1140/epja/i2003-10219-7>, doi:10.1140/epja/i2003-10219-7.
- [GS91] J.-J. Gaimard and K.-H. Schmidt. A reexamination of the abrasion-ablation model for the description of the nuclear fragmentation reaction. *Nuclear Physics A*, 531(3-4):709–745, Sep 1991. URL: [https://doi.org/10.1016/0375-9474\(91\)90748-U](https://doi.org/10.1016/0375-9474(91)90748-U), doi:10.1016/0375-9474(91)90748-u.
- [GLMP91] M E Grypeos, G A Lalazissis, S E Massen, and C P Panos. The 'cosh' or symmetrized woods-saxon nuclear potential. *Journal of Physics G: Nuclear and Particle Physics*, 17(7):1093, 1991. URL: <http://stacks.iop.org/0954-3899/17/i=7/a=008>.
- [IBGP92] A. S. Ilinov, A. B. Botvina, E. S. Golubeva, and I. A. Pshenichnov. Intranuclear cascade mechanism in anti-nucleon nucleus interactions. *Sov. J. Nucl. Phys.*, 55:734–743, 1992.
- [PBN94] G. Peter, D. Behrens, and C. C. Noack. Poincaré covariant particle dynamics. i. intranuclear cascade model. *Physical Review C*, 49(6):3253–3265, Jun 1994. URL: <https://doi.org/10.1103/PhysRevC.49.3253>, doi:10.1103/physrevc.49.3253.
- [rtbcVV] reference to be completed. (): 2VVV.
- [rtbcWW] reference to be completed. (): 2WWW.
- [rtbcXX] reference to be completed. (): 2XXX.
- [rtbcYY] reference to be completed. (): 2YYY.
- [rtbcZZ] reference to be completed. (): 2ZZZ.
- [SMC79] K. Stricker, H. McManus, and J. A. Carr. Nuclear scattering of low energy pions. *Physical Review C*, 19(3):929–947, Mar 1979. URL: <https://doi.org/10.1103/PhysRevC.19.929>, doi:10.1103/physrevc.19.929.
- [WHQ92] LIU Yong WANG Hai-Qiao, CAI Xu. The intranuclear cascade and the target fragmentation in high energy ha collisions. *Chinese physics C*, 16(S1):101–106, 1992. URL: <http://cpc.ihep.ac.cn/article/id/451f970e-d373-4068-a249-241de7f05308>.
- [BL74] A. R. Barnett and J. S. Lilley. Interaction of alpha particles in the lead region near the coulomb barrier. *Physical Review C*, 9(5):2010–2027, May 1974. URL: <https://doi.org/10.1103/PhysRevC.9.2010>, doi:10.1103/physrevc.9.2010.
- [BCD+13] A. Boudard, J. Cugnon, J.-C. David, S. Leray, and D. Mancusi. New potentialities of the liège intranuclear cascade model for reactions induced by nucleons and light charged particles. *Physical Review C*, Jan 2013. URL: <https://doi.org/10.1103/PhysRevC.87.014606>, doi:10.1103/physrevc.87.014606.
- [CDG+72] D. R. F. Cochran, P. N. Dean, P. A. M. Gram, E. A. Knapp, E. R. Martin, D. E. Nagle, R. B. Perkins, W. J. Shlaer, H. A. Thiessen, and E. D. Theriot. Production of charged pions by 730-MeV protons from hydrogen and selected nuclei. *Physical Review D*, 6(11):3085–3116, Dec 1972. URL: <https://doi.org/10.1103/PhysRevD.6.3085>, doi:10.1103/physrevd.6.3085.

- [DL74] G Deconninck and M Longree. Fonctions d'excitation des réactions induites par particules alpha sur bi entre 40 et 100 mev. In *Annales de la Société Scientifique de Bruxelles*, volume 88, 341–346. 1974.
- [eal05] A. Hermanne et al. Experimental study of the cross sections of  $\alpha$ -particle induced reactions on  $^{209}\text{Bi}$ . In *AIP Conference Proceedings*. AIP, 2005. Conf. on Nucl. Data for Sci. and Techn., Santa Fe 2004. URL: <https://doi.org/10.1063/1.1945163>, doi:10.1063/1.1945163.
- [IAE] IAEA. Benchmark of spallation models, organized by the iaea. <http://www-nds.iaea.org/spallations>. [Online; accessed 28-October-2017].
- [IMS+01] Y. Iwata, T. Murakami, H. Sato, H. Iwase, T. Nakamura, T. Kurosawa, L. Heilbronn, R. M. Ronningen, K. Ieki, Y. Tozawa, and K. Niita. Double-differential cross sections for the neutron production from heavy-ion reactions at energies  $E/a=290\text{--}600\text{mev}$ . *Physical Review C*, Oct 2001. URL: <https://doi.org/10.1103/PhysRevC.64.054609>, doi:10.1103/physrevc.64.054609.
- [KAH08] Ricciardi M V Kelic A and Schmidt K H. Abla07 — towards a complete description of the decay channels of a nuclear system from spontaneous fission to multifragmentation. In D Filges, S Leray, Y Yariv, A Mengoni, A Stanculescu, and G Mank Eds., editors, *Proceedings of the Joint ICTP-IAEA Advanced Workshop on Model Codes for Spallation Reactions*, number INDC(NDS)-530, 181. ICTP Trieste, Italy, 4-8 February 2008. IAEA, IAEA Vienna, August 2008. download: <https://www-nds.iaea.org/publications/indc/indc-nds-0530.pdf>.
- [KSegre49] E. L. Kelly and E. Segrè. Some excitation functions of bismuth. *Physical Review*, 75(7):999–1005, Apr 1949. URL: <https://doi.org/10.1103/PhysRev.75.999>, doi:10.1103/physrev.75.999.
- [LM85] Richard M. Lambrecht and Saed Mirzadeh. Cyclotron isotopes and radiopharmaceuticals—XXXV astatine-211. *The International Journal of Applied Radiation and Isotopes*, 36(6):443–450, Jun 1985. URL: [https://doi.org/10.1016/0020-708X\(85\)90207-8](https://doi.org/10.1016/0020-708X(85)90207-8), doi:10.1016/0020-708X(85)90207-8.
- [MBC+14] Davide Mancusi, Alain Boudard, Joseph Cugnon, Jean-Christophe David, Pekka Kaitaniemi, and Sylvie Leray. Extension of the liège intranuclear-cascade model to reactions induced by light nuclei. *Physical Review C*, Nov 2014. URL: <https://doi.org/10.1103/PhysRevC.90.054602>, doi:10.1103/physrevc.90.054602.
- [RBAC90] I.A. Rizvi, M.K. Bhardwaj, M.Afzal Ansari, and A.K. Chaubey. Non-equilibrium reaction mechanism in alpha-particle induced excitation function for  $^{209}\text{Bi}$  up to 60 MeV. *International Journal of Radiation Applications and Instrumentation. Part A. Applied Radiation and Isotopes*, 41(2):215–219, Jan 1990. URL: [https://doi.org/10.1016/0883-2889\(90\)90112-T](https://doi.org/10.1016/0883-2889(90)90112-T), doi:10.1016/0883-2889(90)90112-t.
- [RodriguezSanchezDM+17] Jose Luis Rodríguez-Sánchez, Jean-Christophe David, Davide Mancusi, Alain Boudard, Joseph Cugnon, and Sylvie Leray. Improvement of one-nucleon removal and total reaction cross sections in the liège intranuclear-cascade model using hartree-fock-bogoliubov calculations. *Phys. Rev. C*, 96:054602, Nov 2017. URL: <https://link.aps.org/doi/10.1103/PhysRevC.96.054602>, doi:10.1103/PhysRevC.96.054602.
- [SMS94] N. L. Singh, S. Mukherjee, and D. R. S. Somayajulu. Non-equilibrium analysis of ( $\alpha$ ,xn) reactions on heavy nuclei. *Il Nuovo Cimento A*, 107(9):1635–1645, Sep 1994. URL: <https://doi.org/10.1007/BF02780697>, doi:10.1007/bf02780697.
- [SH74] J. D. Stickler and K. J. Hofstetter. Comparison of  $^3\text{He}$ -,  $^4\text{He}$ -, and  $^{12}\text{C}$ -induced nuclear reactions in heavy-mass targets at medium excitation energies. i. experimental cross sections. *Physical Review C*, 9(3):1064–1071, Mar 1974. URL: <https://doi.org/10.1103/PhysRevC.9.1064>, doi:10.1103/physrevc.9.1064.
- [PatelShahSingh99] H. B. Patel, D. J. Shah, and N. L. Singh. Study of ( $\alpha$ ,xn) reactions on  $^{169}\text{Tm}$ ,  $^{181}\text{Ta}$  and  $^{209}\text{Bi}$  up to 70 MeV. *Nuovo Cimento A Serie*, 112:1439, December 1999.
- [eal73] I. Ribansky et al. Pre-equilibrium decay and the exciton model. *Nucl. Phys. A*, 205():545–560, 1973.
- [GMT83] K.K. Gudima, S.G. Mashnik, and V.D. Toneev. *Nucl. Phys. A*, 401:329, 1983.

- [MBS58] N. Metropolis, R. Bibins, and M. Storm. Monte carlo calculations on intranuclear cascades. i. low-energy studies. *Physical Review*, 110:185, 1958.
- [WE40] V. F. Weisskopf and D. H. Ewing. On the yield of nuclear reactions with heavy elements. *Physical Review*, 57(6):472–485, Mar 1940. URL: <https://doi.org/10.1103/PhysRev.57.472>, doi:10.1103/physrev.57.472.
- [Wil70] F. C. Williams. *Phys. Lett. B*, 31:180, 1970.
- [Fre36] J Frenkel. On the absorption of light and the trapping of electrons and positive holes in crystalline dielectrics. *Phys. Zs. Sowjetunion*, 9:533–536, 1936.
- [WE40] V. F. Weisskopf and D. H. Ewing. On the yield of nuclear reactions with heavy elements. *Physical Review*, 57(6):472–485, Mar 1940. URL: <https://doi.org/10.1103/PhysRev.57.472>, doi:10.1103/physrev.57.472.
- [ASIP94] M. V. Kazarnovsky A. S. Iljinov and E. Ya. Paryev. *Intermediate-Energy Nuclear Physics*. CRC Press, 1994.
- [BW52] J. Blatt and V. F. Weisskopf. *Theoretical Nuclear Physics*. John Wiley & Sons, Inc., New York, 1952.
- [CFdLM67] JL Cook, H Ferguson, and AR de L Musgrove. Nuclear level densities in intermediate and heavy nuclei. *Australian Journal of Physics*, 20(5):477, 1967. URL: <https://doi.org/10.1071/PH670477>, doi:10.1071/ph670477.
- [DFF59] I. Dostrovsky, Z. Fraenkel, and G. Friedlander. Monte carlo calculations of nuclear evaporation processes. III. applications to low-energy reactions. *Physical Review*, 116(3):683–702, Nov 1959. URL: <https://doi.org/10.1103/PhysRev.116.683>, doi:10.1103/physrev.116.683.
- [Fur00] S. Furihata. Statistical analysis of light fragment production from medium energy proton-induced reactions. *Nuclear Instruments and Methods in Physics Research Section B: Beam Interactions with Materials and Atoms*, 171(3):251–258, Nov 2000. URL: [https://doi.org/10.1016/S0168-583X\(00\)00332-3](https://doi.org/10.1016/S0168-583X(00)00332-3), doi:10.1016/s0168-583x(00)00332-3.
- [GC65] A. Gilbert and A. G. W. Cameron. A COMPOSITE NUCLEAR-LEVEL DENSITY FORMULA WITH SHELL CORRECTIONS. *Canadian Journal of Physics*, 43(8):1446–1496, Aug 1965. URL: <https://doi.org/10.1139/p65-139>, doi:10.1139/p65-139.
- [HB51] H. Hurwitz and H. A. Bethe. Neutron capture cross sections and level density. *Physical Review*, 81(5):898–898, Mar 1951. URL: <https://doi.org/10.1103/PhysRev.81.898>, doi:10.1103/physrev.81.898.
- [IMB+92] A.S. Iljinov, M.V. Mebel, N. Bianchi, E. De Sanctis, C. Guaraldo, V. Lucherini, V. Muccifora, E. Polli, A.R. Reolon, and P. Rossi. Phenomenological statistical analysis of level densities, decay widths and lifetimes of excited nuclei. *Nuclear Physics A*, 543(3):517–557, Jul 1992. URL: [https://doi.org/10.1016/0375-9474\(92\)90278-R](https://doi.org/10.1016/0375-9474(92)90278-R), doi:10.1016/0375-9474(92)90278-r.
- [MAL82] T. Matsuse, A. Arima, and S. M. Lee. Critical distance in fusion reactions. *Physical Review C*, 26(5):2338–2341, Nov 1982. URL: <https://doi.org/10.1103/PhysRevC.26.2338>, doi:10.1103/physrevc.26.2338.
- [Sha53] Mathew M. Shapiro. Cross sections for the formation of the compound nucleus by charged particles. *Physical Review*, 90(2):171–182, Apr 1953. URL: <https://doi.org/10.1103/PhysRev.90.171>, doi:10.1103/physrev.90.171.
- [TCH70] J W Truran, A G V Cameron, and E Hilf. Construction of mass formulas designed to be valid for neutron-rich nuclei. *Proc. Int. Conf. on the Properties of Nuclei Far From the Beta-Stability, Leysin, Switzerland, August 31 - September 4, 1970*, pages 275–306, 1970. CERN-1970-030-V-1. URL: <http://cds.cern.ch/record/867056>.
- [Wei37] V. Weisskopf. Statistics and nuclear reactions. *Physical Review*, 52(4):295–303, Aug 1937. URL: <https://doi.org/10.1103/PhysRev.52.295>, doi:10.1103/physrev.52.295.

- [BITG73] V.S. Barashenkov, A.S. Iljinov, V.D. Toneev, and F.G. Gereghi. Fission and decay of excited nuclei. *Nuclear Physics A*, 206(1):131–144, May 1973. URL: [https://doi.org/10.1016/0375-9474\(73\)90611-8](https://doi.org/10.1016/0375-9474(73)90611-8), doi:10.1016/0375-9474(73)90611-8.
- [BW39] Niels Bohr and John Archibald Wheeler. The mechanism of nuclear fission. *Physical Review*, 56(5):426–450, Sep 1939. URL: <https://doi.org/10.1103/PhysRev.56.426>, doi:10.1103/physrev.56.426.
- [Cam57] A. G. W. Cameron. A REVISED SEMIEMPIRICAL ATOMIC MASS FORMULA. *Canadian Journal of Physics*, 35(9):1021–1032, Sep 1957. URL: <https://doi.org/10.1139/p57-114>, doi:10.1139/p57-114.
- [Cam58] A. G. W. Cameron. NUCLEAR LEVEL SPACINGS. *Canadian Journal of Physics*, 36(8):1040–1057, Aug 1958. URL: <https://doi.org/10.1139/p58-112>, doi:10.1139/p58-112.
- [had] Evaluated nuclear structure data file (ensdf) - a computer file of evaluated experimental nuclear structure data maintained by the national nuclear data center, brookhaven national laboratory. <http://www.nndc.bnl.gov/nudat2/>. [Online; accessed 31-October-2017].
- [BT78] I.M. Band and M.B. Trzhaskovskaya. Tables of the gamma-ray internal conversion coefficients for the k-, l-, m- shells,  $10 \leq z \leq 104$ . *Special Report of Leningrad Nuclear Physics Institute*, 1978.
- [BTL76] I.M. Band, M.B. Trzhaskovskaya, and M.A. Listengarten. Internal conversion coefficients for atomic numbers  $z \leq 30$ . *Atomic Data and Nuclear Data Tables*, 18(5):433–457, Nov 1976. URL: [https://doi.org/10.1016/0092-640X\(76\)90013-9](https://doi.org/10.1016/0092-640X(76)90013-9), doi:10.1016/0092-640X(76)90013-9.
- [HS68] R.S. Hager and E.C. Seltzer. Internal conversion tables part II: directional and polarization particle parameters for  $z = 30$  to  $z = 103$ . *Nuclear Data Sheets. Section A*, 4(5-6):397–411, Oct 1968. URL: [https://doi.org/10.1016/S0550-306X\(68\)80017-5](https://doi.org/10.1016/S0550-306X(68)80017-5), doi:10.1016/s0550-306x(68)80017-5.
- [IMB+92] A.S. Iljinov, M.V. Mebel, N. Bianchi, E. De Sanctis, C. Guaraldo, V. Lucherini, V. Muccifora, E. Polli, A.R. Reolon, and P. Rossi. Phenomenological statistical analysis of level densities, decay widths and lifetimes of excited nuclei. *Nuclear Physics A*, 543(3):517–557, Jul 1992. URL: [https://doi.org/10.1016/0375-9474\(92\)90278-R](https://doi.org/10.1016/0375-9474(92)90278-R), doi:10.1016/0375-9474(92)90278-r.
- [RD00] M Rysavý and O Dragoun. On the reliability of the theoretical internal conversion coefficients. *Journal of Physics G: Nuclear and Particle Physics*, 26(12):1859–1872, 2000. URL: <http://stacks.iop.org/0954-3899/26/i=12/a=309>.
- [RFAP78] F. Rösel, H.M. Fries, K. Alder, and H.C. Pauli. Internal conversion coefficients for all atomic shells. *Atomic Data and Nuclear Data Tables*, 21(2-3):91–289, Feb 1978. URL: [https://doi.org/10.1016/0092-640X\(78\)90034-7](https://doi.org/10.1016/0092-640X(78)90034-7), doi:10.1016/0092-640X(78)90034-7.
- [EKM85] Viola V. E., Kwiatkowski K., and Walker M. *Phys. Rev. C*, 31:1550, 1985.
- [eal93] Adeev G. D. et al. Technical Report, INR, Moscow, Russia, 1993. Preprint INR 816/93.
- [VR73] Huizenga J. R. Vandebosch R. *Nuclear Fission*. Academic Press, New York, 1973.
- [AS81] F. Ajzenberg-Selove. Energy levels of light nuclei  $a = 13–15$ . *Nuclear Physics A*, 360(1):1–186, May 1981. URL: [https://doi.org/10.1016/0375-9474\(81\)90510-8](https://doi.org/10.1016/0375-9474(81)90510-8), doi:10.1016/0375-9474(81)90510-8.
- [AS82] F. Ajzenberg-Selove. Energy levels of light nuclei  $a = 16–17$ . *Nuclear Physics A*, 375(1):1–168, Feb 1982. URL: [https://doi.org/10.1016/0375-9474\(82\)90538-3](https://doi.org/10.1016/0375-9474(82)90538-3), doi:10.1016/0375-9474(82)90538-3.
- [AS83] F. Ajzenberg-Selove. Energy levels of light nuclei  $a = 18–20$ . *Nuclear Physics A*, 392(1):1–184, Jan 1983. URL: [https://doi.org/10.1016/0375-9474\(83\)90180-X](https://doi.org/10.1016/0375-9474(83)90180-X), doi:10.1016/0375-9474(83)90180-x.
- [AS84] F. Ajzenberg-Selove. Energy levels of light nuclei  $a = 5–10$ . *Nuclear Physics A*, 413(1):1–168, Jan 1984. URL: [https://doi.org/10.1016/0375-9474\(84\)90650-X](https://doi.org/10.1016/0375-9474(84)90650-X), doi:10.1016/0375-9474(84)90650-x.
- [AS85] F. Ajzenberg-Selove. Energy levels of light nuclei  $a = 11–12$ . *Nuclear Physics A*, 433(1):1–157, Jan 1985. URL: [https://doi.org/10.1016/0375-9474\(85\)90484-1](https://doi.org/10.1016/0375-9474(85)90484-1), doi:10.1016/0375-9474(85)90484-1.

- [BaravsenkovBarbavsevB58] V. S. Barašenkov, B. M. Barbašev, and E. G. Bubelev. Statistical theory of particle multiple production in high energy nucleon collisions. *Il Nuovo Cimento*, 7(S1):117–128, Jan 1958. URL: <https://doi.org/10.1007/BF02725091>, doi:10.1007/bf02725091.
- [BBI+95] J.P. Bondorf, A.S. Botvina, A.S. Iljinov, I.N. Mishustin, and K. Sneppen. Statistical multifragmentation of nuclei. *Physics Reports*, 257(3):133–221, Jun 1995. URL: [https://doi.org/10.1016/0370-1573\(94\)00097-M](https://doi.org/10.1016/0370-1573(94)00097-M), doi:10.1016/0370-1573(94)00097-m.
- [EGKR69] Marcelle Épherre, Eli Gradsztajn, Robert Klapisch, and Hubert Reeves. Comparison between the evaporation and the break-up models of nuclear de-excitation. *Nuclear Physics A*, 139(3):545–553, Dec 1969. URL: [https://doi.org/10.1016/0375-9474\(69\)90278-4](https://doi.org/10.1016/0375-9474(69)90278-4), doi:10.1016/0375-9474(69)90278-4.
- [Err83] Errata. Energy levels of light nuclei,  $a = 16\text{--}17$ . *Nuclear Physics A*, 392(1):185–216, Jan 1983. URL: [https://doi.org/10.1016/0375-9474\(83\)90181-1](https://doi.org/10.1016/0375-9474(83)90181-1), doi:10.1016/0375-9474(83)90181-1.
- [Err84] Errata. Energy levels of light nuclei,  $a = 18\text{--}20$ . *Nuclear Physics A*, 413(1):168–214, Jan 1984. URL: [https://doi.org/10.1016/0375-9474\(84\)90651-1](https://doi.org/10.1016/0375-9474(84)90651-1), doi:10.1016/0375-9474(84)90651-1.
- [Fer50] E. Fermi. High energy nuclear events. *Progress of Theoretical Physics*, 5(4):570–583, Jul 1950. URL: <https://doi.org/10.1143/ptp/5.4.570>, doi:10.1143/ptp/5.4.570.
- [I70] Kopylov G. I. *Principles of resonance kinematics (in Russian)*. Moskva : "Nauka," Glav. red. fiziko-matematicheskoi, 1970.
- [Kop85] G. I. Kopylov. *ELEMENTARY KINEMATICS OF ELEMENTARY PARTICLES*. Moscow, USSR: Mir Publ. ( 1983) 270p, 1985.
- [Kop73] G.I. Kopylov. The kinematics of inclusive experiments with unstable particles. *Nuclear Physics B*, 52(1):126–140, Jan 1973. URL: [https://doi.org/10.1016/0550-3213\(73\)90090-4](https://doi.org/10.1016/0550-3213(73)90090-4), doi:10.1016/0550-3213(73)90090-4.
- [Kre61] M Kretzschmar. Statistical methods in high-energy physics. *Annual Review of Nuclear Science*, 11(1):1–38, Dec 1961. URL: <https://doi.org/10.1146/annurev.ns.11.120161.000245>, doi:10.1146/annurev.ns.11.120161.000245.
- [ÉpherreG67] Marcelle Épherre and Élie Gradsztajn. Calcul de la spallation de  $^{12}\text{C}$  et  $^{16}\text{O}$  par des protons de 70 à 200 MeV. *Journal de Physique*, 28(10):745–751, 1967. URL: <https://doi.org/10.1051/jphys:019670028010074500>, doi:10.1051/jphys:019670028010074500.
- [BBI+95] J.P. Bondorf, A.S. Botvina, A.S. Iljinov, I.N. Mishustin, and K. Sneppen. Statistical multifragmentation of nuclei. *Physics Reports*, 257(3):133–221, Jun 1995. URL: [https://doi.org/10.1016/0370-1573\(94\)00097-M](https://doi.org/10.1016/0370-1573(94)00097-M), doi:10.1016/0370-1573(94)00097-m.
- [eal87] Botvina A. S. et al. *Nucl. Phys. A*, 475:663, 1987.
- [Bas80] R. Bass. Fusion reactions: successes and limitations of a one-dimensional description. *Proceedings of the Symposium on Deep-Inelastic and Fusion Reactions with Heavy Ions*, Springer Verlag, Berlin, 1980, pages 281–293, 1980.
- [BGdJ+98] J. Benlliure, A. Grewe, M. de Jong, K.-H. Schmidt, and S. Zhdanov. Calculated nuclide production yields in relativistic collisions of fissile nuclei. *Nuclear Physics A*, 628(3):458 – 478, 1998. URL: <http://www.sciencedirect.com/science/article/pii/S0375947497006076>, doi:[https://doi.org/10.1016/S0375-9474\(97\)00607-6](https://doi.org/10.1016/S0375-9474(97)00607-6).
- [BW39] Niels Bohr and John Archibald Wheeler. The mechanism of nuclear fission. *Physical Review*, 56(5):426–450, Sep 1939. URL: <https://doi.org/10.1103/PhysRev.56.426>, doi:10.1103/physrev.56.426.
- [CCR04] Philippe Chomaz, Maria Colonna, and Jørgen Randrup. Nuclear spinodal fragmentation. *Physics Reports*, 389(5):263 – 440, 2004. URL: <http://www.sciencedirect.com/science/article/pii/S0370157303003934>, doi:<https://doi.org/10.1016/j.physrep.2003.09.006>.

- [HM88] Rainer W. Hasse and William D. Myers. *Folded Distributions*, pages 25–28. Springer Berlin Heidelberg, Berlin, Heidelberg, 1988. URL: [https://doi.org/10.1007/978-3-642-83017-4\\_3](https://doi.org/10.1007/978-3-642-83017-4_3), doi:10.1007/978-3-642-83017-4\_3.
- [HWK+21] W.J. Huang, Meng Wang, F.G. Kondev, G. Audi, and S. Naimi. The ame 2020 atomic mass evaluation: (i). evaluation of input data, adjustment procedures. *Chinese Physics C*, 45(3):030002, 2021. URL: <https://dx.doi.org/10.1088/1674-1137/abddb0>, doi:10.1088/1674-1137/abddb0.
- [Ign00] A. V. Ignatyuk. Systematics of low-lying level densities and radiative widths. *Proceedings of the Conference Bologna 2000: Structure of the Nucleus at the Dawn of the Century, Bologna, Italy, 29 May - 3 June 2000*, edited by G. C. Bonsignori, M. Bruno, A. Ventura, and D. Vretenar, pages 287–292, 2000.
- [JdJC+98] A.R. Junghans, M. de Jong, H.-G. Clerc, A.V. Ignatyuk, G.A. Kudyaev, and K.-H. Schmidt. Projectile-fragment yields as a probe for the collective enhancement in the nuclear level density. *Nuclear Physics A*, 629(3):635 – 655, 1998. URL: <http://www.sciencedirect.com/science/article/pii/S0375947498006587>, doi:[https://doi.org/10.1016/S0375-9474\(98\)00658-7](https://doi.org/10.1016/S0375-9474(98)00658-7).
- [JSB03] B. Jurado, K.-H. Schmidt, and J. Benlliure. Time evolution of the fission-decay width under the influence of dissipation. *Physics Letters B*, 553(3):186 – 190, 2003. URL: <http://www.sciencedirect.com/science/article/pii/S0370269302032343>, doi:[https://doi.org/10.1016/S0370-2693\(02\)03234-3](https://doi.org/10.1016/S0370-2693(02)03234-3).
- [JSS+05] B. Jurado, C. Schmitt, K.-H. Schmidt, J. Benlliure, and A.R. Junghans. A critical analysis of the modelling of dissipation in fission. *Nuclear Physics A*, 747(1):14 – 43, 2005. URL: <http://www.sciencedirect.com/science/article/pii/S0375947404010759>, doi:<https://doi.org/10.1016/j.nuclphysa.2004.09.123>.
- [KAH08] Ricciardi M V Kelic A and Schmidt K H. Abla07 — towards a complete description of the decay channels of a nuclear system from spontaneous fission to multifragmentation. In D Filges, S Leray, Y Yariv, A Mengoni, A Stanculescu, and G Mank Eds., editors, *Proceedings of the Joint ICTP-IAEA Advanced Workshop on Model Codes for Spallation Reactions*, number INDC(NDS)-530, 181. ICTP Trieste, Italy, 4-8 February 2008. IAEA, IAEA Vienna, August 2008. download: <https://www-nds.iaea.org/publications/indc/indc-nds-0530.pdf>.
- [Kra40] H.A. Kramers. Brownian motion in a field of force and the diffusion model of chemical reactions. *Physica*, 7(4):284 – 304, 1940. URL: <http://www.sciencedirect.com/science/article/pii/S0031891440900982>, doi:[https://doi.org/10.1016/S0031-8914\(40\)90098-2](https://doi.org/10.1016/S0031-8914(40)90098-2).
- [KAB+02] K. Kruglov, A. Andreyev, B. Bruyneel, S. Dean, S. Fransoo, M. Górska, K. Helariutta, M. Huyse, Yu. Kudryavtsev, W.F. Mueller, N.V.S.V. Prasad, R. Raabe, K.-H. Schmidt, P. Van Duppen, J. Van Roosbroeck, K. Van de Vel, and L. Weissman. Yields of neutron-rich isotopes around  $z = 28$  produced in 30 mev proton-induced fission of  $^{238}\text{U}$ . *The European Physical Journal A - Hadrons and Nuclei*, 14(3):365–370, Jul 2002. URL: <https://doi.org/10.1140/epja/i2002-10013-1>, doi:10.1140/epja/i2002-10013-1.
- [MNMS95] P. Moller, J.R. Nix, W.D. Myers, and W.J. Swiatecki. Nuclear ground-state masses and deformations. *Atomic Data and Nuclear Data Tables*, 59(2):185 – 381, 1995. URL: <http://www.sciencedirect.com/science/article/pii/S0092640X85710029>, doi:<https://doi.org/10.1006/adnd.1995.1002>.
- [Mor75] Luciano G. Moretto. Statistical emission of large fragments: a general theoretical approach. *Nuclear Physics A*, 247(2):211 – 230, 1975. URL: <http://www.sciencedirect.com/science/article/pii/0375947475906326>, doi:[https://doi.org/10.1016/0375-9474\(75\)90632-6](https://doi.org/10.1016/0375-9474(75)90632-6).
- [NWH+02] J. B. Natowitz, R. Wada, K. Hagel, T. Keutgen, M. Murray, A. Makeev, L. Qin, P. Smith, and C. Hamilton. Caloric curves and critical behavior in nuclei. *Phys. Rev. C*, 65:034618, Mar 2002. URL: <https://link.aps.org/doi/10.1103/PhysRevC.65.034618>, doi:10.1103/PhysRevC.65.034618.
- [RAB+06] M. V. Ricciardi, P. Armbruster, J. Benlliure, M. Bernas, A. Boudard, S. Czajkowski, T. Enqvist, A. Kelić, S. Leray, R. Legrain, B. Mustapha, J. Pereira, F. Rejmund, K.-H. Schmidt, C. Stéphan, L. Tassan-Got, C. Volant, and O. Yordanov. Light nuclides produced in the proton-induced spallation of  $^{238}\text{U}$  at 1 GeV. *Physical Review C*, January 2006. URL: <http://dx.doi.org/10.1103/PhysRevC.73.014607>, doi:10.1103/physrevc.73.014607.

- [RSCD+22] J. L. Rodriguez-Sanchez, J. Cugnon, J.-C. David, J. Hirtz, A. Kelić-Heil, and S. Leray. Hypernuclei formation in spallation reactions by coupling the liège intranuclear cascade model to the deexcitation code abla. *Physical Review C*, Jan 2022. URL: <https://doi.org/10.1103/PhysRevC.105.014623>, doi:10.1103/physrevc.105.014623.
- [RSCD+23] J. L. Rodriguez-Sánchez, J. Cugnon, J.-C. David, J. Hirtz, A. Kelić-Heil, and I. Vidaña. Constraint of the nuclear dissipation coefficient in fission of hypernuclei. *Physical Review Letter*, Mar 2023. URL: <https://link.aps.org/doi/10.1103/PhysRevLett.130.132501>, doi:10.1103/PhysRevLett.130.132501.
- [RSDH+18] Jose Luis Rodriguez-Sánchez, Jean-Christophe David, Jason Hirtz, Joseph Cugnon, and Sylvie Leray. Constraining the  $\Lambda$ -nucleus potential within the liège intranuclear cascade model. *Physical Review C*, Aug 2018. URL: <https://doi.org/10.1103/PhysRevC.98.021602>, doi:10.1103/physrevc.98.021602.
- [RIO97] A. Ya. Rusanov, M. G. Itkis, and V. N. Okolovic. Mass distribution properties of fission fragments of hot rotating nuclei. *Physics of Atomic Nuclei*, 60():683, 1997.
- [SCB06] C. Samanta, P. Roy Chowdhury, and D. N. Basu. Generalized mass formula for non-strange and hypernuclei with su(6) symmetry breaking. *Journal of Physics G: Nuclear and Particle Physics*, Feb 2006. URL: <https://doi.org/10.1088/0954-3899/32/3/010>, doi:10.1088/0954-3899/32/3/010.
- [Sie86] Arnold J. Sierk. Macroscopic model of rotating nuclei. *Phys. Rev. C*, 33:2039–2053, Jun 1986. URL: <https://link.aps.org/doi/10.1103/PhysRevC.33.2039>, doi:10.1103/PhysRevC.33.2039.
- [WE40] V. F. Weisskopf and D. H. Ewing. On the yield of nuclear reactions with heavy elements. *Physical Review*, 57(6):472–485, Mar 1940. URL: <https://doi.org/10.1103/PhysRev.57.472>, doi:10.1103/physrev.57.472.
- [WSC76] B. D. Wilkins, E. P. Steinberg, and R. R. Chasman. Scission-point model of nuclear fission based on deformed-shell effects. *Phys. Rev. C*, 14:1832–1863, Nov 1976. URL: <https://link.aps.org/doi/10.1103/PhysRevC.14.1832>, doi:10.1103/PhysRevC.14.1832.
- [eal95] K. Niita et al. Analysis of the ( $n$ ,  $xn'$ ) reaction by quantum molecular dynamics plus statistical decay model. *Phys. Rev. C*, 52:2620–2635, 1995.
- [eal99] K. Niita et al. Development of jqmd (jaeri quantum molecular dynamics) code. *Japan Atomic Energy Research Institute (JAERI)*, 1999.
- [eal87] S. Kox et al. Trends of total reaction cross sections for heavy ion collisions in the intermediate energy range. *Phys. Rev. C*, 35:1678–1691, 1987.
- [Fur00] S. Furikata. Statistical analysis of light fragment production from medium energy proton-induced reactions. *Nucl. Instrum. Meth. Phys. Res. B*, 171:251–258, 2000.
- [MNMS09] D. Mancusi, K. Niita, T. Maryuyama, and L. Sihver. Stability of nuclei in peripheral collisions in the jaeri quantum molecular dynamics. *Phys. Rev. C*, 52:014614, 2009.
- [SWF+89] W.-Q. Shen, B. Wang, J. Feng, W.-L. Zhan, Y.-T. Zhu, and E.-P. Feng. Total reaction cross section for heavy-ion collisions and its relation to the neutron excess degree of freedom. *Nuclear Physics A*, 491:130–146, 1989.
- [STS+93] L. Sihver, C. H. Tsao, R. Silberberg, T. Kanai, and A. F. Barghouty. Total reaction and partial cross section calculations in proton-nucleus ( $Zt \leq 26$ ) and nucleus-nucleus reactions ( $Zp$  and  $Zt \leq 26$ ). *Physical Review C*, 47(3):1225–1236, Mar 1993. URL: <https://doi.org/10.1103/PhysRevC.47.1225>, doi:10.1103/physrevc.47.1225.
- [SStockerG89] H. Sorge, H. Stöcker, and W. Greiner. Poincaré invariant hamiltonian dynamics: modelling multi-hadronic interactions in a phase space approach. *Ann. Phys. (N.Y.)*, 192:266–306, 1989.
- [TCW97] R. K. Tripathi, F. A. Cucinotta, and J. W. Wilson. Universal parameterization of absorption cross sections. Technical Report TP-3621, NASA Technical Paper, 1997.
- [TCW99] R. K. Tripathi, F. A. Cucinotta, and J. W. Wilson. Universal parameterization of absorption cross sections. Technical Report TP-209726, NASA Technical Paper, 1999.

- [Cuc94] Francis A Cucinotta. Multiple-scattering model for inclusive proton production in heavy ion collisions. Technical Report 3470, NASA Technical Paper, 1994.
- [WTW+93] Lawrence W Townsend, John W Wilson, Ram K Tripathi, John W Norbury, Francis F Badavi, and and Ferdou Khan. Hzefrg1, an energy-dependent semiempirical nuclear fragmentation model. Technical Report 3310, NASA Technical Paper, 1993.
- [WTC+95] J W Wilson, R K Tripathi, F A Cucinotta, J K Shinn, F F Badavi, S Y Chun, J W Norbury, C J Zeitlin, L Heilbronn, and and J Miller. Nucfrg2: an evaluation of the semiempirical nuclear fragmentation database. Technical Report 3533, NASA Technical Paper, 1995.
- [BaGB86] C. A. Bertulani and and G. Baur. Electromagnetic processes in relativistic heavy ion collisions. *Nucl. Phys. A*, 458:725–744, 1986.
- [WTC+95] J W Wilson, R K Tripathi, F A Cucinotta, J K Shinn, F F Badavi, S Y Chun, J W Norbury, C J Zeitlin, L Heilbronn, and and J Miller. Nucfrg2: an evaluation of the semiempirical nuclear fragmentation database. Technical Report 3533, NASA Technical Paper, 1995.
- [AS86] D Ashery and J P Schiffer. Pion absorption in nuclei. *Annual Review of Nuclear and Particle Science*, 36(1):207–252, Dec 1986. URL: <https://doi.org/10.1146/annurev.ns.36.120186.001231>, doi:10.1146/annurev.ns.36.120186.001231.
- [CH81] H.C. Chiang and J. Hüfner. Nucleons after pion absorption. *Nuclear Physics A*, 352(3):442–460, Feb 1981. URL: [https://doi.org/10.1016/0375-9474\(81\)90422-X](https://doi.org/10.1016/0375-9474(81)90422-X), doi:10.1016/0375-9474(81)90422-x.
- [eal82] H.P. Isaak et al. Single and coincident neutron emission after the absorption of stopped negative pions in  ${}^6\text{Li}$ ,  ${}^7\text{Li}$ ,  ${}^{12}\text{C}$ ,  ${}^{59}\text{Co}$  and  ${}^{197}\text{Au}$ . *Helvetica Physica Acta*, 55:477–500, 1982. URL: <https://www.e-periodica.ch/digbib/view?pid=hpa-001:1982:55#479>, doi:10.5169/seals-115295.
- [GE87] E. Gadioli and E. Gadioli Erba. Nuclear reactions induced by  $\pi^-$  at rest. *Physical Review C*, 36(2):741–757, Aug 1987. URL: <https://doi.org/10.1103/PhysRevC.36.741>, doi:10.1103/physrevc.36.741.
- [HIE+78] R. Hartmann, H.P. Isaak, R. Engfer, E.A. Hermes, H.S. Pruys, W. Dey, H.J. Pfeiffer, U. Sennhauser, H.K. Walter, and J. Morgenstern. Spectroscopy of single and correlated neutrons following pion absorption in  ${}^{12}\text{C}$ ,  ${}^{59}\text{Co}$  and  ${}^{197}\text{Au}$ . *Nuclear Physics A*, 308(3):345–364, Oct 1978. URL: [https://doi.org/10.1016/0375-9474\(78\)90556-0](https://doi.org/10.1016/0375-9474(78)90556-0), doi:10.1016/0375-9474(78)90556-0.
- [HIP+83] P. Heusi, H.P. Isaak, H.S. Pruys, R. Engfer, E.A. Hermes, T. Kozlowski, U. Sennhauser, and H.K. Walter. Coincident emission of neutrons and charged particles after  $\pi^-$  absorption in  ${}^6\text{Li}$ ,  ${}^7\text{Li}$ ,  ${}^{12}\text{C}$ ,  ${}^{59}\text{Co}$  and  ${}^{197}\text{Au}$ . *Nuclear Physics A*, 407(3):429–459, Oct 1983. URL: [https://doi.org/10.1016/0375-9474\(83\)90660-7](https://doi.org/10.1016/0375-9474(83)90660-7), doi:10.1016/0375-9474(83)90660-7.
- [IZE+83] H.P. Isaak, A. Zglinski, R. Engfer, R. Hartmann, E.A. Hermes, H.S. Pruys, F.W. Schlepütz, T. Kozlowski, U. Sennhauser, H.K. Walter, K. Junker, and Nimai C. Mukhopadhyay. Inclusive neutron spectra from the absorption of stopped negative pions in heavy nuclei. *Nuclear Physics A*, 392(2-3):368–384, Jan 1983. URL: [https://doi.org/10.1016/0375-9474\(83\)90133-1](https://doi.org/10.1016/0375-9474(83)90133-1), doi:10.1016/0375-9474(83)90133-1.
- [Mac83] H. Machner. Study of particle emission following  $\pi^-$  absorption at rest. *Nuclear Physics A*, 395(2):457–470, Mar 1983. URL: [https://doi.org/10.1016/0375-9474\(83\)90054-4](https://doi.org/10.1016/0375-9474(83)90054-4), doi:10.1016/0375-9474(83)90054-4.
- [MVA+82] R. Madey, T. Vilaithong, B. D. Anderson, J. N. Knudson, T. R. Witten, A. R. Baldwin, and F. M. Waterman. Neutrons from nuclear capture of negative pions. *Physical Review C*, 25(6):3050–3067, Jun 1982. URL: <https://doi.org/10.1103/PhysRevC.25.3050>, doi:10.1103/physrevc.25.3050.
- [ODD+80] C. J. Orth, W. R. Daniels, B. J. Dropesky, R. A. Williams, G. C. Giesler, and J. N. Ginocchio. Products of stopped-pion interactions with cu and ta. *Physical Review C*, 21(6):2524–2534, Jun 1980. URL: <https://doi.org/10.1103/PhysRevC.21.2524>, doi:10.1103/physrevc.21.2524.

- [PEH+79] H.S. Pruys, R. Engfer, R. Hartmann, U. Sennhauser, H.-J. Pfeiffer, H.K. Walter, J. Morgenstern, A. Wytenbach, E. Gadioli, and E. Gadioli-Erba. Absorption of stopped  $\pi^-$  in  $^{59}\text{Co}$ ,  $^{75}\text{As}$ ,  $^{197}\text{Au}$  and  $^{209}\text{Bi}$  investigated by in-beam and activation  $\gamma$ -ray spectroscopy. *Nuclear Physics A*, 316(3):365–388, Mar 1979. URL: [https://doi.org/10.1016/0375-9474\(79\)90043-5](https://doi.org/10.1016/0375-9474(79)90043-5), doi:10.1016/0375-9474(79)90043-5.
- [SCMZ79] F. W. Schlepütz, J. C. Comiso, T. C. Meyer, and K. O. H. Ziock. Emission of low-energy charged particles following negative-pion capture from rest. *Physical Review C*, 19(1):135–141, Jan 1979. URL: <https://doi.org/10.1103/PhysRevC.19.135>, doi:10.1103/physrevc.19.135.
- [Wey90] Heinz J Weyer. Pion absorption in light nuclei. *Physics Reports*, 195(6):295–367, Nov 1990. URL: [https://doi.org/10.1016/0370-1573\(90\)90076-E](https://doi.org/10.1016/0370-1573(90)90076-E), doi:10.1016/0370-1573(90)90076-e.
- [J3AJMP20] C. De Saint Jean et al. Jef-3: A.J.M. Plompen, O. Cabellos. The joint evaluated fission and fusion nuclear data library, jeff-3.3. Technical Report, Eur. Phys. J. A 56, 181 (2020), 2020. <https://doi.org/10.1140/epja/s10050-020-00141-9>.
- [Gro91] ENDF/B-VI: Cross Section Evaluation Working Group. Endf/b-vi summary document. Technical Report BNL-NCS-17541 (ENDF-201), Brookhaven National Laboratory, Upton, NY, USA, 1991. edited by P.F. Rose, National Nuclear Data Center.
- [MMB+17] **missing publisher in had-Macfarlane\_2017**
- [SRCD11] J.-C. Sublet, P. Ribon, and M. Coste-Delclaux. CALENDF-2010: User Manual. 2011.
- [ZTTD25] M. Zmeškal, L. Thulliez, P. Tamagno, and E. Dumonteil. Improvement of geant4 neutron-hp package: unresolved resonance region description with probability tables. *Annals of Nuclear Energy*, 211:110914, February 2025. URL: <http://dx.doi.org/10.1016/j.anucene.2024.110914>, doi:10.1016/j.anucene.2024.110914.
- [WFMAScEP] McMaster University Wesley Ford M.A.Sc Engineering Physics. G4ndll4.2 final state guide. <https://geant4-userdoc.web.cern.ch/ContributionFromUsers/UsefulNotes/G4NDLFinalStateDecryptionCERNv1.pdf>. [Online; accessed 1-December-2022].
- [zli] zlib. Zlib library. <http://www.zlib.net>. [Online; accessed 11-December-2017].
- [had] Evaluated nuclear structure data file (ensdf). <https://www.nndc.bnl.gov/ensdf/>. [Online; accessed 3-December-2024].
- [BTN+02] I.M. BAND, M.B. TRZHASKOVSKAYA, C.W. NESTOR, P.O. TIKKANEN, and S. RAMAN. Dirac-fock internal conversion coefficients. *Atomic Data and Nuclear Data Tables*, 81(1–2):1–334, May 2002. URL: <http://dx.doi.org/10.1006/adnd.2002.0884>, doi:10.1006/adnd.2002.0884.
- [Bec98] F. Bečvář. Simulation of  $\gamma$ -cascades in complex nuclei with emphasis on assessment of uncertainties of cascade-related quantities. *Nuclear Instruments and Methods in Physics Research Section A: Accelerators, Spectrometers, Detectors and Associated Equipment*, 417(2–3):434–449, November 1998. URL: [http://dx.doi.org/10.1016/S0168-9002\(98\)00787-6](http://dx.doi.org/10.1016/S0168-9002(98)00787-6), doi:10.1016/s0168-9002(98)00787-6.
- [CHO+09] R. Capote, M. Herman, P. Obložinský, P.G. Young, S. Goriely, T. Belgya, A.V. Ignatyuk, A.J. Koning, S. Hilaire, V.A. Plujko, M. Avrigeanu, O. Bersillon, M.B. Chadwick, T. Fukahori, Zhigang Ge, Yinlu Han, S. Kailas, J. Kopecky, V.M. Maslov, G. Reffo, M. Sin, E.Sh. Soukhovertskii, and P. Talou. Ripl – reference input parameter library for calculation of nuclear reactions and nuclear data evaluations. *Nuclear Data Sheets*, 110(12):3107–3214, December 2009. URL: <http://dx.doi.org/10.1016/j.nds.2009.10.004>, doi:10.1016/j.nds.2009.10.004.
- [JAT16] D. Jordan, A. Algara, and J.L. Tain. An event generator for simulations of complex  $\beta$ -decay experiments. *Nuclear Instruments and Methods in Physics Research Section A: Accelerators, Spectrometers, Detectors and Associated Equipment*, 828:52–57, August 2016. URL: <http://dx.doi.org/10.1016/j.nima.2016.05.034>, doi:10.1016/j.nima.2016.05.034.
- [MACO+23] E. Mendoza, V. Alcayne, D. Cano-Ott, E. González-Romero, T. Martínez, A. Pérez de Rada, A. Sánchez-Caballero, J. Balibrea-Correa, C. Domingo-Pardo, J. Lerendegui-Marco, F. Calviño, and

- C. Guerrero. Neutron capture measurements with high efficiency detectors and the pulse height weighting technique. *Nuclear Instruments and Methods in Physics Research Section A: Accelerators, Spectrometers, Detectors and Associated Equipment*, 1047:167894, February 2023. URL: <http://dx.doi.org/10.1016/j.nima.2022.167894>, doi:10.1016/j.nima.2022.167894.
- [MCO] E. Mendoza and D. Cano-Ott. Nudex (a nuclear de-excitation code). URL: <https://github.com/UIN-CIEMAT/NuDEX>.
- [MCOJ+20] E. Mendoza, D. Cano-Ott, D. Jordan, J.L. Tain, and A. Algora. Nudex: a new nuclear  $\gamma$ -ray cascades generator. *EPJ Web of Conferences*, 239:17006, 2020. URL: <http://dx.doi.org/10.1051/epjconf/202023917006>, doi:10.1051/epjconf/202023917006.
- [Cen96] CENDL-2: Chinese Nuclear Data Center. Cendl-2, the chinese evaluated nuclear data library for neutron reaction data. Technical Report IAEA-NDS-61 Rev. 3, International Atomic Energy Agency, Vienna, Austria, 1996.
- [eal94] Brond-2.2: A.I Blokhin et al. Current status of russian nuclear data libraries. Technical Report Volume 2, Nuclear Data for Science and Technology, edited by J. K. Dickens (American Nuclear Society, LaGrange, IL), 1994. p.695.
- [eal95] JENDL-3: T. Nakagawa et al. Japanese evaluated nuclear data library, version 3, revision 2. Technical Report 32, J. Nucl. Sci. Technol., 1995. 1259.
- [J2CN94] M. Salvatores Jef-2: C. Nordborg. Status of the jef evaluated data library. Technical Report, Nuclear Data for Science and Technology, 1994. edited by J. K. Dickens (American Nuclear Society, LaGrange, IL).
- [DK82] G. Dietze and H. Klein. Nresp4 and neff4: monte carlo codes for the calculation of neutron response functions and detection efficiencies for ne213 scintillation detectors. Technical Report PTB-ND-22, Physikalisch-Technische Bundesanstalt (PTB), Braunschweig, Germany, 1982.
- [GMCO+17] A.R. Garcia, E. Mendoza, D. Cano-Ott, R. Nolte, T. Martinez, A. Algora, J.L. Tain, K. Banerjee, and C. Bhattacharya. New physics model in GEANT4 for the simulation of neutron interactions with organic scintillation detectors. *Nuclear Instruments and Methods in Physics Research Section A: Accelerators, Spectrometers, Detectors and Associated Equipment*, 868:73–81, Oct 2017. URL: <https://doi.org/10.1016/j.nima.2017.06.021>, doi:10.1016/j.nima.2017.06.021.
- [Gro91] ENDF/B-VI: Cross Section Evaluation Working Group. Endf/b-vi summary document. Technical Report BNL-NCS-17541 (ENDF-201), Brookhaven National Laboratory, Upton, NY, USA, 1991. edited by P.F. Rose, National Nuclear Data Center.
- [JENDLDEU2020SNO21] Y. Watanabe JENDL/DEU-2020: S. Nakayama, O. Iwamoto and K. Ogata. Jendl/deu-2020: deuteron nuclear data library for design studies of accelerator-based neutron sources. Technical Report 58(7), J. Nucl. Sci. Technol., 2021. 805-821.
- [Kon66] E. Konopinski. *The Theory of Beta Radioactivity*. Oxford Press, 1966.
- [Tru96] P.R. Truscott. *PhD Thesis*. University of London, 1996.
- [Tul96] J.K. Tuli. Evaluated nuclear structure data file. *Nuclear Instruments and Methods in Physics Research Section A: Accelerators, Spectrometers, Detectors and Associated Equipment*, 369(2-3):506–510, Feb 1996. BNL-NCS-51655-Rev87, (1987): <http://citeseerx.ist.psu.edu/viewdoc/download?doi=10.1.1.459.3917&rep=rep1&type=pdf>, online database: <http://www.nndc.bnl.gov/nudat2/>. URL: [https://doi.org/10.1016/S0168-9002\(96\)80040-4](https://doi.org/10.1016/S0168-9002(96)80040-4), doi:10.1016/s0168-9002(96)80040-4.
- [Wil70] D.H. Wilkinson. Evaluation of the fermi function; EO competition. *Nuclear Instruments and Methods*, 82:122–124, May 1970. URL: [https://doi.org/10.1016/0029-554X\(70\)90336-8](https://doi.org/10.1016/0029-554X(70)90336-8), doi:10.1016/0029-554x(70)90336-8.



# **Part V**

# **Photolepton**



---

**CHAPTER**  
**FORTYTWO**

---

## **INTRODUCTION**

Gamma-nuclear and lepto-nuclear reactions are handled in GEANT4 as hybrid processes which typically require both electromagnetic and hadronic models for their implementation. While neutrino-induced reactions are not currently provided, the GEANT4 hadronic framework is general enough to include their future implementation as a hybrid of weak and hadronic models.

The general scheme followed is to factor the full interaction into an electromagnetic (or weak) vertex, in which a virtual particle is generated, and a hadronic vertex in which the virtual particle interacts with a target nucleus. In most cases the hadronic vertex is implemented by an existing GEANT4 model which handles the intra-nuclear propagation.

The cross sections for these processes are parameterizations, either directly of data or of theoretical distributions determined from the integration of lepton-nucleon cross sections double differential in energy loss and momentum transfer.



---

CHAPTER  
**FORTYTHREE**

---

## CROSS-SECTIONS IN PHOTONUCLEAR AND ELECTRONUCLEAR REACTIONS

### 43.1 Approximation of Photonuclear Cross Sections

The photonuclear cross sections parameterized in the G4PhotoNuclearCrossSection class cover all incident photon energies from the hadron production threshold upward. The parameterization is subdivided into five energy regions, each corresponding to the physical process that dominates it.

- The Giant Dipole Resonance (GDR) region, depending on the nucleus, extends from 10 MeV up to 30 MeV. It usually consists of one large peak, though for some nuclei several peaks appear.
- The “quasi-deuteron” region extends from around 30 MeV up to the pion threshold and is characterized by small cross sections and a broad, low peak.
- The  $\Delta$  region is characterized by the dominant peak in the cross section which extends from the pion threshold to 450 MeV.
- The Roper resonance region extends from roughly 450 MeV to 1.2 GeV. The cross section in this region is not strictly identified with the real Roper resonance because other processes also occur in this region.
- The Reggeon-Pomeron region extends upward from 1.2 GeV.

In the GEANT4 photonuclear data base there are about 50 nuclei for which the photonuclear absorption cross sections have been measured in the above energy ranges. For low energies this number could be enlarged, because for heavy nuclei the neutron photoproduction cross section is close to the total photo-absorption cross section. Currently, however, 14 nuclei are used in the parameterization:  $^1\text{H}$ ,  $^2\text{H}$ ,  $^4\text{He}$ ,  $^6\text{Li}$ ,  $^7\text{Li}$ ,  $^9\text{Be}$ ,  $^{12}\text{C}$ ,  $^{16}\text{O}$ ,  $^{27}\text{Al}$ ,  $^{40}\text{Ca}$ , Cu, Sn, Pb, and U. The resulting cross section is a function of  $A$  and  $e = \log(E_\gamma)$ , where  $E_\gamma$  is the energy of the incident photon. This function is the sum of the components which parameterize each energy region. The cross section in the GDR region can be described as the sum of two peaks,

$$GDR(e) = th(e, b_1, s_1) \cdot \exp(c_1 - p_1 \cdot e) + th(e, b_2, s_2) \cdot \exp(c_2 - p_2 \cdot e).$$

The exponential parameterizes the falling edge of the resonance which behaves like a power law in  $E_\gamma$ . This behavior is expected from the CHIPS modelling approach ([DKW00c]), which includes the nonrelativistic phase space of nucleons to explain evaporation. The function

$$th(e, b, s) = \frac{1}{1 + \exp\left(\frac{b-e}{s}\right)},$$

describes the rising edge of the resonance. It is the nuclear-barrier-reflection function and behaves like a threshold, cutting off the exponential. The exponential powers  $p_1$  and  $p_2$  are

$$\begin{aligned} p_1 &= 1, p_2 = 2 \text{ for } A < 4 \\ p_1 &= 2, p_2 = 4 \text{ for } 4 \leq A < 8 \\ p_1 &= 3, p_2 = 6 \text{ for } 8 \leq A < 12 \\ p_1 &= 4, p_2 = 8 \text{ for } A \geq 12. \end{aligned}$$

The  $A$ -dependent parameters  $b_i$ ,  $c_i$  and  $s_i$  were found for each of the 14 nuclei listed above and interpolated for other nuclei. The  $\Delta$  isobar region was parameterized as

$$\Delta(e, d, f, g, r, q) = \frac{d \cdot th(e, f, g)}{1 + r \cdot (e - q)^2},$$

where  $d$  is an overall normalization factor.  $q$  can be interpreted as the energy of the  $\Delta$  isobar and  $r$  can be interpreted as the inverse of the  $\Delta$  width. Once again  $th$  is the threshold function. The  $A$ -dependence of these parameters is as follows:

- $d = 0.41 \cdot A$  (for  $^1\text{H}$  it is 0.55, for  $^2\text{H}$  it is 0.88), which means that the  $\Delta$  yield is proportional to  $A$ ;
- $f = 5.13 - .00075 \cdot A$ .  $\exp(f)$  shows how the pion threshold depends on  $A$ . It is clear that the threshold becomes 140 MeV only for uranium; for lighter nuclei it is higher.
- $g = 0.09$  for  $A \geq 7$  and 0.04 for  $A < 7$ ;
- $q = 5.84 - \frac{.09}{1 + .003 \cdot A^2}$ , which means that the “mass” of the  $\Delta$  isobar moves to lower energies;
- $r = 11.9 - 1.24 \cdot \log(A)$ .  $r$  is 18.0 for  $^1\text{H}$ . The inverse width becomes smaller with  $A$ , hence the width increases.

The  $A$ -dependence of the  $f$ ,  $q$  and  $r$  parameters is due to the  $\Delta + N \rightarrow N + N$  reaction, which can take place in the nuclear medium below the pion threshold. The quasi-deuteron contribution was parameterized with the same form as the  $\Delta$  contribution but without the threshold function:

$$QD(e, v, w, u) = \frac{v}{1 + w \cdot (e - u)^2}.$$

For  $^1\text{H}$  and  $^2\text{H}$  the quasi-deuteron contribution is almost zero. For these nuclei the third baryonic resonance was used instead, so the parameters for these two nuclei are quite different, but trivial. The parameter values are given below.

- $v = \frac{\exp(-1.7+a \cdot 0.84)}{1+\exp(7 \cdot (2.38-a))}$ , where  $a = \log(A)$ . This shows that the  $A$ -dependence in the quasi-deuteron region is stronger than  $A^{0.84}$ . It is clear from the denominator that this contribution is very small for light nuclei (up to  $^6\text{Li}$  or  $^7\text{Li}$ ). For  $^1\text{H}$  it is 0.078 and for  $^2\text{H}$  it is 0.08, so the delta contribution does not appear to be growing. Its relative contribution disappears with  $A$ .
- $u = 3.7$  and  $w = 0.4$ . The experimental information is not sufficient to determine an  $A$ -dependence for these parameters. For both  $^1\text{H}$  and  $^2\text{H}$   $u = 6.93$  and  $w = 90$ , which may indicate contributions from the  $\Delta(1600)$  and  $\Delta(1620)$ .

The transition Roper contribution was parameterized using the same form as the quasi-deuteron contribution:

$$Tr(e, v, w, u) = \frac{v}{1 + w \cdot (e - u)^2}.$$

Using  $a = \log(A)$ , the values of the parameters are

- $v = \exp(-2. + a \cdot 0.84)$ . For  $^1\text{H}$  it is 0.22 and for  $^2\text{H}$  it is 0.34.
- $u = 6.46 + a \cdot 0.061$  (for  $^1\text{H}$  and for  $^2\text{H}$  it is 6.57), so the “mass” of the Roper moves higher with  $A$ .
- $w = 0.1 + a \cdot 1.65$ . For  $^1\text{H}$  it is 20.0 and for  $^2\text{H}$  it is 15.0).

The Regge-Pomeron contribution was parametrized as follows:

$$RP(e, h) = h \cdot th(7., 0.2) \cdot (0.0116 \cdot \exp(e \cdot 0.16) + 0.4 \cdot \exp(-e \cdot 0.2)), \quad (43.1)$$

where  $h = A \cdot \exp(-a \cdot (0.885 + 0.0048 \cdot a))$  and, again,  $a = \log(A)$ . The first exponential in Eq. (43.1) describes the Pomeron contribution while the second describes the Regge contribution.

## 43.2 Electronuclear Cross Sections and Reactions

Electronuclear reactions are so closely connected with photonuclear reactions that they are sometimes called “photonuclear” because the one-photon exchange mechanism dominates in electronuclear reactions. In this sense electrons can be replaced by a flux of equivalent photons. This is not completely true, because at high energies the Vector Dominance Model (VDM) or diffractive mechanisms are possible, but these types of reactions are beyond the scope of this discussion.

## 43.3 Common Notation for Different Approaches to Electronuclear Reactions

The Equivalent Photon Approximation (EPA) was proposed by E. Fermi [Fer24] and developed by C. Weizsäcker and E. Williams [Weizsäcker34, Wil34] and by L. Landau and E. Lifshitz [LL34]. The covariant form of the EPA method was developed in Refs. [PS61] and [GSKO62]. When using this method it is necessary to take into account that real photons are always transversely polarized while virtual photons may be longitudinally polarized. In general the differential cross section of the electronuclear interaction can be written as

$$\frac{d^2\sigma}{dydQ^2} = \frac{\alpha}{\pi Q^2} (S_{TL} \cdot (\sigma_T + \sigma_L) - S_L \cdot \sigma_L),$$

where

$$S_{TL} = y \frac{1 - y + \frac{y^2}{2} + \frac{Q^2}{4E^2} - \frac{m_e^2}{Q^2} \left( y^2 + \frac{Q^2}{E^2} \right)}{y^2 + \frac{Q^2}{E^2}},$$

$$S_L = \frac{y}{2} \left( 1 - \frac{2m_e^2}{Q^2} \right).$$

The differential cross section of the electronuclear scattering can be rewritten as

$$\frac{d^2\sigma_{eA}}{dydQ^2} = \frac{\alpha y}{\pi Q^2} \left( \frac{(1 - \frac{y}{2})^2}{y^2 + \frac{Q^2}{E^2}} + \frac{1}{4} - \frac{m_e^2}{Q^2} \right) \sigma_{\gamma^* A},$$

where  $\sigma_{\gamma^* A} = \sigma_{\gamma A}(\nu)$  for small  $Q^2$  and must be approximated as a function of  $\epsilon$ ,  $\nu$ , and  $Q^2$  for large  $Q^2$ . Interactions of longitudinal photons are included in the effective  $\sigma_{\gamma^* A}$  cross section through the  $\epsilon$  factor, but in the present GEANT4 method, the cross section of virtual photons is considered to be  $\epsilon$ -independent. The electronuclear problem, with respect to the interaction of virtual photons with nuclei, can thus be split in two. At small  $Q^2$  it is possible to use the  $\sigma_\gamma(\nu)$  cross section. In the  $Q^2 \gg m_e^2$  region it is necessary to calculate the effective  $\sigma_{\gamma^*}(\epsilon, \nu, Q^2)$  cross section. Following the EPA notation, the differential cross section of electronuclear scattering can be related to the number of equivalent photons  $dn = d\sigma/\sigma_{\gamma^*}$ . For  $y \ll 1$  and  $Q^2 < 4m_e^2$  the canonical method [VBB71] leads to the simple result

$$\frac{ydn(y)}{dy} = -\frac{2\alpha}{\pi} \ln(y). \quad (43.2)$$

In [BGMS75] the integration over  $Q^2$  for  $\nu^2 \gg Q_{max}^2 \simeq m_e^2$  leads to

$$\frac{ydn(y)}{dy} = -\frac{\alpha}{\pi} \left[ \frac{1 + (1 - y)^2}{2} \ln \left( \frac{y^2}{1 - y} \right) + (1 - y) \right].$$

In the  $y \ll 1$  limit this formula converges to Eq. (43.2). But the correspondence with Eq. (43.2) can be made more explicit if the exact integral

$$\frac{ydn(y)}{dy} = \frac{\alpha}{\pi} \left( \frac{1 + (1 - y)^2}{2} l_1 - (1 - y)l_2 - \frac{(2 - y)^2}{4} l_3 \right), \quad (43.3)$$

where

$$\begin{aligned} l_1 &= \ln \left( \frac{Q_{max}^2}{Q_{min}^2} \right), \\ l_2 &= 1 - \frac{Q_{max}^2}{Q_{min}^2}, \\ l_3 &= \ln \left( \frac{y^2 + Q_{max}^2/E^2}{y^2 + Q_{min}^2/E^2} \right), \\ Q_{min}^2 &= \frac{m_e^2 y^2}{1-y}, \end{aligned}$$

is calculated for

$$Q_{max(m_e)}^2 = \frac{4m_e^2}{1-y}. \quad (43.4)$$

The factor  $(1-y)$  is used arbitrarily to keep  $Q_{max(m_e)}^2 > Q_{min}^2$ , which can be considered as a boundary between the low and high  $Q^2$  regions. The full transverse photon flux can be calculated as an integral of Eq. (43.3) with the maximum possible upper limit

$$Q_{max(max)}^2 = 4E^2(1-y). \quad (43.5)$$

The full transverse photon flux can be approximated by

$$\frac{ydn(y)}{dy} = -\frac{2\alpha}{\pi} \left( \frac{(2-y)^2 + y^2}{2} \ln(\gamma) - 1 \right), \quad (43.6)$$

where  $\gamma = E/m_e$ . It must be pointed out that neither this approximation nor Eq. (43.3) works at  $y \simeq 1$ ; at this point  $Q_{max(max)}^2$  becomes smaller than  $Q_{min}^2$ . The formal limit of the method is  $y < 1 - \frac{1}{2\gamma}$ .

In Fig. 43.1(a,b) the energy distribution for the equivalent photons is shown. The low- $Q^2$  photon flux with the upper limit defined by Eq. (43.4) is compared with the full photon flux. The low- $Q^2$  photon flux is calculated using Eq. (43.2) (dashed lines) and using Eq. (43.3) (dotted lines). The full photon flux is calculated using Eq. (43.6) (the solid lines) and using Eq. (43.3) with the upper limit defined by Eq.(43.5) (dash-dotted lines, which differ from the solid lines only at  $\nu \approx E_e$ ). The conclusion is that in order to calculate either the number of low- $Q^2$  equivalent photons or the total number of equivalent photons one can use the simple approximations given by Eq. (43.2) and Eq.(43.6), respectively, instead of using Eq. (43.3), which cannot be integrated over  $y$  analytically. Comparing the low- $Q^2$  photon flux and the total photon flux it is possible to show that the low- $Q^2$  photon flux is about half of the the total. From the interaction point of view the decrease of  $\sigma_{\gamma*}$  with increasing  $Q^2$  must be taken into account. The cross section reduction for the virtual photons with large  $Q^2$  is governed by two factors. First, the cross section drops with  $Q^2$  as the squared dipole nucleonic form-factor

$$G_D^2(Q^2) \approx \left( 1 + \frac{Q^2}{(843 \text{ MeV})^2} \right)^{-2}.$$

Second, all the thresholds of the  $\gamma A$  reactions are shifted to higher  $\nu$  by a factor  $Q^2/2M$ , which is the difference between the  $K$  and  $\nu$  values. Following the method proposed in [BFG+76] the  $\sigma_{\gamma*}$  at large  $Q^2$  can be approximated as

$$\sigma_{\gamma*} = (1-x)\sigma_\gamma(K)G_D^2(Q^2)e^{b(\epsilon,K)\cdot r+c(\epsilon,K)\cdot r^3}, \quad (43.7)$$

where  $r = \frac{1}{2} \ln(\frac{Q^2+\nu^2}{K^2})$ . The  $\epsilon$ -dependence of the  $a(\epsilon, K)$  and  $b(\epsilon, K)$  functions is weak, so for simplicity the  $b(K)$  and  $c(K)$  functions are averaged over  $\epsilon$ . They can be approximated as

$$b(K) \approx \left( \frac{K}{185 \text{ MeV}} \right)^{0.85},$$

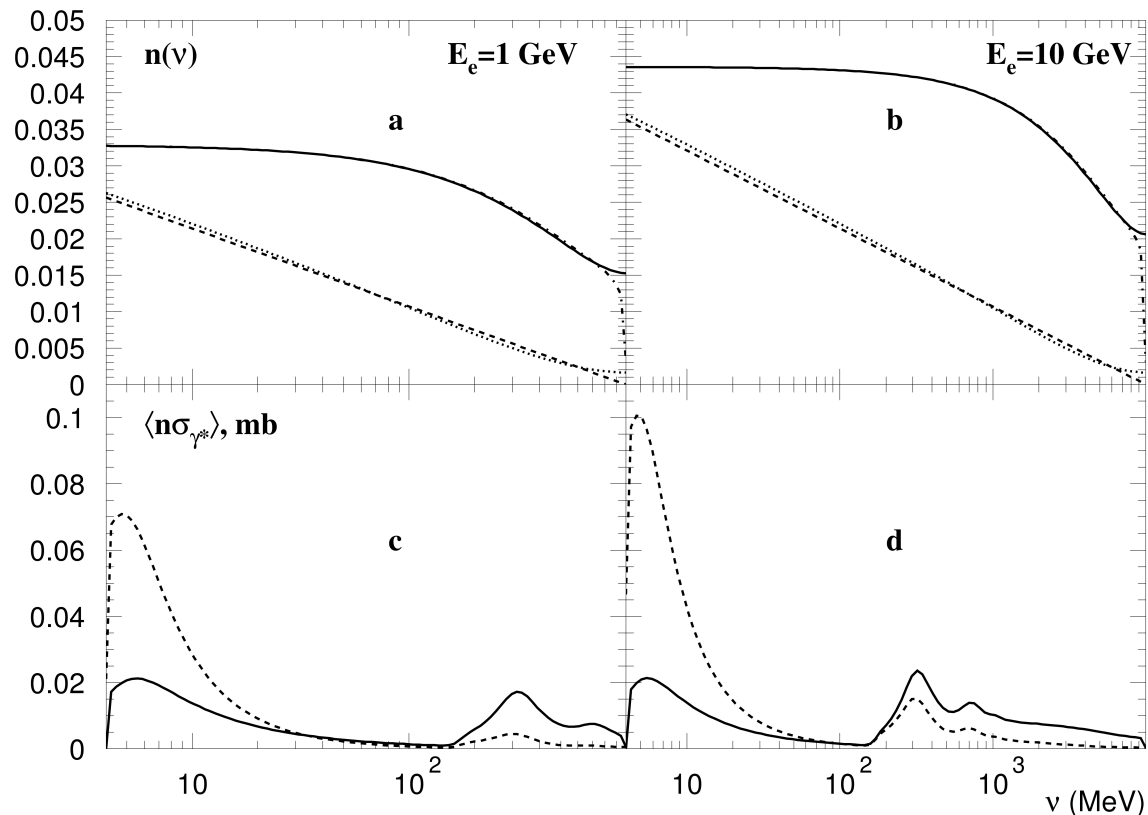


Fig. 43.1: Relative contribution of equivalent photons with small  $Q^2$  to the total “photon flux” for (a) 1 GeV electrons and (b) 10 GeV electrons. In figures (c) and (d) the equivalent photon distribution  $dn(\nu, Q^2)$  is multiplied by the photonuclear cross section  $\sigma_{\gamma^*}(K, Q^2)$  and integrated over  $Q^2$  in two regions: the dashed lines are integrals over the low- $Q^2$  equivalent photons (under the dashed line in the first two figures), and the solid lines are integrals over the high- $Q^2$  equivalent photons (above the dashed lines in the first two figures).

and

$$c(K) \approx - \left( \frac{K}{1390 \text{ MeV}} \right)^3.$$

The result of the integration of the photon flux multiplied by the cross section approximated by Eq. (43.7) is shown in Fig. 43.1(c,d). The integrated cross sections are shown separately for the low- $Q^2$  region ( $Q^2 < Q_{max(m_e)}^2$ , dashed lines) and for the high- $Q^2$  region ( $Q^2 > Q_{max(m_e)}^2$ , solid lines). These functions must be integrated over  $\ln(\nu)$ , so it is clear that because of the Giant Dipole Resonance contribution, the low- $Q^2$  part covers more than half the total  $eA \rightarrow \text{hadrons}$  cross section. But at  $\nu > 200 \text{ MeV}$ , where the hadron multiplicity increases, the large  $Q^2$  part dominates. In this sense, for a better simulation of the production of hadrons by electrons, it is necessary to simulate the high- $Q^2$  part as well as the low- $Q^2$  part.

Taking into account the contribution of high- $Q^2$  photons it is possible to use Eq. (43.6) with the over-estimated  $\sigma_{\gamma^* A} = \sigma_{\gamma A}(\nu)$  cross section. The slightly over-estimated electronuclear cross section is

$$\sigma_{eA}^* = (2 \ln(\gamma) - 1) \cdot J_1 - \frac{\ln(\gamma)}{E_e} \left( 2J_2 - \frac{J_3}{E_e} \right).$$

where

$$\begin{aligned} J_1(E_e) &= \frac{\alpha}{\pi} \int^{E_e} \sigma_{\gamma A}(\nu) d\ln(\nu) \\ J_2(E_e) &= \frac{\alpha}{\pi} \int^{E_e} \nu \sigma_{\gamma A}(\nu) d\ln(\nu), \end{aligned}$$

and

$$J_3(E_e) = \frac{\alpha}{\pi} \int^{E_e} \nu^2 \sigma_{\gamma A}(\nu) d\ln(\nu).$$

The equivalent photon energy  $\nu = yE$  can be obtained for a particular random number  $R$  from the equation

$$R = \frac{(2 \ln(\gamma) - 1) J_1(\nu) - \frac{\ln(\gamma)}{E_e} \left( 2J_2(\nu) - \frac{J_3(\nu)}{E_e} \right)}{(2 \ln(\gamma) - 1) J_1(E_e) - \frac{\ln(\gamma)}{E_e} \left( 2J_2(E_e) - \frac{J_3(E_e)}{E_e} \right)}.$$

Eq. (43.3) is too complicated for the randomization of  $Q^2$  but there is an easily randomized formula which approximates Eq. (43.3) above the hadronic threshold ( $E > 10 \text{ MeV}$ ). It reads

$$\frac{\pi}{\alpha D(y)} \int_{Q_{min}^2}^{Q^2} \frac{y d n(y, Q^2)}{dy dQ^2} dQ^2 = -L(y, Q^2) - U(y), \quad (43.8)$$

where

$$\begin{aligned} D(y) &= 1 - y + \frac{y^2}{2}, \\ L(y, Q^2) &= \ln \left[ F(y) + \left( e^{P(y)} - 1 + \frac{Q^2}{Q_{min}^2} \right)^{-1} \right], \end{aligned}$$

and

$$U(y) = P(y) \cdot \left( 1 - \frac{Q_{min}^2}{Q_{max}^2} \right),$$

with

$$F(y) = \frac{(2-y)(2-2y)}{y^2} \cdot \frac{Q_{min}^2}{Q_{max}^2}$$

and

$$P(y) = \frac{1-y}{D(y)}.$$

The  $Q^2$  value can then be calculated as

$$\frac{Q^2}{Q_{min}^2} = 1 - e^{P(y)} + \left( e^{R \cdot L(y, Q_{max}^2) - (1-R) \cdot U(y)} - F(y) \right)^{-1},$$

where  $R$  is a random number. In Fig. 43.2, Eq. (43.3) (solid curve) is compared to Eq. (43.8) (dashed curve). Because the two curves are almost indistinguishable in the figure, this can be used as an illustration of the  $Q^2$  spectrum of virtual photons, which is the derivative of these curves. An alternative approach is to use Eq. (43.3) for the randomization with a three dimensional table  $\frac{ydn}{dy}(Q^2, y, E_e)$ .

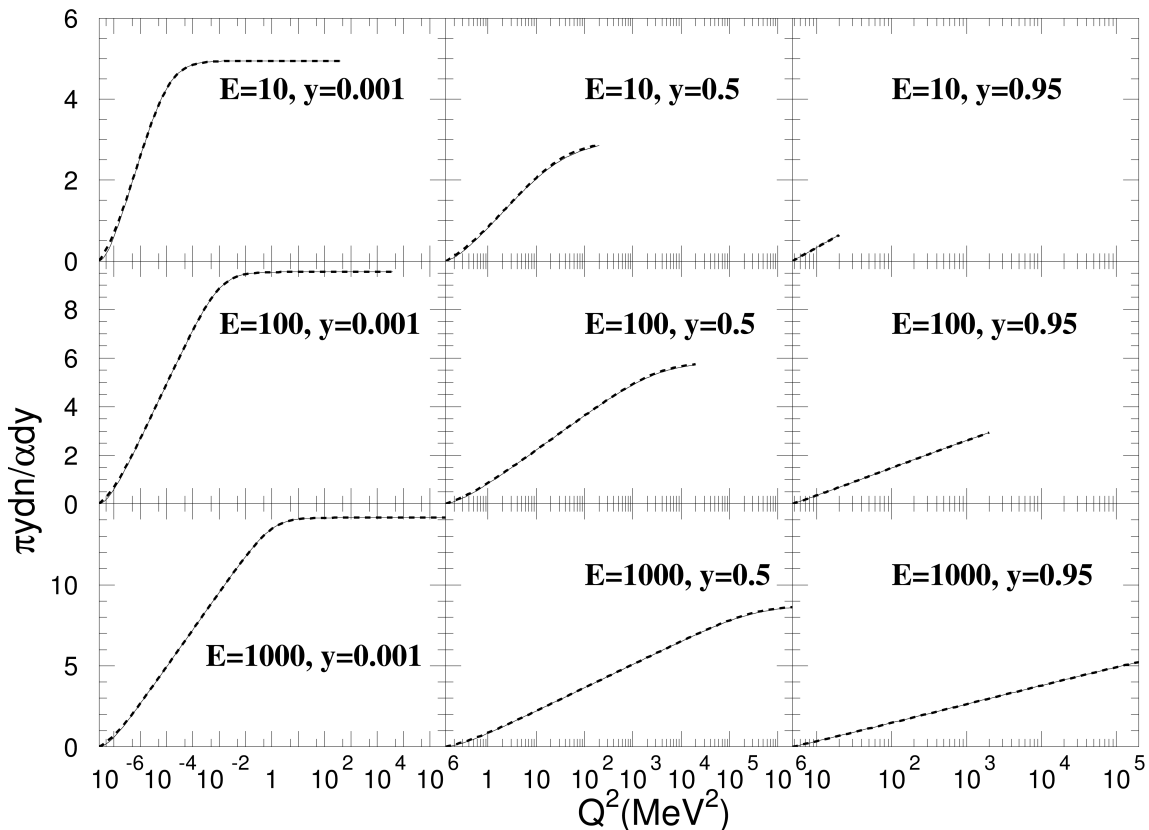


Fig. 43.2: Integrals of  $Q^2$  spectra of virtual photons for three energies 10 MeV, 100 MeV, and 1 GeV at  $y=0.001$ ,  $y=0.5$ , and  $y=0.95$ . The solid line corresponds to Eq. (43.3) and the dashed line (which almost everywhere coincides with the solid line) corresponds to Eq. (43.3).

After the  $\nu$  and  $Q^2$  values have been found, the value of  $\sigma_{\gamma^*A}(\nu, Q^2)$  is calculated using Eq. (43.7). If  $R \cdot \sigma_{\gamma^*A}(\nu) > \sigma_{\gamma^*A}(\nu, Q^2)$ , no interaction occurs and the electron keeps going. This “do nothing” process has low probability and cannot shadow other processes.



---

CHAPTER  
**FORTYFOUR**

---

## GAMMA-NUCLEAR INTERACTIONS

### 44.1 Process and Cross Section

Gamma-nuclear reactions in GEANT4 are handled by the class *G4PhotoNuclearProcess*. The default cross section class for this process is *G4PhotoNuclearCrossSection*, which was described in detail in the previous chapter.

### 44.2 Final State Generation

Final state generation proceeds by two different models, one for incident gamma energies of a few GeV and below, and one for high energies. For high energy gammas, the QGSP model is used. Incident gammas are treated as QCD strings which collide with nucleons in the nucleus, forming more strings which later hadronize to produce secondaries. In this particular model the remnant nucleus is de-excited using the GEANT4 precompound and de-excitation sub-models.

At lower incident energies, there are two models to choose from. The Bertini-style cascade (*G4CascadeInterface*) interacts the incoming gamma with nucleons using measured partial cross sections to decide the final state multiplicity and particle types. Secondaries produced in this initial interaction are then propagated through the nucleus so that they may react with other nucleons before exiting the nucleus. The remnant nucleus is then de-excited to produce low energy fragments. Details of this model are provided in another chapter in this manual.

An alternate handling of low energy gamma interactions is provided by *G4GammaNuclearReaction*, which is based upon the Chiral Invariant Phase Space model (CHIPS [[DKW00c](#), [DKW00a](#), [DKW00b](#)]). In GEANT4 version 9.6 and earlier a separate CHIPS model was provided for gamma nuclear interactions. Here the incoming gamma is absorbed into a nucleon or cluster of nucleons within the target nucleus. This forms an excited bag of partons which later fuse to form final state hadrons. Parton fusion continues until there are none left, at which point the final nuclear evaporation stage is invoked to bring the nucleus to its ground state.

### 44.3 Low Energy Nuclear Data Model

The LEND model ([Low Energy Nuclear Data Model](#)) utilised evaluated data to sample the final states of gamma-nuclear interactions to high precision. This model is particularly suitable for incident gammas below 20 MeV giving higher precision than the default Bertini Cascade model (BertiniCascade).



## ELECTRO-NUCLEAR INTERACTIONS

### 45.1 Process and Cross Section

Electro-nuclear reactions in GEANT4 are handled by the classes *G4ElectronNuclearProcess* and *G4PositronNuclearProcess*. The default cross section class for both these processes is *G4ElectroNuclearCrossSection* which was described in detail in an earlier chapter.

### 45.2 Final State Generation

Final state generation proceeds in two steps. In the first step the electromagnetic vertex of the electron/positron-nucleus reaction is calculated. Here the virtual photon spectrum is generated by sampling parameterized  $Q^2$  and  $\nu$  distributions. The equivalent photon method is used to get a real photon from this distribution.

In the second step, the real photon is interacted with the target nucleus at the hadronic vertex, assuming the photon can be treated as a hadron. Photons with energies below 10 GeV can be interacted directly with nucleons in the target nucleus using the measured  $(\gamma, p)$  partial cross sections to decide the final state multiplicity and particle types. This is currently done by the Bertini-style cascade (*G4CascadeInterface*). Photons with energies above 10 GeV are converted to  $\pi^0$ s and then allowed to interact with nucleons using the FTFP model. In this model the hadrons are treated as QCD strings which collide with nucleons in the nucleus, forming more strings which later hadronize to produce secondaries. In this particular model the remnant nucleus is de-excited using the GEANT4 precompound and de-excitation sub-models.

This two-step process is implemented in the *G4ElectroVDNuclearModel*. An alternative model is the CHIPS-based *G4ElectroNuclearReaction* [DKW00c]. This model also uses the equivalent photon approximation in which the incoming electron or positron generates a virtual photon at the electromagnetic vertex, and the virtual photon is converted to a real photon before it interacts with the nucleus. The real photon interacts with the hadrons in the target using the CHIPS model in which quasmons (generalized excited hadrons) are produced and then decay into final state hadrons. Electrons and positrons of all energies can be handled by this single model.



## MUON-NUCLEAR INTERACTIONS

### 46.1 Process and Cross Section

Muon-nuclear reactions in GEANT4 are handled by the class *G4MuonNuclearProcess*. The default cross section class for this process is *G4KokoulinMuonNuclearXS*, the details of which are discussed in [Muon Photonuclear Interaction](#).

### 46.2 Final State Generation

Just as for the electro-nuclear models, the final state generation for the muon-nuclear reactions proceeds in two steps. In the first step the electromagnetic vertex of the muon-nucleus reaction is calculated. Here the virtual photon spectrum is generated by sampling parameterized momentum transfer ( $Q^2$ ) and energy transfer ( $\nu$ ) distributions. In this case the same equations used to generate the process cross section are used to sample  $Q^2$  and  $\nu$ . The equivalent photon method is then used to get a real photon.

In the second step, the real photon is interacted with the target nucleus at the hadronic vertex, assuming the photon can be treated as a hadron. Photons with energies below 10 GeV can be interacted directly with nucleons in the target nucleus using the measured  $(\gamma, p)$  partial cross sections to decide the final state multiplicity and particle types. This is currently done by the Bertini-style cascade (*G4CascadeInterface*). Photons with energies above 10 GeV are converted to  $\pi^0$ s and then allowed to interact with nucleons using the FTFP model. In this model the hadrons are treated as QCD strings which collide with nucleons in the nucleus, forming more strings which later hadronize to produce secondaries. In this particular model the remnant nucleus is de-excited using the GEANT4 precompound and de-excitation sub-models.

This two-step process is implemented in the *G4MuonVDNuclearModel*.



## BIBLIOGRAPHY

- [BFG+76] F.W. Brasse, W. Flauger, J. Gayler, S.P. Goel, R. Haidan, M. Merkwitz, and H. Wriedt. Parametrization of the q2 dependence of  $\gamma\gamma$  p total cross sections in the resonance region. *Nuclear Physics B*, 110(4-5):413–433, aug 1976. URL: [https://doi.org/10.1016/0550-3213\(76\)90231-5](https://doi.org/10.1016/0550-3213(76)90231-5), doi:10.1016/0550-3213(76)90231-5.
- [BGMS75] V.M. Budnev, I.F. Ginzburg, G.V. Meledin, and V.G. Serbo. The two-photon particle production mechanism. physical problems. applications. equivalent photon approximation. *Physics Reports*, 15(4):181–282, jan 1975. URL: [https://doi.org/10.1016/0370-1573\(75\)90009-5](https://doi.org/10.1016/0370-1573(75)90009-5), doi:10.1016/0370-1573(75)90009-5.
- [DKW00] P.V. Degtyarenko, M.V. Kossov, and H.-P. Wellisch. Chiral invariant phase space event generator, iii: modeling of real and virtual photon interactions with nuclei below pion production threshold. *The European Physical Journal A*, 9(3):421–424, dec 2000. URL: <https://doi.org/10.1007/s100500070026>, doi:10.1007/s100500070026.
- [Fer24] E. Fermi. Über die theorie des stoßes zwischen atomen und elektrisch geladenen teilchen. *Zeitschrift für Physik*, 29(1):315–327, dec 1924. URL: <https://doi.org/10.1007/BF03184853>, doi:10.1007/bf03184853.
- [GSKO62] V. N. Gribov, V. M. Shekhter, V. A. Kolkunov, and L. B. Okun. Covariant derivation of the Weizsäcker-Williams formula. *Sov. Phys. JETP*, 14:1308, 1962. [Original Russian: Zh. Eksp. Teor. Fiz. 41, 1839 (1962)].
- [LL34] Lev Davidovich Landau and Evgeny Mikhailovich Lifschitz. Production of electrons and positrons by a collision of two particles. *Phys. Z. Sowjetunion*, 6:244, 1934.
- [PS61] I.Ya. Pomeranchuk and I.M. Shumushkevich. On processes in the interaction of  $\gamma$ -quanta with unstable particles. *Nuclear Physics*, 23:452–467, feb 1961. URL: [https://doi.org/10.1016/0029-5582\(61\)90272-3](https://doi.org/10.1016/0029-5582(61)90272-3), doi:10.1016/0029-5582(61)90272-3.
- [VBB71] L. P. Pitaevskii V. B. Berestetskii, E. M. Lifshitz. *Relativistic Quantum Theory. Vol. 4*. Pergamon Press, 1st ed. edition, 1971. The method of equivalent photons ISBN 978-0-08-017175-3.
- [Weizsäcker34] C. F. v. Weizsäcker. Ausstrahlung bei stößen sehr schneller elektronen. *Zeitschrift für Physik*, 88(9):612–625, Sep 1934. URL: <https://doi.org/10.1007/BF01333110>, doi:10.1007/BF01333110.
- [Wil34] E. J. Williams. Nature of the high energy particles of penetrating radiation and status of ionization and radiation formulae. *Physical Review*, 45(10):729–730, may 1934. URL: <https://doi.org/10.1103/PhysRev.45.729>, doi:10.1103/physrev.45.729.
- [DKW00a] P. V. Degtyarenko, M. V. Kossov, and H. -P. Wellisch. Chiral invariant phase space event generator, i. nucleon-antinucleon annihilation at rest. *The European Physical Journal A*, 8(2):217–222, jul 2000. URL: <https://doi.org/10.1007/s100500070108>, doi:10.1007/s100500070108.
- [DKW00b] P.V. Degtyarenko, M.V. Kossov, and H.-P. Wellisch. Chiral invariant phase space event generator, ii. nuclear pion capture at rest. *The European Physical Journal A*, 9(3):411–420, dec 2000. URL: <https://doi.org/10.1007/s100500070025>, doi:10.1007/s100500070025.

[DKW00c] P.V. Degtyarenko, M.V. Kossov, and H.-P. Wellisch. Chiral invariant phase space event generator, iii: modeling of real and virtual photon interactions with nuclei below pion production threshold. *The European Physical Journal A*, 9(3):421–424, dec 2000. URL: <https://doi.org/10.1007/s100500070026>, doi:10.1007/s100500070026.

# **Part VI**

# **Neutrino**



---

CHAPTER  
**FORTYSEVEN**

---

## GEANT4 NEUTRINO INTERACTION PROCESSES

GEANT4 neutrino processes include three flavour oscillation, neutrino-electron and neutrino-nucleus interactions. The interactions are available in both charged and neutral current modes.

The user neutrino process management is located in the G4NeutrinoPhysicsMessenger class (in the domain /physics\_lists/nu/). The messenger is in connection with the G4NeutrinoPhysics constructor that is included in the majority of GEANT4 physics lists. Neutrino activation and tuning have to be chosen before the /run/ initialize command.

### 47.1 Neutrino oscillation process

In the user macro file:

```
/physics_lists/factory/addNeutrino    # adds G4NeutrinoPhysics on the top of PL
/physics_lists/nu/NuOscDistanceName   rBaseLine  # oscillation L name
/physics_lists/nu/NuOscDistanceBias   5.0e4      # L is biased
...
/run/initialize
...
```

The first command activates the neutrino physics. It is mandatory for all neutrino processes. Then the user defines the oscillation distance G4Region name and the reduction length bias ( $10^3$  km is not suitable for the GEANT4 geometry, 1000 km/50000=20 m).

### 47.2 Neutrino-electron process

The G4NeutrinoElectronProcess class with biased charge and neutral current cross-sections in a detector G4Region:

```
/physics_lists/factory/addNeutrino
/physics_lists/nu/NuEleCcBias          1.0      # charged current is not biased
/physics_lists/nu/NuEleNcBias          5.0e14   # neutral current is biased
/physics_lists/nu/NuDetectorName       lTarget   # detector region name
...
/run/initialize
...
```

The process gets the cross-sections (G4NeutrinoElectronNc(Cc) Xsc) as well as charge and neutral current final state models (G4NeutrinoElectronNc(Cc) Model). Here the neutral current cross-section is biased only.

## 47.3 Neutrino-nucleus process

User commands:

```
/physics_lists/factory/addNeutrino
/physics_lists/nu/NeETotXscActivation true
/physics_lists/nu/NuDetectorName gTarget # G4Region name
/physics_lists/nu/NuNucleusBias 1.e12
...
/run/initialize
...
```

The  $\nu A$  total cross-sections (class G4MuNeutrinoNucleusTotXsc) will be biased ( $\cdot 10^{12}$ ) in the G4Region named gTarget. The process G4MuNeutrinoNucleusProcess manages charge and neutral current models implemented in classes G4NuMuNucleusCc(Nc)Model with  $x$  and  $Q^2$  distributions stored in G4PARTICLESDATA->/neutrino/nu\_mu data set. The biasing has to provide  $\lesssim 0.1$  neutrino detection with approximately flat distribution,  $(1 - \exp[-\sigma_{bias}n_{atL}]) \sim \sigma_{bias}n_{atL}$ .

## 47.4 Example

All neutrino processes are activated and biased:

```
/physics_lists/factory/addNeutrino
/physics_lists/nu/NuOscDistanceName rBaseline # oscillation L name
/physics_lists/nu/NuOscDistanceBias 5.0e4 # L is biased
...
/physics_lists/nu/NuEleCcBias 1.0 # charged current is not biased
/physics_lists/nu/NuEleNcBias 5.0e14 # neutral current is biased
/physics_lists/nu/NuDetectorName lTarget # detector region name
...
/physics_lists/nu/NeETotXscActivation true
/physics_lists/nu/NuNucleusBias 1.e12
...
/run/initialize
...
```

Another way to add neutrino physics is to add it in the main test program:

```
G4VModularPhysicsList* phys = nullptr;
...
// define neutrino physics
phys->AddPhysics( new G4NeutrinoPhysics() );
runManager->SetUserInitialization(phys);
...
```

More details can be found in [Gri19, Gri23] (however they refer to the old interface via /em/ rather than /nu/).

## BIBLIOGRAPHY

- [Gri19] V.M. Grichine. Geant4 neutrino-electron interaction model. *Nuclear Instruments and Methods in Physics Research Section A: Accelerators, Spectrometers, Detectors and Associated Equipment*, 942:162403, October 2019. URL: <http://dx.doi.org/10.1016/j.nima.2019.162403>, doi:10.1016/j.nima.2019.162403.
- [Gri23] V.M. Grichine. Geant4model for neutrino nucleon/nucleus integral cross sections. *Nuclear Instruments and Methods in Physics Research Section A: Accelerators, Spectrometers, Detectors and Associated Equipment*, 1053:168394, August 2023. URL: <http://dx.doi.org/10.1016/j.nima.2023.168394>, doi:10.1016/j.nima.2023.168394.



# **Part VII**

# **Solid State**



---

CHAPTER  
**FORTYEIGHT**

---

## PHONON-LATTICE INTERACTIONS

### 48.1 Introduction

Phonons are quantized vibrations in solid-state lattices or amorphous solids, of interest to the low-temperature physics community. Phonons are typically produced when a heat source excites lattice vibrations, or when energy from radiation is deposited through elastic interactions with nuclei of lattice atoms. Below 1 K, thermal phonons are highly suppressed; this leaves only *acoustic* and *optical* phonons to propagate.

There is significant interest from the condensed-matter community and direct dark-matter searches to integrate phonon production and propagation with the excellent nuclear and electromagnetic simulations available in GEANT4. An effort in this area began in 2011 by the SuperCDMS Collaboration [BAB+12] and is continuing; initial developments in phonon propagation have been incorporated into the GEANT4 toolkit for Release 10.0.

As quasiparticles, phonons at low temperatures may be treated in the GEANT4 particle-tracking framework, carrying well defined momenta, and propagating in specific directions until they interact [BAB+12]. The present implementation handles ballistic transport, scattering with mode-mixing, and anharmonic downconversion [Tam93a, Tam85, Tam93b] of acoustic phonons. Optical phonon transport and interactions between propagating phonons and thermal background phonons are not treated.

Production of phonons from charged particle energy loss or by photon-lattice interactions are in development, but are not yet included in the GEANT4 toolkit.

### 48.2 Phonon Propagation

The propagation of phonons is governed by the three-dimensional wave equation [Wol98]:

$$\rho\omega^2 e_i = C_{ijlm} k_j k_m e_l \quad (48.1)$$

where  $\rho$  is the crystal mass density and  $C_{ijml}$  is the elasticity tensor; the phonon is described by its wave vector  $\vec{k}$ , frequency  $\omega$  and polarization  $\vec{e}$ .

For a given wave vector  $\vec{k}$ , Eq.(48.1) has three eigenvalues  $\omega$  and three polarization eigenvectors  $\vec{e}$ . The three polarization states are labelled *Fast Transverse (FT)*, *Slow Transverse (ST)* and *Longitudinal (L)*. The direction and speed of propagation of the phonon are given by the *group velocity*  $\vec{v}_g = d\omega/dk$ , which may be computed from Eq.(48.1):

$$\vec{v}_g = \frac{d\omega(\vec{k})}{d\vec{k}} = \nabla_k \omega(\vec{k}) . \quad (48.2)$$

Since the lattice tensor  $C_{ijml}$  is anisotropic in general, the phonon group velocity  $\vec{v}_g$  is not parallel to the momentum vector  $\hbar\vec{k}$ . This anisotropic transport leads to a focussing effect, where phonons are driven to directions which correspond to the highest density of eigenvectors  $\vec{k}$ . Experimentally, this is seen [NW79] as caustics in the energy distribution resulting from a point-like phonon source isotropic in  $\vec{k}$ -space, as shown in Fig. 48.1.

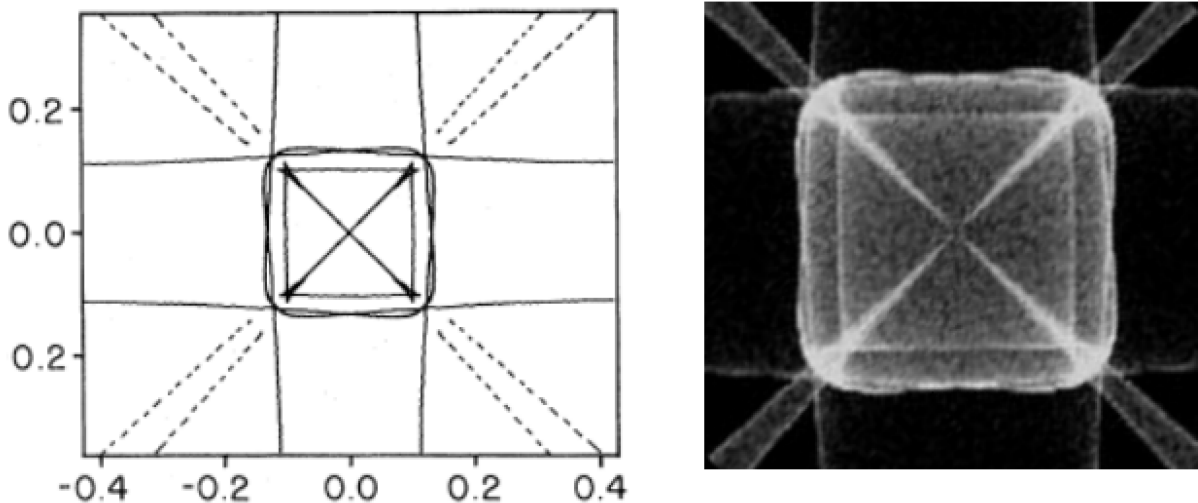


Fig. 48.1: **Left:** outline of phonon caustics in germanium as predicted by Northrop and Wolfe [NW79]. **Right:** Phonon caustics as simulated using the GEANT4 phonon transport code.

## 48.3 Lattice Parameters

## 48.4 Scattering and Mode Mixing

In a pure crystal, *isotope scattering* occurs when a phonon interacts with an isotopic substitution site in the lattice. We treat it as an elastic scattering process, where the phonon momentum direction (wave vector) and polarization are both randomized. The scattering rate for a phonon of frequency  $\nu$  ( $\omega/2\pi$ ) is given by [Tam93b]

$$\Gamma_{scatter} = B\nu^4 \quad (48.3)$$

where  $\Gamma_{scatter}$  is the number of scattering events per unit time, and  $B$  is a constant of proportionality derived from the elasticity tensor (see Eq. 11 and Table 1 in [Tam85]). For germanium,  $B = 3.67 \times 10^{-41}\text{s}^3$ . [Tam85]

At each scattering event, the phonon polarization may change between any of the three states  $L$ ,  $ST$ ,  $FT$ . The branching ratios for the polarizations are determined by the relative density of allowed states in the lattice. This process is often referred to as *mode mixing*.

## 48.5 Anharmonic Downconversion

An energetic phonon may interact in the crystal to produce two phonons of reduced energy. This *anharmonic downconversion* conserves energy ( $\vec{k} = \vec{k}' + \vec{k}''$ ), but not momentum, since momentum is exchanged with the bulk lattice. In principle, all three polarization states may decay through downconversion. In practice, however, the rate for  $L$ -phonons completely dominates the energy evolution of the system, with downconversion events from other polarization states being negligible [Tam93b].

The total downconversion rate  $\Gamma_{anh}$  for an  $L$ -phonon of frequency  $\nu$  is given by [Tam93b]

$$\Gamma_{anh} = A\nu^5 \quad (48.4)$$

where (as in Eq.(48.3))  $A$  is a constant of proportionality derived from the elasticity tensor (see Eq. 11 and Table 1 in [Tam85]). For germanium,  $A = 6.43 \times 10^{-55}\text{s}^4$ . [Tam85]

Downconversion may produce either two transversely polarized phonons, or one transverse and one longitudinal. The relative rates are determined by dynamical constants derived from the elasticity tensor  $C_{ijkl}$ .

As can be seen from Eqs.(48.3) and (48.4), phonon interactions depend strongly on energy  $\hbar\nu$ . High energy phonons ( $\nu \sim \text{THz}$ ) start out in a diffusive regime with high isotope scattering and downconversion rates and mean free paths of order microns. After several such interactions, mean free paths increase to several centimeters or more. This transition from a diffuse to a ballistic transport mode is commonly referred to as “quasi-diffuse” and it controls the time evolution of phonon heat pulses.

Simulation of heat pulse propagation using our GEANT4 transport code has been described previously [BAB+12] and shows good agreement with experiment.



## CRYSTAL CHANNELING PHYSICS

### 49.1 Channeling of relativistic particles

Coherent effects of ultra-relativistic particles in crystals allow the manipulation of particle trajectories thanks to the strong electric field generated between crystal planes and axes [Tsy76].

When the motion of a charged particle is aligned (or at a small angle) with a string (or plane), a coherent scattering with the atoms of the string (or plane) can occur. In the low-angle approximation we can replace the potentials of the single atoms with an averaged continuous potential. The atomic string (plane) in the continuum approximation gently steers a particle away from the atoms, therefore suppressing the encounters with small impact parameters listed above. The channeling phenomenon is due to the fact that the fields of the atomic axes and planes form the potential wells, where the particle may be trapped. Particles can be trapped between planes or axes, under planar or axial channeling, respectively.

The continuous approximation by Lindhard [Lin65] was developed to describe channeling and its related phenomena. Coherent effects are primary phenomena, i.e., they govern path of particles. Four basic assumptions can be introduced for particles under orientational effects. First, angles of scattering may be assumed to be small. Indeed, scattering at large angles imply complete lost of the original direction. Secondly, because particle move at small angle with respect to an aligned pattern of atoms and collisions with atoms in a crystal demand proximity, correlations between collisions occur. Third, since coherent length  $l$  of scattering process ( $l = 2E/q^2$ , where  $E$  is the particle energy and  $q$  the transferred momentum) is larger than lattice constant, classical picture can be adopted. Fourth, idealized case of a perfect lattice may be used as a first approximation.

By following such assumptions, the continuous approximation can be inferred. Under such approximation, the potential of a plane of atoms  $U(c)$  can be averaged along direction parallel to plane directions. Angle  $\theta$  has to be greater than scattering angle  $\phi$  with a single atom:

$$U(x) = Nd_p \int \int_{-\infty}^{+\infty} dy dz V(\mathbf{r})$$

The transverse motion of a particle incident at small angle with respect to one of the crystal axes or planes is governed by the continuous potential of the crystal lattice. A charged particle moving in a crystal is in planar channeling condition if it has a transverse momentum that is not sufficient to exceed the barrier to a neighboring channel, in this case the particle can not escape from the channel.

In the limit of high particle momenta the motion of particles in the channeling case (a series of correlated collisions) may be considered in the framework of classical mechanics, even though the single process of scattering is a quantum event . The classical approximation works better at high energy for two reasons: the first is that the wave lengths of incoming particles are sufficiently small to prevent the formation of interference patterns of waves; secondly classical mechanics is applicable thanks to the large number of energetic levels accessible in the interplanar potential (in analogy with the quantum harmonic oscillator). The second condition is always fulfilled for heavy particles, such as ions and protons, but for light particles (electrons, positrons) the classical approach starts to work in the  $10 - 100\text{MeV}$  range. For motion in the potential  $U(x)$  the longitudinal component of the momentum is conserved for a relativistic particle,

implying the conservation of the transverse energy [BCK96]:

$$E_T = \frac{p\beta}{2} \left( \frac{dx}{dz} \right)^2 + U(x) = const$$

The equation which describes the particle motion in the potential well is therefore:

$$p\beta \frac{d^2x}{dz^2} + U'(x) = 0$$

The particle remains trapped within the channel if its transverse energy  $E_T$  is less than the potential-well depth  $U_0$ :

$$E_T = \frac{p\beta}{2} \theta^2 + U(x) \leq U_0$$

where  $U_0$  is the maximum value of the potential barrier at the distance  $d_p/2$  from the center of the potential well, where the plane is located.

Intensity of incoherent interactions for particles under coherent effects strongly depends on local nuclei and electronic density. Thereby, the intensity of interaction in amorphous media has to be weighted with respect to the nuclear and electronic density averaged transverse to the crystal planes or axes [KO73]. Root-mean-square of transverse energy variation in crystal turns into a function of particle position, e.g. it is valid to treat intensity of interactions under planar condition

$$\left\langle \frac{dp_x^2}{dz} \right\rangle = \left\langle \frac{dp_x^2}{dz} \right\rangle_{am} \frac{n(x)}{n_{am}}$$

where  $\left\langle \frac{dp_x^2}{dz} \right\rangle$  is the root-mean-square of transverse energy variation in crystal,  $n(x)$  is the atomic density along the crystal plane,  $n_{am}$  is the average crystal atomic density.

Information on the implementation details can be found in literature [BAB+14, EBaVGuidi13]

## 49.2 Channeling Fast Simulation Model

Channeling Fast Simulation Model (*G4ChannelingFastSimModel*) [SBC+23] is a model allowing one to simulate the trajectories of charged particles in an oriented crystal in the field of atomic planes (1D model) and atomic strings (2D model). The model also includes incoherent multiple and single Coulomb scattering depending on the particle coordinate in the crystal lattice and taking in account the suppression [MSB+20] of incoherent Coulomb scattering due to presence of the coherent part, i.e. motion in the field of atomic planes/strings. The model also includes ionization energy losses.

Furthermore, the model exploits the Baier-Katkov method [BKS98], [GBT12], [STB19] (*G4BaierKatkov*) in order to simulate the production of secondary photons by  $e^+/e^-$ .

Both models are based on the CRYSTALRAD simulation code [STB19].

To simulate an electromagnetic shower in an oriented crystal, the model of coherent  $e^+e^-$  pair production by a high energy photon has been developed (*G4CoherentPairProduction*). This model exploits the Baier-Katkov method modified for the pair production case [BKS98], [TM72] as well as the same algorithms and crystal data as *G4ChannelingFastSimModel* to simulate the dynamics of  $e^+/e^-$ .

### 49.2.1 Applicability range

The Channeling Fast Simulation Model is a classical model calculating the classical trajectories. This sets its low energy limit of applicability, being 100 MeV for e+/e- and less than MeV for hadrons. However, additional limitations for hadrons are connected with hadronic physics not introduced yet into the model. Therefore, channeling of hadrons can be used only at the crystal thicknesses much smaller than the corresponding interaction lengths of hadronic processes at a given energy.

Angular range of the model is described by the Lindhard angle being a critical channeling angle:

$$\theta_L = \sqrt{2U_0/pv} \quad (49.1)$$

where,  $U_0$  is the potential well depth (depending on the material and the lattice type typically a few tens of eV for atomic planes and a few hundred of eV for atomic strings),  $p$  and  $v$  particle momentum and velocity, respectively. The channeling model should be used until a particle feels the influence of transverse electric field of the planes/strings, i.e. up to at least 10-20  $\theta_L$ .

Both angular and energy limits can be adjusted by the user. Outside these limits a standard Geant4 physics is active.

### 49.2.2 Trajectory simulation

The simulations of trajectories of charged particles is carried out by solving the trajectory equations (in *G4ChannelingFastSimModel*)

$$\begin{cases} \frac{d^2x}{dz^2} + \frac{U'_x}{pv} + \frac{1}{R} = 0, \\ \frac{d^2y}{dz^2} + \frac{U'_y}{pv} = 0, \end{cases} \quad (49.2)$$

where  $x$  and  $y$  are the transverse coordinates,  $z$  being the longitudinal coordinate directed along an atomic plane/string, either straight or bent (only in the horizontal direction),  $R$  the crystal bending radius ( $1/R$  is missing for a straight crystal),  $U'_x$  and  $U'_y$  the electric field functions (derivative of the potential  $U$ ) in  $x$  and  $y$  directions, respectively (the second equation is missing in the case of the 1D model).

The system  $x, y, z$  is fixed w.r.t. the coordinate system of the logical volume though they do not necessarily coincide. The functions of transformations of both particle coordinates and angles both forward and inverse have been also introduced (in *G4ChannelingFastSimCrystalData*). The electric fields are calculated according to the Doyle-Terner approximation [DPW95] and are contained in the data files in *G4CHANNELINGDATA*, each for certain crystal material, the type of the lattice (planes or strings) and their crystallographic direction. They are uploaded into the model through *G4ChannelingFastSimCrystalData* into *G4ChannelingFastSimInterpolation*. There is also an option to use an external datafile which does not belong to *G4CHANNELINGDATA*.

### 49.2.3 Coulomb scattering and ionization losses

The Coulomb scattering in an oriented crystal does not coincide with scattering in amorphous materials since it is split onto an incoherent part of scattering on single atoms and a coherent part of motion in the field of crystal lattice [MSB+20], [TM72]. The cross-section of this scattering is described by:

$$\frac{d\sigma}{d\Omega} = \frac{d\sigma}{d\Omega}_{coh} + \frac{d\sigma}{d\Omega}_{inc}, \quad (49.3)$$

where the coherent part  $\frac{d\sigma}{d\Omega}_{coh}$  is simulated by calculation of the trajectory as described above, while the incoherent fraction

$$\frac{d\sigma}{d\Omega}_{inc} = D \frac{d\sigma}{d\Omega}_{Yukawa}(x, y) \quad (49.4)$$

is calculated using the cross-section based on Coulomb screened (Yukawa) atomic potential  $\frac{d\sigma}{d\Omega} Y_{\text{ukawa}}(x, y)$ . This cross-section depends on the particle position through the atomic density map contained in the data files of the electric fields.  $D$  is the Debay-Waller factor which represents the fundamental difference between incoherent scattering in amorphous and crystalline materials.

The Coulomb scattering on single electrons is simulated using the Rutherford cross-section in *G4VChannelingFastSimCrystalData*. It requires the maps of electron density and minimum energy of ionization calculated using the same model as the electric fields and contained in the same data files.

The energy loss resulting from energy transfer to an electron is also utilized to model fluctuations in ionization losses in *G4VChannelingFastSimCrystalData*. This is achieved by replacing the energy-transfer-dependent terms of the Bethe formula, while the remaining terms are computed using the standard Bethe formula [Nav24]. The corresponding deposited energy is added to the current Geant4 simulation step.

#### 49.2.4 Baier-Katkov Model

The Baier-Katkov (BK) quasiclassical method [BKS98], [GBT12], [STB19] is a radiation integral made over the classical trajectory such as calculated using the Channeling model, but taking into account quantum recoil. Thereby, this method is suitable for the case of hard radiation, when a charged particle (ultrarelativistic e+/e-) moving along a complicated trajectory within a radiation formation length losses a significant part of its energy for radiation a single photon. The energy range of the photons produced using the BK method is from ~ MeV (can be adjusted by user) up to the charged particle energy.

The BK quasiclassical formula expressing the radiation probability can be written as (in natural unit system):

$$dP_{rad} = \frac{\alpha}{4\pi^2} \frac{d^3 k}{\omega} \int \int dt_1 dt_2 \bar{N}_{21} \exp [ik'(x_1 - x_2)], \quad (49.5)$$

where  $\bar{N}_{21}$  is the radiation polarization matrix averaged over the initial particle polarization,  $k = (\omega, \mathbf{k})$  is the 4-vector of the photon momentum including radiated energy  $\omega$  and 3-momentum  $\mathbf{k}$ ,  $k' = \varepsilon k / \varepsilon'$ , where  $\varepsilon$  and  $\varepsilon' = \varepsilon - \omega$  are the particle energy before and after the photon emission, respectively,  $x_{1,2}$  the particle coordinate 4-vector.

The Baier-Katkov Model (*G4BaierKatkov*) can potentially be used beyond the channeling model, for instance to simulate the hard radiation in magnetic and electric field in accelerator elements (e.g. magnets) as well as in beam-beam electric fields.

#### 49.2.5 Coherent Pair Production Model

Unlike *G4ChannelingFastSimModel*, the model of Coherent Pair Production (*G4CoherentPairProduction*) is realized as *G4VDiscreteProcess* and is configured via *G4CoherentPairProductionPhysics*. This model is also based on the Baier-Katkov method [BKS98]. However, unlike the case of radiation, which involves calculating the probability of photon emission along a fixed trajectory of a charged particle, the pair production process requires a different approach. Specifically, it involves randomly generating a  $e^-e^+$  pair and tracking its motion over a short distance. This trajectory is then used within the Baier-Katkov method to calculate the probability of generating of this pair.

The BK quasiclassical formula expressing the  $e^+e^-$  pair production probability can be written as (compare to (49.5)):

$$dP_{PP} = \frac{\alpha}{4\pi^2} \frac{d^3 p}{\omega} \int \int dt_1 dt_2 \bar{N}_p \exp [ik'(x_1 - x_2)], \quad (49.6)$$

where  $\bar{N}_p$  represents the pair production polarization matrix, averaged over the initial photon polarization. The definitions align with those in (49.5), except that  $p$  represents the momentum of the charged particle whose trajectory is being integrated, and  $\varepsilon$  is the energy of this particle, while  $\varepsilon' = \omega - \varepsilon$  denotes the energy of the other particle in the  $e^+e^-$  pair.

The *G4CoherentPairProduction* exploits *G4ChannelingFastSimCrystalData* and requires that *G4ChannelingFastSimModel* is configured with the same crystal data for the same oriented crystal. The combination of *G4ChannelingFastSimModel* with *G4BaierKatkov* activated and *G4CoherentPairProduction* enables the simulation of an electromagnetic shower in an oriented crystal.



## BIBLIOGRAPHY

- [BAB+12] D. Brandt, M. Asai, P. L. Brink, B. Cabrera, E. do Couto e Silva, M. Kelsey, S. W. Leman, K. McArthy, R. Resch, D. Wright, and E. Figueroa-Feliciano. Monte carlo simulation of massive absorbers for cryogenic calorimeters. *Journal of Low Temperature Physics*, 167(3-4):485–490, feb 2012. URL: <https://doi.org/10.1007/s10909-012-0480-3>, doi:10.1007/s10909-012-0480-3.
- [NW79] G. A. Northrop and J. P. Wolfe. Ballistic phonon imaging in solids—a new look at phonon focusing. *Physical Review Letters*, 43(19):1424–1427, nov 1979. URL: <https://doi.org/10.1103/PhysRevLett.43.1424>, doi:10.1103/physrevlett.43.1424.
- [Tam93a] S. Tamura. Monte carlo calculations of quasidiffusion in silicon. *Journal of Low Temperature Physics*, 93(3-4):433–438, nov 1993. URL: <https://doi.org/10.1007/BF00693457>, doi:10.1007/bf00693457.
- [Tam85] Shin-ichiro Tamura. Spontaneous decay rates of LA phonons in quasi-isotropic solids. *Physical Review B*, 31(4):2574–2577, feb 1985. URL: <https://doi.org/10.1103/PhysRevB.31.2574>, doi:10.1103/physrevb.31.2574.
- [Tam93b] Shin-ichiro Tamura. Quasidiffusive propagation of phonons in silicon: monte carlo calculations. *Physical Review B*, 48(18):13502–13507, nov 1993. URL: <https://doi.org/10.1103/PhysRevB.48.13502>, doi:10.1103/physrevb.48.13502.
- [Wol98] J.P. Wolfe. *Imaging Phonons, Chapter 2*. Cambridge University Press, United Kingdom, 1998.
- [BAB+14] E. Bagli, M. Asai, D. Brandt, A. Dotti, V. Guidi, and D. H. Wright. A model for the interaction of high-energy particles in straight and bent crystals implemented in geant4. *The European Physical Journal C*, 74(8):2996, 2014. URL: <http://dx.doi.org/10.1140/epjc/s10052-014-2996-y>, doi:10.1140/epjc/s10052-014-2996-y.
- [BCK96] V. M. Biryukov, Y. A Chesnokov, and V. I. Kotov. *Crystal Channeling and Its Applications at High-Energy Accelerators*. Springer, 1996.
- [KO73] M. Kitagawa and Y. H. Ohtsuki. Modified dechanneling theory and diffusion coefficients. *Physical Review B*, 8(7):3117–3123, oct 1973. URL: <https://doi.org/10.1103/PhysRevB.8.3117>, doi:10.1103/physrevb.8.3117.
- [Lin65] J. Lindhard. Influence of crystal lattice on motion of energetic charged particles. *Danske Vid. Selsk. Mat. Fys. Medd.*, 34:14, 1965.
- [Tsy76] E.N. Tsyanov. Some aspects of the mechanism of a charge particle penetration through a monocrystal. Technical Report, Fermilab, 1976. Preprint TM-682.
- [EBaVGGuidi13] E. Bagli and V. Guidi. Dynecharm++: a toolkit to simulate coherent interactions of high-energy charged particles in complex structures. *Nuclear Instruments and Methods in Physics Research Section B: Beam Interactions with Materials and Atoms*, 309(0):124 – 129, 2013. URL: <http://www.sciencedirect.com/science/article/pii/S0168583X1300308X>, doi:<http://dx.doi.org/10.1016/j.nimb.2013.01.073>.

- [BKS98] V.N. Baier, V.M. Katkov, and V.M. Strakhovenko. *Electromagnetic Processes At High Energies In Oriented Single Crystals*. World Scientific Publishing Company, 1998. ISBN 9789814502542.
- [DPW95] S.L. Dudarev, L.-M. Peng, and M.J. Whelan. On the doyle-turner representation of the optical potential for rheed calculations. *Surface Science*, 330(1):86–100, 1995. URL: <https://www.sciencedirect.com/science/article/pii/0039602895004645>, doi:[https://doi.org/10.1016/0039-6028\(95\)00464-5](https://doi.org/10.1016/0039-6028(95)00464-5).
- [GBT12] Vincenzo Guidi, Laura Bandiera, and Victor Tikhomirov. Radiation generated by single and multiple volume reflection of ultrarelativistic electrons and positrons in bent crystals. *Phys. Rev. A*, 86:042903, Oct 2012. URL: <https://link.aps.org/doi/10.1103/PhysRevA.86.042903>, doi:[10.1103/PhysRevA.86.042903](https://doi.org/10.1103/PhysRevA.86.042903).
- [MSB+20] A. Mazzolari, A. Sytov, L. Bandiera, G. Germogli, M. Romagnoni, E. Bagli, V. Guidi, V. V. Tikhomirov, D. De Salvador, S. Carturan, C. Durigello, G. Maggioni, M. Campostrini, A. Berra, V. Mascagna, M. Prest, E. Vallazza, W. Lauth, P. Klag, and M. Tamisari. Broad angular anisotropy of multiple scattering in a si crystal. *The European Physical Journal C*, 80(1):63, Jan 2020. URL: <https://doi.org/10.1140/epjc/s10052-019-7586-6>, doi:[10.1140/epjc/s10052-019-7586-6](https://doi.org/10.1140/epjc/s10052-019-7586-6).
- [Nav24] S. et al. Navas. Review of particle physics. *Physical Review D*, August 2024. URL: <http://dx.doi.org/10.1103/PhysRevD.110.030001>, doi:[10.1103/physrevd.110.030001](https://doi.org/10.1103/physrevd.110.030001).
- [STB19] A. I. Sytov, V. V. Tikhomirov, and L. Bandiera. Simulation code for modeling of coherent effects of radiation generation in oriented crystals. *Phys. Rev. Accel. Beams*, 22:064601, Jun 2019. URL: <https://link.aps.org/doi/10.1103/PhysRevAccelBeams.22.064601>, doi:[10.1103/PhysRevAccelBeams.22.064601](https://doi.org/10.1103/PhysRevAccelBeams.22.064601).
- [SBC+23] Alexei Sytov, Laura Bandiera, Kihyeon Cho, Giuseppe Antonio Pablo Cirrone, Susanna Guatelli, Viktor Haurylavets, Soonwook Hwang, Vladimir Ivanchenko, Luciano Pandola, Anatoly Rosenfeld, and Victor Tikhomirov. Geant4 simulation model of electromagnetic processes in oriented crystals for accelerator physics. *Journal of the Korean Physical Society*, 83(2):132–139, Jul 2023. URL: <https://doi.org/10.1007/s40042-023-00834-6>, doi:[10.1007/s40042-023-00834-6](https://doi.org/10.1007/s40042-023-00834-6).
- [TM72] Mikhail L. Ter-Mikaelian. *High-energy electromagnetic processes in condensed media*. New York (N.Y.) : Wiley-Interscience, 1972. ISBN 0471851906.